



Durham E-Theses

The tully-fisher relation in nearby clusters

Young, Paul

How to cite:

Young, Paul (1996) *The tully-fisher relation in nearby clusters*, Durham theses, Durham University.
Available at Durham E-Theses Online: <http://etheses.dur.ac.uk/5097/>

Use policy

The full-text may be used and/or reproduced, and given to third parties in any format or medium, without prior permission or charge, for personal research or study, educational, or not-for-profit purposes provided that:

- a full bibliographic reference is made to the original source
- a [link](#) is made to the metadata record in Durham E-Theses
- the full-text is not changed in any way

The full-text must not be sold in any format or medium without the formal permission of the copyright holders.

Please consult the [full Durham E-Theses policy](#) for further details.

The Tully-Fisher Relation In Nearby Clusters

by Paul Young

A thesis submitted to the University of Durham
in accordance with the regulations for
admittance to the Degree of Doctor of Philosophy.

The copyright of this thesis rests with the author. No quotation from it
should be published without his prior written consent and
information derived from it should be acknowledged.

Department of Physics
University of Durham
September 1996

The copyright of this thesis rests with the author.
No quotation from it should be published without
his prior written consent and information derived
from it should be acknowledged.

10 MAR 1997



Abstract

The Tully-Fisher Relation In Nearby Clusters

by Paul Young

In this thesis are presented the Tully-Fisher (TF) relations for a sample of 99 galaxies within the four nearby clusters; Coma, Abell 2199, Abell 2634 and Abell 194. Each cluster was comprised of two samples. The first sample was drawn from either Zwicky or UGC catalogues based on a combination of magnitude, type and ellipticity. These provided spiral cluster member candidates over the entire cluster region to a magnitude limit of 16 in the b-band. The second sample was selected from published photographic plate scans of the central areas of each cluster. This sample had a fainter magnitude limit of 18 b-band mags but covered a much smaller area (approx. $2^\circ \times 2^\circ$).

The galaxies were observed over two observing runs in May and August of 1993 on the JKT and INT Isaac Newton Group Telescopes simultaneously. I-band CCD images and optical long-slit spectra were taken of 65% of the selected objects. Isophotal ellipse fitting of the images was used to produce surface brightness profiles. From these, isophotal magnitudes and diameters were extracted. From consideration of the surface brightness, ellipticity and position angle a "disk region" of each profile was selected and used to calculate extrapolated total magnitudes. Gaussian fitting of H α emission lines of the long-slit spectra produced optical rotation curves for each galaxy. Maximum rotation velocities were calculated from these curves.

Corrections found in the literature were applied to the total magnitude and rotation velocity of each galaxy. These compensated for internal dust extinction and the inclination of the disk to the line-of-sight. Numerical simulations of the fitting procedures demonstrated that an inverse regression of

log-rotation velocity on magnitude provided a fit to the relationship free from selection bias. Residuals around this fit were used to choose forms of the corrections that produced the minimum scatter. A full error budget was compiled and an error weighted fit to the data yielded relationships with a mean scatter of 0.35 mags rms.

A combination of all sources of measurement error, considering inter-correlation, produced a value of 0.27 mags rms, as an estimate of the contribution to the scatter. It was shown that uncertain cluster membership was not a significant source of scatter. In addition, the "expanding cluster" model correction suggested in the literature did not significantly reduce the scatter. The most important source of scatter in the relationship was found to be the symmetry and extent of rotation curves used. A significant correlation was shown to exist between rotation curve extent in terms of disk scale lengths and the TF fit residuals. When only the highest quality data were used, the typical scatter was reduced to 0.20 mags rms. Consideration of the remaining measurement errors produced an upper limit of 0.12 mags rms for the intrinsic scatter within the TF relation.

Monte-Carlo modeling indicated that the observed difference in TF slope between the Coma and Abell 2634 samples was significant. The possibility that this difference is the result of systematic errors in the dataset was ruled out. It is concluded that the change in gradients is due to real variations in the underlying slope influenced by differences in cluster environment.

Preface

The work described in this thesis was undertaken between 1991 and 1996 whilst the author was a research student under the supervision of Dr Ray Sharples in the Department of Physics at the University of Durham. This work has not been submitted for any other degree at the University of Durham or at any other University.

Acknowledgements

I would like to express my sincere thanks to everyone in Durham for the large number of useful suggestions and friendly advice I have received over the past five years. First and foremost I need to thank Ray Sharples for the excellent supervision he has given me. Throughout my PhD, his clear thoughts and phenomenal knowledge of astronomy have guided my way. Moreover, the patience he has displayed with my flagrant disregard for deadlines is nothing less than heroic. I would also like to thank John Lucey for his own special brand of supervision and wit and for the invaluable help he gave during my observing runs.

I would also like to thank Martin Hendry for many useful discussions on statistics and regression, and for putting up with my repeated questions by email. My thanks also go to Mike Irwin for help with aspects of the APM catalogue, to Don Mathewson for providing all his data on mag tape and to the ING staff on La Palma for making my observing runs relatively free from stress.

All work for this thesis was produced on computer equipment installed and maintained by STARLINK. Much use was made of the NASA/IPAC Extragalactic database (NED), the NASA Astrophysics Data System Abstract Service and the Babbage e-print archives.

My special thanks go to all the members of the YTA, old and new for their friendship and camaraderie in the face of extreme adversity.

On a more personal note, my dearest thanks and love go to my parents, Michael and Patricia who have done a superb job of raising my brother Martin and myself. They have made many sacrifices over the years to keep us both in education; I hope now they can be proud of our achievements.

My heartfelt thanks go to Caroline who has been the closest friend I have ever had. She has comforted me when things got me down and her enthusiasm has given me the energy I needed to finish this thesis. Her excellent English and high boredom threshold have improved this work beyond measure. She spent many hours correcting the scripts for which I am grateful. My special thanks also go to Peter whose friendship and advice I value immensely. I appreciate enormously the kind friendship of Gillian and Jane who have been like sisters to me and have supported me during my years here in Durham.

Contents

Chapter 1	Introduction	1
	1.1 A Physical Basis for the Relation	1
	1.2 A Brief History	2
	1.3 Rationale - Improving the TF method	4
	1.4 Thesis Summary	5
Chapter 2	Sample Selection	7
	2.1 Cluster Selection	7
	2.2 Galaxy Selection	8
	2.2.1 Photographic Photometry Data	8
	2.2.2 Secondary Sample Selection	9
	2.2.3 The Use of APM data	10
	2.3 Details of Selection	10
	2.3.1 Coma [Abell 1656]	10
	2.3.2 Abell 2199	10
	2.3.3 Abell 2634	10
	2.3.4 Abell 194	13
	2.3.5 The Selected Samples	13
	2.4 Selection Bias	22
Chapter 3	Photometric Observations and Data Reduction	24
	3.1 Photometric Observations	24
	3.1.1 Initial Data Reduction	25
	3.1.2 Photometric Calibration	26
	3.1.3 Photometric Quality	26
	3.2 Galaxy Surface Photometry	27
	3.2.1 The Photometry Pipeline	28
	3.2.2 Isophotal fitting	28
	3.2.3 Surface Photometry	31
	3.2.4 Calculating Total Magnitudes	33
	3.2.5 Disk Profile Fitting	33
	3.2.6 Final Photometry Results	34
	3.3 Photometric Errors	34
	3.3.1 Internal Photometry Errors	34
	3.3.2 External Photometry Errors	35
	3.4 Data presentation	37
Chapter 4	Spectroscopic Observations and Data Reduction	38

4.1 Spectroscopic Observations	38
4.1.1 Initial Data Reduction	39
4.1.2 Wavelength calibration	40
4.1.3 Sky Subtraction	40
4.2 Rotation Curve Fitting	40
4.2.1 Emission Line Fitting	41
4.2.2 Forming The Rotation Curves	43
4.3 Spectroscopic Quality	44
4.4 Internal and External Errors	44
4.4.1 Internal Errors	44
4.4.2 External Errors	45
4.5 Data presentation	45
Chapter 5 The Tully-Fisher Relation	47
5.1 Photometric Corrections	47
5.1.1 Internal Dust Absorption	47
5.1.2 Galactic Absorption	48
5.1.3 Cosmological Correction	49
5.1.4 Seeing Correction	50
5.2 Kinematic Corrections	50
5.2.1 Deprojecting Rotation Velocities	50
5.2.2 Galaxy Inclination	50
5.2.3 Relativistic Correction	51
5.2.4 The Effects of Seeing	51
5.3 Forming the Relation	51
5.3.1 Data Quality and Rejection	51
5.3.2 The "Standard" Relation	52
5.4 The Nature of the Tully-Fisher Relation	54
5.4.1 The Distribution of I_{Total} and $\log(V_{Rot})$	54
5.4.2 The Bivariate Distribution	56
5.4.3 Selection Bias	57
5.4.4 Cluster Selection Functions	60
5.5 Quantifying the Relationship	63
5.6 Sources of Error	70
5.6.1 Photometric data	70
5.6.2 Spectroscopic data	70
5.6.3 Error Budget	70
5.6.4 The Weighted Inverse Regression	72
5.7 Forming a Composite Relationship	73
5.8 Optimal Corrections	77

Chapter 6	The Origin of the TF Scatter	82
	6.1 Contribution from Measurement Errors	82
	6.1.1 Correlated Errors	82
	6.1.2 Errors in $\log V_{R\alpha}$ as a Source of Scatter	84
	6.1.3 Cluster Membership	86
	6.1.4 Data Quality	91
	6.1.5 Poor Extent of Rotation Curves	94
	6.1.6 Intrinsic Scatter	98
	6.2 Variations in the TF Gradient	98
	6.2.1 Potential Systematic Effects on Gradient	99
	6.3 Estimating Distances	101
Chapter 7	Conclusions	103
	7.1 Summary and Evaluation	103
	7.1.1 The Selection Function	103
	7.1.2 Scatter in the Relationship	103
	7.1.3 Variations in the TF Gradient	104
	7.2 Future work	105
Appendix A	Galaxy Selection	107
	8.1 Tables of Selected Galaxies	107
Appendix B	Galaxy Photometry	119
	9.1 Surface Photometry	119
	9.2 Table of Photometric Measurements	119
Appendix C	Hα Rotation Curves	185
	10. Rotation Curves	185
Appendix D	Final TF Sample	222
	11. IFF Sample Data Table	222

Chapter 1

Introduction

Abstract. This chapter explains the physical basis for the Tully-Fisher relation between the luminosity and rotation velocity of spiral galaxies. The history of its use as a distance indicator is then described and suggested sources of systematic error are discussed. Finally, the motivation for the present work is detailed.

Over the past decade, the study of large-scale structure and motions within the universe has become an area of central importance within cosmology. Accurate and unbiased estimates of extragalactic distances are crucial for this field of work. Hence there is considerable incentive for the observing community to develop widely applicable and reliable distance estimating techniques. Since the correlation between rotation velocity and luminosity for spiral galaxies was first proposed as a distance indicator (Tully & Fisher 1977), measurements for over 3000 galaxies have appeared in the literature. This amounts to more measurements than the sum total of all other extragalactic methods of distance estimation.

Despite the efforts of many authors, a physical basis for the Tully-Fisher (TF) relationship remains elusive and the procedure for estimating distances remains a purely empirical process. This thesis work describes the approach taken by the author to quantify and reduce sources of uncertainty and systematic error that enter into this empirical process. We set out a physical argument for the existence of the relationship, consider how its use has developed and then discuss some current difficulties with its application. Finally, the background and motivation for this study is described.

1.1 A Physical Basis for the Relation

It has been shown by Aaronson et al. (1979) and Djorgovski et al. (1988) that after making a few assumptions about the nature of spiral galaxies, a simple physical basis for the TF relationship can be advanced. The argument, as detailed by Rhee (1996),

relies on the existence of three fundamental relations:

1. The circular velocity of a spiral galaxy's halo is related to its total mass.
2. The luminous (baryonic) mass is related to the total mass (baryonic plus dark matter).
3. A relation exists between the luminosity and the baryonic mass.

In this picture, the total mass is considered to be the fundamental property of a galaxy, and the mass distribution along with the distributions of scale size and halo rotation velocities are determined by the galaxy formation process. The TF relation is then formed as a result of the combination of these three relations. The first two relations are considered to be the natural outcome of galaxy formation and the third exists as a result of the star formation history of spirals.

This combination of properties can be quantified in the following way. Firstly, assuming that disk galaxies are rotation-supported, we can relate the total mass to rotation velocity as:

$$V_{\text{Rot}}^2 = \gamma \frac{GM}{R} \quad (1.1)$$

Were V_{Rot} is the maximum rotation velocity, γ is a structural parameter ($\gamma = 1$ in the case of a thin disk), M is the total mass, R is the characteristic radius and G is the gravitational constant. Then representing the total mass as the sum of the luminous mass and dark matter mass, i.e. $M = M_L + M_D$ and the dark matter fraction, α , as $\alpha = M_D/M_L$. Equation 1.1 can be written as:

$$M_L = V_{\text{Rot}}^4 \left[\gamma^2 (1 + \alpha)^2 G^2 \rho \right]^{-1} \quad (1.2)$$



Where ρ is the mass surface density of luminous matter, i.e. $\rho = M_L/R^2$. Assuming the total luminosity in a certain waveband, L is directly proportional to the luminous mass Equation 1.2 can be re-written:

$$L = V_{R\alpha}^4 \left[\gamma^2 (1 + \alpha)^2 G^2 \rho \frac{M_L}{L} \right]^{-1} \quad (1.3)$$

It can be seen from Equation 1.3 that if the mass-to-light ratio and mean mass surface density remain constant, we would expect a relationship with a gradient of 10 in the magnitude-log-rotation velocity plane. The typical amount by which galaxy's parameters depart from the mean values of γ , α , ρ and M_L/L would then decide the amount of scatter in the relationship. However, it is well established that the TF slope does vary between different wavebands (Bottinelli et al. 1983 and Pierce & Tully 1988) so this may be an over-simplification of the situation.

Attempts to reproduce this relation by detailed simulation of galaxy formation have met with reasonable success. The standard CDM cosmological model provides an environment for galaxy formation that predicts the TF slope fairly well (Cole et al. 1994). Although the predicted scatter, which is due to variations in halo merger histories, is larger than typically observed. The question of whether this small observed scatter is due to some "fine tuning" of cosmological initial conditions or a feedback process affecting star formation was raised by Eisenstein & Loeb (1996). Silk (1995) demonstrated that the relationship could be recreated purely using arguments based upon gas dynamics within the disk and self-regulating star formation.

Clearly we are still some way from a complete understanding of the underlying astrophysical processes of the Tully-Fisher relation but this does not preclude the empirical use of the relationship as a distance indicator.

1.2 A Brief History

The first use of the relationship between luminosity and mass to estimate distance was made by Oepik (1922) to estimate the distance to Andromeda. However, its widespread use did not follow until years later when it was suggested that the

width of the 21 cm radio line is related to the total mass of a galaxy by Roberts (1962). Then later Bottinelli et al. (1971) postulated it could be used to estimate distances. It was in this context that Tully & Fisher 1977 (1977) showed that a correlation existed between 21cm linewidth and b-band photographic magnitudes. This enabled them to use the relation to estimate the distance to the Ursa Major and Virgo galaxy clusters.

In Sandage & Tammann (1976) several problems were immediately highlighted with the application of the relation as a distance estimator that still plague its use today. It was pointed out that variations in the amount of internal absorption, the shape of the relation and possible changes with morphology could all significantly affect distance estimates. A number of different corrections were suggested (reviewed in Bottinelli et al. 1983). Aaronson et al. (1979) adopted the technique of using H-band aperture magnitudes to remove the need for extinction corrections altogether. It was shown in Aaronson et al. (1979) that the resulting relationship had less scatter and a steeper gradient than its b-band counterpart. This infra-red version of the relation also displayed a steeper gradient, close to 10 which was taken as further evidence that this method yielded the "true relationship".

However, further improvements in the technique were still possible. The "IRTF" method purported by the Aaronson group made use of a "hybrid" method that still relied on b-band photographic data to measure the axial ratio and isophotal diameter of target spirals. The axial ratio was needed to calculate each galaxy's inclination to the line-of-sight which was used to correct the measured linewidths to its edge-on value. A more serious drawback of this technique was the necessity to "aperture correct" the H-band magnitudes using the b-band diameters. As the magnitude of each galaxy was measured using a fixed set of apertures, each galaxy's magnitude needed to be corrected for contributions from the outer parts of galaxies that were not included within the aperture. This dependence of b-band diameters could introduce systematic errors as shown by Van Den Bergh (1981) and was responsi-

ble for introducing more scatter into the relationship (Bothun 1986).

An improvement of the technique was suggested in Bothun (1986), where it was noted that I-band CCD images would provide more accurate estimates of magnitude and inclination while still remaining relatively unaffected by internal dust absorption. In Bothun & Mould (1987), this approach was validated and used to estimate the distance to the Pisces and Abell 2634 clusters. After the publication of this paper, the use of CCD surface photometry became widespread.

The TF method is now one of three most widely applicable extragalactic distance estimating techniques. The TF remains more popular than $D_n - \sigma$ or SBF methods because of the ease of observations and the effective sampling of the field due to the widespread distribution of spirals. Tully-Fisher distances also play an important role as a secondary method in the distance scale ladder. As suitable calibrating galaxies are available in the local group, providing good overlap with Cepheid primary distance indicators, it plays an important part in the determination of H_0 . We refer the reader to a full discussion of distance estimators given in Jacoby et al. (1992) where the role played by the TF relation in calculating H_0 is fully discussed.

Tully-Fisher distance surveys have become increasingly ambitious. Most noteworthy of the recent contributions to the field have been the extensive cluster surveys undertaken by Han (1991;1992) and Mould et al. (1993) who in the space of four years surveyed eighteen northern clusters and thirteen southern clusters. In addition, the large field studies undertaken by Willick (1991) and Courteau (1992), in total estimated distances to over six hundred spiral field galaxies. The largest survey to date was undertaken by Mathewson, Ford, & Buchhorn (1992) in which Tully-Fisher measurements were made of 1355 spiral galaxies.

Recently, a further refinement to the Tully-Fisher technique has been made by workers such as Courteau (1992) and Mathewson, Ford, & Buchhorn (1992). These authors make use of rotation velocities measured from $H\alpha$ rotation curves using optical spectroscopy.

This has two major advantages. Firstly, observations are not limited to areas of sky covered by the Arecibo telescope with which most of the 21cm radio measurements were made. Secondly, the technique could be applied to all spiral galaxies rather than just the ones with detected radio emission. A further advantage of using rotation curves is that they provide further kinematic information about the distribution of mass in spirals. It has been suggested by Salucci et al. (1992) and Chiba & Yoshi (1995) that information within the curves can be used to further reduce the scatter in the TF relationship.

More recently, other new techniques have been pioneered, notably, the Fabry-Perot observations undertaken by Schommer et al. (1993). This approach has the advantage of producing two dimensional velocity fields of target galaxies allowing simultaneous calculation of rotation velocity and inclination by the fitting of kinematic models. Another attempt at improving the relationship has been made by Peletier & Willner (1993) by investigating the use of recently available infra-red detector arrays. Once perfected, this line of enquiry should provide a relationship free from the effects of dust extinction.

The observational boundaries of distance estimating techniques have been further extended by the work of recent authors such as Sofue (1994). They used millimeter measurements of CO line emission to form a TF relationship of galaxies in distant clusters. One of the most distant applications of the TF technique has been made by Vogt et al. (1996) who combined HST photometry with optical spectroscopy obtained on the KECK to measure TF parameters for field galaxies with redshift between $Z=0.1$ and $Z=1.0$.

The major motivation for large scale TF surveys is the study of large scale structure and motions within the universe. The real-space maps of galaxies can be combined with redshift measurements to calculate the individual peculiar motions of galaxies. Linear theory, that describes the growth of gravitationally enhanced density perturbations in the universe, provides the means with which to study the origin and growth of large scale structure in the universe. Whereas redshift surveys enable the mapping

of the distribution of luminous matter, peculiar velocities surveys give information about the density field of all matter, luminous and dark. Combining the distributions of visible and dark matter allows modern cosmological theories of galaxy formation to be evaluated. In particular, this provides a test of biased galaxy formation and allows estimation of the bias parameter β . In addition, dynamical estimates of the cosmological density parameter, Ω_0 , can be made providing information on whether the universe is open or closed. A full discussion of the gravitational instability picture, linear theory and methods of reconstructing the density field from the peculiar field is beyond the scope of this review. The reader is referred to Dekel & Rees (1994) and Strauss & Willick (1995) for further information.

Another important aspect of TF work that has developed over the last decade has been the study of large scale streaming motions. The Burstein et al. (1986) study of velocities in the local universe detected significant deviations of galaxies from the Hubble flow using the D_n - σ method. This discovery of what became the Great Attractor by the group which were later known as the Seven Samurai, was the first observation of coherent motion of galaxies over scales of $50 h^{-1} \text{Mpc}$. Since then, several authors have claimed detection of coherent motions over even greater scales, notably the TF studies of Willick (1991), Mathewson et al. (1992) and Courteau et al. (1993). Such motions suggest density perturbations over extremely large scales which, as these scales increase, are becoming less and less likely in standard cosmological models. Because of this, studies of large scale flows has become another important application of the TF method.

1.3 Rationale - Improving the TF method

The aim of this thesis is to examine ways in which the method of applying the Tully-Fisher relation to estimating distances can be improved. In this section we attempt to isolate those factors that most strongly limit the accuracy with which the technique can be applied and areas of possible systematic bias. Systematic bias is the greatest potential problem for all distance estimators as to a certain extent, large scale surveys allow random errors to

be averaged out. However, systematic errors result in consistently incorrect estimates that will give a misleading view of the universe. Systematic effects can mimic exactly the coherent motions that are the focus of interest in studies of large scale structure.

Perhaps the most likely source of consistent error in TF distance estimates is the bias introduced by incorrect calibration. In this work, we attempt to make the most accurate measurement possible, of the underlying relationship. Realistically, this is difficult to accomplish as any sample must be considered a combination of the intrinsic distribution and the methods of selection and observation. The likely presence of such selection effects is the single most common criticism of the TF method.

Unfortunately until CCD surveys of large portions of the sky become available, candidate galaxies for any sample have to be selected from catalogues based on photographic data. These catalogues typically have uncertain magnitude limits and incompleteness near this limit that varies over the sky. By selecting objects from these catalogues, any calibrating sample inherits these inconsistencies. Such limits have a varying effect on the relationship depending on the fitting procedures used. Willick (1994) prescribes a complex iterative procedure which uses a quantitative description of the catalogue used to correct for the effects of selection. While Hendry & Simmons (1994) suggests that the need for this can be circumvented by regressing log-rotation velocity on magnitude. Part of the rationale for this study is to obtain a complete cluster sample with well defined selection limits in order to further investigate the effects of selection.

Another important consideration, is the form of the corrections applied to the raw apparent magnitudes and rotation velocities. The two largest corrections for inclination and internal absorption can result in adjustments of up to 0.39 and 1.4 magnitudes respectively. These corrections are critical for field survey work as they are larger than the small deviations that result from the peculiar velocities we seek to measure. The galaxy clusters are an excellent place for studying the form of these corrections. In this work we attempt to form well populated TF relations within just a few clusters, over the largest

range of magnitude and rotation velocity possible. This will form a sample that is ideal for investigating the optimal forms of these corrections.

One other systematic effect plagues TF distance surveys. Malmquist bias combines distance errors and selection limits to bias estimated distances to greater distances and towards regions of higher density (see Hendry & Simmons 1994, Willick 1994 and Lynden-Bell et al. 1988). Cluster samples like the ones discussed here are unaffected by such problems as they are formed around the assumption that all objects within the cluster are effectively at the same distance. Because the size of Malmquist bias and selection effects are strongly dependent on the amount of scatter within the relationship, a major portion of this work will be devoted to the isolation and reduction of sources of uncertainty in the TF method. Clusters provide an excellent setting for isolating and reducing sources of scatter in the relationship.

In order to minimise the scatter in the TF sample we have chosen a sample of four clusters sufficiently distant that variations in distance due to the cluster line-of-sight depth are reduced to below 10%. Combining this with careful reduction of I-band CCD photometry and $H\alpha$ rotation curves we hoped to obtain a relationship with the minimum of scatter.

Before confident statements can be made about the underlying relationship, careful consideration must be given to potential biases in the method, suitable corrections need to be applied and sources of error minimised. We wish to place a reliable upper limit on the amount of intrinsic scatter within the relationship and to test for variations in the shape and slope with changing cluster environment. This is an important consideration if the Tully-Fisher method is to be applied consistently to galaxies over a wide range of environments. There have been some recent claims of environmental influence on the TF relationship (Pierce & Tully 1992) and also the D_n - σ relation (Lucey et al. 1991). This requires further investigation before the TF relation can be considered universal.

The main drive of this work is the intensive study of the Tully-Fisher relation within just a few clusters. Whereas most TF works are dedicated to mak-

ing distance estimates of many galaxies and clusters, here we concentrate on the form of the relationship and the method of its application. At the same time this procedure will also produce unbiased and accurate relative distances to the four clusters in the sample. By selecting complete and extensive samples to a faint magnitude limit, we seek a greater understanding of the fundamental relationship and the nature of spiral galaxies.

1.4 Thesis Summary

In the next chapter of this work we report in detail the cluster and galaxy selection procedures. Chapters three and four describe the photometric and spectroscopic observations and the way in which the data were reduced. Chapter five relates how optimal corrections to the parameters were developed and an unbiased method of fitting the relation was used. A full error budget is also presented. In chapter six we analyse all known sources of scatter within the relation and place an upper limit on the intrinsic scatter. Lastly the significance of variations in the TF gradient between clusters is discussed.

References

- Aaronson M., Mould J., Huchra J., 1979, *ApJ*, 229, 1
 Bothun G., 1986, in *Galaxy Distances and Deviations from Universal Expansion*, ed. B. F. Madore and R. B. Tully (Dordrecht: Reidel), Vol. symp, p. 87
 Bothun G. D., Mould J. R., 1987, *ApJ*, 313, 629
 Bottinelli L., Chamaraux P., Gerard E., Gougenheim L., Heidman J., Kazes I., Lauque R., 1971, *A&A*, 12, 264
 Bottinelli L., Gougenheim L., Patreul G., G. De Vaucouleurs, 1983, *A&A*, 118, 4
 Burstein D., Davies R. L., Dressler A., Faber S. M., Lynden-Bell D., 1986, in *Galaxy Distances and Deviations from Universal Expansion*, ed. B. F. Madore and R. B. Tully (Dordrecht: Reidel), Vol. symp, p. 123
 Chiba M., Yoshi Y., 1995, *ApJ*, 442, 82
 Cole S., Aragon-Salamanca A., Frenk C. S., Navarro J. F., Zepf S. E., 1994, *MNRAS*, 271, 781
 Courteau S., 1992, Ph.D. thesis, University of California, Santa Cruz
 Courteau S., Faber S. M., Dressler A., Willick J. A., 1993, *ApJL*, 412, L51
 Dekel A., Rees M. J., 1994, *ApJL*, 422, L1
 Djorgovski S., De Carvalho R., Han M. S., 1988, in *The extragalactic distance scale; Proceedings of the ASP*

- 100th Anniversary Symposium, Victoria, Canada, June 29-July 1, 1988 (A90-14129 03-90). San Francisco, CA, Astronomical Society of the Pacific, 1988, p. 329-341, Vol. symp, p. 329
- Eisenstein D. J., Loeb A., 1996, *ApJ*, 459, 432
- Han M. S., 1991, Ph.D. thesis, California Institute of Technology, Pasadena, California.
- Han M. S., Mould J. R., 1992, *ApJ*, 396, 453
- Hendry M. A., Simmons J. F. L., 1994, *ApJ*, 435, 515
- Jacoby G. H. et al., 1992, *PASP*, 104, 599
- Lucey J. R., Gray P. M., Carter D., Terlevich R., 1991, *MNRAS*, 248, 804
- Lynden-Bell D., D. S. M. F., Burstein , Davies R. L., Dressler A., Terlevich R. J., Wegner G., 1988, *ApJ*, 302, 536
- Mathewson D. S., Ford V. L., Buchhorn M., 1992, *ApJ Lett.*, 389, L5
- Mould J. R., Akeson R. L., Bothun G. D., Han M., Huchra J. P., Roth J., Schommer R. A., 1993, *ApJ*, 409, 14
- Oepik E., 1922, *ApJ*, 55, 406
- Peletier R. F., Willner S. P., 1993, *ApJ*, 418, 626
- Pierce M. J., Tully R. B., 1988, *ApJ*, 330, 579
- Pierce M. J., Tully R. B., 1992, *ApJ*, 387, 47
- Rhee M.-H., 1996, Ph.D. thesis, Kapteyn Laboratorium, Groningen, The Netherlands.
- Roberts M. S., 1962, *AJ*, 67, 431
- Salucci P., Frenk C. S., Persic M., 1992, *MNRAS*, 262, 392
- Sandage A., Tammann G. A., 1976, *ApJ*, 210, 7
- Schommer R. A., Bothun G. D., Williams T. B., Mould J. R., 1993, *AJ*, 105, 97
- Silk J., 1995, *ApJ*, 438, L41
- Sofue Y., 1994, *PASJ*, 46, 173
- Strauss M. A., Willick J. A., 1995, *Physrep*, 261, 271
- Tully R. B., Fisher J. R., 1977, *A&A*, 54, 661
- Van Den Bergh S., 1981, *ApJL*, 248, L9
- Vogt N. P., C. D. A. F. A., Phillips , Gronwall C., Faber S. M., Illingworth G. D., Koo D. C., 1996, *ApJL*, 465, L15
- Willick J. A., 1991, Ph.D. thesis, University of California, Berkeley
- Willick J. A., 1994, *ApJS*, 92, 1

Chapter 2

Sample Selection

Abstract. A well defined sample selection procedure is vital if the effects of selection on the Tully-Fisher relation are to be examined and any resulting biases removed. This chapter explains our choice of galaxy clusters and outlines the galaxy selection process undertaken as part of this study. The quality of the catalogues from which we selected our target galaxies is assessed and the exact details of the magnitude, ellipticity and colour-magnitude limits applied to each catalogue are given.

2.1 Cluster Selection

As noted in chapter 1, a well defined selection process is a crucial part of any Tully-Fisher study. Good selection requires the use of a catalogue of sufficient quality and the application of stringent criteria for selecting from that catalogue. This enables us to understand and minimise the biases introduced by selection. With this in mind we chose four galaxy clusters; Coma (Abell 1656), Abell 2199 (A2199), Abell 2634 (A2634) and Abell 194 (A194), for the present study.

The importance of using clusters with a sufficient distance to minimise the effect of cluster depth and individual galaxy peculiar velocities on the TF relation was emphasized in §1.3. This was the main reason for the choice of clusters at intermediate redshifts ($cz > 5000 \text{ km s}^{-1}$). As we also intended to maximise the extent of our TF sample in luminosity, we were limited in cluster distance to redshifts of less than 15000 km s^{-1} in order to keep exposure times on the 1.0 metre JKT telescope to a reasonable length of time.

Considering the rationale, for this project clusters were required that displayed a wide range of richness, central concentration and spiral fraction but with sufficient size that our selected sample would contain enough galaxies. We also desired northern hemisphere clusters in quiet areas of the Hubble flow, to further reduce the effects of peculiar velocities, and with high galactic latitudes in order to reduce the size of galactic extinction corrections.

Finally, the current state of published information on each cluster had to be considered. Adequate selection calls for extensive catalogues with accurate measurements of magnitude, ellipticity and colour (e.g. Godwin et al. 1983). Where possible information on morphology (Dressler 1980) and redshifts is desired (Gregory & Thompson 1984). It is also necessary to use catalogues of a high quality whose completeness and selection functions are relatively well understood since the selected sample will inherit any biases present.

To compare our measurements and techniques with other authors, clusters were required that had been the subject of previous Tully-Fisher work (e.g. Aaronson et al. 1982). It is also desirable that these clusters have other published distance estimates available using independent methods such as $D_n - \sigma$ (e.g. Lucey et al. 1991b).

It was decided that the above criteria were best met by the three Abell clusters; A1656, A2199 and A2634 (see Abell 1958). Coma (A1656) is the most studied cluster in the sky and contains the largest single cluster TF sample to date, Fukugita (1991) (and more recently Bernstein et al.). Coma is considered to be the "test bench" for many secondary distance indicators (Jacoby et al. 1992). It provides an important step in the distance scale ladder and offers an excellent reference point with which to compare our results with other independent measurements. As Coma is such a well studied cluster, extensive published data on photometry, morpho-

Table 2.1. Table of properties for the selected clusters. Column headings are; Cluster name, cluster position in ra and dec, and galactic l and b in B1950 co-ordinates, mean heliocentric redshift of cluster members, cz_{\odot} , velocity dispersion of cluster members, σ (both from Struble & Rood 1991), X-ray gas temperature in keV, T_{Xray} (from Jones & Forman 1984 and David et al. 1993), Abell cluster richness, R (Abell, Corwin, & Olowin 1989), percentage of spiral galaxy members, Sp% (calculated from Dressler 1980), concentration index, C, (from Butcher & Oemler 1984), cluster morphology, M, consisting of Rood-Sastry type (from Struble & Rood 1987 and Bautz-Morgan type (Abell, Corwin, & Olowin 1989).

Cluster	α_{1950}	δ_{1950}	l_{1950}	b_{1950}	cz_{\odot}	σ	T_{Xray}	R	Sp%	C	M
Coma	12 57.3	+28 14.4	58.08	+87.98	6955	880	8.3	2	18	0.53	B II
Abell 2199	16 26.9	+39 39.6	62.93	+43.70	8964	794	4.5	2	24	0.53	cD I
Abell 2634	23 36.0	+26 46.0	103.51	-33.06	9623	976	3.4	1	37	0.50	cD II
Abell 194	01 23.4	-01 36.0	142.17	-62.92	5336	440	2.0	0	31	-	L II

logical types and redshifts (Godwin et al. 1983 and Kent & Gunn 1982) is available to aid sample selection.

Abell 2199 and Abell 2634 have existing TF and $D_n - \sigma$ distance estimates (Freudling et al. 1991, Aaronson et al. 1982 and Lucey et al. 1991a) and a range of central concentrations. Both clusters have high predicted peculiar velocities by the $D_n - \sigma$ method (Lucey et al. 1991a) and a more accurate TF based estimate would provide a useful check on these measurements. When preparing the observing schedule for these three clusters it became apparent that there was a right ascension gap during which all three clusters were below the horizon. To fill this gap we decided to observe A194. Although A194 is closer than the other clusters ($cz=5340\text{kms}^{-1}$), its position falls outside the Arecibo visibility strip and as the majority of TF measurements rely upon radio measurements, A194 has no published TF distance estimate to date. Since our method does not require 21cm data, we aim to provide the first TF results for that cluster. See Table 2.1 for a summary of the characteristics of the four selected clusters.

2.2 Galaxy Selection

In order to reduce the biases introduced into our TF galaxy sample, we applied a stringent and uniform galaxy selection procedure to each cluster. While we wished to form a subsample from the available catalogues that contained the maximum possible number of spiral galaxy cluster members, completeness within our selected subsample was not important as long as the subsample is unbiased. We also wanted

to minimise the number of mis-selected non-spirals that would contaminate the sample and lower observing efficiency. For each cluster there are a number of possible sources of information. The Zwicky CGCG catalogue (Zwicky, Herzog, & Wild 1960) is one possibility that has been widely used by previous authors (e.g. Bernstein et al. 1994, Han 1991 and Aaronson et al. 1986), but because of its patchy incompleteness and its relatively bright (and uncertain) magnitude limit it was deemed unsuitable for our purpose. For our primary galaxy selection we decided to use catalogues that had been prepared by previous authors from scans of photographic plates. The primary sample for each cluster was then supplemented by a secondary sample, prepared from other existing sources in a way typical of previous TF studies and given a lower priority at observing time.

2.2.1 Photographic Photometry Data

All current large area cluster catalogues are based on photographic data. They have a much lower dynamic range than CCDs but their large area coverage makes them ideal for survey work. A well prepared plate and careful data reduction can produce a catalogue of galaxies with accurate shape and orientation information down to a b-band magnitude of 20.0 (Godwin, Metcalfe, & Peach 1983). This is two magnitudes fainter than our imposed magnitude limit of 18.0, and such catalogues are available for the main three selected clusters.

In the case of each cluster the typical area covered by the photographic plate was around 4 square

degrees, which is a lot smaller than the area covered by catalogues traditionally used in TF work. The reduced area is not a problem though, as the fainter magnitude limit and increased probability of cluster membership in the inner regions combines to produce more than sufficient candidate galaxies. The smaller catalogue area conflicts however with our goal to sample a wide range of cluster environments, and for this we rely upon our more wide spread secondary sample.

The first selection cut applied to each catalogue was in terms of magnitude, and all objects with an apparent b-magnitude fainter than 18 were discarded. We considered a galaxy with a b magnitude of 18 to be the faintest object we could observe efficiently with the small telescopes that the project was designed for. The magnitude limit introduced a varying and distance dependent *absolute* magnitude cut into each sample. But as the limit is well defined for each cluster we believe any biases introduced can be corrected as part of our analysis.

Secondly, all galaxies with a measured ellipticity of less than 0.28 were removed. The fact that face-on spiral galaxies are circular is now well established (see Bernstein et al. 1994 and §5.2.1), and as we required the sample galaxies to be inclined at more than 45° (i.e. $e \geq 0.28$) this cut discarded all those more face-on. Selecting galaxies with $e \geq 0.28$ also has the advantage of rejecting a large fraction of the elliptical galaxies in the catalogue. Face-on spirals are unsuitable because errors on the large rotation velocity corrections needed would introduce too much scatter into the relation.

In order to remove the remaining elliptical and S0 type galaxies from our sample, galaxy selection was also done on the basis of colour and magnitude. Published colour-magnitude (c-m) relations are available for each of the three main clusters, and these were used to reject galaxies based on where they appeared on each cluster's c-m diagram. As cluster spirals are bluer than other early-type cluster members and the majority of early-type galaxies fall within the c-m relation strip for each cluster, we can reject the remaining early-type galaxies in the sample by only selecting the objects that appear bluewards of each cluster's c-m relationship.

However it was still possible that our selected sample could be contaminated with S0s or elliptical galaxies with high a ellipticity and blue colour. Early-type galaxies, especially S0s, can sometimes have blue colours due to residual star formation. It is more likely though, that contamination is the result of errors in the measured photometric parameters or the merging of a galaxy's image on the photographic plate with a nearby star. The chance merging of a star's image with a galaxy will elongate the galaxy's isophotes, increasing the measured ellipticity, tending to make the galaxy appear bluer.

In order to minimise the amount of mis-selected galaxies within our sample, the majority of selected objects were checked by eye on the photographic plates. This "eyeball" check, provided a last chance to reject star-galaxy mergers, irregular galaxies etc. allowing only a low level of contamination to reach the final primary sample.

2.2.2 Secondary Sample Selection

To augment our primary samples, a secondary sample was drawn from existing all-sky catalogues in a manner more typical of published TF work. Selecting from such catalogues allows the coverage of a larger cluster area, but limits the sample to relatively brighter galaxies ($b \leq 16.0$). Where possible extensive local catalogues were utilised which included information on type and redshift (for example Kent & Gunn 1982, Gregory & Thompson 1984, Chapman et al. 1988) in an attempt to keep our selection as uniform as possible.

The resulting samples were then further extended with objects from an NED galaxy search within 5° of each cluster centre (see Helou et al. 1991). Each NED search produced all the galaxies classified as spirals and with redshifts consistent with cluster membership in the published literature. This allowed the type and redshift information from a large number of sources to be merged with our already selected samples. This information acted as an aid to establishing observing priorities and allowed us to extend our secondary samples outwards. The galaxies appearing in the NED data base are predominantly from the UGC, CGCG or NGC galaxy

catalogues and as a result, our secondary samples have an effective magnitude limit of $b\text{-mag} \approx \leq 16.0$.

Selection between different spiral types was not performed for three reasons: (i) We wished to sample a range of spiral types in order to examine any type dependence in the TF relation. (ii) Galaxy types are unreliable for the edge-on spirals that make up our sample. (iii) Much of our primary sample do not have types and we did not want to bias our secondary (and on average brighter) sample as compared to our primary sample.

2.2.3 The Use of APM data

The positions from the photographic catalogue for the primary A2634 sample were too inaccurate for our purposes. In this cluster, and for all the objects in the secondary samples, galaxy positions were cross-correlated with positions from a copy of the APM catalogue (Maddox et al. 1988) kindly supplied by Mike Irwin, and the APM positions used from then on. The APM catalogue positions are accurate to within 3 arcseconds and provide a uniform co-ordinate system for all of the catalogues. The photometry sample for A2634 and a number of galaxies in our secondary samples lacked position angle information in their respective catalogues, in these cases, position angles from the APM catalogue were also used.

2.3 Details of Selection

The selection procedure outlined above was followed for all four of our selected clusters, and in each case a primary and secondary sample was selected.

2.3.1 Coma [Abell 1656]

The primary galaxy sample for the Coma cluster was selected from the catalogue published in Godwin et al. 1983 (GMP83). The positions and magnitude proved to be of good quality, even though the ellipticity cut was made at 0.3 (because GMP83 ellipticities are only published to within 0.1) there were still sufficient objects for a large sample. A colour-magnitude sequence of $1.53 \leq 0.0223(b - 22.0) + (b - r) \leq 1.98$ published in

Mazure et al. (1988) was used for the colour selection. See Figure 2.1 for a summary of the selection process; Figure 2.2 shows the distribution of the galaxies from the primary sample within Coma.

An extensive catalogue including morphological types and redshifts of brighter Coma members can be found in Kent & Gunn (1982) and this was used to select our secondary sample. Figure 2.3 shows the redshift distribution of this secondary sample as compared to the entire Kent & Gunn catalogue. A redshift versus radial cluster position plot is also shown. A map of the secondary sample's distribution in the outer regions of Coma is shown in Figure 2.4.

2.3.2 Abell 2199

The A2199 primary sample was taken from a catalogue published in Dixon et al. (1989)(DGP) which proved to be of similar quality to the GMP82 catalogue. The DGP ellipticities are given to 0.01 accuracy, allowing a cut of $e \geq 0.28$. A colour-magnitude relation of $2.46 \leq 0.04b + (b - r) \leq 2.75$ fitted by the author was used for the $c-m$ selection of the primary sample. See Figure 2.5 for a plot of the $c-m$ relation and further details of the primary sample selection. The position of the primary sample galaxies in the area around A2199 can be seen in Figure 2.6. To keep the selection limits as simple as possible the secondary sample for A2199 was solely selected from the UGC catalogue. Selection was done on the basis of magnitude ($b\text{-mag} \leq 16.0$), ellipticity ($e \geq 0.28$), type and redshift ($\pm 3000 \text{ km s}^{-1}$). The distribution on the sky of the secondary sample is shown in Figure 2.7.

2.3.3 Abell 2634

Primary selection for A2634 was done from the sample appearing in Butchins (1983). This work is older and based on lower quality data than the catalogues used for the selection in Coma and A2199. The effects of this reduced quality can be seen in Figure 2.8 which summarizes the primary selection process for A2634. The measured ellipticities display an uneven distribution which is attributed to the breaking up of the larger galaxies in the sample into smaller pieces by the object detection algorithms.

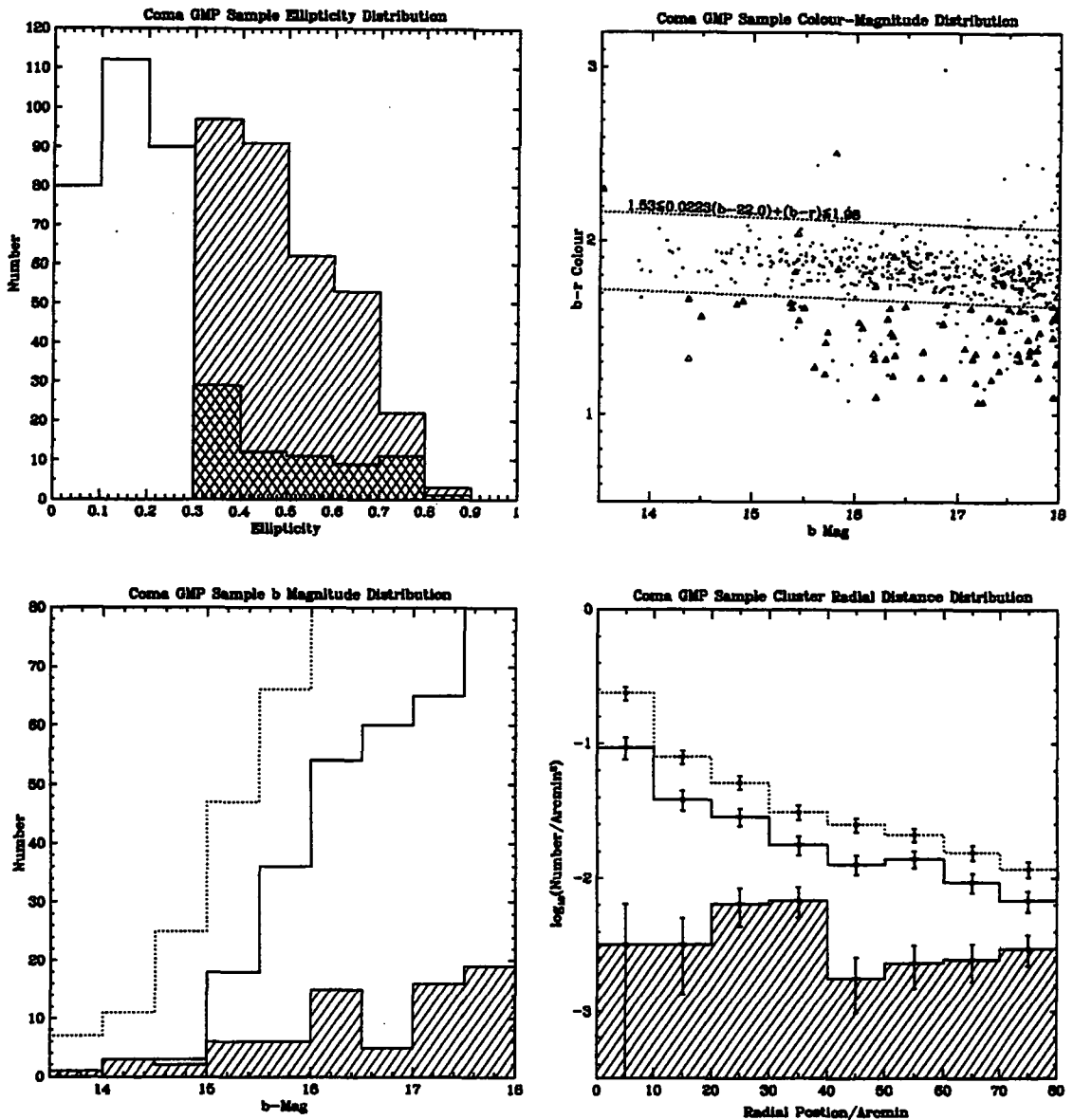


Figure 2.1: Four graphs detailing the primary Coma sample selection process using photographic photometry published in Godwin, Metcalfe, & Peach (1983)(GMP83). **Top Left:** A Histogram showing the distribution of ellipticity for all objects in the GMP83 sample with $b\text{-mag} \leq 18$. Objects with ellipticity greater than 0.28 (i.e. inclination greater than 45° in the case of spiral galaxies) are shown with half shaded bins. The distribution of the finally selected objects is shown fully shaded. **Top Right:** Colour-magnitude relation for GMP83 objects. A fit to the colour magnitude relation from Mazure et al. (1988) is shown as parallel dotted lines. The primary sample selected using ellipticity and color-magnitude (i.e. blue-ward of the c-m relation) are marked with triangles. Objects selected for the supplementary sample on the basis of their spiral type are also marked (these are the points appearing above the c-m relation). **Bottom Left:** A Histogram of the magnitude distribution of the three samples; all GMP83 objects (dotted line), objects with $e \geq 0.28$ (solid line), and the primary selected sample based on ellipticity and colour (shaded). **Bottom Right:** Histogram showing the radial number density distribution of objects within the cluster. The three samples are marked in the same manner as the previous plot. The selected galaxies (shaded histograms) show tentative evidence of concentration towards the centre of the cluster.

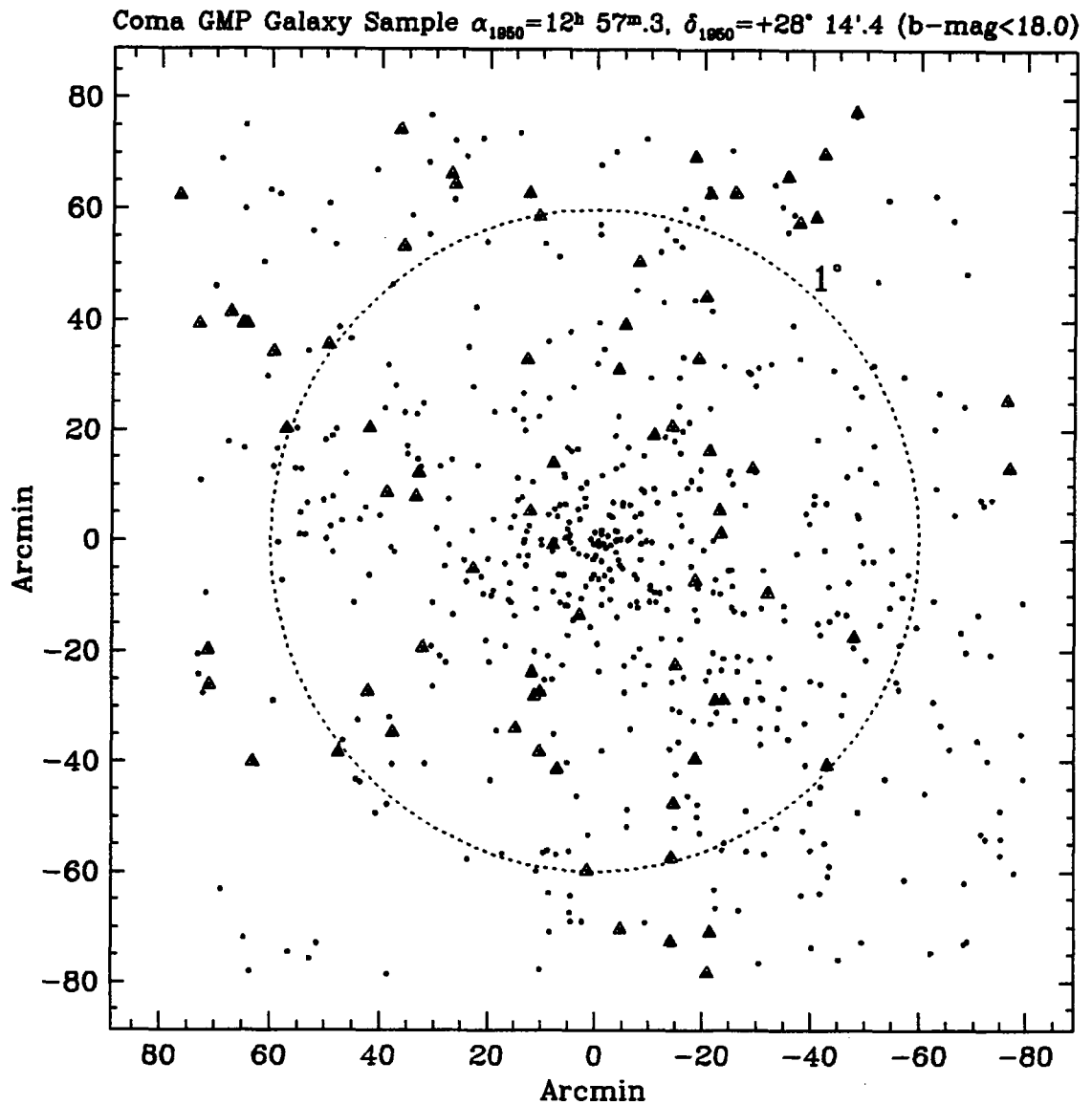


Figure 2.2: A map of a $2.6^{\circ} \times 2.6^{\circ}$ region centred on the Coma cluster. All galaxies from the GMP83 catalogue with b -magnitudes less than 18.0 are marked as points. The galaxies from our primary Coma sample, selected from GMP83 on the basis of ellipticity and colour are marked with triangles.

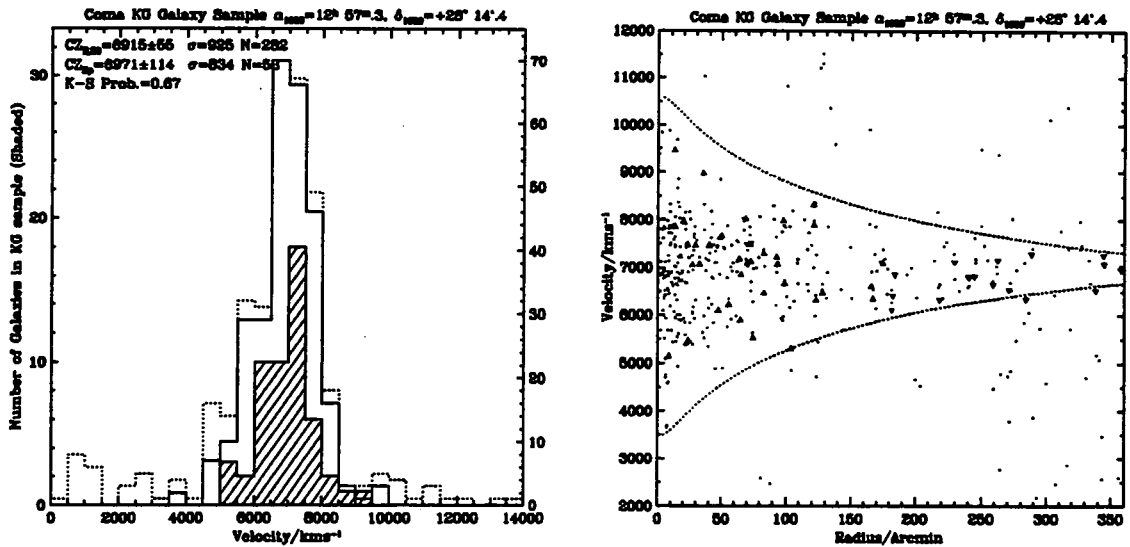


Figure 2.3: Left Panel: Two histograms of galaxy recessional velocities from Kent & Gunn (1982). The unshaded bins are for all the galaxies appearing in the Kent & Gunn catalogue, with numbers in each bin appearing on the right-hand side of the plot. The velocities of galaxies from the secondary coma sample (i.e. Kent & Gunn galaxies typed as spirals) are marked with shaded histograms and their size can be read from the left-hand scale. Right Panel: Radial velocity plotted against projected radial distance for all the galaxies in the Kent & Gunn catalogue. Galaxies from the secondary Coma sample are marked with triangles. The dotted line is the projected cluster membership limits calculated from a spherically symmetric, $\Omega = 1$ Coma model from van Haarlem et al. 1993 (1993) (see also van Haarlem 1992).

The c - m relation fitted by the author is shown superimposed on a c - m diagram of the entire sample in the upper right panel of Figure 2.8.

Galaxies with colors blue-wards of the relation $2.55 \leq 0.04b + (b - r) \leq 2.90$ were selected and their positions compared with the APM catalogue in order to obtain more accurate ellipticities. Galaxies with $e \geq 0.28$ and $b\text{-mag} \leq 18.0$ were then selected for the main cluster sample. This first selection proved too small and an additional sample was selected with b magnitudes less than 18.6 which was given a lower priority (and in fact was never used). A map showing the distribution on the sky of the two samples is given in Figure 2.9. Selection for the A2634 secondary sample was done in a similar way to the A2199 UGC sample and a map of this data is given in Figure 2.10.

2.3.4 Abell 194

No large-area photometric catalogue was available for Abell 194 in the literature. Instead the primary sample was selected from the catalogue of cluster members published in Chapman et al. (1988). This

catalogue is considered by the author to be reasonably complete to a b magnitude of 18.0, gives morphological type and classifies galaxies into cluster members using redshift. Further type information from the NED database was merged with the Chapman data before selecting the primary sample. This sample was then augmented with a secondary sample selected from the UGC and Zwicky CGCG catalogues. Galaxies from these catalogues within 4° of the cluster centre and with correct morphological types, ellipticities, redshift and $b\text{-mag} \leq 16.5$ were used to form this secondary sample. Because of the patchy nature of this process the selection function for A194 is considered more uncertain. The positions of all the selected galaxies within A194 is shown in Figure 2.11.

2.3.5 The Selected Samples

Full details of the selected galaxies for each cluster including positions and photometric parameters are given in Appendix A. Which galaxies were actually observed and the quality of the results obtained is also given there.

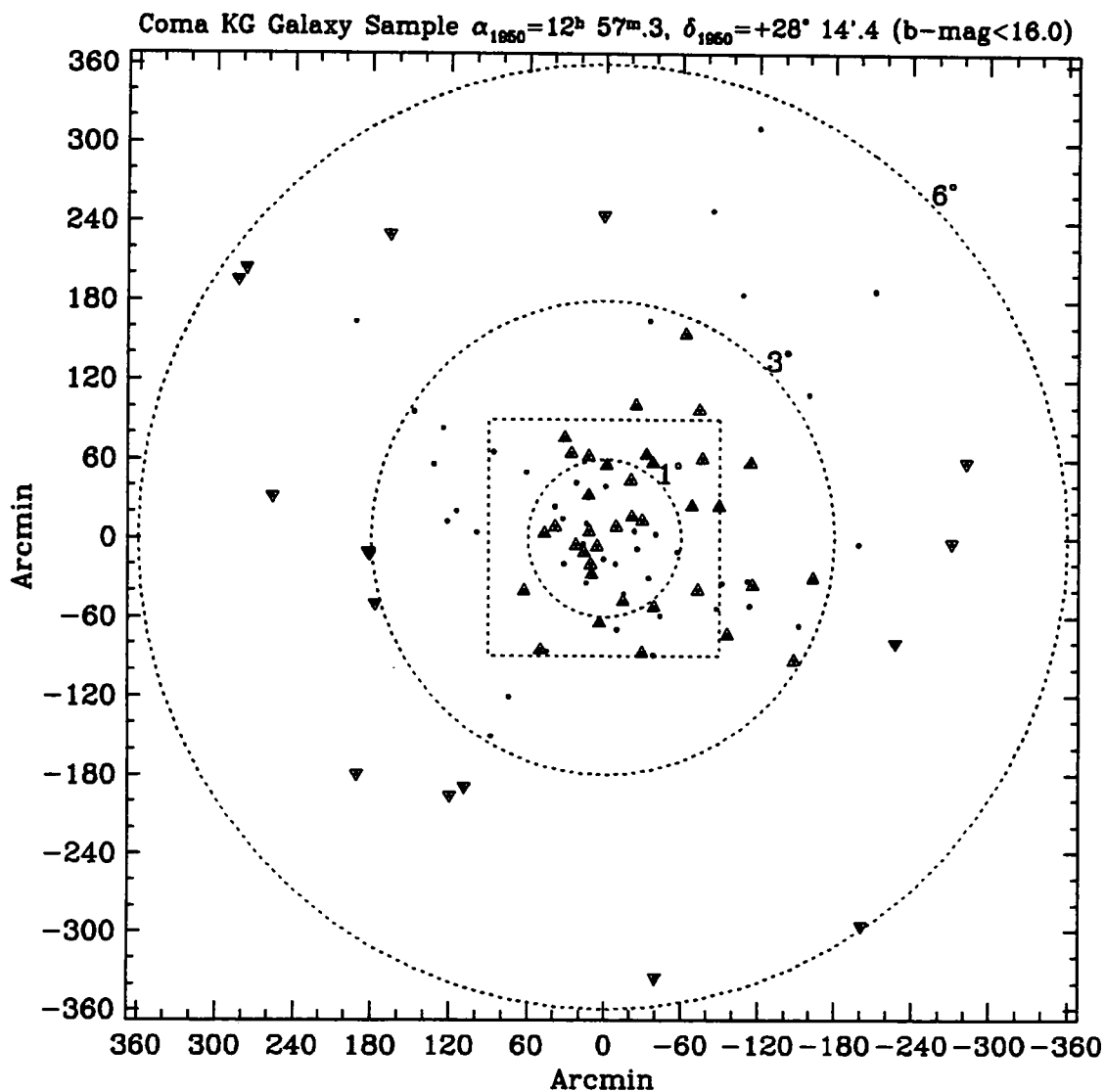


Figure 2.4: A Map of the $12^{\circ} \times 12^{\circ}$ region centred on Coma. All galaxies with $b\text{-mag} \leq 16.0$ from the Kent & Gunn (1982) sample are marked as points. The secondary Coma sample is marked with triangles. This sample consists of cluster member galaxies (i.e. with correct redshift) that are also typed as spiral in the literature. The sample is divided into a inner (radial position, $r < 3^{\circ}$) and a outer sample ($3^{\circ} < r < 6^{\circ}$). The inner sample is indicated with vertical triangles, the outer sample with inverted triangles and the sample limits are marked with a dotted line. The limit of the inner primary sample is marked by a dotted box.

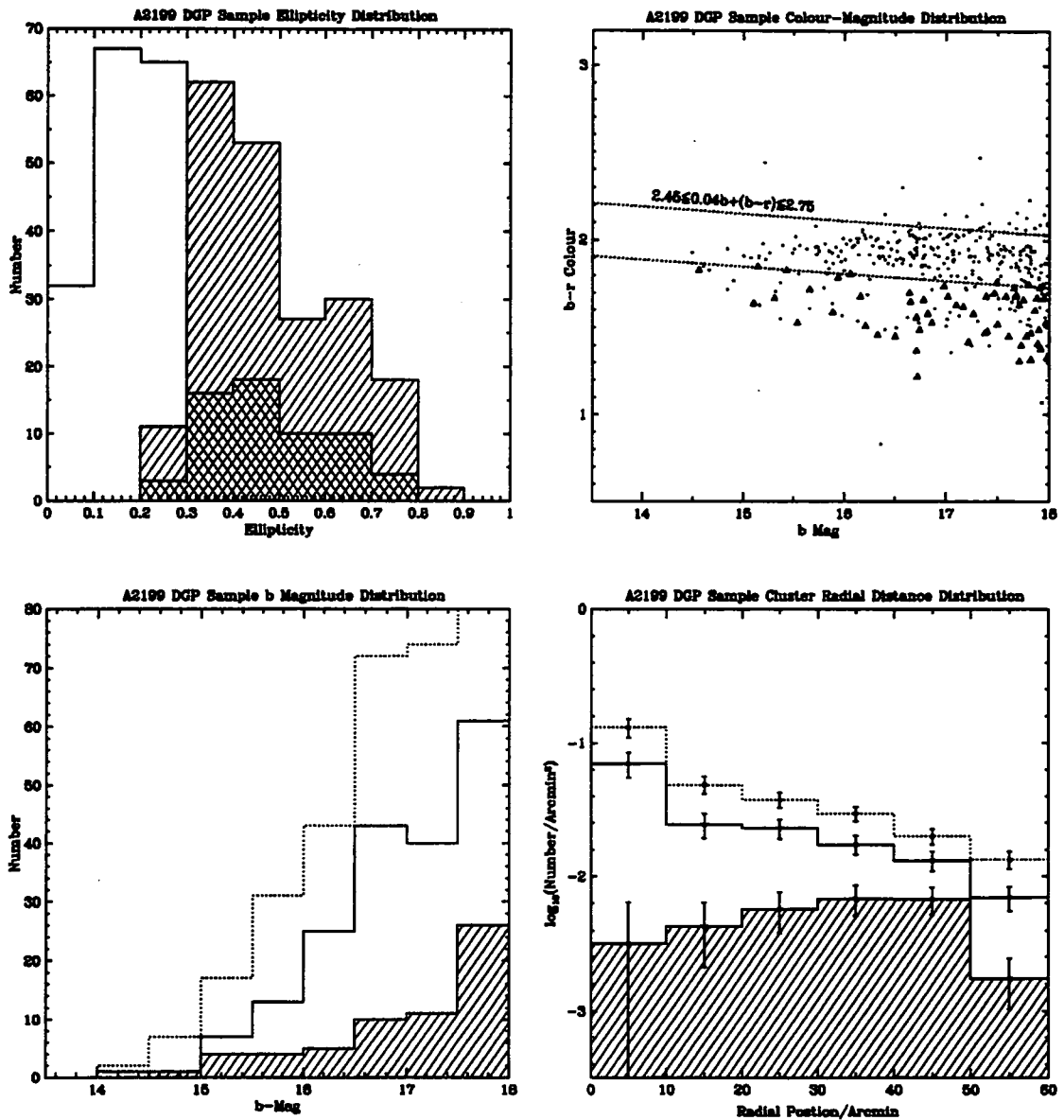


Figure 2.5: Four graphs detailing the target selection process using photographic photometry from Dixon et al. (1989)(DGP89). Top Left: A Histogram showing the distribution of ellipticity for all objects in the DGP89 sample with $b\text{-mag} \leq 18$. Objects with ellipticity greater than 0.28 (i.e. inclination greater than 45° in the case of spiral galaxies) are shown with half shaded bins. The distribution of the finally selected objects is shown fully shaded. Top Right: Colour-magnitude relation for DGP89 objects. A fit to the colour magnitude relation is marked as parallel dotted lines. The primary sample selected using ellipticity and color-magnitude (i.e. blue-ward of the c-m relation) is marked with triangles. Objects selected for the supplementary sample on the basis of their spiral type, ellipticity and redshift are also marked. Bottom Left: A Histogram of the magnitude distribution of the three samples; all DGP89 objects (dotted line), objects with $e \geq 0.28$ (solid line), and the primary selected sample based on ellipticity and colour (shaded). Bottom Right: Histogram showing the radial number density distribution of objects within the cluster. The three samples are marked in the same manner as the previous plot. The selected galaxies (shaded histograms) show some evidence of concentration towards the centre of the cluster.

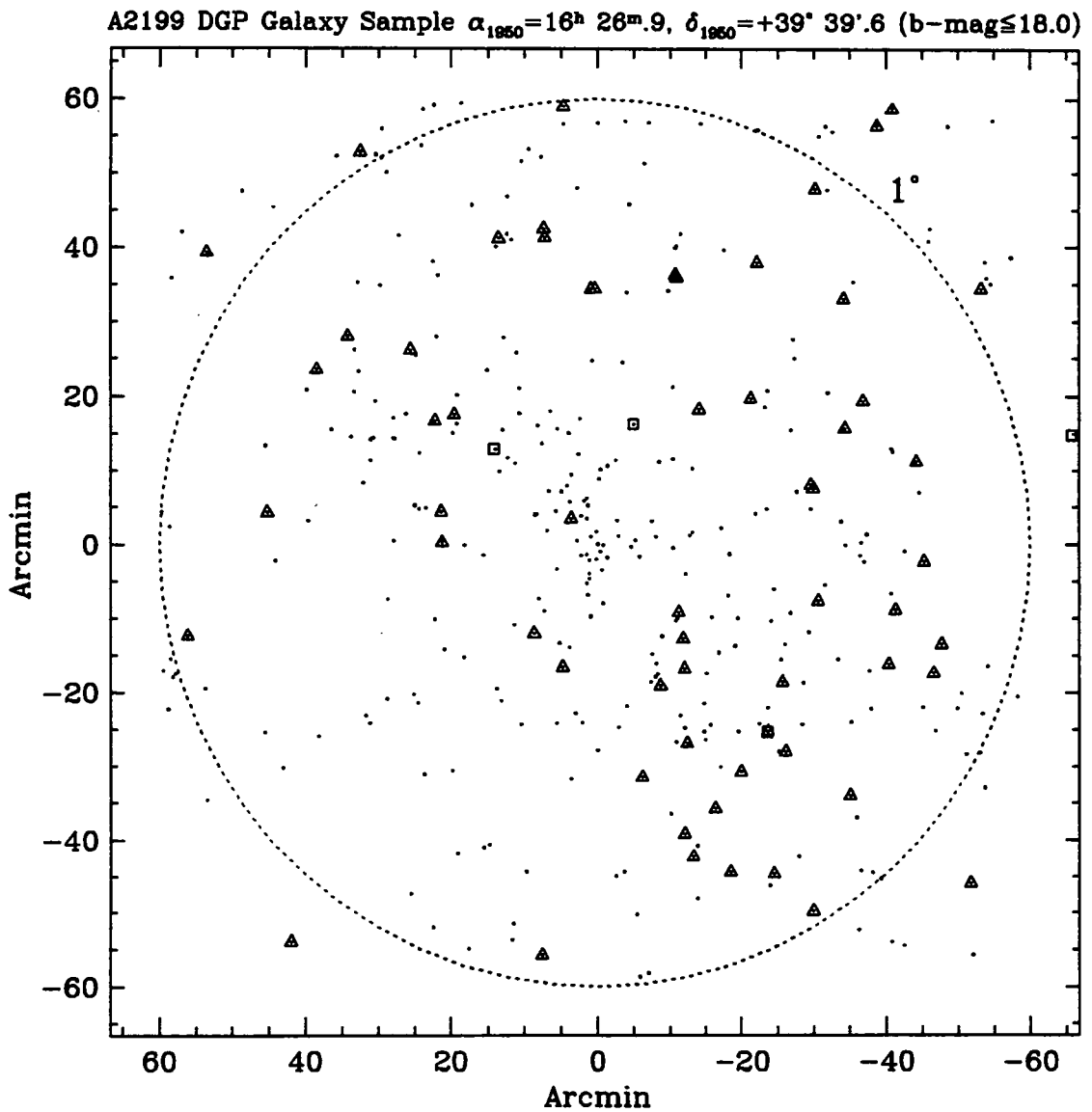


Figure 2.6: A map of a $2^{\circ} \times 2^{\circ}$ region centred on Abell 2199. All galaxies from the DGP89 catalogue with b -magnitudes less than 18.0 are marked as points. The galaxies from our primary A2199 sample, selected from DGP89 on the basis of ellipticity and colour are marked with triangles. The few points from the secondary A2199 sample (selected from the UGC catalogue using ellipticity, type and redshift) that fall within the inner region are marked using squares.

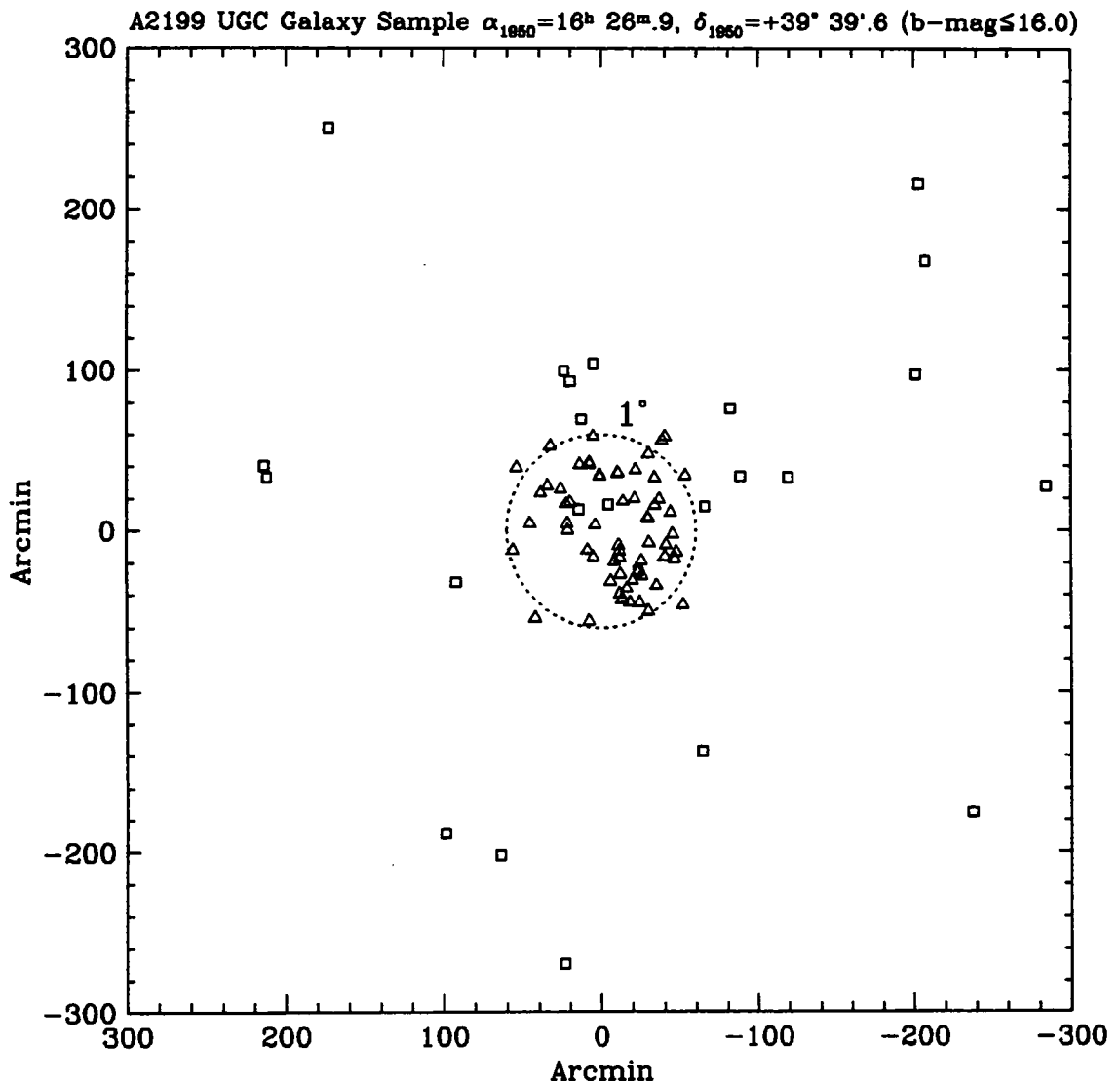


Figure 2.7: A Map of the $10^{\circ} \times 10^{\circ}$ region centred on A2199 showing the distribution of our selected samples on the sky. Galaxies from our secondary sample selected from the UGC catalogue (with $b\text{-mag}\leq 16.0$, $e>0.28$, spiral type and correct redshift) are marked with boxes. The inner primary A2199 sample is marked with triangles.

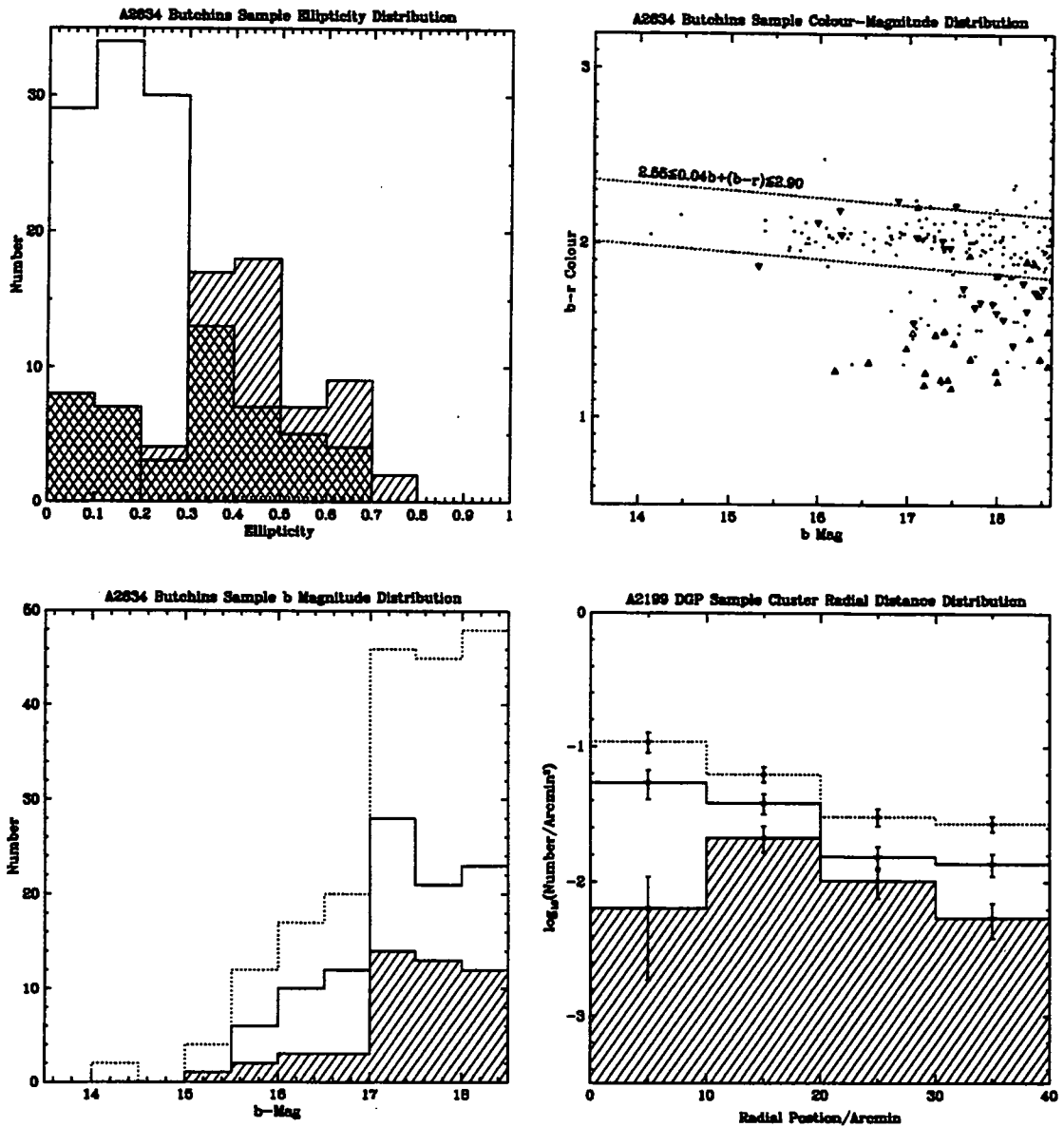


Figure 2.8: Four graphs detailing the target selection process using photographic photometry from Butchins 1983(B83). Top Left: A Histogram showing the distribution of ellipticity for all objects in the B83 sample with $b\text{-mag} \leq 18$. Objects with ellipticity greater than 0.28 (i.e. inclination greater than 45° in the case of spiral galaxies) are shown with half shaded bins. The distribution of the finally selected objects is shown fully shaded. The large scatter in this plot demonstrates the poor quality of the ellipticities from the B83 catalogue. Top Right: Colour-magnitude relation for B83 galaxies. A fit to the colour magnitude relation is marked as parallel dotted lines. The primary sample selected using ellipticity and colour-magnitude (i.e. blue-ward of the $c-m$ relation) are marked with triangles. Objects selected for the supplementary sample on the basis of their spiral type, ellipticity and redshift are also marked. Bottom Left: A Histogram of the magnitude distribution of the three samples; all B83 objects (dotted line), objects with $e \geq 0.28$ (solid line), and the primary selected sample based on ellipticity and colour (shaded). Bottom Right: Histogram showing the radial number density distribution of objects within the cluster. The three samples are marked in the same manner as the previous plot. The selected galaxies (shaded histograms) again show some evidence of concentration towards the centre of the cluster.

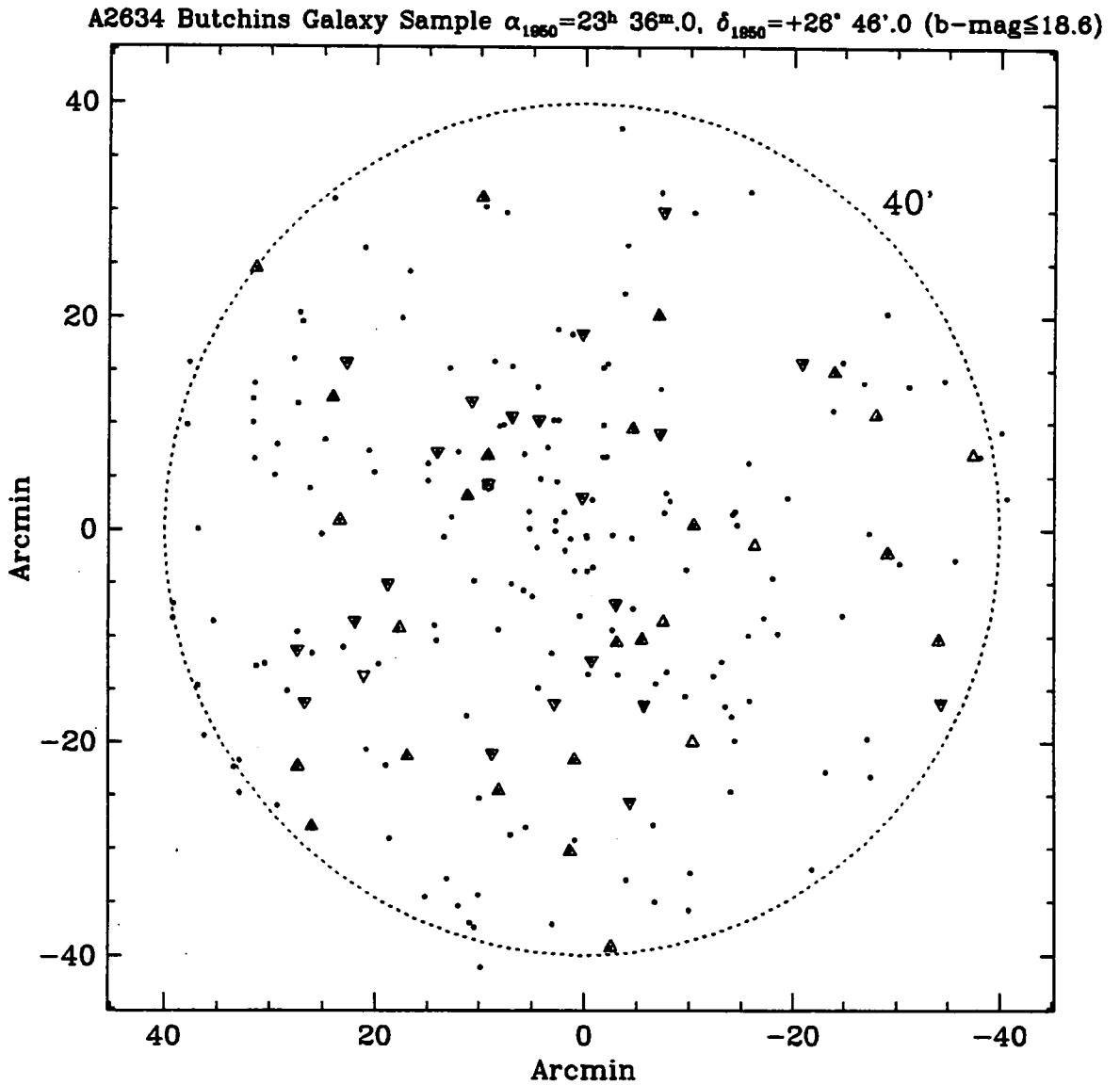


Figure 2.9: A map of a $1.2^{\circ} \times 1.2^{\circ}$ region centred on Abell 2634. All galaxies from the B83 catalogue with b -magnitudes less than 18.6 are marked as points. The galaxies from our primary A2634 sample, selected from B83 on the basis of ellipticity and colour are marked with triangles. This sample is divided into two, galaxies with $b\text{-mag}\leq 18.0$ are marked with vertical triangles and galaxies with $18.0 < b\text{-mag}\leq 18.6$ are marked with inverted triangles. The few points from the secondary A2634 sample (selected from the UGC catalogue using ellipticity, type and redshift) that fall within the inner region are marked using squares.

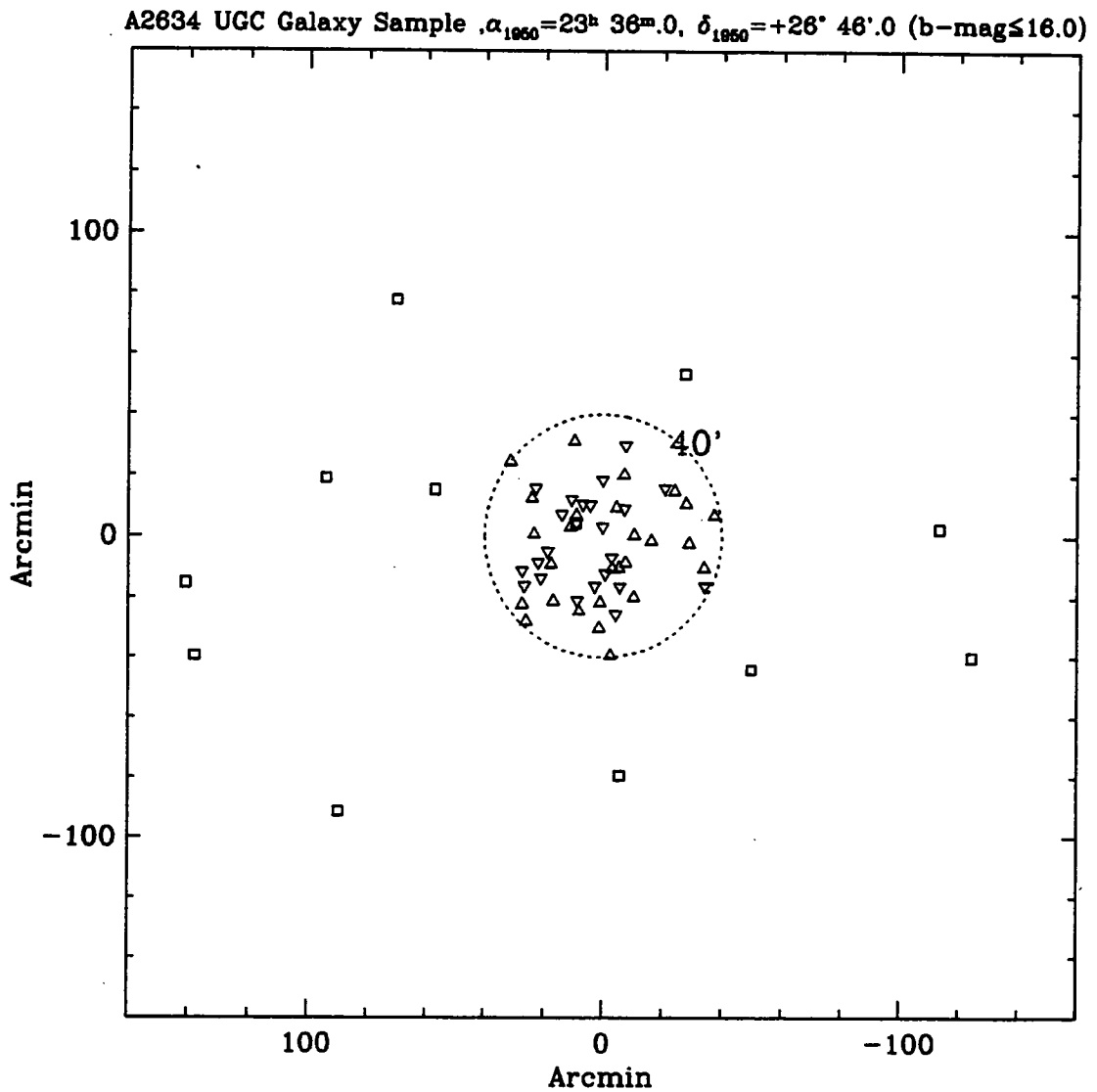


Figure 2.10: A Map of the $5^{\circ} \times 5^{\circ}$ region centred on A2634 showing the distribution of our selected samples on the sky. Galaxies from our secondary sample selected from the UGC catalogue (with $b\text{-mag}\leq 16.0$, $e>0.28$, spiral type and correct redshift) are marked with boxes. The inner primary A2634 sample is marked with triangles.

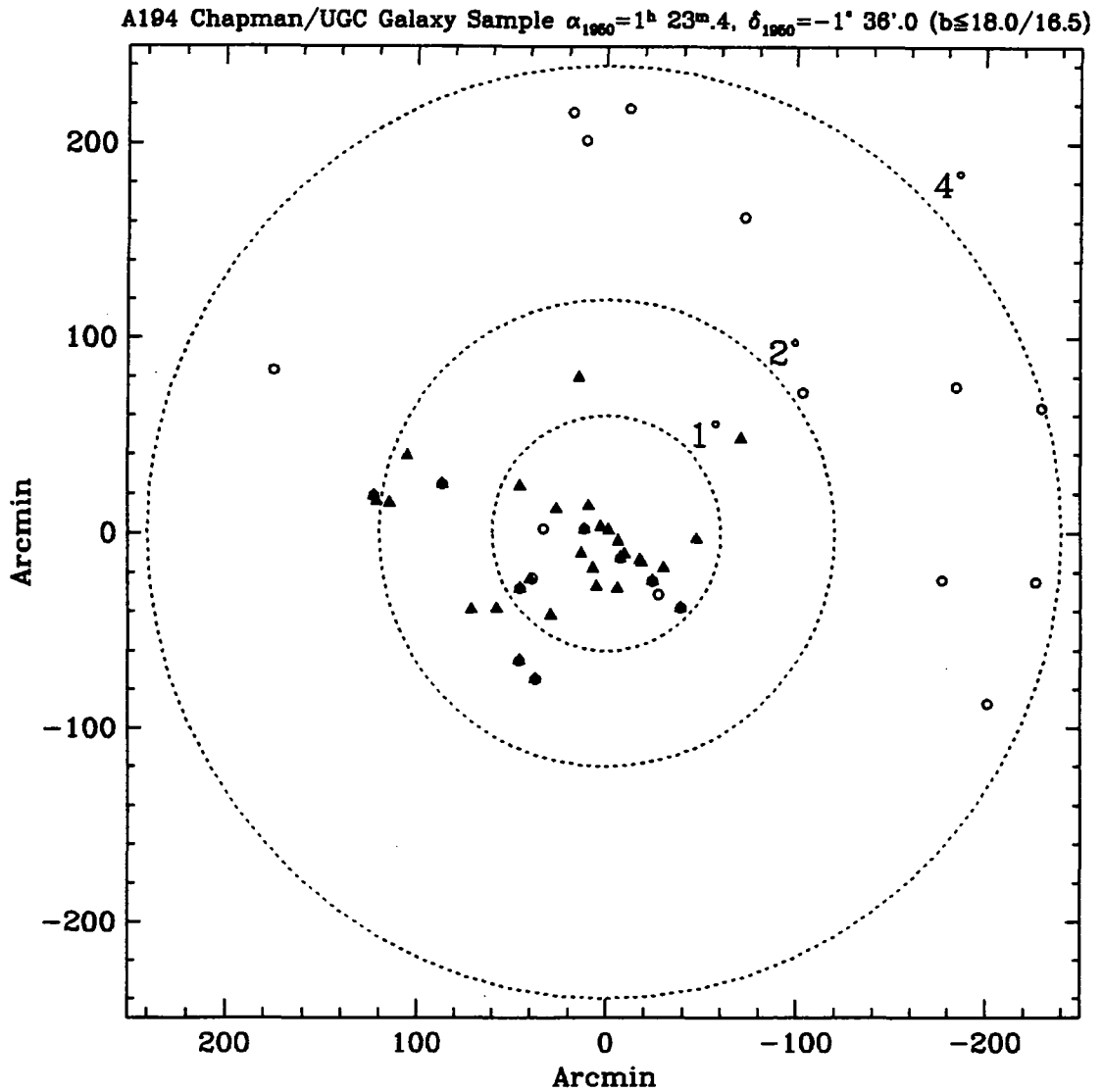


Figure 2.11: A Map of the $8^{\circ} \times 8^{\circ}$ region centred on A194 showing the distribution of our selected samples on the sky. Galaxies from our primary sample are selected from the sample of galaxies measured by Chapman, Geller, & Huchra 1988, with $b\text{-mag} \leq 16.0$, $e > 0.28$, spiral type and correct redshift, are indicated with filled triangles. The secondary sample selected with the same criteria from the UGC catalogue are marked with open circles.

2.4 Selection Bias

As was mentioned in §2.2.1 our apparent magnitude cut at $b\text{-mag}=18$ introduces a selection bias at differing absolute magnitudes within each of our cluster samples. The impact of this effect will be discussed in Chapter 5 along with methods for correcting for the effect. Aside from the simple bias introduced by our magnitude cut there are a number of other effects introduced by our selection process and inherent in our cluster samples.

As all of galaxy selection is from photographic data, our samples inherit all of the biases involved with selecting galaxies from photographic plates. The main bias is towards galaxies in a narrow range of surface brightness (see McGaugh 1996). The impact of this on the final TF relation is reduced as the TF data is based on magnitudes measured in a different photometric band from the photographic data. This difference in band tends to wash out the strong peak in the surface brightness distribution, and the remaining effect will be discussed in Chapter 5. Another trait of photographic data is that the algorithms used to detect the objects within each plate tend to break up the typically uneven spiral galaxy images into smaller pieces which would fall below our magnitude cut. We believe this effect is small and unlikely to introduce a significant bias into our samples.

Another possible bias arises from our colour selection. Galaxies in the field tend to be bluer than cluster galaxies. Selecting blue galaxies as probable spirals also biases our sample towards field galaxies in the foreground and background of the cluster. This effect would tend to increase the scatter in the TF relation. The effects of cluster membership and the size of this bias will be examined in Chapter 6.

Another aspect of this selection procedure to note is that it assumes the measured parameters for each object; ellipticity, colour, magnitude, morphological type etc. are correct. In fact, all these parameters are uncertain to a greater or lesser extent and the selection limits are blurred by an uncertain amount. For example, the effect of the merging of galaxy images with nearby stars upon the measured ellipticity could cause an object to remain unselected. The important thing to note is that errors in the param-

eters only affect the completeness of our samples. Although we can never assume 100% completeness, our selected sample can be considered to be an unbiased random subset.

References

- Aaronson M., Bothun G., Mould J., Huchra J., Schommer R. A., Cornell M. E., 1986, *ApJ*, 302, 536
- Aaronson M., Huchra J., Mould J., Schechter P. L., Tully R. B., 1982, *ApJ*, 258, 64
- Abell G. O., 1958, *ApJS*, 3, 211
- Abell G. O., Corwin H. G., Olowin R., 1989, *ApJS*, 70, 1
- Bernstein G., Guhathakurta P., Raychaudhury S., Giovanelli R., Haynes M. P., Herter T., Vogt N. P., 1994, *AJ*, 107, 1962
- Butcher H., Oemler A., 1984, *ApJ*, 285, 426
- Butchins S. A., 1983, Ph.D. thesis, The University of Oxford, Oxford, U.K.
- Chapman G. N. F., Geller M. J., Huchra J. P., 1988, *AJ*, 95, 999
- David L. P., Slyz A., Jones C., Forman W., Vrtilik S. D., 1993, *ApJ*, 412, 479
- Dixon K. L., Godwin J. G., Peach J. V., 1989, *MNRAS*, 239, 459
- Dressler A., 1980, *ApJS*, 42, 565
- Freudling W., Martel H., Haynes M. P., 1991, *ApJ*, 377, 349
- Fukugita M., 1991, *ApJ*, 376, 8
- Godwin J. G., Metcalfe N., Peach J. V., 1983, *MNRAS*, 202, 113 (GMP83)
- Gregory S. A., Thompson L. A., 1984, *ApJ*, 286, 422
- Han M. S., 1991, Ph.D. thesis, California Institute of Technology, Pasadena, California.
- Helou G., Madore B., Schmitz M., Bica M., Wu X., Bennett J., 1991, *The NASA/IPAC Extragalactic Database, Databases and On-Line Data in Astronomy*, ed. D. Egret & M. Albrecht (Dordrecht: Kluwer)
- Jacoby G. H. et al., 1992, *PASP*, 104, 599
- Jones C., Forman W., 1984, *ApJ*, 276, 38
- Kent S. M., Gunn J. E., 1982, *AJ*, 87, 945
- Lucey J. R., Gray P. M., Carter D., Terlevich R., 1991a, *MNRAS*, 248, 804
- Lucey J. R., Guzman R., Carter D., Terlevich R., 1991b, *MNRAS*, 253, 584
- Maddox S. J., Loveday J., Sutherland W. J., Efstathiou G., 1988, in *Large-scale structures in the universe - Observational and analytical methods*. Springer-Verlag, p. 90

- Mazure A., Proust D., Mathez G., Mellier Y., 1988, *A&AS*, 76, 339
- McGaugh S. S., 1996, *MNRAS*, 280, 337
- Struble M. F., Rood H. J., 1987, *ApJS*, 63, 555
- Struble M. F., Rood H. J., 1991, *ApJS*, 77, 363
- van Haarlem M. P., 1992, Ph.D. thesis, Leiden, Sterrewacht, Postbus 9513, Leiden, 2300RA, Netherlands.
- van Haarlem M. P., Cayon L., Gutierrez De La Cruz C., Martinez-Gonzalez E., 1993, *MNRAS*, 264, 71
- Zwicky F., Herzog E., Wild P., 1960, Catalogue of galaxies and of clusters of galaxies

Chapter 3

Photometric Observations and Data Reduction

Abstract. In this chapter are discussed the observations and reduction methods used to produce Tully-Fisher parameters for over one hundred galaxies from four galaxy clusters. I detail the instruments used and reduction methods applied and explain our technique for fitting galaxy isophotes and obtaining photometric parameters. The photometry is then compared with other authors' data and estimates are made of our internal and external errors.

Photometric and spectroscopic measurements of the galaxies within our cluster samples were made during two observing runs in May and August of 1993 at the Observatorio del Roque de los Muchachos on the island of La Palma in the Canary Islands. The Jacobus Kapteyn telescope (JKT) was used to take I-band CCD images of our target galaxies and the Isaac Newton telescope (INT) was used to make required long-slit spectroscopic measurements.

3.1 Photometric Observations

The JKT has a 1.0 metre parabolic primary mirror combined with a hyperbolic secondary, which gives a conventional Cassegrain optical system with a focal ratio of $f/15.0$. The telescope is equatorially mounted on a cross-axis mount. The East of pier configuration was used so that target galaxies could be tracked down to the 84° zenith distance limit in the west. All the galaxies in our sample were imaged in the I-band using the EEV7 detector head mounted at Cassegrain focus along with an I-band Kitt Peak interference filter.

The EEV7 head contains an EEV 05-30 coated charge-coupled device (CCD) chip with 1242×1152 pixels. The plate scale of 13.5 arcsec/mm and pixel size of $22.5 \times 22.5 \mu\text{m}$ results in a pixel angular size of 0.3×0.3 arcseconds and a total field of view of 6.2×5.8 arcminutes. The EEV chip has a low read-out noise of $4e^-$ rms (≈ 5.3 ADU), a negligi-

ble dark current and an even bias frame with variations in the bias being below 0.2%. The chip also has a very even response over its surface with large scale variations before flat-fielding being less than 3% and less than 0.8% after flat-fielding. Charge transfer was not perfect and the heavy bleeding that appeared on some frames, due to saturation caused by bright stars, made surface photometry difficult and increased the uncertainty in the magnitude measurements. This was only a real problem in the few frames where a bright star appeared nearby a target galaxy and in a few cases these objects had to be rejected.

The filter used was an I-band Kitt Peak interference filter built to the specifications of J. Mould (see Bothun & Mould 1987) and supplied to the ING telescopes by the Kitt Peak observatory. The I-band filter is made from a MgF_2 coated Schott RG-N9 substrate with a peak transmission of over 80% between the "50% on" and "50% off" wavelengths of 7300\AA and 9000\AA (see Argyle 1988).

Typically one nights observing would consist of around 20 images of target galaxies, 15 exposures of standard stars and about 10 short exposures of blank fields during twilight for flat-fielding. Exposure time for galaxy images ranged from 500 to 2000 seconds the majority being 1000 seconds allowing accurate surface photometry out to surface brightnesses of $24 \text{ mag arcsec}^{-2}$ in the I-band.

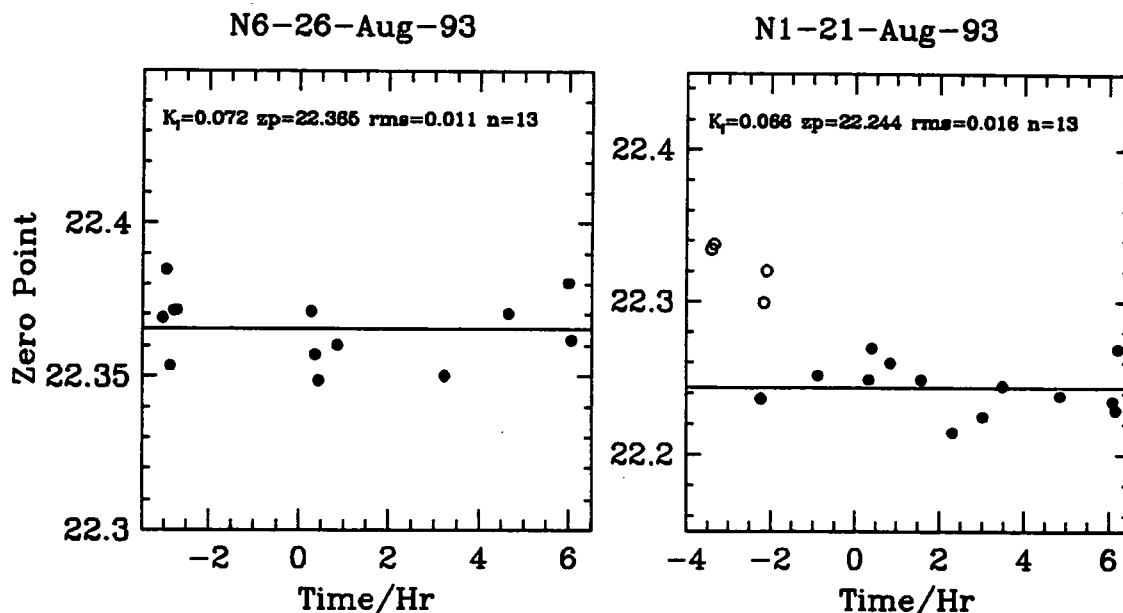


Figure 3.1: Left: An example of the variation in the photometry zero-point over the hours of a photometric ($Q=1$) night relative to midnight, local time. Right: The zero-point variation over a partially photometric night ($Q=2$). The open symbols show the effect of clouds on the zero-points during the first two hours of the night. The solid line in both plots represents the final zero-point adopted for that night. In the case of the partially photometric night the early measurements represented by the open symbols were excluded from the zero-point fit.

3.1.1 Initial Data Reduction

A combination of Starlink and IRAF software running on workstations provided by the Starlink node at the University of Durham was used throughout the reduction process of all the data presented here. The initial reduction of the “raw” CCD images was done using standard procedures with the CCDPACK software developed by Peter Draper for Starlink (see Draper 1993). The weak structure observed in the bias frames remained constant over both observing runs. This allowed the creation of a master bias frame from the median of the scaled individual bias frames taken during both observing runs. This allowed the bias offset and any bias structure in each frame to be removed by subtracting the master bias frame. The master bias frame was scaled before the subtraction so that the median value of the over-scan strip in the master bias frame and each individual image frame matched.

Flat-field frames for each night were created using the *makeflat* task within CCDPACK. Suitable twilight sky images from each night were combined by scaling to unity and taking the median to pro-

duce a flat-field frame for each night. The CCD window and filters used on the JKT suffered from dust specks during both of our observing runs. These dust specks appear in the images as small dark areas which could possibly interfere with surface photometry. The specks can be divided out using each night's flat-field frame but as these dust specks tend to move around during each night and from night to night an element of trial and error was introduced into the flat-fielding process.

Flat-field frames were made up from different subsets of twilight frames and used to divide out the CCDs varying spatial response and any dust present in that night's images. The best performing flat-field frame was the one finally used. In a few cases two flat-fields were used for one night. One flat made up from twilight frames taken at the start of the night would be used to flatten images taken early in the night and a second flat, created using the morning twilight, would be used to flat-field images taken in the second half of the night. This way the effect of dust was kept to a minimum and had little effect on the final surface photometry. Large scale variations in the final flat-fielded frames ranged between 0.1%

Table 3.1. A Summary of observations made during two observing runs at the JKT. Column headings are: Date, I-band extinction coefficient k_I , magnitude zero-point a_I , colour term b_I , rms of fitted zero-point σ_a , number of standard stars observed N_{stand} , number of galaxies observed N_{gal} , mean seeing fwhm S in arcseconds, photometry quality Q and weather.

Date	k_I	a_I	b_I	σ_a	N_s	N_g	S''	Q	Notes
20/5/93	0.110	22.389	-0.047	0.025	21	15	2.2	2	Cirrus at start of night
21/5/93	0.117	22.437	-0.005	0.009	21	19	1.6	1	
22/5/93	0.103	22.405	0.009	0.010	10	14	1.6	1	
23/5/93	0.102	22.430	0.054	0.004	3	1	1.8	2	cloudy most of night
24/5/93	0.109	22.440	0.022	0.004	13	10	2.8	1	very poor seeing
25/5/93	-	-	-	-	1	2	1.5	3	very cloudy all night
26/5/93	-	-	-	-	0	18	-	3	Cirrus/ridge cloud all night
21/7/93	0.065	22.239	-0.006	0.016	13	14	1.0	2	Cirrus early in night
22/7/93	0.186	22.494	-0.003	0.016	8	14	1.0	2	Cirrus early in night
23/7/93	0.086	22.406	0.064	0.010	11	20	0.9	1	
24/7/93	-	-	-	-	11	10	-	3	Cirrus all night
25/7/93	0.095	22.411	0.050	0.011	9	23	1.4	1	
26/7/93	0.080	22.408	0.066	0.008	13	16	1.3	1	
27/7/93	0.026	22.381	0.083	0.021	15	25	1.1	1	

and 0.8% and on average the image frames were flat to within 0.4%.

3.1.2 Photometric Calibration

During each night, a selection of standard stars with different colours were observed from the list of Kitt Peak Photometric Standards (from Landolt 1983). The same stars were observed at different times during each night, over a range of air masses in order to calibrate the conversion from instrumental magnitudes to the Kron-Cousins photometric scheme (Cousins 1976 and Landolt 1983). The transformation used was:

$$I = a + I_{\text{instr}} + b(V - I) - k_I X \quad (3.1)$$

Where I_{instr} is the I band instrumental magnitude measured from the CCD image within a $22''$ diameter aperture. I and V are the I and V magnitudes within the Kron-Cousins photometric system, X is the air mass and a, b and k_I are the photometric zero point, colour coefficient and I-band atmospheric extinction respectively. The instrumental magnitude is defined as:

$$I_{\text{instr}} = -2.5 \log \left(\frac{C_{22''} - \overline{sky}}{T_{\text{exp}}} \right) + 30 \quad (3.2)$$

Where $C_{22''}$ are the counts measured within a $22''$ diameter aperture centred on the standard star and T_{exp} is the exposure time of the image.

All three of the calibration coefficients a, b and k_I are determined for each night using a least-squares fit to the standard star measurements (see Table 3.1). Unlike previous works in this area (e.g. Han 1991 and Willick 1991) k_I was not fixed at a specific value for the observatory but was allowed to vary from night to night. This is because La Palma suffers from varying extinction due to dust at high altitude in the atmosphere blown from the nearby Sahara desert. Changing levels of dust can cause the extinction to vary over time scales of less than a week (see k_I in Table 3.1) and to assume a constant value for the extinction over a one week observing run would be unwise.

3.1.3 Photometric Quality

Once the standard star magnitudes for each night are fitted, a graph of photometric zero-point (a in Equation 3.1) against time can be plotted for each night. The zero-point plots along with weather reports and notes from the observing log allowed a quality value (Q) to be given to each nights observing. Nights with good clear weather and no system-

atic or large variations in zero-point over the night were allocated a quality value, $Q=1$. If a nights observing was partially interrupted by poor weather or displayed a large increase in zero-point over a period of the night a value of $Q=2$ was given if the rest of the night had a steady zero-point.

When a night was badly disrupted by poor weather or the measured photometric zero-point displayed high scatter, the photometric data was considered untrustworthy and assigned a poor quality value of $Q=3$. An example of the zero-point variation over a photometric, $Q=1$ night and a partially photometric, $Q=2$ night can be seen in Figure 3.1. Over fourteen nights of observing, seven nights were photometric $Q=1$, four nights were partially photometric $Q=2$ nights, and three were poor observing nights and assigned a quality value $Q=3$.

The weather during the first observing run in May was poorer than expected with three of the available seven nights being lost to a combination of cirrus and ridge cloud. In total, approximately 50% of the possible observing time was lost to equipment faults and bad weather. Seeing was also less than ideal during the first run; the mean seeing was around $1.6''$ and varied between $1.4''$ and $3.0''$. The second observing run in August had fine weather with only one night considered completely non-photometric due to Cirrus cloud. Seeing was also better with a mean seeing fwhm of $1.1''$ for the week. Our observing efficiency was also much improved with images of over 120 galaxies being taken as compared to the 80 of the first run.

During nights when the weather was changing rapidly or was unpredictable more standard stars were measured in order to monitor the conditions and to help decide which galaxy images could be considered photometric. When the conditions were clearly non-photometric few if any standards were observed as telescope time was best used by taking many short exposure "snapshots" of target galaxies to check for correct morphology, inclination and nearby bright stars. Suitable galaxies could then be given a high priority for observation under photometric conditions. A summary of the dates, photometry coefficients, quality and weather notes for all fourteen observing nights is given in Table 3.1.

3.2 Galaxy Surface Photometry

Surface photometry of the 200 galaxies observed was done using a combination of an image analysis program, AVIEW, written by John Lucey, Starlink software and the IRAF package of image reduction software. Different aspects of each of these packages were combined into one "pipeline" using shell scripts and programs written by the author. Only two stages of the reduction required interactive input, the initial selection of the target galaxy on the CCD frame and the marking of the disk region of each galaxy when considering the surface photometry profiles. The rest of the reduction steps were executed as "batch" processes using shell scripts which treated each frame in the same uniform manner.

The first stage of the surface photometry process, selecting the target galaxy from within the CCD image, was done using the AVIEW photometry package. After the image was loaded into the program and displayed with a suitable stretch, the *PSA* task within AVIEW was used to detect all objects in the frame and hi-light them with an ellipse. The object detection subroutines used by AVIEW to do this are the same subroutines used by PISA; the Starlink stand-alone object detection and analysis package. In this case objects detected in the frame are defined as any four or more adjacent pixels with a level at least 1.5σ above a nominal sky value for the frame. Selection was done with an on-screen cursor due to the large field of view of the CCD, and reference to the original finder charts was often made at this point. The position of a galaxies core was measured using the centroiding task *CEN*, along with the seeing PSF which was measured from bright stars appearing in the image using the *STP* command within AVIEW. A final "eyeball" check was made of the detection and selection process before exiting AVIEW.

Upon exit, AVIEW produces a number of auxiliary files to accompany the main image. These include: (i) A ".jpars" file containing information needed for the photometric calibration of the frame and other information, e.g. name, date, airmass, etc. (ii) A ".epars" file containing the centres, major axes, ellipticities and position angles of ellipses describing all the objects detected within the image

frame. (iii) A “.rpars” file contains details of any regions within the image, defined manually with AVIEW, which should not be considered when calculating the sky level etc. as they contain defects, dust specks, diffraction spikes or saturated regions. As the detection algorithm worked well, very few objects in each frame had to be marked manually and as star removal is often the most time consuming step in galaxy surface photometry the process adopted saved much time and hard work.

3.2.1 The Photometry Pipeline

Once an image had passed through the interactive AVIEW stage it was then passed on to the first of my reduction shell scripts, *ephot1.csh*. The first step in the reduction was to obtain a robust but accurate estimate of the sky level within the image. Accurate sky subtraction is important if the surface photometry is to trace the light of each galaxy out to as faint a limit as possible. Good sky subtraction is crucial if correct magnitudes, and surface brightnesses are to be obtained.

The first part of the task consists of converting the files containing the detected objects and “bad” regions outputted from AVIEW, and inputting them into the *histpeak* task from the Starlink ESP package of programs written by Grant Privett. The *histpeak* program constructs an image pixel value versus occurrence histogram, the peak of which is fitted with a Gaussian to produce a modal sky value.

As all pixels considered to lie within a detected object or “bad” region are excluded from this analysis, the histogram is a good representation of the distribution of the value of “sky” pixels within the image. The centre and width of the Gaussian fitted to the modal peak is considered an accurate estimate of the global sky value and sky error. In order of significance, the sky error is due to a combination of: flat fielding errors (both from poor large scale correction and pixel-to-pixel response), Poisson noise, scattered light, undetected weak cosmic rays, faint undetected objects and CCD read out noise. As all of the target galaxies lie within the inner two thirds of the image the outer one third of each image was also excluded from the *histpeak* analysis so that the error estimates produced are more representative of

the image region local to the considered galaxy. After each elliptical region of the mask is increased in size by 100% to allow for faint extended objects, typically 70% of the total image area remains and is considered “sky” by *histpeak*.

Once a good estimate of the sky level was made, a second program, *Autosky* (written by John Lucey), was used to estimate the size of the large scale response variations within the image. The flat-fielding done in the preliminary reduction of each image is never perfect and large scale variations in the sky level always remain at some level. *Autosky* measures the remaining variations by dividing the image up into 100 regions and taking the median pixel value within each region as the local sky value. The mean and σ of the sky values within the 100 regions is then output by *Autosky*. The σ of the sky levels from the 100 regions ($\sigma_{\text{flatfield}}$) is used as an indication of the large scale flat-fielding error within a particular image. In all cases $\sigma_{\text{flatfield}}$ was less than 0.4%. Both the values produced by *histpeak* and *Autosky* are added to the image information file to be used at a later stage to calculate photometry errors.

3.2.2 Isophotal fitting

A simple model for a spiral galaxy consists of a thin circular disk of matter with an exponential radial surface brightness profile. Such a spiral galaxy, with its axis lying in a random direction, appears in projection as an ellipse with a surface brightness profile simply related to its face-on profile. As each isophote of the galaxy can be approximated by an ellipse, a series of ellipses with increasing radii can then be fitted to the CCD image of the whole galaxy.

The apparent ellipticity, e , of each ellipse is directly related to the disk’s inclination with respect to the line of sight. As the inclination of the galaxy plays an important factor in corrections to the measured Tully-Fisher parameters (Han 1991, Willick 1991), an accurate and unbiased estimate of the disk ellipticity is essential. Representing the galaxy as a series of ellipses is only an approximation. As can be seen from the images appearing in Appendix A, each spiral has its own spiral structure superimposed on the underlying disk. The galaxies also have cores of differing strengths and many

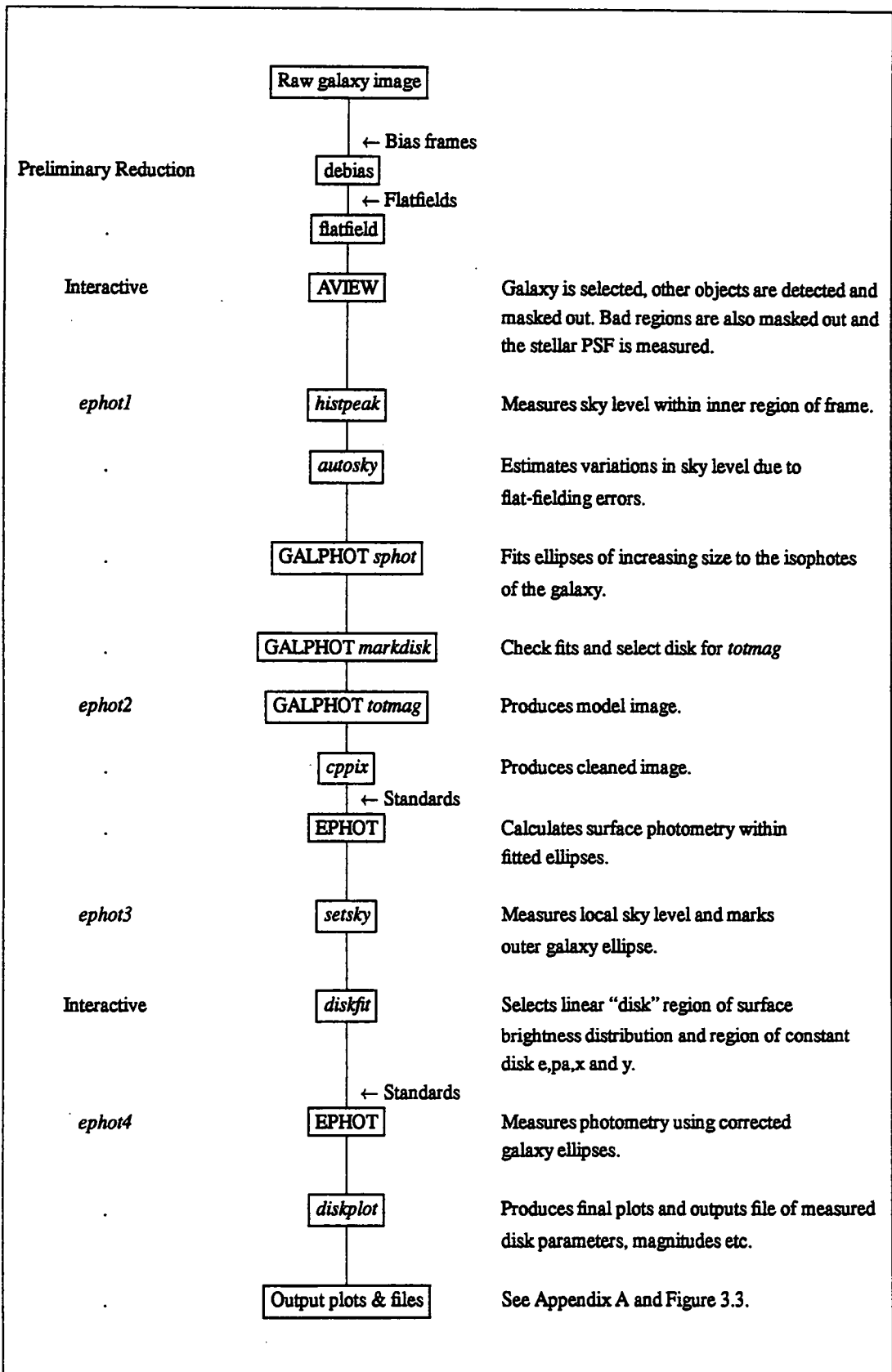


Figure 3.2: A flow diagram outlining the steps involved in the photometric reduction process. The left column indicates whether the step is done by hand or as part of a reduction shell script. The middle column indicates which software packages were used at each stage and the flow of the image data. The right column gives more detail for certain stages.

Ellipse Fitting Results For: D21

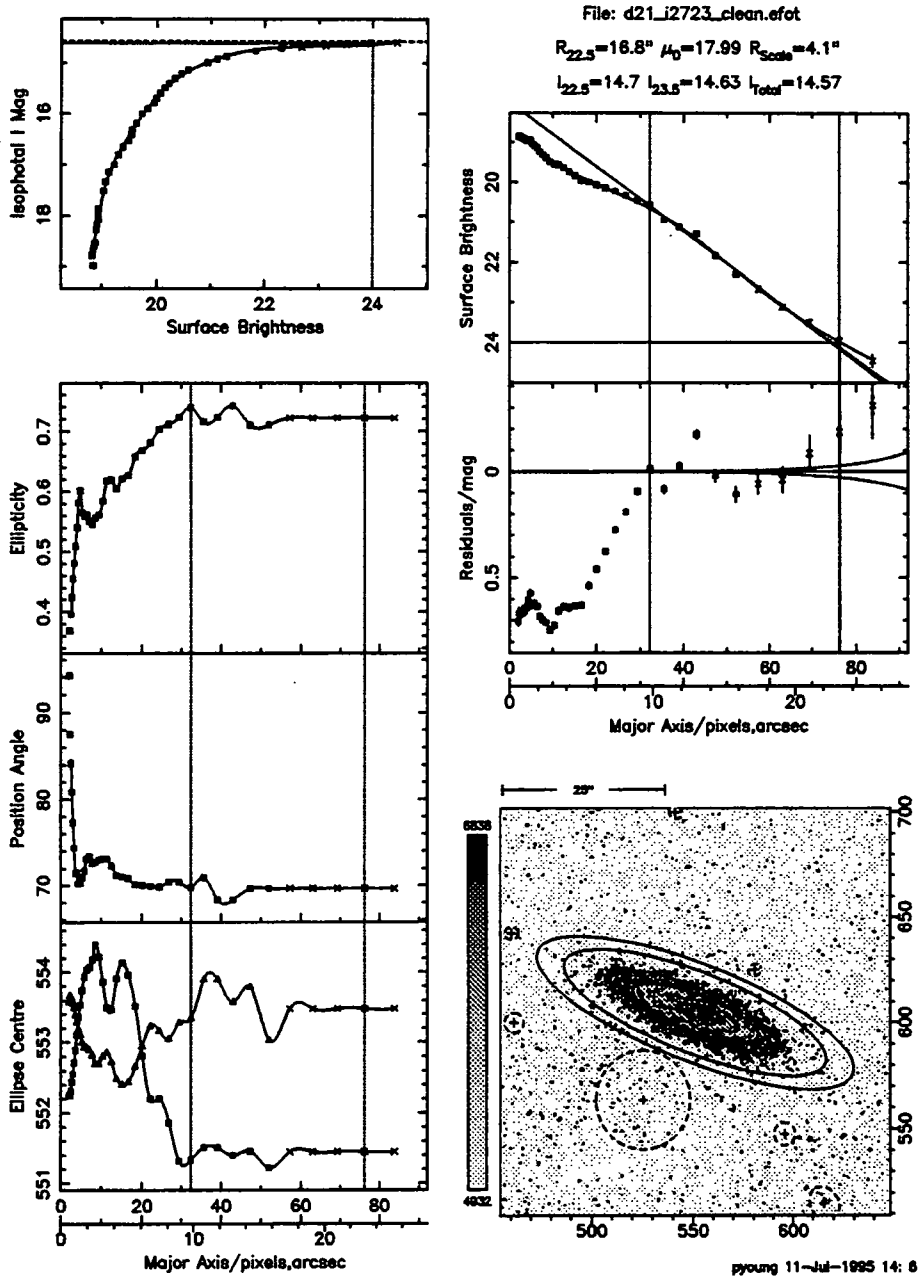


Figure 3.3: An example of the final result of the surface photometry reduction process. The four left-hand panels show from top to bottom; the galaxy's isophotal magnitude at each fitted isophote, the ellipticity, position angle and centre of the fitted ellipses, all versus radius (in pixels on upper scale and arcsec on lower scale). For the outer isophotes where the S/N is too low to accurately fit ellipses the ellipse parameters are fixed to the mean of their "disk" region values, while the radius is increased in order to measure the isophotal magnitudes. These ellipses are marked with crosses on each plot. The top right-hand panel shows the surface brightness of each ellipse against radius along with a straight line fit to what is considered the "disk" region of the galaxy (marked with vertical parallel dashed lines). The lower panel shows the residuals from the linear fit. Note the length of the error bars indicate the random error at each point and the tick marks on each error bar indicate the systematic errors. The fitted disk parameters are used to calculate the total magnitude by extrapolation from the outer isophotal magnitude (marked on the upper left panel with a dashed line and dotted lines respectively). The lower right panel displays a grey scale of the galaxy superimposed with contours representing the I-band isophotes between 19 and 21.5 in steps of 0.5. The three solid ellipses marked on the image represent the inner and outer disk limits and the radius at which the sky level is reached. Nearby stars etc. have been masked out and replaced with intensity values from the fit plus noise, and are marked with dashed ellipses on the image.

have bar structures both of which can result in non-elliptical inner isophotes. An example of this effect can be seen in Figure 3.3.

The importance of the inclination in calculating the final Tully-Fisher parameters means the fitting of ellipses to the galaxy isophotes is a crucial step in the analysis. The IRAF package GALPHOT was used within the photometry reduction procedure for this purpose. GALPHOT was written as an extension to the ISOPHOT package by Wolfram Freudling and has the facilities for fitting of ellipses either interactively or in batch and reproducing model images from the results. GALPHOT uses the IRAF task *ellipse* from the STSDAS *isophote* package to fit each individual isophote, providing the initial ellipse for each isophote. The *ellipse* task uses the initial ellipse with semi-major radius, a to sample the image around an elliptical path, producing an intensity distribution, $I(a, e)$ as a function of the ellipse eccentric angle, e . This distribution can be represented by a Fourier series in terms of e .

$$I(a, e) = I_0(a) + A_1 \sin e + B_1 \cos e + A_2 \sin 2e + B_2 \cos 2e \quad (3.3)$$

Ellipse fits this function to the actual intensity distribution to produce the harmonic amplitudes; A_1, B_1, A_2 and B_2 , which represent errors in the ellipse position, position angle and ellipticity respectively. A correction to the parameters of the model ellipse are calculated from the harmonic amplitudes and the parameter with the largest deviation is corrected. This process is iterated until the corrections fall below a specified level or a maximum number of iterations are completed. This method is described in Jedrzejewski 1987 and is the same method used by the GASP package detailed in Han 1991.

Another important facility of GALPHOT is its ability to exclude regions of the image from the fitting process so that other objects or defects detected earlier in the image can be prevented from having an effect on the fitting.

The next section of the reduction shell script converts the image and information files to a format suitable for input into IRAF and GALPHOT. The GALPHOT ellipse fitting task, *sphot* (which calls *ellipse* as a subroutine) is then used to fit ellipses to

the target galaxy without the need for any interactive stage. At this point the GALPHOT task *markdisk* is then used to display a plot of the surface brightness, ellipticity, position angle and centre co-ordinates of the fitted ellipses against radius. This plot is then used as an "eyeball" test that the ellipse has produced reasonable results and to select a preliminary disk region where the fitted ellipse parameters remain relatively constant.

In the case of about 10% of galaxies, the fitting process fails. The ellipse fitting task can fail or produce incorrect results if the initial starting ellipse given to the task by the script is too different from the true isophote. This can happen if the galaxy has a very steep inner surface brightness gradient or strongly non-elliptical inner isophotes. In these cases the *sphot* task was repeated in interactive mode until an acceptable fit was made.

At this stage in the reduction, the image still contains objects, cosmic rays and other defects near to the galaxy that were masked out from the fitting process but would prevent accurate surface photometry from being done. In order to remove these contaminations the reduction script used the GALPHOT task *totmag* to create a model image from the fit results. The parameters used in creating the model image are taken directly from the ellipse fit as far as the outer radius of the selected disk region (see §3.2.5) at which point the mean disk pa, e , and centre (x and y) are used for the remaining ellipses.

Foreground stars and other objects in the images could then be removed from the image by replacing the masked out pixels with ones from the model image using the program *cppix*, written by the author and run as part of the *ephot2* shell script. The resulting "cleaned" image was then ready for surface photometry measurements. The image appearing in Figure 3.3 is an example of an image cleaned in such a way.

3.2.3 Surface Photometry

EPHOT, a galaxy surface photometry program written by John Lucey was used as part of the *ephot2* reduction procedure to produce accurate isophotal magnitudes and surface brightness profiles for our sample galaxies. After consultation with John

Lucey, EPHOT was altered slightly to produce error estimates using my own prescriptions. EPHOT reads in the parameters of the fitted ellipses which are then used as elliptical apertures for the surface photometry. For each input ellipse, a surface brightness in magnitudes/arcsec² is calculated along with an isophotal magnitude representing the integrated luminosity within that ellipse. The surface brightness, μ of a particular ellipse is defined as the median value of pixels around that ellipse minus the sky value.

$$\mu(a) = \langle I_i(a) - \overline{sky} \rangle_{\text{Median}} \quad (3.4)$$

Where $I_i(a)$ is the counts within the i^{th} pixel around an ellipse of major-axis a , and \overline{sky} is the fitted modal sky value output from *histpeak*. As each pixel has a finite area, the raw intensity $I_i(a)$ can be considered as a surface brightness in counts/pixel² and converted into magnitudes per arcsecond² using the known plate scale, photometric zeropoint, airmass etc as explained above. The surface brightness error $\delta\mu$ for each ellipse is taken as the error on the mean intensity of the pixels on that ellipse i.e.

$$\delta\mu(a) = \frac{\sigma_1}{\sqrt{n-1}} \quad (3.5)$$

Where σ_1 is the rms of the sky subtracted intensity and n is the number of pixels around the ellipse.

The error on the sky comes from a number of sources, as discussed above, which are hard to separate from each other. The two major contributors are the error on the measured sky level (dominated by large scale flat-fielding errors) and Poissonian statistical uncertainty connected with the detection of both the sky and galaxy photons. Both sources of error are considered to be uncorrelated and to combine in quadrature to produce the measured surface brightness error (Equation 3.5) thus:

$$\delta\mu = \sqrt{\sigma_{\text{Poisson}}^2 + \sigma_{\text{flatfield}}^2} \quad (3.6)$$

This is only an approximation but equating Equations 3.5 and 3.6 allows the separation of the error $\delta\mu(a)$ into systematic flat-fielding errors and the random photon counting errors. These two errors are represented separately in the surface brightness verses radius plots in Figure 3.3 and Appendix A. Other less important sources of error e.g. read-out

noise are also random and are included as part of the Poissonian error, σ_{Poisson} . The combined random errors are marked on each point by error bars, along with the systematic errors which appear as tick marks on each of the error bars (See Figure 3.3). Showing the errors in this way allows the systematic effect of sky errors on the surface brightness distribution (and total magnitude) to be easily assessed.

Isophotal magnitudes for each ellipse are produced by summing up the counts in every pixel within the ellipse and subtracting away the sky level.

$$E(a) = \sum_{i=1}^{N_{\text{pix}}} (I_i - \overline{sky}) \quad (3.7)$$

Where N_{pix} is the total number of pixels within and ellipse of major axis a . The raw intensity $E(a)$ being converted in I-band magnitudes using the photometric transformation outlined above in Equation 3.1. The error on the isophotal magnitude $E(a)$ is calculated using.

$$\delta E(a) = \sqrt{\sum_{i=1}^{N_{\text{pix}}} I_i + (N_{\text{pix}} \delta sky)^2} \quad (3.8)$$

Where δsky is the local sky error produced by *histpeak*. Again this error, $\delta E(a)$ is dominated by two main sources, the Poissonian error as represented by the first term and the sky error which is the second quantity added in quadrature. The Poissonian error is only important within the inner most ellipses, and for all the isophotal magnitudes published here, uncertainty in the sky level is the major source of error.

In order to improve our sky estimate further *ephoto3* extends the fitted ellipses out into the sky surrounding each galaxy. The EPHOT program is then used to measure the sky surface brightness around each ellipse in exactly the same way the galaxies surface brightness was measured. The photometry within these ellipses is then used by my own program *setsky* to estimate the size of local sky variations, $\sigma_{\text{flatfield}}$, which is calculated as the rms "sky ellipse" value. The error on the sky level is taken as the error on the mean ellipse value. Measuring the local sky value in the way as the galaxy magnitudes are measured provides our best estimate of the true underlying sky level and this value is used during

the final photometry stages and replaces the sky values, measured by *histpeak*, in the above equations (see §3.2.5 and Figure 3.2).

Variations in the measured sky level over the relatively small area covered by a galaxy are expected to be small, the variations measured with this method are typically $\leq 0.05\%$ which is less than a tenth of the typical global value for a frame. This explains why error estimates based on the global frame value tend to overestimate the expected errors on galaxy photometry and disagree with error estimates made from internal comparisons (see Willick 1991).

3.2.4 Calculating Total Magnitudes

The surface intensity distribution of a spiral galaxy can be approximated by the combination of a $r^{1/4}$ distribution representing the bulge light (see de Vaucouleurs 1948);

$$I(r) = I_e e^{-7.67((r/r_e)^{1/4} - 1)} \quad (3.9)$$

and an exponential distribution from the disk (de Vaucouleurs 1959):

$$I(r) = I_0 e^{-r/r_0} \quad (3.10)$$

Where r_e is the effective radius, the radius that encloses half of the total bulge light, and I_e is the intensity of the bulge at r_e . I_0 is the central intensity of the disk distribution and r_0 is the disk scale length.

The fitting of bulge plus disk models to the azimuthally averaged surface brightness profiles of spiral galaxies is fraught with a number of problems (See Knapen & van der Kruit 1991 and Schommer & Bothun 1987). The inner regions of the profiles are broadened by seeing and fits to the outer regions are sensitive to errors in sky subtraction and flat fielding. In addition a large fraction of spirals need the inclusion of a third lenticular component in order to produce reasonable fits. The majority of cases are also affected by spiral structure which can distort the profile and further complicate profile fitting with simple models. For our present work, de-convolving the components of our target galaxies is not necessary as we are only interested in calculating total magnitudes. The details on the relative contribution of disk and bulge may however prove useful at a later date when

a more sophisticated method of 3D analysis (e.g. Byun & Freeman 1995) could be attempted.

It is easy to show from Equation 3.10 that the surface brightness profile can be approximated by a linear equation thus.

$$\mu(r) = 1.086 \frac{r}{r_0} + \mu_0 \quad (3.11)$$

Where the intercept of the equation gives μ_0 , the central surface brightness of the disk distribution and the gradient provides the scale length. The outer regions of the late type spiral galaxies within our sample are completely dominated by disk light. Although they are subject to the effects mentioned above they all display largely linear outer profiles (see Figure 3.3). This allows the fitting of the simple linear function (3.10) to this outer region to produce values for μ_0 and r_0 . The total magnitude of the galaxy can then be calculated by extrapolating from the outermost fitted ellipse (Han 1991) using the equation:

$$I_{\text{total}} = I(r) - 2.5 \log(Q) \\ Q = 1 + q(r/r_0) \frac{b}{a} 10^{-0.4(I_t - I(r))} \quad (3.12)$$

where $I(r)$ is the magnitude within the outer fitted aperture and $\frac{b}{a}$ is the minor-to-major axial ratio of the disk.

$$q(x) = (1+x)e^{-x} \quad (3.13)$$

And

$$I_t = \mu_0 - 5 \log r_0 - 1.995 \quad (3.14)$$

The isophotal level μr of the isophotal radius $I(r)$ from which the extrapolation was made was at least $\mu r = 23.5 \text{ mag/arcsec}^2$ in all cases. At such faint limits any bulge light is negligible. Isophotal magnitudes and radii can also be calculated in a similar way (see Han 1991).

3.2.5 Disk Profile Fitting

The remaining interactive step of the reduction was to fit a straight line to the linear disk region of each target galaxy, giving values for μ_0 and r_0 , which were then used to calculate a total magnitude for all galaxies in our sample

The shell script *ephot3* executes *diskfit* which was written by the author and gives full control over how the disk surface brightness distribution is fitted. The display of *diskfit* is similar to Figure 3.3, where graphs of surface brightness, position angle, ellipticity and centre against radius are plotted for all ellipses. The user selects the disk region using a cursor and *diskfit* displays the selected region on all the graphs and plots the nearest ellipses overlaying an image of the galaxy. A linear fit within the marked region to the surface brightness distribution is displayed along with residuals. The limits of the fitted region can then be adjusted until a satisfactory fit is obtained. As well as producing values for μ_0 and r_0 , *diskfit* also calculates mean disk parameters using all the ellipses within the selected disk region.

As repeat measurements showed no variation of μ_0 and r_0 with seeing, the weighting scheme of Han (1991) was not adopted. Repeating the analysis on the same images with differing estimates of the sky level, showed the values of μ_0 and r_0 to have a systematic dependence on the sky value as expected. This highlights the importance of the correct estimation of the sky level and minimising flat fielding errors as detailed in 3.2.3.

3.2.6 Final Photometry Results

The last stage of the photometry reduction was the running of my *ephot4* shell script. This script first repeated the measurement of each galaxy's surface photometry by re-running EPHOT. The mean disk parameters produced by *diskfit* were used to correct the photometry in the outer most apertures input into EPHOT, by fixing the position angle and ellipticity of each aperture to the mean disk values. The final results of the photometry and fitting could then be displayed (see Figure 3.3) and stored by another of my programs *diskplot*.

The output results from *diskplot* can be seen in Figure 3.3 and Appendix A. On each plot the ellipticity, position angle, ellipse centre and surface brightness are shown for each fitted ellipse against the major axis of each ellipse. The selected disk region limits are marked on all of the graphs and the residuals from the linear surface brightness fit are plotted. The effects on a straight line fit of the sky

varying within its estimated errors are also marked on the fit. The outer most isophotal magnitude and calculated total magnitude are marked on an isophotal curve of growth, displaying the isophotal magnitude of within each ellipse against isophotal radii and providing a check of the total magnitude extrapolation. A greyscale image of the galaxy is produced overlaid with the inner and outer disk ellipses to provide an "eyeball" check of the ellipse fitting and the removal of foreground stars etc. Overall, the output from *diskplot* allows evaluation at a glance of the quality of the surface photometry for each galaxy. All of the measured and calculated parameters for each galaxy along with their respective errors are then stored ready for further analysis.

3.3 Photometric Errors

3.3.1 Internal Photometry Errors

The uncertainty in the photometry for each galaxy depends on many things, some vary from image to image such as poor sky subtraction or cosmic ray removal. Other sources vary from galaxy to galaxy. Ellipse fitting errors, for example, will depend on the individual irregularities which are a feature of spiral galaxies. Variations from observation to observation such as weather conditions, seeing and telescope pointing also have a major effect which can also depend on the season of the observing run.

These errors are hard to calculate and tend to be larger than the formal errors produced by the reduction process. The best way to get an accurate estimate of the combined effect of all the errors involved within the reduction process is to make repeat measurements. By reducing and comparing repeat images of the same galaxies over the entire observing period an internal error can be calculated for all of the measured parameters. These errors are considered to be more representative of the true variation in measured values from observation to observation and from galaxy to galaxy.

We made around 40 repeat measurements over our two observing runs, 24 of which both measurements were considered reasonable quality, and the calculated internal errors from these are displayed in Table 3.2. The internal (and external) errors were calculated as the mean standard deviation of each

Table 3.2. A summary of our mean formal, internal and external error estimates for the galaxies in our main sample. Column headings are: The type of error estimate, the number of galaxies considered, N and the rms deviations for each of the main photometric parameters, isophotal magnitude, $I_{23.5}$, total magnitude, I_{total} , isophotal major axis, $a_{23.5}''$, ellipticity, e , position angle, pa , scale length, R_s , and central surface brightness, μ_0 . External comparisons were made with 32 measurements of 25 independent galaxies from, (Bothun & Mould 1987), (Bernstein et al. 1994) and (Han 1991). Errors are also given as a percentage of the sample mean parameter value where applicable.

Error Estimate	N	Typical RMS Errors						
		$\sigma_{I_{23.5}}$	$\sigma_{I_{\text{total}}}$	$\sigma_{a_{23.5}''}$	σ_e	σ_{pa}	σ_{R_s}	σ_{μ_0}
Mean Formal Errors	202	0.033	0.048	1.3	0.019	1.5	1.1	0.465
Internal Estimate	25	0.024	0.030	1.4	0.043	3.7	0.9	0.408
Mean Percentage Error				5.8	7.7	3.8	16.4	
External Estimate (Bothun)	8	0.031	0.036	-	0.025	-	-	-
Mean Percentage Error					4.5			
External Estimate (Bernstein)	12	-	0.072	-	0.060	2.6	-	-
Mean Percentage Error					10.7	2.7		
External Estimate (Han)	13	0.043	0.043	-	0.035	-	-	-
Mean Percentage Error					6.3			

set of repeat measurements (See Courteau 1992 for detailed discussion). The internal agreement for all of the parameters is good and compares reasonably with those given in, for example, Courteau (1992). Details of all of the repeat observations are given in Appendix A.

3.3.2 External Photometry Errors

Another test of the accuracy of our measurements and reduction procedures is to compare similar measurements made by other authors of the same galaxies. These comparisons not only consider the variations in conditions over different observing runs but also differences due to instruments, telescopes, reduction methods and any subjective input by the observers themselves. Because of this, these external comparisons are the best estimates of the true accuracy to which these photometric parameters can be measured. See Table 3.2 for a summary of the comparison with the work of three different authors using 25 independent galaxies. Details of the comparisons are given in Appendix A and our magnitude estimates are plotted against their estimates in Figure 3.4.

Our isophotal magnitudes compare well with the two authors that published isophotal values. There are no significant systematic offsets and rms

deviations are low and consistent with our internal estimates. Total magnitudes also compare well, Bernstein et al. (1994) and Han 1991 (1991) display no significant offset. A comparison with Bothun (1987) does show a significant offset of -0.08 ± 0.02 . This could be due to a difference between our respective methods of calculating the total magnitudes. Bothun & Mould (1987) extrapolate the aperture-magnitude relationship for each of the galaxies in order to calculate I_{total} , whereas the method used by ourselves and the authors cited in Table 3.2 involves extrapolating the disk surface brightness distribution as outlined above. The agreement between all these published total magnitudes is impressive considering the typical error in our photometric zero points is 0.01 magnitudes and the extrapolation to total magnitudes involves the step of fitting to the subjectively selected disk region.

The other important photometric parameters, ellipticity and position angle, also display good general agreement with typical rms deviations of less than 10% in both cases. The internal and external ellipticity errors are larger than expected, considering the small errors involved with measuring the ellipticity of the disk isophotes (a typical error is 0.019) and the typical rms variations of the ellipticity over

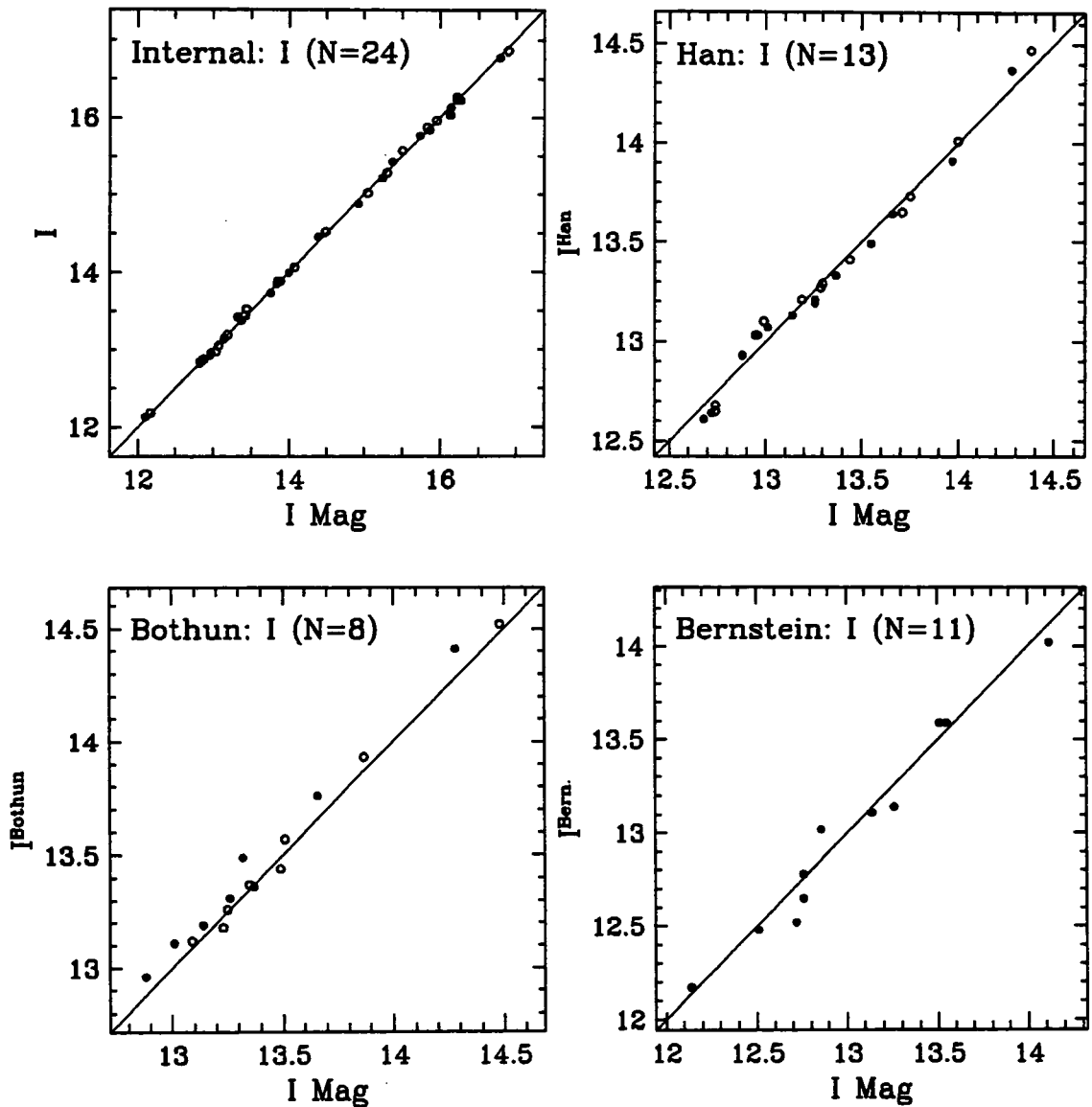


Figure 3.4: Four plots showing internal and external comparisons of measured isophotal (open circles) and total I magnitudes (filled circles). Top Left: An Internal comparison of 24 magnitude measurements shows a scatter of $\sigma_{23.5} = 0.03$ and $\sigma_{I_{\text{Total}}} = 0.04$. Top Right: A comparison of 13 measurements of $I_{23.5}$ and I_{Total} with Han (1991) displays no significant offset and rms deviations of 0.06 for both magnitudes. Bottom Left: A similar comparison with Bothun & Mould (1987) using 8 galaxies displays deviations of $\sigma_{23.5} = 0.04$ and $\sigma_{I_{\text{Total}}} = 0.06$. The total magnitudes do show a significant offset of -0.08 ± 0.02 possibly due to their use of aperture magnitudes. Bottom Right: Comparison with 11 total magnitude measurements by Bernstein et al. (1994) gives $\sigma_{I_{\text{Total}}} = 0.10$. The results compared here are tabulated in Appendix A along with comparisons of other photometric parameters.

each galaxy's disk region, normally around 0.018. Combining the two in quadrature produces an expected error of 0.026 which is about half the internal and external error estimates. The remaining source of error is attributed to the variations involved with the subjective selection of a disk region for each galaxy. For the remainder of this work the measured disk ellipticity is assumed to have an average error of 0.040.

There is a small offset between position angles measured by Bernstein et al. (1994) and ourselves of about -5 degrees. This can be attributed to a slight difference in alignment of the CCD cameras on the respective telescopes. A further comparison between the measured position angle of our sampled galaxies and the values in the APM catalogue, (See Maddox et al. 1988) which probably provides a better estimate of true north, shows an offset of -3 degrees. This should be considered by anyone attempting to repeat our spectroscopic measurements.

The error estimates given here will be included in the complete error budget for our sample in chapter 5, at which point their relative importance in contributing to the scatter of the TF relation will be discussed.

3.4 Data presentation

Detailed listings of all the photometric data is given in Appendix A along with full external comparisons.

References

- Argyle R. W., 1988, ING User Manual No. XVIII, RGO, Cambridge UK
- Bernstein G., Guhathakurta P., Raychaudhury S., Giovanelli R., Haynes M. P., Herter T., Vogt N. P., 1994, AJ, 107, 1962
- Bothun G. D., Mould J. R., 1987, ApJ, 313, 629
- Byun Y. I., Freeman K. C., 1995, ApJ, 448, 563
- Courteau S., 1992, Ph.D. thesis, University of California, Santa Cruz
- Cousins A. W. J., 1976, MNRAS, 81, 25
- de Vaucouleurs G., 1948, Ann. d'Astrophys., 11, 247
- de Vaucouleurs G., 1959, ApJ, 130, 728
- Draper P. W., 1993, CCDPACK data reduction package, Starlink User Note 139.0, CCLRC / RAL
- Han M. S., 1991, Ph.D. thesis, California Institute of Technology, Pasadena, California.
- Jedrzejewski R. I., 1987, MNRAS, 226, 747
- Knapen J. H., van der Kruit P. C., 1991, A&A, 248, 57
- Landolt A. U., 1983, AJ, 88, 439
- Maddox S. J., Loveday J., Sutherland W. J., Efstathiou G., 1988, in Large-scale structures in the universe - Observational and analytical methods. Springer-Verlag, p. 90
- Schommer R. A., Bothun G. D., 1987, AJ, 92, 60
- Willick J. A., 1991, Ph.D. thesis, University of California, Berkeley

Chapter 4

Spectroscopic Observations and Data Reduction

Abstract. In this chapter I present the spectroscopic observations and reduction methods used to produce rotation curves for the galaxies within our sample. Details are given of the reduction procedure and emission line fitting as well as the folding of the resulting curves to find the kinematic centre of each galaxy. A number of different rotation velocity parameters are measured from these curves for consideration in the following chapter.

4.1 Spectroscopic Observations

The spectroscopic observations for this project were undertaken using the Isaac Newton Telescope (INT) on La Palma. The observations were made over two seven day periods, the 21st – 27th May 1993 and 20th – 26th August 1993, at the same time as our photometric measurements were being made on the JKT.

The INT has a 2.54 metre diameter primary mirror with a focal ratio of $f/2.94$. The intermediate-dispersion spectrograph (IDS) was used for all our observations and is mounted at the $f/15$ Cassegrain focus. The IDS R1200Y grating was used, set with blaze to collimator at a grating angle of 46.9° this combined with the 235mm camera to give a dispersion of 35.2 \AA/mm . These settings combined with the EEV5 detector head to give a 0.89 arc-sec/pix plate scale along the slit and dispersion of 0.79 \AA/pix over the wavelength range of 6200 \AA to 7100 \AA which includes the wavelengths of the $H\alpha$ and $[\text{NII}]$ emission lines from our target galaxies (all with $z < 0.05$). The slit width was set at 300 \mu m (1.65 arcsec). This resulted in a typical resolution of 1.9 pixels FWHM. To remove the effect of any higher order spectra, a GG495 red-pass filter was utilised for all observations (See Argyle 1988 for further details).

The EEV5 head contains an EEV 05-30 CCD chip with very similar characteristics to the head and chip used on the JKT (See Chapter 3.1) with a low

read out noise of 6.6 ADU and a flat response (less than 3% rms). The low readout noise is important for $H\alpha$ rotation curve measurements as the fitting of the weak emission lines in the low surface brightness outer regions of each galaxy is limited by the noise level.

Each observation was made with the spectrograph slit aligned along the major axis of the target galaxy with a typical exposure time of a 1000 sec. Where possible observations were made of galaxies observed on the JKT on a previous night. The CCD images aided in slit alignment and in rejecting objects with poor morphology which could not be discerned from the survey plates. In cases where we were uncertain about the galaxy type, short 500 sec exposures were made to check for extended $H\alpha$ emission which could then be followed up with longer exposures if needed.

Some lower surface brightness galaxies proved to have weak, but promising, well extended emission lines and these were followed up with longer 1500 sec and 2000 sec exposures. Acquisition proved to be a major overhead due to the time needed to detect some of the lower surface brightness objects on the INT TV camera. In some cases, the time taken to align the slit on the galaxy was comparable to the actual integration time. Typically data on twenty galaxies could be gathered on a clear night which matched the rate produced on the JKT pretty well.

In order to de-bias, flat-field and wavelength calibrate each frame, at least two CuNe arc lamp exposures and two tungsten lamp exposures were taken each night together with twilight sky frames at the beginning and end of the night. A number of bias frames were measured as well over the course of each observing run. The weather during the first observing run in May was far from ideal with about 30% of telescope time being lost due to bad weather or faults. For the second run in August this figure improved to about 20%.

The whole reduction process detailed below was then repeated for all of the 244 galaxy spectra taken over the two observing runs. The colour-magnitude and ellipticity selection process outlined in chapter 2 was deliberately relaxed in order to ensure enough spiral candidates made it into the sample. However, this relaxed selection meant there was considerable contamination of our sample from S0 type galaxies. Edge-on S0s can be confused with edge-on spirals especially when viewing the lower quality photographic plates. Once a spectrum had been taken, any S0 galaxies were easily rejected as S0s have little or no star formation, resulting in no measurable emission lines. Some of the spectra were rejected for this reason ($\approx 20\%$), and another 30% were rejected due to very poor signal-to-noise or incorrect slit alignment. Another 10% of the galaxy sample was rejected because any star formation they displayed was not extended outside their galactic core. The lack of emission lines outside their core means that any rotation curve measured has a poor extent and is unsuitable for this study. This left approximately 80 galaxy spectra suitable for emission line fitting in order to produce rotation curves for each galaxy.

4.1.1 Initial Data Reduction

The initial reduction of the spectroscopic CCD data was done in a similar manner to the photometric data using the same CCDPACK software (see Draper 1993 and Chapter 3.1.1). The bias frames measured during each run were compared to check for consistency and then combined to form a median master bias frame using the *make-bias* task within CCDPACK. This image represents the digi-

tised value of the offset voltage introduced by the readout electronics to ensure the linear response of the analogue-to-digital converter. The frame also contains structure introduced by the electronics that, although at low level, can degrade the data. The bias frames, like all images, also contain random readout noise which is minimised by taking the median of many frames.

The modern EEV 05-30 and its accompanying electronics produced very little structure. There is a 0.03% gradient in the bias level across the 350 rows of the windowed portion of the CCD chip, with a 0.008% spike in the bias level about every 10 rows. The bias level (≈ 4130 ADU) was constant for the 1270 columns apart from a 0.01% rise in the level for the first 200 columns. The bias level and structure could then be removed from all frames by first scaling the master bias frame by the median level of the over-scan regions in common with each image, and then subtracting the scaled bias frame from each image. This process was done by the *de-bias* CCDPACK program and was tested on an individual bias frame resulting in a flat image containing only Gaussian read out noise with a standard deviation of 6.6 ADU.

Next each image was corrected for the slight variations in pixel sensitivity which all CCDs exhibit and which contribute to the apparent noise in each spectrum. Every night at least one exposure of a bright tungsten lamp was taken, and the median frame of all the exposures for one run was used to form a map of the variations in pixel response over the EEV chip. The high counts in the tungsten image meant that noise contributions from Poisson statistics and read-out noise become insignificant and the median of several frames further reduces any noise. The median tungsten lamp spectrum is then divided by a smoothed version of itself to remove the spectral distribution of the tungsten lamp which results in a flat master pixel response frame. A histogram of the pixel values within this frame shows that greater than 98% of the pixels in the frame have a correction of less than 10%.

Each spectral image was then corrected by dividing by the normalised master response frame. This was then tested on a few twilight sky frames which

displayed the expected drop in the image noise of 10%. An example of this reduction in the image noise can be seen in Figure 4.4.1, which shows a reduction in the visible image noise between the "raw" and reduced frames.

The next stage of the reduction was the removal of the characteristic shape introduced into each spectrum by the uneven illumination of the spectrograph slit. This was done by dividing each spectrum by a master vignetting frame made from the median of the twilight sky frames, the twilight sky providing an evenly illuminated light source with which to measure the slit vignetting function. The median image frame was divided by its spectral distribution and then collapsed to a single column. This 1-D slit vignetting distribution was then smoothed, normalised and grown out to form the final master image. The slit illumination function can then be removed from each image by dividing by the master frame. Twice during the two runs, dust collected on the slit during the night. This had the effect of changing the slit vignetting function for that night. In those cases smoothed versions of just one night's twilight sky exposures was used to form the vignetting correcting frame and was used to divide out the effects of the dust.

At this point the CCD images were trimmed down in size to remove the over-scan regions and a ten pixel wide region around the edge of the image where the vignetting correction was too large. A typical example of a galaxy spectrum at this stage in the reduction can be seen in the top of Figure 4.4.1.

4.1.2 Wavelength calibration

After the de-biasing, flat-fielding, vignetting correction and trimming steps were completed each frame had to be wavelength calibrated. Each frame needs a calibration map that, for each row, will map column numbers to wavelength in Angstroms. Typically three exposures were made of a copper-neon arc lamp each night, the wavelengths of the emission within the CuNe spectrum are well known, and from these a calibration map can be made. This stage of the process was done using the *arc*, *iarc* and *iscrunch* commands within the STARLINK FIGARO data reduction package (see Meyerdierks 1995).

In the first step, a 1-D spectrum is formed from the mean of several rows from the middle of each arc spectrum image. This spectrum is input into the *arc* FIGARO task; *arc* provides an easy way of identifying all the emission lines in the spectrum and fitting the pixel-to-wavelength calibration function. In all cases the best fit to the pixel vs. wavelength data was a third order polynomial, with only three parameters needed to produce residuals of less than 0.01\AA (0.5km s^{-1} at H α). These parameters were then read into the *iarc* program which attempts to fit the same polynomial to every row of the spectrum. The initial fit is used as a first guess which is then shifted slightly in order to best fit the arc spectrum within each row.

The next step of the process required the re-binning of the data into a new image with a linear wavelength axis using the *iscrunch* or *iscruni* tasks. The *IAR* file produced by *iarc* which contains the coefficients of the fitted polynomials for each row is used by *iscrunch* to remap the data to a new pixel grid. In the cases where a spectrum was taken between two arc exposures the *iscruni* program was used which interpolates between the two functions to perform an optimum wavelength calibration

4.1.3 Sky Subtraction

The final stage in the initial reduction of each image was the removal of sky emission lines from the spectrum. A sky spectrum was made from each frame by taking the median of the lower and higher image rows that only contain sky to form a spectrum. A sky spectrum image was then made by growing the sky spectrum which in turn was subtracted from the original, leaving a reduced galaxy spectrum, free from sky lines, and ready for emission line fitting (See Figure 4.4.1). Any remaining cosmic rays in the region of the emission lines which could effect the line fitting were also removed at this stage.

4.2 Rotation Curve Fitting

To produce a rotation curve and recessional velocity for each galaxy, the wavelength of the emission lines within each galaxy spectrum must be compared with their rest frame equivalents. The wave-

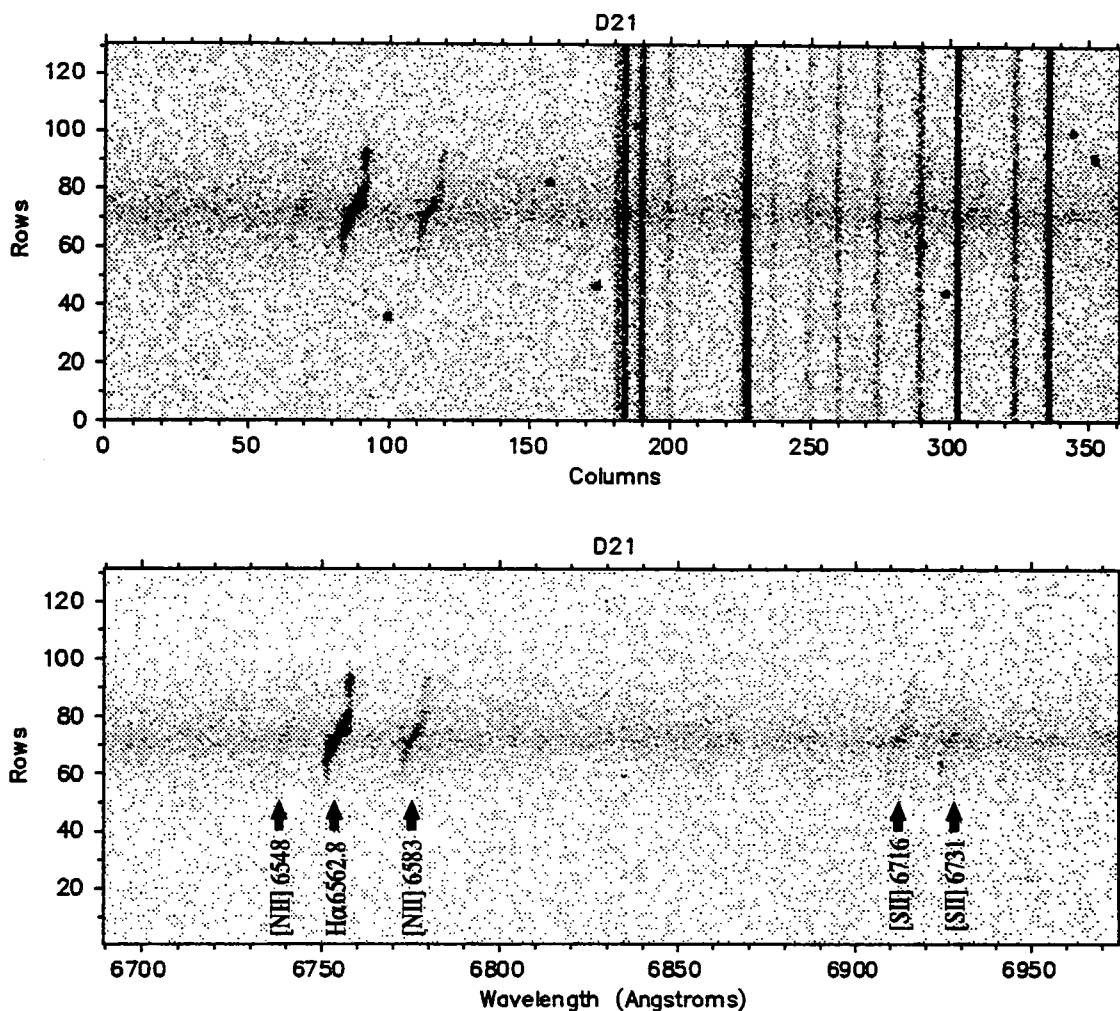


Figure 4.1: Top Image, An example of a “raw” galaxy spectrum. The curved H α and N[II] emission lines can be seen in the left portion of the image along with the faint horizontal continuum light. The vertical lines on the right are emission lines from the night’s sky and the dark points are caused by cosmic rays hitting the CCD. Lower Image, The full reduced version of the same frame, once the sky has been subtracted from the frame and the cosmic rays removed all five of the emission lines can be seen clearly. Also notice the slight reduction in noise compared to the original image which is the result of the flat-fielding process.

length of the centre of each line, λ , was found by fitting a Gaussian function to the emission peak. This value along with the rest frame wavelength, λ_0 and the speed of light, c , was used to calculate the observed velocity, V_{obs} , thus:

$$V_{obs} = \left(\frac{\lambda - \lambda_0}{\lambda_0} \right) c \quad (4.1)$$

The observed velocity was then corrected to allow for the rotation and orbital motion of the Earth. These heliocentric corrections are small, ranging

from -23.0 km^{-1} to 24.0 km^{-1} and were always less than 0.5%.

4.2.1 Emission Line Fitting

The emission line fitting and calculation of velocities were produced using the TWODSPEC extensions to the FIGARO data reduction package (See Wilkins 1994). The TWODSPEC task *longslit* provided an entire procedure for fitting the lines in each row of the image, rejecting low S/N fits to produce a final rotation curve. Using *longslit*, two “tramlines”

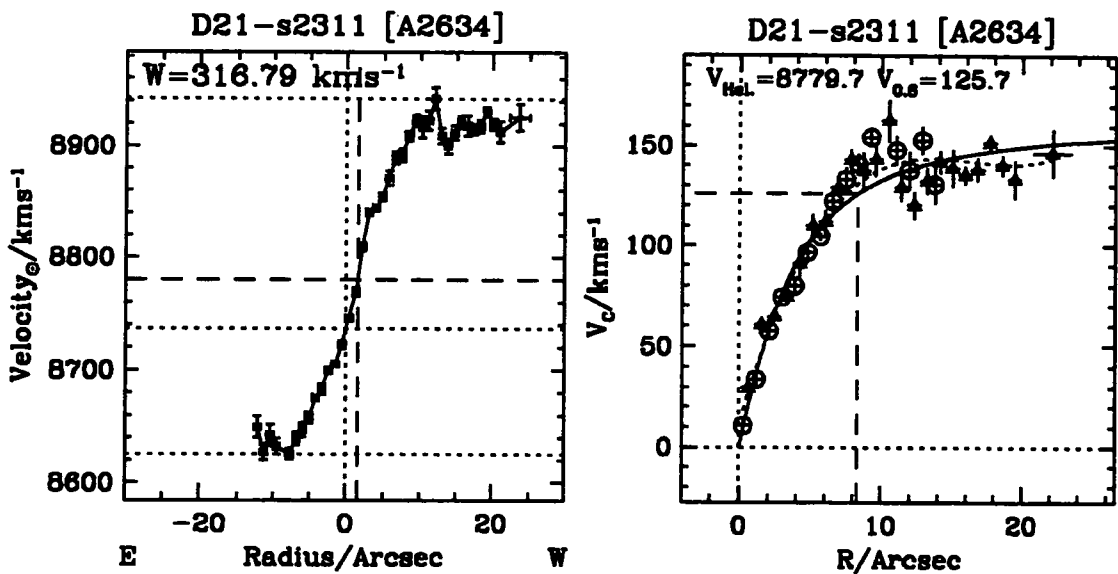


Figure 4.2: Left Panel: An example of a $H\alpha$ rotation curve generated from the spectrum shown in Figure 4.4.1. The heliocentric radial velocity of each point on the galaxy is plotted against radius in arcseconds. The vertical dotted line represents the optical centre of the rotation curve where the emission line crosses the peak in the continuum emission. The dashed vertical line shows the kinematic centre found by folding the curve, the two central horizontal lines show the different radial velocities which would be attributed to these centres. This shows that finding the correct centre is crucial in giving the galaxy a correct radial velocity. The top and bottom horizontal dotted lines show the maximum and minimum velocities within the curve and demonstrate how a velocity width parameter based on the difference between the two is affected by noise. Right Panel: The same rotation curve is displayed after being folded in such a way as to maximise the symmetry between the two halves of the curve. The solid curve is the result of the three parameter fitting function and the dotted curve is the smoothed spline fit. The dashed line marks $V_{0.6R_{opt}}$, the interpolated rotation velocity at 0.6 of the optical radius.

were placed on the image to select the region of columns and rows that contained a single emission line, *longslit* then proceeded to fit a Gaussian function to the strongest peak within each row of the marked region.

The velocities and errors calculated from each fitted line were then corrected to the heliocentric frame, output to a file and later plotted using the SM plotting package (See Lupton & Monger 1994) to produce a rotation curve (See Left panel of Figure 4.2). At this stage a signal to noise cut was also applied to the data: within *longslit* a tolerance was set on the error, width and height of each fitted line to reject any missed cosmic rays or fits with velocity errors greater than $\approx 20\text{kms}^{-1}$.

All the rotation curves displayed within this thesis were created from fits to just the $H\alpha$ emis-

sion line within each spectrum. I experimented with adding in the results of fitting of the second strongest, N(II) 6583Å emission line, but this resulted in only a small reduction in the errors of fits to the brighter inner emission regions of each spectrum. The Nitrogen line rarely extends as far out as the $H\alpha$ line and so cannot help in reducing the errors on the outer points in each rotation curve. In general the other four emission lines were much weaker than the Hydrogen $H\alpha$ line, and so adding in fits to these lines had the effect of adding more noise to the final measurement without adding any worthwhile signal.

A cross-correlation technique for calculating the velocities, similar to the methods employed by other authors (e.g. Courteau 1992), was also considered but proved to be impractical. The cross-correlation

method needs a suitable template spectrum to correlate with each row and this proves difficult in practice as the relative line strengths within the spectrum often change across a galaxy's disk and from galaxy to galaxy. Even with a suitable template this method suffers from the same problem as fitting multiple Gaussians since the velocity measured and its associated errors tend to strongly depend upon the H α line peak, with the rest of the spectrum having the effect of adding noise without adding significant signal.

4.2.2 Forming The Rotation Curves

A typical final rotation curve produced by this process is shown in Figure 4.4.2, this curve was produced from the spectrum shown in Figure 4.4.1 and represents a typical rotation curve from our data set. The brightest point of the galaxy's core, was measured for each galaxy by fitting a Gaussian function to the distribution of the continuum light either side of the emission line. The position of this peak in the light distribution along the slit was considered the optical centre for each galaxy and is marked on the rotation curves.

Each rotation curves provides considerable information on the kinematic nature of each galaxy. In addition to an indication of a maximum rotation speed which can be parameterised in a number of ways for traditional TF studies. Each curve gives information on the velocity gradient within each galaxy, the radius at which the velocity turn-over occurs and gives an indication of any substructure or asymmetries present.

The final stage in the production of the rotation curves was to fold each curve about its centre so that the data for each side overlapped. This was done using a program written by the author, *rotcurve*, which folds each rotation curve around a trial centre, starting with the optical centre, and then calculates a weighted mean difference between each half of the curve. *Rotcurve* then iterates about this point until the centre of reflection for each curve is found which minimises the difference between each half of the curve.

This method worked for all of the extended rotation curves in our sample even though finding the

kinematic centre in this way does assume symmetry for each curve. The right-hand panel of Figure 4.4.2 shows an example of a folded rotation curve output from *rotcurve* and is a folded version of the curve in the left-hand panel. Folding and plotting each curve in this way has the advantage of highlighting any real asymmetries or structure along with providing the kinematic centre and evening out the noise from any points with large errors.

As well as folding each curve, *rotcurve* also provides fits of two different functions to each curve, allowing interpolation of the rotation velocity for each galaxy to any radius and the parameterisation of the shape of each curve. One method of interpolation is by using a smoothed cubic spline fit, this has the advantage of following any systematic variations in the velocity due to real spiral structure in the target galaxies. The fact that the folded curves are fairly continuous and the spline fit is smoothed means the function is well behaved, following the data closely and remaining insensitive to noise.

The second method of interpolation involves the use of a chosen fitting function as opposed to the arbitrary functional form of the spline fit. The simple three parameter function used to fit for the circular rotation velocity, V_c at radius r was:

$$V_c(r) = \frac{V_{max}r}{(r^\alpha + r_0^\alpha)^{\frac{1}{\alpha}}} \quad (4.2)$$

Where V_{max} is the maximum rotation velocity reached at infinity, r_0 is a characteristic radius at which the function turns over after its initial rise and α controls how sharp the turn-over portion of the curve is. For typical rotation curves displaying clear turn-overs in velocity, V_{max} equals the maximum rotation velocity, r_0 ranges from 0.1 to 0.8 as a fraction of the maximum extent of each curve and α can vary between 0.5 and 5 with an imposed maximum of 8 (See Figure 4.4.2 and Appendix B).

This method has the advantage of providing a smoothed interpolation of the rotation velocity and produces a simple parameterisation of each curve. What these parameters indicate in terms of galaxy kinematics will be discussed in Chapters 5 and 6. The typically small gaps in the folded rotation curve data means any interpolations made are small, and

Table 4.1. A summary of our mean formal, internal and external (compared with Courteau 1992) error estimates for our H α rotation curve velocity measurements. Column headings are: The type of error estimate, the number of galaxies considered, N and the rms deviations for each of the main velocity parameters. Three ways of measuring the recessional velocity were tried, V_r^{MN} , which is the mean mid point of the three rotational velocity measurements, V_{max1} , V_{max2} and V_{max3} (c.f. Courteau), V_r^{OPT} the velocity measured at the peak of the continuum, i.e. the optical centre of each galaxy, and V_r^{KC} the velocity measured at the kinematic centre of the galaxy, calculated from each folded rotation curve. Rotational velocities were measured as the difference between mean three highest and lowest points on the curve, V_{max} , between the highest and lowest points, V_{max1} , the second, V_{max2} and the third highest/lowest velocities, V_{max3} . $V_{0.6R_{OPT}}$ is the interpolated rotation velocity at a fraction of the optical radius fitted to the folded version of each curve. A velocity measured between two points judged by eye on each curve, V_{eye} , is also shown for comparison purposes. The external HI comparisons were made using 37 measurements made by other authors, 17 galaxies from Bernstein et al. 1994 and 20 from Willick 1991.

Error Estimate	N	Typical RMS Errors								
		V_r^{MN}	V_r^{OPT}	V_r^{KC}	V_{max}	V_{max1}	V_{max2}	V_{max3}	$V_{0.6R}$	V_{eye}
Mean Formal Errors	147	3.1	5.8	2.6	6.1	11.2	10.2	9.7	6.8	-
Internal Estimate	27	17.3	25.3	21.3	11.5	15.4	11.8	11.3	8.2	26.9
Percentage Error		0.2	0.3	0.2	8.3	10.3	8.6	8.8	8.8	9.9
H α External	10	37.6	31.8	-	11.2	-	-	10.0	-	29.6
Percentage Error		0.4	0.4	-	8.1	-	-	7.8	-	10.9
HI ΔH_{50} External	37	27.7	53.9	34.5	21.0	17.3	20.3	27.4	-	17.3
Percentage Error		0.3	0.6	0.3	15.2	11.6	14.8	21.3	-	15.4

results from both the spline and fitting function methods agree well.

The three parameter fitting function has fewer degrees of freedom than the spline function and as a result is less sensitive to structure within the curves. For this reason the fitting function tends to better represent the underlying rotation velocity and was the preferred method. The results from these two approaches and different ways of measuring, V_{max} and other velocity related parameters from the rotation curve data will be discussed in chapters 5 and 6.

4.3 Spectroscopic Quality

Finally each rotation curve is assigned a quality number, Q, this number represents a subjective view of the signal-to-noise and "good behaviour" of each curve. A low noise curve with good extent, no large asymmetries and displaying a clear turn-over is given a quality, Q=1. Curves that show a turn-over but have a low signal-to-noise or show some asymmetry are assigned Q=2. And curves which show no clear turnover or large asymmetries are given Q=3. In the case of some galaxies the rotation curve had

such poor extent only a redshift for the galaxy could be estimated and no curve could be produced.

4.4 Internal and External Errors

4.4.1 Internal Errors

As with the photometric observations the uncertainty in the final velocity measurements comes from many sources, some of which are hard to assess and result in the true errors tending to be larger than the calculated formal errors from the emission line fits. Small movements within the spectrograph as it moves with the telescope across the sky causes the spectrum to shift by small amounts over the detector. This effect coupled with small variations in focus and errors in the calibration resulted in the calibration arcs showing typical differences of 0.03 rms/pix ($\approx 1.1 \text{ km s}^{-1}$) over the course of each observing run, and the variations are expected to affect each galaxy spectrum in the same way.

Fitting the rotation curves out to as large a radius as possible meant that a large fraction of the line fits were done at a very low signal-to-noise. Because of this both CCD read-out noise, cosmic ray removal

and sky subtraction all added to the errors on the measured velocities. The final generation of rotation curves also adds to the errors. Folding and fitting the rotation curve can be affected by noisy points, structure and asymmetries within the curve which also adds to the errors on the measured velocities.

In order to assess the true errors on the measured rotation velocities and redshifts, measurements of some galaxies were repeated during each run. Over both observing runs 35 repeat spectra were made, but as in some of these cases the second observation was made because the initial one had poor signal-to-noise, only 27 were suitable for comparison. The internal agreement for all the velocity parameters measured as the mean standard deviation of the repeated observations (See §3.3.1) is summarised in Table 4.4.1. Full details of the repeat observations are given in Appendix B. It can be seen from Table 4.4.1 that the internal error estimates are consistent with the mean formal errors produced by the fitting process.

4.4.2 External Errors

In order to further check the accuracy of our spectroscopy we compared our measurements with similar ones made by other authors found in the literature. As was discussed in the previous chapter, such external comparisons give a more realistic estimate of how accurately such quantities can be measured given the differences in the instruments, telescopes and reduction methods presently used. See Table 4.1 for a summary of a comparison between this work and the H α measurement of Courteau 1992. Unfortunately there are only ten galaxies our samples have in common, but given the small sample the agreement is reasonable and consistent with a combination of Courteau's internal error estimates and our own. The mean difference between Courteau's and our recessional velocities is $37 \pm 28.8 \text{ km s}^{-1}$ with a mean standard deviation of $\sigma_v = 37.6 \text{ km s}^{-1}$. The mean difference between the Courteau's rotation velocity parameter, V_{max} , (the difference between the mean of the three highest and lowest points in the rotation curve) and our own measured in the same way was $8.0 \pm 9.9 \text{ km s}^{-1}$ with $\sigma_{V_{max}} = 22.3 \text{ km s}^{-1}$.

To further establish the external errors on our rotation curve measurements a comparison was also made between our measured velocities and those made using HI 21cm line measurements by Bernstein et al. (1994) and Willick (1991). There are 37 measurements in common between our sample and a combined sample of their measured recessional velocities and rotation widths (see Table 4.4.1). The HI line widths were measured at 50% of the mean line flux in both samples. The radio measurements show good overall agreement with our own data, the mean difference between the velocities was $10.1 \pm 12.2 \text{ km s}^{-1}$ with $\sigma_v = 27.7$. The HI velocity widths were scaled to match typical optical values by dividing by a value between 1.02 and 1.13 (see Bernstein et al. 1994), resulting in a difference of $-0.1 \pm 12.3 \text{ km s}^{-1}$ with a RMS error of $\sigma_{v_{max}} = 21.0$. Further details of these comparisons are given in Table 1 Appendix B.

The error estimates given here will be included in the complete error budget for our sample in chapter 5, at which point their relative importance in contributing to the scatter of the TF relation will be discussed, and the most suitable rotation velocity parameter selected.

4.5 Data presentation

Detailed listings of all the spectroscopic data is given in Appendix B along with full details of the external error analysis.

References

- Argyle R. W., 1988, ING User Manual No. XVIII, RGO, Cambridge UK
- Bernstein G., Guhathakurta P., Raychaudhury S., Giovanelli R., Haynes M. P., Herter T., Vogt N. P., 1994, AJ, 107, 1962
- Courteau S., 1992, Ph.D. thesis, University of California, Santa Cruz
- Draper P. W., 1993, CCDPACK data reduction package, Starlink User Note 139.0, CCLRC /RAL
- Lupton R. H., Monger P., 1994, SM 2.3.8, Starlink MUD, CCLRC /RAL
- Meyerdierks H., 1995, FIGARO, A general data reduction system, Starlink User Note 86.10, CCLRC /RAL
- Wilkins T. N., 1994, TWODSPEC, Some Additions to Figaro, Starlink User Note 16.4, CCLRC /RAL

Willick J. A., 1991, Ph.D. thesis, University of California, Berkeley

Chapter 5

The Tully-Fisher Relation

Abstract.

In this chapter the details are given of all the various corrections that must be applied to the measured parameters before forming the Tully-Fisher relation. All observations are assessed for quality and galaxies below a certain threshold are rejected. The form of the underlying bivariate distribution and ideal fitting techniques are discussed. The effects of sample selection on fitting are modelled and an approach adopted that minimises any possibility of bias in the estimated parameters. A full error budget is then made of all sources of uncertainty in the final parameters. A maximum-likelihood technique for combining the entire sample into a composite relation is considered but rejected. Finally, optimum forms of the parameter corrections are used to minimise the scatter in the relationship.

Having selected the four cluster samples of galaxies using the procedures outlined in chapter two and reduced the data as detailed in chapters three and four, a Tully-Fisher relation can now be produced for each cluster. Before the parameters quantifying luminosity and rotation velocity can be plotted together, a number of effects must be corrected for.

Each of the effects described below contributes to the scatter observed in the TF relationship, and in each case the ideal correction would reduce this contribution to a minimum. Assuming these corrections are random and uncorrelated, the best form of each correction is the one that results in the smallest scatter. In order to form a "raw" Tully-Fisher relation with which to test the corrections, an initial correction is adopted in each case. The final corrections made to each parameter are tabulated for all the sample galaxies in Appendix C.

5.1 Photometric Corrections

The photometric magnitudes measured for each object must be corrected for a number of effects; internal extinction, extinction within our own galaxy and relativistic effects.

5.1.1 Internal Dust Absorption

Spiral galaxies contain dust as well as stars and gas. Dust has the effect of attenuating the light from each galaxy in two ways. Firstly it scatters light away from the line of sight and secondly, it absorbs light from the stars within the optical wavebands which is then re-emitted in the far infra-red. In this way, the apparent brightness of a galaxy within one waveband depends upon the amount of dust within the line of sight. In addition, dust is not evenly distributed throughout each galaxy but is more concentrated within the plane of the disk of each spiral galaxy. As a result, the amount of dust absorption along the line of sight depends on the inclination of the disk. Light that travels across the disk passes through more dust, and is more attenuated than light leaving the galaxy normal to the disk. This effect means that the same galaxy viewed at different angles to the disk has different apparent magnitudes.

The effect of absorption is wavelength dependent; shorter optical wavelengths are more strongly absorbed than the longer infra-red wavelengths. By selecting the I-band, which is the optical band with the longest wavelength, the effect of dust absorption is minimised. However, the effect of absorption is still significant and must be corrected for.

The size of the correction depends upon inclination and the galaxies within our sample have inclinations to the line of sight ranging from 45° to 90° (measured normal to the disk). Over these angles, the variation in absorption can result in a difference in apparent magnitude of up to 0.8 magnitudes in the I-band ($\leq 40\%$ variation in distance). This makes the internal absorption correction the second largest correction to the “raw” TF parameters.

The precise form of the correction depends on exactly how the dust affects light within different wavebands and the distribution of dust within each type of spiral galaxy. At present the effect of dust within spirals is not completely understood. Opinions are divided between the traditional view, which states that spiral disks are optically thin (Holmberg 1958, Holmberg et al. 1975) and the mounting evidence that they are optically thick (Disney et al. 1989, Valentijn 1990 and Giovanelli et al. 1994). For the purpose of producing the Tully-Fisher relation, no consensus has been made as to the exact form of the internal absorption correction. Within recent published works, at least six different forms of the correction have been used.

The internal absorption correction applied by Willick (1991) and the slightly different method used by Courteau (1992) (both based on the correction used by Bothun et al. 1985), along with the correction prescribed by Tully & Fouque (1985) (used by Mathewson et al. 1992a), have an arbitrary maximum inclination above which the correction is constant (see Figure 5.1). These corrections also depend upon inclination which is calculated from the measured disk ellipticity. One alternative is the correction used by Han (1991) (similar to Sandage & Tammann 1981 and the correction used by de Vaucouleurs et al. 1976) which is given in terms of $\log(a/b)$ and has slightly different forms depending on the morphology of the observed galaxy (See Figure 5.1).

The correction used by Bernstein et al. (1994) is not only the simplest method used thus far, but depends directly on the disk ellipticity which is a directly measured quantity. Bernstein et al. (1994) apply this correction to an extensive I-band Tully-

Fisher sample (which is the most similar published work to this study) and produce a relation with a lower scatter than that which is produced using the corrections prescribed by Tully & Fouque (1985), Willick (1991) or Han (1991).

Hence we adopt the Bernstein et al. (1994) correction to adjust our measured magnitudes to form a “raw” TF relation for each of our cluster samples:

$$\Delta I = 1.37(e - e_{mean}) \quad (5.1)$$

Where e is the measured disk ellipticity, and the correction, ΔI , corrects the observed I-band magnitudes to a value that would be observed at an inclination of approximately 70° , this corresponds to the mean observed ellipticity of our sample. Correcting the data to the mean inclination in this way reduces the mean absorption correction needed and minimises any error introduced by uncertainty in the measured ellipticity. Other methods (mentioned above) correct for absorption to a “face-on” value (i.e. zero inclination). Since the typical mean inclination for TF samples is 70° , this results in larger corrections and inflates any errors introduced by the measured ellipticity. To compare relative shifts in magnitude between galaxies, as will be undertaken later in this work, absorption-free magnitudes are not needed. The left panel of Figure 5.1 shows a comparison between all the internal absorption corrections discussed above.

An alternative correction with some physical basis is suggested by Giovanelli et al. (1994). However, for the purpose of forming an initial relation, we prefer to use a simple model with fewer free parameters. More complex corrections will be explored below in §5.8, along with the effects of internal dust absorption on the measured diameters and surface brightness profiles of the galaxies within our sample.

5.1.2 Galactic Absorption

The second correction that must be made to the measured magnitudes is for absorption by dust within our own galaxy. This correction is only important at low galactic latitudes where the dust is concentrated. At the typical latitudes of our sample, the required correction is smaller than the internal ex-

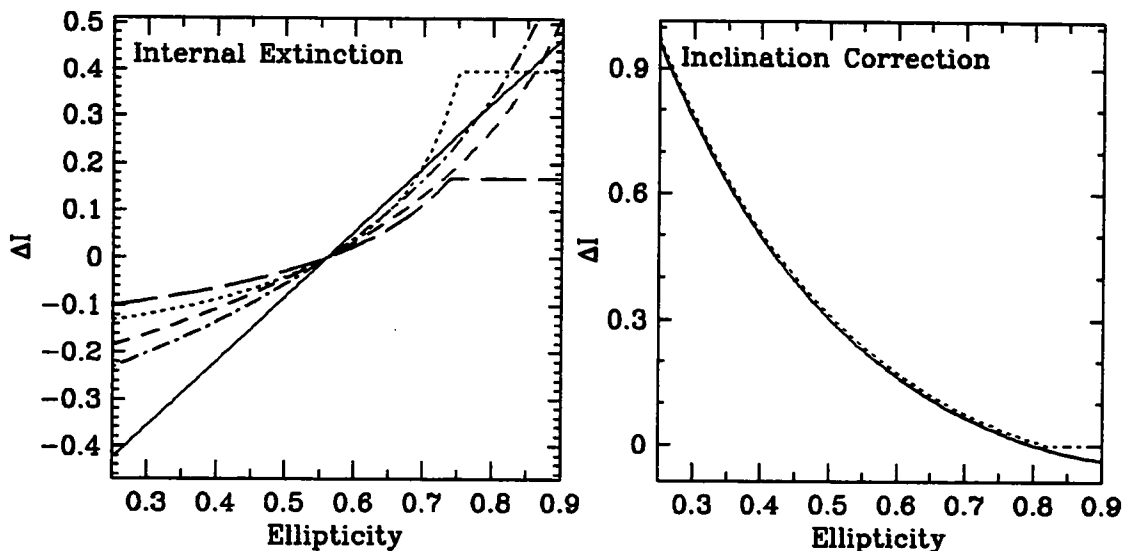


Figure 5.1: Plot of the two largest TF parameter corrections. **Left Panel:** A graph of the five most common internal extinction corrections. The different corrections are; solid line:Bernstein et al. (1994), long dash:Tully & Fouque (1985), short dash:Han (1991), dot-dash:Giovannelli et al. (1994), dotted:Willick (1991). All corrections are relative to the sample mean inclination. Note the methods of different authors can result in variations in the correction of up to 0.3 mag (15% in distance). **Right Panel:** A plot of the inclination correction applied to the measured rotation velocities. In order to assess the impact on the scatter within the relation the correction is given in terms of magnitudes by assuming a typical slope of the TF relation. The dashed line is the correction adopted here (from Willick (1991)) and the solid line is the slightly different correction used by Bernstein et al. (1994).

tion correction and is always less than 0.1 magnitudes ($\leq 5\%$ in distance) for galaxies within our sample.

A technique to correct the measured magnitudes for this external extinction was suggested by Burstein & Heiles (1978). This is Based upon the integrated “zero velocity” HI flux density measured in the direction of each galaxy and their corrections for variations in the gas to dust ratio were based on Lick galaxy number counts. As these measurements were only published for relatively bright galaxies, the exact corrections are not available for the majority of objects within our sample. Instead the B-band corrections given by Burstein & Heiles (1978) are interpolated to the position of each galaxy within our sample and converted to the I-band by scaling by 0.4875 (See Schlegel 1995).

Implicit in the correction method suggested by Burstein & Heiles (1978), is the assumption that the dust which causes the extinction is distributed in the same way as the measured neutral hydrogen gas. A more sophisticated method is proposed by Schlegel (1995) where IRAS and DIRBE measure-

ments are used to directly measure the dust distribution. The possible improvements made by adopting this method will be investigated in §5.8.

5.1.3 Cosmological Correction

Within the redshift range covered by our sample galaxies cosmological effects on the observed magnitudes are small, typically between 0.02 and 0.04 magnitudes ($\leq 2\%$ in distance), and vary little within any one cluster. For this reason, a simple correction (based upon Bernstein et al. 1994) was adopted for the purpose of forming the initial Tully-Fisher relation for each cluster.

$$\Delta I = -(1 - \Omega_0/2 + k_I)z \quad (5.2)$$

Where Ω_0 is the cosmological density parameter, z is the galaxy redshift measured in the CMB frame and k_I is the K-correction term. We use the value for k_I adopted by Bernstein et al. (1994), $k_I = 0.6$ which is based upon a typical spiral spectral energy distribution from McLeod (1993).

Other, more complex forms of the cosmological correction have been used in the literature. A cor-

rection method used by Han (1991) which depends upon galaxy type was deemed unsuitable due to the inherent inaccuracy in estimating types for samples of highly inclined spirals. A method suggested by Willick (1991) which uses the colour-linewidth relation to better estimate k_1 for each galaxy will be examined in §5.8.

5.1.4 Seeing Correction

The resolution degrading effects of atmospheric and dome seeing do not greatly affect the photometric quantities discussed here and in chapter three. The only two quantities that are discernibly affected are the measured ellipticity, e and surface brightness, μ . How these parameters, measured at different radii of an exponential disk, are distorted by seeing has been simulated by Han (1991) for various disk inclinations and scale lengths. The seeing only strongly affects the inner 1 scale length (about 5 arcseconds for our sample) of the surface brightness profile of each galaxy.

Under normal seeing conditions, for a galaxy with average inclination and typical size, the change in surface brightness, $\Delta\mu$, is always less than 0.3 mags/arcsec². At the radius of the selected disk region over which the disk scale length and central surface brightness are fitted (see §3.2.5) $\Delta\mu$ is less than 0.05.

For our sample galaxies the mean disk ellipticity of each galaxy is calculated as the mean fitted ellipticity measured over the selected disk region. For galaxies within our sample this disk region is typically 17 arcseconds (3 scale lengths) outside of each galaxy's core, considering our mean seeing disk is 1.4 arcsecs (see §3.1.3) and mean disk scale length is 6 arcsec, at these radii the apparent reduction in ellipticity is typically less than 1% (see Han 1991). In the worst case of an edge-on galaxy with a low apparent diameter imaged with under poor seeing, the effects on e and μ are still less than 15% and 0.4 mags. As the isophotal radii and magnitudes are measured at even greater radii, the effect of seeing on these parameters is considered negligible and no seeing corrections are made to the photometric quantities.

5.2 Kinematic Corrections

The rotation velocity parameter measured from the H α rotation curve in each galaxy also requires correction.

5.2.1 Deprojecting Rotation Velocities

The most important kinematic correction and in fact the largest of all the Tully-Fisher parameter corrections is the deprojection of the rotation velocities. The rotation velocity we measure is the line of sight component of the rotation in the plane of each galaxy's disk. Each measured rotation velocity can simply be corrected to an edge on rotation velocity by dividing by the sine of the inclination to the line of sight:

$$V_{\text{rot}} = \frac{V_{\text{obs}}}{\sin i} \quad (5.3)$$

Considering a typical I-band Tully-Fisher slope this correction can mean a change in magnitude between $i = 45^\circ$ and $i = 90^\circ$ of 0.9 magnitudes (see Figure 5.1) or up to 50% in terms of distance. The inclination of each galaxy, i , must be calculated from the measured mean disk ellipticity in each case. Due to the size of the correction, it is important that i is unbiased and has the minimum possible error.

5.2.2 Galaxy Inclination

A method for calculating the inclination of each galaxy that has been commonly adopted within recent publications concerning the Tully-Fisher relation (e.g. Courteau 1992, Mathewson et al. 1992a and Bernstein et al. 1994) is based upon the original work by Holmberg (1958). Assuming that face-on spiral galaxies are circular i.e. have a mean ellipticity, $e = 1.0$, and that edge-on galaxies, due to their intrinsic thickness display a maximum ellipticity, $e = v$, then the inclination can be calculated thus:

$$\cos i = \left(\frac{(1-e)^2 - (1-v)^2}{1 - (1-v)^2} \right)^{\frac{1}{2}} \quad (5.4)$$

A mean ellipticity of $e = 1.0$ for face-on galaxies is well established and the low scatter found in the TF relation formed by Bernstein et al. (1994), using this correction was cited as proof that face-on spirals are circular. The value of the mean edge-on

ellipticity, v , is not critical as it simply scales V_{rot} , introducing a constant shift in $\log V_{\text{rot}}$. At this point, a value of $v = 0.82$ (See Willick 1991) is adopted for the initial inclination corrections. A plot showing the size of the inclination correction over the typical ellipticity range of the present sample is shown in the right-hand panel of Figure 5.1.

It is important to note that the two largest corrections applied to the TF parameters depend on the measured ellipticity. At low ellipticities, the inclination correction dominates (though slightly canceled by negative extinction corrections), while at high ellipticities the inclination correction is small and the extinction correction is the major correction (see Figure 5.1). This dependence means that an accurate measurement of each galaxy's ellipticity is required to keep the contribution to the scatter in the relation to a minimum. The propagation of ellipticity error and the relative importance to the scatter in the TF relation will be studied in §5.6.3.

5.2.3 Relativistic Correction

A small relativistic correction must also be made to the measured rotation velocities;

$$V_c = \frac{V_{\text{rot}}}{1+z} \quad (5.5)$$

where z is the redshift of the galaxy. This is to correct for the fact that the two sides of each galaxy are effectively receding at different redshifts due to rotation. The resulting correction is small and for the galaxies considered here is always less than 4%. This corresponds to 0.1 in magnitudes or $\leq 5\%$ in distance, assuming a typical slope of -6.0 for the TF relation.

The measured values of all the important parameters discussed here for each of the galaxies within the selected sample are tabulated in Appendix C. Note that in some cases the values given in Appendix C are based upon the finally adopted forms of the corrections and parameters such as a_i and v .

5.2.4 The Effects of Seeing

The seeing affects the measured rotation curve in two ways. Firstly, an increased seeing disk reduces the amount of light entering the spectrograph. As the

slit width was fixed at 1.65 arcsec for all of our measurements, poor seeing (the mean was 1.4 arcsec) resulted in a reduction in the signal-to-noise ratio within some galaxy spectra. Secondly, the smoothing effect of the seeing disk reduces the measured inner velocity gradient of each galaxy's rotation curve. Although this is not expected to greatly affect the maximum rotation velocity measured from each curve.

Since any possible effects of seeing are considered to be very small, no seeing corrections were made at this stage. This proved to be adequate as no correlation was later seen in the Tully-Fisher residuals.

5.3 Forming the Relation

The final stage, before forming our initial Tully-Fisher relation requires the assessment of the quality of the available photometric and spectroscopic data for each galaxy. Each galaxy is assigned two quality numbers, each ranging from one to three where three is the lowest quality (see §3.1.3 and §4.3 for details). The quality assignments are tabulated in Appendix C along with all the measured parameters for each galaxy.

5.3.1 Data Quality and Rejection

Before the Tully-Fisher relation for each cluster was formed, any galaxies with quality $Q=3$ data were removed from each sample. For the photometric measurements, a galaxy with $Q=3$ data typically consists of objects without a photometric zeropoint due to bad weather conditions. Low Quality, $Q=3$ rotation curves displayed no clear turn-over or had large asymmetries which made assigning a maximum rotation velocity very uncertain.

It is important to emphasize that such data rejection is done before plotting the relation. Simply culling galaxies which fall far off the fit would result in a misleadingly low estimate for the scatter of each relationship. Not only does this give a false impression of the scatter but is self defeating in that any possible correlation between the residuals and a third parameter will be weakened and much more difficult to detect. Details of which objects were re-

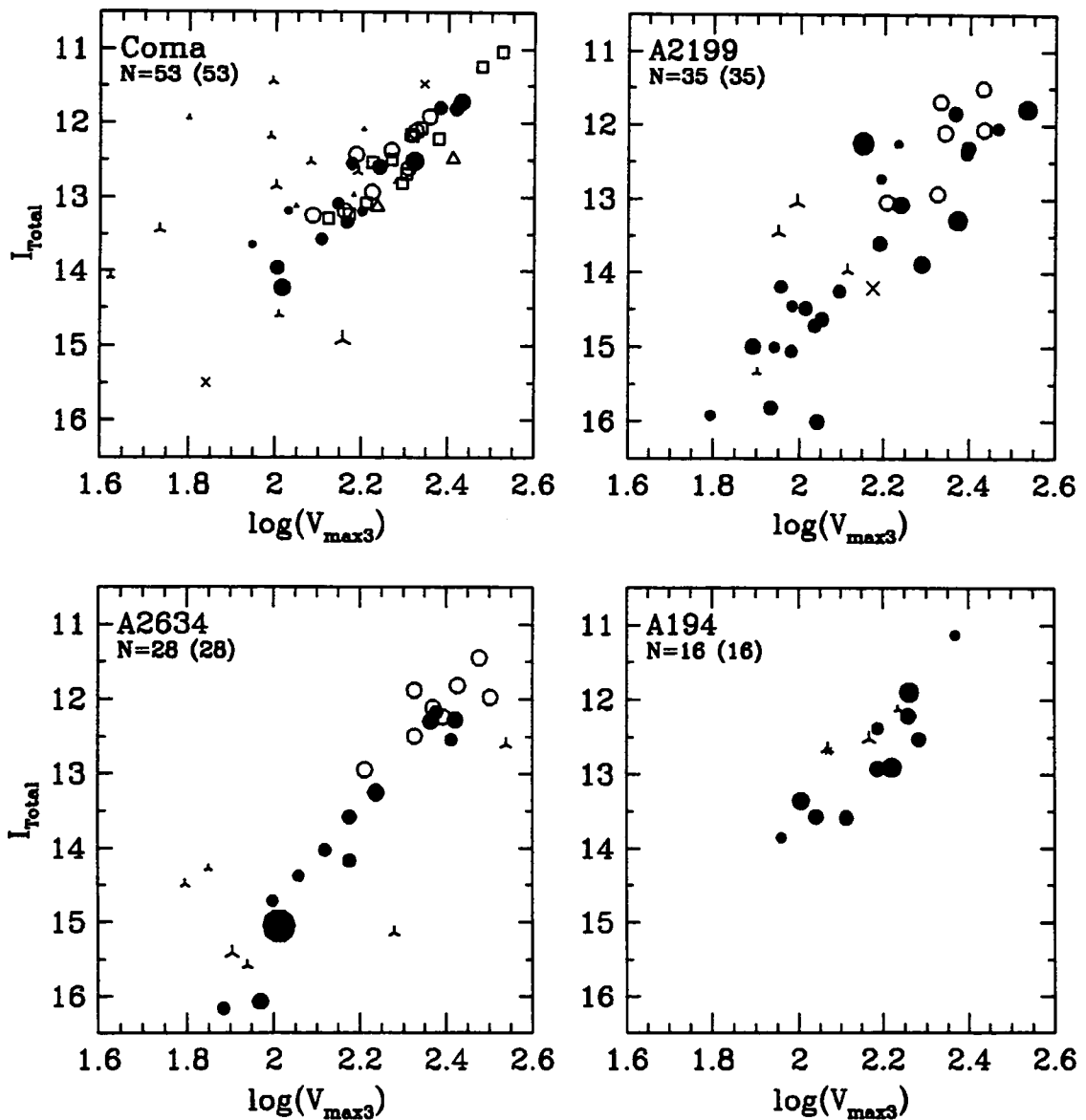


Figure 5.2: The Tully-Fisher relation for the four clusters within our sample. No points have been rejected, all galaxies with measurements are shown. Solid circles represent galaxies from the present sample, galaxies with poor quality measurements are marked with crosses. In both cases the size of the point indicates the extent of the H α rotation curve. Open circles represent data from previous observations and for the Coma cluster open squares and triangles represent measurements by Bernstein et al. (1994).

jected and the reasons why in each case are given in Appendix D.

5.3.2 The "Standard" Relation

The "Standard" Tully-Fisher Relation for each of the four clusters is shown in figures 5.2 and 5.3. These plots represent our initial picture of the relationship within rich clusters. The plots are considered standard as they are typical of Tully-Fisher re-

lations appearing in the present literature. The treatment of the data and all the corrections applied to this point follow closely the approaches adopted by other authors with similar datasets.

Figure 5.2 shows a plot for each cluster containing points for all galaxies for which we could possibly measure the parameters, I_{Total} and $V_{\text{max}3}$. The solid circles represent galaxies from the current sample with $Q=1$ or 2 data, the crosses mark galax-

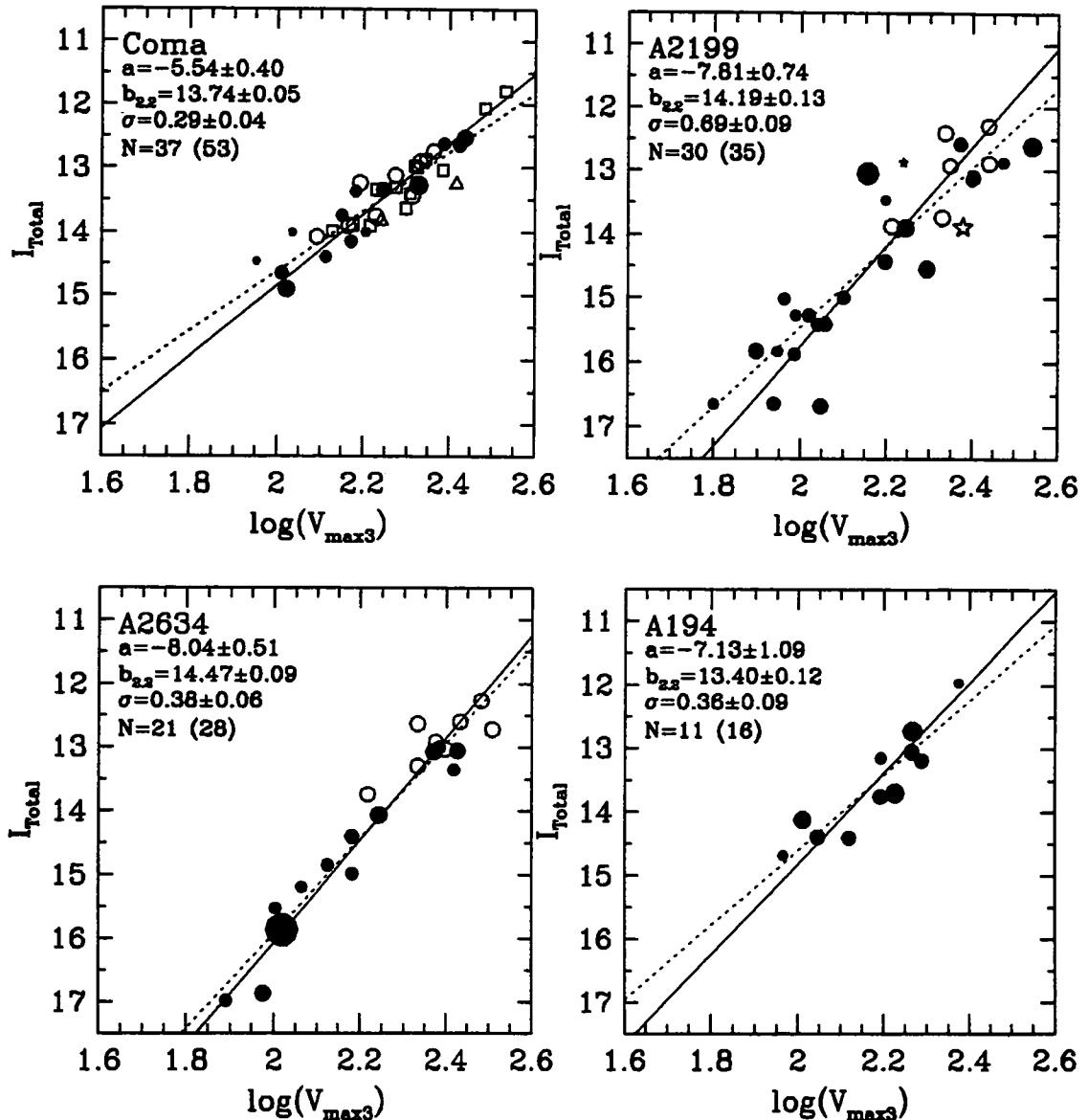


Figure 5.3: The TF relation within the four target clusters after rejection of the poor quality points. The symbols are the same as in figure 5.2. A simple least squares regression of $\log V_{\text{max}3}$ upon I_{Total} is marked as a solid line on each relation. The details of each of these fits are marked in the upper left of each panel. The regression of I_{Total} upon $\log V_{\text{max}3}$ is represented in each case as a dotted line.

ies with $Q=3$ data. In both cases the relative size of each point indicates the extent of the measured rotation curve for each galaxy. In the case of $Q=3$ points four-point crosses mark objects without zero-pointed photometry and three-point crosses represent objects with poor rotation curves. Open circles mark data from previous observations and for Coma the open squares and triangles indicate measurements made by Bernstein et al. (1994).

The low quality, $Q=3$, data was culled from the dataset and the resulting relationships are shown in Figure 5.3. Note how a large fraction of the rejected points lie within the relation and are not simply the points which displayed the most scatter.

For each relation an unweighted least-squares fit (minimising in I_{Total}) is marked together with the parameters of each fit. Notice the large scatter within the A2199 cluster TF relation and the apparently different gradient displayed by the A2634 relation-

ship (possible reasons for these effects and their significance will be explored below).

The accuracy of distance estimates made with each relation depend upon the observed scatter. In order to improve the accuracy of any distance estimates made we first need to form a single composite relation from the four clusters. A single, well populated relationship is the best tool for deciding upon the ideal corrections to adopt and for studying other possible sources of scatter. In order to do this a more sophisticated method of fitting each relation is needed. But before we can proceed with this an understanding of the underlying relationship is required along with an accurate estimate of the errors on each data point.

5.4 The Nature of the Tully-Fisher Relation

The underlying Tully-Fisher relationship is due to a chain of dependences between a number of the global physical properties exhibited by spiral galaxies. A galaxy's total luminosity is related to its stellar mass which is related to the baryonic mass which in turn is connected to its total mass, made up from baryonic and dark matter, which in some way is parameterised by the galaxy's rotation velocity. So a complete understanding of the relationship is drawn from several fields which include stellar astrophysics, galaxy formation, galaxy dynamics, and cosmology.

A detailed description of each stage of this complex relationship between galaxy properties is outside the scope of the present work, see §1.1 for limited further discussion on this topic.

In simple terms, the true distribution of total mass depends upon the power spectrum of the primordial mass distribution and the way in which this is amplified by gravity over time. Galaxy formation theory then describes the complex collapse, cooling and feedback processes that formed the first stellar populations, and defines the distribution of scale size that galaxies exhibit. Further astrophysics is required to explain how stellar evolution and further formation combine to produce the stars that dominate galaxy's spectra observed today. And galaxy dynamics show how the movement of stars and gas

within the disk of spirals is related to the total mass distribution within each galaxy.

The *observed* TF relationship contains another level of complexity, the combination of the underlying parameters with the sample selection and the inherent observability of the measured quantities. The wavelengths of the filters used when measuring total magnitudes involves a further dependence upon each galaxy's star formation history. The use of H α rotation curves also means that we are limited to objects with present star formation throughout a reasonable fraction of their stellar disks.

Figure 5.6 shows a plot of a simple model TF relation in terms of a probability distribution of the measured parameters along with the observed distributions of rotation velocity and total magnitude.

5.4.1 The Distribution of $I_{T\alpha\alpha}$ and $\log(V_{R\alpha})$

The galaxy mass distribution can be considered the most fundamental property of the spiral galaxy population, and is directly proportional to the product of the rotation velocity squared and the scale length of each galaxy's disk:

$$M \propto V^2 R_{scale} \quad (5.6)$$

The scale length of galaxies within the present sample vary by a much smaller amount than either luminosity or rotation velocity (see Figure 5.11) and is approximately proportional to the rotation velocity (see Figure 5.10). Thus, it is reasonable to consider the rotation velocity of a galaxy to be directly related to its mass, and to take $\log(V_{R\alpha})$ as the independent variable in the simple models of the TF relation that follow.

The *observed* $\log(V_{R\alpha})$ distribution is also assumed to be normal, which for this sample is approximately true (see Figure 5.4). The exact form of both observed distributions is strongly a function of the sample selection process. At the high mass end, i.e. $\log(V_{R\alpha}) > 2.2$ and $b\text{-mag} < 15.5$, the distribution is probably a reasonable representation of the mass function of spirals within clusters. At this point in the distribution we can be confident that our sample is close to being complete.

As galaxies selected from the much deeper plate scans make up only one half the present sample, the

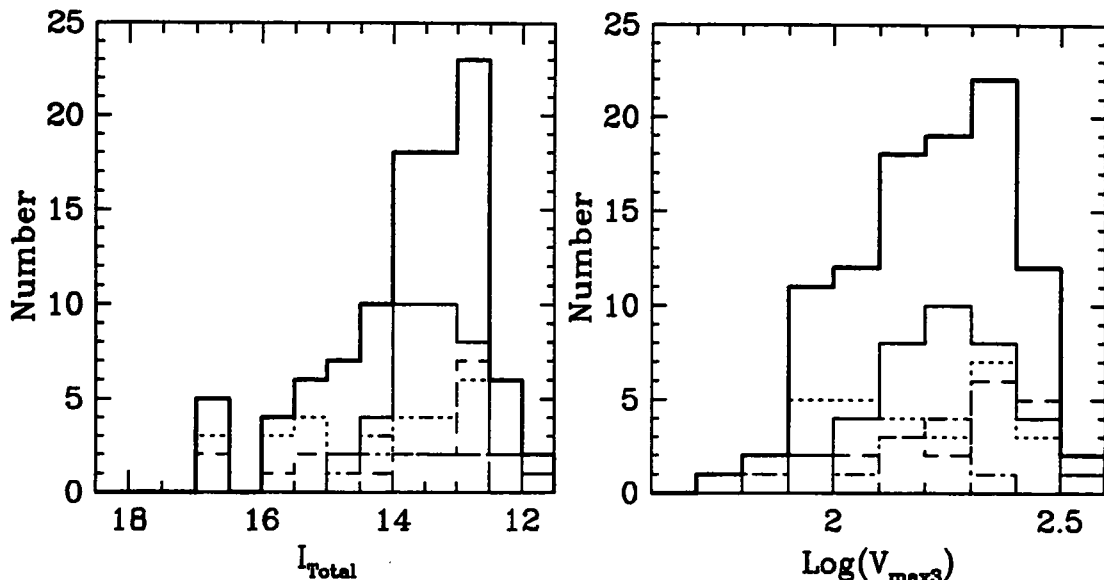


Figure 5.4: Total I-band magnitude and log-rotation velocity histograms for the final sample of 99 galaxies. On both plots the solid thick line indicates the distribution of the whole sample. Other line types show the respective distribution for each of the four clusters; Solid line for Coma, dotted line for A2199, dashed line for A2634 and dot-dashed for A194.

observed magnitude distribution (and rotation velocity distribution as a result) is dominated by the completeness function of the catalogues used to select the brighter cluster members (see §2.2). For rotation velocities of $\log(V_{rot})$ lower than 2.2 (which correspond to the completeness limit of the UGC and Zwicky catalogues ($B\text{-mag} \approx 15.5$)) the distribution peaks then declines before reaching the faint limit of $B\text{-mag} = 18.0$. Histograms of the observed rotation velocity and apparent magnitude distributions are shown in Figure 5.4.

Since the observed distribution function of the variables is close to normal, the TF relation can be modeled as a Bivariate Normal or Binormal joint distribution. This approximation greatly simplifies the modeling of the relationship, the process of fitting and is not an unreasonable representation for the underlying distributions. The underlying mass distribution for all galaxies within a cluster is expected to continue to rise towards lower masses, the overall distribution being described by a Schechter function. However, not all galaxies are suitable for Tully-Fisher work. For the present purpose we select disk galaxies which display circular stellar motions as opposed to the more turbulence dominated motions of elliptical and dwarf galaxies. And in

particular for the present technique we rely upon galaxies with a reasonable amount of star formation throughout their stellar disks to enable the measurement of a $H\alpha$ rotation curve. The properties become less and less common in lower mass galaxies and so we can expect the underlying mass (and luminosity) distribution of galaxies suitable for Tully-Fisher work to be reasonably approximated by a Gaussian.

Other galaxy properties can also affect the distributions of magnitude and rotation velocity. Both surface brightness and morphology influence the probability that a galaxy will appear in the final sample. Objects which displayed strongly disturbed morphologies were rejected, and objects with lower surface brightness have lower signal-to-noise spectra and poorer quality rotation curves as a result. If these properties also correlate with either luminosity or rotation velocity, as surface brightness certainly does (see Figure 5.10 and Figure 10 in Mathewson et al. 1992b), then they can in turn alter the observed distributions of magnitude and rotation velocity.

Another consideration that changes the observed distribution of parameters is observability, namely how easy it is to measure the required quantities to a suitable accuracy as a function of the apparent mag-

nitude and rotation velocity. For example, it was found that for the fainter objects, which tended to have lower surface brightnesses (see Figure 5.10), it was much harder to align the spectrograph slit along the galaxy's major axis during measurement of the H α rotation curve. This resulted in a much higher rejection rate for the fainter objects due to poor rotation curve extent as a result of slit misalignment. This effect is demonstrated in Figure 5.5 which shows a histogram of the quality number assigned to measured data on all the galaxies selected for the present work. The graph is divided into galaxies selected from plate scans and galaxies selected from the widespread but relatively brighter Zwicky and UGC catalogues. Clearly a higher proportion of the, on average fainter galaxies selected from the plate scans have been attributed with a lower data quality or completely rejected from the final sample.

The effects of the two processes discussed above are hard to separate requiring a large database with well defined selection criteria and notes detailing why objects were rejected. Unfortunately no such sample is available in the literature to date. However, it is certain that other galaxy properties are involved in deciding the distribution of the final sample parameters and the possible effects of this will be discussed below.

5.4.2 The Bivariate Distribution

The process of forming a Tully-Fisher relation to estimate galaxy and cluster distances or in order to study galaxy properties relies upon a fitted relationship that quantifies the observed distribution in terms of slope, intercept and scatter. That is:

$$M = a \log V_{rot} + b \quad (5.7)$$

where a and b are the slope and intercept respectively.

All possible fitting schemes utilise a regression upon one or both parameters, where the adopted best fit relation is the one that minimises the residuals in one or both directions. Implicit in the process of performing a regression is the assumption that the variable that is being regressed is *normally* distributed at a constant value of the other parameter. In the case of a more complex fitting procedure such as an or-

thogonal bisector, which is a combination of regressions on both variables in turn, the assumption is made that both parameters are normally distributed at fixed values of each other.

Representing the Tully-Fisher relation as a bivariate normal distribution and adopting the nomenclature developed by Hendry & Simmons 1994, where P denotes $\log V_{rot}$, we can derive the two regression lines in terms of the distributions of the two parameters thus:

$$E(M|P) = M_0 + \rho \frac{\sigma_M}{\sigma_P} (P - P_0) \quad (5.8)$$

$$E(P|M) = P_0 + \rho \frac{\sigma_P}{\sigma_M} (M - M_0) \quad (5.9)$$

Where $E(M|P)$ is the *expected* or most likely value of M given a certain value of P . M_0, P_0 and σ_M, σ_P are the means and standard deviations of M and P respectively. The strength of the correlation between the two parameters is denoted by ρ , the correlation coefficient. By comparing Eq.5.7 with Eqs.5.8 & 5.9 the slope and intercept of the regression of M on P , or "direct" Tully-Fisher relation become:

$$a = \rho \frac{\sigma_M}{\sigma_P} \quad (5.10)$$

$$b = M_0 \quad (5.11)$$

And for the regression of P on M or "inverse" relationship:

$$a = \rho \frac{\sigma_P}{\sigma_M} \quad (5.12)$$

$$b = P_0 - \rho \frac{\sigma_P}{\sigma_M} M_0 \quad (5.13)$$

An important fact that emerges from this is that the gradient and intercept of the direct and inverse fits are mathematically distinct and different, and should not both be considered as approximating a single and somehow fundamental relationship. Both regressions are perfectly valid and can be used to quantify the differences between distributions but the fitted values should not be expected to converge to a single value of slope and intercept. This is true for all bivariate normal distributions and in fact all reasonable distributions of M and P .

A graphical representation of a bivariate normal distribution that closely matches the present sample

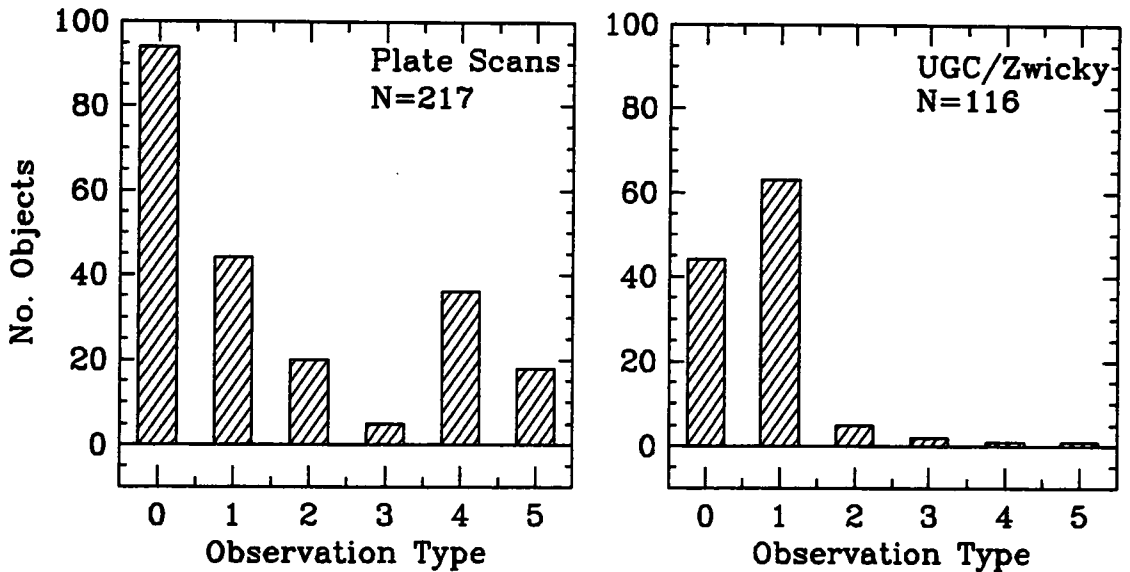


Figure 5.5: Two Histograms displaying the outcome of observations of 333 galaxies selected from photographic plate scans or either UGC or Zwicky catalogues. The observation type codes indicate; 0=not observed, 1=in final TF sample, 2=rotation curve with poor extend, 3=only nuclear H α emission, 4=no H α emission, 5=wrong morphology (e.g. star or elliptical). A larger fraction of the fainter objects selected have proved to have weak or no H α emission lines.

of galaxies is shown in Figure 5.6. The main panel of this figure is divided into three regions. In the upper right-hand region, the probability density of finding a galaxy with parameters M,P is shown as a grey scale over the entire range of M and P values spanned by the data. The black regions of the grey scale denotes the region where certain combinations of M and P are most likely. The lower portion of this panel shows a histogram that represents the relative probability of a particular value for P ($\log V_{R\alpha}$) within the sample. The left part of this panel displays a histogram of the relative probability function of M within the sample.

Combining the two one-dimensional probability functions produces the two-dimensional probability function represented by the grey scale. The parameters of the distribution are marked in the upper corner of each panel, namely a mean P of 2.2 with $\sigma = 0.2$ and mean M of -22 (assuming $H_0 = 100 \text{ Mpc/kms}^{-1}$) with $\sigma = 1.5$. The slope, intercept and scatter of the relationship are set to -7.5, -22 and 0.35 respectively, which closely matches the values measured from the sample selected here and those given in the literature.

In the upper right-hand region of the main panel of Figure 5.6 the probability distribution is over-

laid with two dotted lines that represent the result of applying the M on P and P on M regressions to the distribution. The difference between the two regressions is small but not insignificant, the inverse slope is 0.4 greater than the direct slope. In the lower half of Figure 5.6 there are two more example distributions. One relationship has the same scatter but over a narrower range of magnitude and rotation velocity and the other covers the same range of parameters but has an increased scatter. It follows from Eq.5.8 and Eq.5.9 that the difference between the inverse and direct slopes is increased in these cases, and this is shown in the lower plots.

5.4.3 Selection Bias

It can be seen from Figure 5.6 that in the case of any reasonable distribution where the expected values of each parameter are normally distributed with respect to each other the difference between the regression lines is small. However, in the more realistic case where this is not true for one or both of the parameters the regressions lines can differ significantly, as will now be demonstrated.

When a selection limit is imposed upon one or both of the variables, the assumption that points are normally distributed is broken and the regression

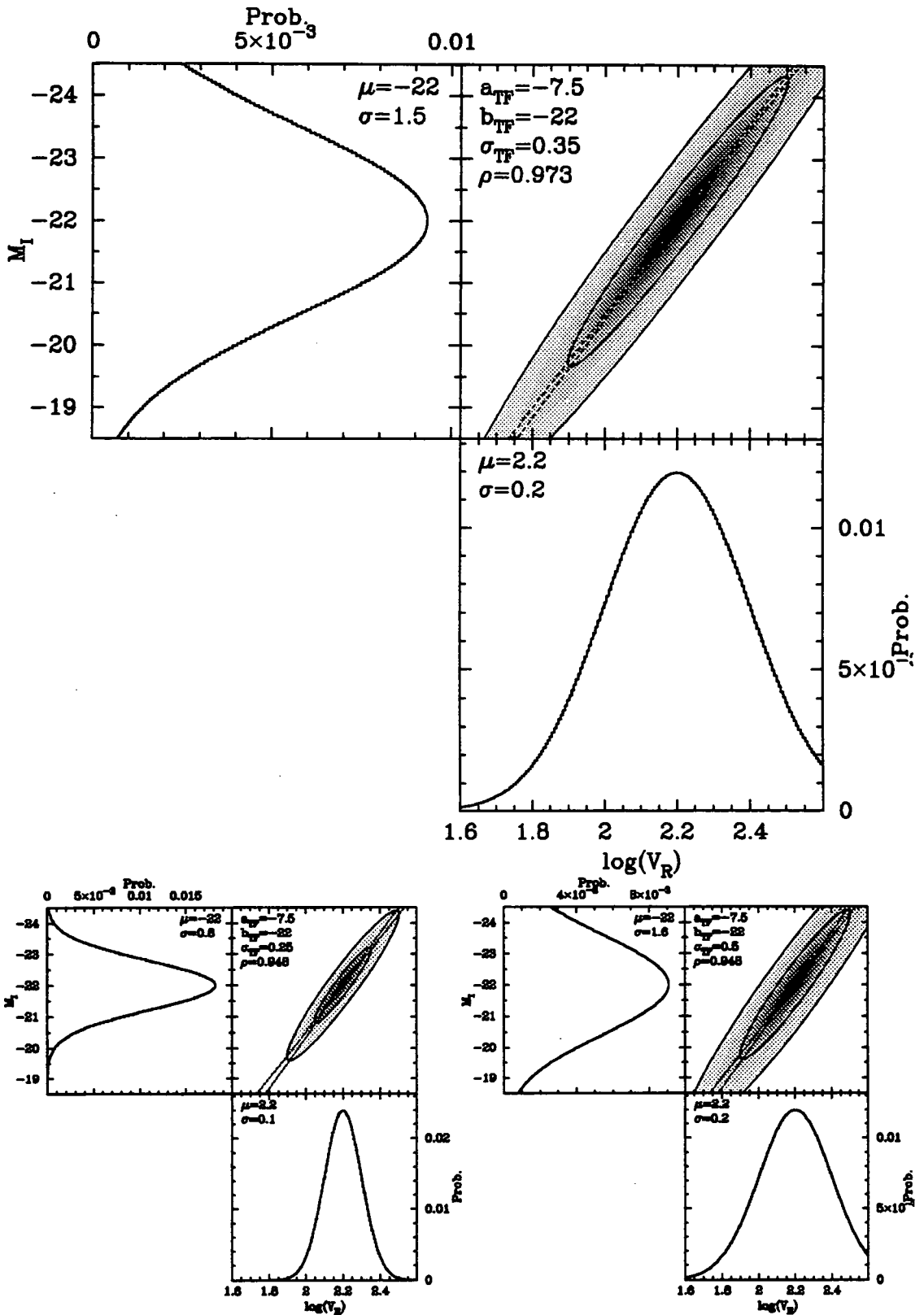


Figure 5.6: A graphical representation of the Tully-Fisher relation as a bivariate normal distribution. The upper portion of the figure displays a distribution with parameters similar to the selected sample. Plotted in the left-hand and lower panels is the probability distributions of total magnitude and rotation velocity. The greyscale image indicates the joint probability distribution where points of highest probability density are marked with black. Direct and inverse regression lines are marked with dotted lines. The two lower plots show how changes in the sample properties affect the probability distribution.

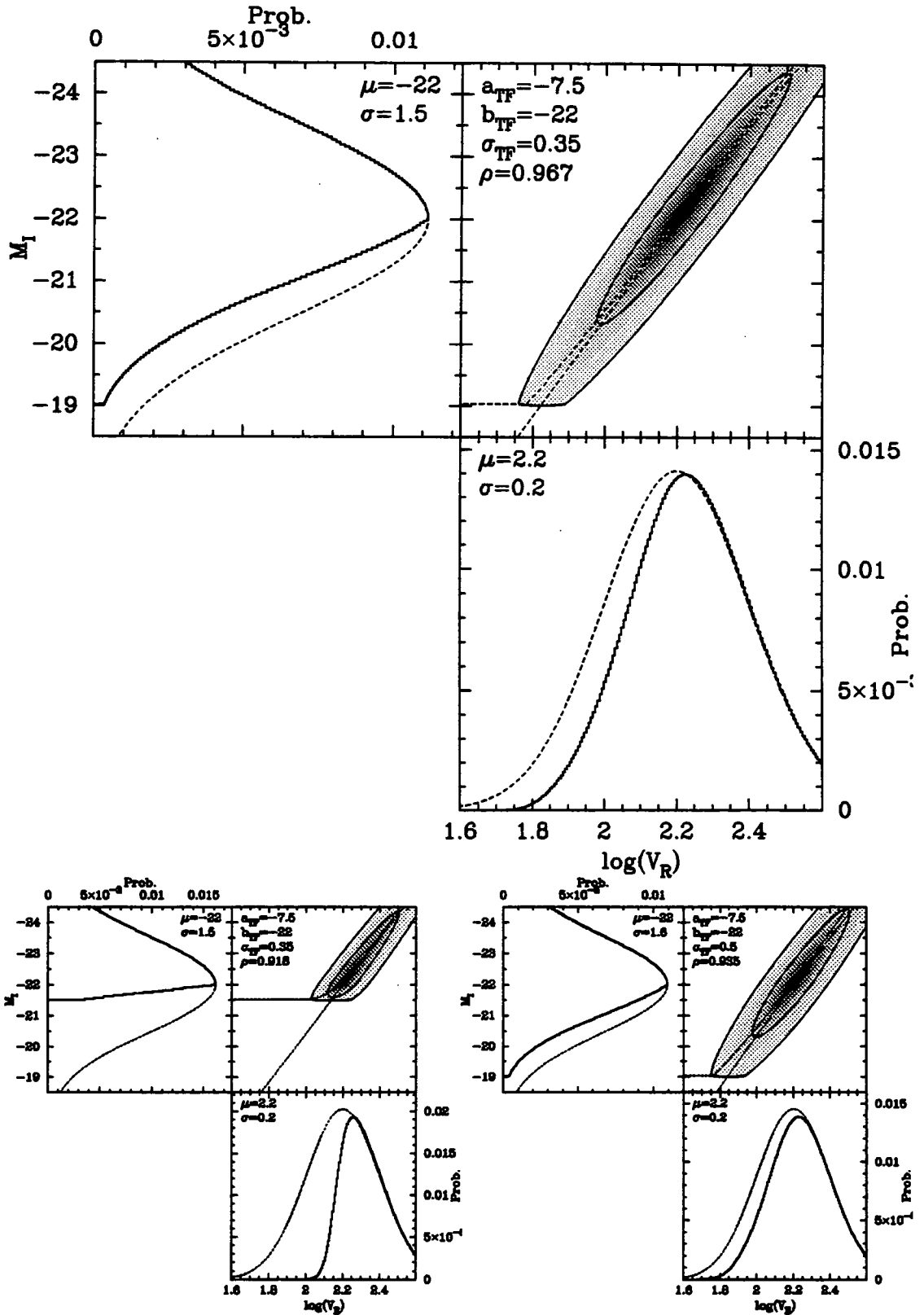


Figure 5.7: The same distributions as shown in Figure 5.6 with magnitude selection effects added. Histograms marked with dashed lines indicate the original distribution before selection. Note how the inverse regression line (lower of dashed lines on greyscale) remains unchanged, whereas the direct line is biased towards brighter magnitudes. The lower plots depict the result of a brighter selection limit or larger TF scatter on the amount of bias. See text for detailed discussion.

line becomes biased away from the true underlying relationship. Figure 5.7 demonstrates this effect where the same distributions used in Figure 5.6 are shown but with realistic selection effects applied to each distribution.

The large upper plot in Figure 5.7 shows a joint distribution similar to the one displayed by the dataset presented here, with the same selection function applied to the M distribution that applies to our own data (see below). The selection function used is complete (i.e. equal to one) down to a b-band magnitude of 15, which corresponds to $M_I = -22$, and then drops linearly to zero for b-magnitudes greater than 18 ($M_I = -19$).

The selection function has a clear effect on the M on P regression line. The upper most dotted line that represents the expected value of M at a given P ($E(M|P)$), on the upper right-hand panel breaks away from the lower $E(P|M)$ at magnitudes where the selection function takes effect until it reaches the lower magnitude limit. The inverse $E(P|M)$ regression line remains unaffected over the entire distribution because no selection function has been applied to the P distribution. The effect of the selection function on the observed distributions of M and P can be seen in the histograms in the left-hand and lower panels in the upper plot in Figure 5.7.

The plot in the lower left-hand quarter of Figure 5.7 illustrates the consequence of a much sharper selection function, similar to those of many previously published TF studies (e.g. Aaronson et al. 1982). The lower right-hand plot shows how the bias introduced into the slope of the direct regression becomes larger if the scatter in the relationship is increased.

In figures 5.6 and 5.7 the expected values $E(M|P)$ and $E(P|M)$ are evaluated as shown for all values of M and P . In the more realistic case of a straight line fit the curved $E(M|P)$ will be reduced to a line of biased slope. The bias introduced into a regression in this way is normally referred to in the literature as selection bias or calibration bias.

Clearly then it is better to use a regression upon a variable unaffected by selection, as this will produce a fit that is more representative of the underlying relationship rather than the particular dataset

used. This becomes of more importance when estimating distances for different clusters, since selection functions will differ for clusters at different distances and particularly when different catalogues are utilised for each cluster. In light of these considerations it is important to quantify the present sample selection function as accurately as possible.

5.4.4 Cluster Selection Functions

Unfortunately, in the case of the dataset considered here, even after the careful selection procedures outlined in chapter two, the selection function is far from simple. The two competing requirements are that our chosen galaxies should span a wide range of cluster environment and yet sample the relationship to as faint a limit as possible. This means that we selected galaxies not only from catalogues based on plate scans but also from the Zwicky and UGC catalogues. All three types of catalogue are drawn from photographic plates and as such share the sample selection limits in terms of surface brightness (See §6.2). Whereas the plate scans are based upon sensitive automated measurements and produce uniform data down to a much fainter magnitude limit than needed here, the Zwicky and UGC catalogues were made using human selection and suffer from varying incompleteness near their relatively bright magnitude limit.

For the purpose of modelling the selection function here we assume the catalogues based upon plate scans are 100% complete to our imposed magnitude limits of 18 or 18.5 in the b-band. In the case of the Zwicky catalogue it is assumed to be 100% complete down to 15 in the b-band but then to have a rapidly falling completeness down to the catalogue limit of 16. The UGC catalogue has a diameter limit which approximately corresponds to a apparent magnitude of 16.5 but, like the Zwicky catalogue, is assumed to be incomplete for magnitudes fainter than 15.

The selection function is further complicated by the observing process. When choosing objects to observe at the telescope we were careful to pick objects at all magnitudes equally. So while to date only 65% of the galaxies selected have been observed, it is assumed that the sample used here is a ran-

dom subset of all selected galaxies. However, there is some bias towards brighter galaxies, even in the samples selected from the plate scans, because of observability considerations. For a number of practical reasons it is harder to observe the fainter objects and as a result a lower percentage of the faint objects from the plate scans produced data of sufficient quality to make it into the final sample (see §5.4.1 above). This effect is clearly seen in Figure 5.5. This indicates that a much greater percentage of the data selected from plate scans is given an observation code of 2 or above. Such data was not to be used in the final TF sample.

Figures 5.8 and 5.9 show magnitude histograms within each cluster for the 341 galaxies selected for this work. Superimposed on the selected galaxy histograms (shown as open bars) is the histogram of objects actually observed in each cluster (represented as hatched bars) and on top of both appears a histogram of the objects which appear in the final Tully-Fisher analysis (cross hatched bars).

Figure 5.8 displays the magnitude distributions for the Coma cluster and Abell 2199. The upper two panels show the distributions for the two samples that make up the Coma data, the left-hand panel shows the distribution for the galaxies selected from plate scans and the right-hand panel shows galaxies selected from the Zwicky catalogue. Notice how the number of galaxies selected from the scan increases with magnitude right up to the selection limit, marked by a dashed line. Whereas the data selected from the Zwicky catalogue begins to fall for magnitudes fainter than 15, the completeness limit marked as a dotted line on the plots. Also notice how the number of objects used for the TF analysis falls in relation to the number selected within the two faintest magnitude bins of the scan selected data. This pattern is repeated for the three other clusters shown in figures 5.8 and 5.9.

The magnitude distribution of the suitable objects from each cluster combine to give the observed distribution shown in Figure 5.4. Clearly a simple magnitude limit is not sufficient to represent the magnitude selection function for the sample. Instead, the function used is considered 100% complete to B-magnitudes of 15 (13 in I-band) with a linearly

falling completeness to the selection limit of 18 (16 in I-band).

The nature of the selection function in terms of $\log V_{R\alpha}$ is less clear. Naïvely, as no information on the rotation velocities was known at the time of selection, galaxies with a particular value of $\log V_{R\alpha}$ could not be biased against. However, this ignores the fact that $\log V_{R\alpha}$ could correlate with other parameters other than magnitude that do enter into the selection procedure. One candidate is the relationship between surface brightness and rotation velocity. A quantitative relationship does exist between $\log V_{R\alpha}$ and the surface brightness, Figure 5.10 demonstrates a weak but significant correlation, and this same effect is also seen in the data of Mathewson et al. 1992b and well demonstrated by their Figure 10. But it is not clear whether this is due to a real relationship directly between $\log V_{R\alpha}$ and surface brightness or due to a general trend between surface brightness and magnitude (See Figure 5.13).

Another possible link between the measured rotation velocity and surface brightness is due to the dependence of the signal-to-noise and extent of the measured rotation curve on the galaxy's rotation velocity. This means that low surface brightness galaxies tend to have poorer quality rotation curves which are insufficient to reliably estimate a rotation velocity, resulting in the rejection from the sample.

It is well established that catalogues selected from photographic plates are strongly limited to only a narrow range in surface brightness (see McGaugh 1996 for a detailed discussion). If there is a strong link between rotation velocity and surface brightness then these selection effects will restrict the range of measured rotation velocities within our sample.

The surface brightness distribution of our galaxies is displayed in Figure 5.11. This exhibits the expected shape when compared with Figure 5.12 (Reproduced from McGaugh 1996), so we can be confident that the distribution is indeed defined by selection effects. Though we do note that the surface brightness distribution of the sample galaxies is broader than expected. This is attributed to the sample objects being selected from b-band photographs but observed in the I-band, variations in colour of

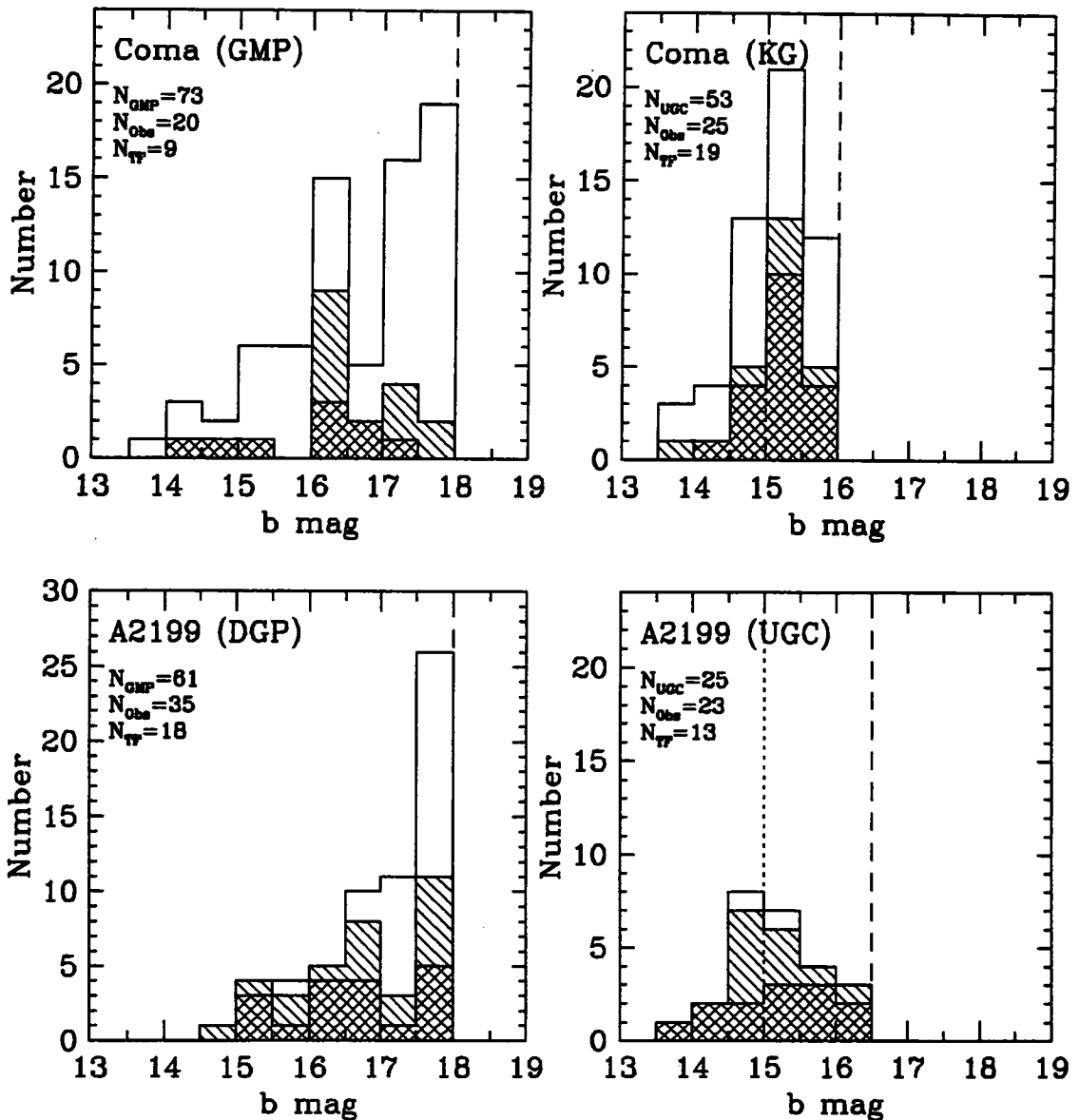


Figure 5.8: Four histograms showing the B-band magnitude distribution for galaxies selected from the Coma and Abell 2199 clusters. The left-hand plots show the distribution for the samples selected from plate scans. The right-hand plots indicate the sample magnitude distribution of galaxies taken from either the Zwicky or UGC catalogues. The imposed magnitude limits of 18.0 and 16.0/16.5 are marked as dashed lines. The suspected completeness limit of the Zwicky and UGC catalogues is shown with a dotted line. The open histograms indicate selected objects and hatched and cross-hatched bars indicate observed and final TF galaxies.

the sample galaxies then broaden the distribution slightly.

This is not the problem that it first appears to be, as the surface brightness lower limit of 21.0 ± 0.5 mag/arcsec² set by plate selection corresponds to an imposed limit on $\log V_{R\alpha}$ of around 1.8 or lower (see Figure 5.10). The limit represented by rotation velocities of $\log V_{R\alpha} = 1.8$ is approximately

the point at which the dataset is already cut due to the magnitude limit. Even with any dependence on surface brightness that rotation velocity may have, surface brightness selection effects will have little or no affect on the rotation velocity distribution. It maybe assumed then, that the present sample suffers from weak or nonexistent selection effects in terms of rotation velocity. Moreover, as similar selection

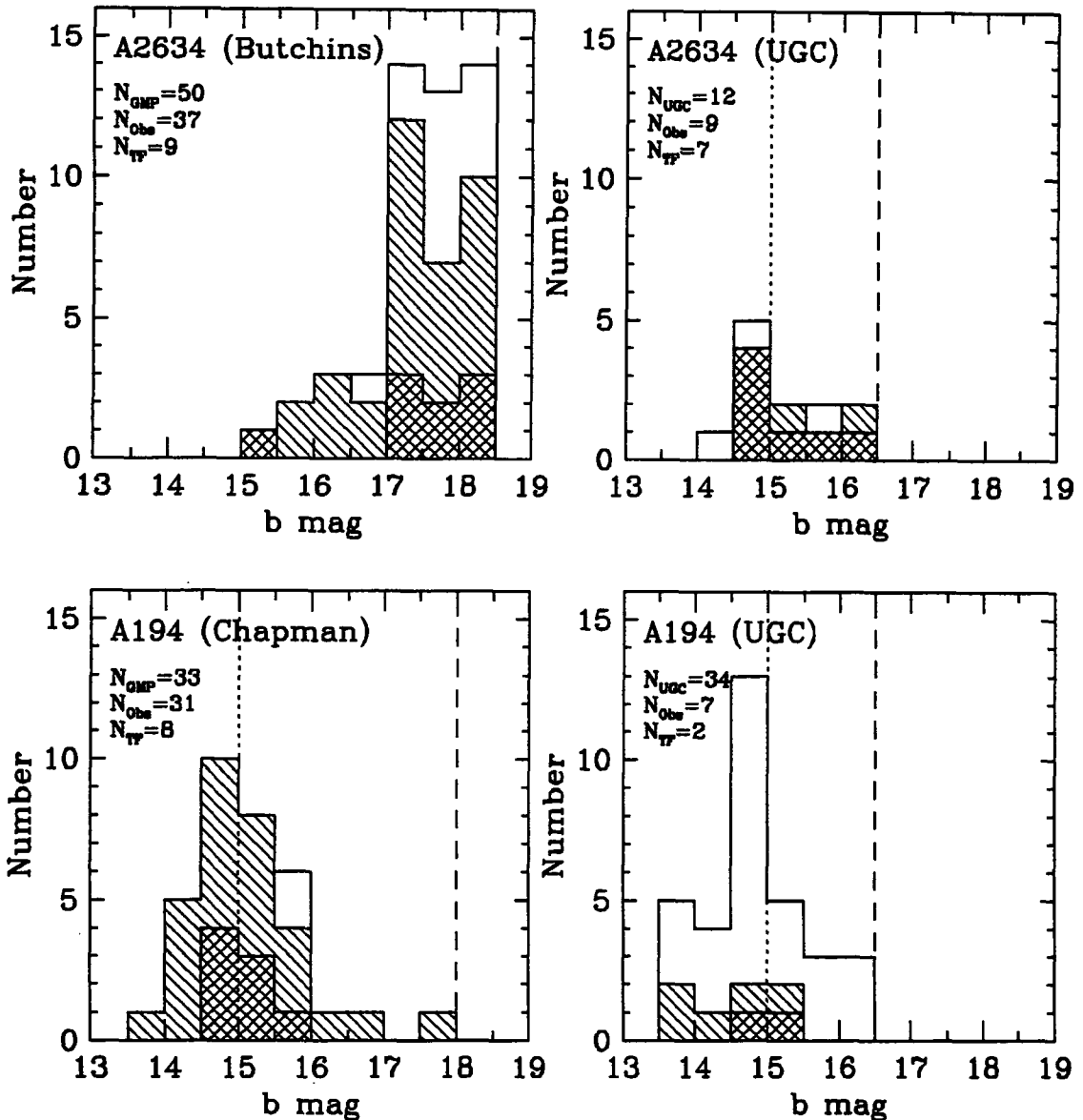


Figure 5.9: Four histograms showing the B-band magnitude distribution for galaxies selected from the Abell 2634 and Abell 194 clusters. The left-hand plots show the distribution for the samples selected from plate scans. The right-hand plots indicate the sample magnitude distribution of objects taken from the UGC catalogue. The imposed magnitude limits of 18.0 and 16.5 are marked as dashed lines. The suspected completeness limit of the UGC catalogue is shown with a dotted line. The open histograms indicate selected objects and hatched and cross-hatched bars indicate observed and final TF galaxies.

procedures were used for all clusters and rotation velocity (and surface brightness) is independent of distance, any remaining effect should remain constant between the four clusters, allowing an unbiased comparison of slopes and intercepts.

This is fortuitous, because if there was strong selection in $\log V_{R\alpha}$, as well as magnitudes, then *all* possible fitting methods would produce biased re-

sults. In such a situation making any sort of statement about the underlying relationship independent of selection would be impossible.

5.5 Quantifying the Relationship

An accurate and unbiased fit of the relationship is needed if we are to study the changes in the Tully-Fisher with variations in galaxy properties across

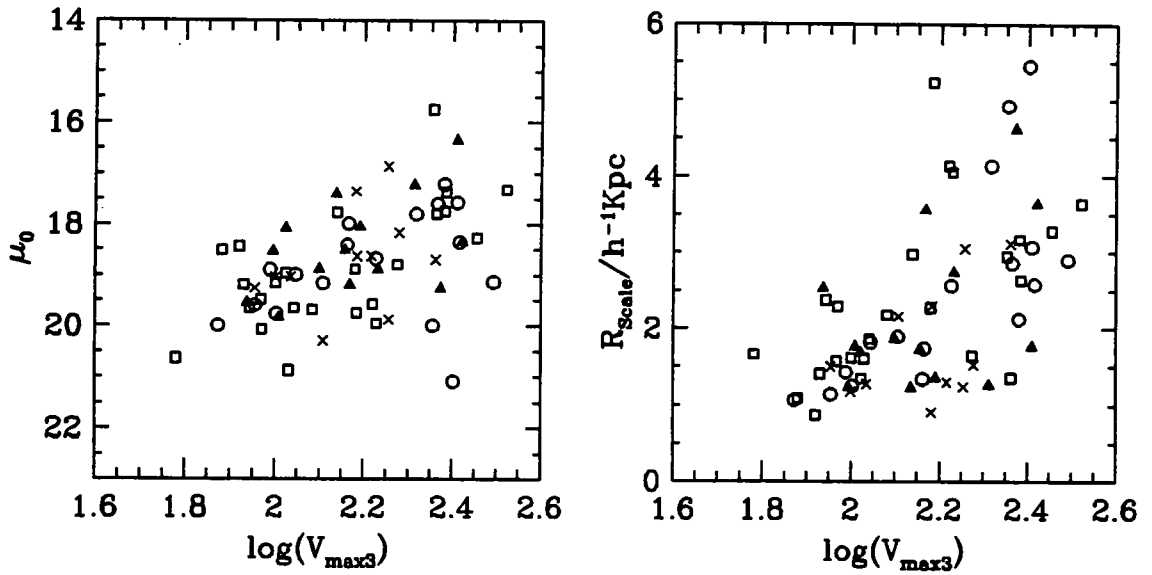


Figure 5.10: Two plots of surface brightness against log-rotation velocity and disk scale length against log-rotation velocity for galaxies within the TF sample. In both cases different symbols indicate the cluster to which each galaxy belongs. Filled triangles mark Coma galaxies, A2634 galaxies are represented by circles, A2199 by squares and A194 by crosses.

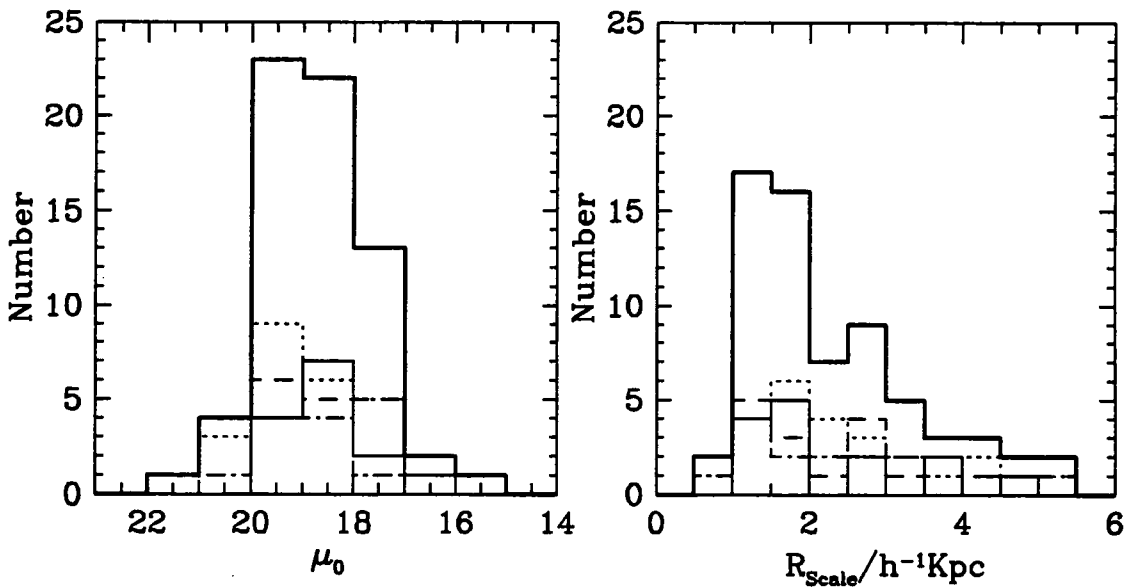


Figure 5.11: Two histograms indicating the disk central surface brightness and disk scale length distributions for the 99 Tully-Fisher galaxies. On both plots the solid thick line indicates the distribution of the whole sample. Other line types show the respective distribution for each of the four clusters; Solid line for Coma, dotted line for A2199, dashed line for A2634 and dot-dashed for A194.

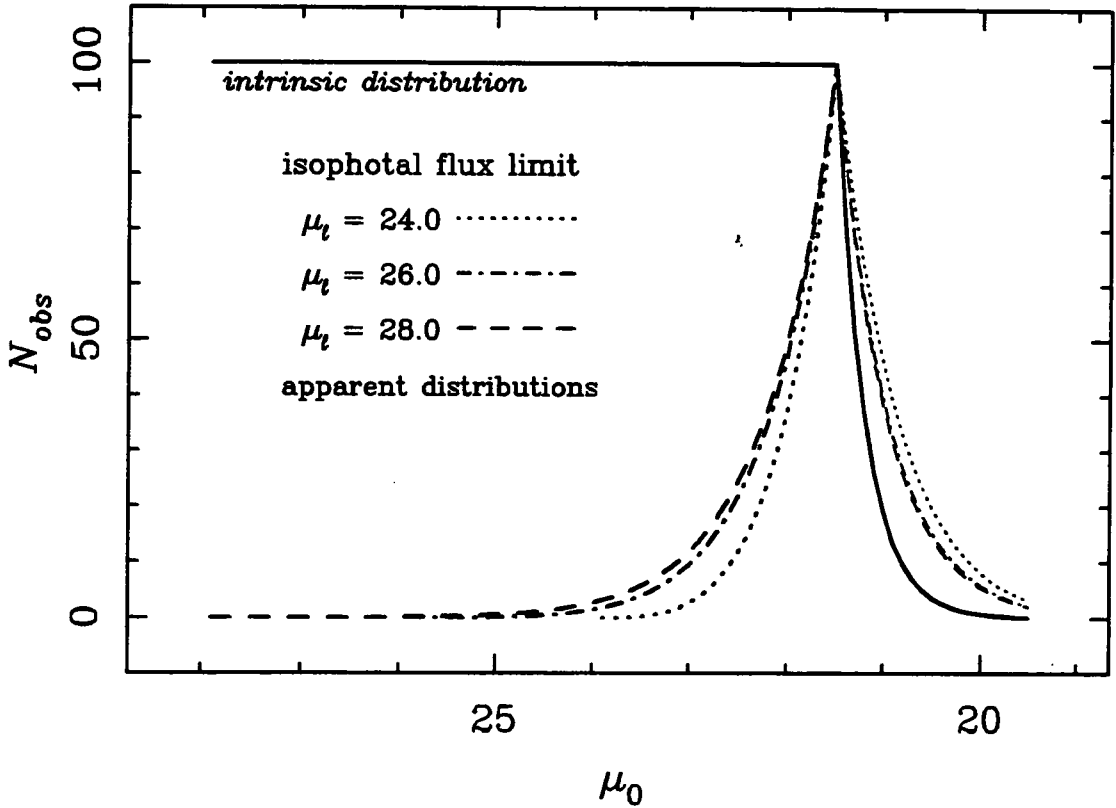


Figure 5.12: A reproduction of McGaugh (1996), Figure 3. Showing the apparent distribution of disk surface brightness of galaxies selected from catalogues limited by isophotal magnitude.

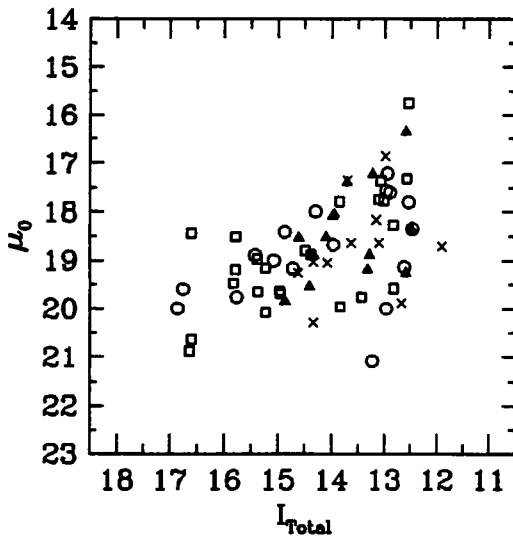


Figure 5.13: Plots of surface brightness against apparent total I-band magnitude for 99 galaxies within the final TF sample. In both cases different symbols indicate the cluster to which each galaxy belongs. Filled triangles mark Coma galaxies, A2634 galaxies are represented by circles, A2199 by squares and A194 by crosses.

clusters. Moreover, reliable confidence limits for the fitted parameters are needed if the significance of any variations is to be assessed. For this purpose a Monte-Carlo simulation program was written that when given a specified relationship, generated many realisations of datasets with the same parameters. Each simulated relationship was then fitted using a chosen regression method, the results and calculated errors stored, and the entire process repeated many times. This was done for a bivariate distribution closely matching the selected galaxy sample, and repeated for all sizes of sample between five and one hundred. In each case both a regression upon rotation velocity and a regression upon magnitude was made.

Results of the simulations can be seen in figures 5.14, 5.15 and 5.16. The three parameters estimated using the direct or “forward” regression ($E(M|P)$) are shown in the left-hand panels and the results from the inverse or “reverse” regression ($E(P|M)$) are plotted in the right-hand panels. In all cases the 68% (1σ) and 95% (2σ) confidence intervals are

marked as dotted lines. Each fit of every realisation produces an error estimate for the fitted parameters, the mean of these estimates for all realisations are plotted as dashed lines on each plot. For all panels the true value of each parameter used to generate the realisations is represented with an arrow, and for the plots of estimated gradient the mean gradient of the opposite regression is marked as a dashed line. In the case of the unbiased relation simulated in Figure 5.14 the dashed line of the predicted errors exactly coincides with the dotted line of the true 1σ limits.

The results given in Figure 5.14 provide an indication of the accuracy expected for regressions performed on a typical dataset but without any selection effects. The bivariate distribution used to generate the simulated data has the same parameters as our dataset, namely a mean $\log V_{R\alpha}$ of 2.2 with $\sigma=0.2$, mean absolute magnitude of -22 with $\sigma=1.5$, a slope of -7.5 and scatter of 0.35 mags. This is identical to the distribution graphically represented in Figure 5.6.

A number of important conclusions can be drawn from Figure 5.14. Firstly, for samples of twenty galaxies or less, the difference in slope between the two regression methods (and hence any possible bias) is insignificant ($< 1\sigma$) compared with the random errors in the estimated slope. This applies to many of the Tully-Fisher samples that appear in the literature, for example only 2 of the 24 clusters within the Mathewson et al. 1992a (1992) dataset (the largest TF survey to date) contain more than twenty galaxies and the largest contains just 28. This means that for the majority of TF cluster samples appearing in the literature the question of which regression line to use is unimportant.

What is also clear from Figure 5.14, is that for a fit to produce values for the slope with errors less than 10% (at 95% confidence limits) a sample size of at least 50 galaxies is needed. Also for sample sizes less than 20 the measured scatter is biased towards low scatter, by as much as 0.5 mags for samples as small as 5 galaxies. Other points to notice are that the estimate of the intercept produced by the inverse regression has the same degree of error as the direct fit but there are greater and asymmetric errors on the gradient.

Figures 5.15 and 5.16 demonstrate the impact of selection effects on the estimated parameters. In both figures the underlying relationship is the same as before. In Figure 5.15 the estimated selection effects of the current sample are applied, complete to an I-band magnitude of -22 and completeness falling linearly to zero at -19. In Figure 5.16 a much higher magnitude cut is made at -21.5, this is representative of samples selected solely from the Zwicky catalogue (e.g. Aaronson et al. 1982). Both of these selection scenarios are graphically represented in the upper and lower left panels of Figure 5.7.

Note that in both Figure 5.15 and Figure 5.16 the values estimated by the direct regression for the slope and intercept are biased away from their true values. In Figure 5.15 the bias is towards lower values and constant for all sample sizes, but it is only significant for very large samples. The bias displayed in by the direct fit in Figure 5.16 is about twice as large but is still only significant for samples larger than 50 galaxies. In both cases the mean parameters produced by the inverse regression remains unbiased.

The results of these simulations provide numerical evidence that the inverse regression ($\log V_{R\alpha}$ on M_I) remains unbiased so long as the rotation velocity parameter is free from selection bias. These effects are placed on a firm mathematical basis in Hendry & Simmons (1994), where the reader will find a full and detailed analysis. Hendry provides rigorous proof that the parameter and distance estimates produced using the inverse regression remain unbiased at all distances and for all sample sizes and realistic distributions. And that the amount of bias in the direct fit depends upon the scatter in the relation and where the selection limits occur with respect to the peak of the magnitude distribution. Further, he demonstrates that *only* the inverse regression is unbiased in cases where there are magnitude dependent selection effects and the rotation velocity remains selection free. This remains true for all underlying distributions of M and P and does not depend upon them being normal.

We can conclude that any bias introduced by selection effects into the cluster samples is small, and

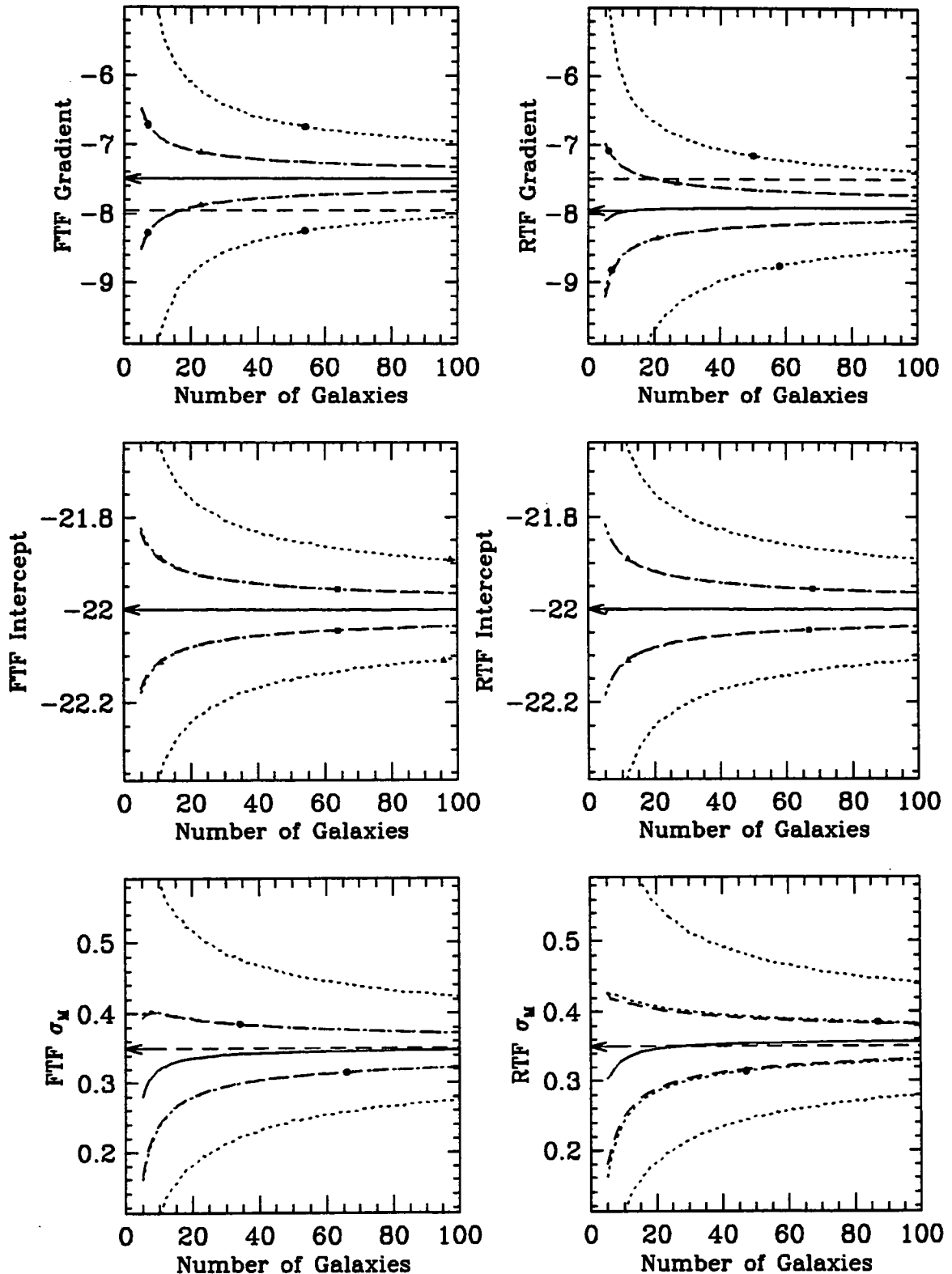


Figure 5.14: Six line plots of output from a Monte-Carlo simulation of the Tully-Fisher fitting procedure for sample sizes ranging from 5 to 100 galaxies. With no magnitude selection effects. The three left-hand plots indicate from top to bottom; The TF gradient estimated using the “forward” regression method, TF intercept fitted with the forward method and TF scatter. The right-hand graphs show the same quantities estimated using the “reverse” regression. In each case the arrow indicates the true value of the underlying relation. Dotted lines indicate the $\pm 1\sigma$ and $\pm 2\sigma$ confidence limits of the fitted parameters. The dashed curved lines mark the mean $\pm 1\sigma$ error predicted by the respective fitting methods and the horizontal dashed line marks the mean value predicted by the opposing method.

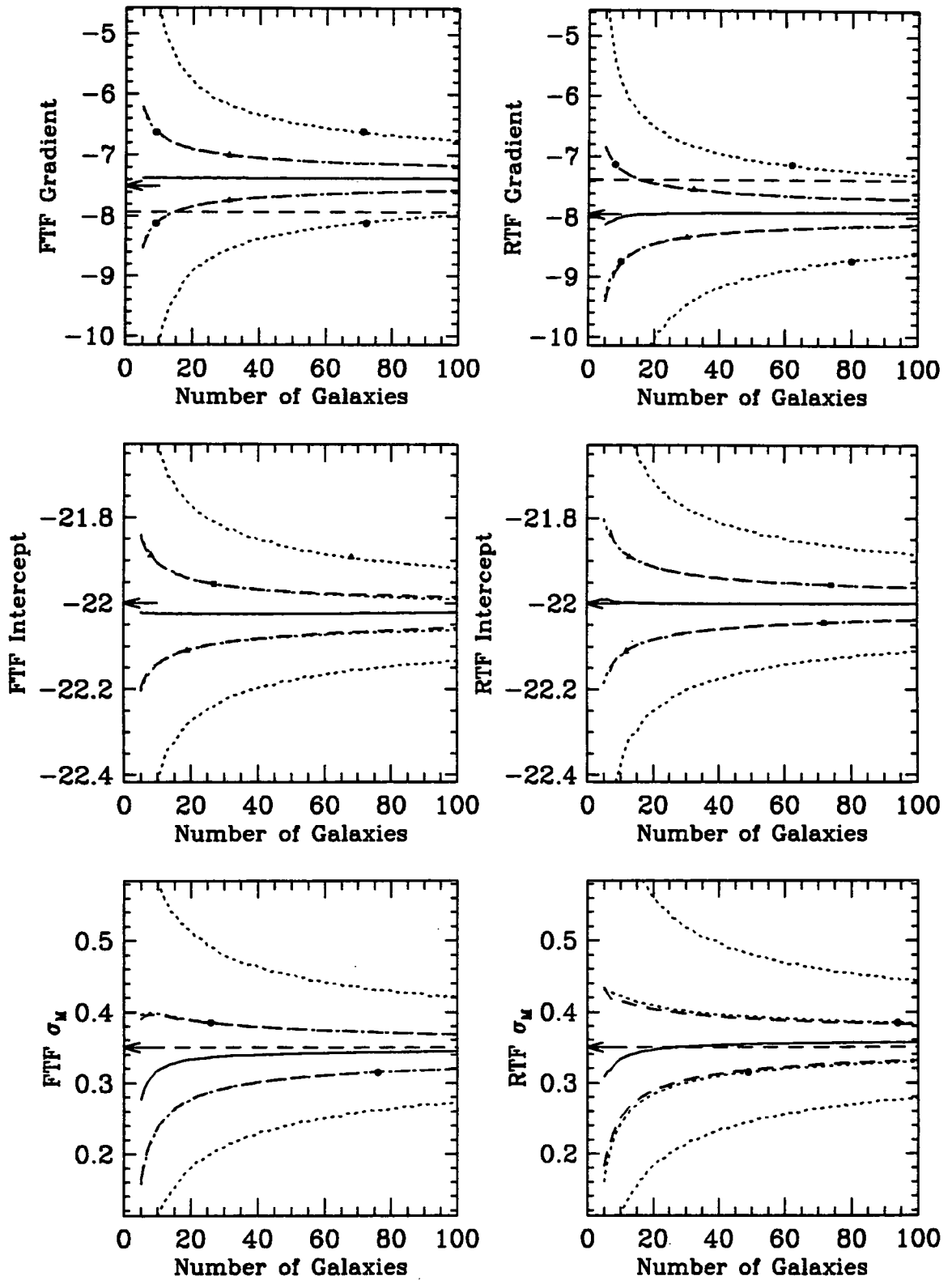


Figure 5.15: Six line plots of output from a Monte-Carlo simulation of the Tully-Fisher fitting procedure for sample sizes ranging from 5 to 100 galaxies. With magnitude selection effects that closely match the present sample. The marked lines have the same meaning as in Figure 5.14. The circles, triangles and squares indicate at which point the $\pm 1\sigma$ and $\pm 2\sigma$ confidence limit lines are within 10%, 5% and 2% of the mean predicted value. Note that in the case of magnitude-only selection the forward regression line becomes biased, whereas the reverse regression remains unaffected.

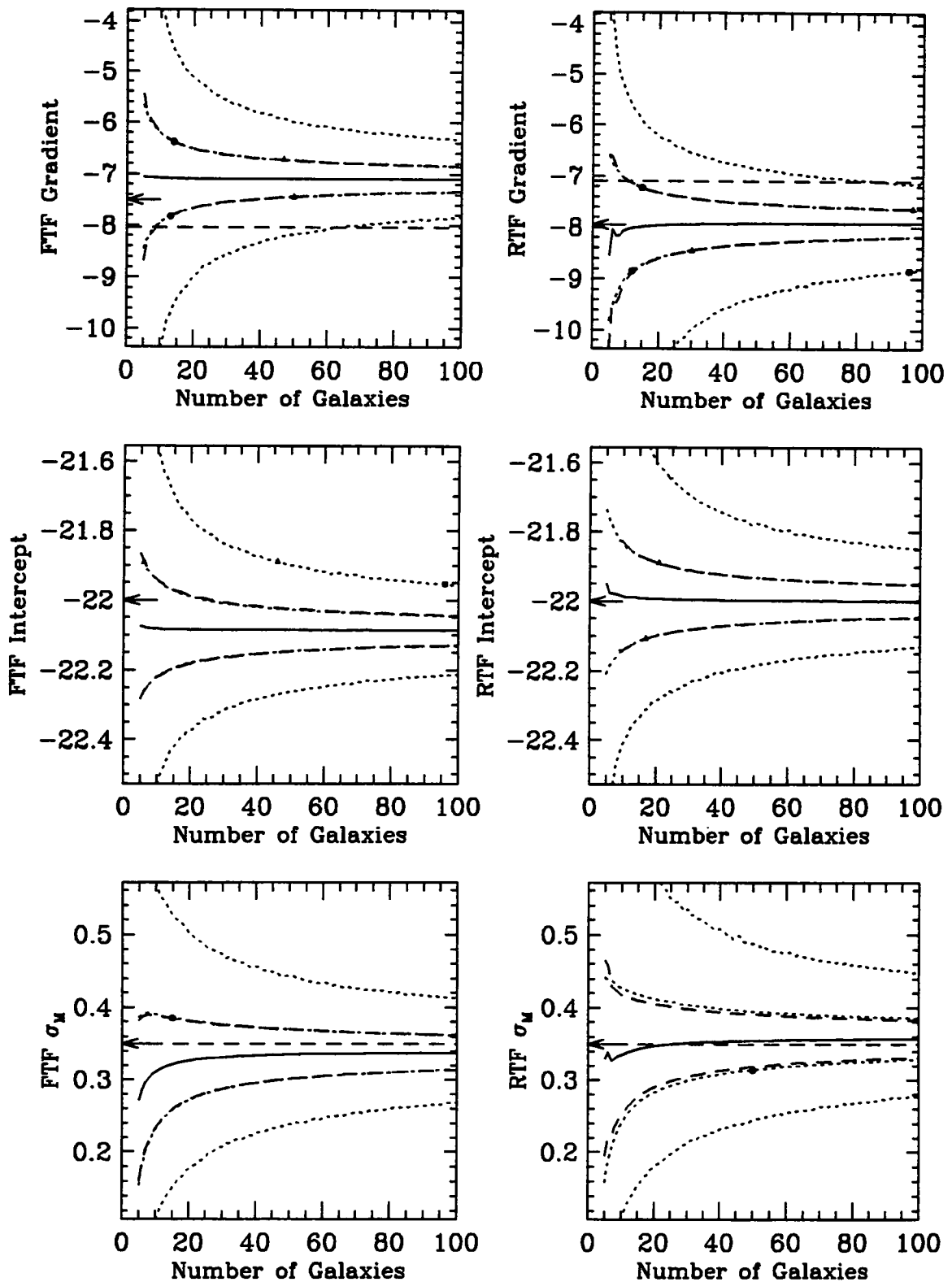


Figure 5.16: Six line plots of output from a Monte-Carlo simulation of the Tully-Fisher fitting procedure for sample sizes ranging from 5 to 100 galaxies. With magnitude selection effects that resemble those depicted in the lower left plot of Figure 5.7. The marked lines and symbols have the same meaning as in figures 5.14 and 5.15. Note that even in the case of strong selection effects, sample sizes of 30 galaxies or over are needed before the amount of bias on the forward regression line becomes significant.

only in the case of Coma, the largest sample, is marginally significant. Even these small biases can be completely removed by using the inverse regression to estimate the relationships parameters. For this reason throughout this work the inverse regression is used unless otherwise stated.

Assuming that the model used in Figure 5.15 correctly represents the distribution and selection effects present in the current dataset, then Figure 5.15 can be used to estimate an upper limit on the accuracy of parameters estimated from the fit. For the slope the expected accuracy ranges from 14% for the Coma sample down to 33% for Abell 194. Errors in the measured intercept in terms of distance range from 10% to 20% and the errors in the measured slope are expected to range between 38% and 70% (all 95% confidence limits). Ultimately these random errors will limit the size of variations that can be significantly detected. Clearly increasing the size of the present samples would be the greatest improvement that one could make to the dataset.

The other important factors that contributes to the fit errors and the size of possible biases is the scatter in the relationship. The scatter in the observer relationship can be reduced by imposing more rigorous rejection criteria upon the sample and by using parameter error estimates to weight individual data points to increase the accuracy of the fit. These methods of reducing the scatter in the relationship are the topic of the remaining sections in this chapter. The first step in this process is the identification of all sources of measurement error present in the dataset.

5.6 Sources of Error

To accurately estimate the individual errors on each point we first need to do a detailed accounting of all sources of error and propagate them through to the final measured parameters. For all estimated parameters, contributions to the error come from two main sources. Random measurement errors on the raw observables is due to signal to noise considerations and systematic errors are introduced by the particular method used to correct the observables in order to obtain the final TF parameters. A complete account of all sources of error are given in Table

5.1. See chapters 3 and 4 for a detailed discussion of uncertainties within the dataset which are briefly mentioned here.

5.6.1 Photometric data

The error contributions to the final total magnitude parameter come from five sources (See Chapter 3 for full details of photometric reduction process). The measured total magnitude makes up less than half of the total error. Errors in the photometric zero point, isophotal magnitude and extrapolation to total magnitude combine to produce a rms error of 0.03 magnitudes as compared to a the total error of 0.08 mags. The main contribution to the total error comes from the adopted internal absorption correction (See §5.8), errors in the measured ellipticity combine with the uncertain extinction correction to contribute a rms error of 0.066 mags to the total. The other main source of error is the Galactic extinction correction which adds a further 0.031 mags rms to the overall error. A small contribution is also added due to uncertainties in the K-correction.

5.6.2 Spectroscopic data

The uncertainty in the measured rotation velocity is dominated by errors associated with the fitting of the rotation curve. Low signal-to-noise regions of the curve greatly increase the errors on the fitted central wavelength of the H α emission line. These errors combine with real variations in the rotation curve due to spiral structure to increase the rms velocity variations within the curve. The net effect is to inflate the errors on the interpolated rotation velocity to typically 10% which contributes 0.25 mags rms to the scatter within the relationship. The measured rotation velocity also has to be corrected for projection which introduces a further dependence upon the measured ellipticity needed to calculate the inclination. Errors in the ellipticity result in uncertainties in the inclination correction that contribute a further 5% error to the rotation velocity parameter.

5.6.3 Error Budget

A full and detailed list of all error sources and their relative contributions to the TF scatter within the

Table 5.1. A complete account of all sources of error and their relative contributions to the scatter about the Tully-Fisher relation. Column headings are (where applicable); mean and maximum size of correction applied, the mean standard deviation of the measured parameters (also given as a percentage, in magnitudes and as a percentage distance error) and the upper limit on any possible systematic errors. See text (§5.6.3) for full details.

Source of Error	Mean,	Standard Deviations				Max
	Max (mag)	$\sigma_{Param.}$	$\sigma_{\%}$	$\sigma_{Mag.}$	$\sigma_{\%}^{Dist.}$	Bias
Measured I-band total magnitude:						
Photometric zero point		-	-	0.012	00.5	≤ 0.010
Measuring isophotal magnitude		-	-	0.021	01.0	0.000
Extrapolating to total magnitude		-	-	0.018	00.8	≤ 0.010
	0.059, 0.280	-	-	0.030	01.4	≤ 0.020
Measured disk ellipticity:						
Isophote fitting		0.019	03.4	-	-	-
Typical rms variation over disk region		0.018	03.2	-	-	-
Subjective selection of disk region		0.030	05.4	-	-	-
		0.040	07.2	-	-	-
Internal absorption correction to total magnitude:						
Propagation of error in ellipticity		-	-	0.051	02.4	0.000
Uncertainty in absorption model		-	-	0.041	01.9	≤ 0.003
	0.009, 0.387	-	-	0.066	03.6	≤ 0.003
Galactic absorption correction to total magnitude:						
Uncertainty in measured extinction		-	-	0.030	01.3	0.000
Uncertainty in b-band to I-band conversion		-	-	0.006	00.3	≤ 0.010
	0.026, 0.099	-	-	0.031	01.4	≤ 0.010
K-correction to total magnitude:						
Uncertainty in measured redshift		21.30	00.3	0.000	00.0	0.010
Uncertainty in K-correction model		-	-	0.003	00.1	0.010
	0.018, 0.020	-	-	0.003	00.1	0.010
Typical error contribution from log-luminosity parameter:						
				0.080	03.8	≤ 0.043
Measured maximum rotation velocity:						
Wavelength calibration ^b		01.10	00.9	0.026	01.2	0.000
H α emission line fitting ^b		09.70	07.6	0.211	10.2	0.000
Real variations in rotation curve ^{ab}		06.10	04.8	0.129	06.1	0.000
		11.50	09.0	0.249	12.2	0.000
Inclination/relativistic correction to rotation velocity:						
Error in inclination due to ellipticity error ^b		03.08	04.5	0.078	03.6	0.000
Uncertainty in form of inclination calculation ^b		01.55	02.3	0.027	01.2	≤ 0.030
Error in relativistic correction ^b		00.00	00.1	0.000	00.0	0.000
	0.571, 1.442	03.44	05.0	0.082	03.9	≤ 0.030
Typical error contribution from rotation velocity parameter^b:						
				0.266	13.0	≤ 0.030
Total Uncertainty:						
Errors added in quadrature		-	-	0.280	13.8	≤ 0.073
Allowing for correlation between errors		-	-	0.270	13.2	≤ 0.073

Notes:

^a The relative contribution from line fitting errors and variations in the rotation curve due to spiral structure vary greatly between galaxies. The typical values given here are consistent with internal error estimates.

^b Assumes a gradient of -7.5 for the TF relation when calculating corresponding magnitude and distance errors.

relationship appear in Table 5.1. This error budget provides a guide to the relative breakdown of errors for a typical galaxy within our sample.

For each source of error, the mean rms error for all 99 galaxies in the final sample was calculated and each error is tabulated in four forms; in units of the parameter, as a percentage, the corresponding magnitude error (assuming a TF gradient), and the percentage distance error corresponding to the magnitude error. When the source of error is associated with a correction, the mean and maximum value of the correction is shown to enable comparison with the uncertainty introduced. Where applicable, any bias that could possibly be introduced is given as an upper limit in magnitudes.

For each galaxy, the error estimates for total magnitude and rotation velocity are calculated by adding up their respective error contributions in quadrature. The mean total magnitude error and mean rotation velocity error for the sample appear underlined in Table 5.1.

Note that some error estimates that appear in the error budget, particularly the errors on the photometric parameters, are slightly lower than would be expected when considering the external errors tabulated in Table 3.2. These differences can be attributed to the subjectiveness of selecting the disk region within each galaxy's surface brightness profile.

An example is the $\sigma \approx 0.10$ scatter between external measurements of the ellipticity and our own measurements (See Table 3.2). This scatter is not due to problems in fitting the particular isophote, because repeat measurements show that this can be done accurately. Rather the scatter is due to the problems of approximating the often irregular shape of spiral isophotes with ellipses, combined with the process of deciding upon a disk region of the elliptical fits and taking the mean ellipse parameters over this region as the disk values. This is a valid method but is a subjective process, and different observers get slightly different disk parameters as a result. The same argument applies to the measurement of the position angle and the extrapolation of the disk light to obtain a total magnitude. As much as 0.05 mags of the external errors could be due to this effect.

5.6.4 The Weighted Inverse Regression

The Tully-Fisher relation for the selected galaxies previously plotted in Figure 5.3 are now plotted in Figure 5.17 with error bars marking the 1σ magnitude and rotation velocity errors for each galaxy. The symbols retain the same meaning and as before, the inverse regression and direct regressions are marked with solid and dotted lines respectively. For each cluster the full details of each fit are marked in the upper left-hand corner of each panel.

Error estimates for each galaxy can now be used to weight each point within the regression calculation thus lowering the impact of discrepant low quality data points on the fit. The same relationship fitted using a weighted inverse regression is shown in Figure 5.18. As the regression is purely on I_{Total} only the errors on rotation velocity are used to weight the fit.

An orthogonal regression technique would also allow the inclusion of the magnitude errors into the weighting scheme. But as such an approach, by its very nature, relies upon the direct regression line in addition to the inverse, it is susceptible to the magnitude selection effects discussed above in §5.5. The assumptions and mathematical framework adopted above and detailed in Hendry & Simmons (1994) are not affected by adopting a weighting scheme when calculating the regression. In particular, the assumption that the inverse regression is unbiased when the rotation velocity parameter is free from selection remains true.

The majority of galaxies within the present sample have rotation velocity errors over three times larger than their magnitude errors. So any combined weighting scheme would still be dominated by the rotation velocity errors and any gain from including the magnitude errors would be small. By ignoring the extra information provided by the magnitude errors, we are in effect accepting slightly larger random errors in the fit parameters in return for a bias-free regression.

Note that the data and errors plotted in figures 5.17 and 5.18 appearing in Table 5.1 were produced using the finally adopted versions of the corrections which are discussed in §5.8 below. As with much of this work an iterative approach was adopted. The

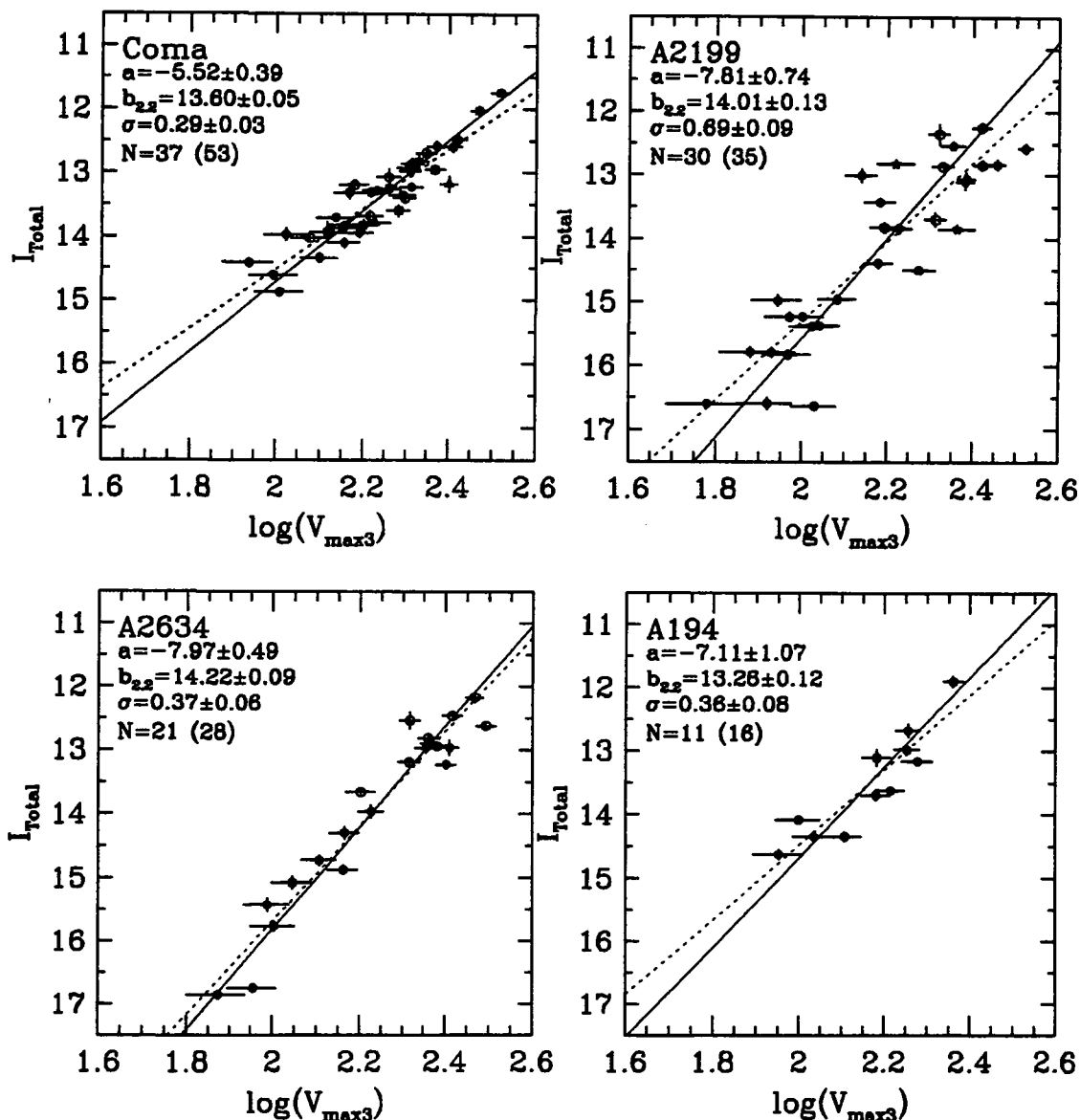


Figure 5.17: The Tully-Fisher relation within the four target clusters. The symbols are the same as in figure 5.2. $\pm 1\sigma$ error estimates in magnitude and log-rotation velocity are marked on each point. The regression line of $\log V_{\text{max}3}$ upon I_{Total} is marked as a solid line on each relation. The details of each of these fits are marked in the upper left of each panel. The regression of I_{Total} upon $\log V_{\text{max}3}$ is represented in each case as a dotted line.

most current corrections from the literature were used to produce the first version of the relationship and error estimates. Then using the techniques discussed below in §5.8 improved versions of the corrections were adopted and used to produce the final Tully-Fisher relation appearing here.

5.7 Forming a Composite Relationship

In order to form a single, well populated relationship to use in studying the optimal forms of the various

parameter corrections, the next stage in the analysis was to combine the four individual cluster relations into one composite relationship. This can be done by simultaneously fitting the entire dataset with a single gradient and intercept while leaving the relative distance moduli between Coma and A2199, A2634 and A194 as free parameters. In effect, the intercepts of the three smaller cluster samples are allowed to slide in magnitude until their respective galaxies display the minimum scatter around the Coma rela-

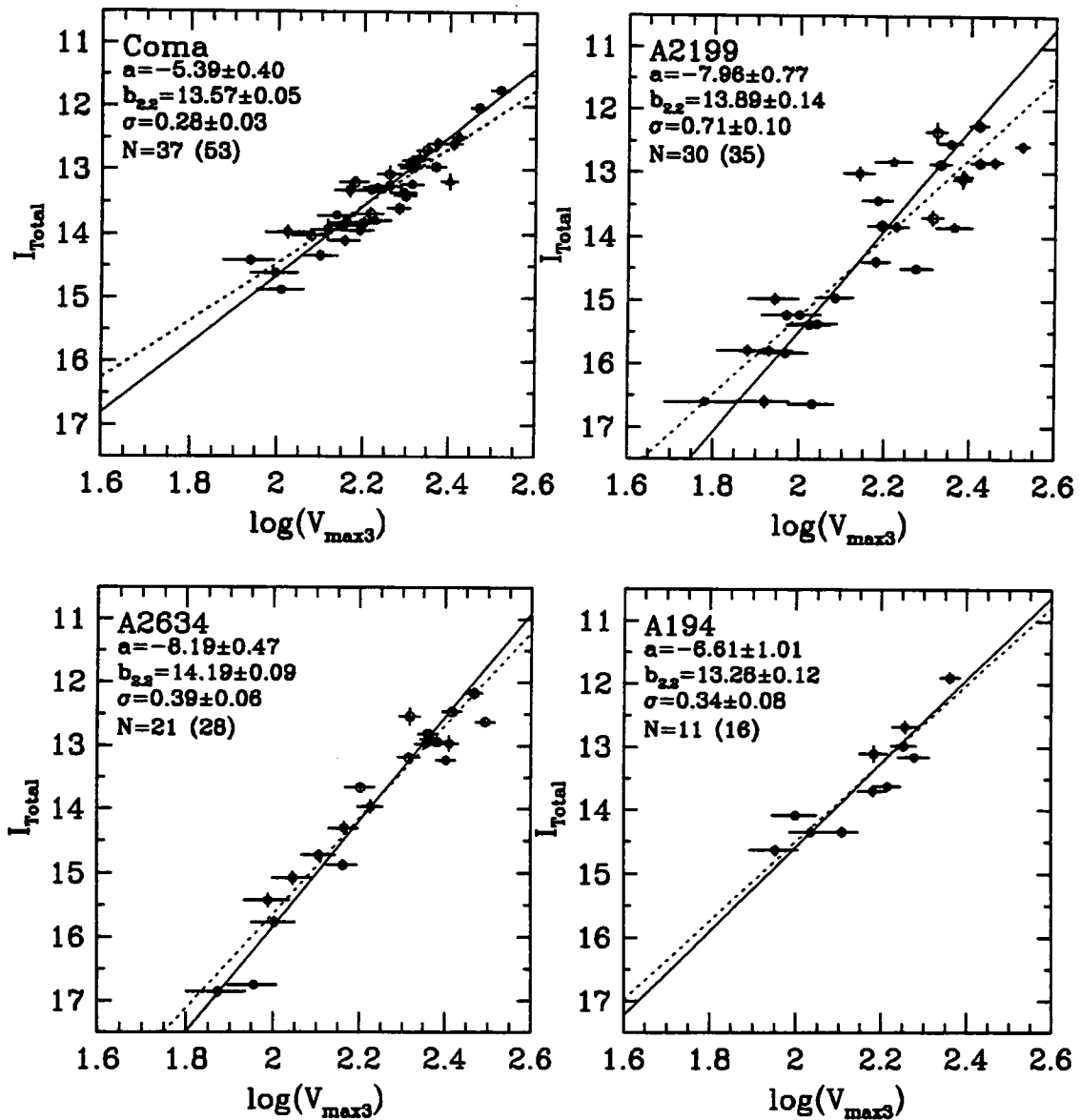


Figure 5.18: The Tully-Fisher relation within the four target clusters. The symbols are the same as in figure 5.2. $\pm 1\sigma$ error estimates in magnitude and log-rotation velocity are marked on each point. The weighted inverse regression line of $\log V_{\text{max}3}$ upon I_{Total} is marked as a solid line on each relation. The details of each of these fits are marked in the upper left of each panel. The regression of I_{Total} upon $\log V_{\text{max}3}$ is represented in each case as a dotted line.

tion. Implicit in this process is the assumption that the Tully-Fisher relation is universal, i.e. galaxies in all clusters obey the same relationship with the same slope.

Fitting the entire dataset in such a way has a number of advantages. Coefficients that appear in the corrections to the observables (See §5.1 and §5.8) can also be allowed to be free parameters. Thus the optimal forms of the corrections, that produce the minimum scatter in the relation, can also be pro-

duced simultaneously. The resulting well populated relationship means that the estimated slope and scatter have much smaller errors. Of course this is also the most logical way of calculating the relative distance between the clusters.

One problem with this technique is the impact selection effects in apparent magnitude can have on the fitting process. A weighted inverse regression is used to fit the points which itself is free from the effects of magnitude selection. But differential selec-

tion limits and completeness within each cluster can seriously affect the relative magnitude shift applied to each cluster.

Developing a program to fit the TF parameters and relative cluster distances while simultaneously dealing with selection effects would be a complex task. Fortunately Martin Hendry has developed such a program (private communication) which tackles this problem using a maximum-likelihood technique that includes a simple model of the selection effects.

The program first computes the properties of the sample, i.e. the mean and standard deviation of the magnitudes and rotation velocities within the sample. Next, a simple fit is calculated, regressing on magnitude and assuming no selection. Then using the first fit to provide starting values for the free parameters, along with inputted initial distance estimates for the clusters, it enters into an iterative fitting loop. During each iteration a bias correction term is calculated which shifts the data points in such a way as to counteract the effects of magnitude selection. Each cluster is then shifted in magnitude with respect to a calibrating cluster (in this case Coma). At the same time fit parameters are chosen in such a way as to maximise the likelihood of the distribution of points around the relation.

This produces an improved set of distance estimates and corrections which can then be re-applied to the original data. New selection corrections are calculated and the entire process repeated until the fitted parameters converge within a specified tolerance. A bootstrap resampling method is then used to estimate the errors on each of the parameters. Many random subsamples of the data are generated and re-fit using the same fitting process which produces a distribution of fitted parameters around their best-fit values from which confidence limits can be calculated.

The results from the composite fit can be seen in Figure 5.19, where the best fit line is represented as a solid line and the fit details are displayed in the upper left-hand corner of the panel. Four different symbols are used to represent galaxies from each of the clusters and the mean magnitude and rotation velocity errors are marked with an error bar.

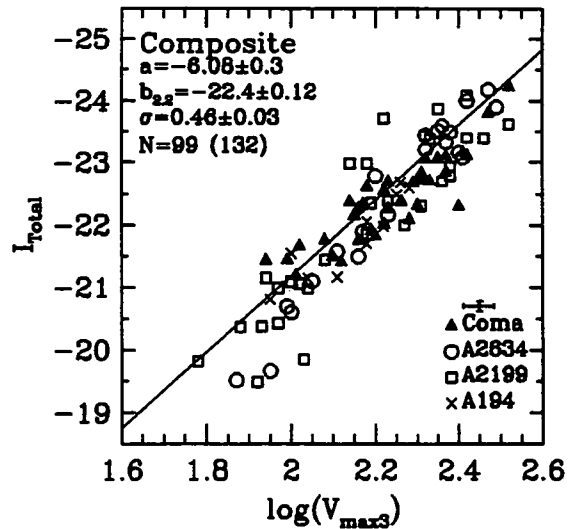


Figure 5.19: A Composite Tully-Fisher formed by combining the four separate cluster TF relations. The entire dataset was simultaneously fitted for a single slope and three distance moduli relative to Coma using a maximum likelihood technique developed by Martin Hendry. The error bars indicate the mean errors for the sample.

One draw back of this technique is that only a simple magnitude limit is used to represent the apparent magnitude selection function, whereas with the present sample, the fact that we have seen falling completeness at fainter magnitudes is also a problem.

However, the main difficulty with this approach is that the gradient of the relationship is assumed to be constant for all clusters. This is not unreasonable and can still be considered the paradigm within current Tully-Fisher literature. But the individual fits to the relationship shown in Figure 5.18 clearly show evidence for significant variations in the gradient between clusters. This is most apparent in the differences between Coma and Abell 2634 where the gradients show a 4.5σ difference.

Further support for variations is provided when Hendry's ML fitting procedure is applied to the individual clusters. The result of this are shown in Figure 5.20 where the symbol meanings are the same as Figure 5.19. The fits produced are consistent with those shown in Figure 5.18 and show the same difference between the Coma and A2634 gradients.

Signs of these variations can also be seen in the results of the composite fit. The fitted slope is inter-

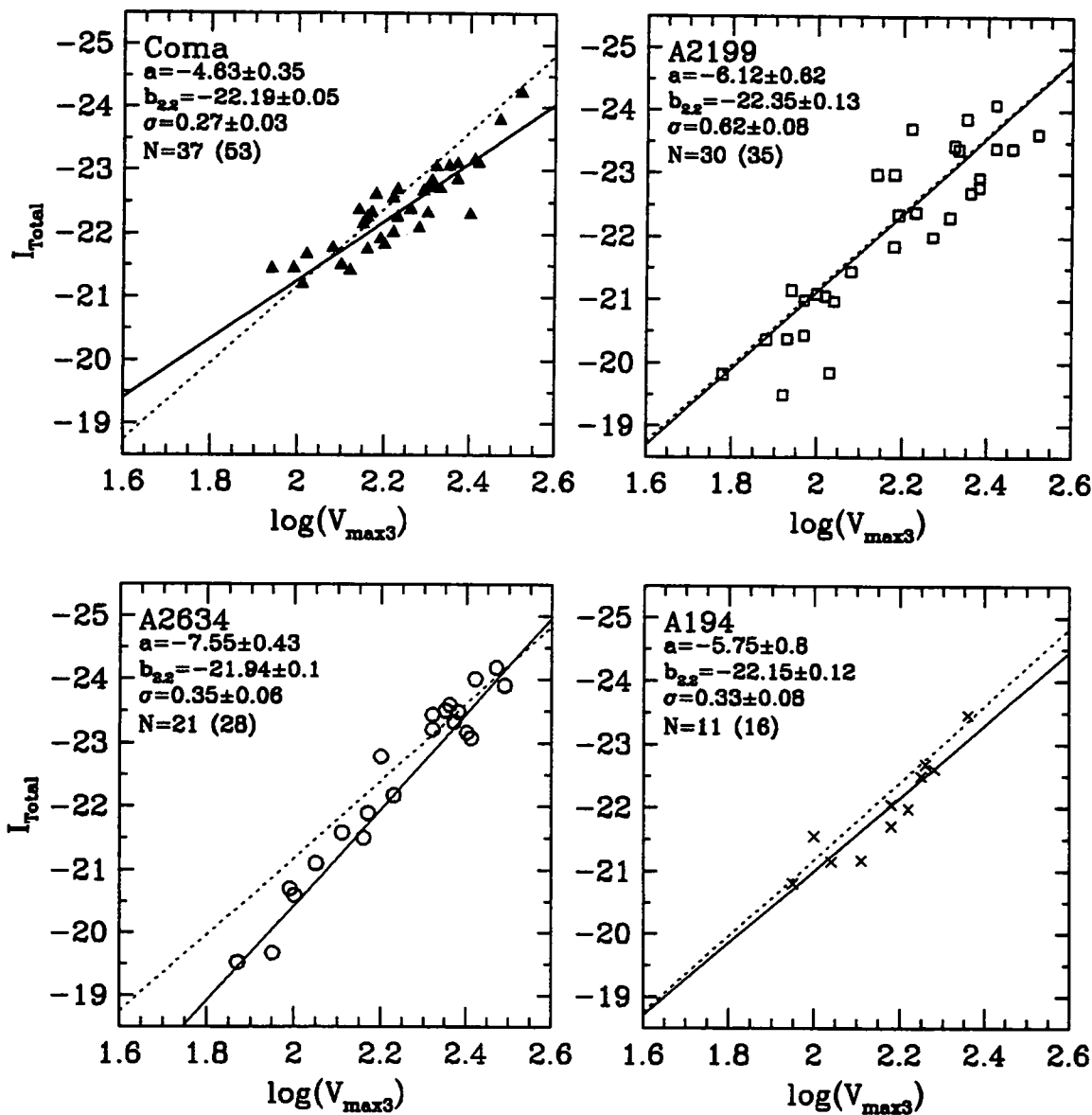


Figure 5.20: The results of applying Hendry's fitting technique to the separate clusters. A solid line on each relationship represents the maximum likelihood fit that attempts to correct for selection bias. The results of each fit are displayed in the upper left-hand corner of each panel. A dotted line represents the composite fit line.

mediate between the range of slopes but the Coma and A2634 points show a trend away from the fit line. This means that scatter around the relationship is larger than the scatter in three of the individual cluster fits.

The significance of possible variations in the TF gradient between the sample clusters will be further discussed in §6.2. However, at this point it should be noted that doubts about the gradient remaining constant are sufficient enough to not rely upon this technique to calculate the best corrections. The in-

creased scatter and fit errors along with systematic variations in slope would inflate the errors on the fit residuals and introduce spurious trends in terms of magnitude and rotation velocity.

Instead the individual cluster fits discussed in §5.6.4 were used when deciding upon the optimal parameter corrections.

5.8 Optimal Corrections

The mean and maximum corrections applied to the TF parameters are shown in Table 5.1 and it is apparent that the two most important corrections are those made to the rotation velocity and the internal absorption correction applied to the apparent magnitudes. In terms of both the size of the correction and the uncertainties introduced, the other corrections are relatively unimportant.

The largest correction is the $\sin i$ inclination correction applied to the rotation velocity of each galaxy and this is also the correction that introduces the most uncertainty into the final parameters. There is no doubt over the form of this correction, the errors are in the inclination which is in turn calculated from the measured ellipticity (see §5.2 for details).

The inclination calculation usually adopted in the literature (see Equation 5.3) makes the assumption that, on average, face-on spiral galaxies have perfectly circular isophotes and edge-on spirals have the same ellipticity, $e = 1 - q_0$. As a result, the uncertainty in the inclination depends on the extent to which these assumptions remain true for each individual galaxy and to the accuracy with which the disk ellipticity can be measured.

Clearly the assumption that all spiral galaxies have the same edge-on ellipticity is only an approximation as each galaxy will deviate from this value due to variations in morphology and spiral structure. It is the size of these intrinsic variations that contribute to the inclination errors.

In principle an ideal value of q_0 , the edge-on minor-to-major axial ratio, could be used that minimises the scatter in the relationship. But in practice this proves not to be the case. Due to correlations between the errors introduced by the inclination and internal absorption corrections (they both depend upon ellipticity), the inclination errors scatter along the relationship rather than away from it (see §6.1.1). This reduces the dependence of the TF residuals upon inclination errors to the point where they are completely masked by other errors.

In the current literature a range of values for q_0 between 0.11 and 0.18 are adopted. Figure 5.21 shows the resulting sample inclination distributions when using q_0 values of either 0.11 and 0.18. The

expected inclination distribution of a sample of randomly orientated disks is proportional to $\sin^2 i$ and as a result increases towards higher inclinations. It can be seen from Figure 5.21 that this distribution is most closely matched when the adopted value of $q_0 = 0.18$ is used.

With the value of the mean edge-on axial ratio fixed, the typical amount that galaxies within the sample deviate from $q_0 = 0.18$ further contributes to the inclination error. Although it is hard to estimate the size of this contribution, very large deviations would effectively smooth out the inclination distribution. As this is not seen, it can be assumed that this is not a major effect. The effect of variations in q_0 on the inclination error at different inclinations is shown in Figure 5.23.

The error on the measured disk ellipticity comes from three sources; errors in isophotal fitting, typical rms variations in the ellipticity (due to spiral structure within the disk) and the subjective nature of selecting the disk region from each galaxy's surface brightness profile. These factors combine to produce a mean disk ellipticity error, estimated by external comparisons, of 0.04. The contribution from the ellipticity error to the total inclination error is shown in Figure 5.22. Considering that the mean inclination for the sample is around 70° , it is clear from both figures 5.22 and 5.23 that minimising errors in ellipticity is the most critical factor in keeping the inclination errors low.

The second most important TF correction, in terms of its effect and the errors introduced, is the internal extinction correction. The correction used in the current literature usually assumes that extinction is proportional to the logarithm of the major-to-minor axis ratio, following Giovanelli et al. (1994):

$$\Delta m = \gamma \log(1/(1 - e)) \quad (5.14)$$

Where e is the ellipticity and γ is a coefficient approximately equal to 1.00.

The technique adopted allows γ to be a free parameter during the fitting of the relationship, adopting a value of γ that minimises the scatter in the final relationship. It was found that a value of $\gamma = 0.85$ produced the minimum TF scatter. This proved to be only a marginal improvement over the simpler cor-

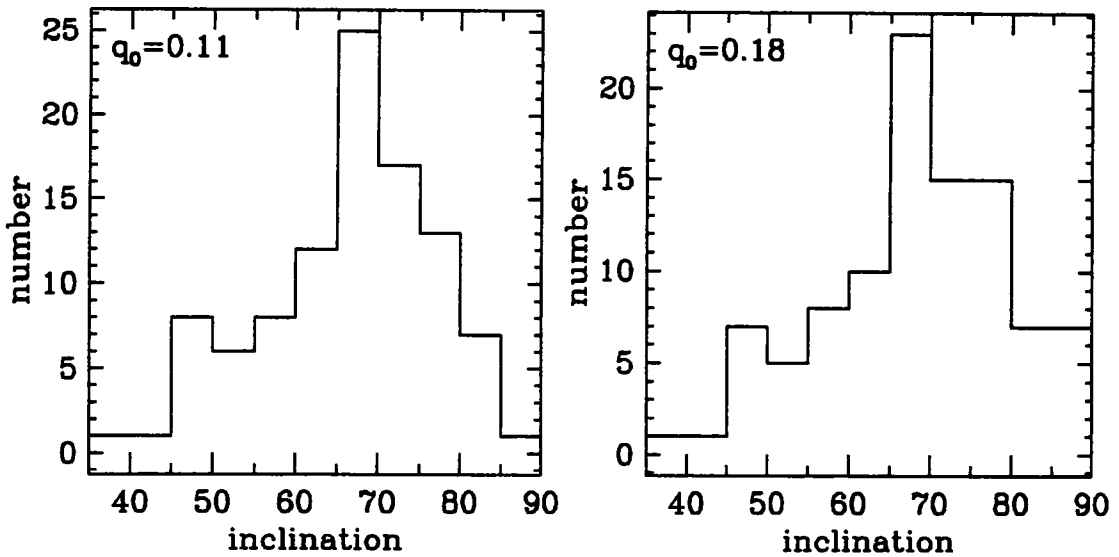


Figure 5.21: Histograms indicating two possible inclination distributions for the sample. The left-hand panel shows the calculated distribution assuming that the mean edge-on axial ratio, q_0 , of the sample galaxies is 0.11. The right-hand graph shows the distribution if q_0 is 0.18. As randomly oriented disks are more likely to be viewed edge-on, $q_0 = 0.18$ is considered more likely.

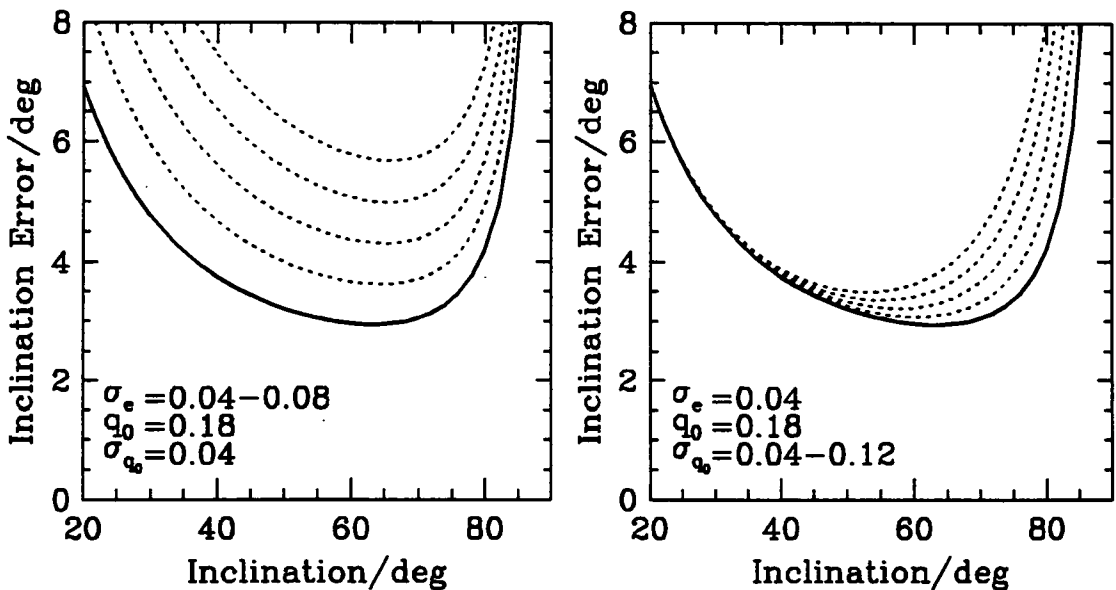


Figure 5.22: Two graphs of the errors in the calculated inclination versus inclination for different ellipticity errors and values of the edge-on axial ratio, q_0 . The left-hand graph shows how the relationship between the inclination error and inclination changes for different rms ellipticity errors. The lines represent steps of 0.01 from 0.04 to 0.08 rms error. The right-hand panel indicates how the same relation changes depending upon the rms deviations of q_0 for galaxies within the sample. The adopted value of 0.04 in both cases is marked with a solid line.

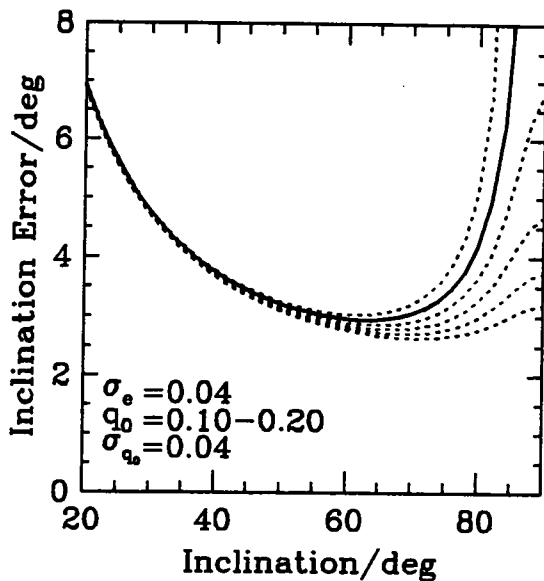


Figure 5.23: A graph showing how the errors in the calculated inclination versus inclination for different values of the edge-on axial ratio, q_0 . The lines represent steps of 0.02 from 0.10 to 0.20. The final adopted value of 0.18 is marked by a solid line.

rection of $\Delta m = \gamma e$ used by Bernstein et al. (1994) which does not have a physical basis.

A graphical representation of these corrections is shown in Figure 5.24. The left-hand panel of Figure 5.24 shows a plot of the fit residuals against disk ellipticity, with no extinction correction applied. The correction suggested by Giovanelli et al. is marked as a solid line in this panel and the linear correction adopted by Bernstein et al. is plotted as a dashed line. The right-hand panel shows the same data after the Giovanelli et al. correction has been applied. There is obviously a trend in the data before correction which is then successfully removed.

However, the scatter in the residuals is such that it is impossible to distinguish a significant difference between the two models. In addition, it should be noted that because the other major correction also depends upon ellipticity, the errors in ellipticity and the errors in the residuals are correlated. This is demonstrated in Figure 5.25 where error bars indicating $\pm 1\sigma$ ellipticity deviations are marked on each data point. Clearly the trend in terms of ellipticity error is such that to a certain extent the apparent effects of extinction are reduced.

However, this technique should be applied with caution. Simply blindly correcting the data with a free parameter will always appear to work in that scatter will be reduced. This is especially true when the data is very noisy and where outlying points can have a disproportionate effect on the model parameters. Thus it has been decided that the size of the present dataset is insufficient to discriminate between the possible models. Instead we adopt the value $\gamma = 1.05$ from Giovanelli et al. who utilise a much larger sample of 1400 galaxies in fitting the relation. This value of gamma is completely consistent with the current sample and was used in producing Figure 5.25 and all the TF relationships presented here.

The three other corrections applied remained the same as those initially adopted in §5.1 from recent Tully-Fisher related literature. Of these, the most important is the correction for Galactic extinction due to gas and dust within the Milky way. Extinction values published in Burstein & Heiles were used as detailed in §5.1.2. Over the entire sample this correction was typically less than 0.03 magnitudes and always smaller than 0.1 mag. Within each cluster rms variations in the correction were always less than 0.016, which is the maximum reduction in scatter that could be expected. In contrast to the large all-sky surveys, the galaxies within this sample are drawn from just four clusters (all at high galactic latitudes) which cover only a small area of sky. As a result, the Galactic extinction corrections are relatively much less important for the current sample and can be considered minor. However, applying the correction did result in a minor reduction in the scatter.

The two remaining corrections both depend on the measured redshift of each galaxy. Although the clusters considered here are at a distance sufficient to reduce depth effects, the distance is not so large that relativistic corrections are important. Moreover, the range of distance covered by galaxies within each cluster is so narrow that any reduction in scatter is small. However, since the fractional error of these redshifts is tiny, any additional uncertainty introduced by these corrections is much less than 1% in distance. Although there is little possible em-

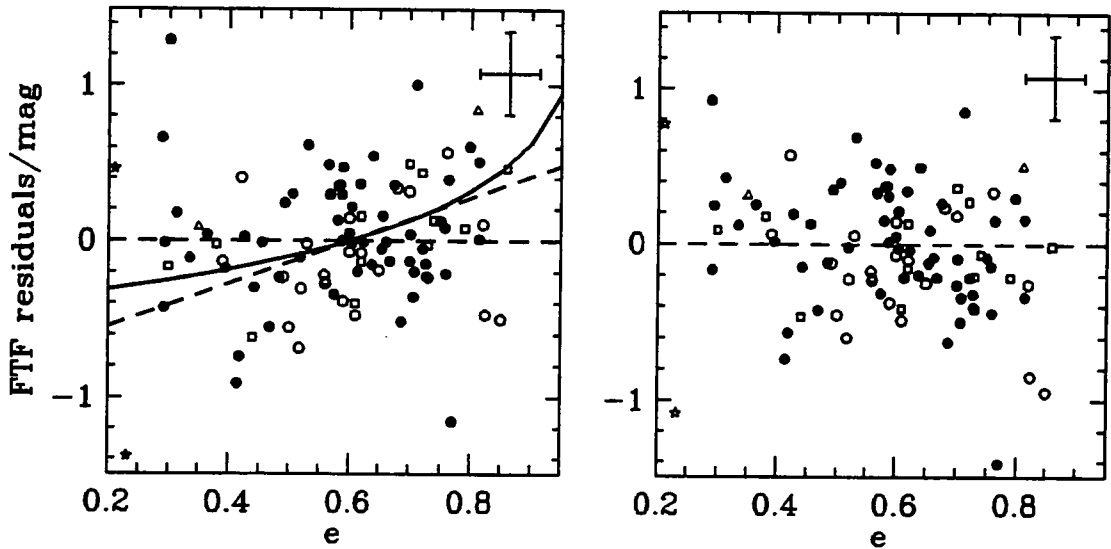


Figure 5.24: Two plot of TF fit residuals against ellipticity before and after the relationship is corrected for the effects of internal absorption. The left-hand graph shows the residuals before correction with two possible corrections marked with lines. The solid line represents a correction of form $\Delta m = \gamma/(1 - e)$ following Giovanelli et al. (1994). The dashed line represents the linear correction applied by Bernstein et al. (1994). On both plots the mean errors are marked with an errorbar in the upper right hand corner. The marker types have the same meaning as given in figure 5.2.

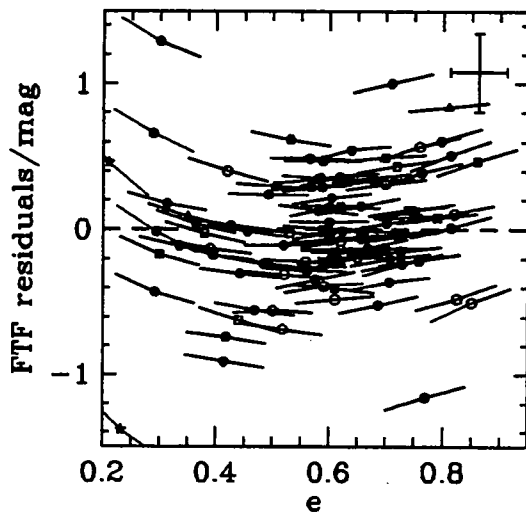


Figure 5.25: A graph of the fit residuals against ellipticity before correction for the effects of internal absorption. The mean errors are marked by a errorbar. The correlation between errors is indicated by a line marked on each point which represents how each point would be shifted by a $\pm 1\sigma_e$ change in ellipticity.

pirical gain from applying these corrections, there is no penalty for making corrections which reduce the parameters to a more fundamental state.

Considered together, these minor corrections are relatively unimportant for the present study. However for the large Tully-Fisher surveys appearing in the literature, these corrections are vitally important. Application of erroneous corrections can result in systematic variations in predicted distance over large areas of sky that exactly mimic structures that the survey is designed to measure. For this reason, it is important to minimise uncertainty in these corrections but, as is clear from the above discussion, this is outside the scope of the present work.

References

- Aaronson M., Huchra J., Mould J., Schechter P. L., Tully R. B., 1982, *ApJ*, 258, 64
 Bernstein G., Guhathakurta P., Raychaudhury S., Giovanelli R., Haynes M. P., Herter T., Vogt N. P., 1994, *AJ*, 107, 1962
 Bothun G. D., Aaronson M., Schommer R. A., Mould J. R., Huchra J., Sullivan W. T., 1985, *ApJS*, 57, 423
 Burstein D., Heiles C., 1978, *ApJ*, 225, 40
 Courteau S., 1992, Ph.D. thesis, University of California, Santa Cruz
 de Vaucouleurs G., de Vaucouleurs A., Corwin H., 1976, Second reference catalogue of bright galaxies

- Disney M., Davies J., Phillipps S., 1989, MNRAS, 239, 939
- Giovanelli R., Haynes M. P., Salzer J. J., Wegner G., da-Costa L. N., Freudling W., 1994, AJ, 107, 2036
- Han M. S., 1991, Ph.D. thesis, California Institute of Technology, Pasadena, California.
- Headry M. A., Simmons J. F. L., 1994, ApJ, 435, 515
- Holmberg E. B., 1958, Lund Medd. Astron. Obs. Ser. II, 136, 1
- Holmberg E. B., Lauberts A., Schuster H. E., West R. M., 1975, A&AS, 22, 327
- Mathewson D. S., Ford V. L., Buchhorn M., 1992a, ApJ Lett., 389, L5
- Mathewson D. S., Ford V. L., Buchhorn M., 1992b, ApJS., 81, 413
- McGaugh S. S., 1996, MNRAS, 280, 337
- McLeod B. A., 1993, AJ, 88, 439
- Sandage A., Tammann G. A., 1981, A revised shapley-ames catalogue of bright galaxies
- Schlegel D. J., 1995, Ph.D. thesis, University of California., Berkeley
- Tully R. B., Fouque P., 1985, ApJS, 58, 67
- Valentijn E. A., 1990, Nat, 346, 153
- Willick J. A., 1991, Ph.D. thesis, University of California., Berkeley

Chapter 6

The Origin of the TF Scatter

Abstract.

This chapter provides a full account of all sources of uncertainty that contribute to the scatter in the Tully-Fisher relation. These sources include measurement errors, cluster depth effects, uncertain cluster membership and data quality. Poorly extended rotation curves and fluctuation within the curves are shown to be the major cause of error in the relation. An upper limit on the remaining intrinsic scatter is placed at 0.12 mags rms. The variation in TF gradient between each cluster is shown to be significant and possible reasons for this are discussed.

Scatter within the Tully Fisher relation can be attributed to a number of sources. The largest of these comes from errors in the measured parameters. If these errors are combined and possible correlations taken into account, the full contribution to the scatter from all errors can be assessed. In addition, there may be ambiguity in cluster membership. If present this would violate the assumption that all galaxies within each cluster are at the same distance. These variations in distance are another cause of outliers within the relationship. Once all such sources of scatter have been removed, the amount of remaining intrinsic scatter, can be determined.

The degree of intrinsic scatter ultimately limits the accuracy with which distances can be estimated using the Tully-Fisher relation and sheds light on the fundamental properties of spiral galaxies. It also provides some constraint on galaxy formation techniques that have to reproduce the TF as part of spiral galaxy formation.

6.1 Contribution from Measurement Errors

A full error budget is given in Table 5.1. This shows that combining in quadrature, all the errors that contribute to the total magnitude error, produces a value of 0.080 rms mags. Errors in the rotation velocity can also be estimated in terms of magnitude by multiplying each error by the TF gradient. Combining these in quadrature produces an rms value of 0.266 mags.

Most authors assume that the errors in the rotation velocity and total magnitude are uncorrelated and combine them in quadrature to estimate the total contribution to the TF scatter from measurement errors. For the present sample this produces a rms value of 0.280 mags. However, this approach is not entirely correct. Both the internal absorption correction and the inclination correction to the rotation velocity depend on the disk ellipticity. As a result, there is a portion of the total magnitude and rotation velocity error which depend upon the ellipticity error and thus are correlated.

6.1.1 Correlated Errors

A detailed analysis of error propagation for Tully-Fisher parameters is undertaken by Rhee (1996). Rhee includes the effects of correlation due to the dependency of both the total magnitude and rotation velocity on ellipticity. In addition, as both the K-correction and $1+z$ correction are dependent on the redshift, a correlation also exists between their errors. However as the errors on these corrections are very small the effect on the scatter is negligible.

The full equation¹ for combining all the errors is given by Rhee as:

$$\sigma_{TF}^2 = \sigma_m^2 + \sigma_{GAb}^2 + z^2 \sigma_k^2 + p_1^2 \sigma_v^2 +$$

¹ N.B. that Eq 3.5 in Rhee (1996) is incorrect, Eq.6.1 was supplied by Rhee in a private communication.

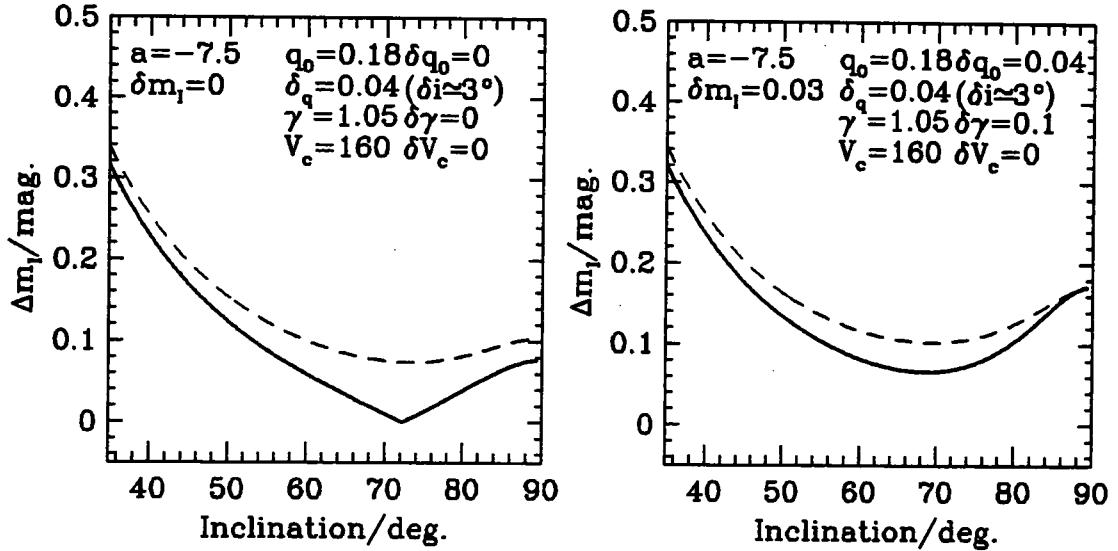


Figure 6.1: The uncertainty introduced into the TF relation by errors in the measured ellipticity versus inclination. **Left:** If all other quantities are assumed to have zero error. **Right:** Adding in quadrature all other sources of error apart from the rotation velocity error. In both graphs the dashed line represents the error calculated by combining all errors in quadrature. The solid line shows the error if correlation between correction errors that depend on ellipticity is taken into account.

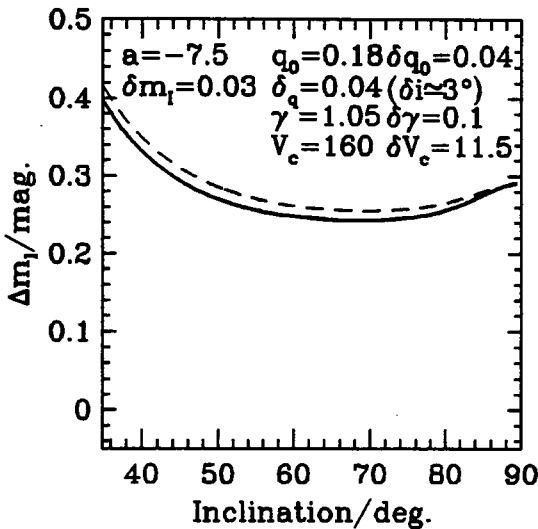


Figure 6.2: The scatter introduced by disk ellipticity errors for galaxies at different inclinations. If all sources of error are considered the effects of correlation between errors becomes relatively unimportant. The marked lines have the same meaning as in Figure 6.1.

$$\begin{aligned}
 & + \left[\frac{a}{\ln 10} + k(1+z)^2 \right]^2 \left(\frac{\sigma_z}{1+z} \right)^2 + p_2^2 \left(\frac{\pi \sigma_i}{180} \right)^2 \\
 & + \left(\frac{a}{\ln 10} \right)^2 \left(\frac{\sigma_{V_{\text{Rot}}}}{V_{\text{Rot}}} \right)^2
 \end{aligned}$$

where:

$$\begin{aligned}
 \sigma_i^2 &= p_3^2 \left(\frac{180}{\pi} \right)^2 \\
 p_1^2 &= \left[0.5 \log[(1 - q_0^2) \cos^2 i + q_0^2] \right]^2 \\
 p_2^2 &= \left[\frac{a \cot i}{\ln 10} + \frac{\gamma(1 - q_0^2) \cos i \sin i}{\ln 10 [q_0^2 + (1 - q_0^2) \cos^2 i]} \right]^2 \\
 p_3^2 &= \frac{q^2 \sigma_q^2}{(q^2 - 1)(q_0^2 - q^2)} \\
 & + \frac{(q^2 - 1) q_0^2 \sigma_{q_0}^2}{(q_0^2 - 1)^2 (q_0^2 - q^2)} \quad (6.1)
 \end{aligned}$$

Using this relation it becomes possible to plot the total error, in terms of magnitude, introduced in the TF relation by a typical galaxy at different inclinations to the line-of-sight (see figures 6.1 and 6.2). The function displayed in the left-hand panel of Figure 6.1 shows the contribution versus inclination assuming all parameters apart from ellipticity, q , have zero error. The total error calculated by simply adding all sources in quadrature is represented by a dashed line. The error contribution as calculated by equation 6.1 is shown as a solid line.

There are two important points to note from Figure 6.1. The contribution to the TF scatter due to errors in the ellipticity is strongly dependent upon the

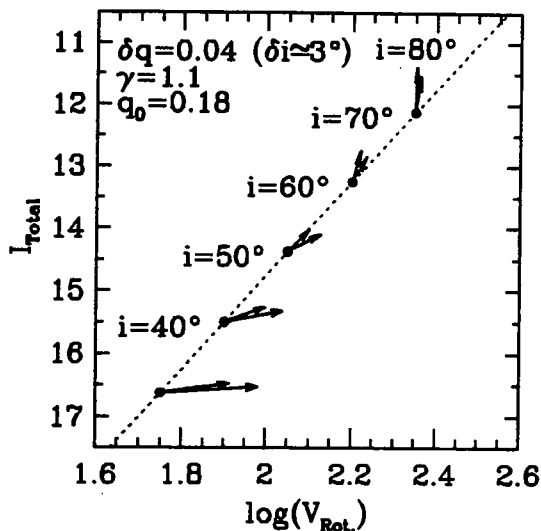


Figure 6.3: A graphical demonstration of the net effect of the two largest TF corrections. Arrows marked on the diagram represent the correction applied to each point for inclination and internal absorption when the disk ellipticity varies by $\pm 1\sigma$. The position of each point in the plane is unimportant. The shown inclination decides the direction of the correction. Note that for inclinations between 60° and 70° the correction lies along the slope of the relation marked by with a dotted line.

inclination (ellipticity) of each galaxy, and reaches a minimum at inclinations of around 70° . Also when the correlation between errors is ignored, the contribution is over estimated at all inclinations.

The minimum point in the scatter contribution at 70° is due to coupling between the internal absorption correction and the rotation velocity inclination correction. At low inclinations the absorption correction is small and the velocity correction is large, in the positive $\log V_{\text{Rot}}$ direction. At high inclinations the velocity correction is small and the absorption correction results in a shift in the negative magnitude direction. At intermediate inclinations around 70° both corrections combine to shift points on the relation *parallel* to the slope of the relationship, leaving its perpendicular residual unchanged. This effect is illustrated in Figure 6.3 where arrows are used to represent the shift in the Tully-Fisher plane induced by the inclination dependent corrections. The direction of the combined correction is independent of a galaxy's position within the diagram, instead purely depending upon inclination.

The fact that the scatter contribution is over estimated when correlation between errors are ignored was noted by Rhee. However, he failed to point out that when contributions from all other sources of error are considered, the total uncertainty is dominated by the rotation velocity error. This effect is demonstrated in figures 6.1 and 6.2. The right-hand panel of Figure 6.1 displays the total error contribution versus inclination when all types of error, apart from the rotation velocity error, are combined. As the extra errors combine in quadrature the final uncertainty is dominated by the largest error. This means any reduction due to correlations with ellipticity become less important. Figure 6.2 shows the case where all errors are considered. In this situation, which is the realistic case, the total error is dominated by the uncertainty in the rotation velocity. Consequently, the overestimation caused by ignoring the error correlation is reduced to less than 0.02 mags.

With proper consideration of all errors, as shown in Figure 6.2, there is a reduction of 0.05 mags in the total error for inclinations of 70° compared to the highest and lowest inclinations within the sample. This combined with the fact that the mean inclination of galaxies within a sample is 68° is a purely fortuitous coincidence which lowers the impact of ellipticity errors on the Tully Fisher relation producing a relationship with lower scatter than might be expected.

Note that as both major corrections are related to ellipticity, minimising the errors is an important requirement for accurate corrections. In terms of the overall scatter, however, the relationship is insensitive to these errors. In the case of this data set, the scatter is dominated by the error in rotation velocity. In general reducing this error is the most critical factor in improving the TF relation.

6.1.2 Errors in $\log V_{\text{Rot}}$ as a Source of Scatter

As rotation velocity errors dominate the contribution to the scatter from measurement errors, it is reasonable to expect the same errors to be the largest of all contributors to the scatter. In such a scenario, the TF residuals would show a trend when compared to errors in V_{Rot} . However, this is hard to detect as er-

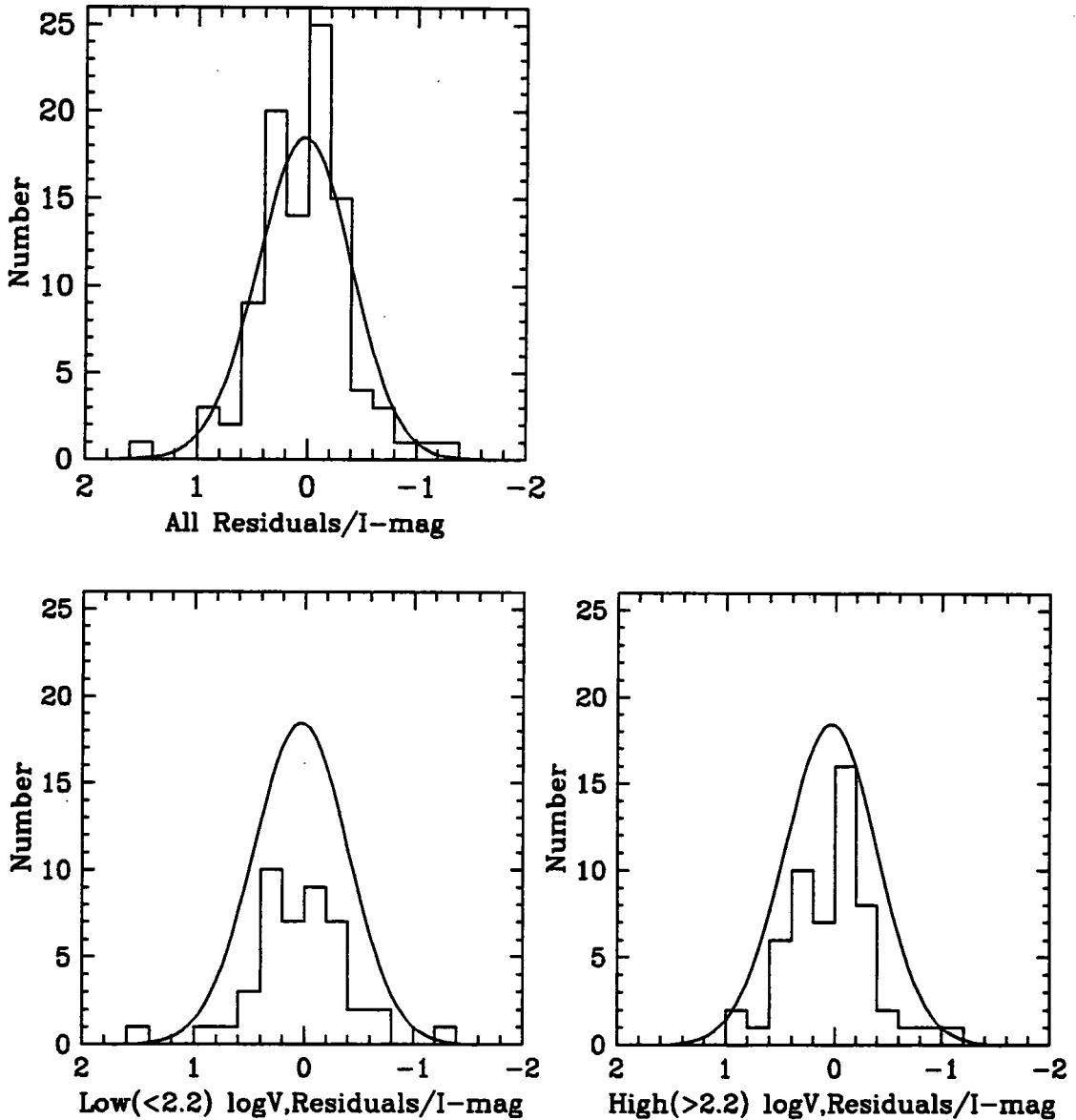


Figure 6.4: Histograms of the magnitude residuals about the fitted relation for all 99 galaxies in the main sample. The Gaussian curve marked on all graphs has a standard deviation of 0.43 mags. The lower plots shows the same data divided into two parts. The lower left histogram displays the residuals for galaxies with $\log V_{\text{Rot}}$ below 2.2. The right-hand plot show residuals for objects with $\log V_{\text{Rot}} > 2.2$.

rors in rotation velocity only cover a narrow range. Instead we check for the signature such a dominance would leave in the data as a whole. The error in log-rotation velocity can be separated as:

$$\begin{aligned} \log(V_{\text{Rot}} \pm \sigma_{V_{\text{Rot}}}) &= \log(V_{\text{Rot}}) \\ &+ \log\left(1 \pm \frac{\sigma_{V_{\text{Rot}}}}{V_{\text{Rot}}}\right) \end{aligned} \quad (6.2)$$

as errors in rotation velocity remain constant or increase for galaxies with lower rotation velocity.

It is apparent from Equation 6.2 that the scatter in the TF relation would increase at low values of $\log(V_{\text{Rot}})$. Figure 6.4 shows three histograms of the residuals within the four cluster Tully-Fisher relations. The upper left-hand panel of Figure 6.4 shows the distribution of residuals for all 99 galaxies within the final sample, over plotted with a Gaussian of $\sigma = 0.43 \pm 0.03$ mags, the rms residual of the whole sample. The lower left and right panels of Figure 6.4 display the same data divided into

two; galaxies with $\log V_{\text{Rot}} < 2.2$ form the left-hand histogram and galaxies with $\log V_{\text{Rot}} > 2.2$ are plotted in the right-hand panel. The same Gaussian is marked in all frames. The rms residual for low $\log V_{\text{Rot}}$ galaxies (44 objects) is $\sigma = 0.47 \pm 0.05$ and for the high $\log V_{\text{Rot}}$ sample (55 objects) is $\sigma = 0.40 \pm 0.04$. The scatter does show a marginal increase, but as the expected increase is close to a factor of two, it is clear that the scatter is not dominated by rotation velocity errors.

Thus we can be confident that the error in rotation velocity has not been underestimated. As all other parameter errors contribute considerably less to the final scatter we must look elsewhere for the remaining sources of error.

6.1.3 Cluster Membership

One likely remaining source of scatter within the Tully-Fisher relation are variations in apparent magnitude due to distance uncertainties. Implicit in the process of forming the TF relation is the assumption that all galaxies within a cluster are at the same distance. The sample selection outlined in chapter 2 was designed to minimise the chance of including nearby field galaxies within the sample. However, the possibility remains that the present cluster samples have been contaminated by outlying galaxies. There are a number possible checks we can perform to ensure that this is not the case.

Figure 6.5 shows a map of the sky surrounding the four clusters. The two circles appearing on each map mark the limits of the inner plate scan selected sample and the outer Zwicky/UGC sample. Any points that appear outside the outer sample are part of earlier observations, or in the case of Coma, galaxies included from the Bernstein et al. (1994) sample. The size of the points used to mark each galaxy in Figure 6.5 is proportional to the size of each galaxy's magnitude residual from the TF fit. Filled triangles mark objects with positive deviations from the relationship and circles denote negative residuals. Clearly, there is no obvious trend between the size of residuals and cluster position, furthermore there is no sign of any sub-grouping of high residual objects. Such a grouping would be ex-

pected if some sample members belonged to background or foreground structures.

As a further check for correlation between the residuals and cluster position, Figure 6.6 shows the same information plotted in terms of TF residual versus projected radial position in arcminutes. The mean residual error for each cluster is represented with an error bar. Clearly there is no significant trend or increase in scatter for objects at greater distances from the cluster centre.

Finally, all four cluster samples were scaled to the same distance as Coma in order to check for any effect in the sample as a whole. The upper left hand plot in Figure 6.7 displays TF residuals against scaled projected radial position for all 99 galaxies within the final sample. The figure shows marginal evidence for a *reduction* in the residuals at larger distances from the cluster centre. This trend is more visible in the lower left-hand panel where the absolute residuals are plotted.

This effect can be attributed to the reduction in projected cluster depth along the lines-of-sight for positions further from the cluster centre. The upper right-hand frame in Figure 6.7 shows the same data with residuals in terms of distance error. Dotted lines drawn on the plot mark the limits in line-of-sight distance of a $7.5 \text{ h}^{-1} \text{ Mpc}$ (6° radius on sky) sphere at the distance of Coma. This sphere is a representation of the cluster membership surface calculated in van Haarlem et al. (1993) and shown in Figure 2.3. The lower right-hand panel displays the same data when the galaxies are divided up equally into nine radial distance bins. The rms residual is calculated for the eleven galaxies within each bin and plotted versus radial position. The slight downward trend in residuals can be taken as further evidence that the projected cluster depth is a significant contributor to the Tully-Fisher scatter. However, this evidence should be regarded with caution. When the large errors and other sources of scatter are considered, the trend is marginal at best. Also note that some of the increase of residuals in the three inner bins is due to increased errors for the objects within the fainter inner samples. However, attributing cluster depth effects to be a source of a scatter within the relationship does add further

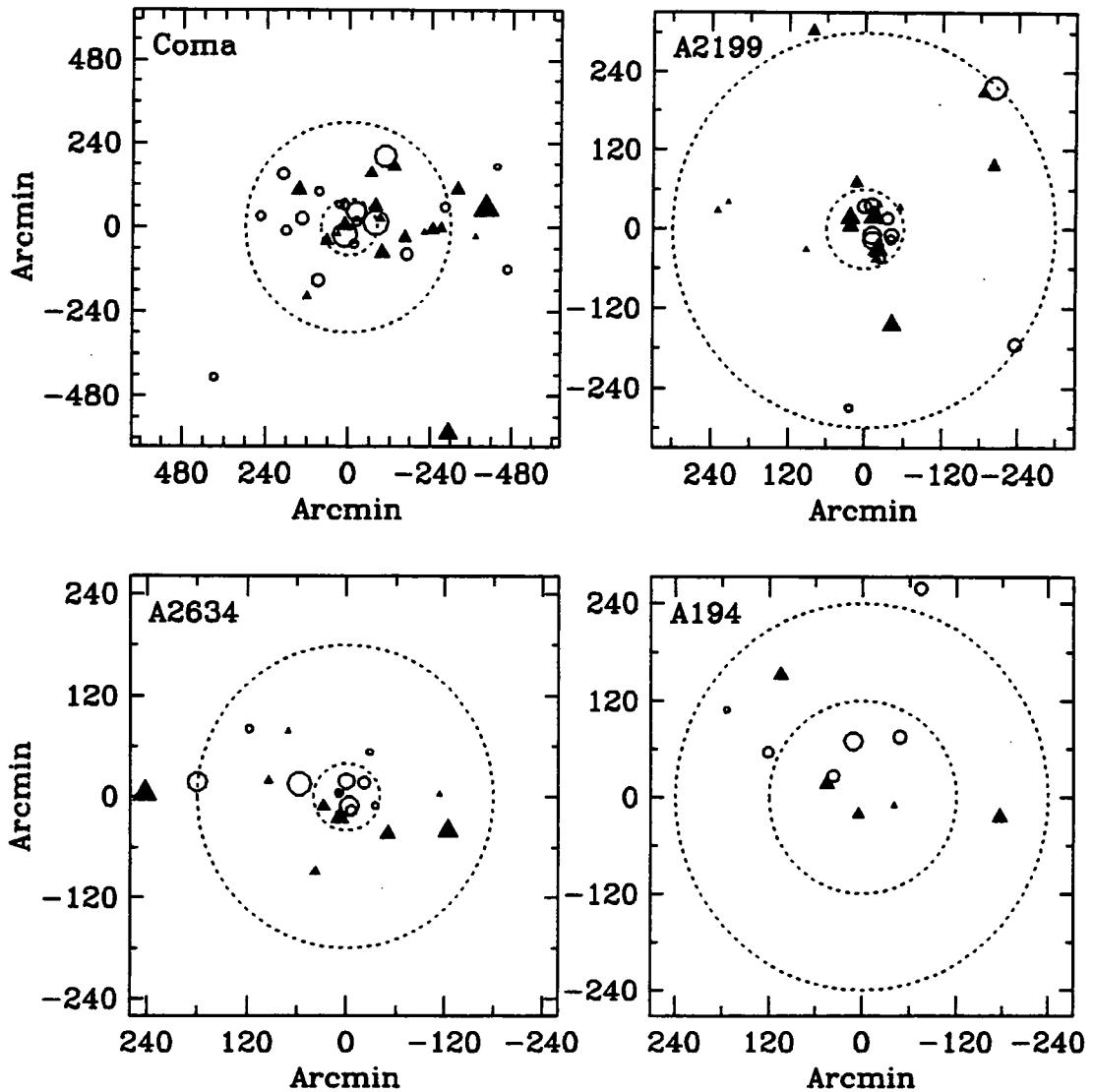


Figure 6.5: A map showing the position of the sample galaxies within their respective clusters. The size of each point is proportional to the size of each galaxy's TF residual. Triangles mark positive magnitude residuals and circles represent negative ones. The inner circle marks the limits of the plate scans used to select the faint sample for each cluster. The outer circles indicate the area in which objects were selected from the Zwicky and UGC catalogues.

weight to the assumption that the majority of the galaxies within the sample *are* cluster members.

Outlying field galaxies can seem to be close to the cluster centre in terms of projected distance but actually be in the foreground or background along the line of sight. Attempts were made to minimise this during selection when only galaxies with redshifts consistent with cluster membership were chosen. Since most of the relatively faint objects selected from plate scans had no published redshifts, contamination still remains a possibility.

As a check for foreground and background galaxies we plot the TF residuals versus log-redshift (CMB frame) in Figure 6.8. A line of slope five that passes through zero at the redshift of each cluster is marked on all plots. This line represents the Hubble flow, the trend followed by galaxies whose redshift is purely due to the expansion of the universe and scales with distance. If a significant fraction of galaxies within the sample were in the field rather than cluster members a correlation should be visible. Clearly there is not a strong tendency for galax-

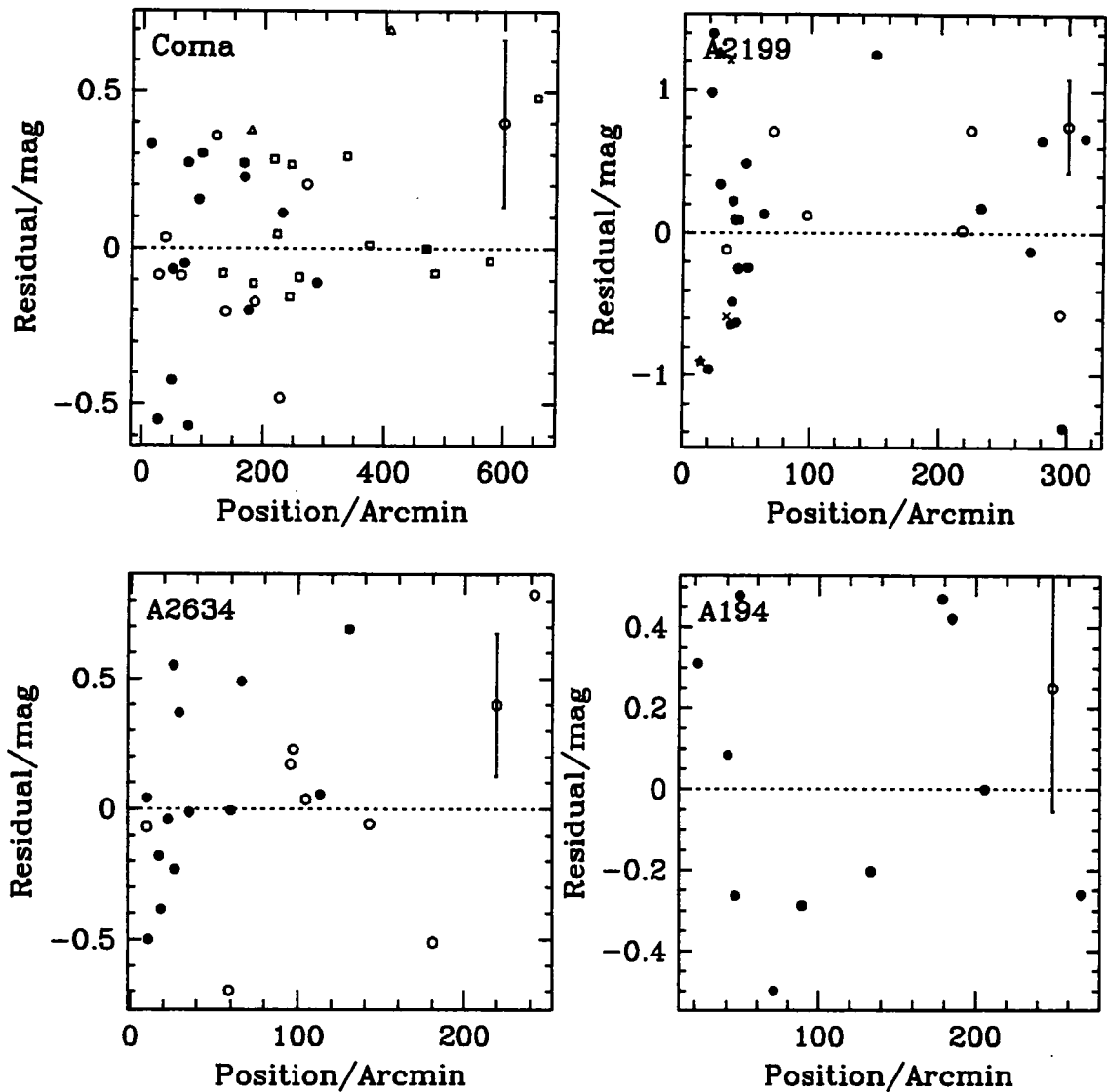


Figure 6.6: A Plot of fit residuals against the radial distance from each cluster's centre. Symbol types have the same meaning as in Figure 5.2. The mean error on the residuals for each cluster are marked by an error bar.

ies to lie along the Hubble flow line, a Spearman rank-order test showed only Coma to have a significant correlation.

To further investigate this possibility we follow the approach adopted in Willick et al. (1995) and correct the relationships with an "expanding model" model for each cluster. This involves applying a magnitude correction, Δm to each galaxy defined thus:

$$\Delta m = \log \left(\frac{z_{\text{Gal}}}{z_{\text{Clus}}} \right) \quad (6.3)$$

This model assumes that the galaxies within each sample are associated with their respective clusters

yet remain upon the Hubble flow, their recession velocities remain largely unaffected by the cluster's gravitational field. Figure 6.9 displays the four cluster Tully-Fisher relations after applying the expansion model. Comparison with Figure 5.18, the same points without the correction, shows no significant changes in the fitted slopes or intercepts. More importantly, none of the corrected relationships show a significant reduction in scatter, in fact, Coma, A2199 and A194 have slightly increased scatter. The remaining residuals after applying the correction are shown in Figure 6.10.

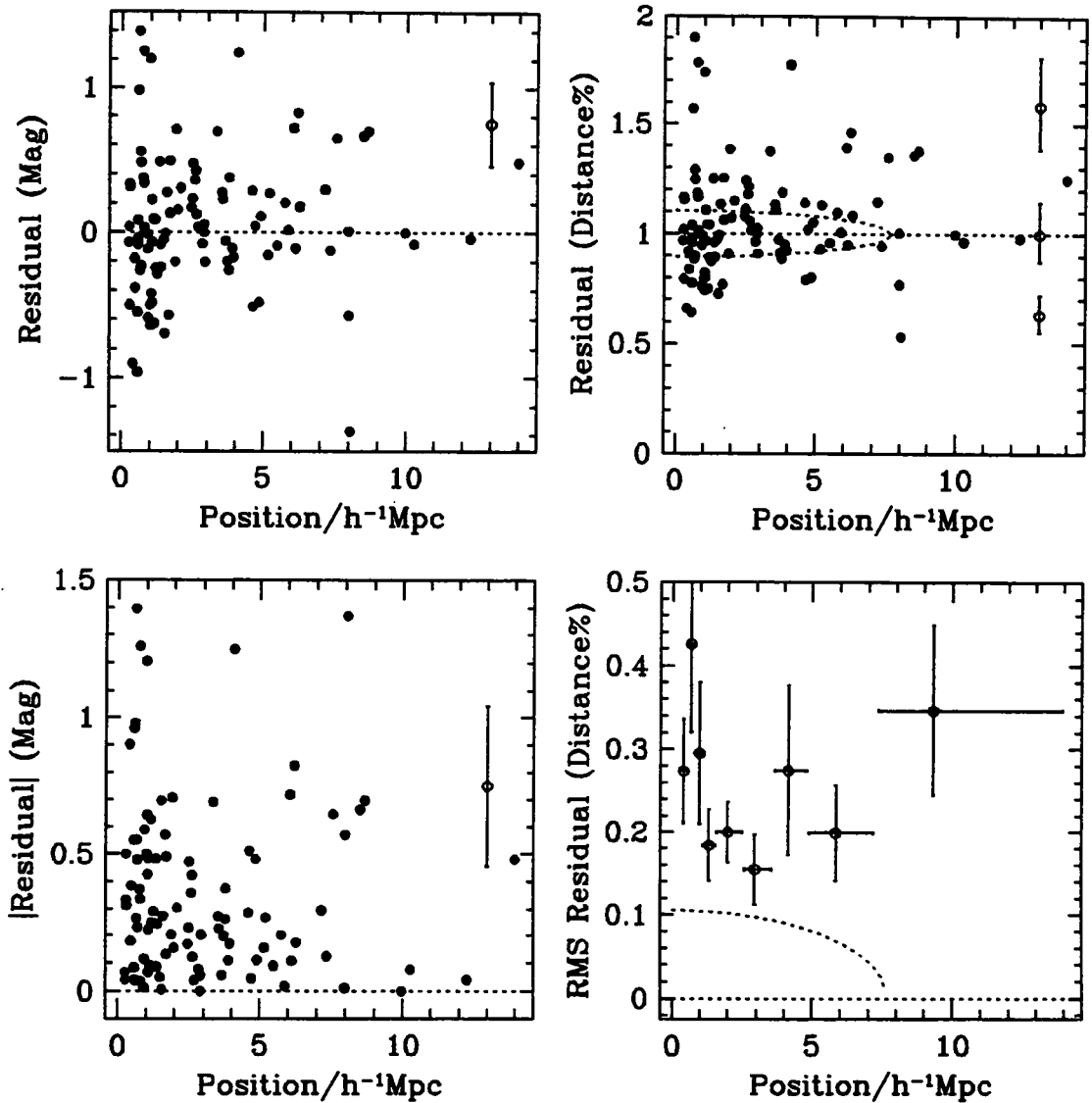


Figure 6.7: A composite plot of all TF fit residuals against radial cluster position in $h^{-1}\text{Mpc}$ for all galaxies in the sample. The lower left-hand plot shows the same data in terms of absolute residuals. The residuals in terms of distance errors are shown in the upper right-hand panel. Marked curves represent the approximate cluster line-of-sight depth in terms of distance. The lower right-hand panel displays the results of binning the data in nine bins each consisting of eleven galaxies. Mean errors are indicated on each plot by an error bar.

An expanding model fit for A2634 would be consistent with the findings in Willick et al. (1995) who note that the expanding model correction reduced the scatter in A2634 when using the data sets of Han & Mould (1992) or Willick (1991). This also agrees with the work of Scodreggio et al. (1995), who after studying large redshift galaxies in the region of A2634, concluded that spiral galaxies in the region represent a dynamically young cluster population. The scatter in the Coma TF relation is dom-

inated by a few outlying points that are adversely corrected. As a result, it is likely that the Coma sample would also exhibit a reduction in scatter (consistent with Willick et al. 1995) if the sample was restricted to a better quality subset.

However, we believe caution is necessary when taking this approach. The scatter in the relation is clearly dominated by other sources of uncertainty as any improvement in scatter induced by the correction is small. As a result of this large scatter the

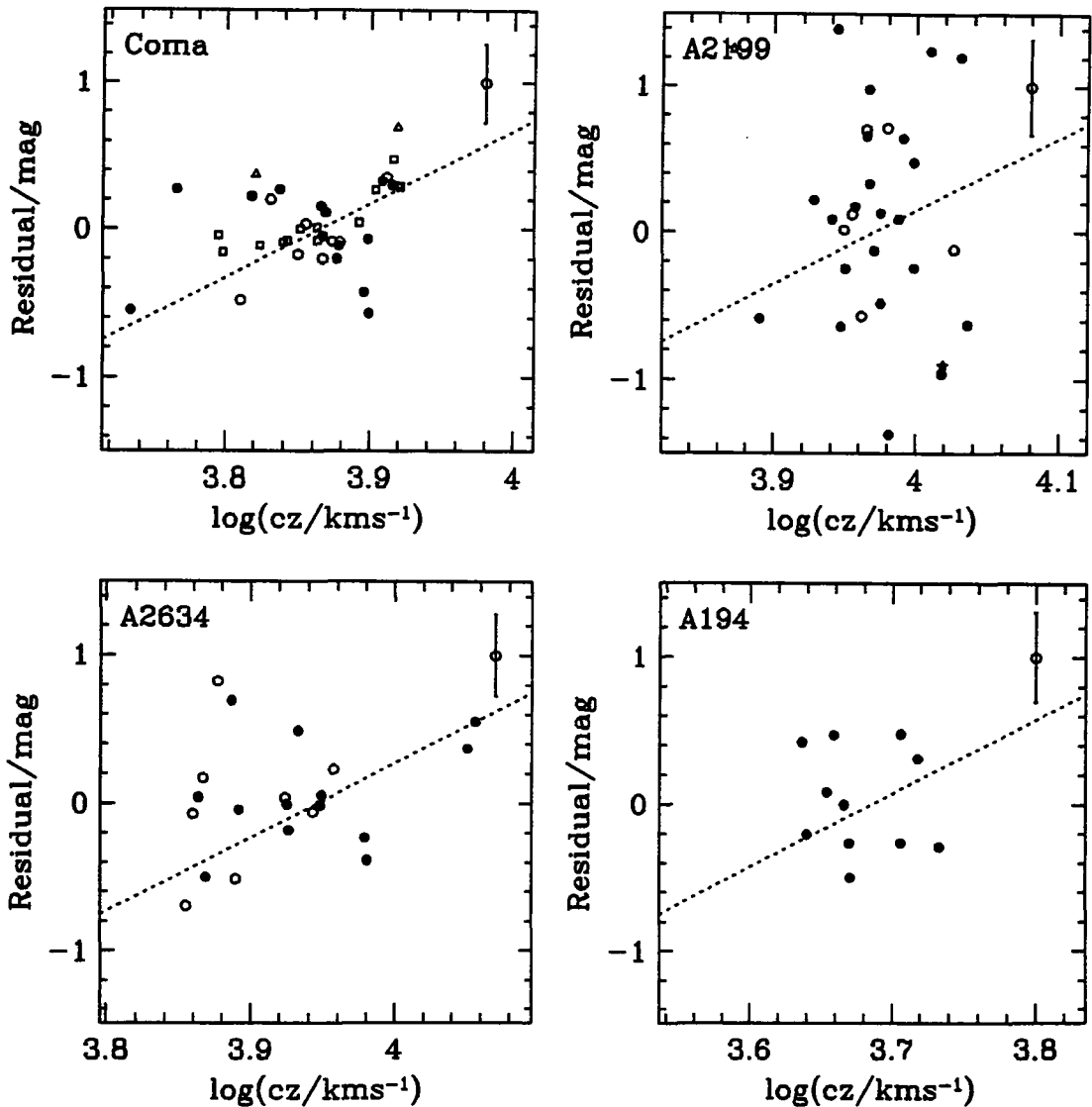


Figure 6.8: Tully-Fisher residuals versus log-redshift for galaxies in the sample. The symbols have the meaning as those shown in Figure 5.2. The dotted line has a gradient of 5 and passes through zero at the redshift of each cluster. Field galaxies on the Hubble flow would be expected to follow this line.

significance of any correlations is low and the probability that a small reduction in scatter could result by chance is not negligible. If enough clusters are tried some will display a correlation. Moreover, we consider it dangerous to use the technique adopted in Willick et al. (1995) of only applying this correction when it results in a reduction of the fit residuals. We note that they apply the correction to 9 out of 31 clusters within the Han & Mould (1992) sample for which the TF scatter is reduced. In addition, of the 10 clusters in common between the Han & Mould (1992) and Willick (1991) samples, four clusters are

considered “expanding” and have the correction applied whereas the same cluster in the other dataset is left uncorrected (even though the majority of the clusters in each dataset are made up from the same galaxies).

In the case of the clusters presented here we consider the sample to be of unsuitable size and quality to differentiate between the expanding and non-expanding scenarios in each case. Either way, uncertainty in cluster membership is not a major contributor to the TF scatter.

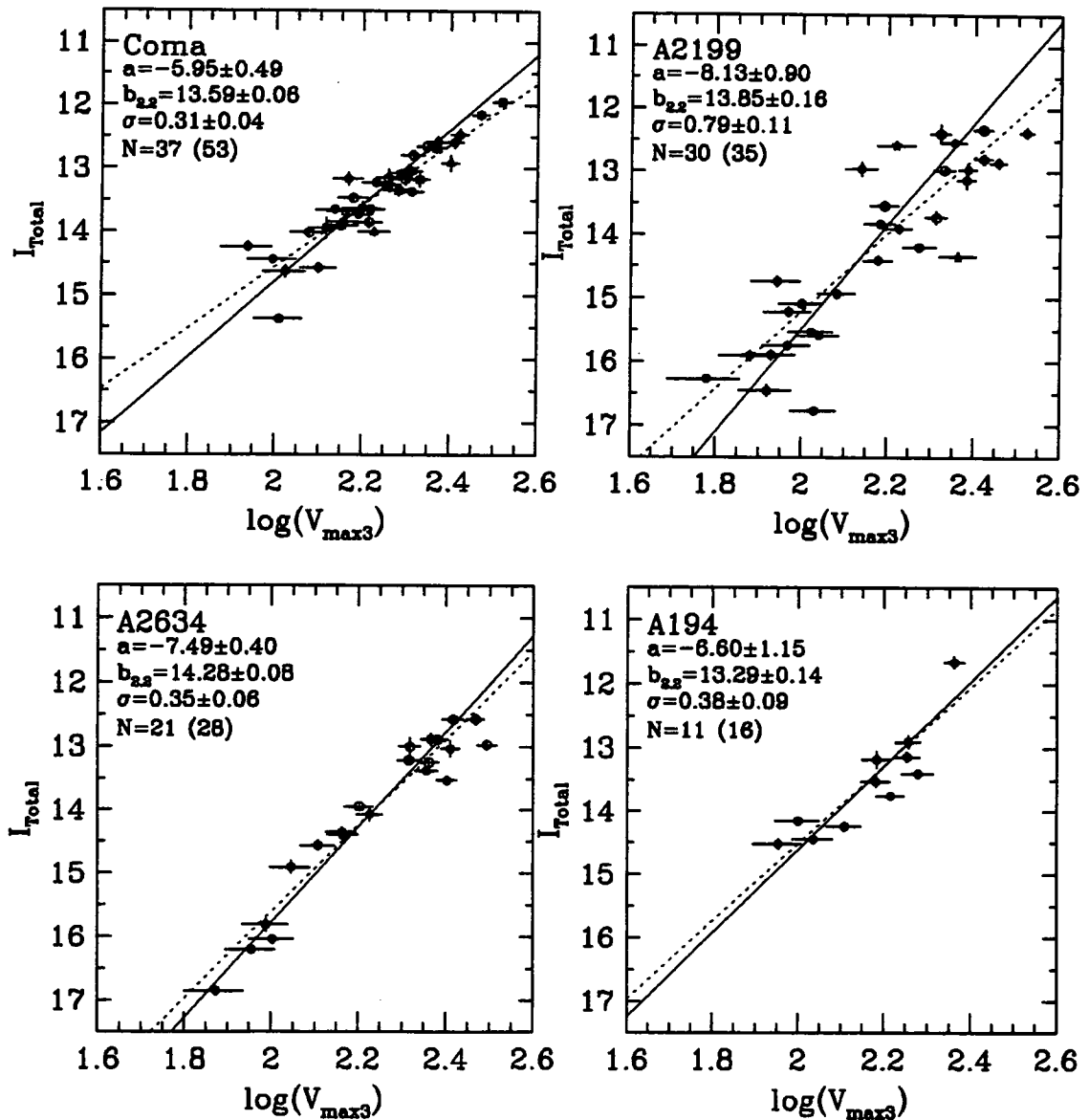


Figure 6.9: The Tully-Fisher relation within the four target clusters. The symbols are the same as in figure 5.2. $\pm 1\sigma$ error estimates in magnitude and \log -rotation velocity are marked on each point. The weighted inverse regression line of $\log V_{\text{max}3}$ upon I_{Total} is marked as a solid line on each relation. The details of each of these fits are marked in the upper left of each panel. The regression of I_{Total} upon $\log V_{\text{max}3}$ is represented in each case as a dotted line. The “expanding” cluster model correction adopted by Willick et al. has been applied to all points. Open circles represent data from previous observations and for the Coma cluster open squares and triangles represent measurements by Bernstein et al. (1994).

6.1.4 Data Quality

The data that makes up the four cluster samples display a fairly wide range of quality in terms of signal-to-noise, symmetry of rotation curves and morphological abnormalities. Figure 6.11 shows the TF relation for the 99 galaxies as above. Now the symbols are used to give an indication of data quality. The sample is divided into two categories; “high”

quality galaxy data is plotted with filled circles and “low” quality with filled triangles. The meaning of the lines and details of the fits are identical to Figure 5.18.

High quality galaxies are defined as those which have symmetric rotation curves with a good extent and no large variations. If a galaxy displayed an abnormal morphology, or a rotation curve with no

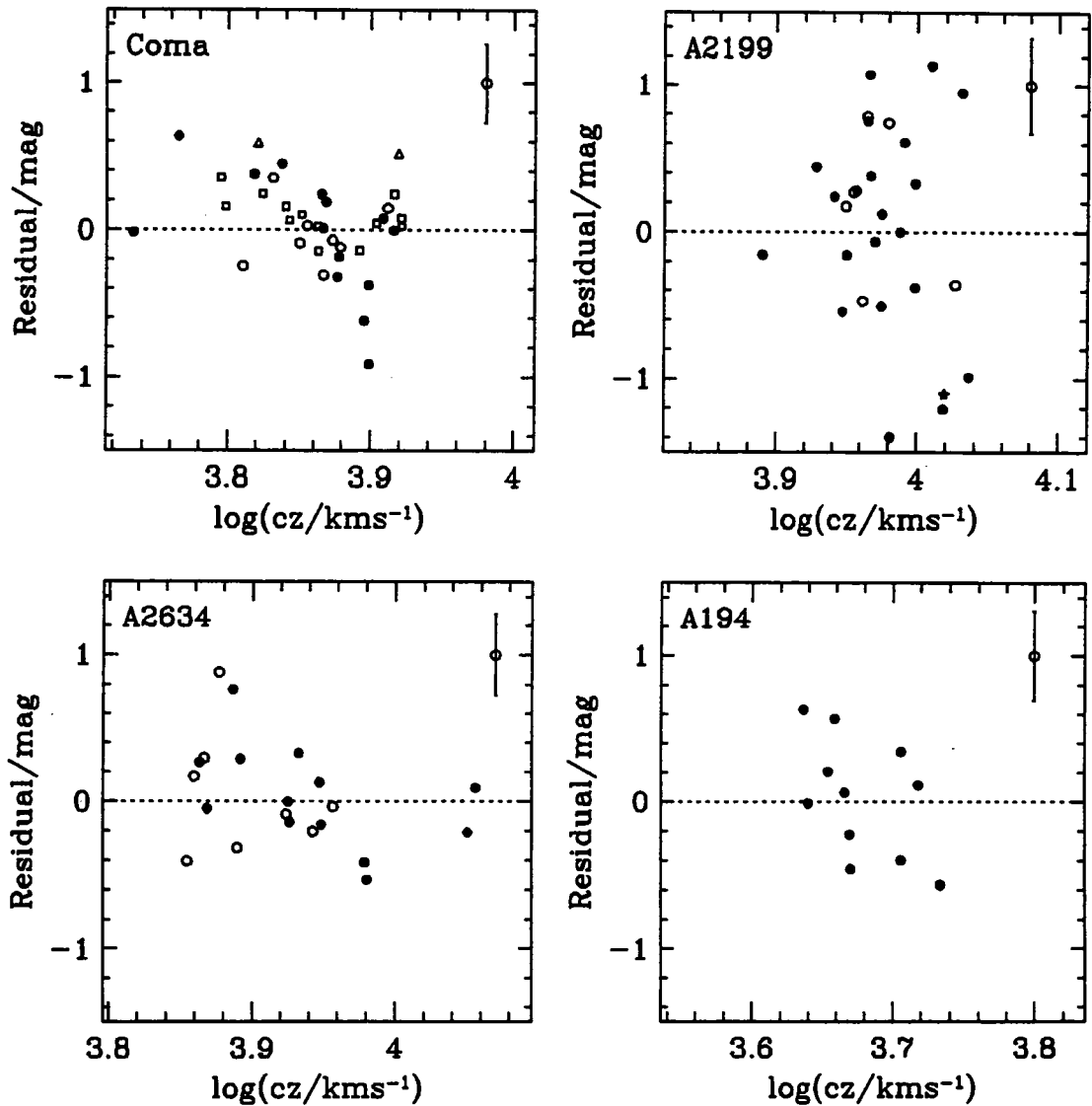


Figure 6.10: Tully Fisher residuals against log redshift for each cluster sample after the expanding model has been applied.

turn-over it was deemed low quality. Galaxies with nearby foreground stars were also assigned as low quality due to the possible effect of poor star removal on photometry. In terms of the quality number (Q) assigned to the photometric and spectroscopic data discussed in chapters 3 and 4 (see §3.1.3 and §4.3), high quality points were given Q values of 1.1 while all other values of Q were considered low quality. Data from previous observations ($Q=0.0$) were also placed in the low quality group. The 17 galaxies in the Coma sample included from the Bernstein et al. (1994) were divided on the basis

of quality assessments given in the same publication.

It is clear from Figure 6.11 that all the outlying galaxies have low quality data, and we conclude that a significant portion of the TF scatter is due to including “unsuitable” galaxies in the sample. Figure 6.12 shows the Tully-Fisher relation for the galaxies that remain after the low quality points have been removed. The mean rms residuals have reduced by 0.3 mags rms and in the case of A2199 the reduction is as much as 0.6 mags rms. Also the fits remain unaffected, although the small sample sizes mean that the errors on the fitted slopes and intercepts have in-

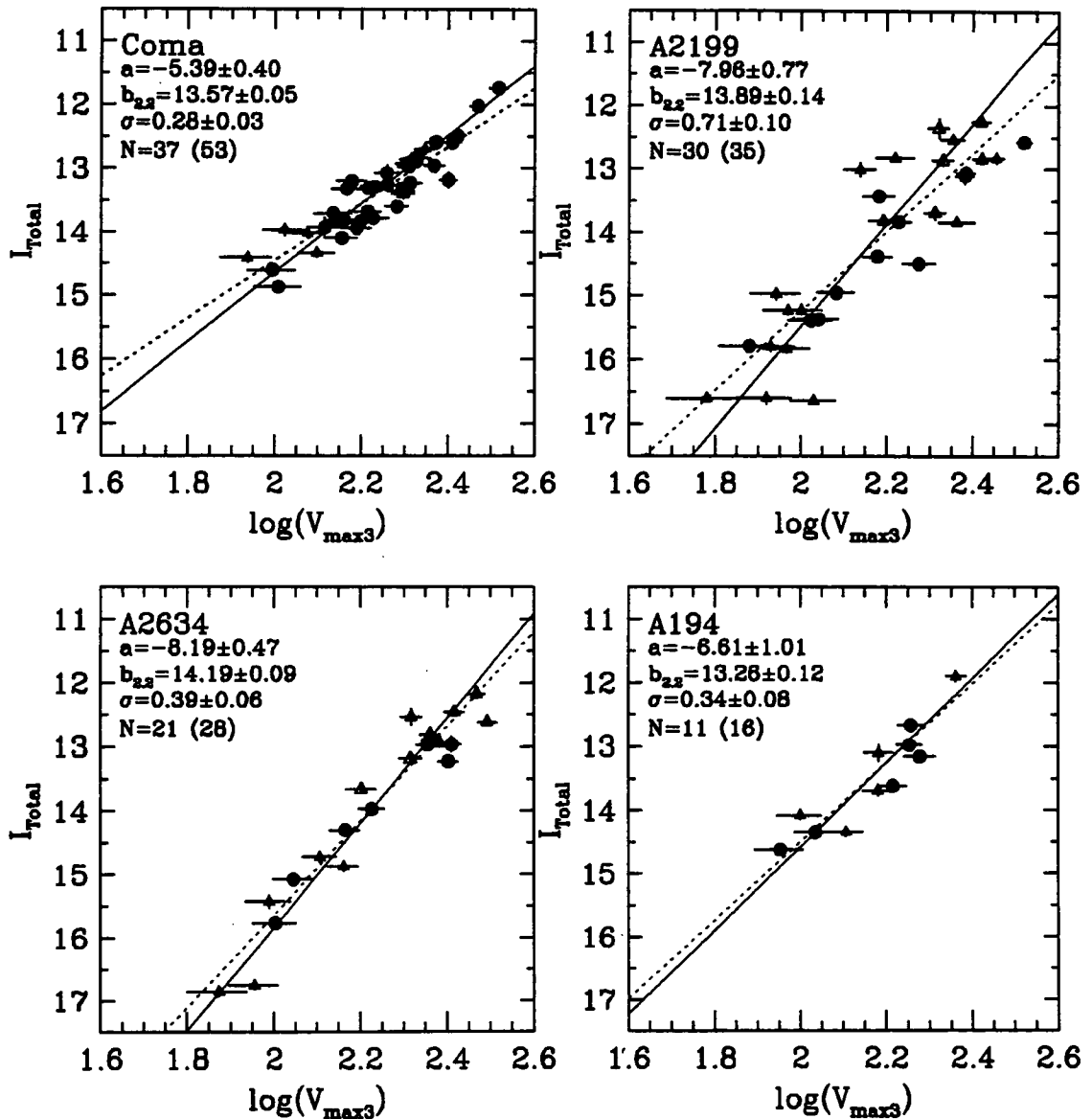


Figure 6.11: The same Tully-Fisher relations as displayed in Figure 5.18. In this instance, the data set is divided into groups of high and low quality. High quality points are marked with a filled circle, low quality points are indicated with a filled triangle.

creased. This has the effect of greatly reducing the significance of any variations in slope between clusters. Another important thing to note is that simulations performed in §5.5 demonstrated that the true TF scatter is typically underestimated by samples this small. The results shown in Figure 5.15 indicate that sample sizes of 15 and less can underestimate the scatter by up to 0.03. But even considering this, the reduction in scatter is significant.

To further investigate the source of the scatter introduced by the low quality points we compared

the rms TF residuals for the whole sample with the rms residuals for subsamples based upon photometric and spectroscopic data quality, Q as defined in §3.1.3 and §4.3. The rms residuals for data with different values of Q is shown in Table 6.1.

From Table 6.1 it can be concluded that the major contribution to the additional scatter comes from poor rotation curves. The disturbed morphologies and uncertain star subtraction that resulted in some galaxies being assigned a photometric Q of 2 does

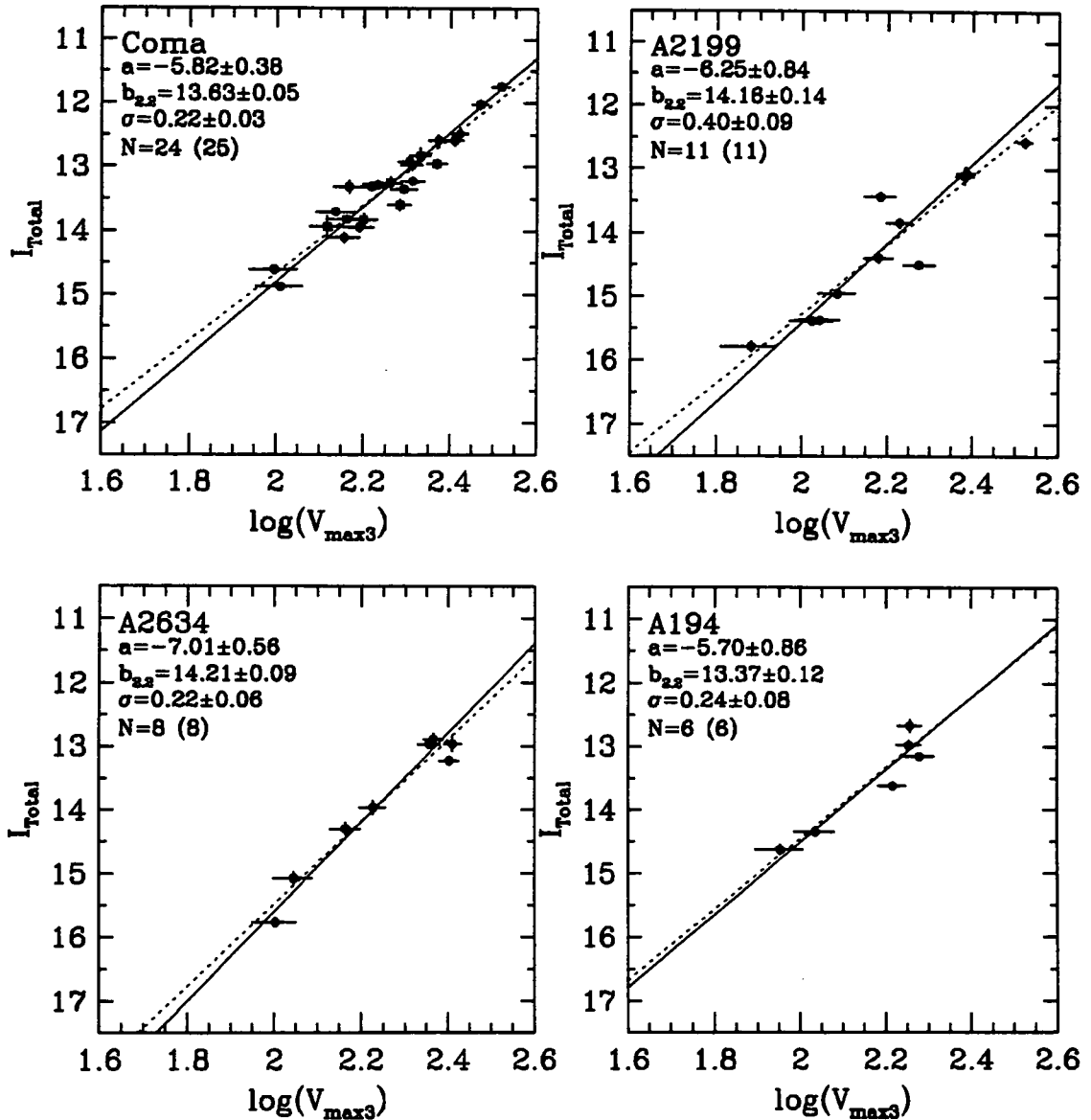


Figure 6.12: The Tully-Fisher relation for each cluster after the low quality data points have been removed. The marked lines and symbols have the same meaning as in Figure 5.18.

not seem to be a major cause of TF relation outliers in this sample.

6.1.5 Poor Extent of Rotation Curves

Galaxies within this sample were given a spectroscopic Q of 2 if they displayed either asymmetries, fluctuations or an uncertain turn-over in their rotation curves. In an attempt to further discriminate between these cases a plot of residuals versus surface brightness is shown in Figure 6.13. The signal-to-noise ratio within spectroscopic data is closely related to surface brightness. If poor the quality was

related to signal-to-noise a trend would be seen. For example, this would be the case if we had underestimated the $H\alpha$ emission line fitting errors, although this is unlikely as they are consistent with internal error estimates. No trend is apparent, so we can conclude that signal-to-noise concerns are not a major cause of the poor rotation curves.

Figure 6.14 displays a plot of TF residuals against $H\alpha$ extent for all the galaxies within the sample. The extent of $H\alpha$ is defined as the mean radial distance of the last three positions in the rotation curve where $H\alpha$ emission was measured. While there appears to

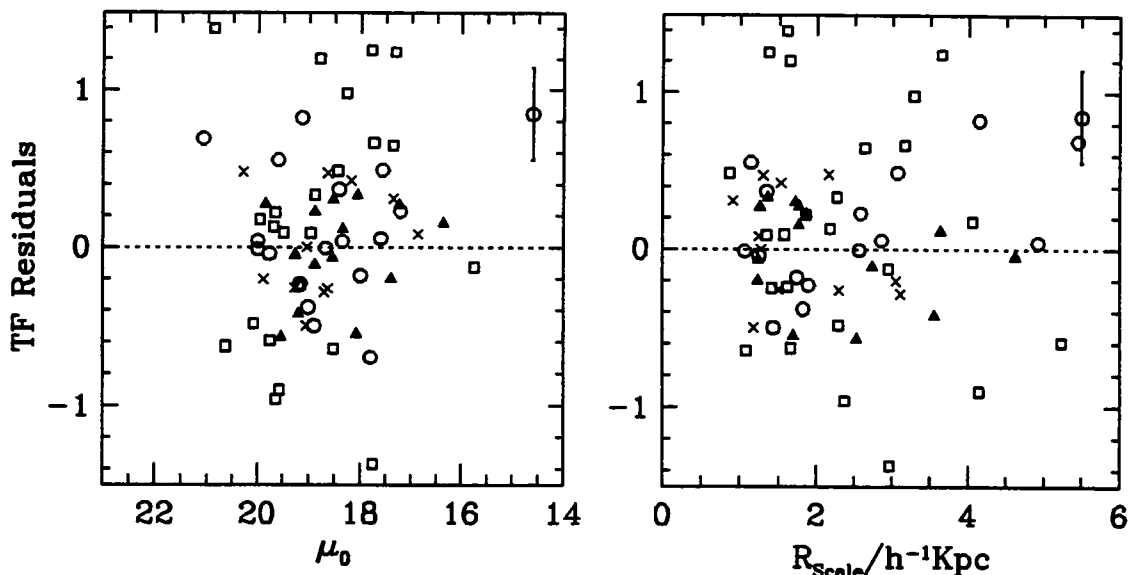


Figure 6.13: Left: A graph showing TF residuals against surface brightness for the sample galaxies. Right: TF residuals versus disk scale length for the same galaxies. The four symbol types indicate data from each cluster; filled triangles denote Coma, Open circles Abell 2634, Open squares Abell 2199, and Crosses mark Abell 194 points.

Table 6.1. The mean Tully-Fisher fit residuals in mags rms for different quality subsets of the selected sample. Column headings are; quality parameter, Q, for each subset as defined in §3.1.3 and §4.3, number of galaxies in each subset, N, TF residuals, σ_{TF} and error.

Q	N	σ_{TF}	error
All	99	0.477	(0.034)
Photometry			
1	76	0.494	(0.041)
2	12	0.366	(0.082)
0	10	0.440	(0.110)
Spectroscopy			
1	54	0.376	(0.037)
2	30	0.621	(0.083)
0	15	0.457	(0.090)

be only marginal evidence that galaxies with extended rotation curves have less TF scatter, a clear correlation can be seen between the residuals and the extent of H α emission in terms of disk scale lengths.

This clearly demonstrates that the rotation velocity can be seriously underestimated for galaxies where the measured rotation curve fails to extend into a sufficient fraction of the disk. Using a rotation

velocity parameter that simply depends on the maximum point, or in this case the third most maximum point, will often underestimate the true rotation velocity by up to 30%. In terms of the resulting TF residuals, a shift of -0.13 in $\log V_{Rot}$ combined with a typical TF slope of -7.5 , will result in a -1.0 residual in magnitude. In other words, the galaxy appears too bright for its measured rotation velocity.

The existence of such a correlation could have an effect which is more serious than the introduction of scatter into the relationship. The lowest surface brightness galaxies within the sample, may also have the largest scale lengths. Thus it is possible that objects with poorly extended rotation curves also have a low surface brightness. As was demonstrated above in §5.4.4 the faintest sample objects tend to have a low surface brightness (see Figure 5.10). If the faintest galaxies have rotation velocities which are underestimates, the slope of the Tully-Fisher relation could be systematically affected.

Figure 6.13 demonstrates that there is no significant trend between the residuals for either surface brightness or disk scale length. In addition, a plot of rotation curve extent versus rotation velocity is shown in Figure 6.15 and reveals there is no significant correlation between the two. From this it can be

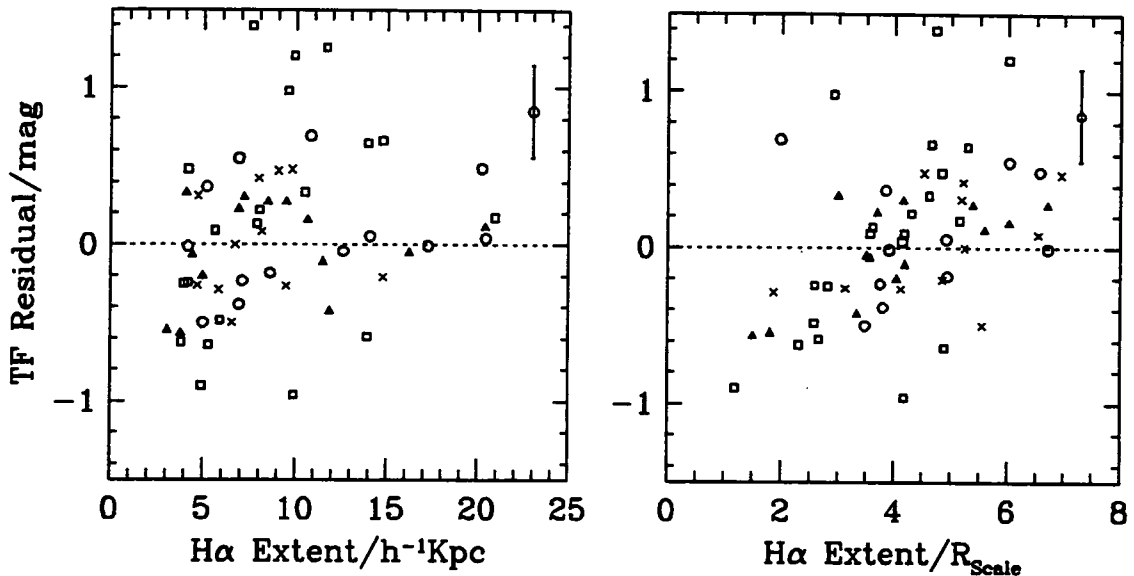


Figure 6.14: Left: The Tully-Fisher residuals for each galaxy plotted against the maximum extent of each objects H α rotation curve in h^{-1} Kpc. Right: The same points plotted against rotation curve extent in terms of disk scale length. Galaxies with poor H α extent with respect to their size tend to have negative TF residuals, i.e. lower rotation velocities than expected.

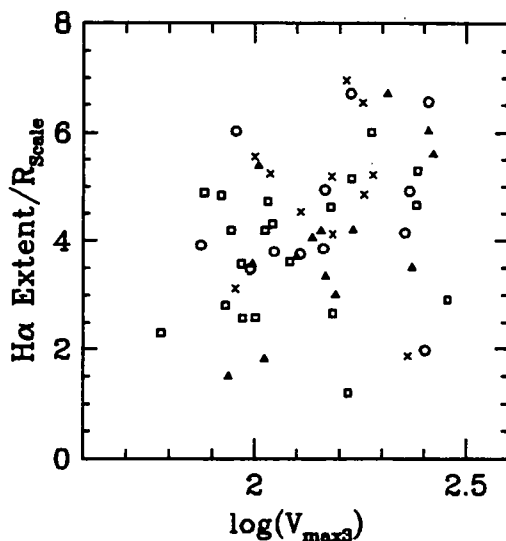


Figure 6.15: A graph of H α rotation curve extent in terms of disk scale length plotted against log-rotation velocity. No trend is evident, so poor quality rotation curves are unlikely to have a systematic effect on the TF slope.

assumed that the extent of H α emission within the sample galaxy disks is not strongly correlated with either luminosity or mass and that the relationship is free from such a systematic effect.

From Figure 6.14 it can be estimated that poorly extended rotation curves introduce an extra 0.2

mags rms into the TF scatter. This contribution could be reduced by rejecting galaxies with rotation curves that do not extend as far as 4 disk scale lengths. However, this would involve rejecting up to a quarter of the present sample. A better approach would be to measure the rotation velocity at a certain number of scale lengths or fraction of the disk radius. Then by carefully choosing the radius at which the rotation velocity is measured, a much smaller fraction of the sample would require rejection. Such a scheme for measuring rotation velocities is adopted in (Salucci et al. 1992) and would be interesting to apply to the present data set.

This approach also allows the quantification of the asymmetries and fluctuations in the rotation curves of the sample galaxies. Such variations are probably due to the spiral structure within each galaxy's disk and are likely to introduce further uncertainties into the rotation velocity. Once these variations have been quantified, their full impact on the TF scatter can be assessed. Clearly, the biggest source of scatter, besides measurement errors, is likely to be poor quality rotation curves.

With the major source of scatter within the relation removed by rejecting the poorest quality data, we can now again test to see if the remaining scatter

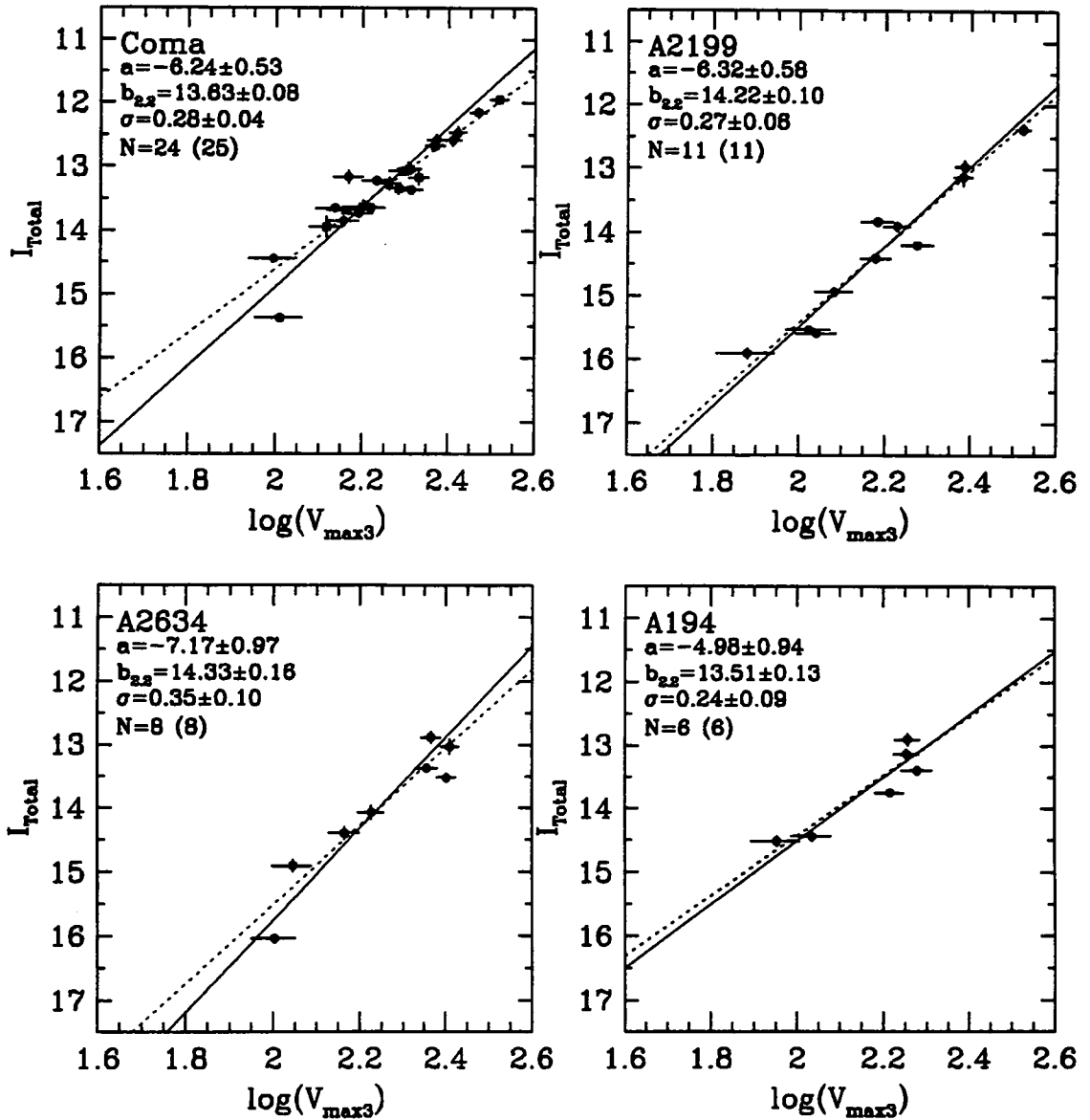


Figure 6.16: The same Tully-Fisher relations for each cluster that appear in Figure 6.12 after the expanding cluster correction has been applied. The scatter is only reduced in the A2199 sample the scatter increases in the other cluster. The marked lines and symbols have the same meaning as in Figure 5.18. 6.12

can be attributed to uncertain cluster membership. In Figure 6.16 we apply the “expanding” cluster correction to the highest quality TF points. The scatter increases for three of the clusters, A2199 being the only cluster where a reduction is seen when compared to the uncorrected relationship in Figure 6.12. The rms residuals in the relationship for A2199 is dominated by just two outlying points, both these galaxies have redshifts that differ from the sample mean by over 1000 km s^{-1} . The correction does reduce the residuals of these two points and hence

the rms scatter of whole sample but has little impact on the other galaxies in A2199. Therefore it is concluded that the “expanding” model is not an accurate description of the samples presented here. It is more likely that some of the remaining scatter is due to foreground or background galaxies that are not associated with the clusters. This implies that a stricter cluster selection based on redshift will further reduce the scatter.

An arbitrary selection limit in redshift was then applied to the highest quality data. All galaxies with

redshifts in the CMB frame that differed by more than 1000kms^{-1} from each cluster's mean sample redshift was rejected. The resulting TF relations are plotted in Figure 6.17. The reduction in the scatter of the A2199 and A2634 relations demonstrate that contamination of these cluster samples by foreground or background galaxies might be a problem (i.e. the selection limits in redshift were not strict enough). However the relationships are so poorly populated that significance of any effect in either cluster is doubtful. The tentative observation is also made that all the relationship's slopes now appear to be more consistent with the lower slope of Coma.

6.1.6 Intrinsic Scatter

When the measurement errors and the mean TF scatter discussed in chapter five are taken together with the best estimates of sources of scatter discussed in this chapter, an upper limit on any remaining intrinsic scatter can be placed. Combining the measurement errors on log-rotation velocity and apparent magnitude, whilst considering correlations in their corrections, produces a value of 0.270 mags rms as the scatter introduced. The uncertainties introduced by poor quality rotation curves, cluster depth effects and uncertain cluster membership are 0.300, 0.217, and 0.100 mags rms respectively. The fitting procedure applied in the previous chapter estimates the mean TF scatter as 0.477 mags rms. Adding all the sources of uncertainty in quadrature and subtracting from this value produces an upper estimate for the intrinsic scatter of 0.121 mags rms.

However, due to the uncertain nature of these estimates and the fact that numbers of a similar value are added in quadrature, this figure for the intrinsic scatter should be considered as an approximation. Possible causes of such scatter could be a morphological dependence in the relationship or variations in star formation history. To isolate such effects would require a much larger data set with additional information such as galaxy colour. This type of analysis is beyond the scope of this work.

6.2 Variations in the TF Gradient

It is now possible to consider whether the observed variations in the TF gradient between clusters, es-

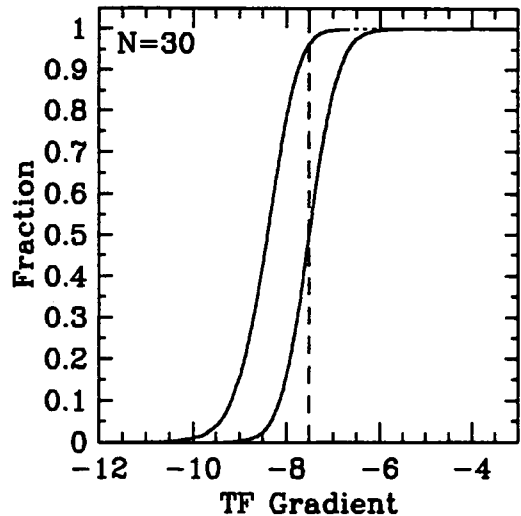


Figure 6.18: A cumulative probability distribution for the expected gradient of a bivariate distribution with parameters closely matching those of the present sample. The true TF slope of -7.5 is marked by a dashed line. The curve on the right represents the distribution for the gradient of the inverse regression. The left-hand curve marks the distribution for the direct regression line slope.

pecially Coma and Abell 2634 are significant. The result of a weighted regression of magnitude on log-rotation velocity is shown in Figure 5.18. The difference in slope between Coma and A2634 is 2.80 ± 0.62 which is a 4.5 sigma difference. Even if the “expanding” cluster correction is applied to the data (which is considered unsuitable for the present sample), the difference between the two gradients is 1.54 ± 0.63 (2.4 sigma). Therefore it can be concluded that the probability that the difference in slopes is due to chance is less than 5%.

A Monte-Carlo simulation of the fitting procedures was applied to a data set which had a slope of -7.5 and the same observed bivariate distribution and the same selection effects as in the present sample. The results of this simulation are shown in Figure 5.15. A cumulative plot of the expected gradient for a sample size of 30 galaxies is shown in Figure 6.18. This illustrates that the probability of obtaining a gradient lower than -6 is less than 1%. This begs the question as to whether the difference is due to real variations in the underlying relationship or some unknown systematic effect.

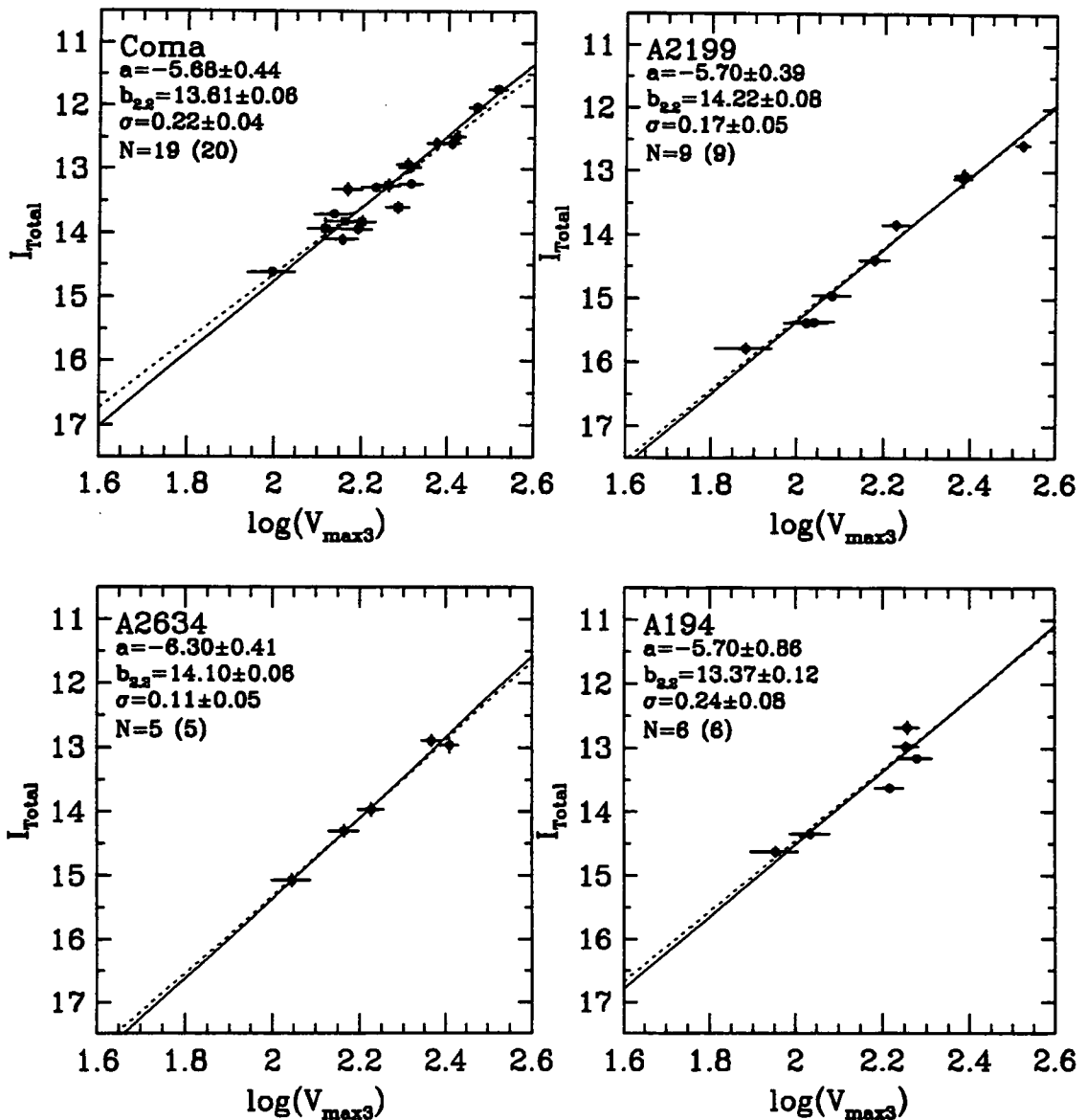


Figure 6.17: Four plots of the Tully-Fisher relation for the four cluster samples after rejection of low quality points and a $\pm 1000 \text{ km s}^{-1}$ redshift cut has been applied.

6.2.1 Potential Systematic Effects on Gradient

Perhaps the most likely cause of such variations is the selection procedure used in forming the samples. This is the single process over which there is little control and which could vary between clusters. Such an effect would have to bias the selected sample towards brighter galaxies at lower rotation velocities in order to change the gradient in such a way. In addition, this effect would need to be dependent on some property that varies between the clusters. We have been careful to select galaxies consistently

across clusters, applying the same selection limits to similar catalogues in each case. We have shown above that the distribution of galaxy properties for all four samples show no significant variation. Surface brightness is the property most likely to be affected by selection from photographic plates but it has been shown that there is no correlation between surface brightness and TF residuals.

Additional evidence that surface brightness considerations are unlikely to bias the Tully-Fisher relation comes from Zwaan et al. (1995). These authors demonstrated that the TF relation is the same

for low surface brightness galaxies as for high ones. Furthermore, to produce the low gradient observed in Coma, any bias would need to be against high rotation velocity galaxies at faint magnitudes. As galaxies with higher rotation velocities tend to have a higher surface brightness, any bias in the Coma sample must be against *high* surface brightness galaxies. Since high surface brightness galaxies are easy to detect on photographic plates and these objects are not small enough to be confused with stars, it is hard to imagine how such an effect could occur.

As the adopted fitting procedure is unaffected by the magnitude selection function, the only likely way the sample selection could have biased the fitted slope is by affecting the sample's rotation velocity distribution. Our data provides no evidence for the existence of any rotation velocity selection. Even if this effect were to operate, any selection function in terms of rotation velocity is liable to be independent of distance. So it is difficult to see how this effect could lead to variations between clusters.

No work on TF can escape mention of Malmquist bias. This bias refers to the systematic variations introduced into distance estimates of samples with apparent magnitude limits. Estimated distances are biased toward greater values and regions of higher density. For a full and detailed discussion of this process the reader is referred to Freudling et al. (1995), Hudson (1994) and Hendry & Simmons (1994). In the context of this work the Malmquist effect is irrelevant because throughout the assumption is made that our galaxies lie at a single distance within each cluster. Malmquist bias is a *distance* bias. Since at no stage in this analysis has distance been estimated our results are free from such a bias.

We have carefully dealt with other areas where systematic errors could be introduced. We have shown there is a correlation between the poor extent of rotation curves and the residuals in the relationship. However, it has also been shown that this effect does not depend on either magnitude or rotation velocity and does not appear to affect Coma galaxies any more than galaxies in the rest of the sample. In general, data quality concerns are not a likely cause of slope variations, as all four clusters are similar in this respect.

It is important to emphasise that these variations cannot originate from the reduction procedures. This is because all data from both observing runs was measured using the same instruments with the same set-up and then reduced in the same way. The data were treated as a single sample and only divided into clusters at the end of the reduction process. Finally, the simulations of our data set and fitting procedure show the fitted parameters to be unbiased and to have accurate error estimates. Therefore it must be concluded that the slopes are intrinsically different.

How can this difference be explained? Whatever process is responsible, it must systematically affect the fainter objects differently from the brighter objects to change the slope and must depend on a particular cluster environment. For example, if galaxies within dense cluster environments tend to lose their gas due to tidal stripping. If this process affects lower mass objects to a greater extent, low rotation velocity galaxies would tend to have weaker and curtailed rotation curves. This could have a systematic effect on the observed TF slope which would be even greater in the dense environment of Coma. Such an effect could be detected by further studying H α emission line strength and changes in rotation curve strength over different environments. This could also explain why the Coma cluster seems to have a deficiency of low rotation velocity objects.

Another possibility is that the denser cluster environment of Coma preferentially triggers star formation within lower mass objects, increasing the luminosity of low rotation velocity galaxies as compared to other cluster members. Higher pressure intra-cluster gas within such a high mass cluster would also work against the feed back effects that normally regulate star formation within lower mass objects. Allowing a higher star formation rate, increasing the mass-to-light ratio for the lower mass galaxies could also effect the TF gradient.

While it is easy to make such suggestions, without a much larger dataset with extra information such as colour, these speculations cannot be evaluated. It is important to note that even if the differences in slope are due to some unaccounted for systematic effect, the approach followed here closely mirrors

Table 6.2. A summary of previously published Tully-Fisher relations for Coma and Abell 2634. The size, N_{Gal} , slope, a , and scatter, σ of each sample is tabulated in addition to the photometric band used and which fitting method was utilised (i.e. forward or reverse).

	Present Work	Present Work	Aaronson (1986)	Bothun (1987)	Fukugita (1991)	Bernstein (1994)	Rood (1993)	Han (1991)	Willick (1991)
Band	I	I	B	I	b	I	B	I	R
Fit	F	R	F	F	F	F	F	F	F
Coma									
N_{Gal}	37	37	13		30	22	7	13	12
-a	4.50 ± 0.35	5.39 ± 0.40	9.86		6.53	5.65 ± 0.20	6.74	7.93 ± 0.96	5.36 ± 0.56
σ	0.27	0.28	0.76		0.47	0.10	0.14	0.31	0.223
A2634									
N_{Gal}	21	21	11	11				11	10
-a	7.39 ± 0.48	8.19 ± 0.46	7.73	6.2 ± 1.0				6.41 ± 1.05	5.74 ± 0.97
σ	0.37	0.39	1.03	0.27				0.26	0.246

those followed in recent TF literature and it seems likely other data sets will also be affected with the same variations.

In recent years a number of authors have measured the I-band Tully-Fisher slope in many nearby clusters. Measured values for the slope, with two recent exceptions, have typically been greater than -7.0 . Notable examples are: Pierce & Tully (1988) who measure a slope of -7.85 ± 0.29 for the Virgo and Ursa Major clusters, Schommer et al. (1993) find values of -8.84 ± 0.70 and -9.81 ± 0.84 for the Antlia and Hydra clusters, and Mathewson et al. (1992) fit a slope of -8.18 to the Fornax cluster. Considering these and other results in the literature a value of -7.5 can be taken the canonical value for the Tully-Fisher gradient. The measured gradient for the three clusters, Abell 2634, Abell 2199 and Abell 194 are entirely consistent with this value. A brief summary of previous TF studies in Coma and Abell 2634 is provided in Table 6.2. No published individual TF relations are currently available for Abell 2199 and Abell 194.

The low slope observed in Coma is not without precedence. A slope of -5.65 ± 0.20 was published in Bernstein et al. (1994) which is entirely consistent with our value of -5.39 ± 0.40 . Although our sample includes 17 galaxies with data from Bernstein et al. (1994) the gradient remains unchanged if these points are removed. More re-

cently an I-band slope of -5.62 ± 0.03 is calculated in Willick et al. (1995) using 31 clusters from data published in Han & Mould (1992). This result would suggest that the Coma cluster sample displays a typical Tully-Fisher relation and the clusters with steeper slopes are perhaps abnormal.

6.3 Estimating Distances

The fitted relationships for the four clusters means that their relative distances can now be calculated. By comparing the intercepts of each relationship at the same point, $\log V_{Rot} = 2.2$, it can be seen that the comparison is unaffected by variations in the slope. As the mean rotation velocity of each cluster sample is close to this value, the error estimates on the intercepts are also unaffected by gradient changes. Fixing the distance to the Coma cluster at 7200 km s^{-1} , which assumes Coma is at rest with respect to the CMB frame, allows the distance of the remaining three clusters to be calculated. The calculated distances and peculiar velocities are shown in Table 6.3.

Table 6.3 shows that the cluster distances estimated from the Tully-Fisher relation for Abell 2199 and Abell 2634 are consistent with those given by an entirely independent Fundamental Plane method (Lucrey et al. 1996). However, the errors are such that the calculated peculiar velocity of Abell 2199 is insignificant. The predicted Abell 194 distance



Table 6.3. Distance and peculiar velocity estimates for three of the clusters. Column headings are; cluster name, number of sample galaxies in cluster, N, cluster redshift in the CMB frame, CZ, Distance modulus relative to Coma, $\Delta\mu$, Calculated distance and Peculiar velocity. For comparison cluster distances and peculiar velocities estimated using the elliptical Fundamental-Plane (FP) technique are also shown (See Lucey et al. and Jorgensen et al.).

Cluster	N	CZ _{CMB}	$\Delta\mu$	Distance	Pec. Vel.	FP Dist.	Pec. Vel.
Coma	37	7200	-	-	-	-	-
A2199	30	9029	$+0.32 \pm 0.15$	8343^{+597}_{-557}	+686	9190	-160
A2634	21	9090	$+0.62 \pm 0.08$	9579^{+359}_{-346}	-489	9760	-670
A194	11	5336	-0.29 ± 0.13	6300^{+388}_{-366}	-964	4506	+532

shows an appreciable difference with the FP estimated distance. The small sample size results in an uncertain sample velocity which is the probable cause of this discrepancy. It is encouraging to note that in the case of Abell 2634 where the peculiar velocity error is smallest, the predicted velocity has the same sign and is close to the FP value. The agreement between these two different techniques means that the marginally detected peculiar velocity should be viewed as more significant. This would prove interesting because, as noted in Lucey et al. (1996), the nearest dominant structure to Abell 2634 is the Pisces-Perseus supercluster. And the distance and direction of the P-P ridge is such that it would be expected to exert a sufficient pull on A2634 to result in a peculiar velocity of -400kms^{-1} .

References

- Bernstein G., Guhathakurta P., Raychaudhury S., Giovanelli R., Haynes M. P., Herter T., Vogt N. P., 1994, *AJ*, 107, 1962
- Freudling W., Da Costa L. N., Wegner G., Giovanelli R., Haynes M. P., Salzer J. J., 1995, *AJ*, 110, 920
- Han M. S., Mould J. R., 1992, *ApJ*, 396, 453
- Hendry M. A., Simmons J. F. L., 1994, *ApJ*, 435, 515
- Hudson M. J., 1994, *MNRAS*, 266, 468
- Jorgensen I., Franx M., Kjaergaard P., 1996, *MNRAS*, 280, 167
- Lucey J. R., Steel R. G. J., Carter D., 1996, *MNRAS*, -, Preprint
- Mathewson D. S., Ford V. L., Buchhorn M., 1992, *ApJS*, 81, 413
- Pierce M. J., Tully R. B., 1988, *ApJ*, 330, 579
- Rhee M.-H., 1996, Ph.D. thesis, Kapteyn Laboratorium, Groningen, The Netherlands.
- Salucci P., Frenk C. S., Persic M., 1992, *MNRAS*, 262, 392
- Schommer R. A., Bothun G. D., Williams T. B., Mould J. R., 1993, *AJ*, 105, 97
- Scodreggio M., Solanes J. M., Giovanelli R., Haynes M. P., 1995, *ApJ*, 444, 91
- van Haarlem M. P., Cayon L., Gutierrez De La Cruz C., Martinez-Gonzalez E., 1993, *MNRAS*, 264, 71
- Willick J. A., 1991, Ph.D. thesis, University of California, Berkeley
- Willick J. A., Courteau S., Faber S. M., Burstein D., Dekel A., 1995, *ApJ*, 446, 12
- Zwaan M. A., Van Der Hulst J. M., De Blok W. J. G., McGaugh S. S., 1995, *MNRAS*, 273, L35

Chapter 7

Conclusions

7.1 Summary and Evaluation

The outcome of this study will now be summarised and evaluated in terms of the extent to which the aims for selection, reduction and analysis of the data have been fulfilled. Lastly, possible future work will be considered.

7.1.1 *The Selection Function*

With respect to selection, the aim was to produce a sample of likely spiral cluster members with clearly defined selection limits. This criterion was difficult to fulfill as the selection procedure had two conflicting requirements. On the one hand, a sample was desired that included fainter objects than had been studied previously. On the other hand, we wished to study galaxies from a wide range of cluster environments. The only available source of faint cluster members is catalogues based on scans of photographic plates. These are good because they have well defined selection limits and are complete to magnitudes well below the ones required here. Unfortunately, they are limited to a single photographic plate which restricts the sample to inner cluster regions. The only available source of galaxies for the outer regions of the cluster are the Zwicky and UGC catalogues which have a much brighter magnitude limit. These catalogues also suffer from incompleteness which results in an uncertain selection limit. As each catalogue was deficient in one of the selection criterion, objects had to be selected from both sources. Consequently, our initial requirement of a well defined sample was compromised.

This was shown not to be problematic by doing exhaustive modeling of the fitting procedure based on a regression of log-rotation velocity upon magnitude. The regression was found to be insensitive to the sample selection function in terms of magnitude.

So we can be confident that the compromises made during sample selection had no impact on the data analysis.

The possibility that the surface brightness limits of photographic catalogues systematically affected the TF relationship was considered but was found to have no physical basis in the data. There was also no evidence for any form of selection effects on rotation velocity. As any remaining undetected bias is likely to be independent of distance, its effect on all clusters will be equal and will not introduce systematic variations between them. Considering the limited observing time, we were still able to observe 65% of spiral candidates in the four clusters. 50% of this fraction were found to have suitable rotation curves and two thirds of these were within 3 degrees of the cluster centres.

Having selected a sample suitable for TF work, an iterative approach was adopted to decide the best form of the corrections to apply to the observables. As a first approximation, the corrections found in the current TF literature were applied. The resulting residuals from the relationship were then used to identify the corrections that produced the greatest reduction in scatter. Final versions of the model were then adopted to minimise the scatter in the relationship.

7.1.2 *Scatter in the Relationship*

The accuracy of distance estimates made using the TF relation is limited by the typical scatter of galaxies around the relation. Therefore it is desirable to reduce all contributions to this scatter from measurement errors and uncertainties in corrections.

It was shown that errors in ellipticity were limited by the amount of irregular isophotes caused by structure within each galaxy's disk. Ellipticity errors

are an important consideration in minimising the uncertainties introduced by the two major corrections. However, it was demonstrated that coupling between the two corrections resulted in ellipticity errors shifting points along the slope of the relationship. As a result, ellipticity errors are considered to have an unimportant contribution to the TF scatter.

The major contributor to the scatter was shown to be errors in rotation velocity caused by poor quality rotation curves. It was shown that a correlation exists between rotation curve extent, in terms of disk scale lengths, and the TF residuals. This is likely to affect all techniques that use the maximal points within the rotation curves to measure galaxy rotation velocities. It seems reasonable that such an effect could also be present in relationships based on radio measurements. This would occur if similar variations in the extent of neutral hydrogen are also seen between galaxies with the same luminosity. Future work that seeks to reduce TF scatter should concentrate on producing a more reliable method for estimating rotation velocities from rotation curves.

It is important to realise that while reductions in measurement error can be made through careful observations, high signal-to-noise, optimal corrections etc, there is a limit to the improvements possible. The irregular nature of spiral galaxies places a fundamental limit on the accuracy with which they can be reduced to a set of parameters. An upper limit was placed on this intrinsic scatter of 0.12 mags rms. The typical rms residuals of the final Tully-Fisher relationships was 0.35 mags rms, when forming the relations from what was considered our highest quality data this was reduced to 0.22 mags rms. These values are comparable to the typical and best values produced by 21cm-line radio based TF techniques. Such low values for the scatter in the underlying relationship has implications for its theoretical basis. This was highlighted by Eisenstein & Loeb (1996). They demonstrated that if the rotational velocity of a spiral galaxy is determined by the velocity dispersion of its halo and its luminosity is related to its total baryonic mass, a minimum intrinsic scatter in the Tully-Fisher relation can be calculated. The scatter expected when combining this popular view of the relationship with current cosmological

models is much larger than these observed values due to variations in galaxy formation history.

7.1.3 Variations in the TF Gradient

After careful consideration of the aforementioned systematic effects, it was concluded that the observed difference in slope between Coma and Abell 2634 is significant and could not be attributed to an effect of selection. This suggests there is a true variation in the underlying Tully-Fisher relationship. The mechanism responsible must systematically affect the TF slope and be dependent on varying cluster environment. Possible mechanisms include variation in dark matter content, systematic effects due to tidal stripping on the rotation curves and differing star formation history. The plausibility of each of these mechanisms will be considered in turn.

It was suggested in Dekel & Silk (1986) that lower mass galaxies are expected to have a higher fraction of dark matter due to mass loss driven by supernova winds. More recently, studies of rotation curves have provided further evidence that this is true (Ashman et al. 1993). The four clusters in our sample display a wide range of mass. If there is a variation in dark matter content between clusters, it is reasonable to assume that a similar difference between galaxies from the respective clusters would also be seen. Such a change in the mass-to-light ratio between the two populations would manifest itself in a change of slope in the TF relationship.

It has been shown by Salucci et al. (1992) that the dark matter content of spirals can have a systematic effect on the shape of rotation curves. This means that differences in the mean mass-to-light ratio between the two environments could also introduce systematic differences into the measured rotation velocities, in turn further affecting the relationship.

Another conceivable effect on the TF relation is due to the tidal stripping of gas from spirals in dense clusters. If this process affected lower mass objects to a greater extent, low rotation velocity galaxies would tend to have weaker and curtailed rotation curves. This would have a systematic effect on the observed TF slope which would be enhanced in the very dense environment of Coma. This could also

explain why the Coma cluster seems to have a deficiency of low rotation velocity galaxies. If such objects have lost a large fraction of their gas, star formation will have dropped to such an extent as to make detection of H α emission difficult.

A further possibility is that the denser cluster environment of Coma preferentially triggers star formation within lower mass objects, increasing the luminosity of low rotation velocity galaxies as compared to other cluster members. Higher pressure intra-cluster gas within such a high mass cluster would also work against the feedback effects that normally regulate star formation within lower mass objects. Such a change in the mass-to-light ratio would alter the Tully-Fisher relation in a similar way to changes resulting from variations in dark matter content.

These theories are directly testable. Variations in star formation between galaxies in different samples would be evident in a difference between the mean galaxy colour in each case. Unfortunately at this stage we only have I-band measurements of the sample so this effect cannot be investigated further. The suggested mechanisms that change the observed rotation curves could be detected by further studying H α emission line strength and changes in rotation curve shape over different cluster environments.

7.2 Future work

In the light of the findings of this study it is possible to make some recommendations for future work. First of all, there is considerable further analysis that could be done on the existing rotation curve data. It has already been shown how the rotation curves can be represented with a three parameter fitting function. These parameters could be used to search for systematic variations in rotation curve shape between cluster samples and galaxies with different properties such as morphology, surface brightness, luminosity and local cluster environment. If such a variation was seen between galaxies in different clusters, this would provide further evidence for real variations in the Tully-Fisher relation.

The spectroscopic data yields other useful information about galaxies which also could be incorpo-

rated into the study. In particular, a total H α emission line flux can be calculated for each galaxy by summing up the flux within each rotation curve. This would produce an indication of the present star formation rate. It would be interesting to see how this varies with cluster environment and with galaxy morphology. And as we have already demonstrated, the strength of H α emission can have a systematic effect on the measured rotation velocity. If this environmental dependence were found it would have implications for the application of the TF over different environments.

To get further information out of rotation curves perhaps a more physical fitting technique should be adopted. For instance, the "universal rotation curve" fitting techniques suggested by Persic et al. (1996) or the interpolated velocity at a fixed number of scale lengths used by Chiba & Yoshi (1995). Other methods of extracting information from the rotation curves such as the principal component techniques suggested by Rhee (1996) could be explored. Measuring velocities at a fixed fraction of some characteristic radius would remove the correlation between the extent of rotation curves and the measured velocity. This would produce a much more trustworthy relation with reduced scatter with the advantage of being applicable to more galaxies.

Further information on morphology could be gained by adopting a more sophisticated surface photometry fitting technique such as that utilised by de Jong (1995). This 2D fitting approach provides more reliable decomposition of disk and bulge components allowing a more accurate quantification of galaxy morphology. However, it is not clear how well this technique will work for the typically edge-on galaxies that form Tully-Fisher samples.

For the future, it would be interesting to apply the techniques discussed here to a cluster at a greater redshift. This would allow a measurement of H $_0$ over an appreciable volume of the universe and to check for possible evolution in the relationship. The major problem with such a study is obtaining data with sufficient spatial resolution. High spatial resolution photometry and spectroscopy is required to accurately ascertain galaxy inclination and to resolve a rotation curve. Considerable HST pho-

tometry of such clusters is already available in the archives and spectroscopic measurements would be an ideal application for the planned integral field unit on the WHT.

Over the past decade considerable effort has been invested in a number of large Tully-Fisher distance surveys, covering much of the nearby universe. In the main, these surveys have tried to make as many accurate distance estimates of galaxies and clusters as possible as part of the ongoing study of large scale structure and the peculiar velocity field. Projects like the present one, which require a similar amount of effort but yield few distance estimates might seem superficially, to be of questionable worth. It is the view of the present author, that the intensive study of a few clusters is valid. Continuation of this work will not only affect all Tully-Fisher work to date, but might also reveal some secrets about the nature of spiral galaxies that have remained hidden for so long.

References

- Ashman K. M., Salucci P., Persic M., 1993, MNRAS, 260, 610
- Chiba M., Yoshi Y., 1995, ApJ, 442, 82
- de Jong R. S., 1995, Ph.D. thesis, Kapteyn Laboratorium, Groningen, The Netherlands.
- Dekel A., Silk J., 1986, ApJ, 303, 39
- Eisenstein D. J., Loeb A., 1996, ApJ, 459, 432
- Persic M., Salucci P., Stel F., 1996, MNRAS, 281, 27
- Rhee M.-H., 1996, Ph.D. thesis, Kapteyn Laboratorium, Groningen, The Netherlands.
- Salucci P., Frenk C. S., Persic M., 1992, MNRAS, 262, 392

8.1 Tables of Selected Galaxies

Full details are given of the candidate spiral galaxies within each cluster. For each cluster, two samples were selected. One sample of galaxies were taken from published catalogues derived from photographic plate scans. And one was made up from galaxies selected from either the Zwicky or UGC catalogues. Each table gives the relevant details extracted from each source.

All objects are assigned an observation code which indicates whether a galaxy has been observed and if so what the outcome was. The meaning of the observation codes (Obs.) are; 0 = not observed, 1 = in final TF sample, 2 = suitable for TF but not in final sample due to poor quality, 3 = redshift only (i.e. only nuclear H α emission), 4 = No H α emission, 5 = blank spectrum (possible miss), 6 = wrong/poor morphology or too face-on (e.g. star or E).

Some published catalogues did not supply all the needed parameters, i.e. position angle. In these cases information was merged from the APM catalogue. When positions were considered inaccurate they were also replaced with APM values. Full details of the sources used and selection procedures are given in §2.2.

Table 8.1. Coma GMP83 Selected sample. Based on magnitude, colour and ellipticity.

No.	Galaxy	Obs	GMP83 Position		B-mag	e	B-R	Type	GAL N	GMP N	PA	V_{hel} /Notes
1	1251+2827	1	12 51 28.375	+28 27 27.70	16.37	0.5	1.45	S	425	6652	39	
2	1251+2840	0	12 51 29.902	+28 39 53.15	17.94	0.6	1.62		586	6641	92	
3	1253+2932	4	12 53 37.051	+29 32 01.29	17.60	0.5	1.35		1532	5648	91	
4	ZW160-20	0	12 53 40.710	+27 56 54.48	15.71	0.3	1.41	I	2042	5643	157	4900
5	IC3913	0	12 54 03.058	+27 33 41.85	15.73	0.3	1.47	S	3232	5422	62	7534
6	1254+2924	1	12 54 03.963	+29 24 27.12	17.33	0.6	1.20		1422	5382	2	
7	1254+2913	4	12 54 11.247	+29 13 03.50	17.31	0.5	1.56		1175	5312	83	
8	ZW160-34	0	12 54 25.720	+29 11 59.05	15.50	0.6	1.61	S	4806	5197	8	8030
9	1255+2920	0	12 54 35.106	+29 20 18.91	17.94	0.3	1.55		4929	5122	171	
10	D94	0	12 54 52.598	+28 04 51.38	16.49	0.3	1.62	S0	6218	4974	8	7110
11	1255+2917	0	12 55 19.454	+29 17 24.89	16.88	0.3	1.63		4900	4677	100	
12	D162	0	12 55 31.720	+28 15 41.74	17.25	0.5	1.07	I	3492	4570	110	4554
13	TT5	1	12 55 32.854	+28 19 51.82	16.07	0.3	1.50	I/S/S0	3489	4555	71	8163
14	1256+2917	0	12 55 40.879	+29 17 13.16	17.46	0.7	1.54		4872	4468	117	
15	U8082	1	12 55 40.925	+28 30 37.59	14.50	0.7	1.56	Scd	3895	4471	155	7247
16	1256+2703	0	12 55 41.523	+27 03 24.03	17.77	0.3	1.56		6565	4478	74	
17	1256+2656	0	12 55 43.691	+26 56 02.26	17.14	0.4	1.32		6441	4463	142	
18	ZW160-58	0	12 55 44.434	+28 58 41.35	15.45	0.7	1.54	Sc	4477	4437	84	7648
19	1256+2847	0	12 55 50.231	+28 47 29.24	17.41	0.3	1.25		4201	4372	120	
20	BO254	2	12 55 53.181	+28 07 04.47	17.77	0.6	1.30		6143	4348	41	7520
21	TT33	1	12 55 53.313	+27 34 50.22	16.85	0.3	1.52	I	5312	4351	144	7476
22	ZW160-62A	0	12 55 53.663	+29 23 53.36	15.38	0.4	1.61	S0	5036	4335	26	7850
23	U8092	0	12 56 10.182	+27 51 57.88	14.38	0.5	1.66	S0p	5660	4156	86	7595
24	ZW160-67	0	12 56 11.980	+27 26 46.57	15.60	0.3	1.27	Sp/I	7026	4135	8	7685
25	1256+2835	0	12 56 13.178	+28 35 06.67	17.51	0.4	1.61		3987	4110	140	
26	1256+2717	0	12 56 13.407	+27 16 57.08	17.94	0.6	1.44		6851	4121	113	
27	1256+2701	0	12 56 14.518	+27 01 43.57	16.86	0.7	1.21		6423	4106	117	
28	BO313	0	12 56 28.797	+28 33 29.38	17.96	0.3	1.55		3817	3930	22	
29	1257+2904	0	12 56 41.866	+29 04 51.87	17.62	0.4	1.31		4554	3744	107	
30	1257+2854	0	12 56 53.318	+28 53 37.27	17.81	0.4	1.47		4422	3578	147	
31	1257+2704	0	12 56 56.703	+27 03 59.97	17.97	0.4	1.57		6511	3538	80	
32	D236	0	12 56 58.476	+28 45 28.06	16.66	0.3	1.36	S	4123	3509	174	
33	1257+2715	0	12 57 24.079	+27 14 37.93	17.79	0.3	1.37		10639	3143	157	
34	D66	4	12 57 31.376	+28 00 54.17	17.17	0.6	1.18	S0/a	9755	3071	36	8910
35	D3	2	12 57 49.400	+27 32 59.29	16.39	0.5	1.34	S	11018	2843	25	
36	U8113	0	12 57 53.281	+28 28 16.64	14.38	0.7	1.32	S0	7860	2795	155	8446
37	NGC4898B	0	12 57 53.306	+28 13 31.75	16.19	0.8	1.32	E	7403	2794	91	6513
38	1258+2736	0	12 58 04.332	+27 36 08.52	17.38	0.6	1.35		9259	2639	16	
39	D26	4	12 58 04.386	+27 47 01.69	16.18	0.4	1.35	S0p/S	9410	2640	169	7460
40	1258+2913	0	12 58 06.960	+29 13 09.61	17.72	0.7	1.37		8826	2625	116	
41	D25	1	12 58 08.780	+27 46 22.41	16.64	0.3	1.21	I	9412	2601	52	
42	U8118	1	12 58 15.390	+29 17 16.84	14.85	0.3	1.63	Sp	8844	2544	57	7193
43	TT13	2	12 58 16.201	+28 47 15.03	16.21	0.7	1.10	S	8194	2536	5	8970
44	U8140	0	12 59 19.269	+29 18 46.92	14.91	0.7	1.65	Sab	8754	1900	87	7027
45	1259+2921	0	12 59 22.473	+29 20 40.52	17.70	0.3	1.43		8928	1870	88	

Table 8.2. Coma GMP83 Selected sample. Based on magnitude, colour and ellipticity. Continued...

No.	Galaxy	Obs	GMP83 Position		B-mag	e	B-R	Type	GAL N	GMP N	PA	V_{hel} /Notes
46	U8142	0	12 59 43.226	+27 55 00.04	15.37	0.3	1.64	Sa	9646	1616	90	7186
47	D202	2	12 59 47.507	+28 26 28.27	16.37	0.3	1.22	Sd/I	7508	1582	5	
48	D189	0	12 59 49.888	+28 22 12.57	17.12	0.4	1.61	S0	7510	1564	20	
49	1300+2908	0	13 00 01.605	+29 07 35.54	17.20	0.5	1.07		8573	1473	62	
50	1300+2929	0	13 00 05.679	+29 28 39.14	17.44	0.3	1.49		9083	1454	131	
51	1300+2740	0	13 00 07.988	+27 39 41.62	17.80	0.3	1.21		9186	1412	90	
52	ZW160-114	0	13 00 14.115	+28 22 58.04	16.34	0.7	1.61	SBa/0	11319	1367	90	7450
53	M5-31-112	0	13 00 28.381	+27 47 10.70	17.97	0.4	1.29		12856	1241	129	
54	1301+2736	0	13 00 52.068	+27 36 02.20	16.04	0.5	1.53	Sp	12725	1028	8	
55	1301+2850	0	13 01 03.862	+28 49 55.98	17.06	0.3	1.38		11817	949	93	
56	1302+2835	0	13 01 38.706	+28 34 35.87	17.17	0.5	1.35		11530	653	57	
57	1302+2849	0	13 01 49.239	+28 48 37.91	17.95	0.3	1.10		11798	597	11	
58	ZW160-127	0	13 02 02.148	+27 34 17.93	15.70	0.3	1.23	S?	12677	455	69	5627
59	1302+2854A	2	13 02 11.935	+28 53 42.77	16.30	0.4	1.32	Sp	11881	419	86	
60	1302+2854B	0	13 02 15.265	+28 53 46.94	16.35	0.3	1.47	Sp	11882	397	21	
61	1302+2856	0	13 02 25.421	+28 55 43.48	17.40	0.6	1.54		11883	329	114	
62	1303+2748	0	13 02 39.071	+27 48 17.80	17.62	0.3	1.60		12893	228	92	
63	1303+2755	0	13 02 39.921	+27 54 38.76	17.43	0.4	1.49		13027	221	33	
64	1303+2854	0	13 02 51.823	+28 53 38.72	17.71	0.3	1.34		11861	140	92	
65	1303+2917	0	13 03 09.370	+29 16 44.21	16.32	0.7	1.55	Sp	12210	20	49	

Table 8.3. Coma GMP83 Selected sample. Based on magnitude, type and ellipticity.

No.	Galaxy	Obs	GMP83 Position		B-mag	e	B-R	Type	GAL N	GMP N	PA	V_{hel} /Notes
1	U8071	0	12 55 04.931	+28 27 28.89	15.81	0.59	2.51	Sa	3925	484	162	7078
2	D22	4	12 55 29.112	+27 45 37.01	16.37	0.37	1.91	SBb	5524	459	80	
3	D21	0	12 55 36.447	+27 45 33.06	15.83	0.32	1.84	Sa/SBa	5521	452	86	
4	D38	1	12 58 11.026	+27 50 35.61	16.20	0.72	1.74	Sbc	9604	258	55	
5	IC4040	1	12 58 13.067	+28 19 38.22	15.44	0.69	2.04	Scd	7336	255	152	7636
6	ZW160-90	0	12 58 25.031	+27 40 28.95	15.41	0.41	1.82	Sa	9258	243	163	6932
7	NGC4921	0	12 59 01.523	+28 09 15.72	13.53	0.39	2.30	SBb	10056	205	154	5435
8	D222	4	13 00 29.242	+28 34 43.47	17.45	0.54	1.76	Sc	11591	124	69	

Table 8.4. Coma Kent and Gunn 1982 Selected sample within 3 degrees of Coma centre. Selection based on magnitude, type and redshift.

No.	Galaxy	Obs	APM Position		B-mag	R_{Clms}	NED: V_{helC}	Type	APM: a	e	PA	Notes
A1	Z159-75	1	12 45 01.53	27 43 49.9	15.2	165.4	6610	S?	37.9	0.48	27	
A2	Z159-80	1	12 46 15.15	26 41 23.4	15.7	172.6	7098	Sc(sp)	51.0	0.73	6	
A3	N4735	1	12 48 36.00	29 11 59.1	15.1	127.0	6459	S?	40.7	0.40	104	
A4	Z159-90	1	12 48 37.29	27 38 30.6	15.5	120.2	8317	S?	39.8	0.36	35	
A5	U8013	1	12 50 09.97	27 01 17.0	15.7	119.0	7885	S?	56.1	0.69	93	
B1	U8017	1	12 50 27.85	28 38 32.3	14.5	92.9	7074	S?	65.5	0.64	39	
B2	Z159-106	1	12 51 26.15	29 15 01.4	15.6	97.6	7976	Spiral	39.6	0.56	180	
B3	U8025	1	12 51 37.48	29 52 29.0	14.8	122.5	6316	Sb	104.9	0.82	74	
B4	N4788	2	12 51 50.25	27 34 29.2	15.4	81.2	6460	S?	48.6	0.61	141	
B5	Z159-114	2	12 52 07.57	28 38 51.3	15.5	71.6	7125	SB?	48.3	0.32	68	
B6	Z159-117	1	12 52 23.16	30 48 56.2	15.7	166.8	6348	Spiral	35.1	0.55	155	
B7	Z160-31	0	12 54 24.18	27 21 51.3	15.7	63.6	6849	Sp	43.7	0.62	149	
B8	Z160-34	0	12 54 25.78	29 12 00.0	15.2	68.0	8019	S?	51.4	0.62	12	
B9	U8069	0	12 54 46.66	29 18 54.4	14.8	71.4	7479	SB?	63.6	0.62	24	
B10	U8071	0	12 55 05.01	28 27 29.2	15.4	30.9	7069	S?	55.2	0.62	159	
B11	I837	0	12 55 05.59	26 46 56.7	15.4	92.1	7222	S?	51.1	0.67	15	
B12	U8076	2	12 55 25.57	29 55 26.9	15.2	103.9	5304	SABd:	51.9	0.37	96	
B13	U8082	0	12 55 40.69	28 30 46.9	14.2	26.0	7049	SBab:sp	80.9	0.67	157	
B14	Z160-58	1	12 55 44.72	28 58 42.2	15.5	48.7	7629	S?	63.7	0.68	86	
B15	Z160-67	1	12 56 12.05	27 26 46.3	15.4	49.5	7666	S? sp	24.1	0.25	11	
B16	N4858	2	12 56 38.77	28 23 30.1	15.5	11.9	9456	SBb	80.5	0.56	43	
B17	I3990	0	12 57 14.77	29 09 54.6	15.0	56.2	6214	S?	65.8	0.69	30	
B18	U8108	2	12 57 38.49	27 10 03.4	14.7	64.0	5895	S	84.4	0.76	14	
B19	Z160-A34A	0	12 57 44.93	28 08 03.3	15.6	9.1	5136	I	39.2	0.56	124	
B20	TT42	2	12 58 04.40	27 47 03.2	16.0	28.9	7467	Spiral	29.8	0.57	160	
B21	Z160-86	0	12 58 08.91	27 54 24.3	15.4	22.4	7476	S?	31.3	0.29	63	
B22	I4040	0	12 58 13.34	28 19 34.9	15.1	14.9	7850	Sdm:	40.8	0.60	153	
B23	TT15	0	12 58 17.55	28 46 51.6	16.0	36.3	8970	Spiral	75.9	0.60	151	
B24	U8118	0	12 58 15.46	29 17 18.4	14.6	64.6	7179	S?	74.3	0.56	58	
B25	U8128	0	12 58 29.49	28 03 10.0	13.7	20.3	7970	SAB(r)bc	26.1	0.42	53	
B26	U8134	0	12 59 01.74	28 09 16.6	13.7	24.8	5459	SB(rs)ab	46.9	0.21	135	
B27	U8140	1	12 59 19.48	29 18 48.1	14.8	71.4	7101	Sab	82.8	0.67	90	
B28	Z160-107	0	12 59 40.35	29 31 19.3	14.9	84.0	7292	S?	61.7	0.76	157	
B29	I4106	0	13 00 14.21	28 22 59.2	15.5	40.7	7454	GPair	48.7	0.31	147	
B30	U8160	1	13 00 52.13	28 17 55.0	15.0	49.3	6093	S?	63.8	0.77	104	
B31	U8161	1	13 01 04.36	26 49 06.7	15.5	98.9	6648	S?	60.3	0.58	139	
B32	Z160-127	1	13 02 02.25	27 34 20.8	15.5	75.3	5523	S?	37.4	0.41	71	
C 1	Z130-8	1	13 03 50.24	25 43 40.4	14.9	174.8	7265	S?	36.8	0.32	145	
B33	U8194A	1	13 03 54.07	29 19 47.9	13.9	110.4	7039	Gpair	54.1	0.49	142	
B34	N4983	0	13 06 04.00	28 35 13.2	14.9	118.3	6631	S?	58.4	0.47	122	
B35	U8229	3	13 06 30.98	28 27 01.6	14.3	123.8	5972	SB(r)b	78.9	0.53	60	
B36	U8259	1	13 08 39.42	29 50 38.0	15.3	179.1	7262	SBab	78.0	0.59	173	

Table 8.5. Coma Kent and Gunn 1982 Selected sample within 6 degrees of Coma centre. Selection based on magnitude, type and redshift.

No.	Galaxy	Obs	APM Position		B-mag	R_{Cls}	NED: V_{hel}	C	Type	APM: a	e	PA	Notes
A1	N4585	1	12 35 45.55	29 12 41.5	14.6	288.7	7294	S?	47.9	0.42	107		
A2	I3620	0	12 36 50.13	28 10 59.6	15.6	269.4	6551	Sp	43.3	0.70	165		
A3	Z159-58	1	12 40 20.64	26 54 57.0	15.5	237.9	6804	S	48.6	0.65	18		
B1	U7928	0	12 42 43.44	23 18 33.6	14.4	353.7	6974	S?	38.1	0.12	174		
C1	I3918	0	12 54 26.39	22 38 37.8	15.6	336.9	6529	Spiral	28.5	0.28	169		
D1	Z160-80	0	12 57 22.25	32 18 50.3	14.7	244.2	6821	SB?	45.8	0.19	116		
C2	U8209	0	13 5 17.82	25 4 38.3	15.3	217.3	6333	SB?	52.3	0.55	97		
C3	U8220	1	13 6 6.77	24 58 1.8	15.2	228.7	7129	Sbc	95.9	0.82	142		
D2	U8292	0	13 10 23.59	32 4 25.1	14.6	287.0	6340	Sb	0.0	0.00	90		
D3	Z160-163	0	13 10 36.32	27 24 22.8	15.7	184.6	6863	GPair	64.3	0.66	38		
D4	Z160-165	0	13 11 2.81	28 1 40.6	15.7	183.3	6106	S?	37.3	0.35	103		
D5	U8300	3	13 11 4.38	28 4 4.8	13.6	183.0	6408	SB(r)b	62.8	0.46	180		
C4	Z130-21	0	13 11 21.22	25 14 48.6	15.4	253.4	7163	Spiral	44.7	0.19	75		
D6	U8366	0	13 16 46.65	28 46 13.9	14.3	260.6	6653	SBb	69.2	0.49	119		
D7	Z160-208	0	13 18 58.71	31 38 57.0	15.0	350.0	7084	S?	34.4	0.62	4		

Table 8.6. Abell 2199 DGP89 Selected sample. Selection on magnitude, colour and ellipticity.

No.	Galaxy	Obs	DGP89 Position		b_{26}	a	b-r	PA	e	Type	V_{hel}	Notes
1	1622+4014	1	16 22 16	40 13 57	16.21	13.8	1.51	78	0.35	S		
2	1622+3854	0	16 22 29	38 53 40	17.10	10.0	1.63	78	0.32			
3	1623+3926	0	16 22 48	39 26 06	17.02	11.7	1.68	133	0.45			
4	1623+3922	4	16 22 54	39 22 12	16.72	15.0	1.22	25	0.64			
5	1623+3937	3	16 23 00	39 37 16	17.97	7.3	1.53	1	0.39			
6	1623+3951	2	16 23 05	39 50 49	15.54	24.9	1.53	33	0.56			
7	1623+4038	2	16 23 20	40 38 16	16.64	12.9	1.70	95	0.62			
8	1623+3931	1	16 23 21	39 30 41	17.71	10.1	1.31	142	0.35			
9	1623+3923	1	16 23 26	39 23 22	17.68	8.4	1.69	24	0.61			
10	1624+4036	0	16 23 31	40 36 01	17.91	7.6	1.73	16	0.39			
11	U10381	4	16 23 43	39 58 56	14.56	39.9	1.83	91	0.43	S0/a	8804	
12	1624+3906	3	16 23 54	39 05 37	17.98	9.7	1.33	125	0.42			
13	1624+3955	1	16 23 56	39 55 17	16.86	14.5	1.53	11	0.59			
14	1624+4013	3	16 23 56	40 12 37	16.06	17.5	1.81	112	0.48			
15	1624+3932	0	16 24 16	39 31 54	17.66	7.8	1.73	175	0.56			
16	1624+4027	0	16 24 16	40 27 27	17.75	8.0	1.66	77	0.65			
17	1624+3947	0	16 24 19	39 47 09	17.47	8.6	1.70	70	0.57			
18	1624+3850	0	16 24 21	38 49 50	17.98	7.7	1.52	66	0.47			
19	1624+3948	2	16 24 21	39 47 39	17.89	8.7	1.41	24	0.66			
20	1625+3912	0	16 24 40	39 11 34	17.17	12.2	1.62	46	0.42			
21	1625+3921	0	16 24 42	39 20 58	17.71	10.6	1.63	79	0.38			
22	1625+3855A	1	16 24 49	38 54 56	16.50	13.6	1.45	119	0.40			
23	U10389	6	16 24 53	39 14 18	15.94	20.1	1.79	44	0.63		10583	
24	1625+4017	1	16 24 59	40 17 28	16.71	12.4	1.56	166	0.42			
25	BO37	1	16 25 04	39 59 18	16.16	13.7	1.68	159	0.55	S		
26	1625+3909	1	16 25 12	39 08 51	15.89	20.3	1.59	61	0.29			
27	1625+3855	1	16 25 20	38 55 11	17.92	7.8	1.38	3	0.51			
28	RB36	1	16 25 31	39 03 52	16.74	11.6	1.49	152	0.43	S		
29	1626+3958	1	16 25 42	39 57 49	17.61	13.1	1.45	21	0.39			
30	1626+3857	4	16 25 47	38 57 17	17.82	6.7	1.47	64	0.33			
31	1626+3913	0	16 25 51	39 12 40	16.65	11.9	1.65	72	0.43			
32	1626+3900	1	16 25 53	39 00 25	17.40	10.3	1.48	166	0.70			
33	BO43	1	16 25 53	39 22 46	16.33	18.3	1.46	148	0.41	SBc	10712	
34	BO125	4	16 25 54	39 26 49	17.68	9.2	1.68	109	0.36			
35	BO63	1	16 25 57	39 30 21	16.98	12.5	1.74	179	0.41			
36	1626+4015	2	16 25 58	40 15 31	17.38	8.8	1.47	17	0.63			
37	1626+4016	1	16 25 59	40 15 52	17.58	7.6	1.68	35	0.70			
38	BO124	0	16 26 10	39 20 29	17.94	11.5	1.74	173	0.34			
39	1626+3908	0	16 26 23	39 08 09	17.39	8.1	1.68	18	0.35			
40	Z224-41	1	16 26 57	40 13 56	15.10	21.5	1.64	145	0.41	S	7802	

Table 8.7. Abell 2199 DGP89 Selected sample. Selection on magnitude, colour and ellipticity. Continued...

No.	Galaxy	Obs	DGP89 Position		b_{26}	a	b-r	PA	e	Type	V_{hel}	Notes
41	Z224-41A	0	16 27 00	40 13 56	15.66	16.1	1.72	97	0.29	S	7705	
42	BO140	0	16 27 14	39 43 05	17.88	8.4	1.67	36	0.64			
43	BO88	0	16 27 20	39 22 59	17.49	8.2	1.76	135	0.42			
44	1627+4039	2	16 27 20	40 38 33	15.43	26.4	1.83	49	0.48			
45	1628+4021A	6	16 27 33	40 20 55	16.78	10.5	1.66	70	0.58			
46	1628+3844	0	16 27 34	38 43 52	16.82	14.1	1.58	100	0.39			
47	BO152	3	16 27 34	40 22 05	16.71	14.5	1.37	42	0.63			
48	1628+3927	0	16 27 40	39 27 30	17.97	8.9	1.53	139	0.42			
49	1628+4021	0	16 28 06	40 20 47	17.50	14.1	1.52	140	0.31			
50	1629+3957	0	16 28 37	39 57 07	17.90	8.5	1.49	52	0.46			
51	1629+3940	6	16 28 45	39 39 50	17.80	11.0	1.75	16	0.29			
52	Z224-55	1	16 28 46	39 43 58	15.14	24.1	1.85	155	0.62	Sa	9138	
53	U10429	1	16 28 51	39 56 15	15.31	27.7	1.67	129	0.31	S?	7433	
54	1629+4006	2	16 29 09	40 05 45	17.27	11.2	1.58	57	0.77			
55	1630+4032	0	16 29 46	40 32 26	17.95	10.0	1.67	59	0.52			
56	1630+4008	0	16 29 54	40 07 35	17.86	11.1	1.60	107	0.57			
57	1630+4003	0	16 30 16	40 03 11	17.22	11.2	1.42	174	0.37			
58	1630+3846	0	16 30 30	38 45 41	17.78	8.8	1.45	14	0.74			
59	1631+3944	0	16 30 50	39 43 54	17.82	8.5	1.32	125	0.53			
60	1632+4019	0	16 31 36	40 18 52	18.00	8.0	1.70	89	0.45			
61	1632+3927	0	16 31 46	39 27 12	17.73	8.4	1.40	142	0.30			

Table 8.8. Abell 2199 UGC Selected sample. Selection on magnitude, type and redshift. within 5 degrees of cluster centre.

Galaxy	Obs	NED Position		Type	b-mag	a	b	V_{hel}	Notes
UGC10166	4	16 02 07.46	40 07 13.0	SB	14.80	1.1	0.6	9319	
UGC10227	1	16 07 08.41	36 44 26.0	SBcd?	15.34	2.2	0.2	9026	
UGC10241	0	16 08 08.42	42 27 48.0	Sbc	15.05	1.0	0.8	11752	
UGC10244	1	16 08 17.12	43 15 30.0	S?	15.50	1.0	0.2	9820	
UGC10252	1	16 09 01.83	41 16 38.0	Sab	15.25	1.0	0.3	9670	
UGC10330	6	16 16 28.87	40 12 54.0	SAB(s)b	15.10	1.1	0.8	9892	
UGC10349	4	16 19 11.10	40 13 17.0	SBab	14.51	1.3	0.5	10175	
UGC10354	4	16 19 40.73	40 55 39.0	SAB(s)c	15.30	1.2	0.9	8942	
UGC10362	4	16 21 12.62	39 54 25.0	SB(r)b	15.00	1.3	0.8	9600	
UGC10366	1	16 21 33.69	37 22 23.0	Sb	14.60	1.9	0.5	10232	
UGC10389	1	16 24 53.16	39 14 18.6	SB?	16.00	1.0	0.4	10574	
UGC10404	2	16 26 29.17	39 55 53.0	SB	15.50	1.5	1.1	7987	
UGC10415	2	16 27 20.82	41 23 33.0	SABb	14.62	1.0	0.9	9546	
UGC10417	1	16 28 00.00	40 49 00.0	Sbc	16.50	1.0	0.2	9257	
UGC10420	1	16 28 08.67	39 52 27.0	SB(r)b	14.48	1.7	1.2	9605	
UGC10427	2	16 28 39.05	41 12 32.0	SBcd:	14.90	1.3	1.3	8869	
UGC10428	1	16 28 48.37	35 09 47.0	(R')SB(s)b	14.40	1.7	1.2	9304	
UGC10432	2	16 29 00.00	41 19 00.0	Sb	16.00	1.3	0.2	9762	
UGC10450	6	16 32 13.00	36 17 47.0	Scd:	16.50	1.0	0.1	9765	
UGC10468	1	16 34 34.50	44 42 13.6	Scd:	16.00	1.0	0.1	9221	
UGC10469	1	16 34 49.44	39 07 41.0	Sb	13.76	1.5	1.1	9000	
UGC10473	0	16 35 06.60	36 31 24.0	SBa	14.84	1.5	0.5	9366	
UGC10531	1	16 42 54.00	43 50 00.0	SB-C	16.50	1.0	0.7	10133	
UGC10550	1	16 45 24.00	40 13 00.0	Scd:	16.00	1.3	0.2	9032	
UGC10553	1	16 45 34.76	40 19 57.0	SBab:	14.91	1.0	0.5	9047	

Table 8.9. Abell 2634 Spiral Candidate Galaxies selected from Butchins 1983 with APM details added. within 0.7deg of cluster centre. selected on Type, Colour(b-r<1.5) and ellipticity(e>0.28) (and redshift). Bluest objects.

No.	Galaxy	Obs	APM Position		b-mag	a	e	PA	Type	b-r	V _{hel}	Notes
A1	BU97	0	23 33 12.16	26 52 59.8	17.48	73.1	0.42	82		1.17		
A2	BU200	1	23 33 27.37	26 35 39.4	18.50	18.0	0.54	141		1.30		
A3	BU94	6	23 33 49.45	26 43 46.8	17.44	21.7	0.47	8		1.22		
A4	D113	4	23 33 54.23	26 56 47.9	18.32	49.8	0.74	66	S	1.90		
A5	D124	6	23 34 12.06	27 00 50.3	17.99	31.8	0.48	152	S	1.82		
A6	D63	6	23 34 47.08	26 44 33.2	15.90	56.8	0.64	64	S	-9.99		
A7	D85	4	23 35 13.21	26 46 25.9	18.40	18.9	0.28	140	S	1.89		
A8	D12	4	23 35 13.77	26 26 03.5	18.10	23.7	0.60	54	S	-9.99		
A9	D41	4	23 35 26.12	26 37 23.2	18.46	51.4	0.50	41	S	1.71		
A10	D131	2	23 35 28.45	27 06 12.4	16.98	28.6	0.30	106	S	1.40		
A11	BU191	0	23 35 35.32	26 35 42.3	18.47	17.3	0.46	104		1.34		
A12	D109	6	23 35 39.52	26 55 29.6	17.18	31.9	0.45	134	I	1.19		
A13	D39	1	23 35 46.16	26 35 26.4	17.51	27.6	0.53	147	S/I	1.43		
A14	BU145	0	23 35 48.83	26 06 46.5	18.00	20.4	0.44	0		1.21		
A15	BU141	0	23 36 04.00	26 24 19.1	17.98	16.8	0.35	39		1.27		
A16	BU86	6	23 36 05.92	26 15 43.8	17.36	19.8	0.38	128		1.22		
A17	D11	1	23 36 36.30	26 21 26.2	18.50	20.5	0.51	21	S	1.50		
A18	D98	3	23 36 41.34	26 52 57.9	17.10	38.7	0.60	95	S	2.21	7919	
A19	BU116	2	23 36 44.27	27 17 12.5	17.68	30.5	0.55	43		1.93		
A20	BU24	6	23 36 49.95	26 49 09.3	16.19	25.2	0.29	45		1.27		
A21	D8	4	23 37 15.37	26 24 41.2	17.30	32.0	0.47	49	S0	1.48	7945	
A22	BU117	0	23 37 18.99	26 36 45.2	17.69	37.5	0.68	73		1.34		
A23	BU36	0	23 37 44.91	26 46 49.2	16.56	28.2	0.47	45		1.32		
A24	BU56	6	23 37 48.20	26 58 27.4	17.05	19.5	0.35	139		1.49		
A25	BU93	0	23 37 55.99	26 18 04.6	17.40	18.3	0.32	149		1.50		
A26	BU181	0	23 38 01.93	26 23 41.2	18.36	18.1	0.42	135		1.46		
A27	BU71	2	23 38 21.13	27 10 33.3	17.19	27.9	0.45	75		1.26		

Table 8.10. Abell 2634 Spiral Candidate Galaxies selected from Butchins 1983 with APM details added. within 0.7deg of cluster centre. selected on Type, Colour($b-r < 1.5$) and ellipticity($e > 0.28$) (and redshift). Sample 2, relaxed colour selection

No.	Galaxy	Obs	APM Position		b-mag	a	e	PA	Type	b-r	V_{hel}	Notes
D1	BU138	0	23 33 26.47	26 29 47.0	17.94	31.3	0.56	42		1.66		
D2	D123	1	23 34 26.27	27 01 45.3	17.37	32.8	0.47	174	S	2.02	9620	
D3	BU193	0	23 35 26.22	27 15 54.2	18.50	17.7	0.49	115		1.75		
D4	BU161	6	23 35 27.67	26 55 06.1	18.17	17.9	0.36	170		1.42		
D5	D21	1	23 35 34.47	26 29 31.9	17.09	40.7	0.58	71	S	2.04	8812	
D6	D7	0	23 35 40.72	26 20 21.3	17.98	41.0	0.71	165	S	1.61		
D7	D59	4	23 35 46.69	26 39 03.3	17.46	27.3	0.36	166	S	1.98	8888	
D8	BU180	6	23 35 56.79	26 33 45.6	18.32	18.0	0.31	33		1.62		
D9	D129	1	23 36 01.07	27 04 30.8	18.06	34.0	0.64	131	S	1.57		
D10	BU186	0	23 36 01.10	26 49 02.6	18.41	16.5	0.29	74		1.73		
D11	D19	4	23 36 12.61	26 29 42.6	16.25	73.5	0.49	110	S	2.05	10039	
D12	D103	4	23 36 19.66	26 56 19.5	16.23	49.7	0.32	5	S	2.19	9139	
D13	D101	4	23 36 31.16	26 56 40.4	16.88	62.9	0.69	12	S	2.25	10488	
D14	D9	1	23 36 39.16	26 24 57.4	17.80	19.8	0.29	117	S	1.67	8527	
B6	D67	1	23 36 41.27	26 50 16.5	15.32	48.6	0.40	79	S	1.87	7552	
D15	D115	6	23 36 48.49	26 58 06.8	15.99	54.3	0.40	104	S	2.12	9639	
D16	D97	4	23 37 03.09	26 53 18.6	17.52	28.7	0.36	109	S	2.22	9375	
D17	D47	2	23 37 24.05	26 40 55.4	18.28	20.5	0.35	53	S	1.78		
D18	D16	0	23 37 34.25	26 32 22.4	17.9	18.6	0.37	38	S	-9.99		
D19	D30	2	23 37 38.28	26 37 25.0	17.06	47.1	0.65	71	S	1.55		
D20	BU108	2	23 37 42.45	27 01 46.1	17.61	28.3	0.51	109		1.75		
D21	BU120	6	23 37 59.09	26 29 48.4	17.74	33.8	0.60	90		1.64		
D22	BU91	1	23 38 02.44	26 34 42.4	17.39	29.6	0.40	178		1.98	11548	

Table 8.11. Abell 2634 UGC Selected sample. Selection on magnitude, type and redshift. within 3 degrees of cluster centre.

No.	Galaxy	Obs	APM Position		e	PA	Type	b-mag	V_{hel}	Notes
B1	U12626	1	23 26 45.96	26 06 11.7	0.53	3	S	15.7	8021	
B2	U12631	1	23 27 32.04	26 48 37.5	0.62	157	SB	14.8	9182	
B3	U12678	1	23 32 18.59	26 02 03.3	0.73	84	SB	15.4	8961	
B4	U12701	1	23 33 55.67	27 39 30.5	0.75	177	SC	16.5	8856	
B5	U12712	6	23 35 34.47	25 26 32.7	0.24	155	S	15.2	9452	
B6	U12721	1	23 36 41.27	26 50 16.5	0.40	79	SBB	15.0	7604	
B7	U12746	1	23 40 15.73	27 01 12.7	0.78	49	SC	15.0	7436	
B8	U12755	1	23 41 18.45	28 03 43.0	0.47	100	SB/BA	15.0	8784	
B9	U12766	0	23 42 34.99	25 14 26.8	0.68	100	S	16.0	11747	
B10	U12772	0	23 43 00.88	27 04 59.3	0.56	39	SBB	14.5	7766	
B11	U12789	4	23 46 13.88	26 06 35.6	0.72	47	SB-C	16.5	0	
B12	U12792	0	23 46 29.66	26 30 36.7	0.59	55	SBB	14.8	11500	

Table 8.12. Abell 194 Chapman 1988 Selected sample. Selection on magnitude, type and ellipticity. Within 2 degs. (Merged with APM data)

No.	Galaxy	Obs	Chap88 Position		b-mag	V_{hel}	PA	e	Notes
1	0118-0048B	2	01 18 42.0	-1 00 48 00	14.50	5240	54	0.42	
2	0120-0139	1	01 20 14.0	-1 01 39 09	14.60	5741	108	0.71	
3	0120-0214	1	01 20 48.4	-1 02 14 13	14.80	4835	162	0.62	
4	0121-0153	4	01 21 23.6	-1 01 53 42	15.60	5920	14	0.57	
5	0121-0200	4	01 21 46.7	-1 02 00 21	14.90	5317	153	0.58	
6	N530	4	01 22 08.8	-1 01 50 55	14.00	5007	138	0.79	
7	II06	4	01 22 12.3	-1 01 49 35	16.60	5647	164	0.59	
8	0122-0146	4	01 22 45.0	-1 01 46 37	14.80	5854	134	0.60	
9	N538	4	01 22 53.2	-1 01 48 35	14.70	5107	32	0.60	
10	N535	4	01 22 58.3	-1 01 40 10	14.90	4913	57	0.64	
11	0123-0204	0	01 23 00.4	-1 02 04 17	15.70	6508	5	0.45	
12	0123-0134	2	01 23 18.5	-1 01 34 38	15.20	5509	108	0.27	
13	0123-0133	4	01 23 35.6	-1 01 33 03	17.80	5525	127	0.33	
14	0123-0203	1	01 23 44.9	-1 02 03 09	15.60	5500	143	0.64	
15	II703	6	01 23 52.3	-1 01 53 59	14.90	5547	123	0.42	
16	0124-0122	4	01 24 02.1	-1 01 22 20	15.60	5842	59	0.31	
17	0124-0133	1	01 24 10.5	-1 01 33 56	15.20	5021	138	0.53	
18	0214-0146	4	01 24 17.7	-1 01 46 17	16.50	5270	39	0.54	
19	0124-0016	6	01 24 22.3	-1 00 16 22	15.40	5572	176	0.48	
20	0125-0123	4	01 25 09.9	-1 01 23 54	15.10	5179	16	0.40	
21	II19	4	01 25 22.3	-1 02 17 56	15.00	5712	77	0.59	
22	0125-0250	1	01 25 53.2	-1 02 50 47	15.20	5078	64	0.66	
23	0126-0159	4	01 26 04.0	-1 01 59 24	15.10	6233	158	0.64	
24	N570	4	01 26 25.4	-1 01 12 29	14.20	5491	98	0.34	
25	0126-0204	6	01 26 25.6	-1 02 04 13	15.70	5284	177	0.46	
26	0126-0241	1	01 26 26.8	-1 02 41 12	15.50	5284	65	0.74	
27	II26	0	01 27 15.2	-1 02 14 28	15.70	5712	175	0.04	
28	N577	6	01 28 07.7	-1 02 15 06	14.20	5935	141	0.20	
29	N585	4	01 29 08.8	-1 01 11 22	14.20	5389	86	0.76	
30	II38	1	01 30 24.0	-1 00 57 00	14.90	4588	18	0.20	
31	0131-0120	2	01 31 01.6	-1 01 20 49	15.20	4870	115	0.71	
32	0131-0119	1	01 31 29.4	-1 01 19 53	14.90	4617	137	0.72	
33	0131-0117	4	01 31 34.8	-1 01 17 16	14.40	4929	74	0.78	

Table 8.13. Abell 194 UGC Selected sample. NED search for Spiral Cluster members. Within 4 degs. Selection on magnitude, type and redshift.

Galaxy	Obs	NED Position		V_{hel}	b-mag	a	b	Type	Notes
UGC00734	2	01 08 06.0	-1 00 32 00	5491	15.42	1.0	0.3	S?	
UGC00737	0	01 08 17.1	-1 00 04 03	5297	15.70	1.3	1.0	S	
UGC00736	0	01 08 18.0	-1 02 01 00	5100	14.96	1.3	0.9	Scd:	
MCG-01-04-013	3	01 09 58.8	-1 03 03 32	5817	14.00	1.1	0.7	SB(r)c:	
UGC00757	0	01 10 00.0	+1 00 01 00	5746	16.00	1.1	0.9	SB	
UGC00771	2	01 11 06.0	-1 00 21 00	5156	14.75	1.1	0.6	Sab	
UGC00784	1	01 11 36.0	-1 02 00 00	4978	14.63	1.2	0.8	Sb	
UGC00790	0	01 12 06.0	+1 00 55 00	4714	14.71	0.9	0.8	Scd:	
UGC00847	0	01 16 30.5	-1 00 24 04	5237	16.50	1.6	0.1	Sd	
UGC00856	0	01 17 06.0	-1 01 58 00	4787	16.50	1.2	0.9	SB(s)m	
UGC00885	1	01 18 24.0	+1 02 43 00	5343	16.50	1.0	0.4	Scd:	
UGC00890	5	01 18 34.0	+1 01 06 40	4947	14.08	1.9	0.5	SB(s)bc:	
UGC00892	0	01 18 43.3	-1 00 48 24	5240	14.01	1.6	1.4	SB(r)ab	
UM319	0	01 20 48.3	-1 02 14 15	4835	14.88	0.8	0.3	SB?	
ARK040	0	01 21 34.6	-1 02 07 14	5422	14.70	0.5	0.2	Sa?	
CGCG385-102	0	01 21 46.7	-1 02 00 21	5317	15.00	0.7	0.3	S?	
MCG-01-04-037	0	01 21 57.8	-1 04 48 42	5888	15.00	1.2	1.0	SB(s)cd:	
UGC00962	0	01 21 59.7	+1 01 28 17	5040	12.55	3.2	2.9	SB(r)bc	
UGC00981	0	01 22 36.0	+1 02 02 00	6141	15.33	0.7	0.4	S?	
UGC00991	0	01 22 53.0	-1 01 48 39	5364	14.58	1.0	0.5	SB(s)ab:	
UGC01021	0	01 24 07.6	+1 01 45 45	5829	13.59	1.5	0.6	SB(s)a?	
CGCG385-138	0	01 24 10.5	-1 01 33 56	5021	15.33	0.5	0.2	Sb?	
UGC01028	0	01 24 36.0	+1 02 00 00	6237	15.00	1.0	0.5	S	
UGC01052	0	01 25 36.9	-1 01 33 54	4505	14.42	1.3	0.4	Sa:	
MCG-01-04-054	0	01 25 53.2	-1 02 50 47	5071	15.00	1.4	0.2	Scd? sp	
UGC01055	0	01 26 00.0	-1 01 59 00	6233	14.84	1.3	0.5	SBa	
UGC01061	0	01 26 25.6	-1 01 12 27	5491	13.70	1.5	1.3	(R')SB(rs)	
UGC01060	0	01 26 25.6	-1 02 04 13	5284	15.70	1.0	0.2	S	
MCG-01-04-055	0	01 26 26.8	-1 02 41 12	5284	15.50	1.2	0.3	S?	
UGC01071	0	01 27 15.0	-1 02 14 30	5712	15.00	1.4	1.2	S?	
UGC01092	0	01 29 09.2	-1 01 11 20	5389	13.99	2.1	0.5	Sa: sp	
UGC01123	0	01 31 34.6	-1 01 17 17	4929	14.38	1.3	0.4	Sab: sp	
UGC01143	3	01 33 26.1	+1 00 24 30	5161	13.71	1.8	1.3	SB(rs)b	
UGC01159	1	01 35 03.5	-1 00 12 48	4898	15.50	1.1	0.4	S	
UGC01225	0	01 42 29.8	-1 00 33 06	5407	16.50	0.4	0.3	SB?	

Appendix B

Galaxy Photometry

9.1 Surface Photometry

The following 99 figures display the results of the surface photometry reduction process for each galaxy in the final Tully-Fisher sample. On each figure the four left-hand panels show from top to bottom; the galaxy's isophotal magnitude at each fitted isophote, the ellipticity, position angle and centre of the fitted ellipses, all versus radius (in pixels on upper scale and arcsec on lower scale). For the outer isophotes where the S/N is too low to accurately fit ellipses the ellipse parameters are fixed to the mean of their "disk" region values, while the radius is increased in order to measure the isophotal magnitudes. These ellipses are marked with a crosses on each plot.

The top right-hand panel shows the surface brightness of each ellipse against radius along with a straight line fit to what is considered the "disk" region of the galaxy (marked with vertical parallel dashed lines). The lower panel shows the residuals from the linear fit. Note the length of the errors bars indicate the random error at each point and the tick marks on each error bar indicate the systematic errors. The fitted disk parameters are used to calculate the total magnitude by extrapolation from the outer isophotal magnitude (marked on the upper left panel with a dashed lines and dotted lines respectively).

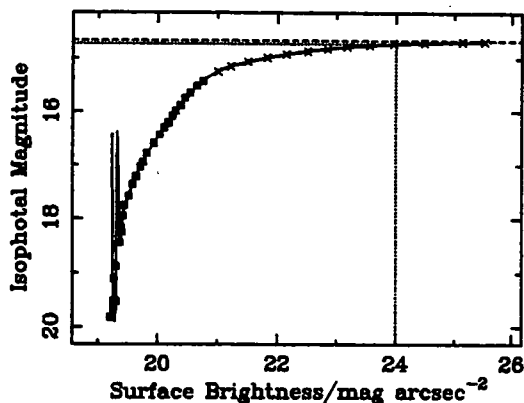
The lower right panel displays a grey scale of the galaxy superimposed with contours representing the I-band isophotes between 19 and 21.5 in steps of 0.5. The three solid ellipses marked on the image represent the inner and outer disk limits and the radius at which the sky level is reached. Nearby stars etc. have been masked out and replaced with intensity values from the fit plus noise, and are marked with dashed ellipses on the image.

9.2 Table of Photometric Measurements

Following the graphical representation of the surface photometry are four tables; 9.1, 9.2, 9.3, 9.4 that summarise all the measured photometric parameters for the sample galaxies.

Values in each column are; galaxy name, assigned photometric quality (see §3.1.3), position in the sky and exposure time of image. Isophotal quantities at 22.5 and 23.5 I-mags per square arcsecond are; isophotal magnitude, radius along major-axis, ellipticity and position angle. Total magnitudes; extrapolated from either 23.5 or 24.0 isophote, extrapolated from last fitted isophote, magnitude within optical radius. Details of isophote at one optical radii; radius, ellipticity and position angle. Mean disk parameters of selected disk region; ellipticity and standard deviation, position angle and standard deviation, disk scale length in arcseconds, disk central surface brightness in magnitudes per square arcsecond.

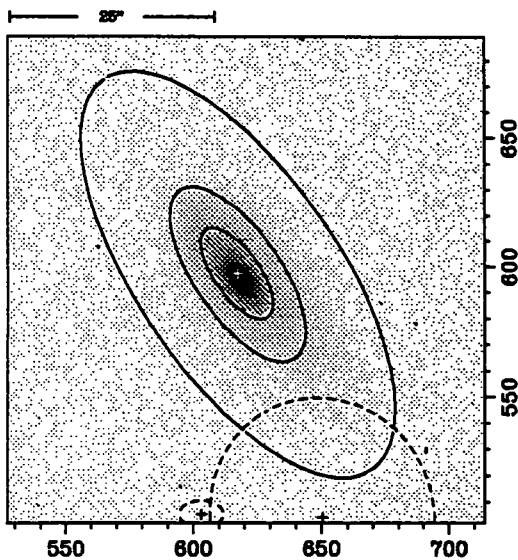
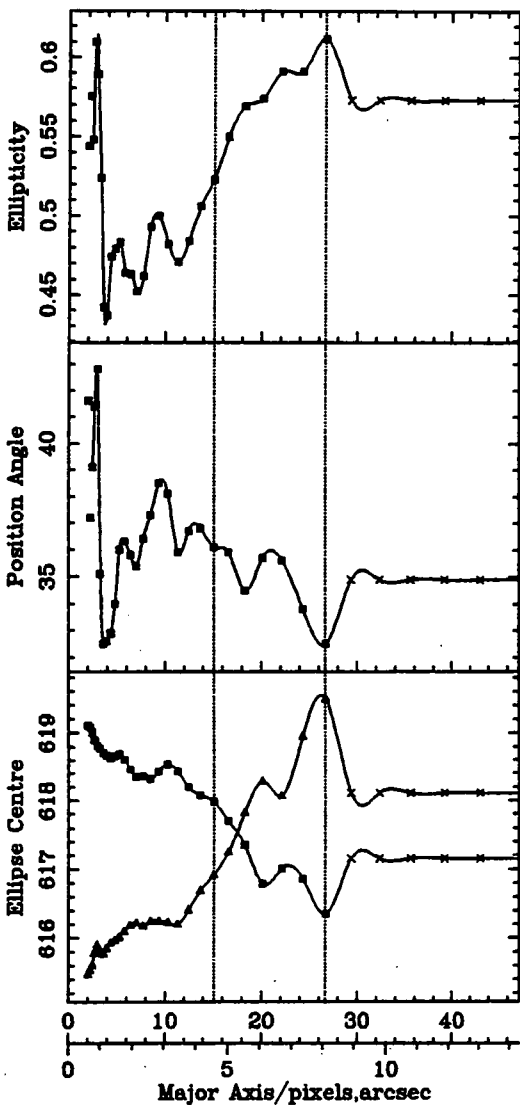
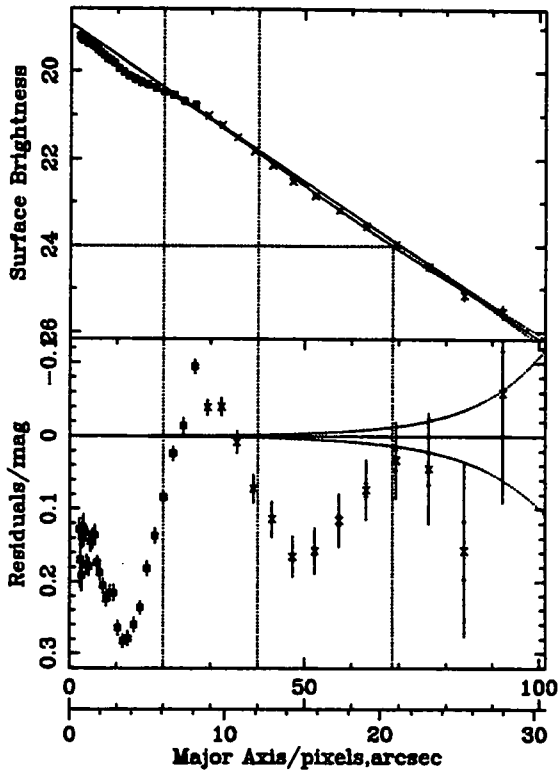
Ellipse Fitting Results For: 1251+2827



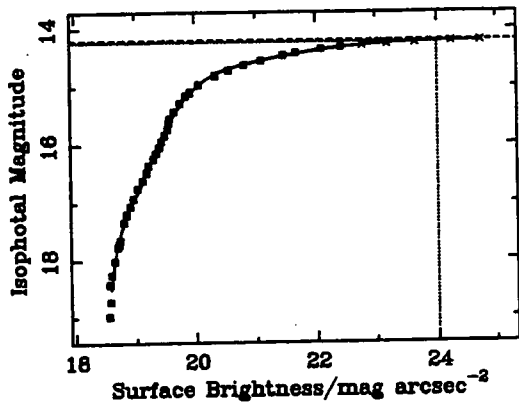
File: 1251_2827_r1317_clean.efot

$I_{22.5}=14.87$ $I_{23.5}=14.75$ $I_{24.0}=14.72$ $I_7=14.66$

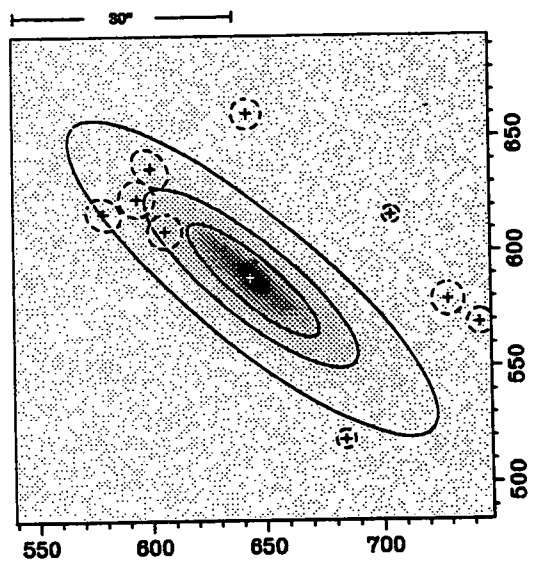
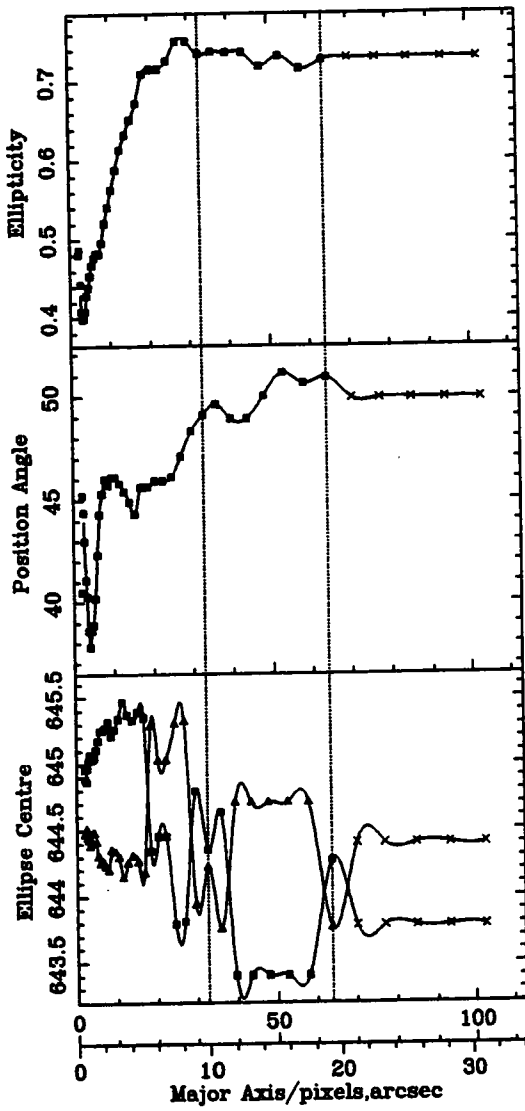
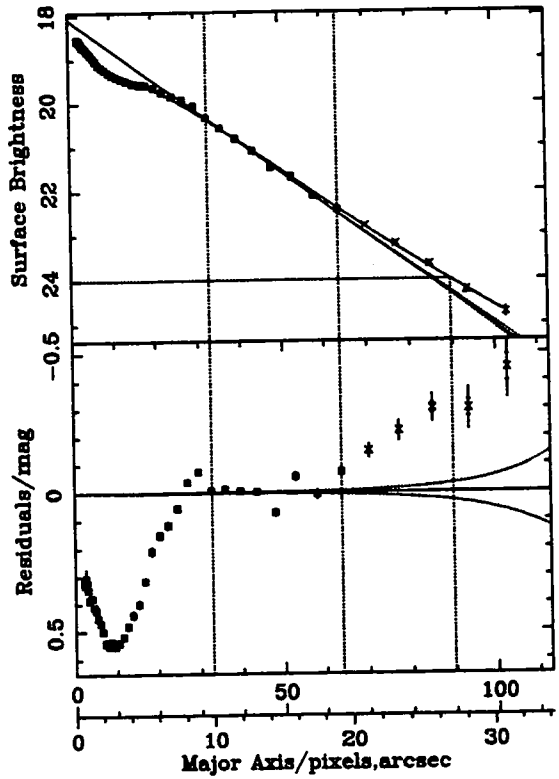
$R_{22.5}=14.7''$ $\mu_0=18.93$ $R_{Scale}=4.6''$



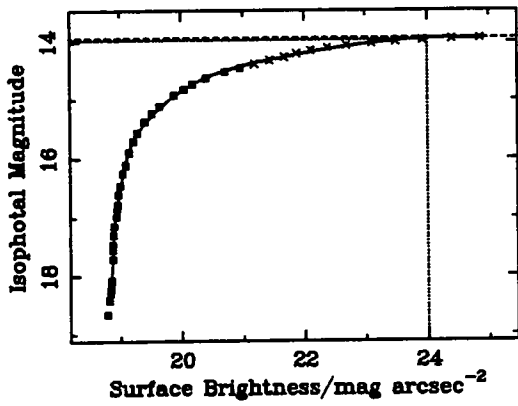
Ellipse Fitting Results For: D38



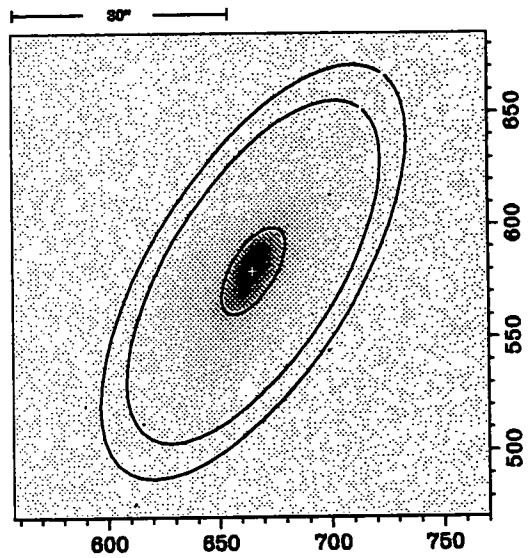
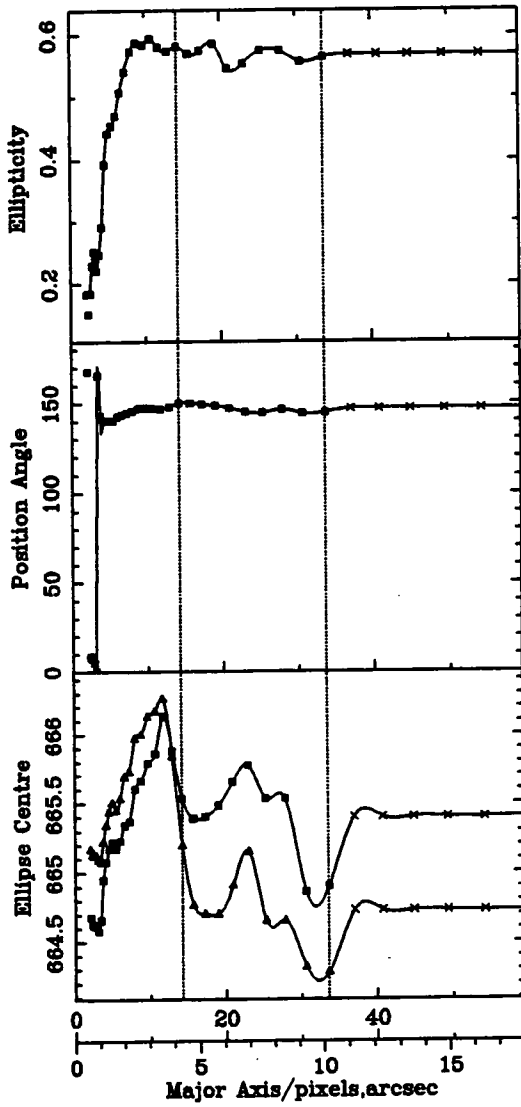
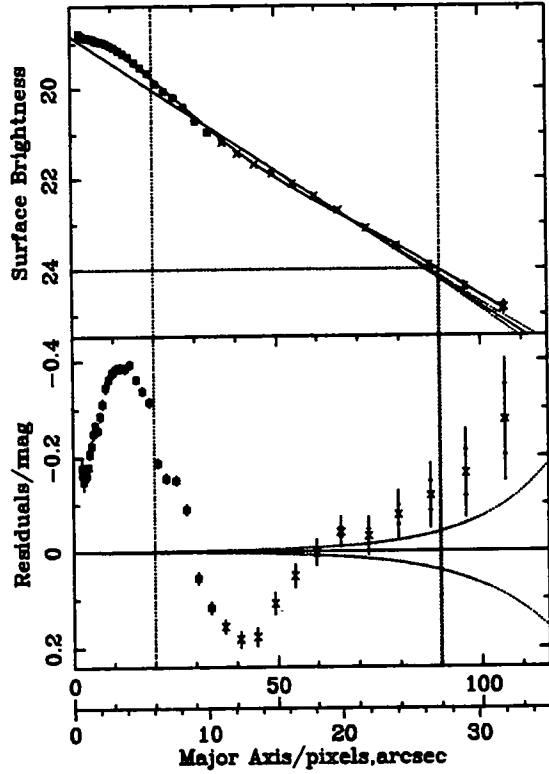
File: d38_r1319_clean.efot
 $I_{22.5}=14.31$ $I_{23.5}=14.25$ $I_{24.0}=14.23$ $I_T=14.19$
 $R_{22.5}=19.9''$ $\mu_0=18.08$ $R_{Scale}=4.8''$



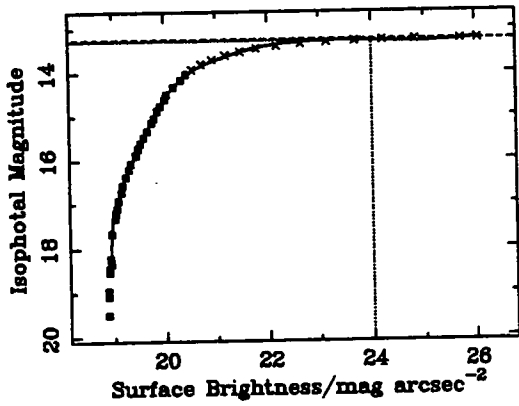
Ellipse Fitting Results For: I4040



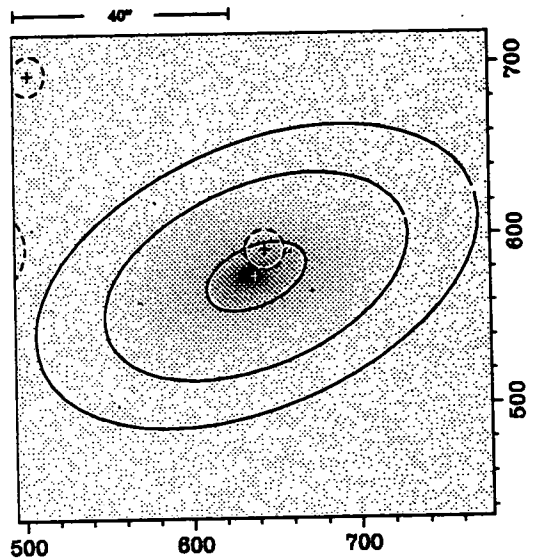
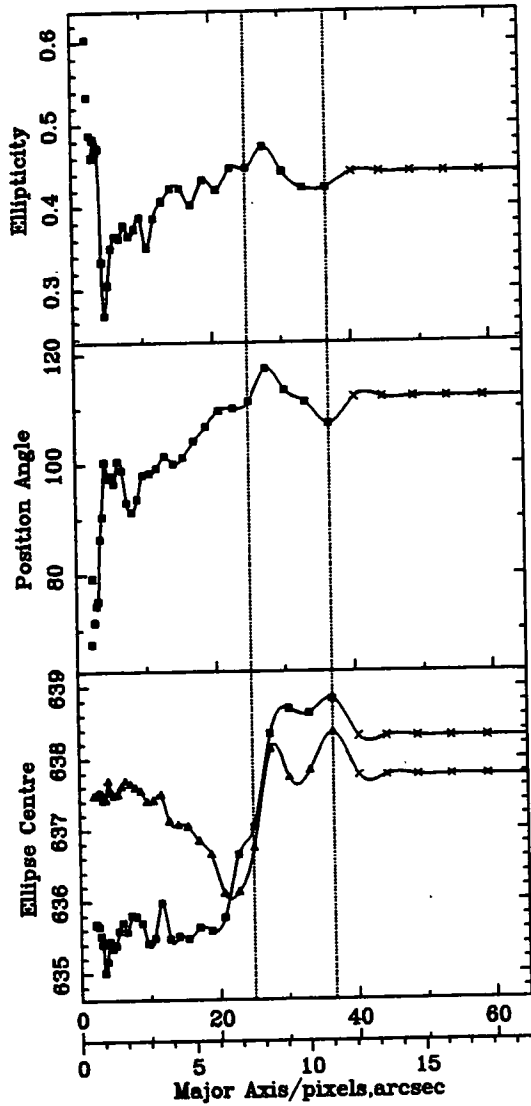
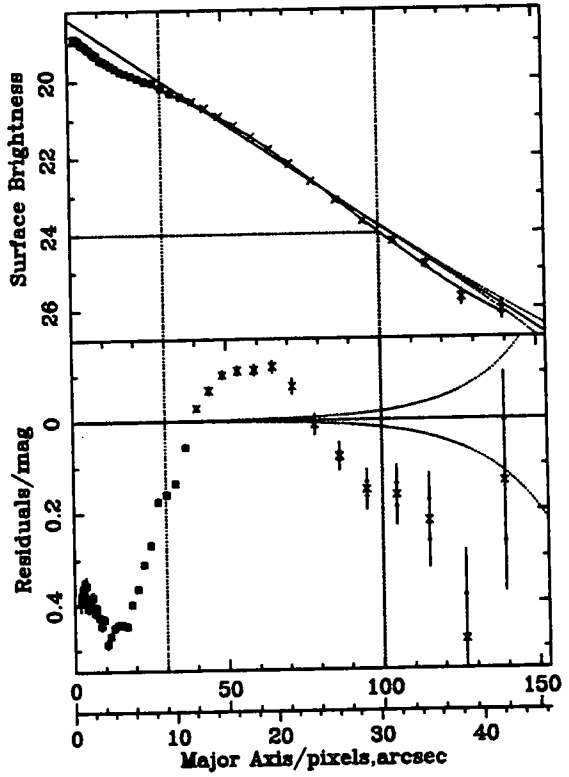
File: i4040_r1925_clean.efot
 $I_{22.5}=14.09$ $I_{23.5}=14$ $I_{24.0}=13.97$ $I_T=13.93$
 $R_{22.5}=18.3''$ $\mu_0=18.83$ $R_{3\sigma}=5.5''$



Ellipse Fitting Results For: N4585



File: n4585_r1514_clean.efot
 $I_{22.5}=13.36$ $I_{23.5}=13.3$ $I_{24.0}=13.28$ $I_T=13.24$
 $R_{22.5}=23.3''$ $\mu_0=18.38$ $R_{Scale}=6.1''$

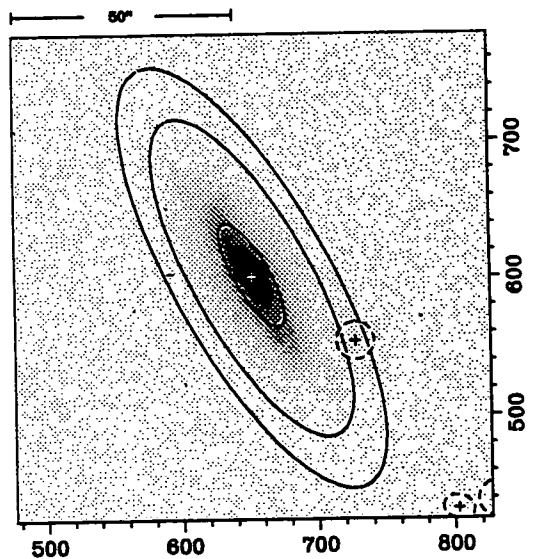
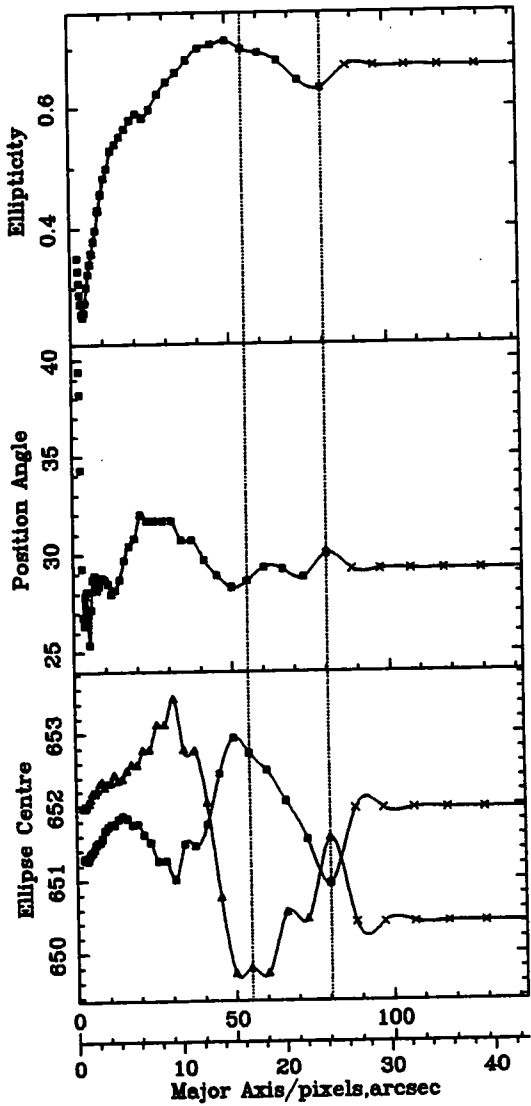
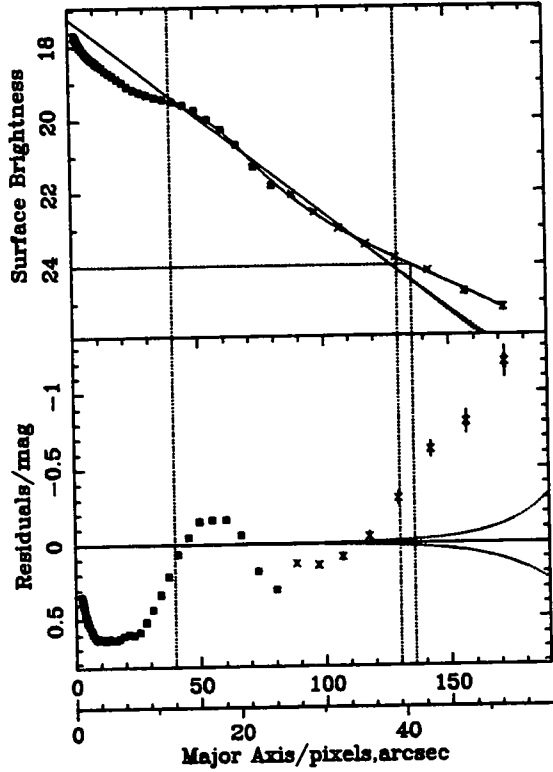
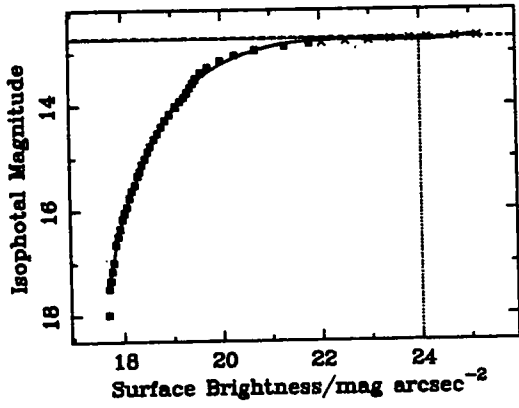


Ellipse Fitting Results For: U8017

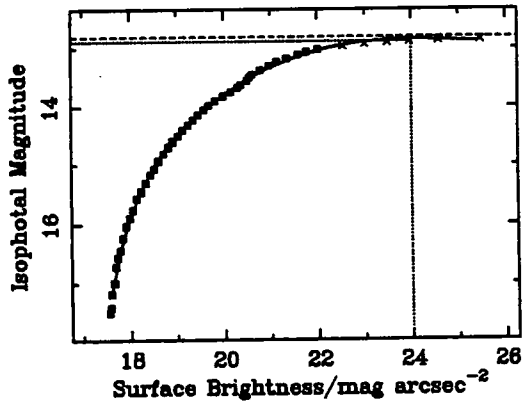
File: u8017_r1223_clean.efot

$I_{22.5}=12.78$ $I_{23.5}=12.74$ $I_{24.0}=12.72$ $I_T=12.71$

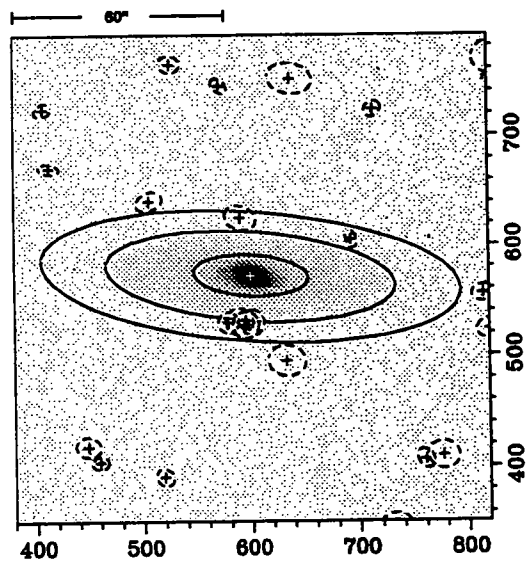
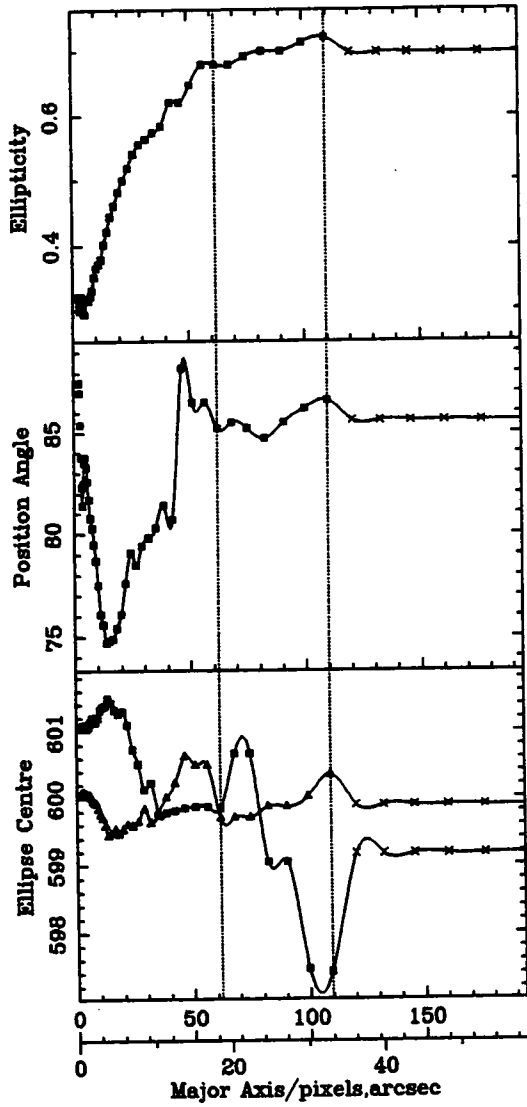
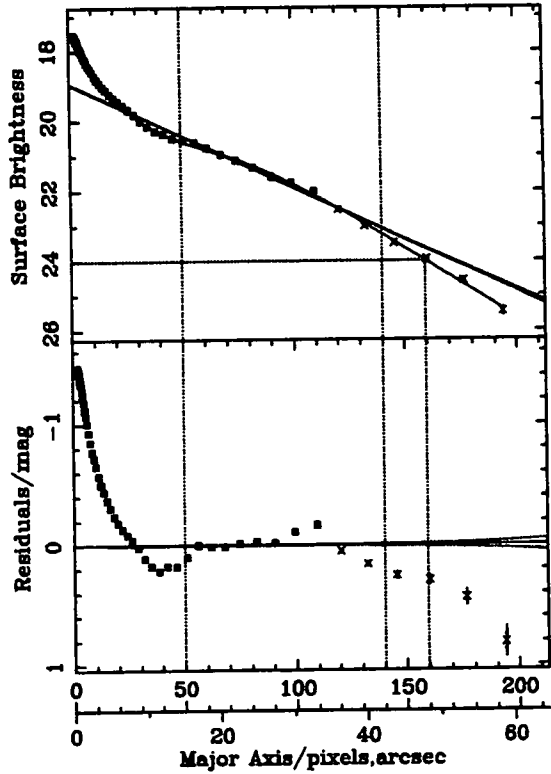
$R_{22.5}=29''$ $\mu_0=17.23$ $R_{Scale}=6.2''$



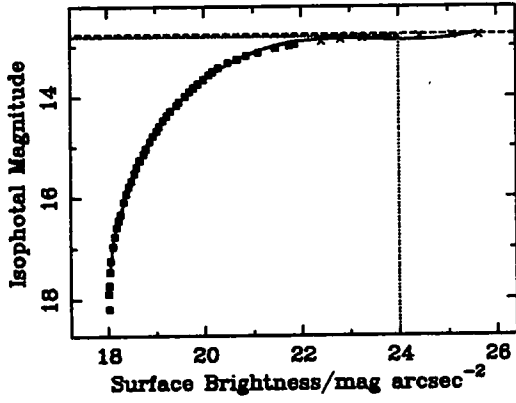
Ellipse Fitting Results For: U8140



File: u8140_r1205_clean.efot
 $L_{22.5}=12.97$ $L_{23.5}=12.9$ $L_{24.0}=12.88$ $L_T=12.81$
 $R_{22.5}=36.6''$ $\mu_0=18.96$ $R_{scale}=11.2''$



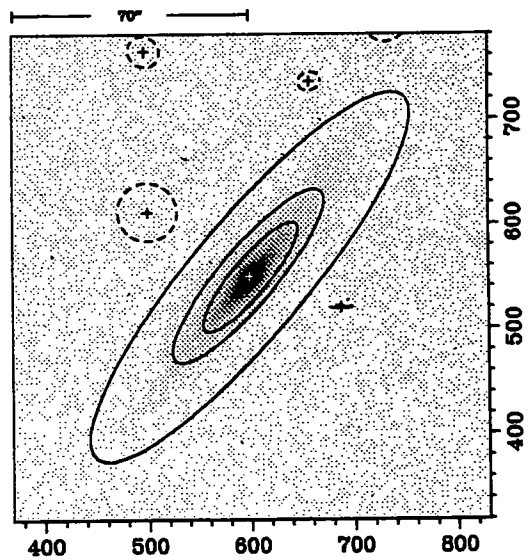
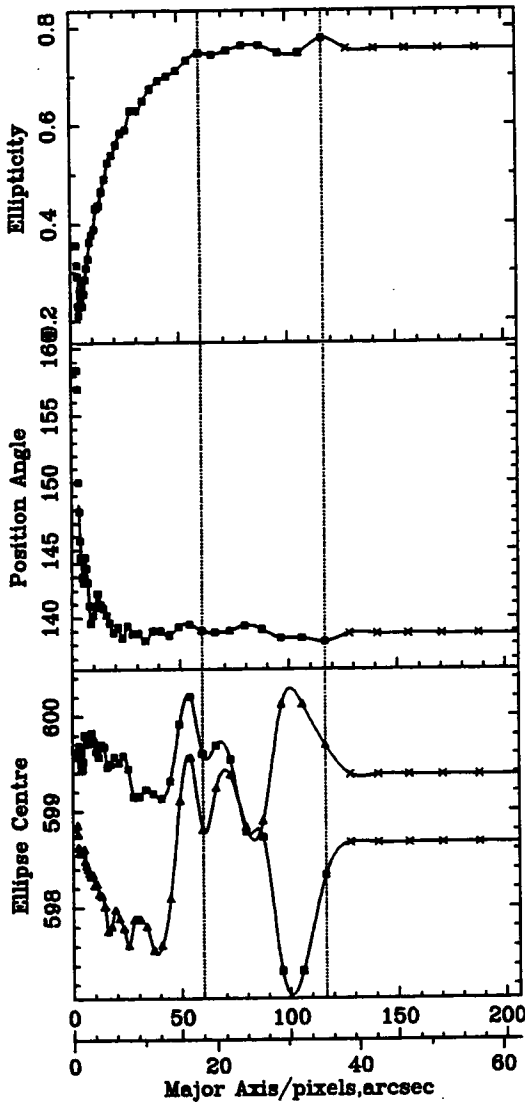
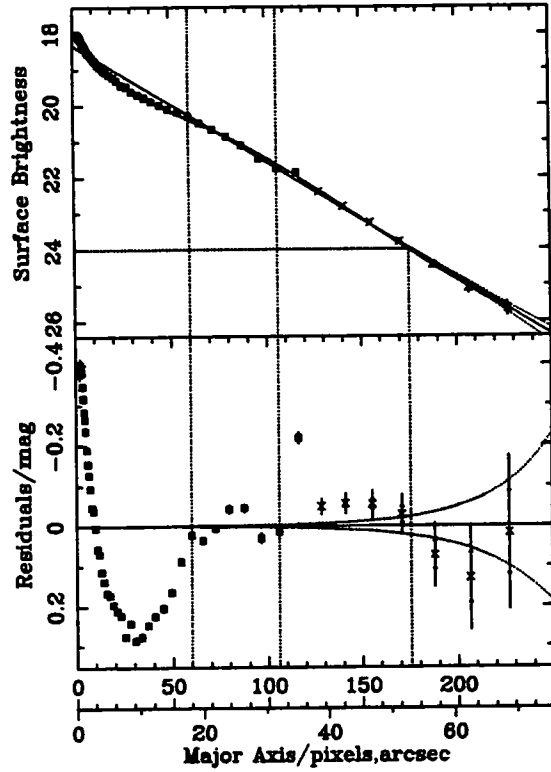
Ellipse Fitting Results For: U8220



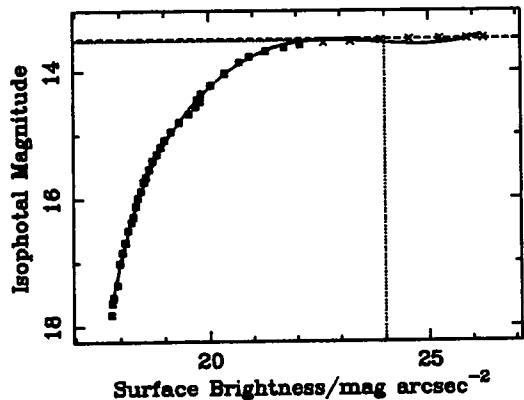
File: u8220_r1520_clean.efot

$I_{22.5}=12.89$ $I_{23.5}=12.83$ $I_{24.0}=12.81$ $I_T=12.76$

$R_{22.5}=40.1''$ $\mu_0=18.34$ $R_{Scale}=10.3''$



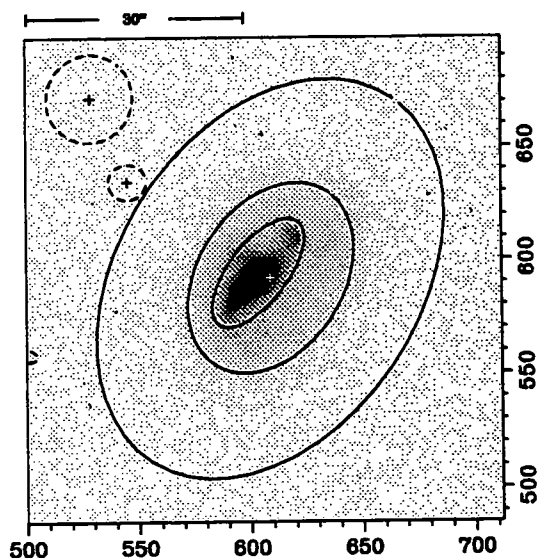
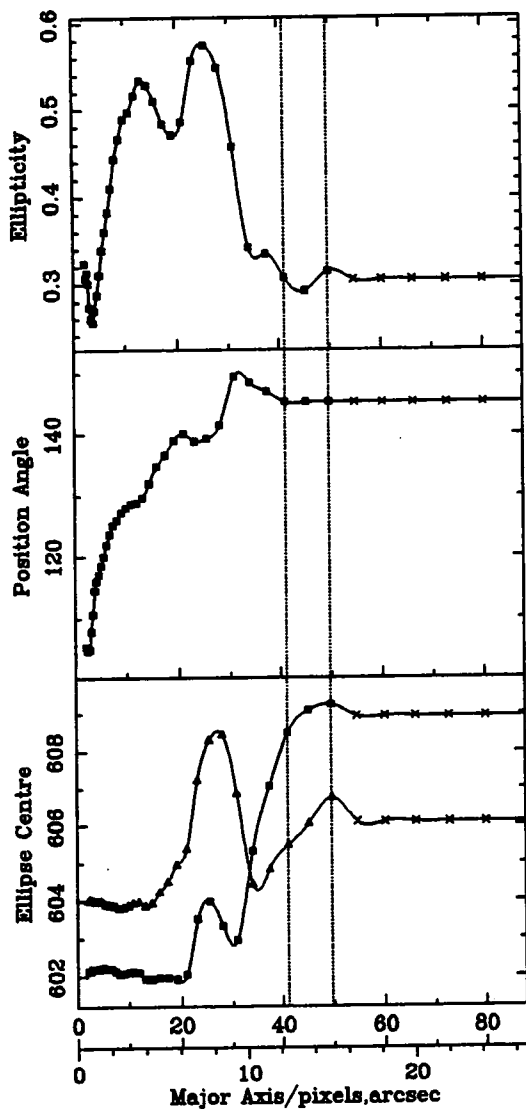
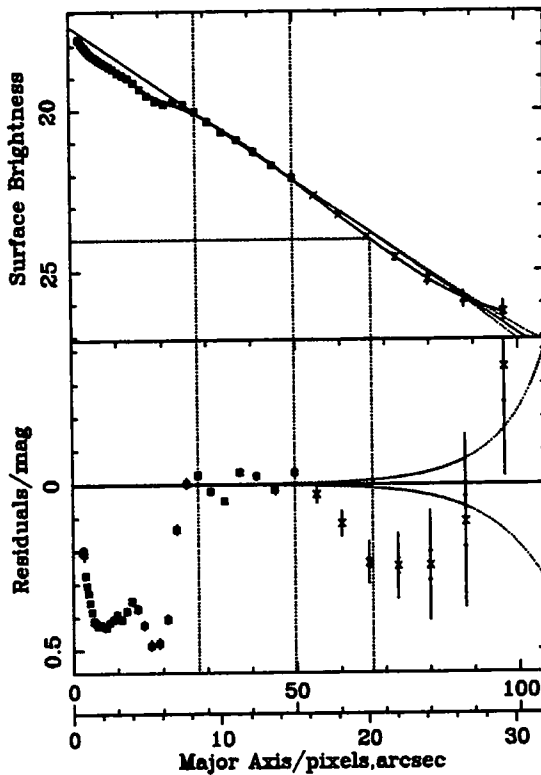
Ellipse Fitting Results For: Z130-8



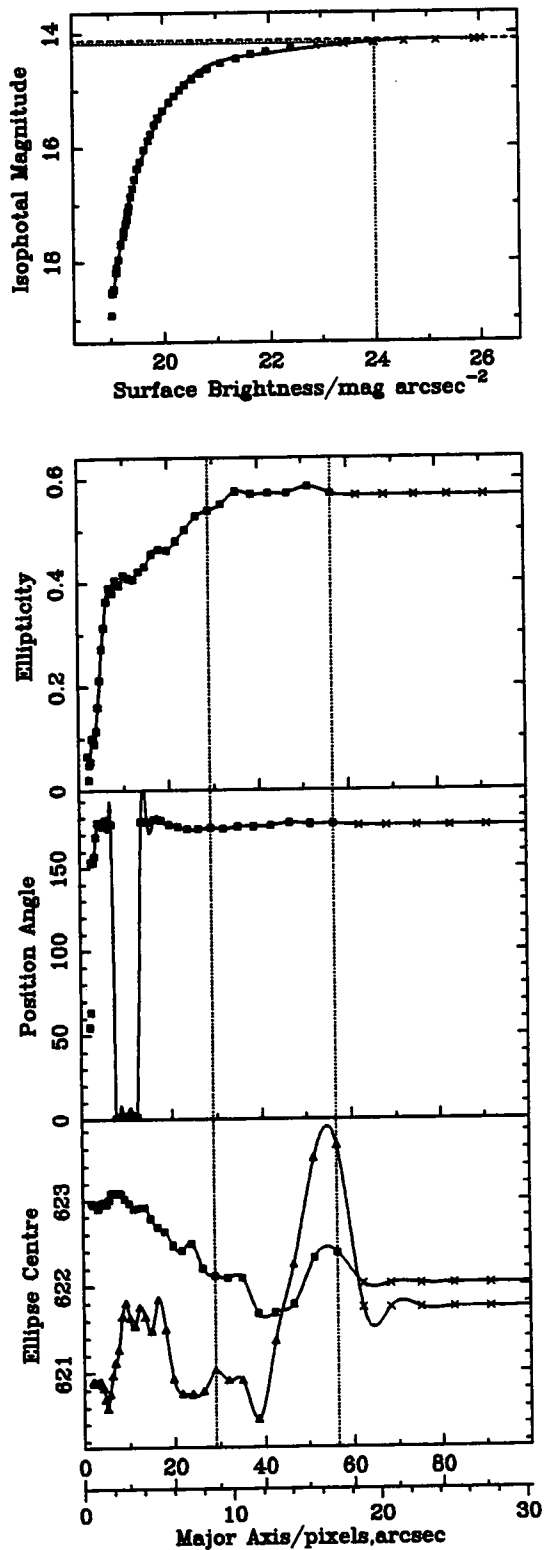
File: z130_6_r1211_clean.efot

$I_{22.5}=13.56$ $I_{23.5}=13.52$ $I_{24.0}=13.51$ $I_T=13.49$

$R_{22.5}=16.1''$ $\mu_0=17.4$ $R_{Scale}=3.5''$



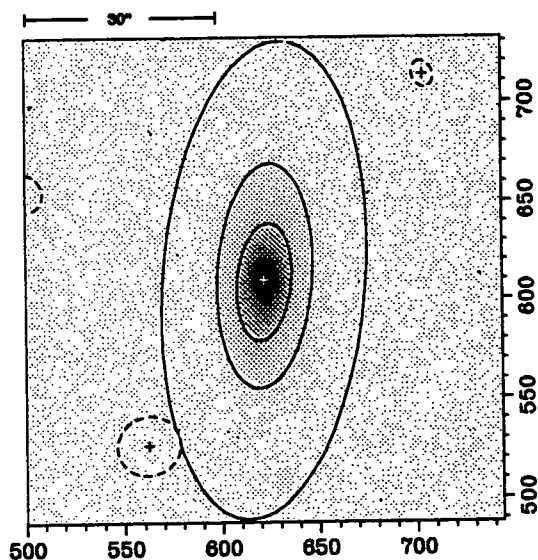
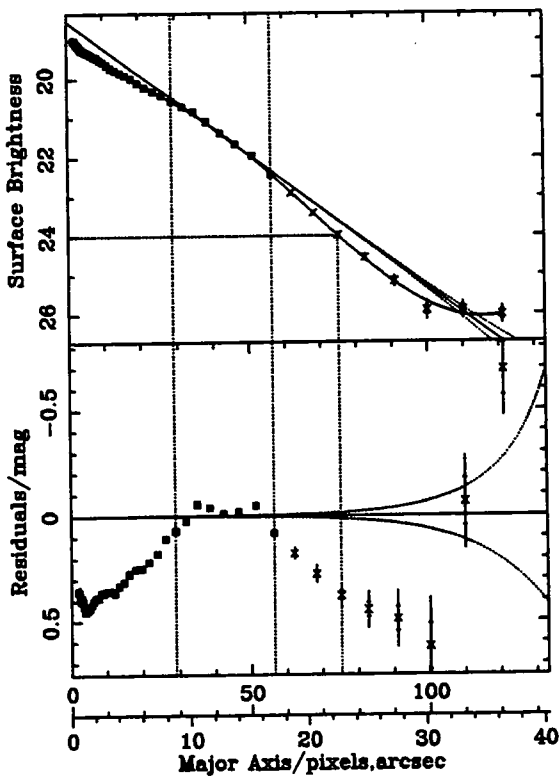
Ellipse Fitting Results For: Z159-106



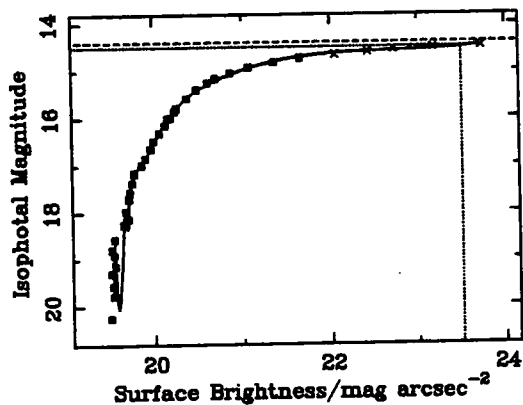
File: z159_106_r1221_clean.efot

$I_{22.5}=14.26$ $I_{23.5}=14.2$ $I_{24.0}=14.18$ $I_T=14.12$

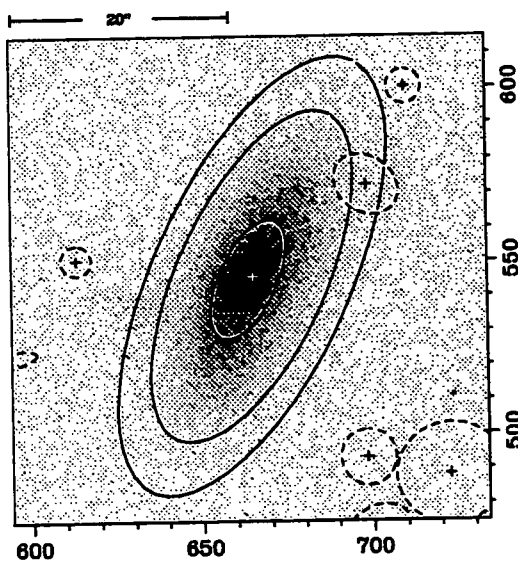
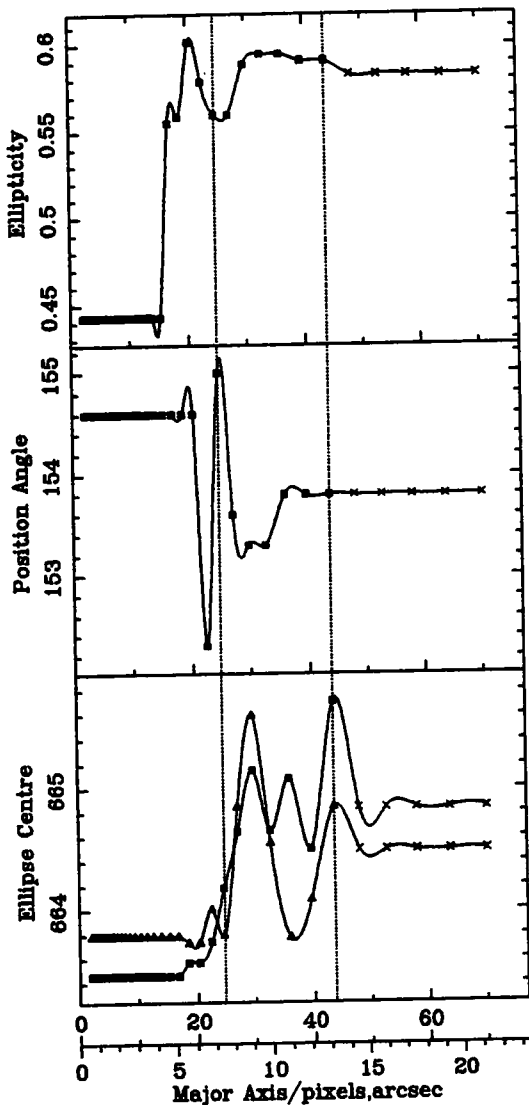
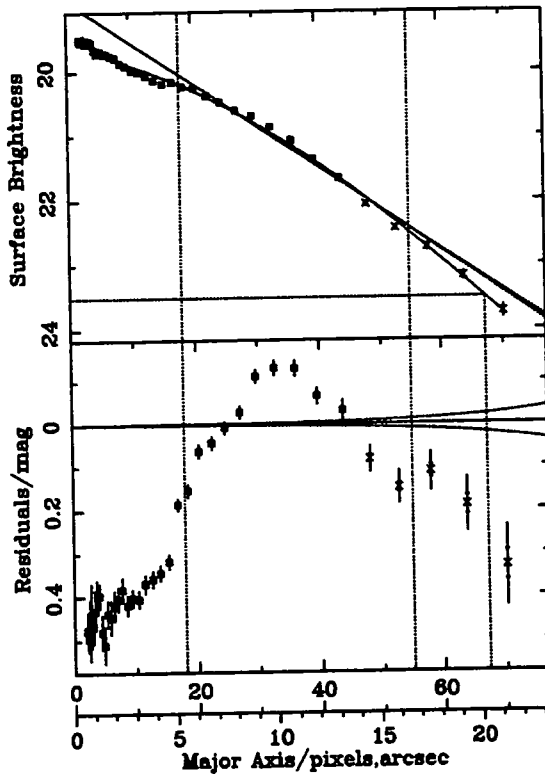
$R_{22.5}=17.4''$ $\mu_0=18.52$ $R_{Scale}=4.9''$



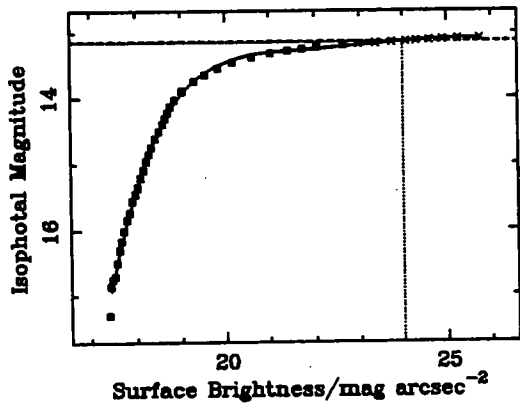
Ellipse Fitting Results For: Z159-117



File: z159_117_r1127_clean.efot
 $I_{22.5}=14.59$ $I_{23.5}=14.5$ $I_{24.0}=99.99$ $I_T=14.39$
 $R_{22.5}=18.7''$ $\mu_0=18.89$ $R_{Scale}=5.1''$



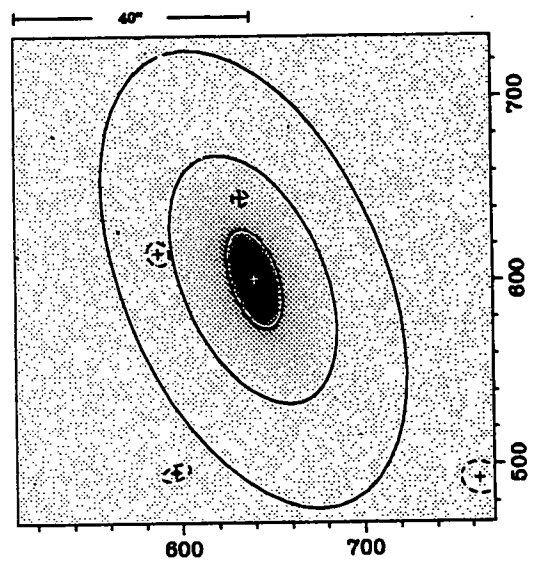
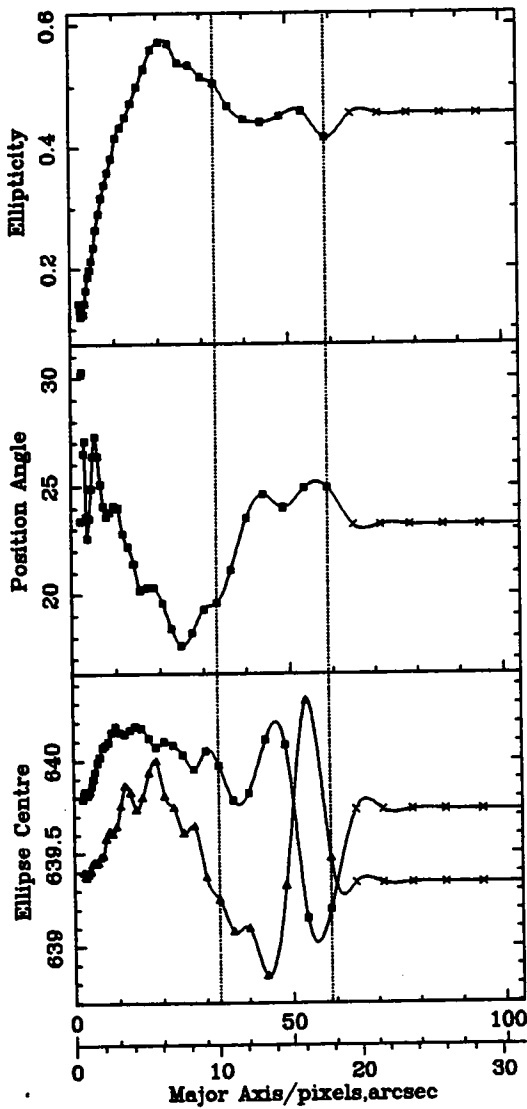
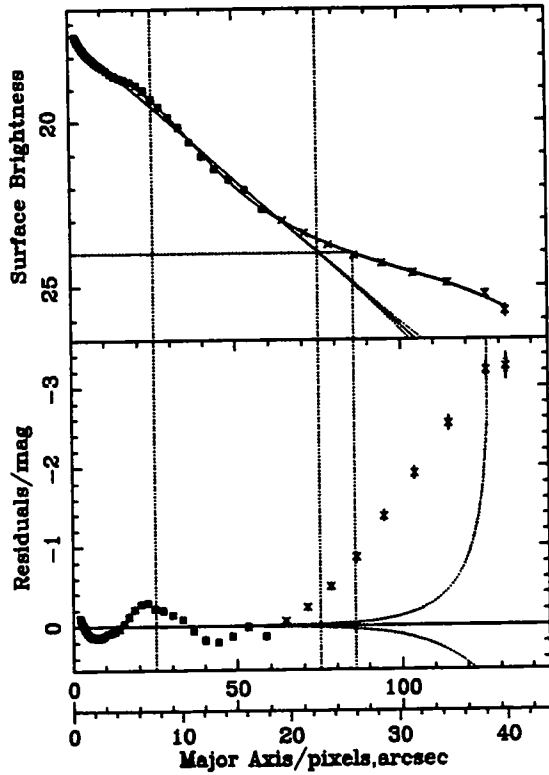
Ellipse Fitting Results For: Z159-75



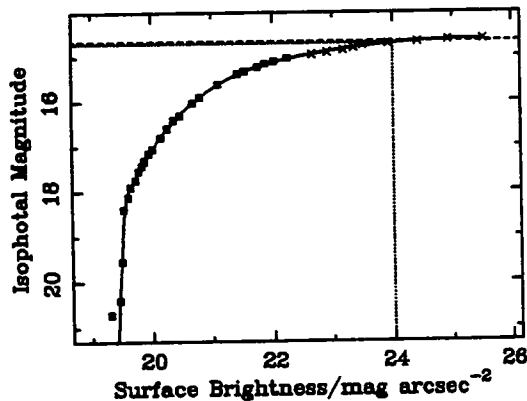
File: z159_75_r1219_clean.efot

$L_{22.5}=13.2$ $L_{23.5}=13.16$ $L_{24.0}=13.15$ $L_T=13.14$

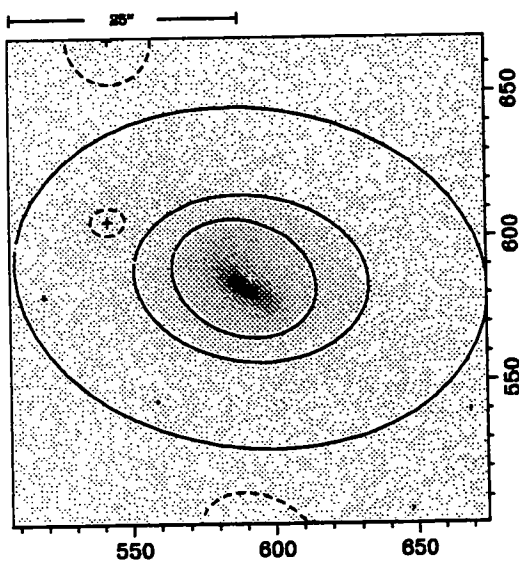
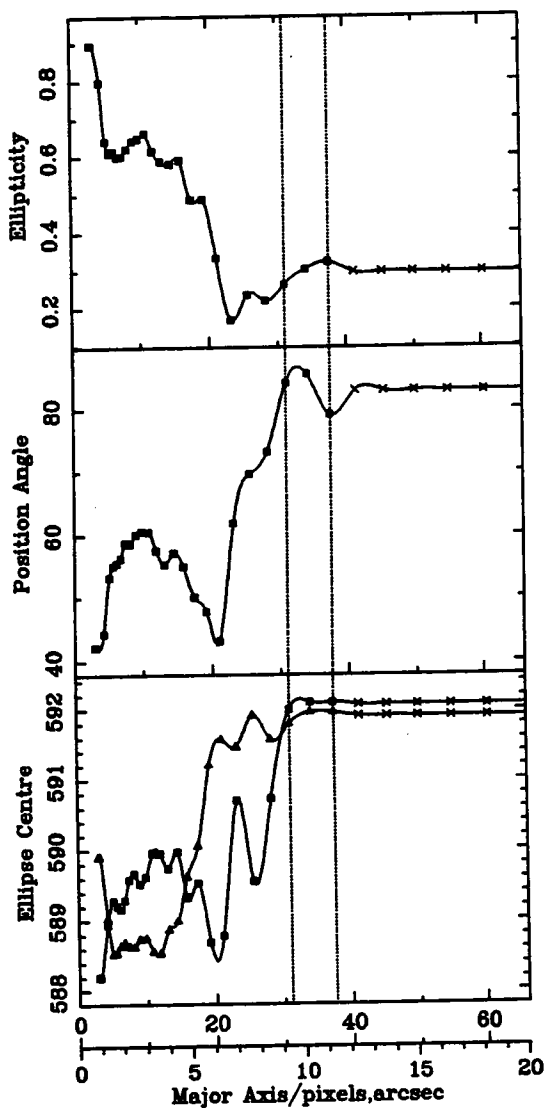
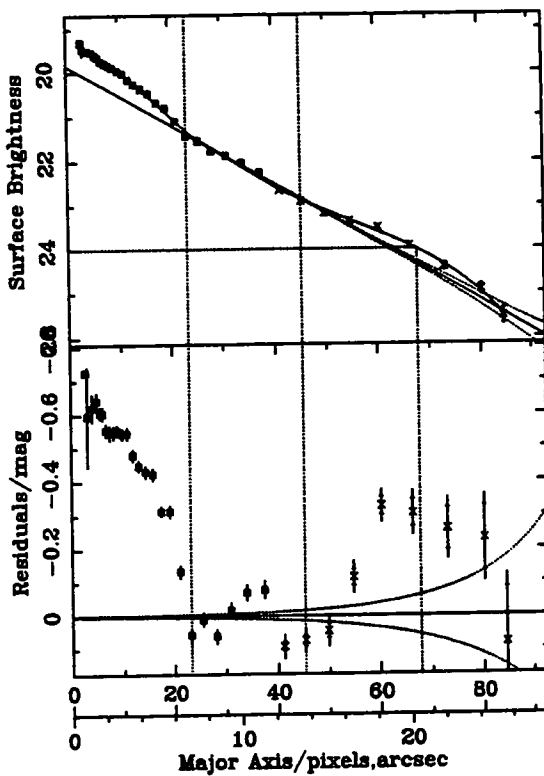
$R_{22.5}=17.3''$ $\mu_0=17.31$ $R_{scale}=3.7''$



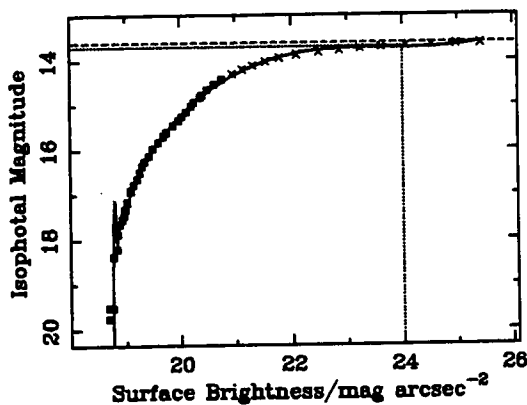
Ellipse Fitting Results For: Z160-127



File: z160_127_r1209_clean.efot
 $I_{22.5}=14.99$ $I_{23.5}=14.78$ $I_{24.0}=14.7$ $I_1=14.68$
 $R_{22.5}=11.9''$ $\mu_0=19.84$ $R_{scale}=5''$



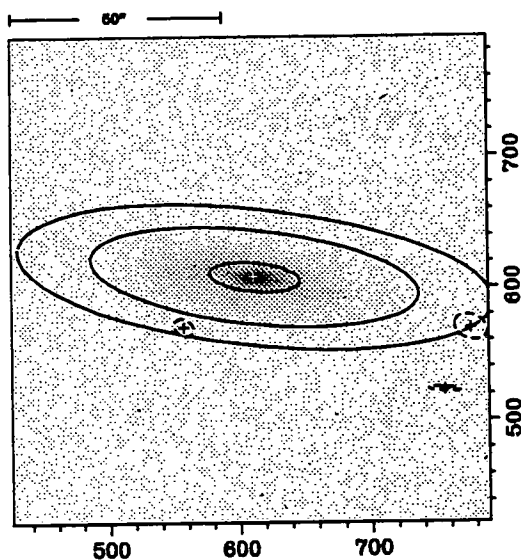
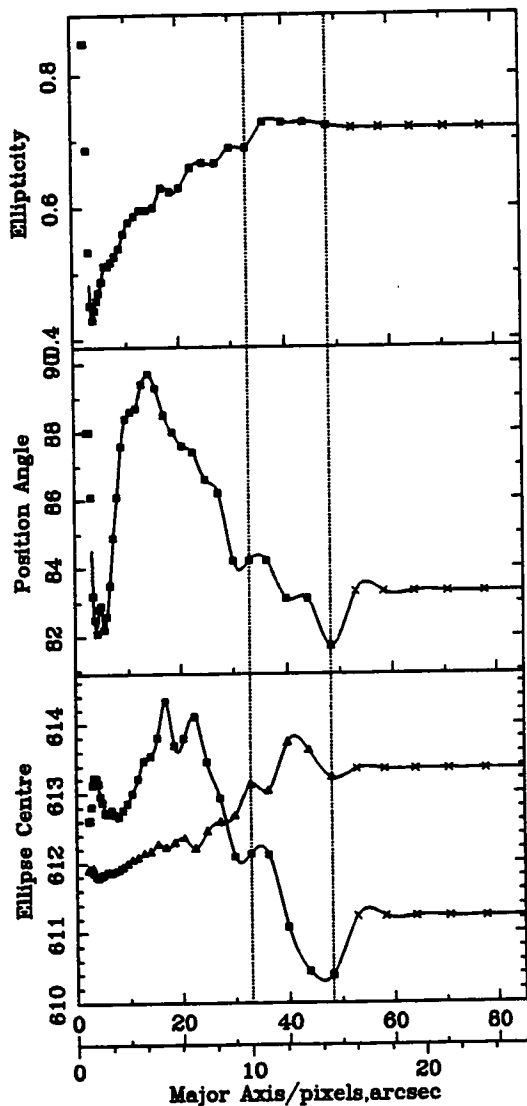
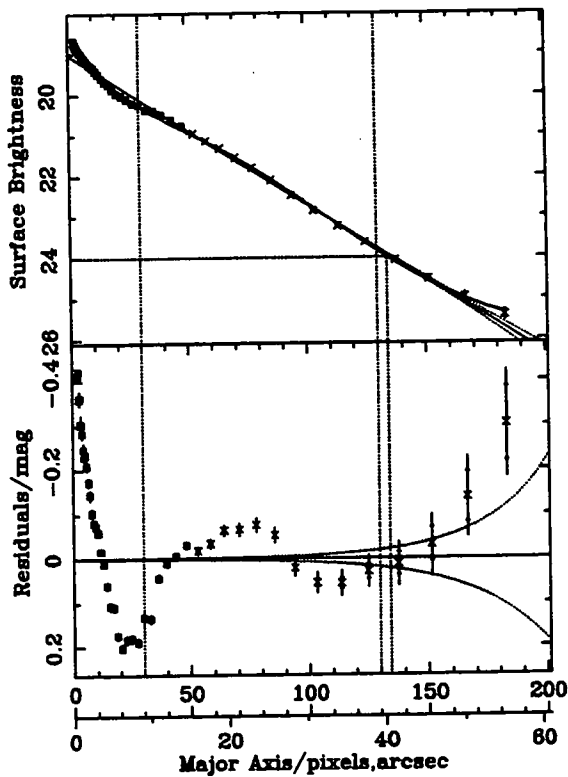
Ellipse Fitting Results For: Z160-58



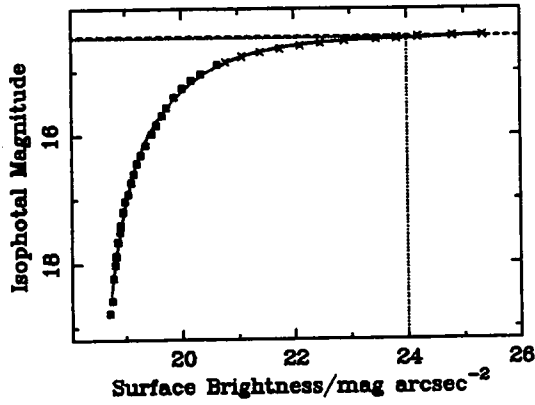
File: z160_58_r1215_clean.efot

$I_{22.5}=13.81$ $I_{23.5}=13.71$ $I_{24.0}=13.88$ $I_T=13.59$

$R_{22.5}=29.3''$ $\mu_0=19.02$ $R_{Scale}=9''$



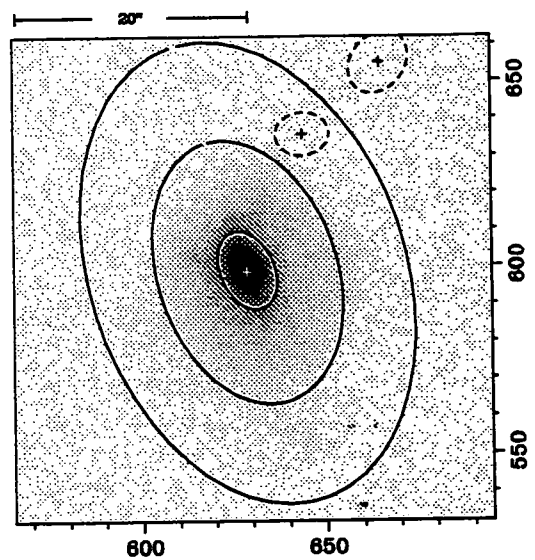
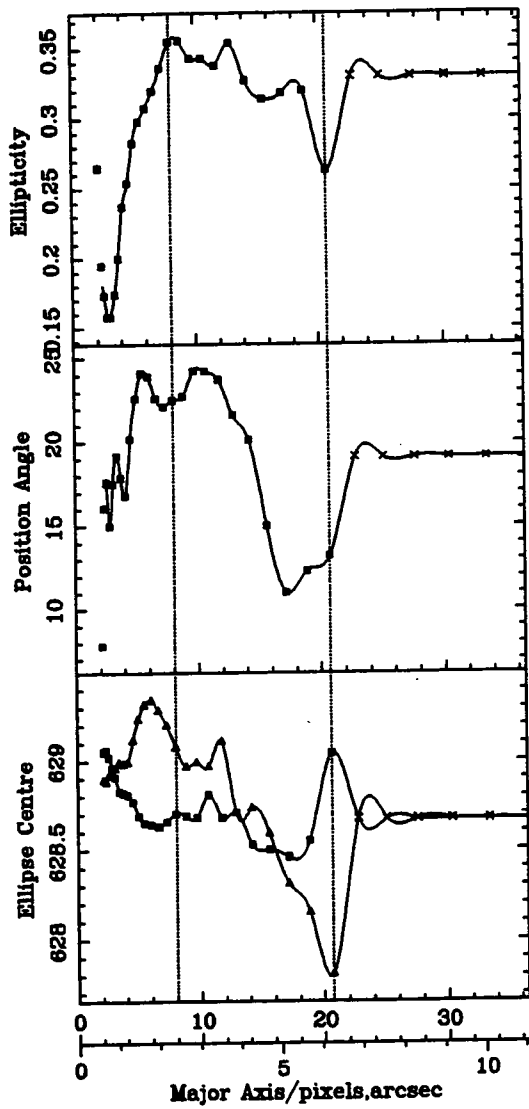
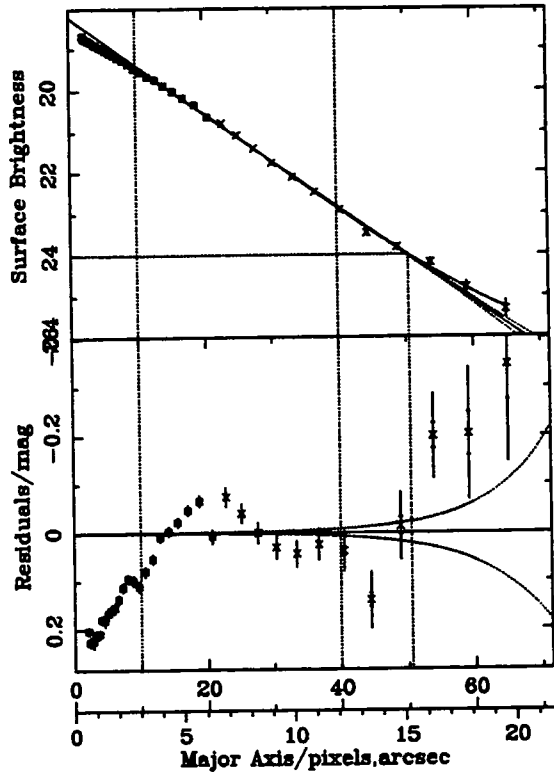
Ellipse Fitting Results For: Z160-67



File: z160_67_r1217_clean.efot

$I_{22.5}=14.55$ $I_{23.5}=14.49$ $I_{24.0}=14.47$ $I_T=14.45$

$R_{22.5}=11.2''$ $\mu_0=18.25$ $R_{scale}=2.9''$

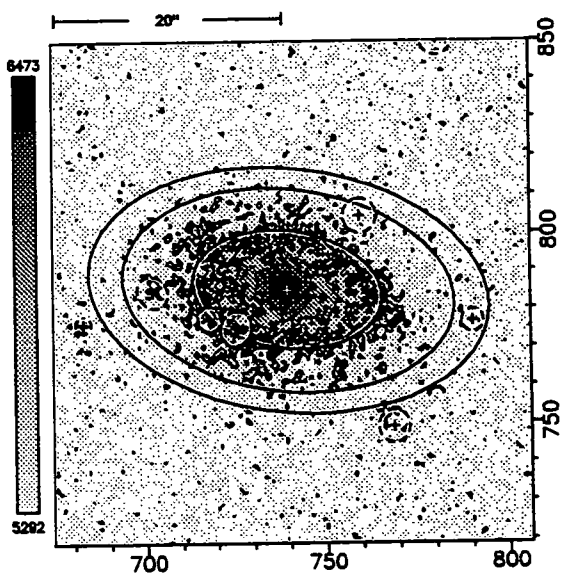
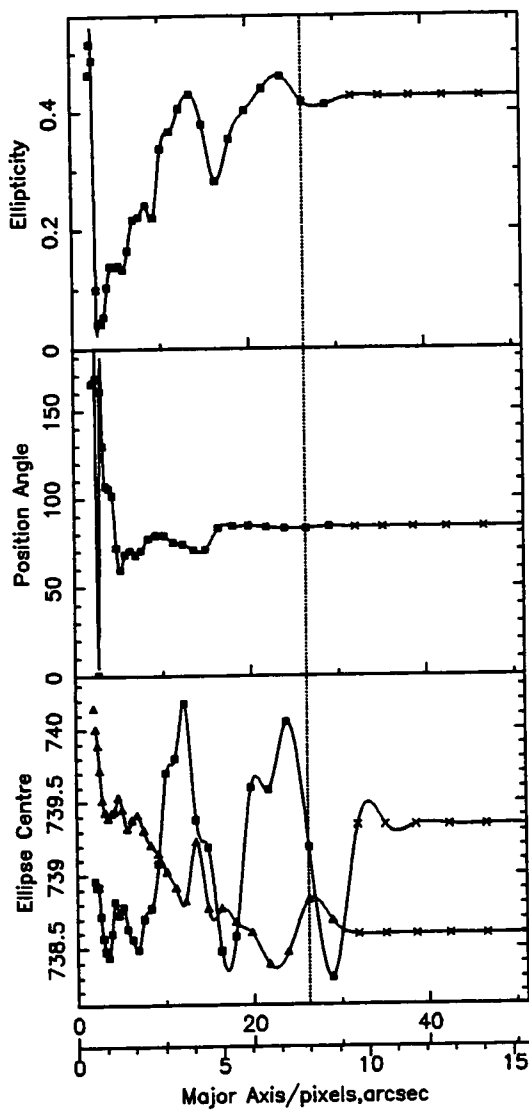
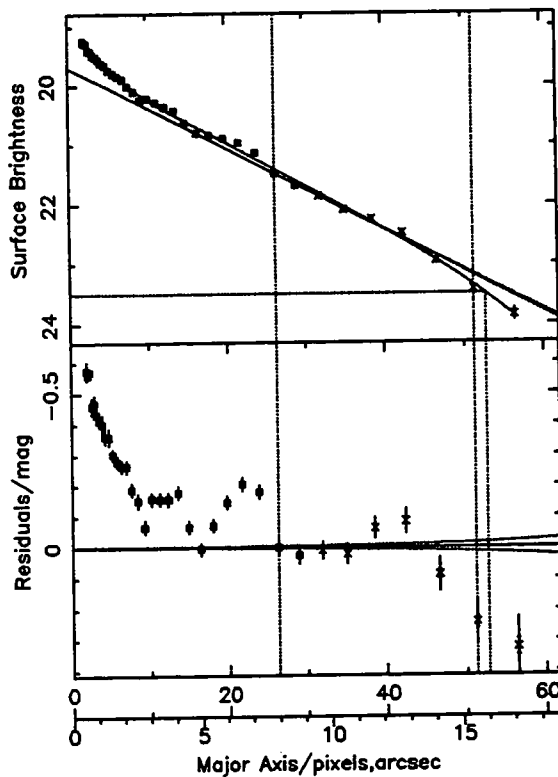
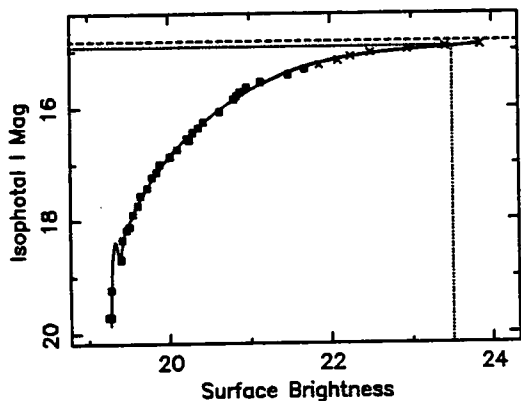


Ellipse Fitting Results For: 1622+4014

File: 1622_4014_j2513_clean.efot

$R_{22.5} = 12.5''$ $\mu_0 = 19.68$ $R_{Scale} = 4.8''$

$I_{22.5} = 15.04$ $I_{23.5} = 14.94$ $I_{Total} = 14.83$



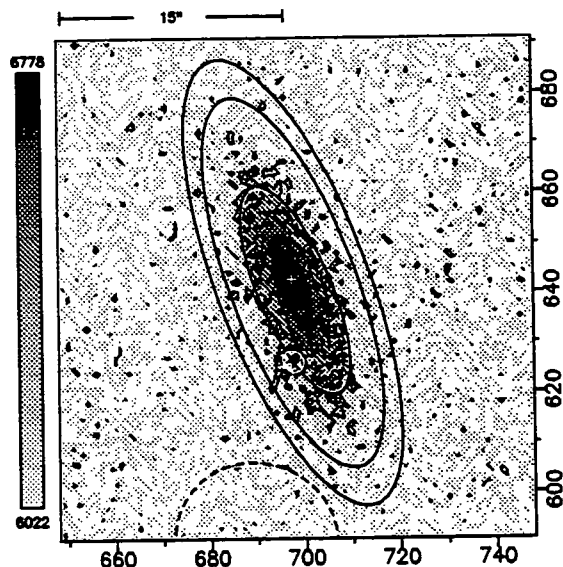
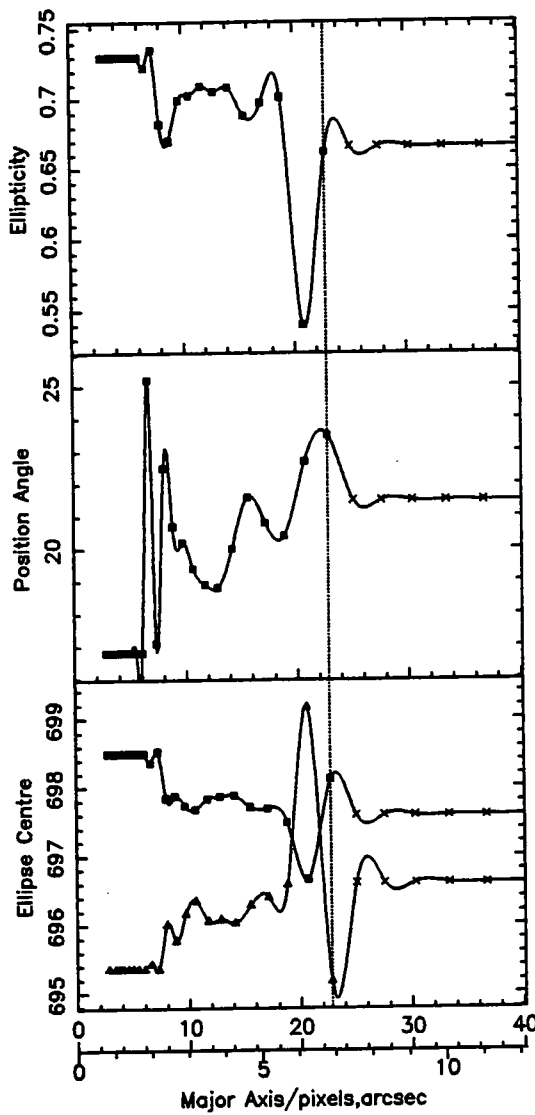
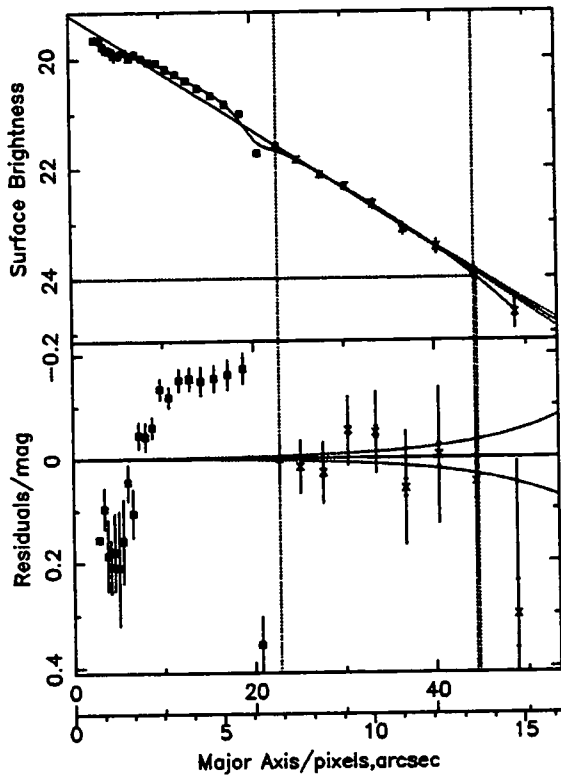
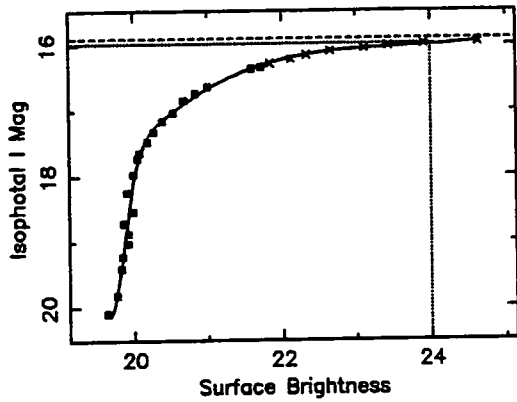
pyoung 3-May-1995 0:23

Ellipse Fitting Results For: 1623+3923

File: 1623_3923_i2710_clean.efot

$R_{22.5} = 9.6''$ $\mu_0 = 19.19$ $R_{Scale} = 3.1''$

$I_{22.5} = 16.13$ $I_{23.5} = 16.01$ $I_{Total} = 15.9$

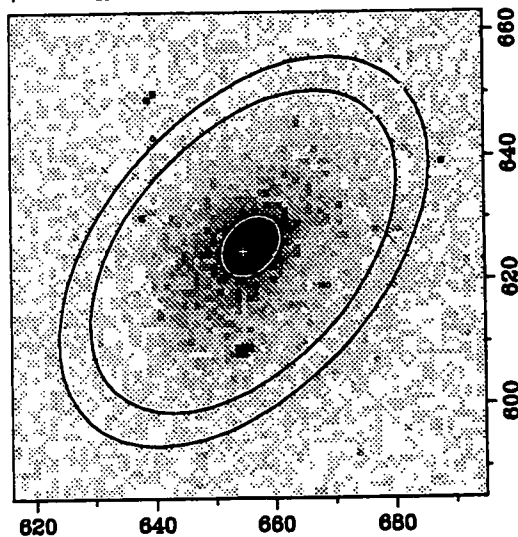
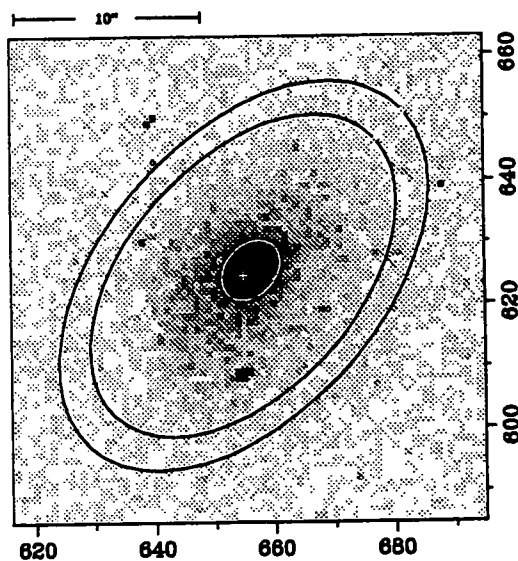
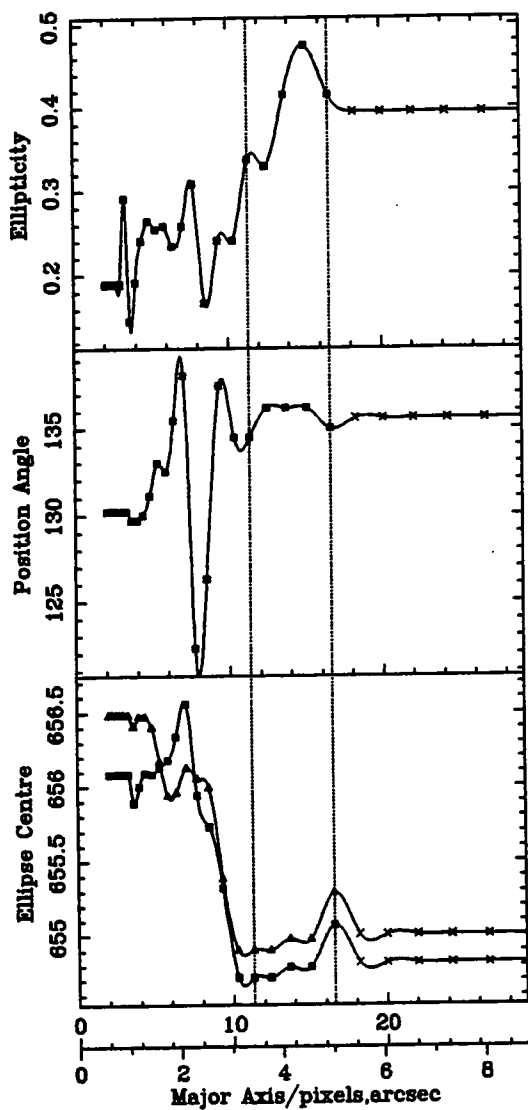
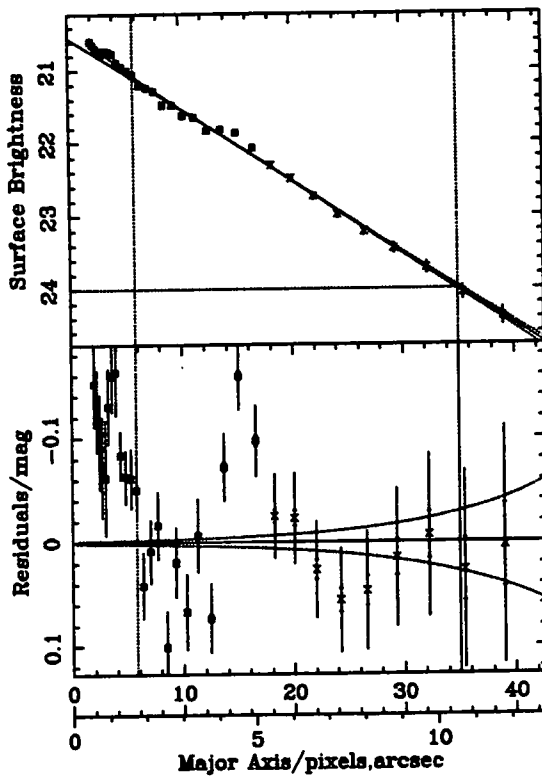
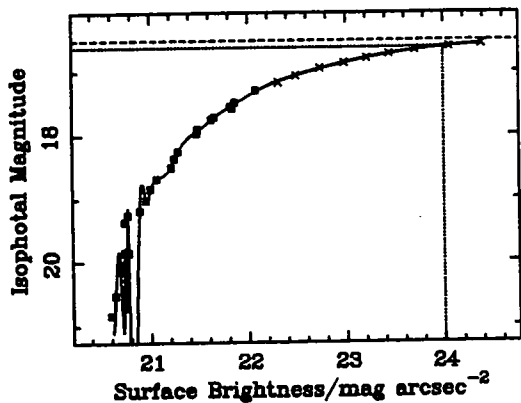


Ellipse Fitting Results For: 1623+3931

File: 1623_3931_r1333_clean.efot

$I_{22.5}=17.06$ $I_{23.5}=16.7$ $I_{24.0}=16.62$ $I_r=16.5$

$R_{22.5}=6''$ $\mu_0=20.54$ $R_{\text{Scale}}=3.3''$

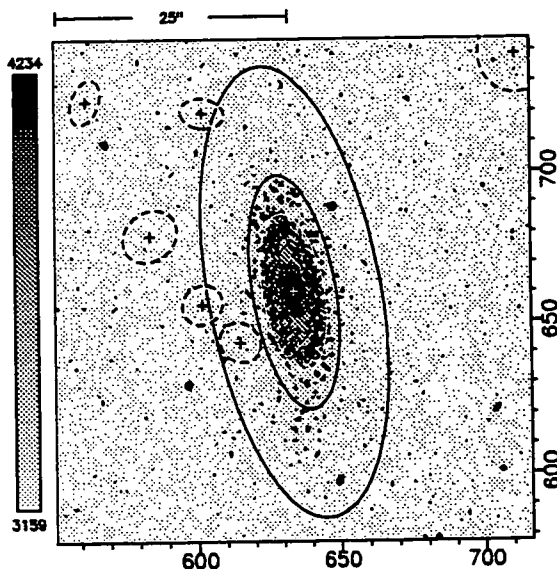
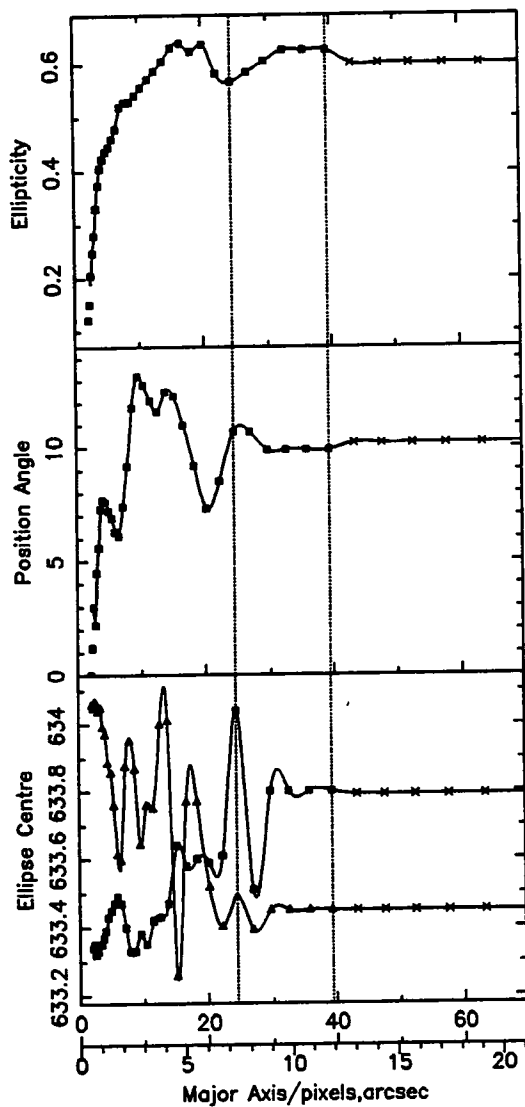
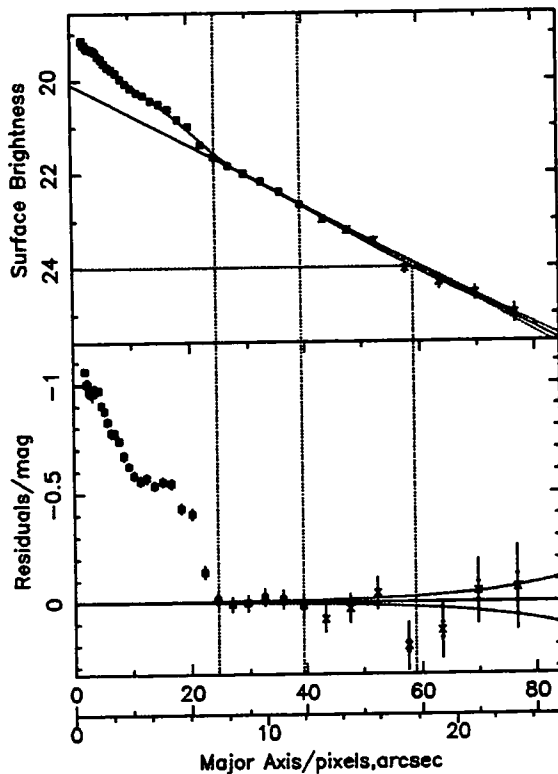
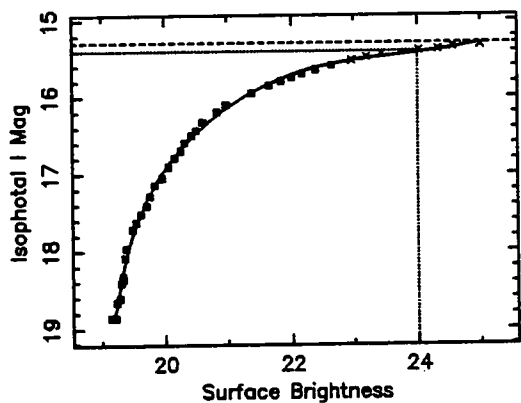


Ellipse Fitting Results For: 1624+3955

File: 1624_3955_i2107_clean.efot

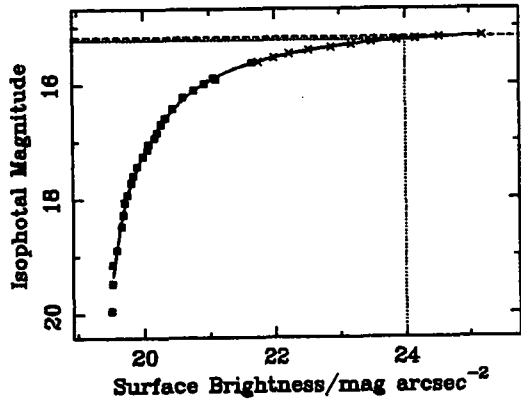
$R_{22.5} = 11.3''$ $\mu_0 = 20.07$ $R_{Scale} = 5.1''$

$I_{22.5} = 15.62$ $I_{23.5} = 15.43$ $I_{Total} = 15.29$



pyoung 24-Mar-1995 6:19

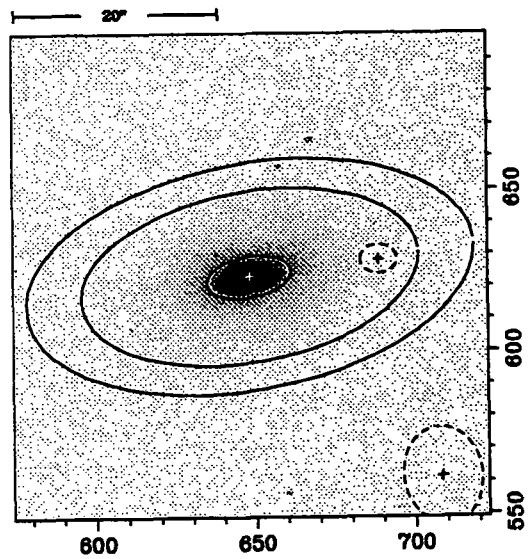
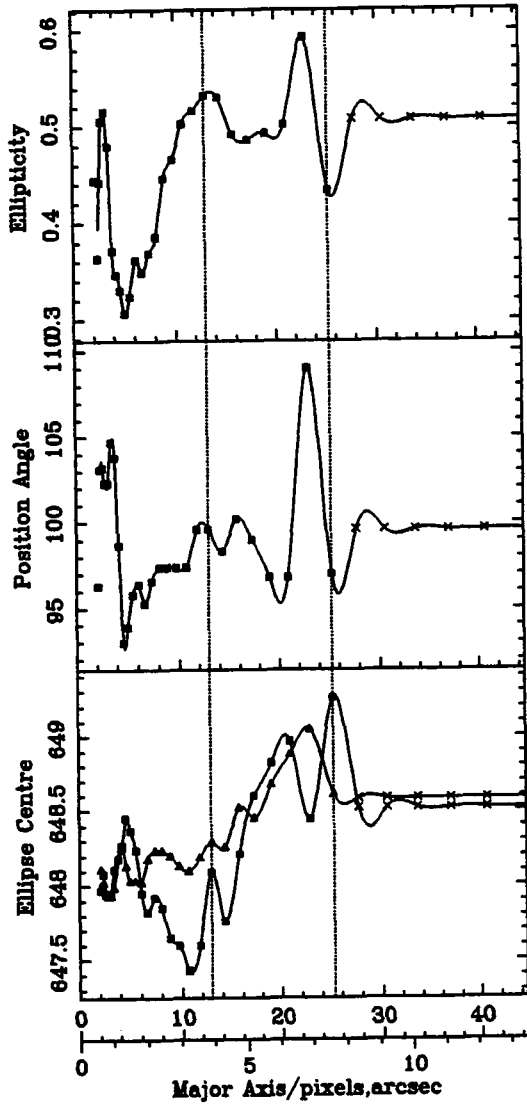
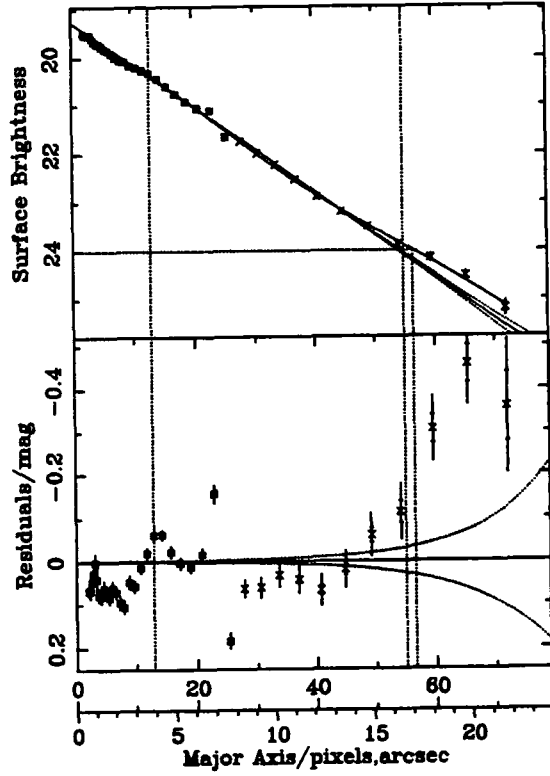
Ellipse Fitting Results For: 1625+3855



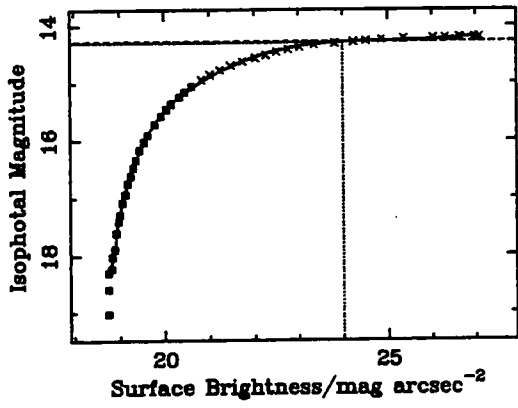
File: 1625_3855_r1531_clean.efot

$I_{22.5}=15.41$ $I_{23.5}=15.27$ $I_{24.0}=15.23$ $I_T=15.18$

$R_{22.5}=11''$ $\mu_0=19.25$ $R_{Scale}=3.8''$



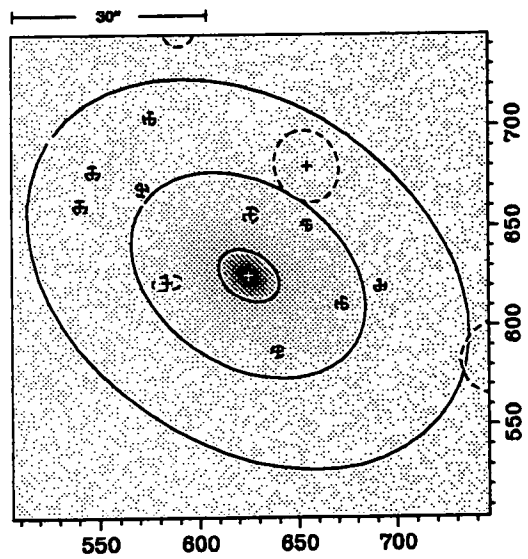
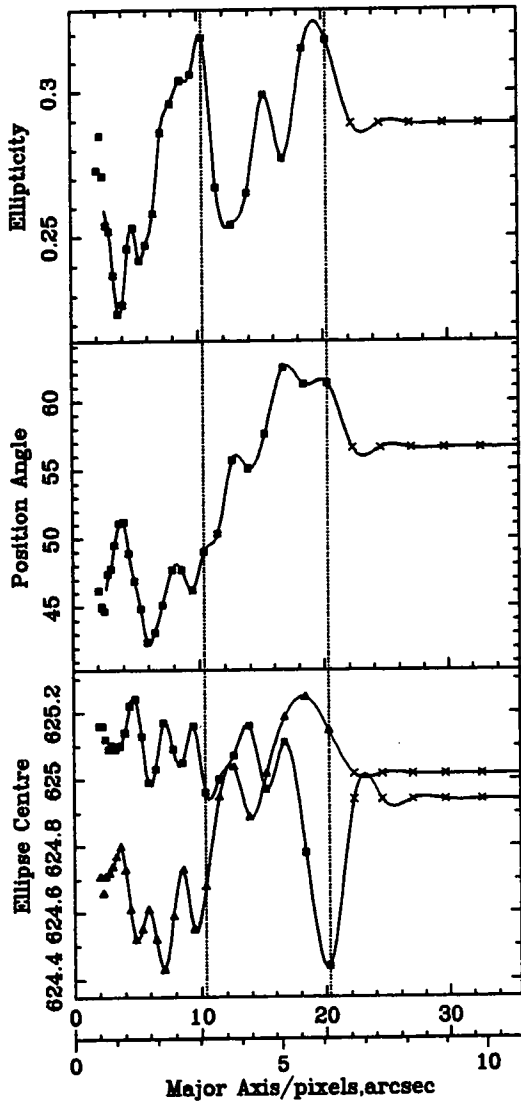
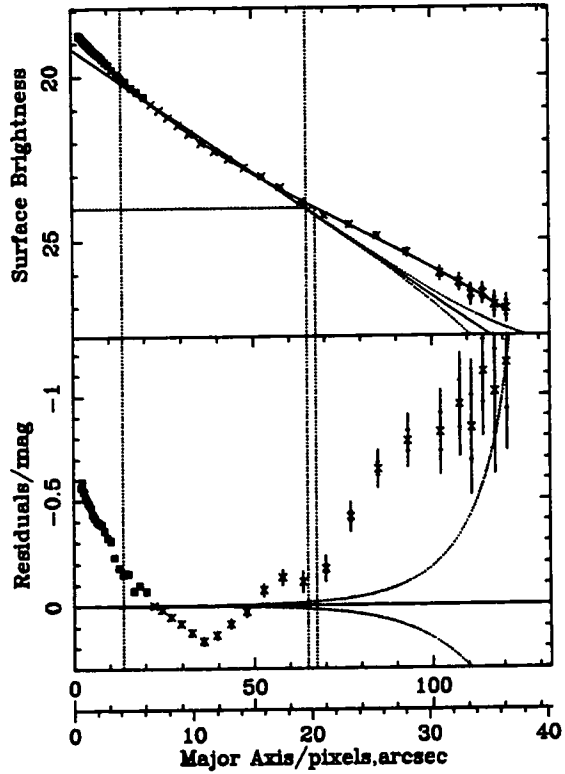
Ellipse Fitting Results For: 1625+3909



File: 1625_3909_r1528_clean.efot

$I_{22.5}=14.46$ $I_{23.5}=14.32$ $I_{24.0}=14.29$ $I_T=14.26$

$R_{22.5}=13.2''$ $\mu_0=19.16$ $R_{Scale}=4.4''$

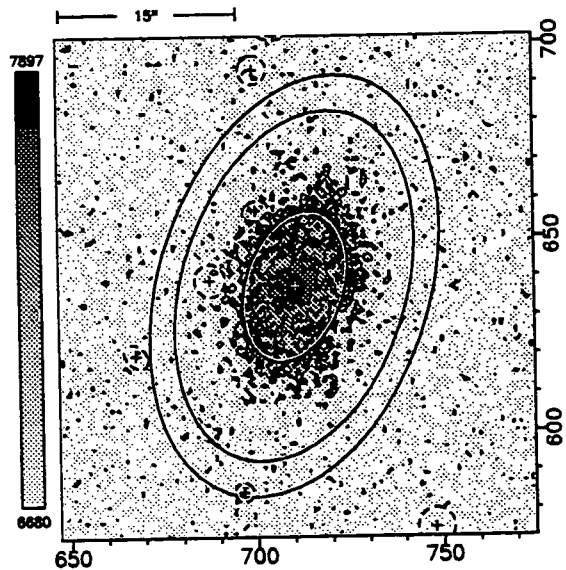
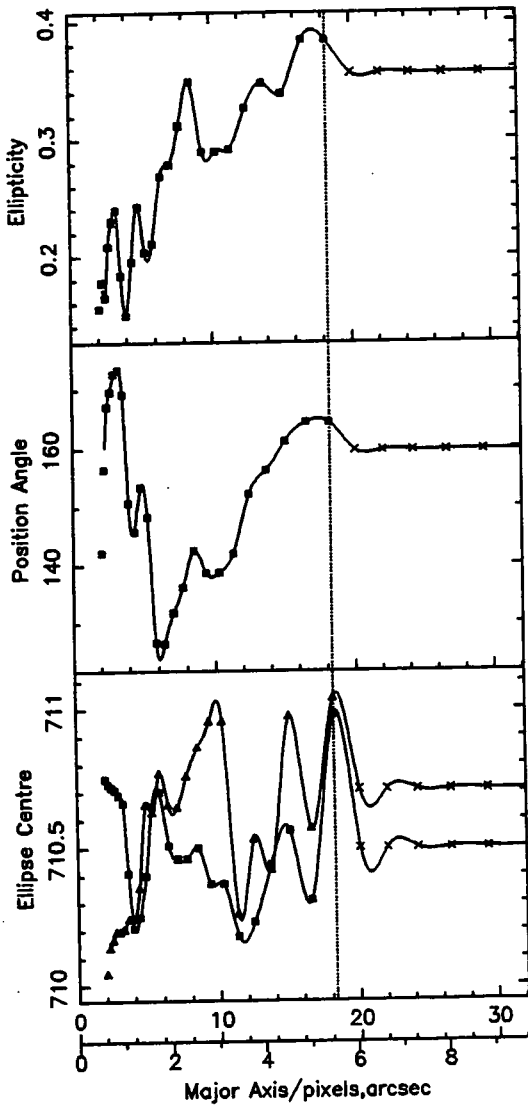
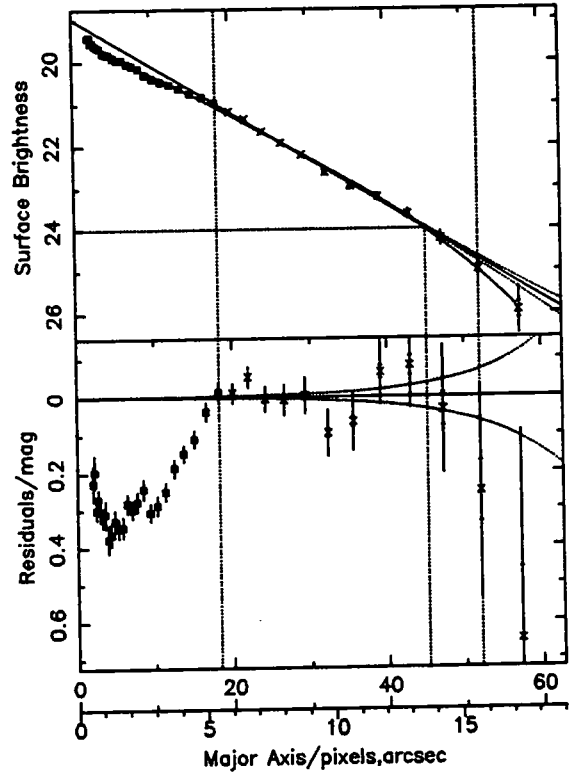
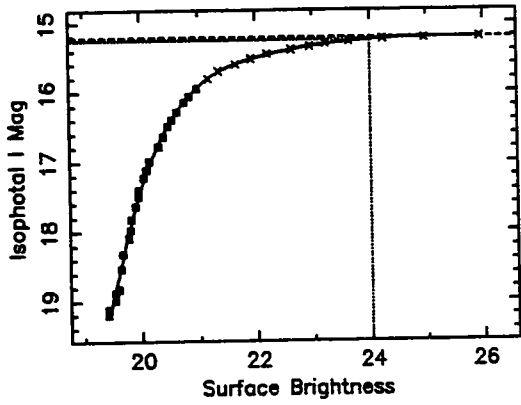


Ellipse Fitting Results For: 1625+4017

File: 1625_4017_i2711_clean.efot

$R_{22.5} = 9.8''$ $\mu_0 = 18.96$ $R_{Scale} = 3''$

$I_{22.5} = 15.41$ $I_{23.5} = 15.28$ $I_{Total} = 15.21$

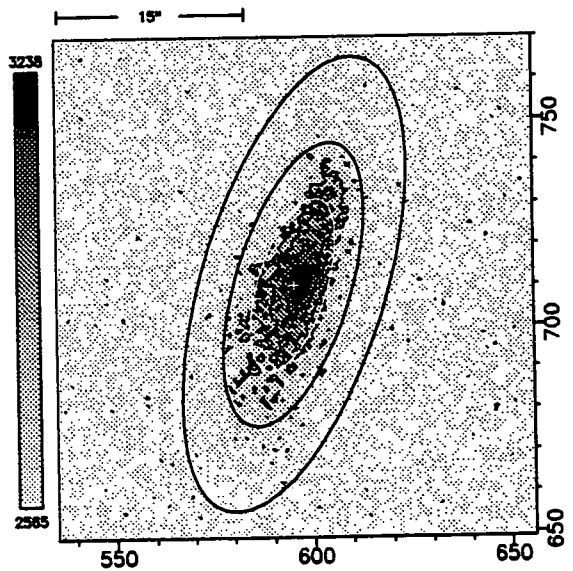
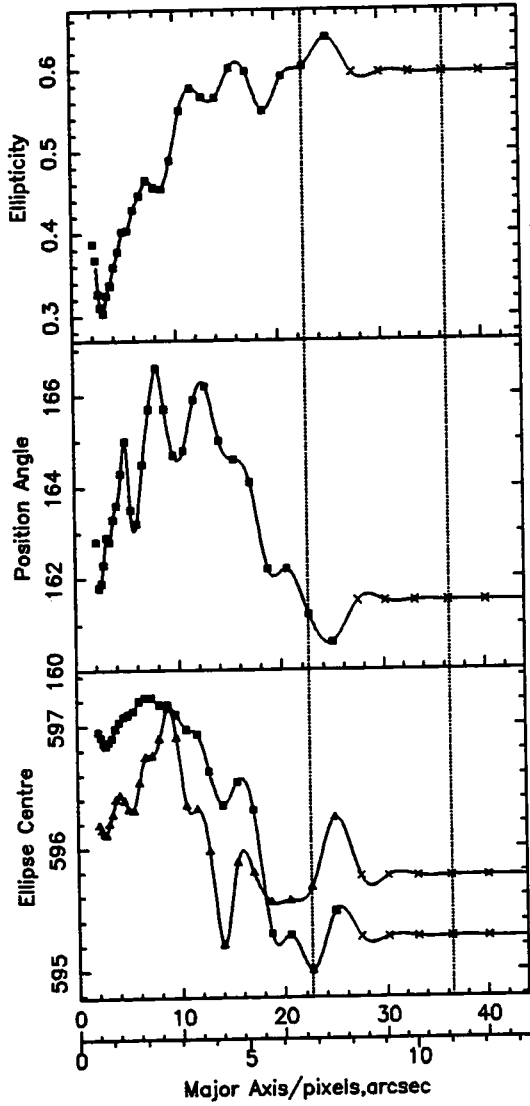
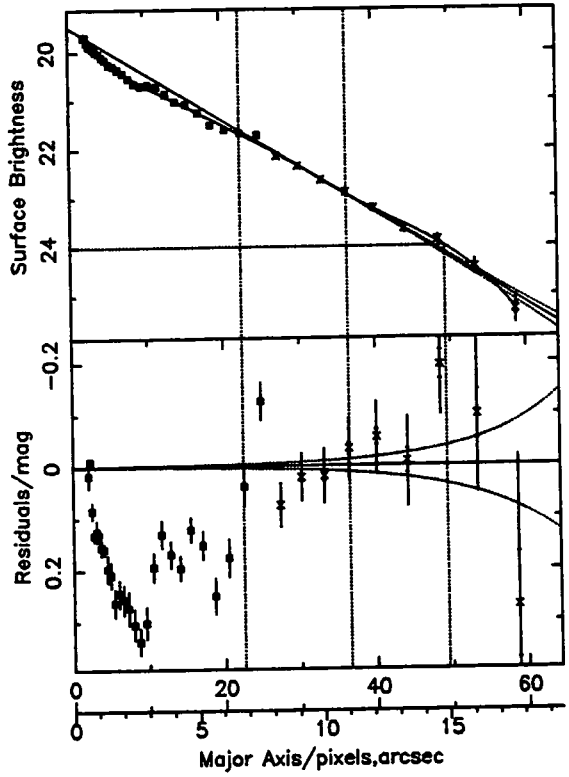
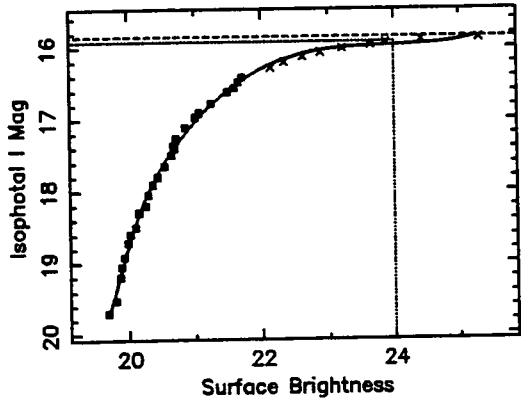


Ellipse Fitting Results For: 1626+3900

File: 1626_3900_i2112_clean.efot

$R_{22.5} = 9.7''$ $\mu_0 = 19.48$ $R_{Scale} = 3.5''$

$I_{22.5} = 16.17$ $I_{23.5} = 15.98$ $I_{Total} = 15.85$

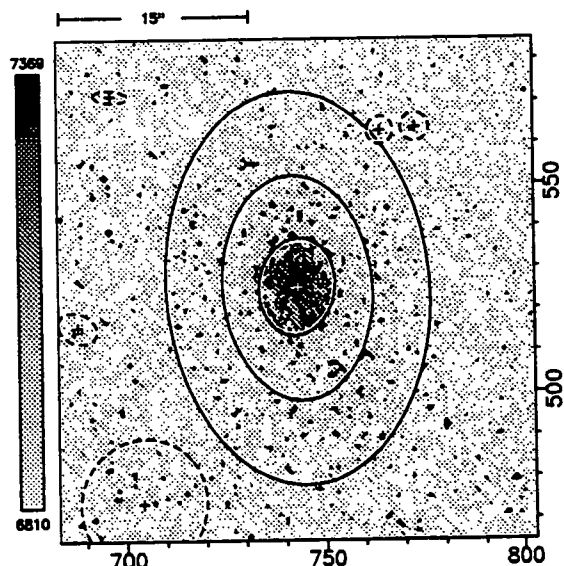
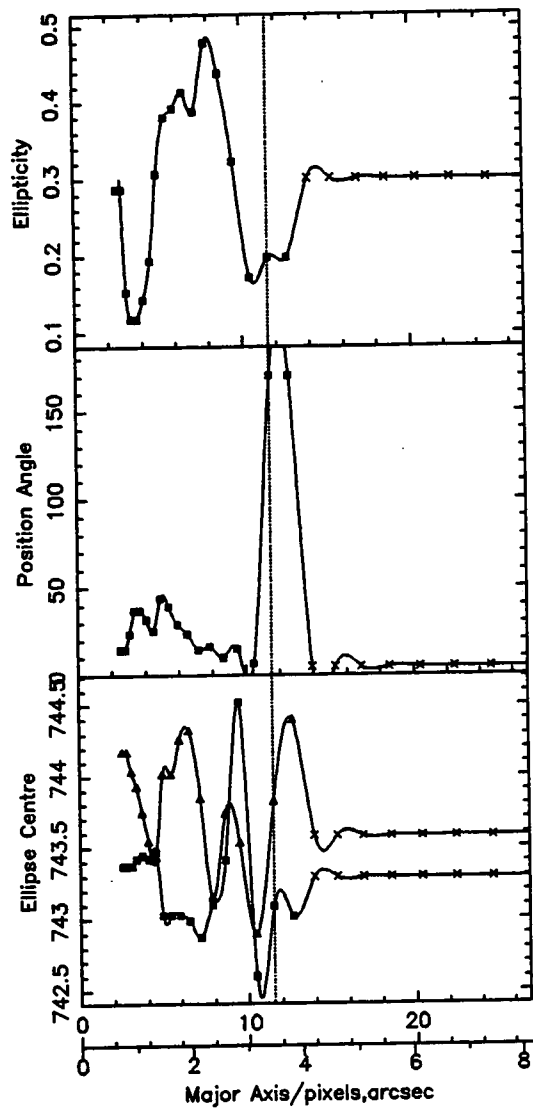
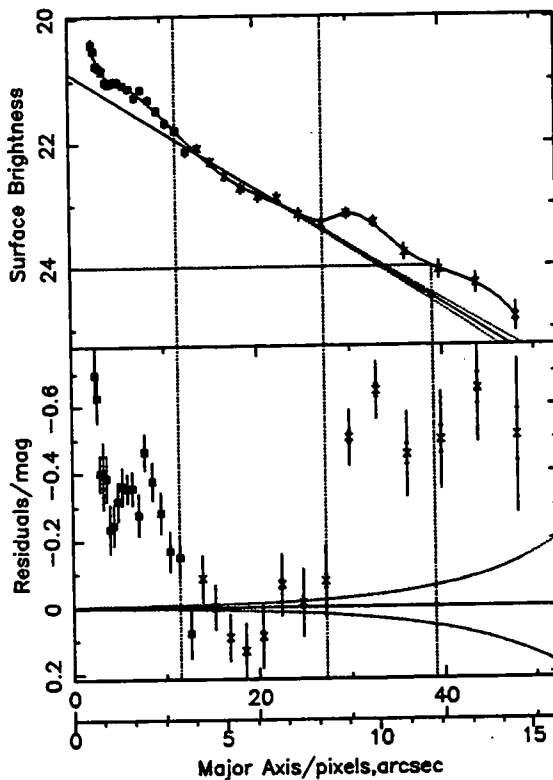
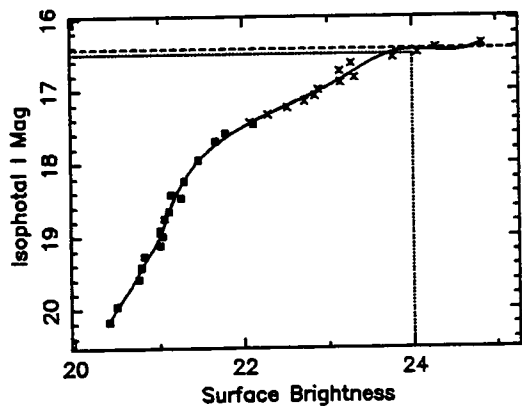


Ellipse Fitting Results For: 1626+3958

File: 1626_3958_i2514_clean.efot

$R_{22.5} = 5''$ $\mu_0 = 20.87$ $R_{Scale} = 3.5''$

$I_{22.5} = 17.25$ $I_{23.5} = 16.59$ $I_{Total} = 16.42$

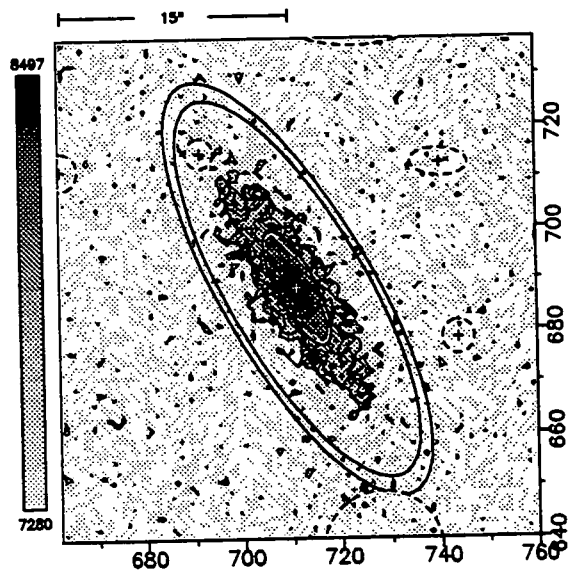
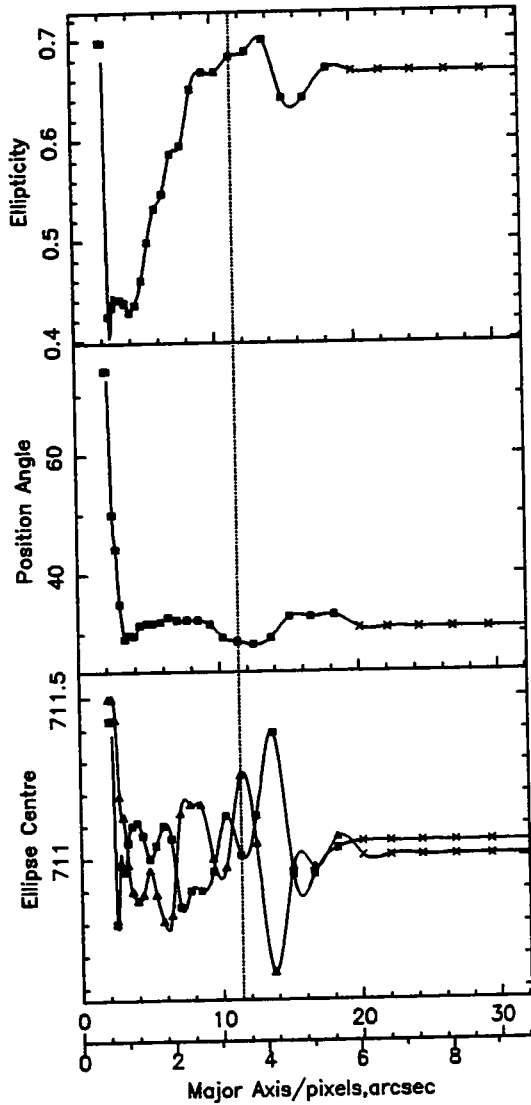
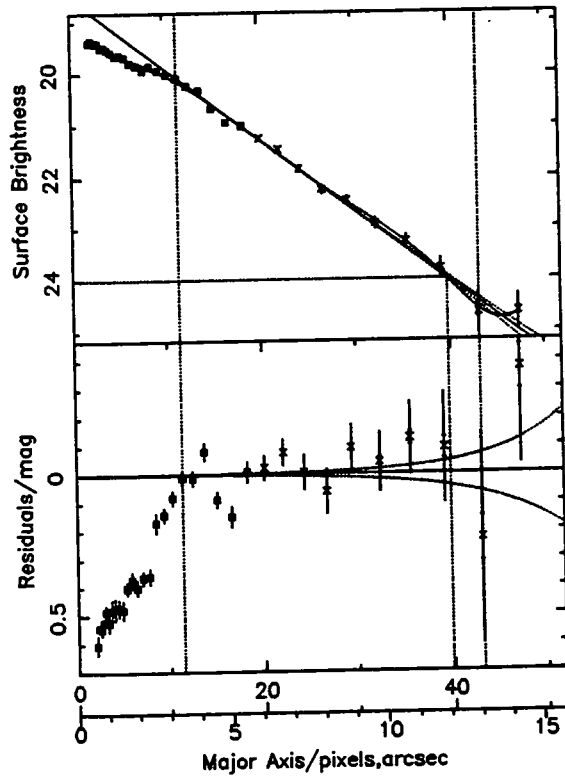
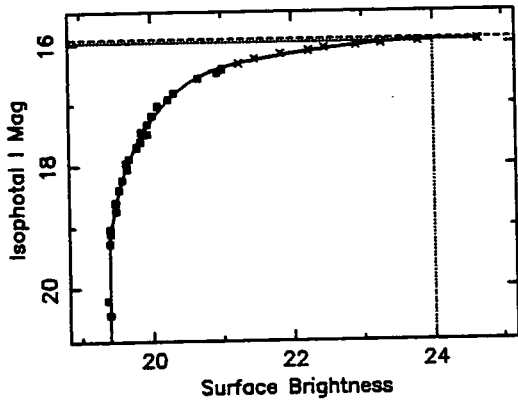


Ellipse Fitting Results For: 1626+4015

File: 1626_4016_i2712_clean.efot

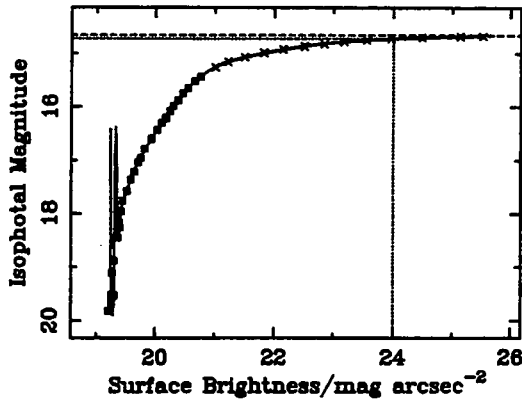
$R_{22.5} = 8.9''$ $\mu_0 = 18.51$ $R_{Scale} = 2.4''$

$I_{22.5} = 16.06$ $I_{23.5} = 15.99$ $I_{Total} = 15.91$



pyoung 5-May-1995 14: 2

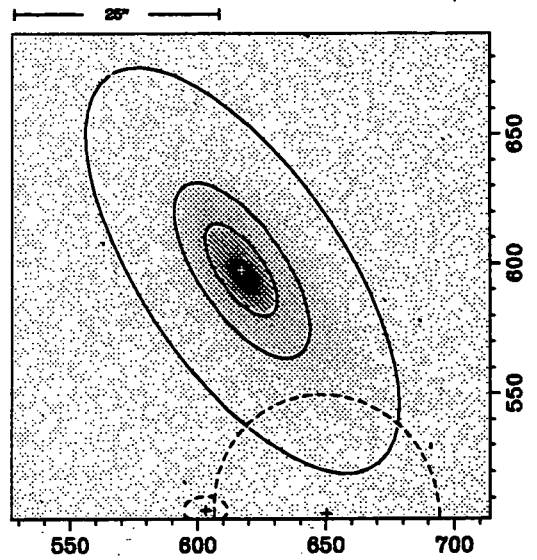
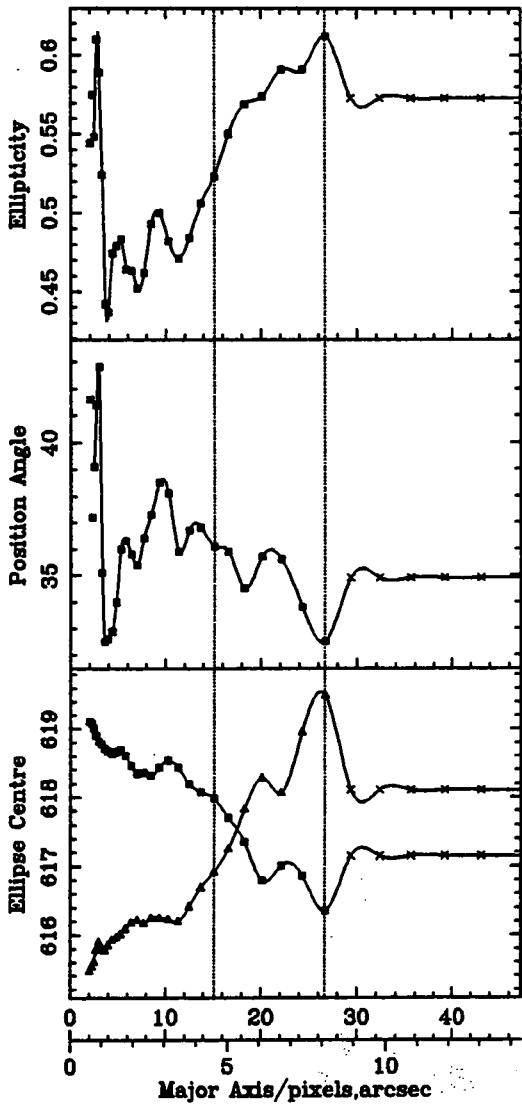
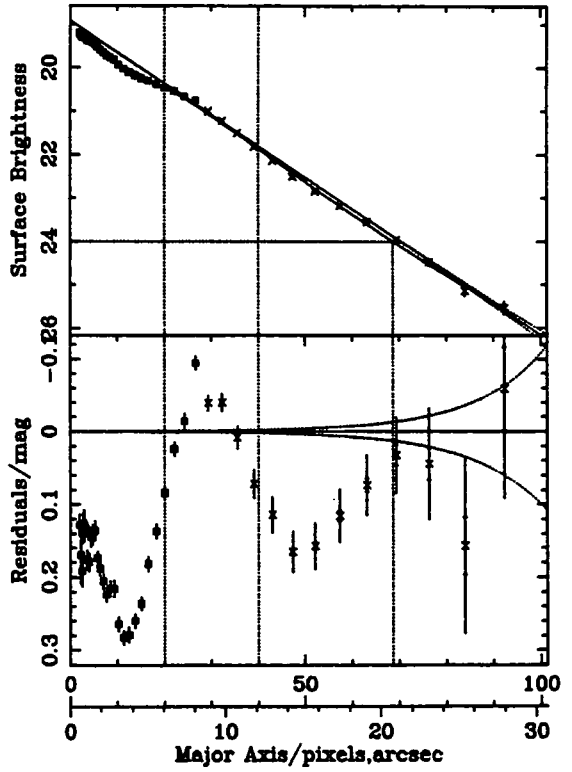
Ellipse Fitting Results For: 1251+2827



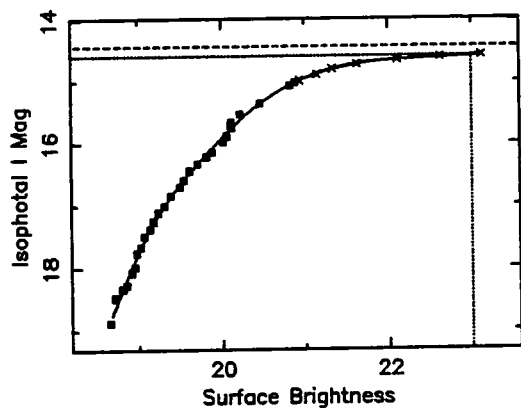
File: 1251_2827_r1317_clean.efot

$I_{22.5}=14.87$ $I_{23.5}=14.75$ $I_{24.0}=14.72$ $I_T=14.66$

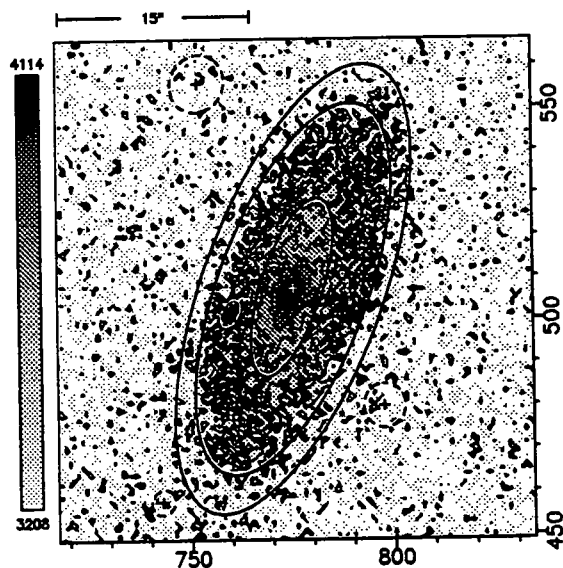
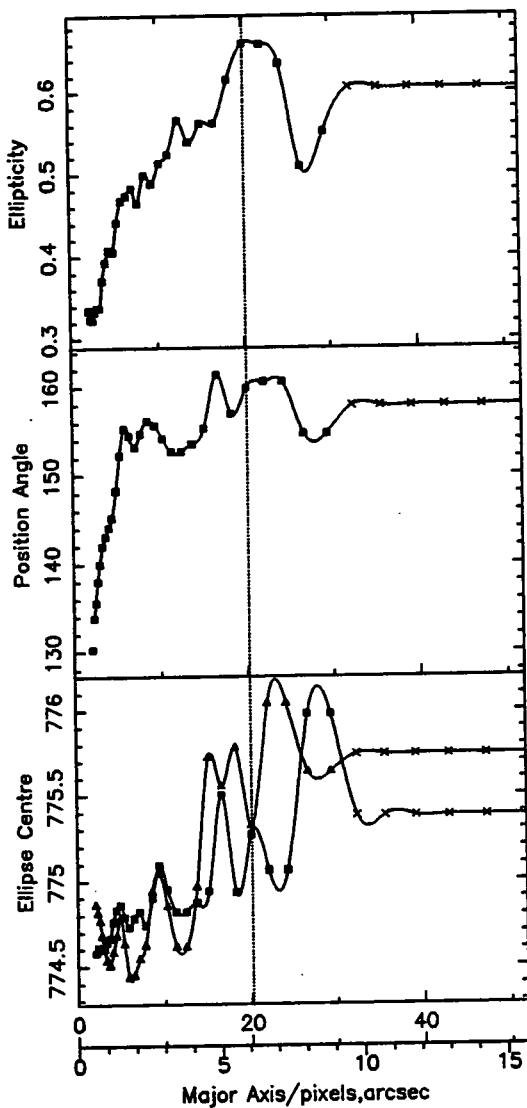
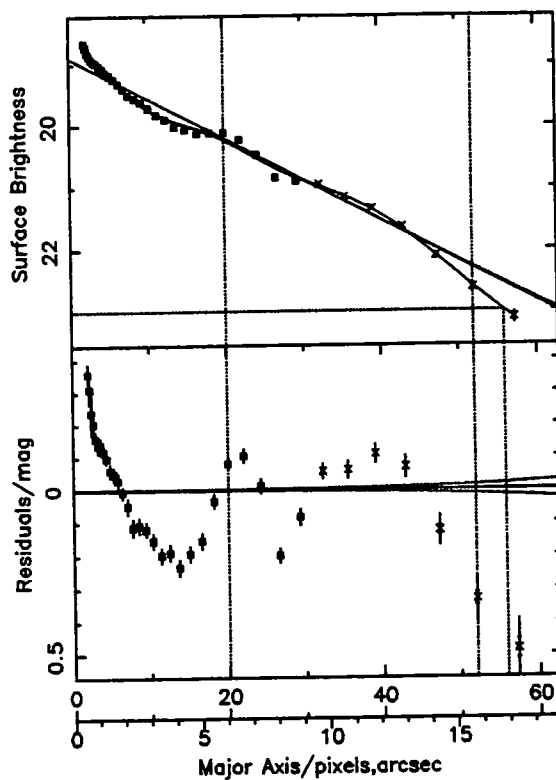
$R_{22.5}=14.7''$ $\mu_0=18.93$ $R_{Scale}=4.6''$



Ellipse Fitting Results For: B037



File: bo37_i2517_clean.efot
 $R_{22.5} = 15.5''$ $\mu_0 = 18.88$ $R_{Scale} = 5''$
 $I_{22.5} = 14.62$ $I_{23.5} = 99.99$ $I_{Total} = 14.43$

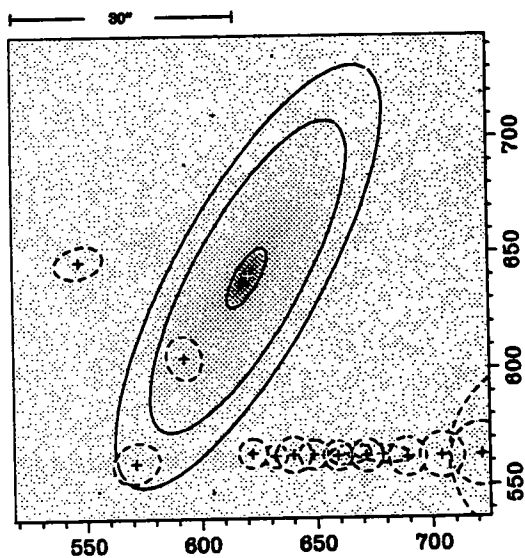
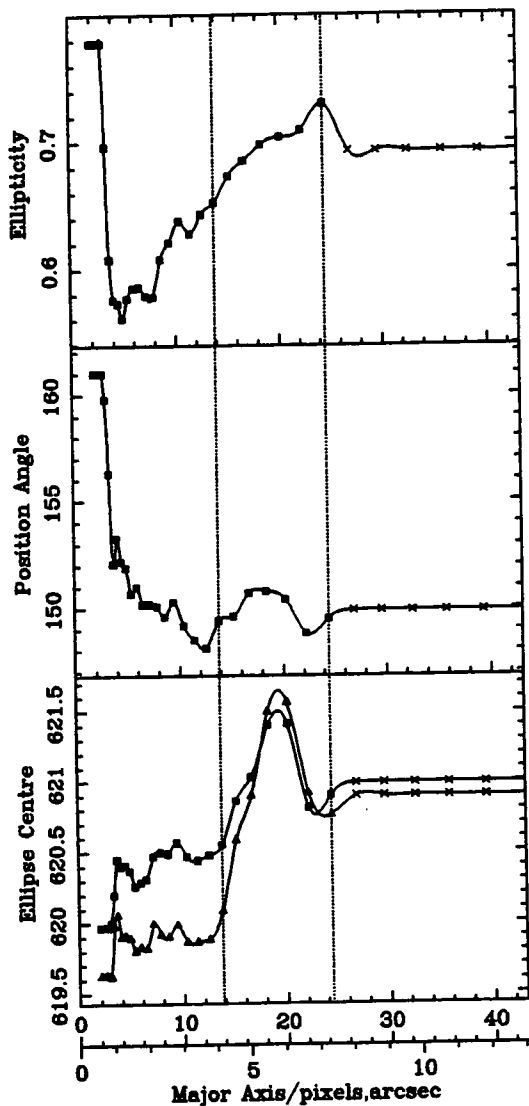
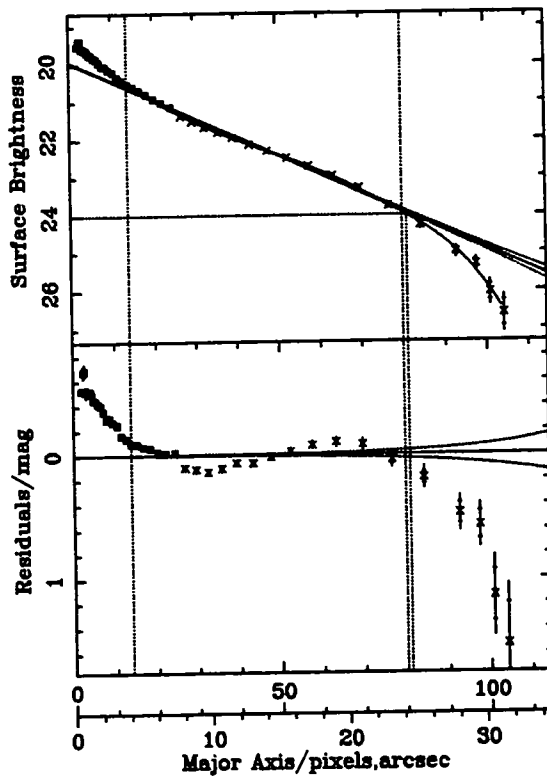
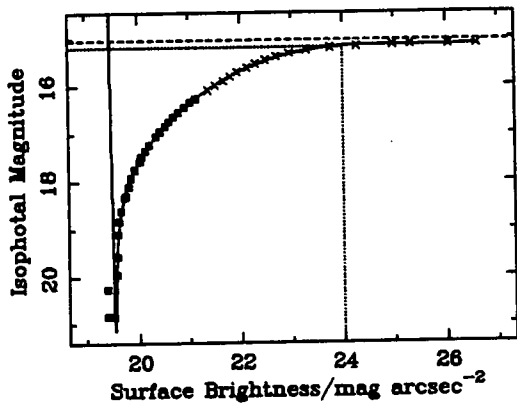


Ellipse Fitting Results For: B043

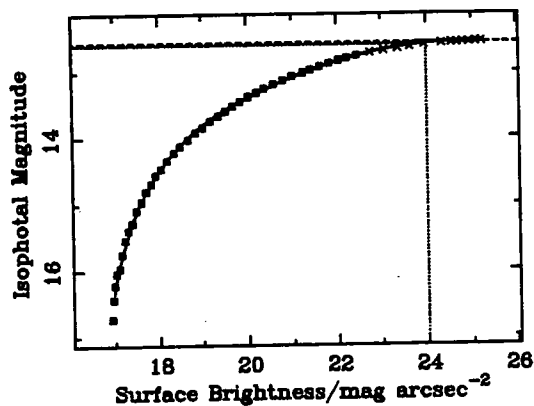
File: bo43_r1234_clean.efot

$I_{22.5} = 15.46$ $I_{23.5} = 15.23$ $I_{24.0} = 15.19$ $I_T = 15.04$

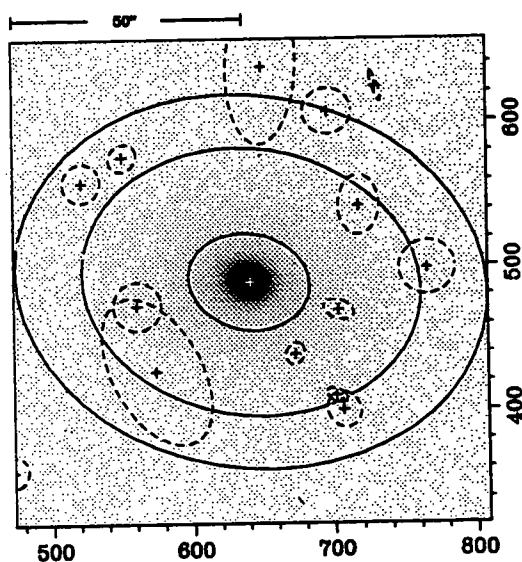
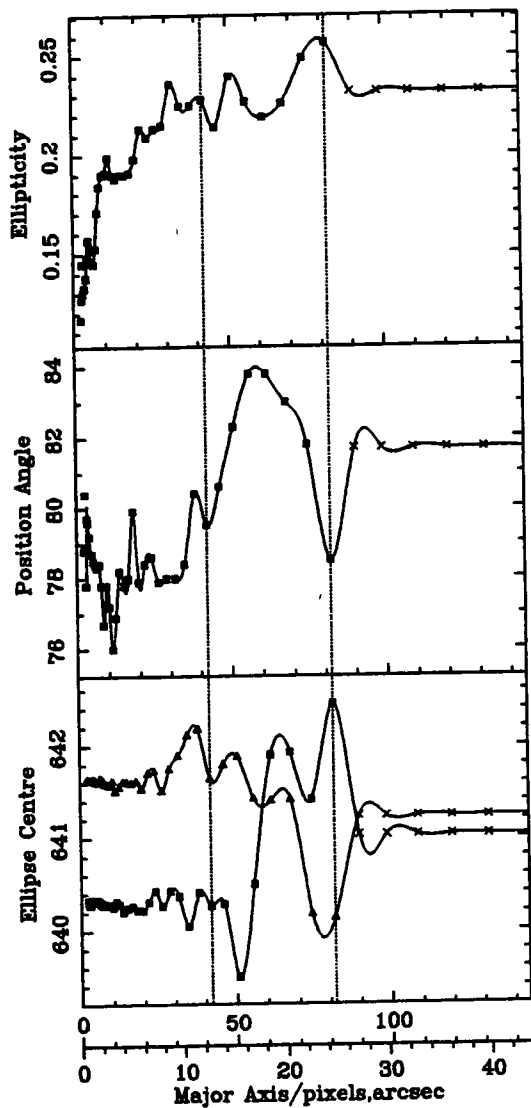
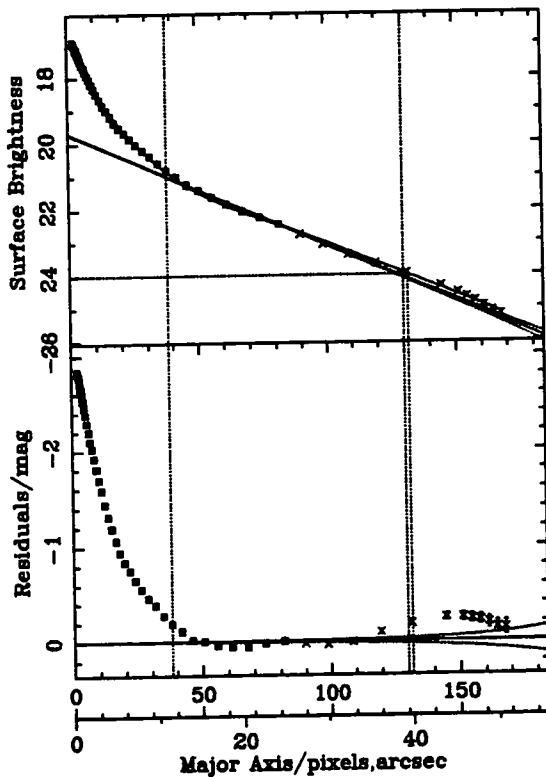
$R_{22.5} = 15.9''$ $\mu_0 = 19.94$ $R_{Scale} = 6.7''$



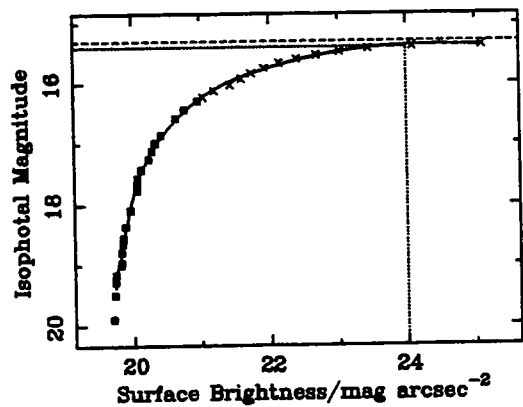
Ellipse Fitting Results For: B063



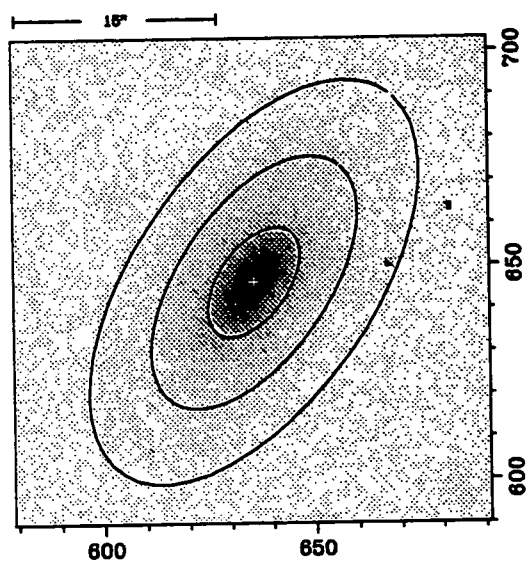
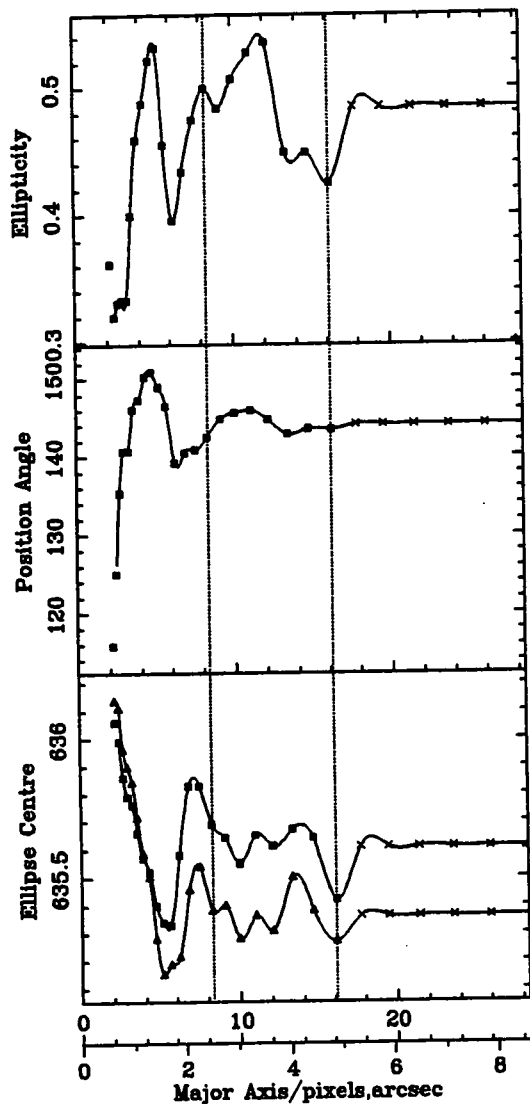
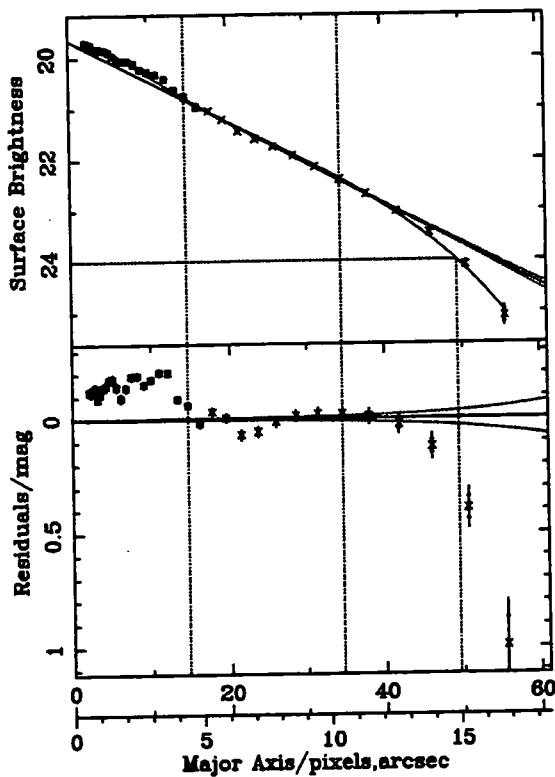
File: bo63_r1237_clean.efot
 $I_{22.5}=12.75$ $I_{23.5}=12.84$ $I_{24.0}=12.59$ $I_T=12.57$
 $R_{22.5}=25''$ $\mu_0=19.7$ $R_{scale}=9.7''$



Ellipse Fitting Results For: RB36

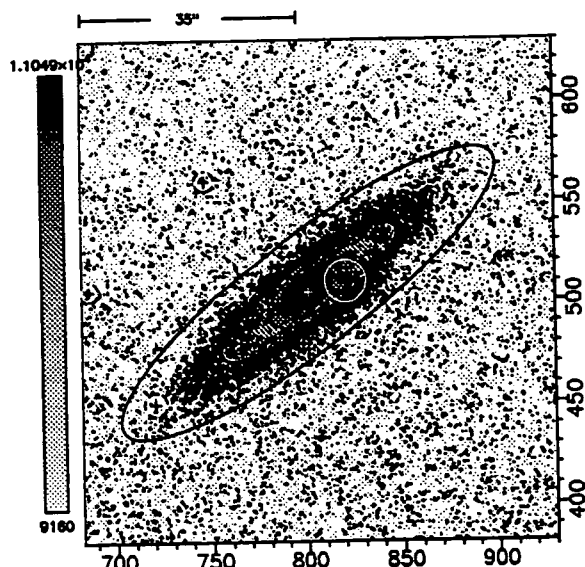
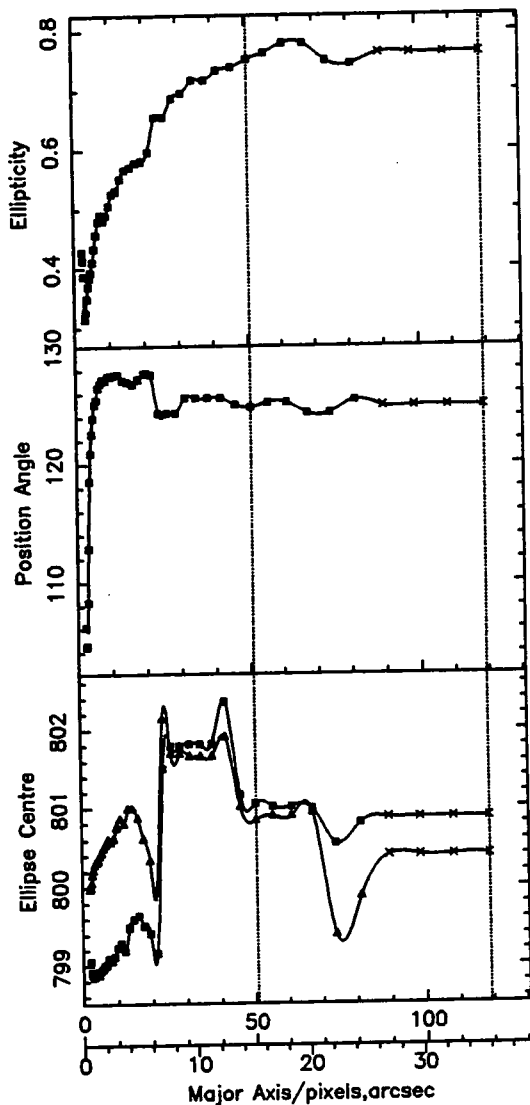
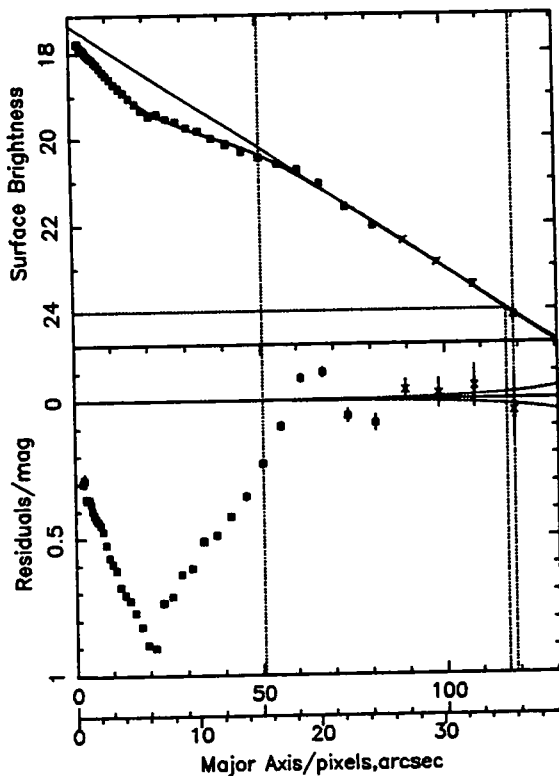
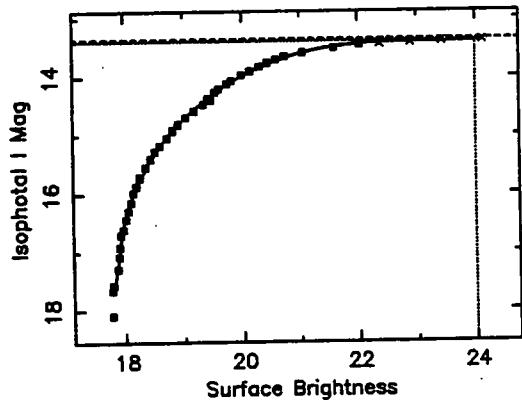


File: rb36_r1236_clean.efot
 $I_{22.5}=15.57$ $I_{23.5}=15.42$ $I_{24.0}=15.39$ $I_7=15.3$
 $R_{22.5}=10.9''$ $\mu_0=19.65$ $R_{Scale}=4.1''$



Ellipse Fitting Results For: U10244

File: u10244_j2715_clean.efot
 $R_{22.5} = 27.7''$ $\mu_0 = 17.36$ $R_{Scale} = 5.8''$
 $I_{22.5} = 13.43$ $I_{23.5} = 13.39$ $I_{Total} = 13.35$

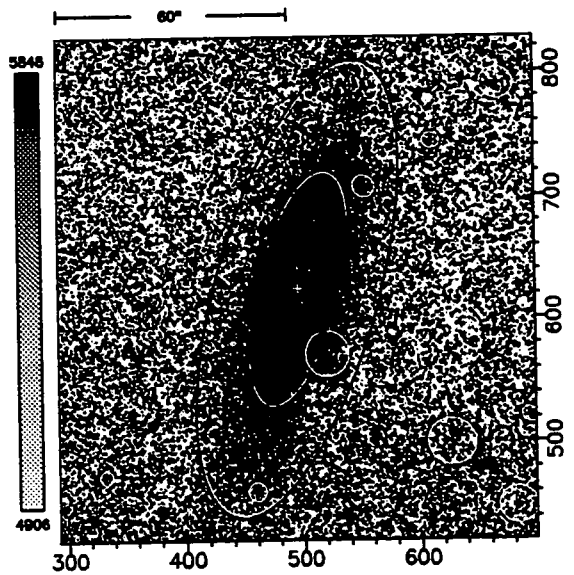
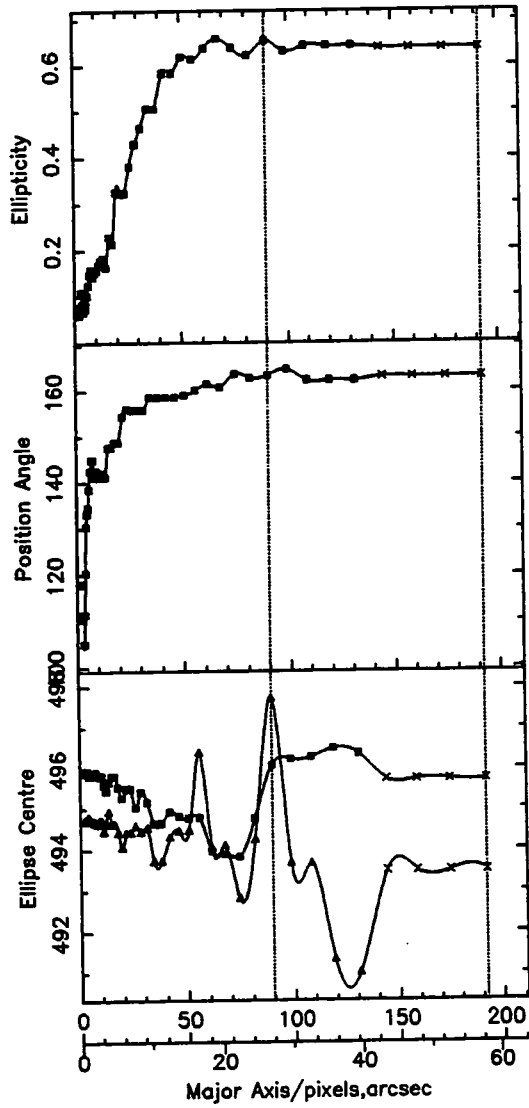
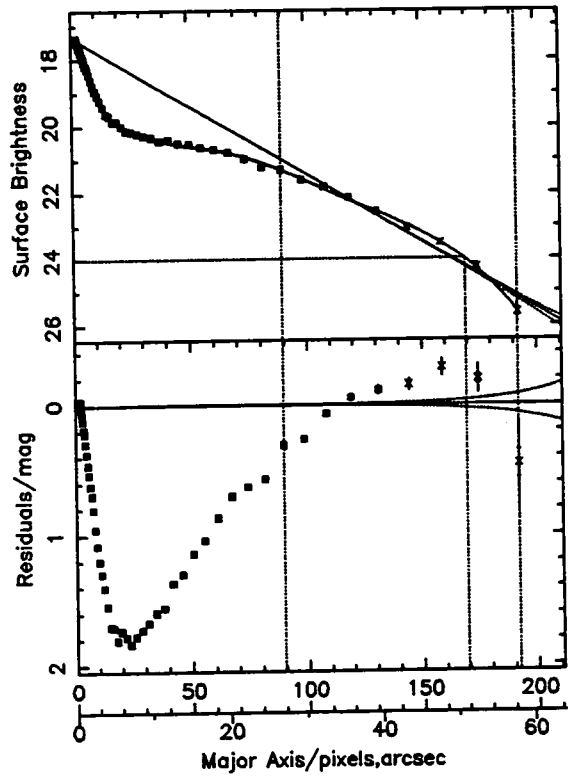
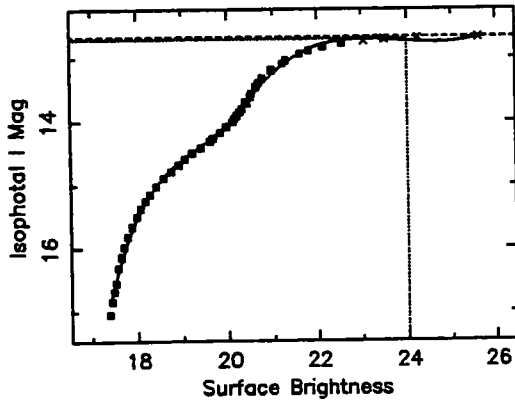


Ellipse Fitting Results For: U10366

File: u10366_j2716_clean.efot

$R_{22.5}=39.1''$ $\mu_0=17.32$ $R_{Scale}=8.1''$

$I_{22.5}=12.78$ $I_{23.5}=12.71$ $I_{Total}=12.66$



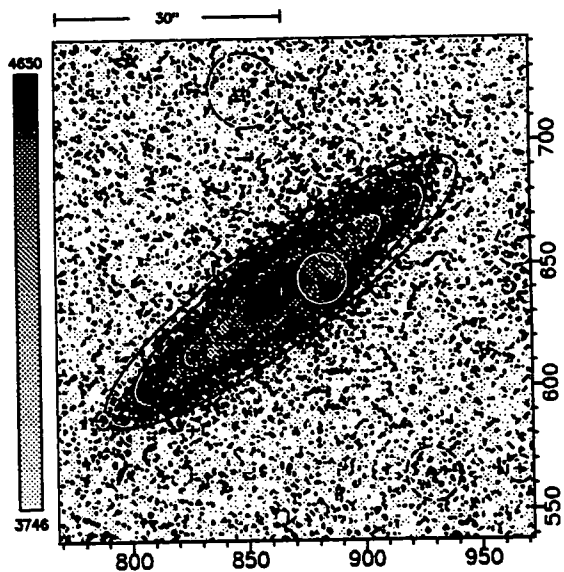
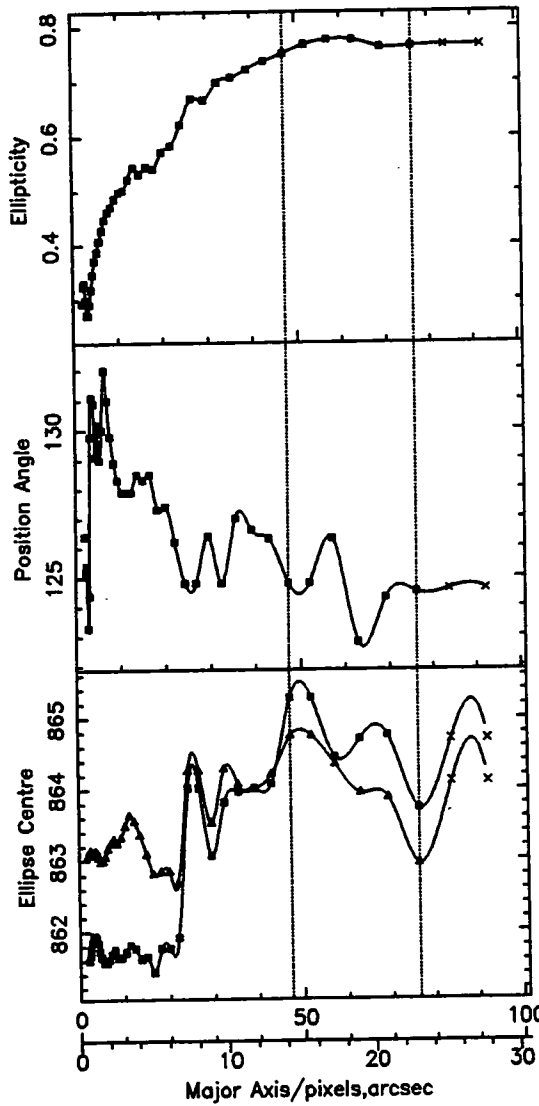
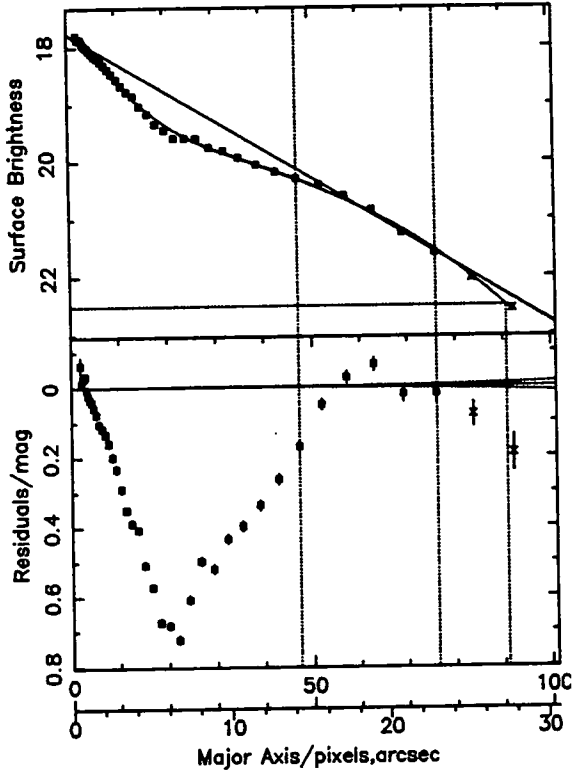
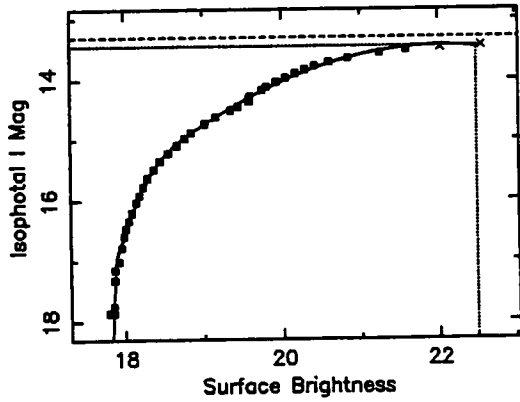
pyoung 7-May-1995 2:7

Ellipse Fitting Results For: U10420

File: u10420_i2612_clean.efot

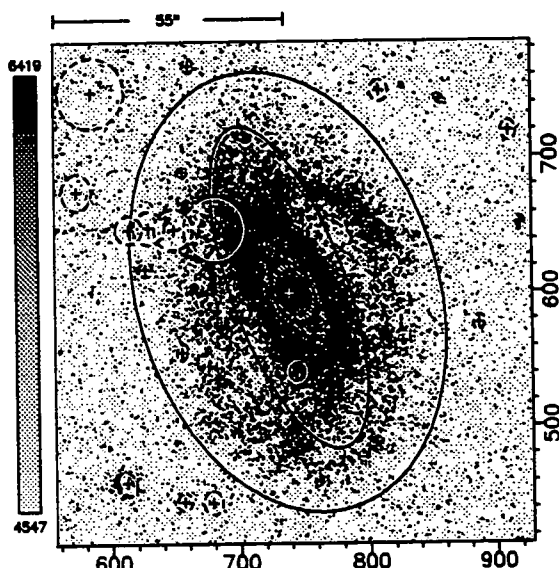
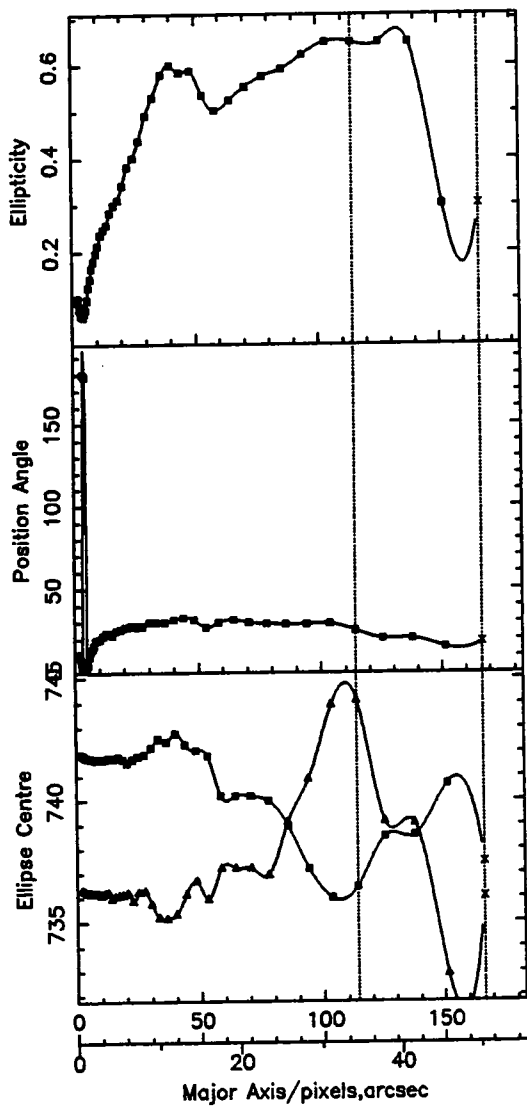
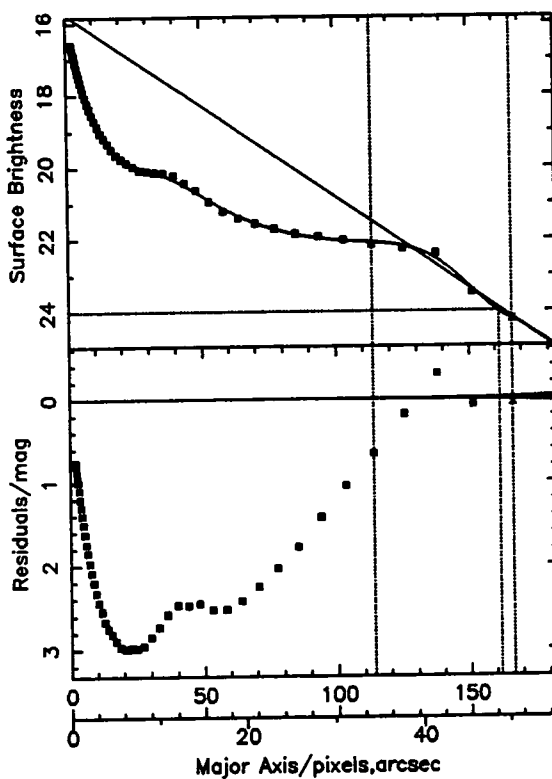
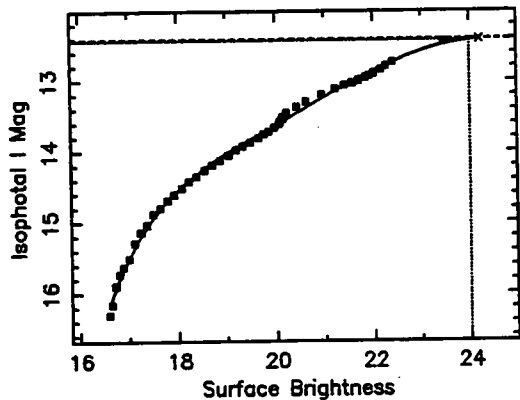
$R_{22.5}=27.5''$ $\mu_0=17.76$ $R_{Scale}=6.6''$

$I_{22.5}=13.45$ $I_{23.5}=99.99$ $I_{Total}=13.3$

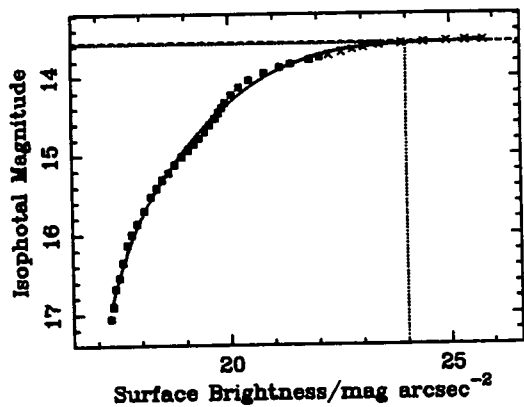


Ellipse Fitting Results For: U10428

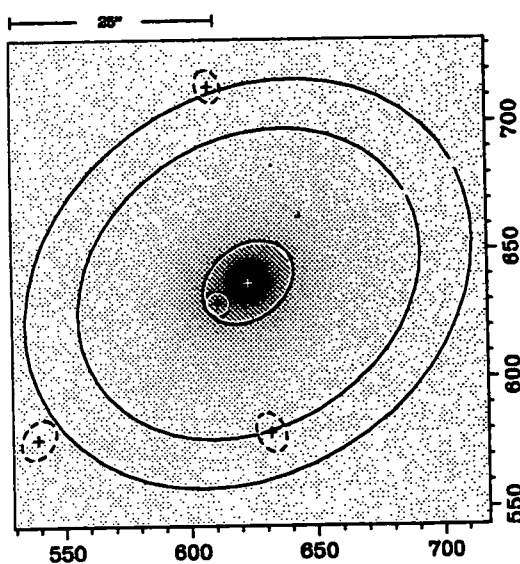
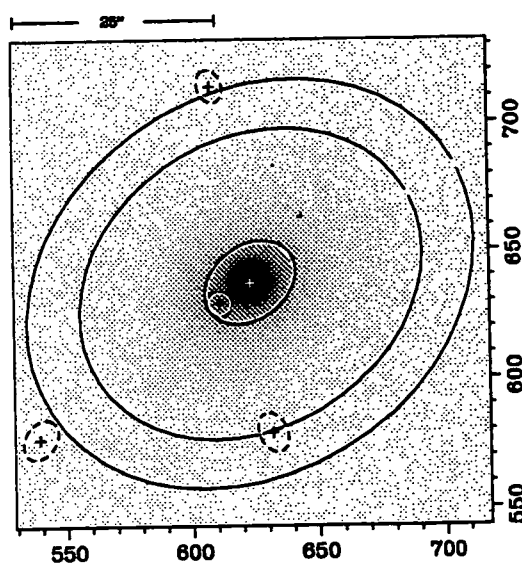
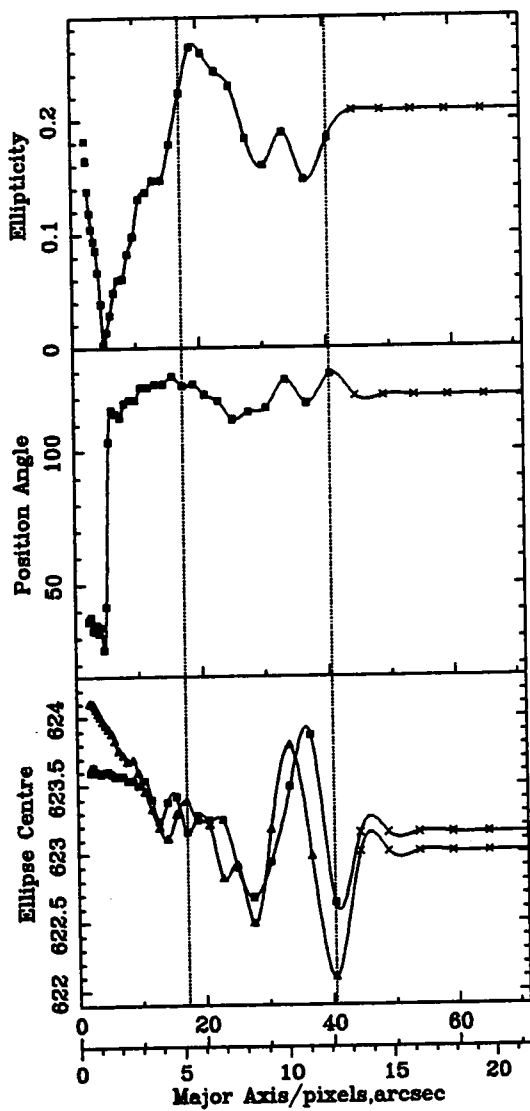
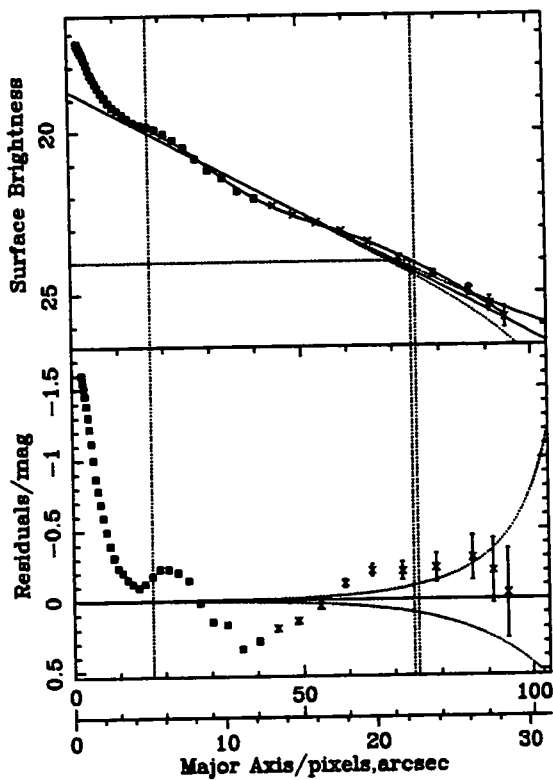
File: u10428_j2312_clean.efot
 $R_{22.5}=41.4''$ $\mu_0=15.74$ $R_{Scale}=6.5''$
 $I_{22.5}=12.72$ $I_{23.5}=12.45$ $I_{Total}=12.41$



Ellipse Fitting Results For: U10429



File: u10429_r1330_clean.efot
 $I_{22.5} = 13.69$ $I_{23.5} = 13.59$ $I_{24.0} = 13.57$ $I_7 = 13.55$
 $R_{22.5} = 14.4''$ $\mu_0 = 18.72$ $R_{scale} = 4.4''$

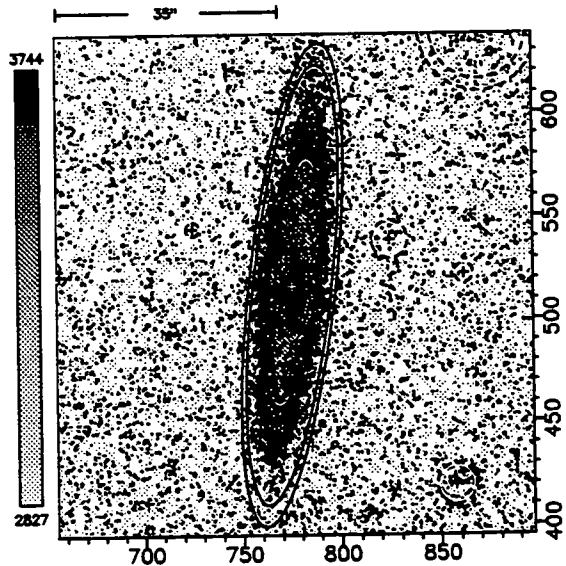
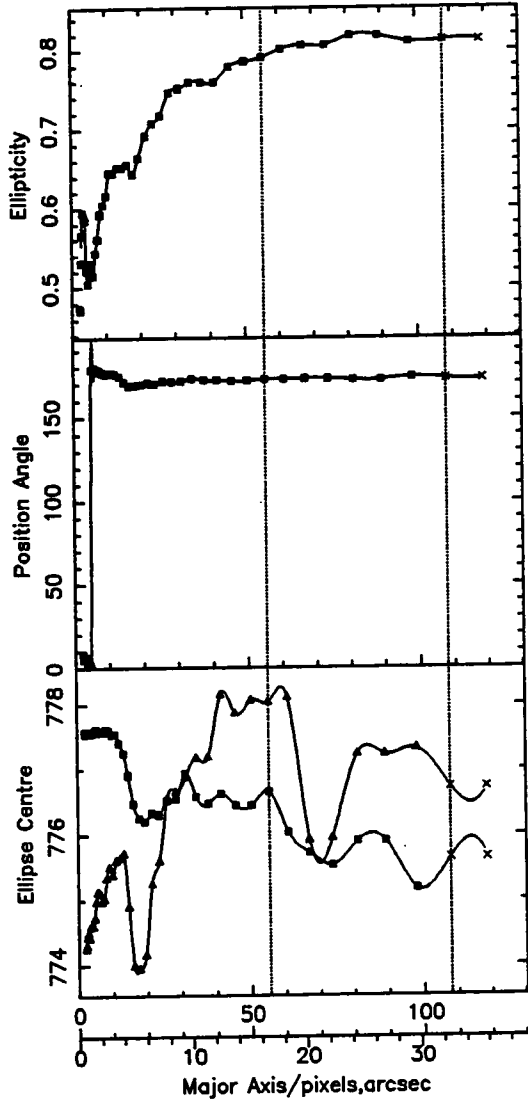
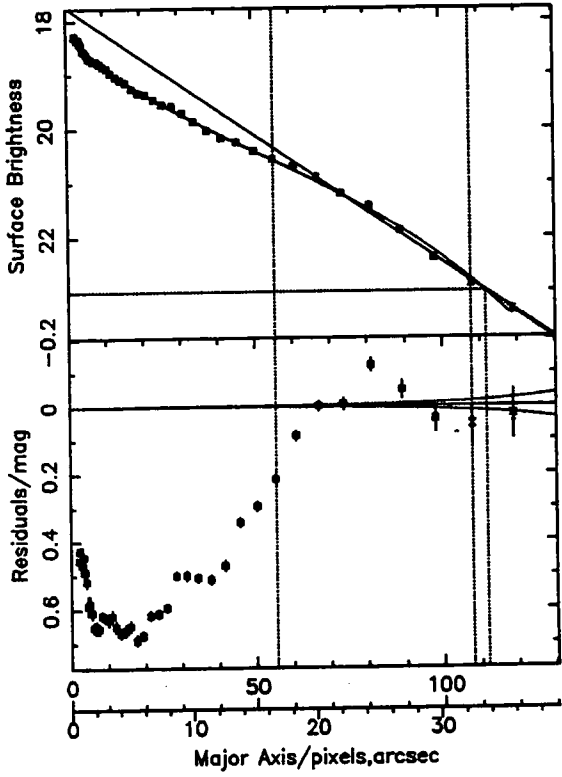
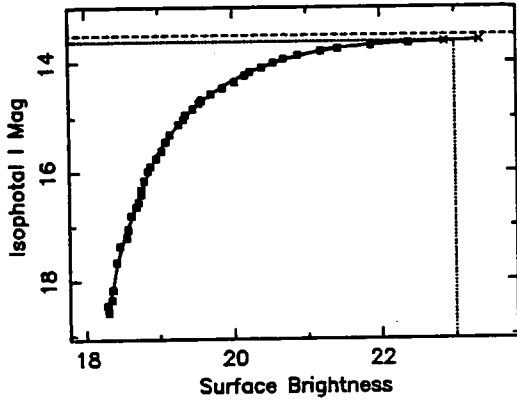


Ellipse Fitting Results For: U10468

File: u10468_i2516_clean.efot

$R_{22.5}=31.2''$ $\mu_0=17.74$ $R_{Scale}=7''$

$I_{22.5}=13.64$ $I_{23.5}=99.99$ $I_{Total}=13.49$

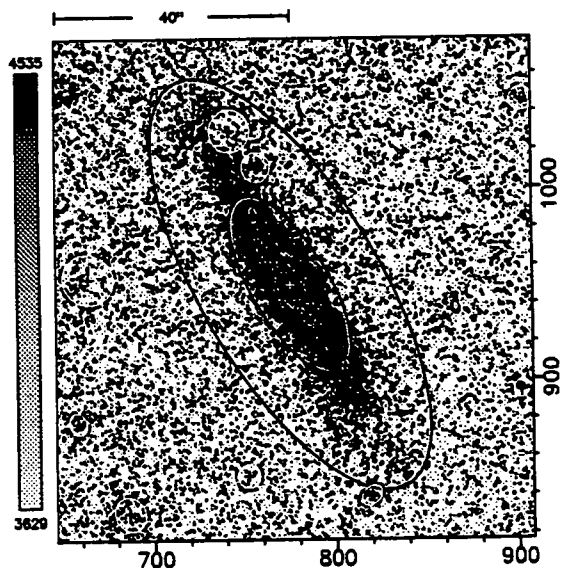
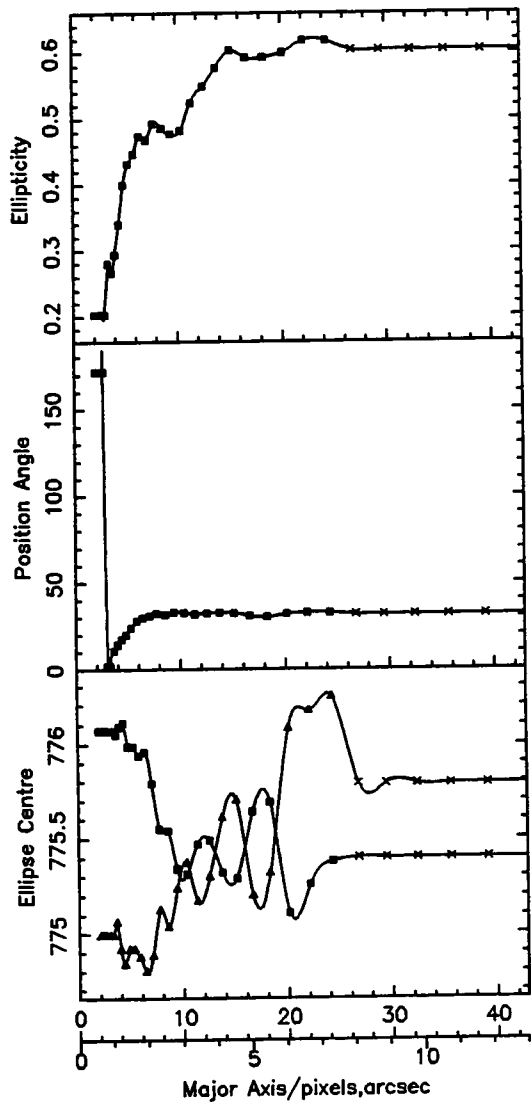
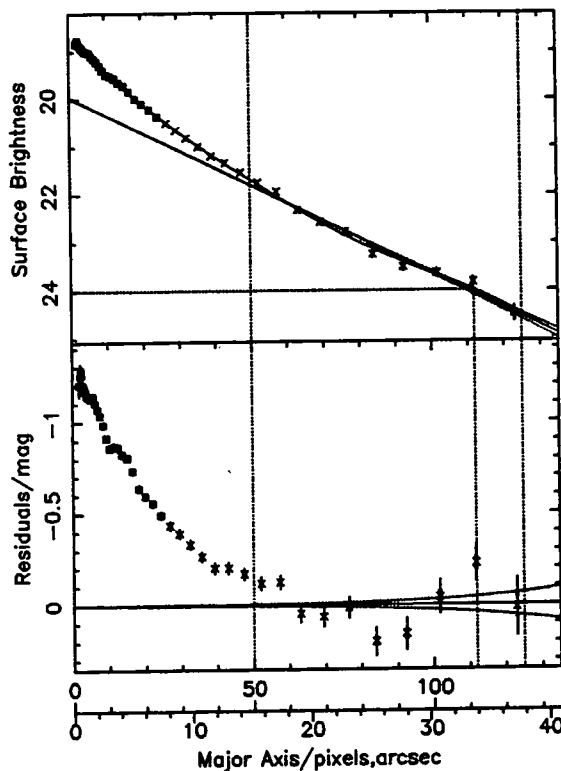
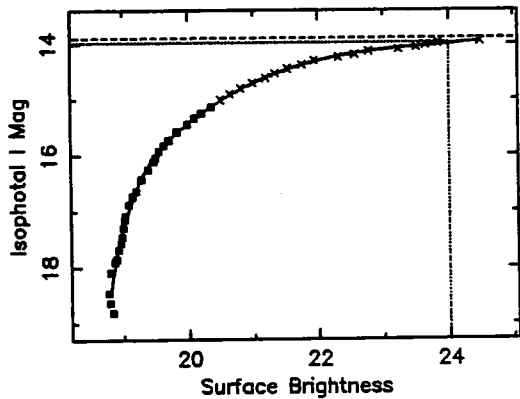


Ellipse Fitting Results For: U10550

File: u10550_i2613_clean.efot

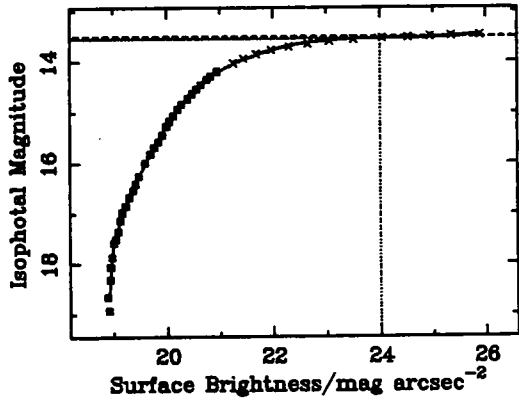
$R_{22.5}=20.6''$ $\mu_0=19.95$ $R_{Scale}=9''$

$l_{22.5}=14.21$ $l_{23.5}=14.07$ $l_{Total}=13.9$

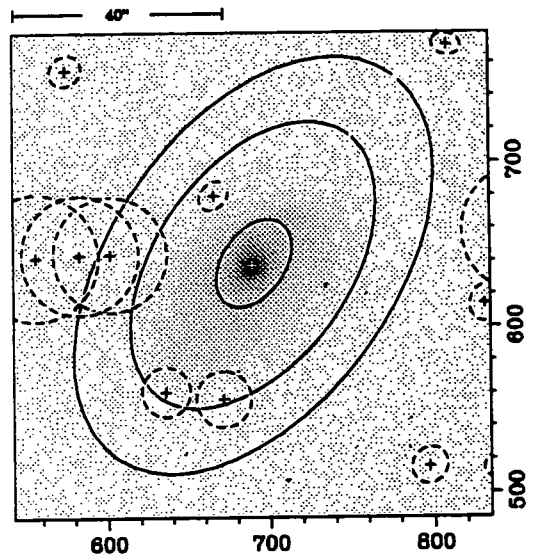
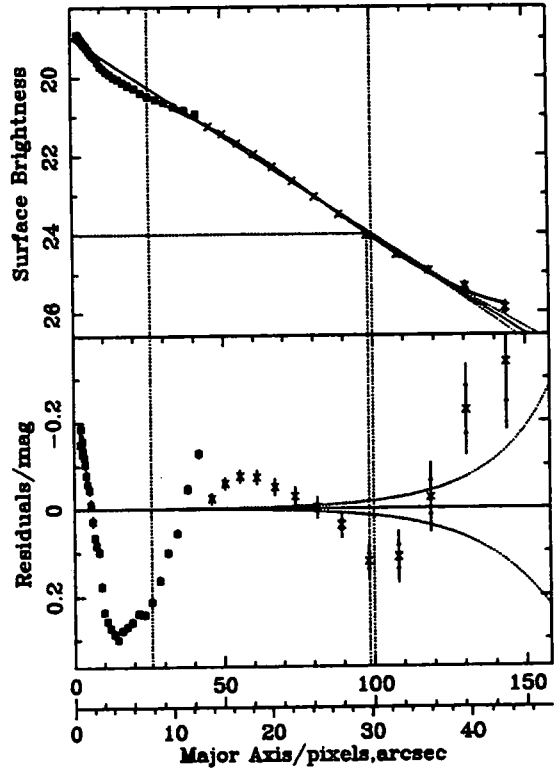
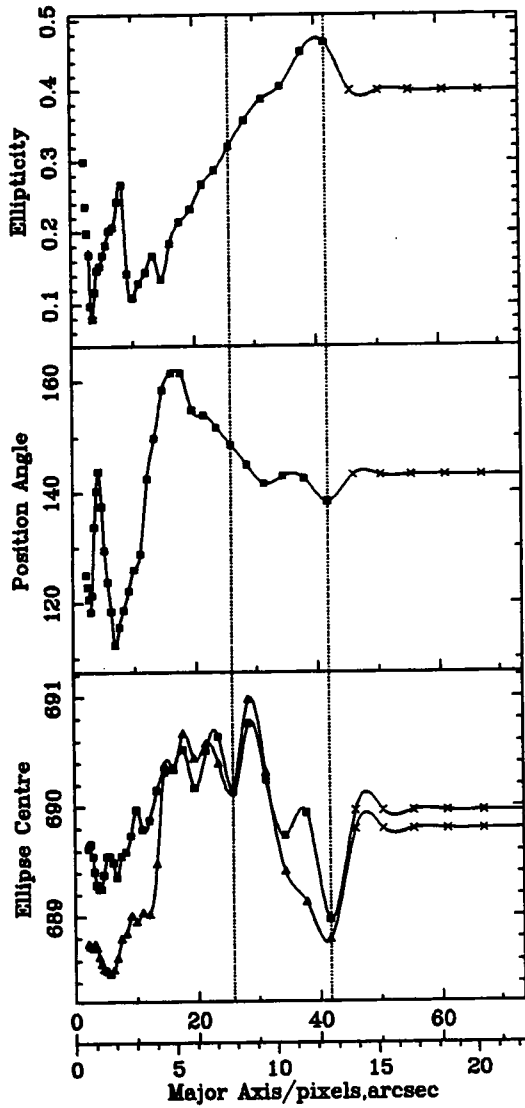


pyoung 4-May-1995 11: 7

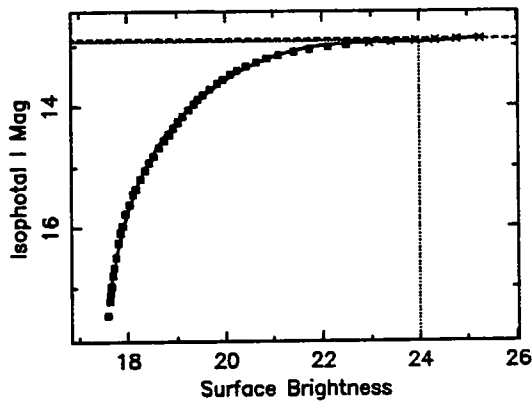
Ellipse Fitting Results For: Z224-41



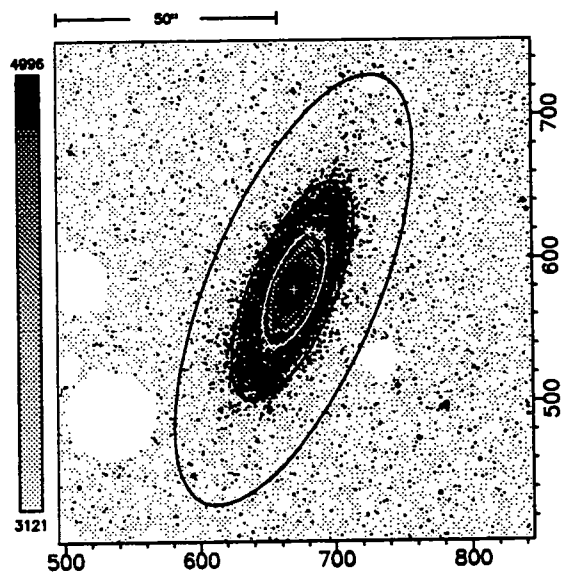
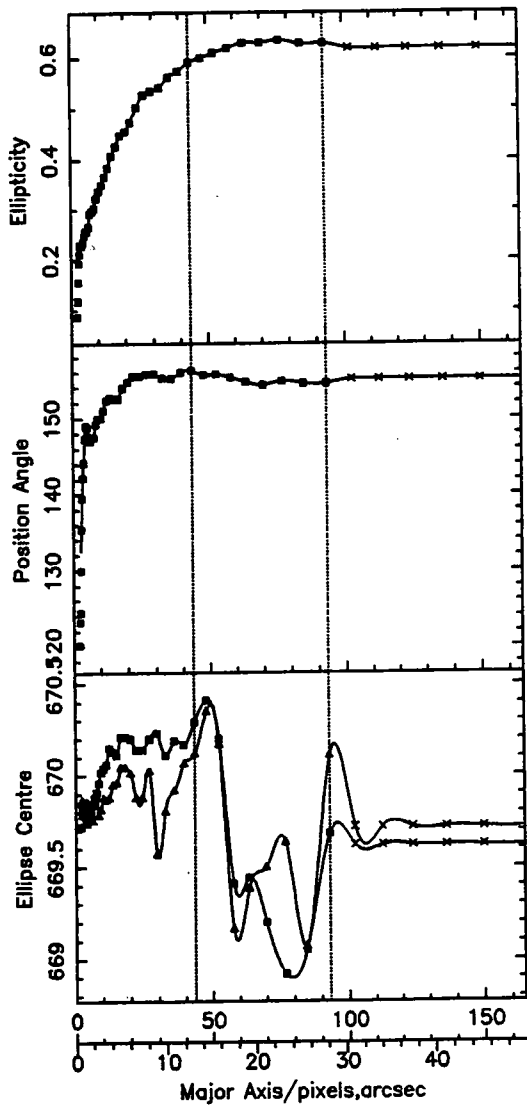
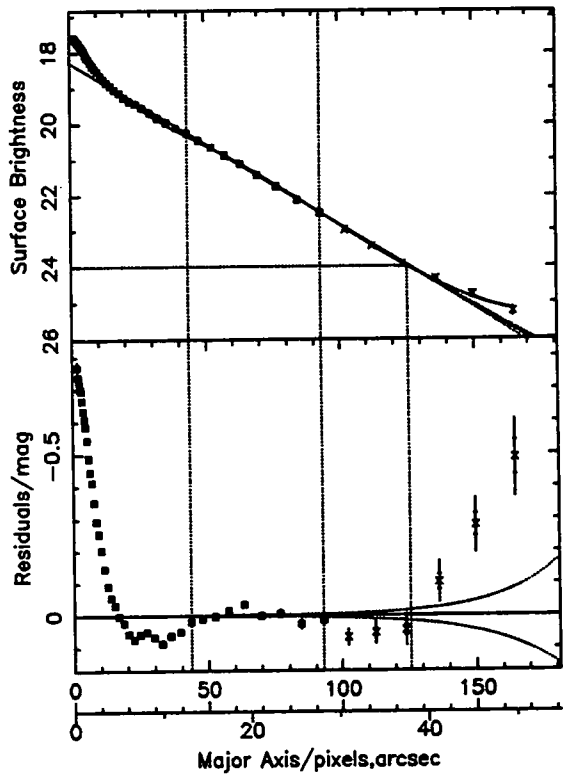
File: z224_41_r1239_clean.efot
 $L_{22.5}=13.68$ $L_{23.5}=13.57$ $L_{24.0}=13.54$ $L_T=13.51$
 $R_{22.5}=21.7''$ $\mu_0=18.96$ $R_{scale}=6.5''$



Ellipse Fitting Results For: Z224-55



$I_{22.5} = 12.99$ $I_{23.5} = 12.94$ $I_{Total} = 12.89$
 $R_{22.5} = 28.3''$ $\mu_0 = 18.27$ $R_{Scale} = 7.3''$

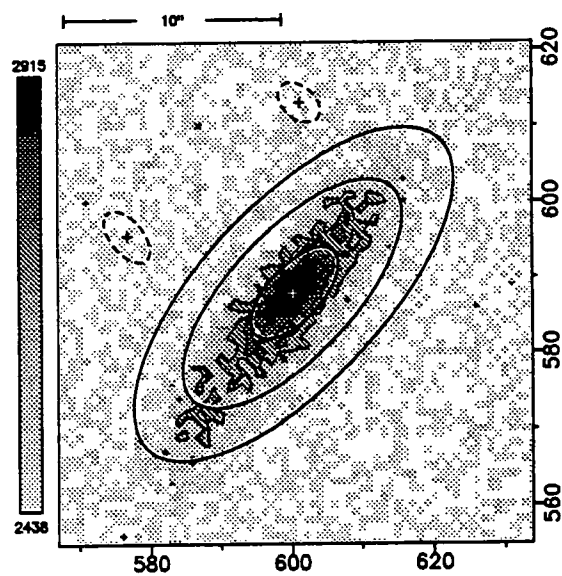
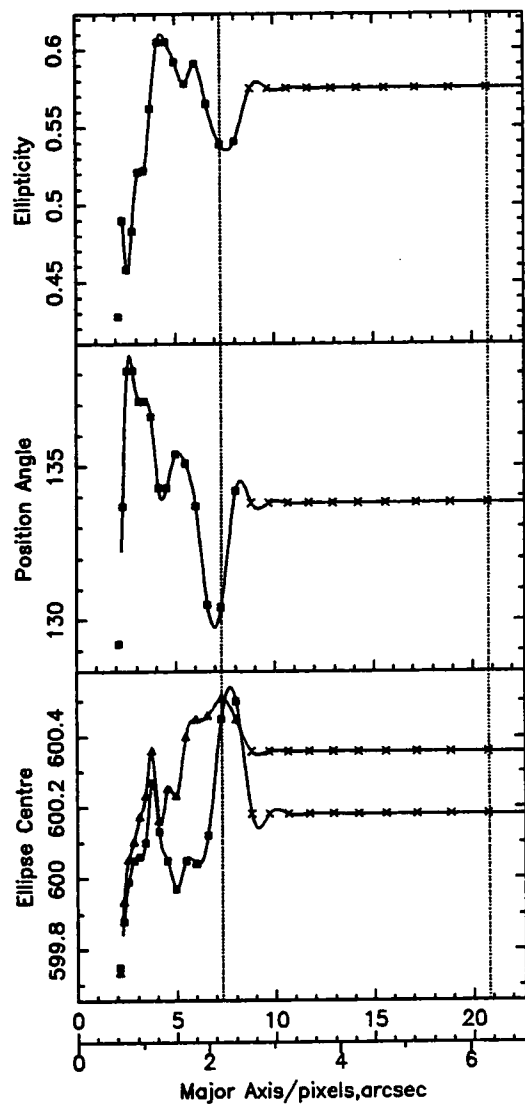
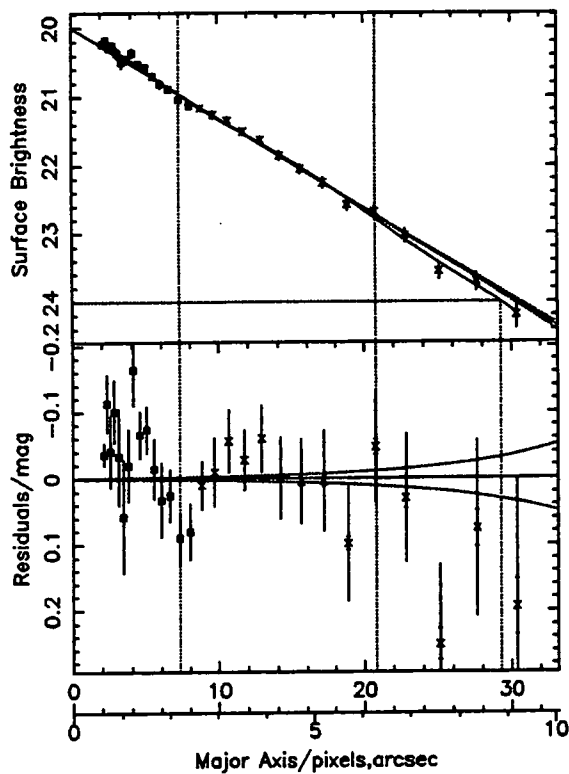
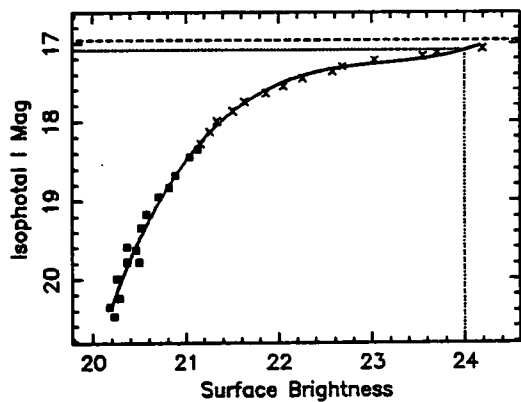


Ellipse Fitting Results For: BU200

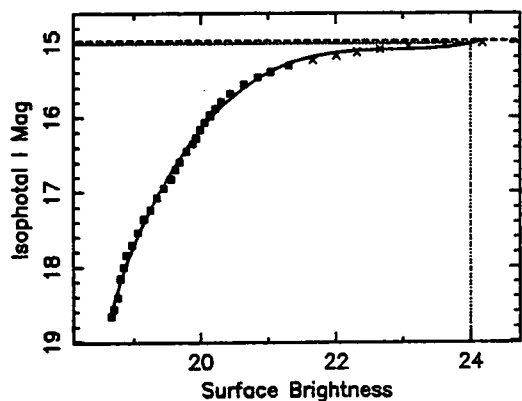
File: bu200_i2528_clean.efot

$R_{22.5}=5.7''$ $\mu_0=19.99$ $R_{Scale}=2.5''$

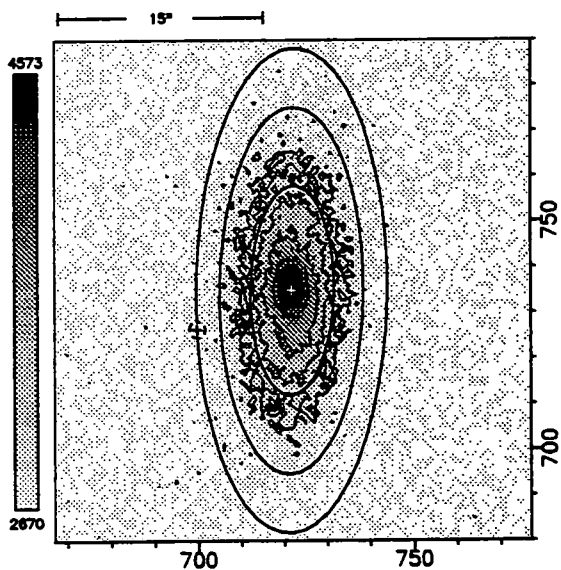
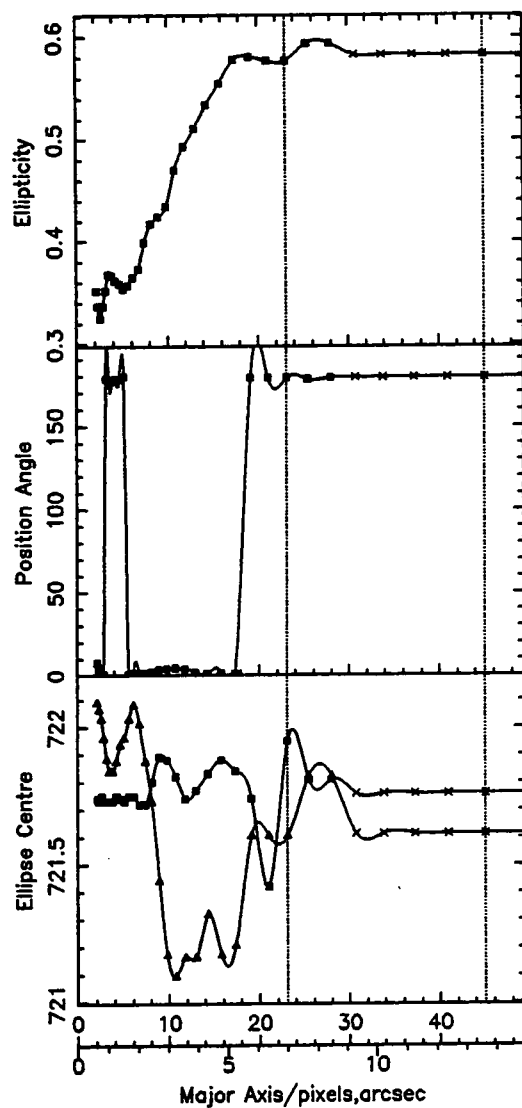
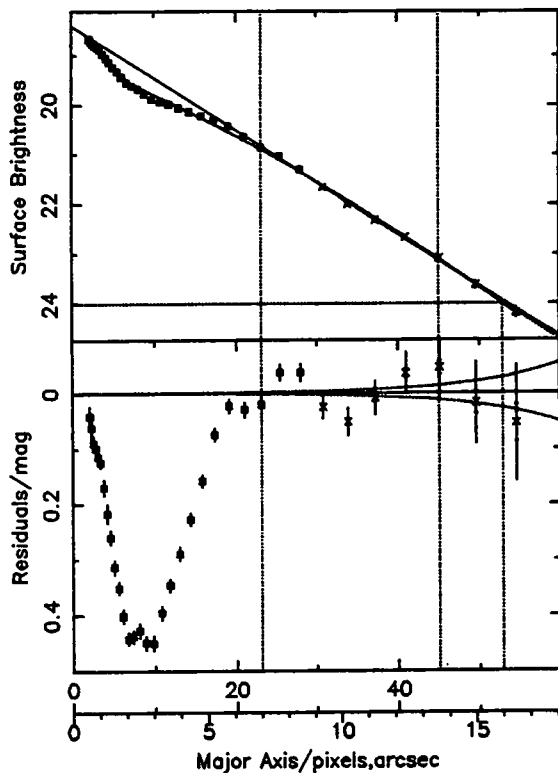
$I_{22.5}=17.38$ $I_{23.5}=17.17$ $I_{Total}=16.96$



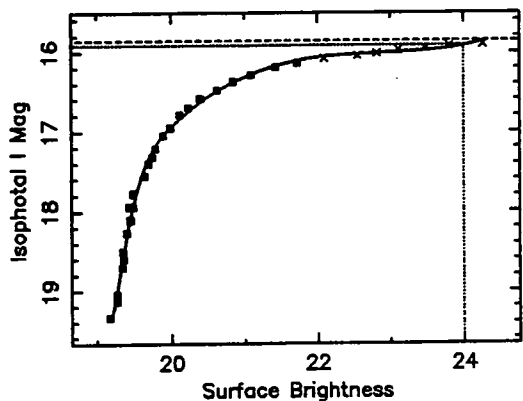
Ellipse Fitting Results For: BU91



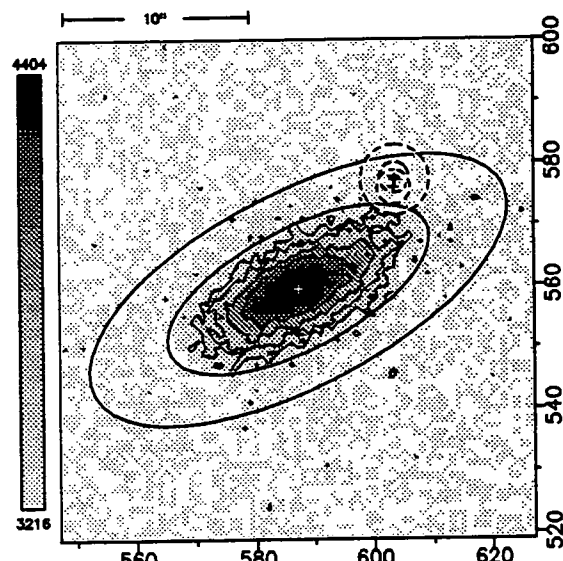
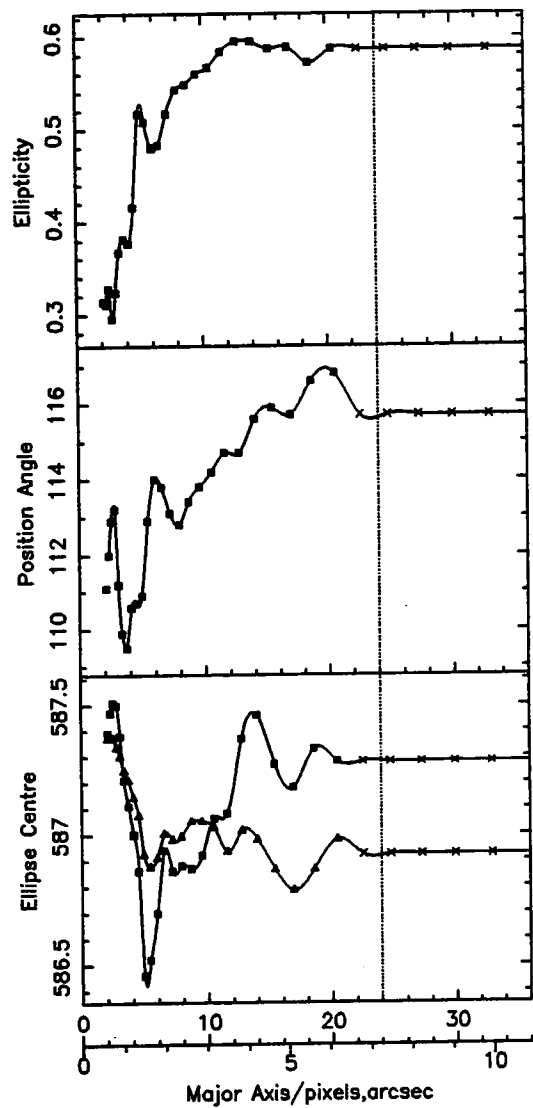
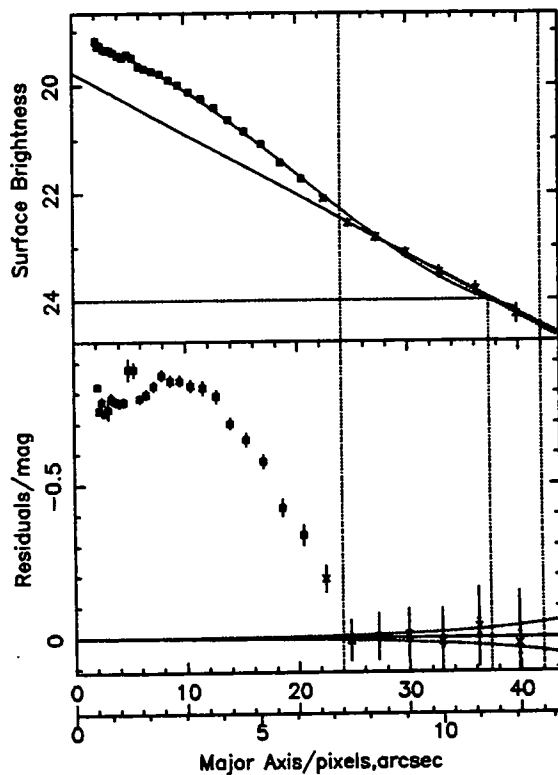
File: bu91_j2622_clean.efot
 $R_{22.5}=11.9''$ $\mu_0=18.41$ $R_{Scale}=3.1''$
 $I_{22.5}=15.11$ $I_{23.5}=15.03$ $I_{Total}=14.97$



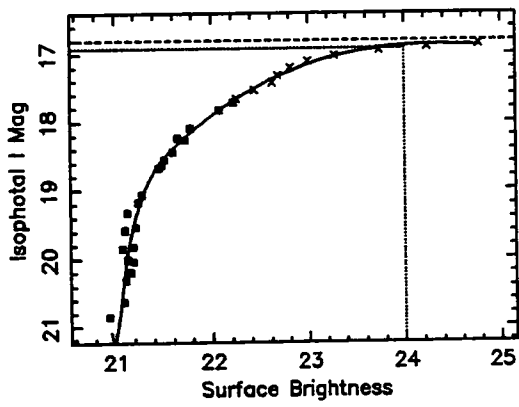
Ellipse Fitting Results For: D9



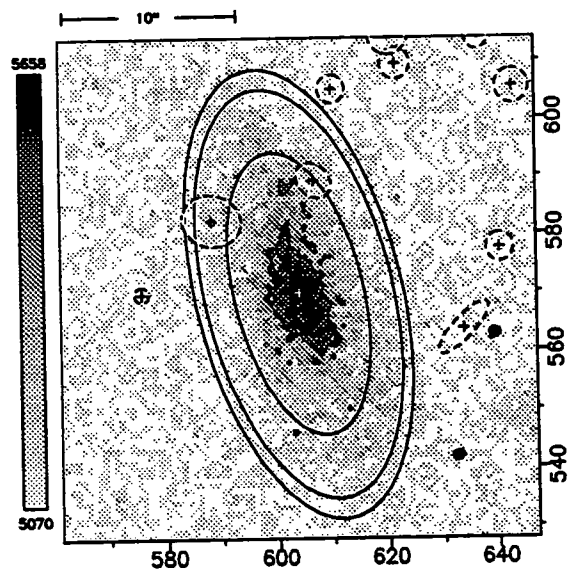
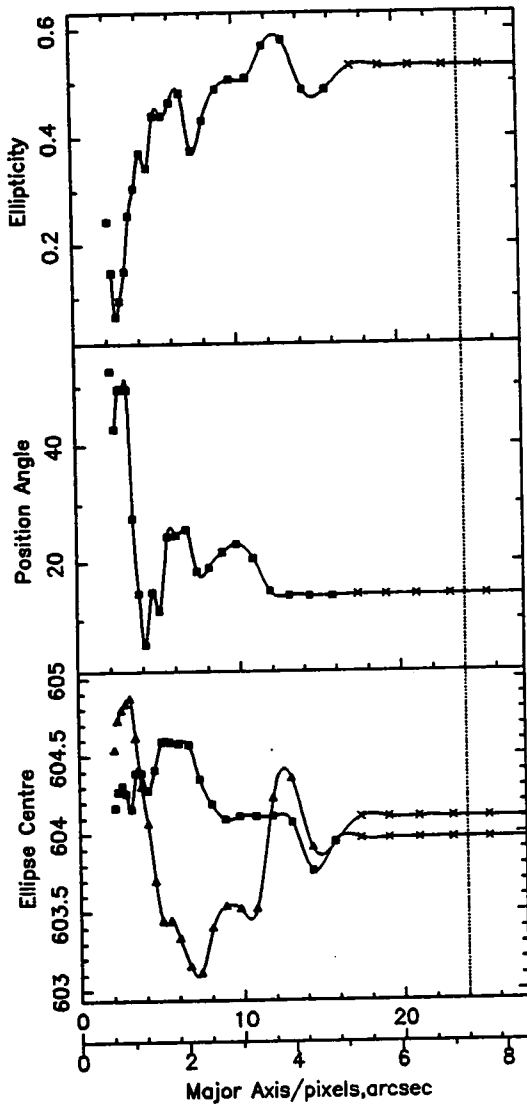
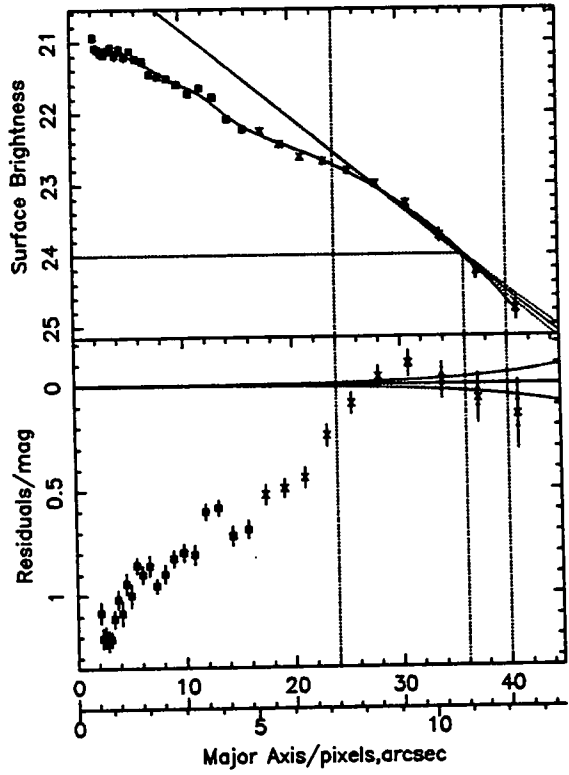
File: d9_i2522_clean.efot
 $R_{22.5} = 7.7''$ $\mu_0 = 19.76$ $R_{Scale} = 2.9''$
 $I_{22.5} = 16.05$ $I_{23.5} = 15.95$ $I_{Total} = 15.86$



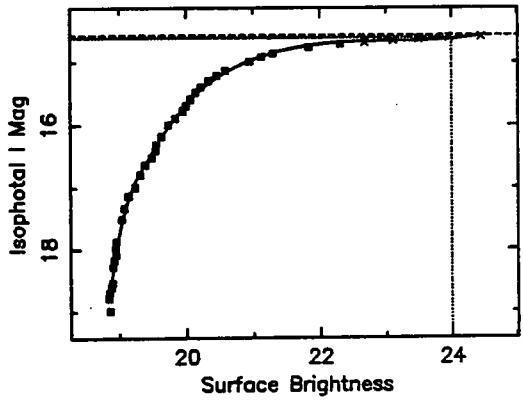
Ellipse Fitting Results For: D11



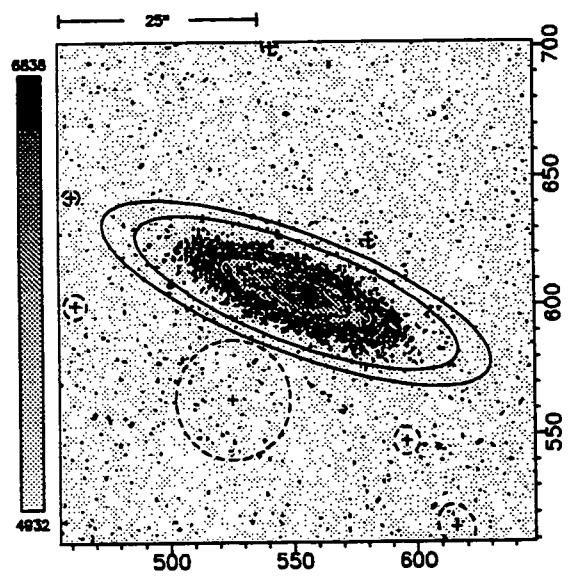
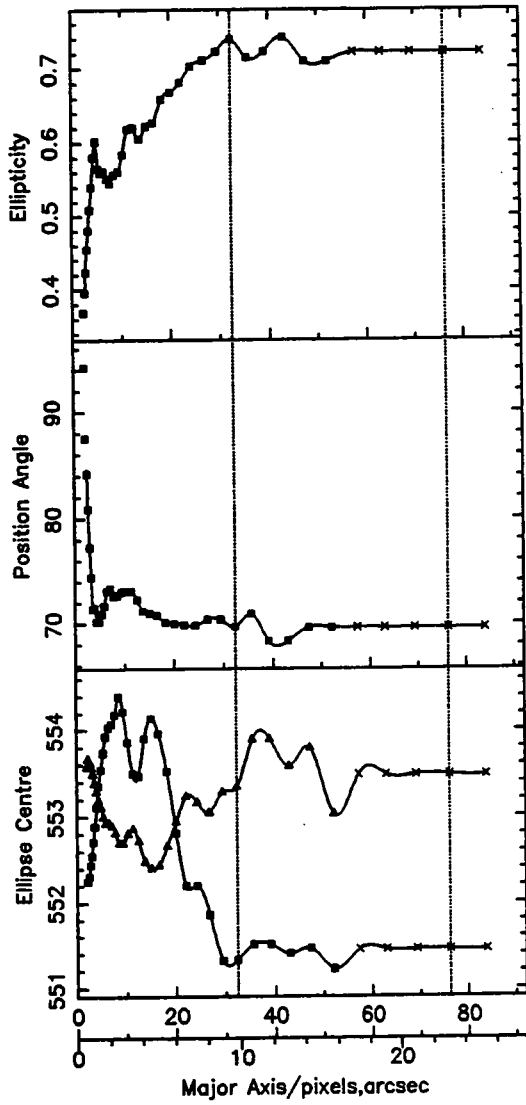
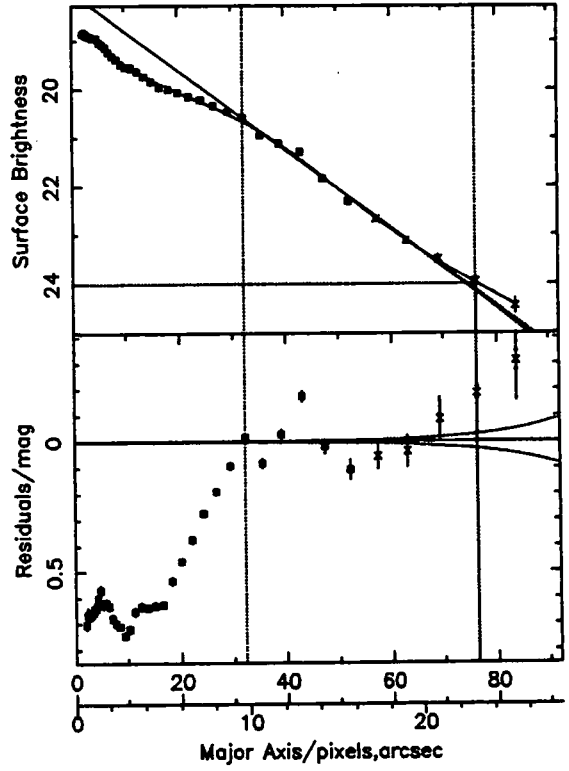
File: d11_i2320_clean.efot
 $R_{22.5}=6.2''$ $\mu_0=19.59$ $R_{Scale}=2.7''$
 $I_{22.5}=17.5$ $I_{23.5}=16.99$ $I_{Total}=16.8$



Ellipse Fitting Results For: D21



File: d21_j2723_clean.efot
 $R_{22.5} = 16.8''$ $\mu_0 = 17.99$ $R_{Scale} = 4.1''$
 $I_{22.5} = 14.7$ $I_{23.5} = 14.63$ $I_{Total} = 14.57$

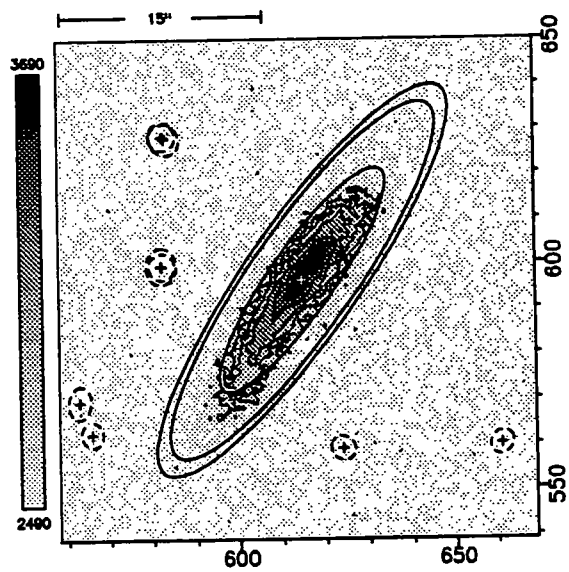
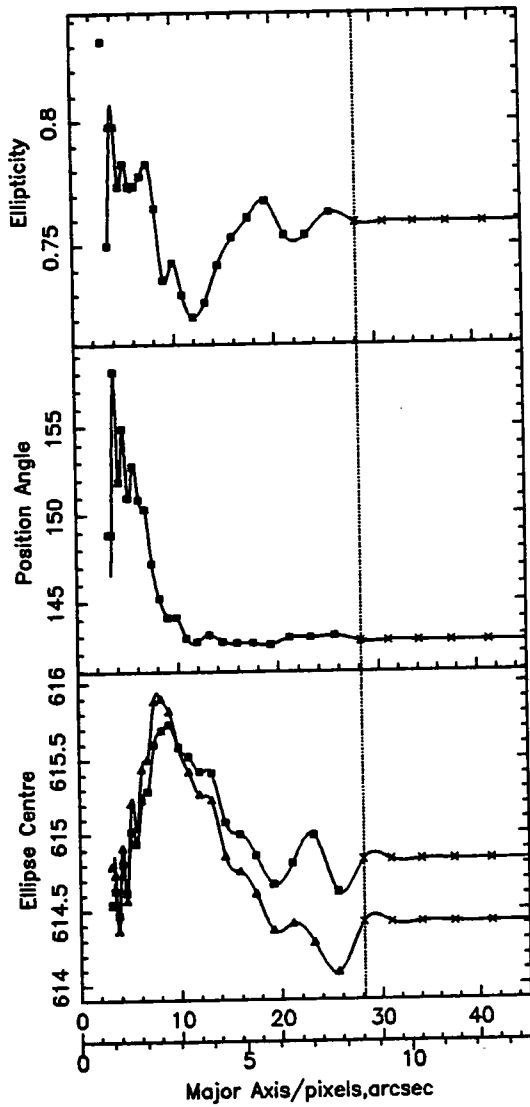
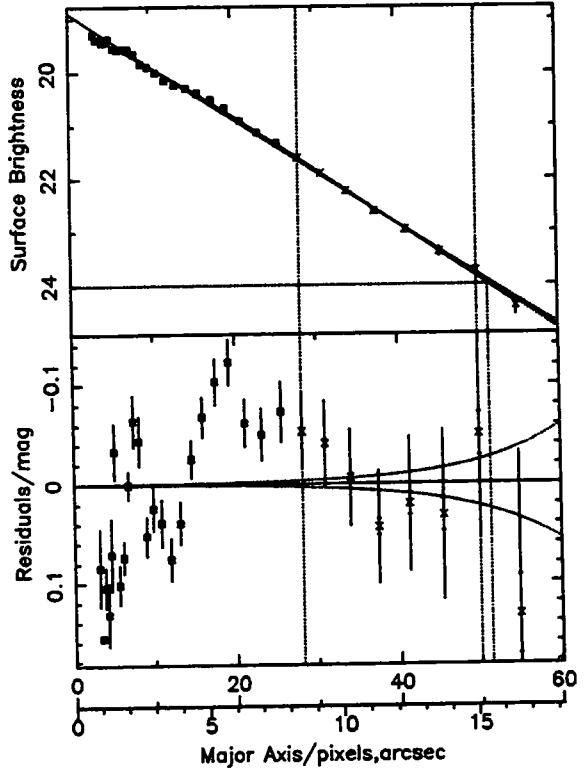
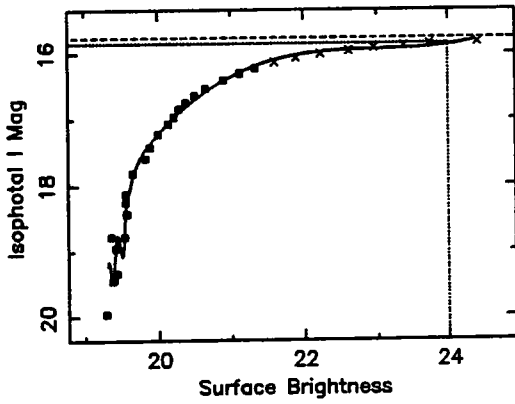


Ellipse Fitting Results For: D39

File: d39_i2529_clean.efot

$R_{22.5}=11.2''$ $\mu_0=18.89$ $R_{Scale}=3.4''$

$I_{22.5}=15.97$ $I_{23.5}=15.87$ $I_{Total}=15.76$



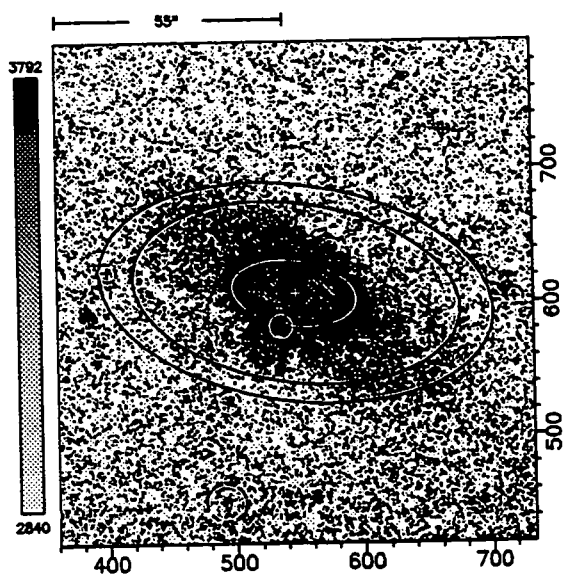
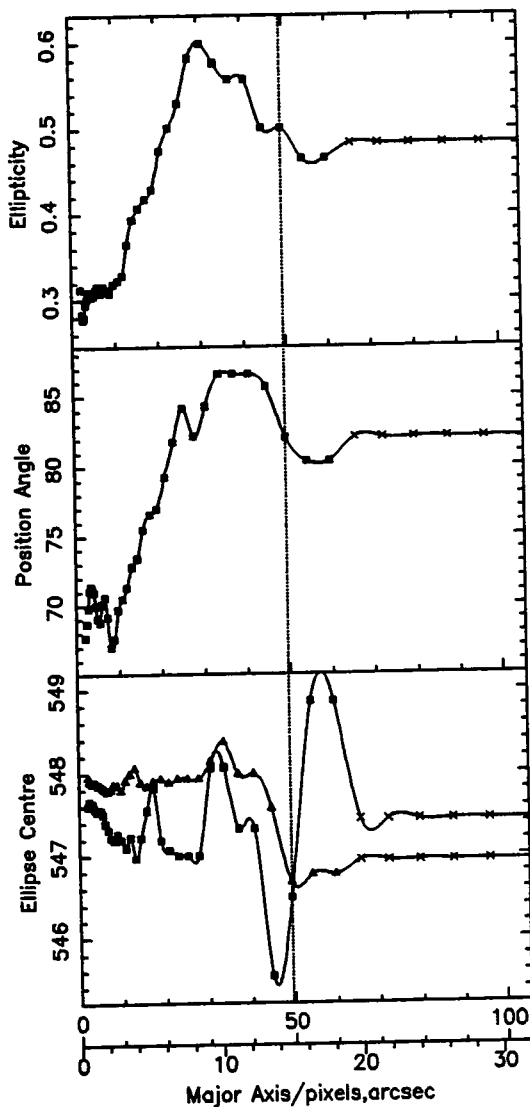
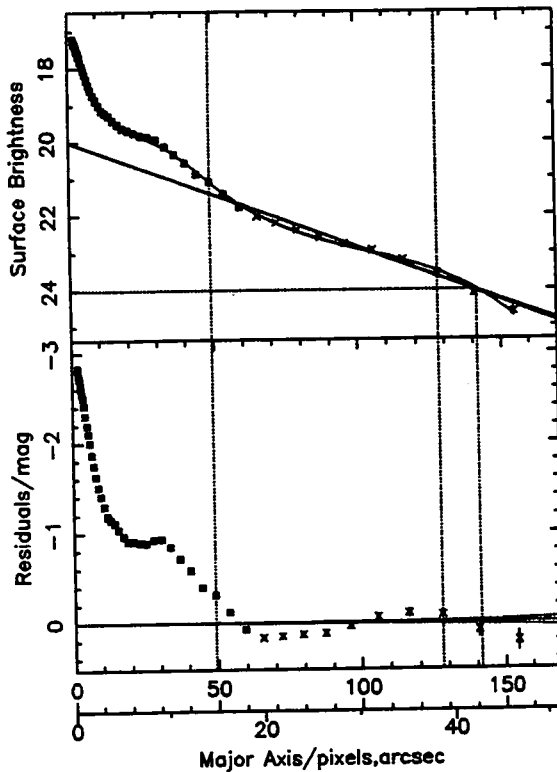
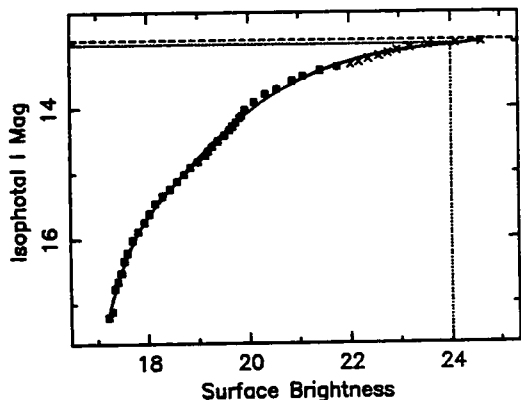
pyoung 3-May-1995 0:47

Ellipse Fitting Results For: D67

File: d67_j2721_clean.efot

$R_{22.5}=24.7''$ $\mu_0=19.99$ $R_{Scale}=11.5''$

$I_{22.5}=13.23$ $I_{23.5}=13.05$ $I_{Total}=12.96$

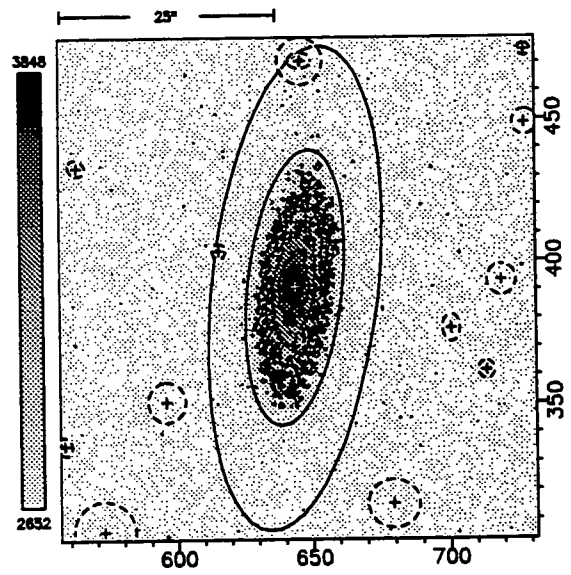
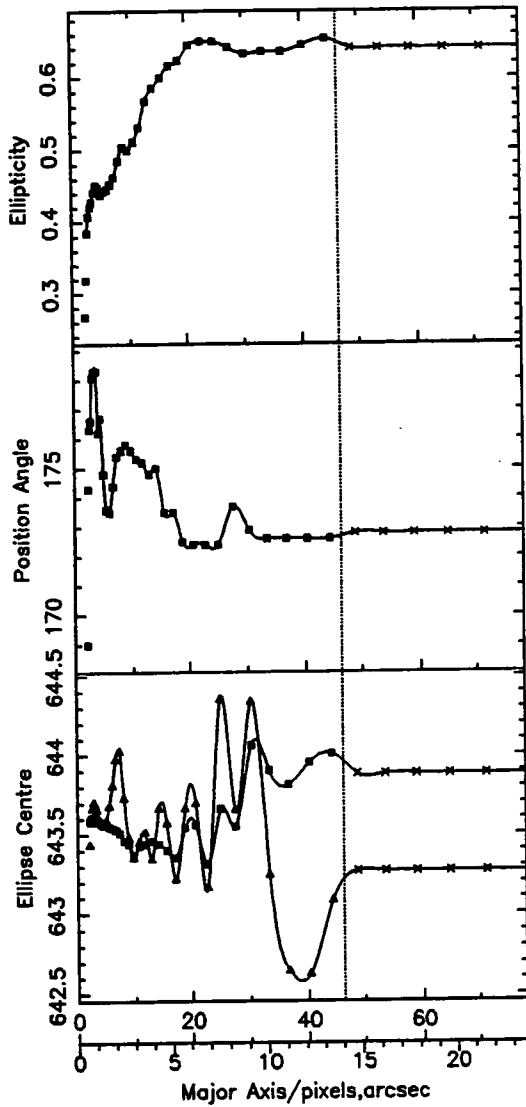
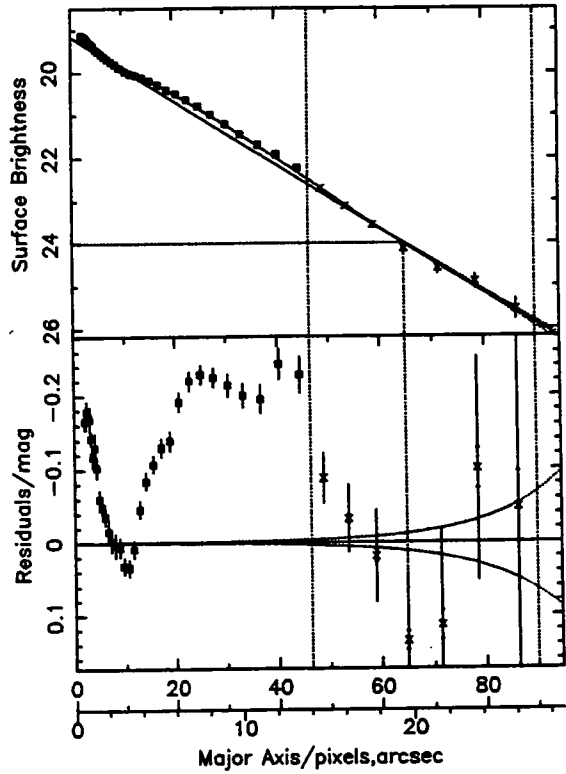
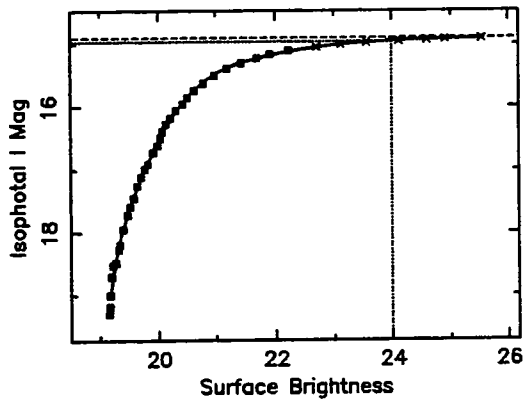


Ellipse Fitting Results For: D123

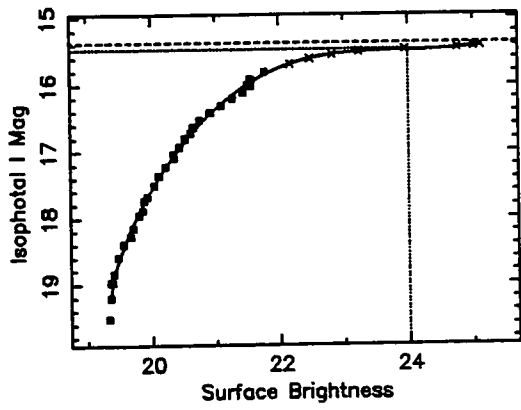
File: d123_i2531_clean.efot

$R_{22.5}=14.1''$ $\mu_0=19.16$ $R_{Scale}=4.4''$

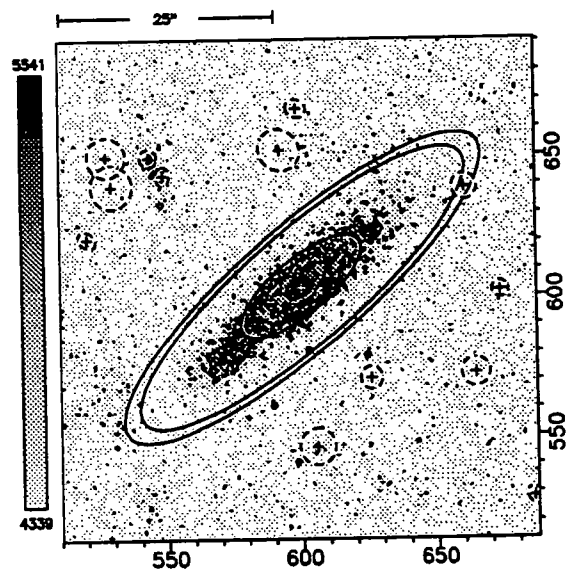
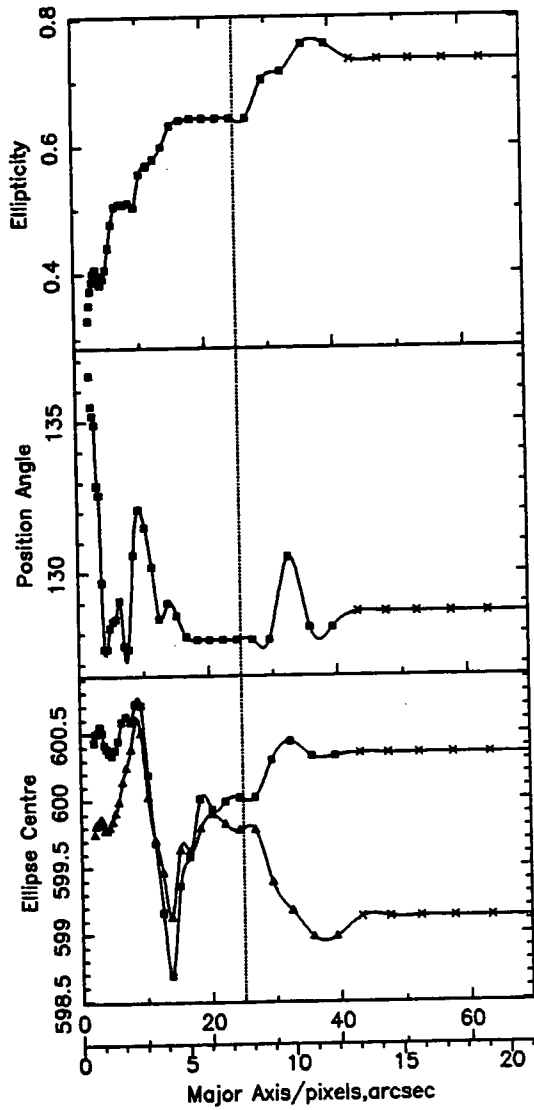
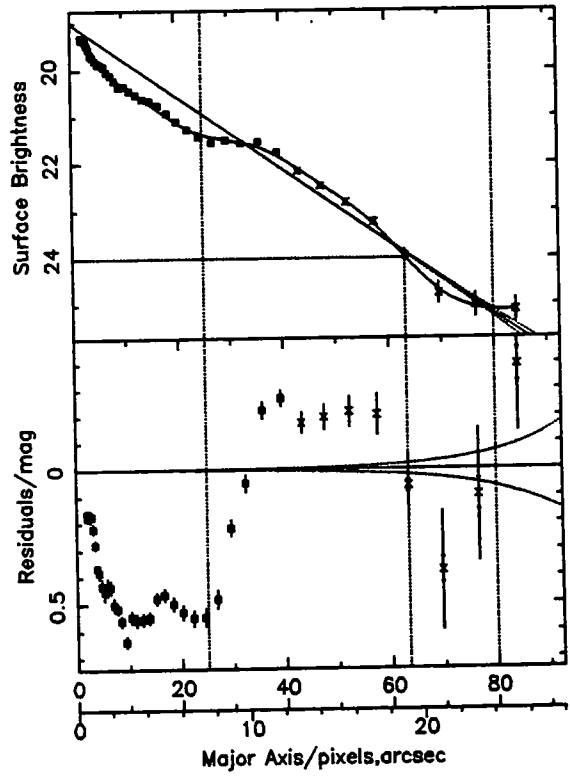
$I_{22.5}=15.07$ $I_{23.5}=14.98$ $I_{Total}=14.9$



Ellipse Fitting Results For: D129



File: d129_i2730_clean.efot
 $R_{22.5}=14.7''$ $\mu_0=19$ $R_{Scale}=4.3''$
 $I_{22.5}=15.61$ $I_{23.5}=15.5$ $I_{Total}=15.37$

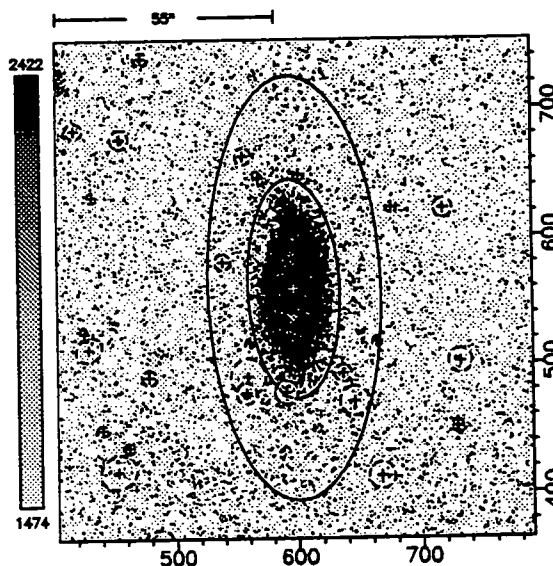
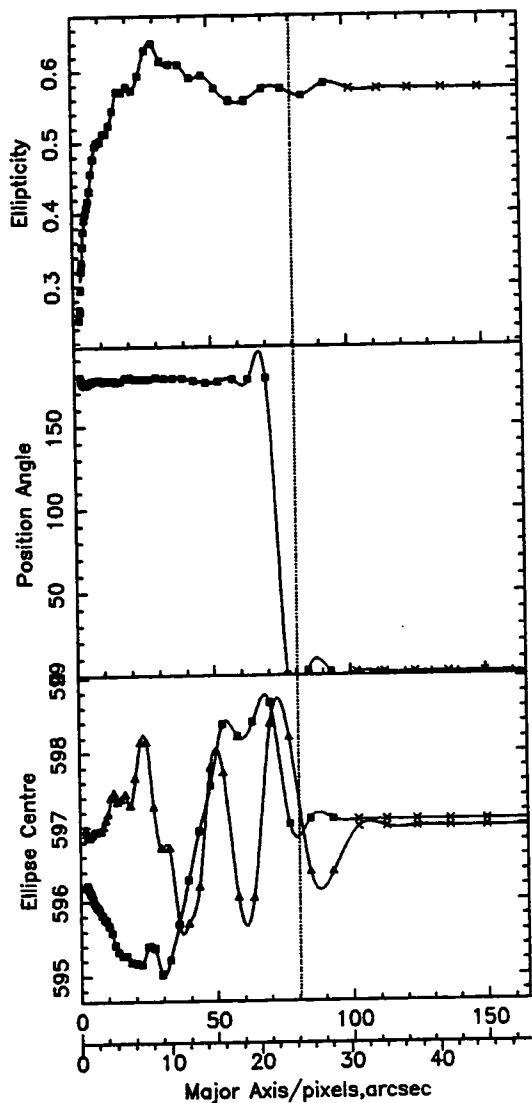
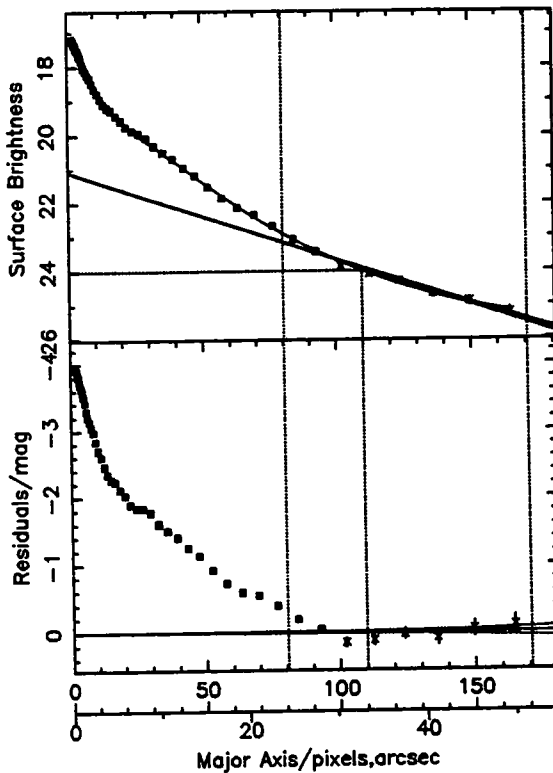
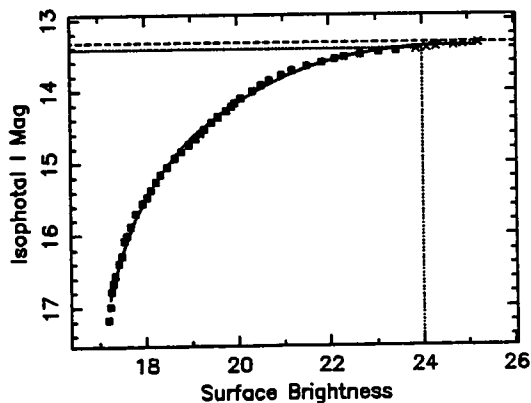


Ellipse Fitting Results For: U12626

File: u12626_i2523_clean.efot

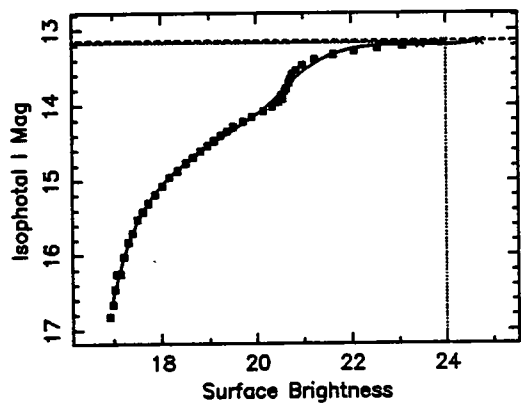
$R_{22.5} = 21.8''$ $\mu_0 = 21.08$ $R_{Scale} = 12.7''$

$I_{22.5} = 13.51$ $I_{23.5} = 13.44$ $I_{Total} = 13.32$

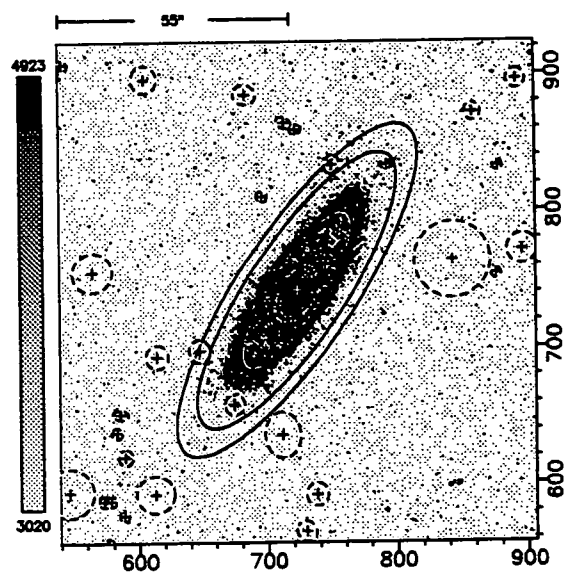
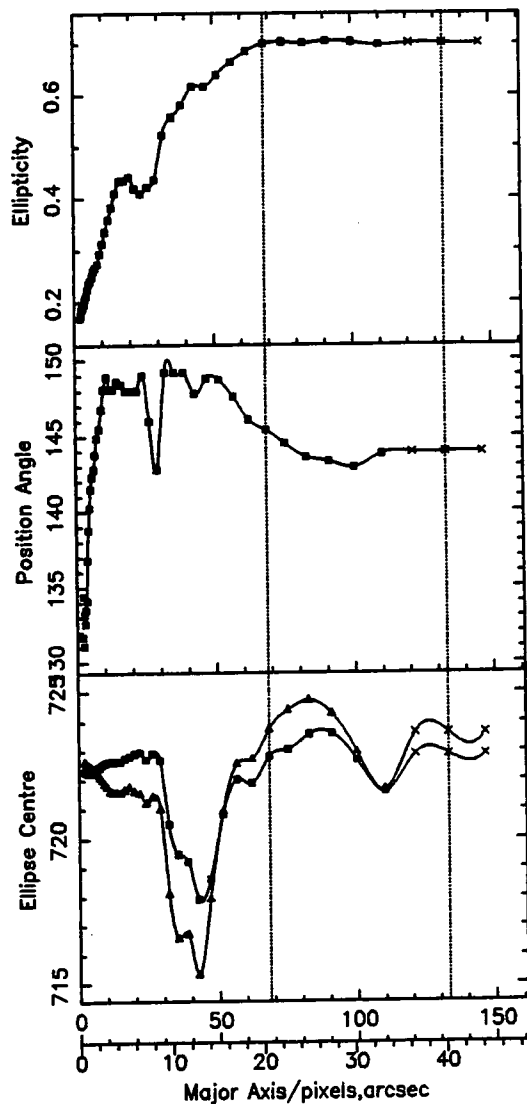
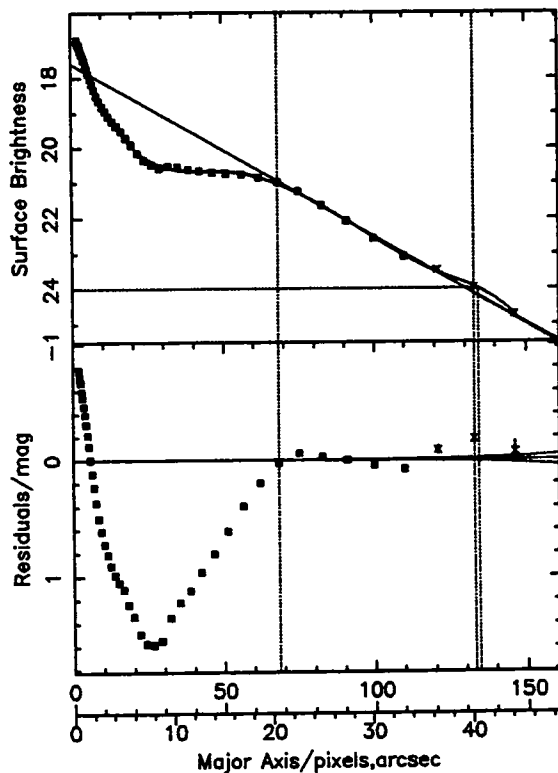


pyoung 4-May-1995 11:23

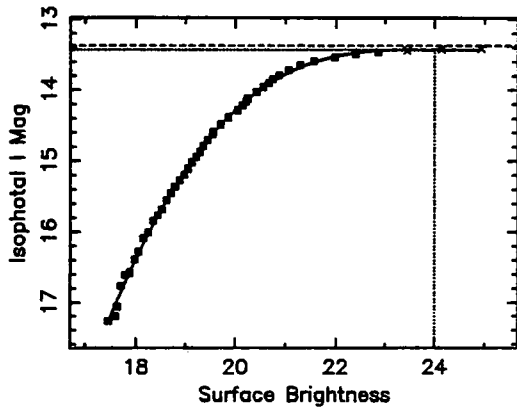
Ellipse Fitting Results For: U12631



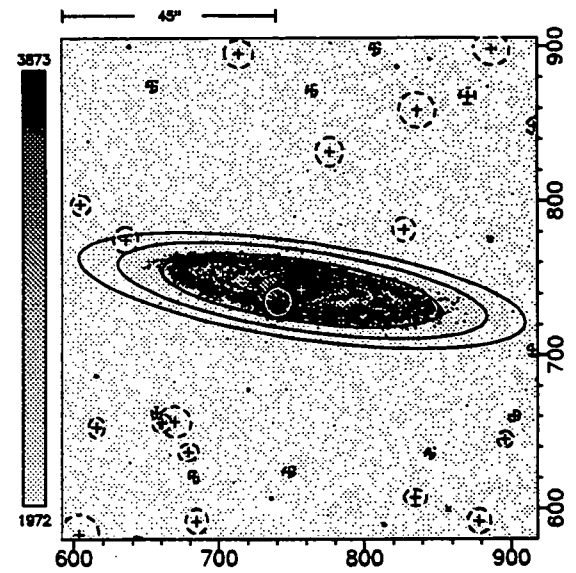
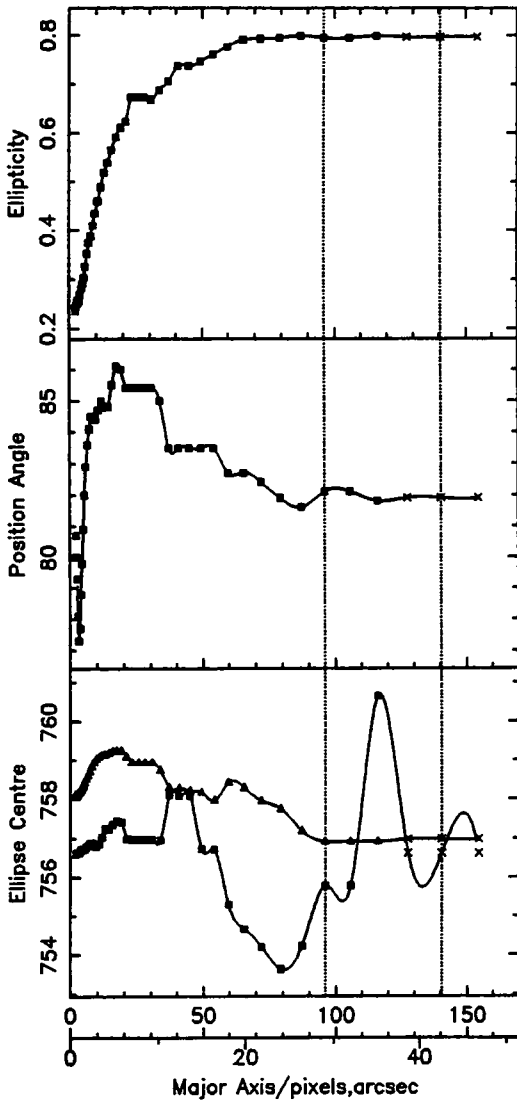
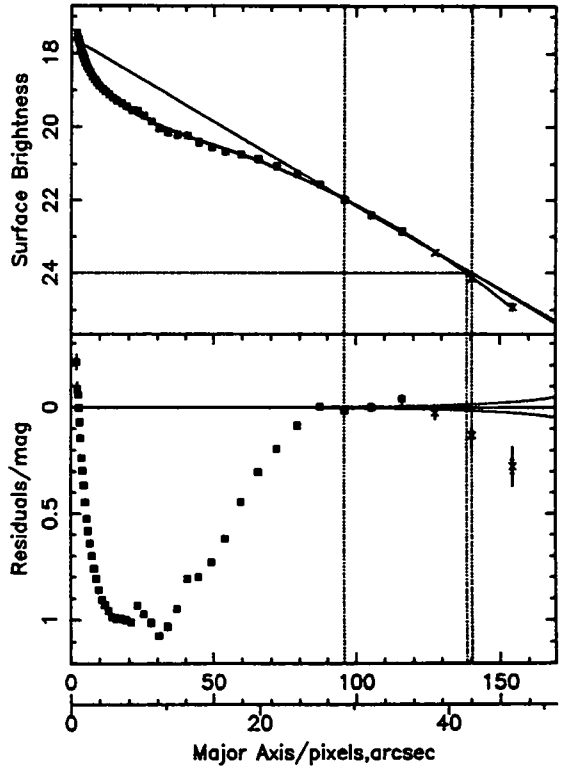
File: u12631_i2621_clean.efot
 $R_{22.5} = 30.1''$ $\mu_0 = 17.6$ $R_{Scale} = 6.7''$
 $I_{22.5} = 13.25$ $I_{23.5} = 13.19$ $I_{Total} = 13.14$



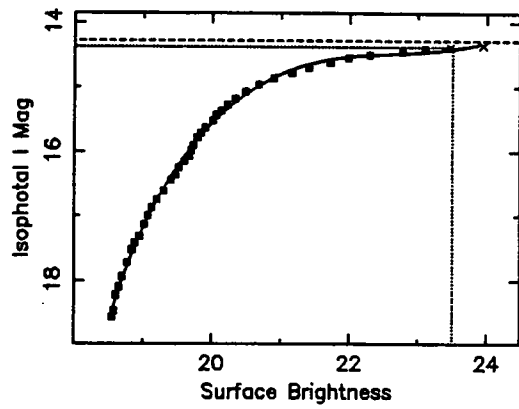
Ellipse Fitting Results For: U12678



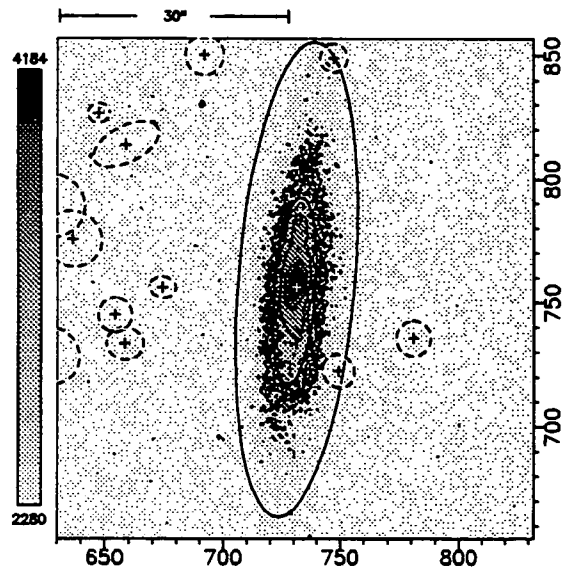
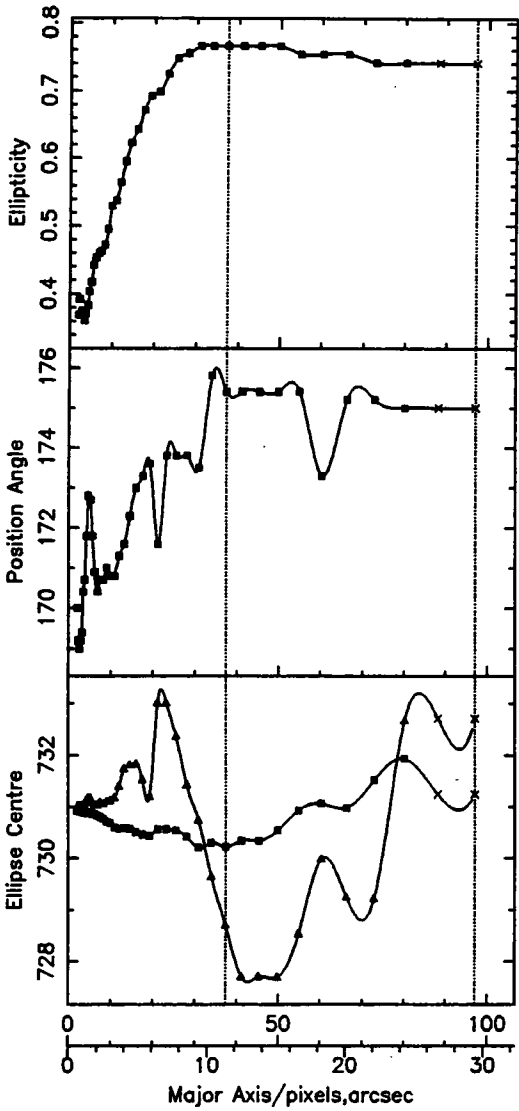
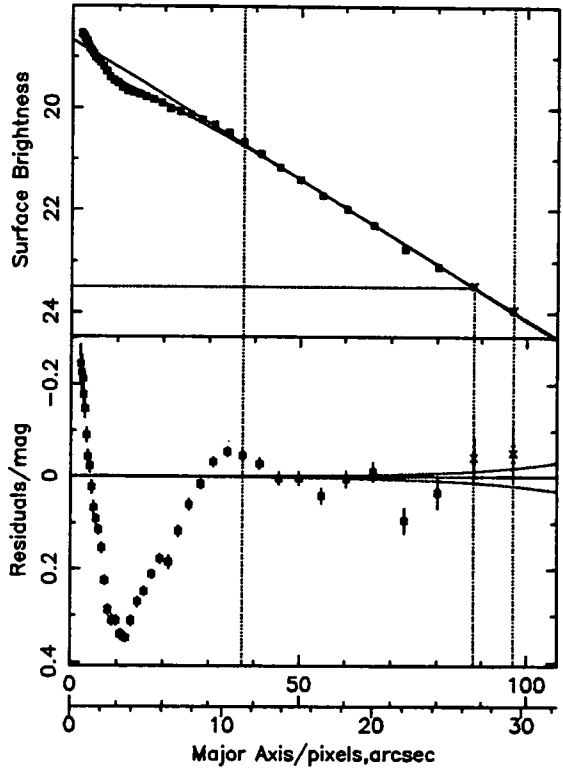
File: u12678_i2626_clean.efot
 $R_{22.5}=33''$ $\mu_0=17.57$ $R_{Scale}=7.2''$
 $I_{22.5}=13.49$ $I_{23.5}=13.44$ $I_{Total}=13.37$



Ellipse Fitting Results For: U12701



File: u12701_j2624_clean.efot
 $R_{22.5} = 21.2''$ $\mu_0 = 18.67$ $R_{Scale} = 6''$
 $I_{22.5} = 14.48$ $I_{23.5} = 14.38$ $I_{Total} = 14.28$

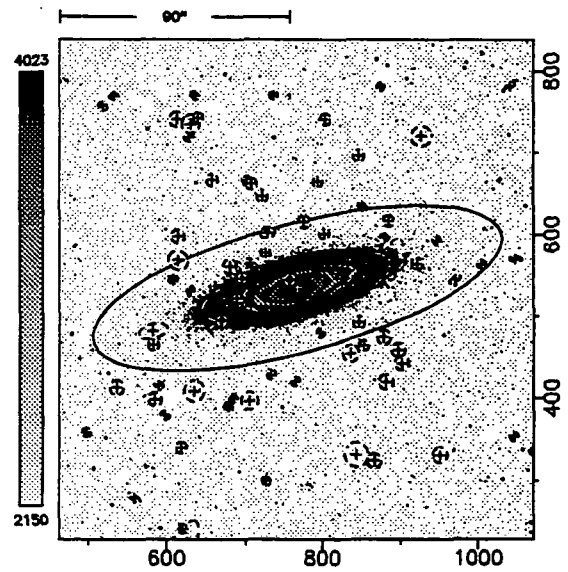
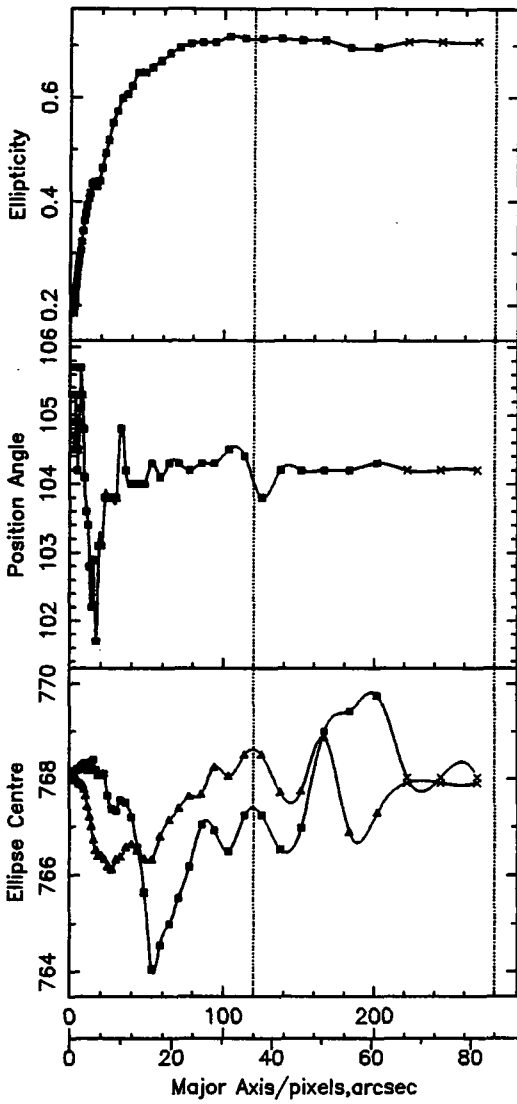
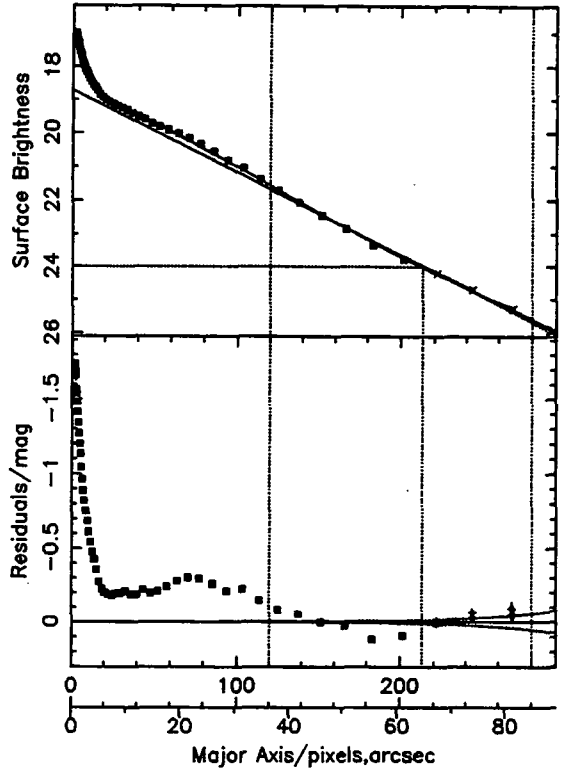
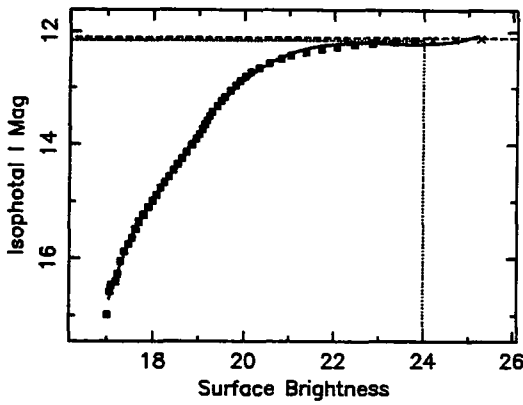


Ellipse Fitting Results For: 0120-0139

File: 0120_0139_i2337_clean.efot

$R_{22.5}=46.9''$ $\mu_0=18.7$ $R_{Scale}=13.3''$

$I_{22.5}=12.23$ $I_{23.5}=12.17$ $I_{Total}=12.1$

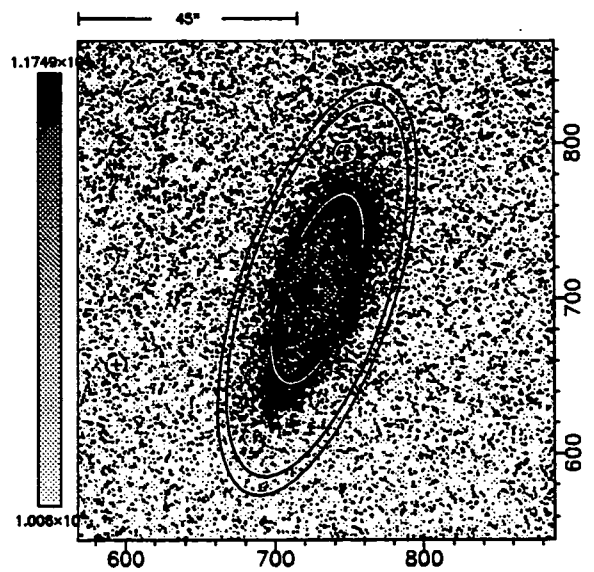
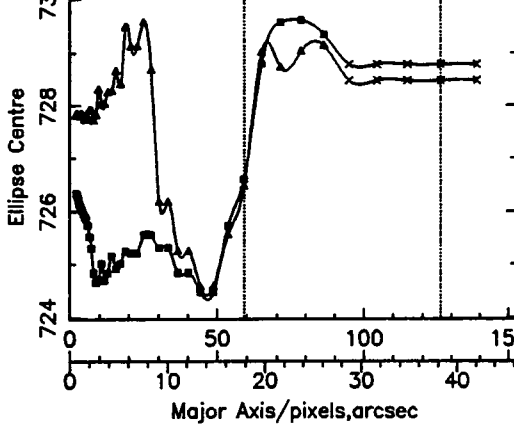
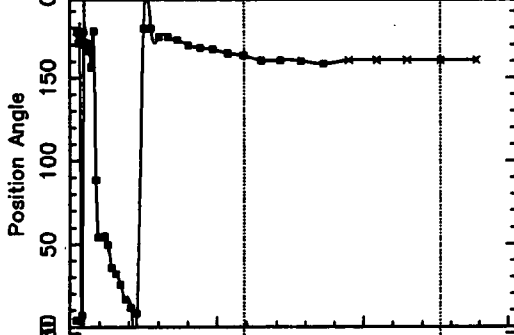
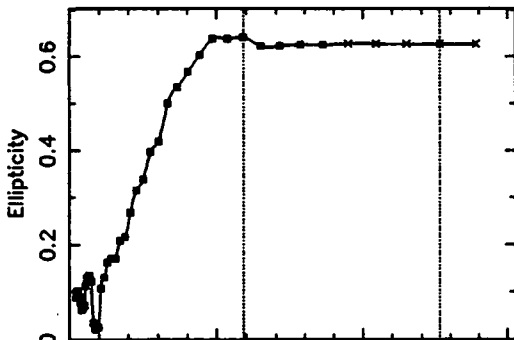
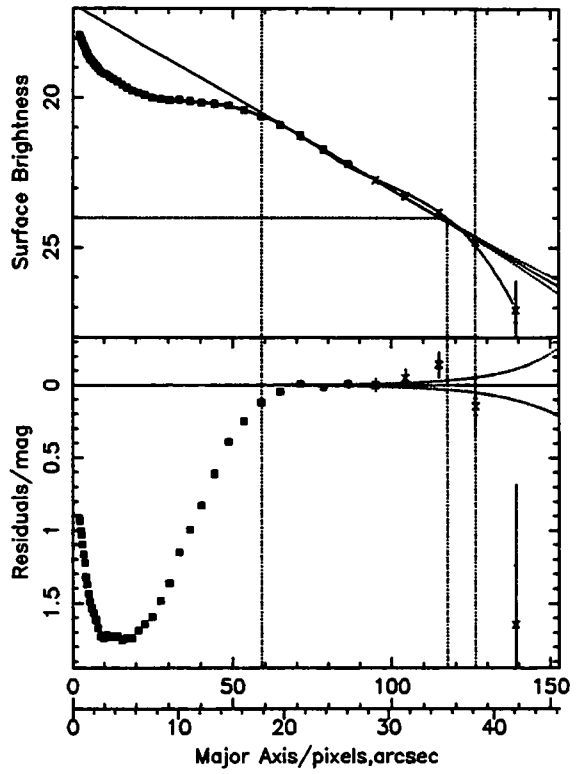
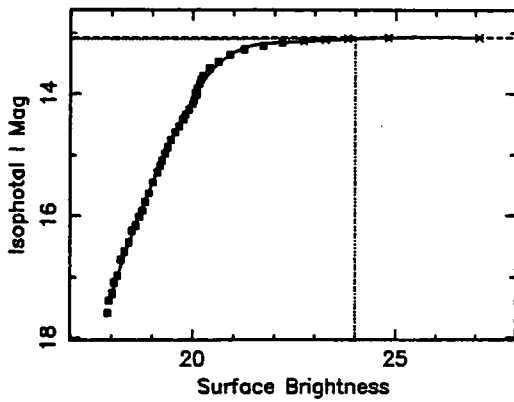


Ellipse Fitting Results For: 0120-0214

File: 0120_0214_i2135_clean.efot

$R_{22.5} = 27.5''$ $\mu_0 = 16.86$ $R_{Scale} = 5.3''$

$I_{22.5} = 13.15$ $I_{23.5} = 13.1$ $I_{Total} = 13.07$

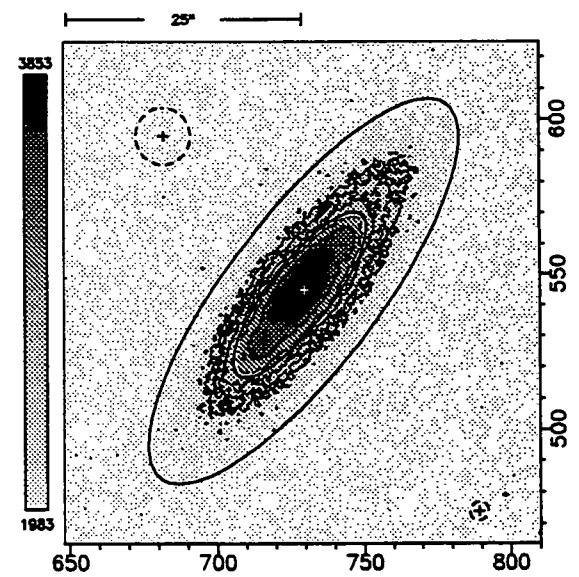
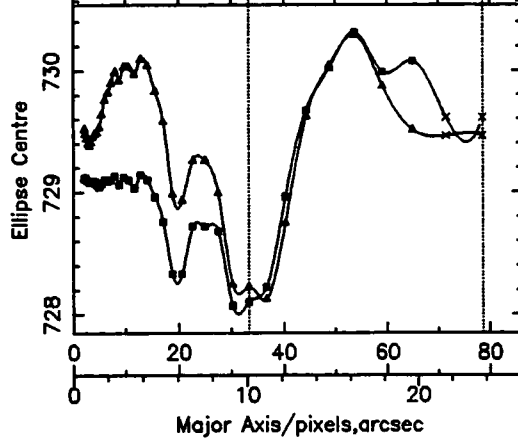
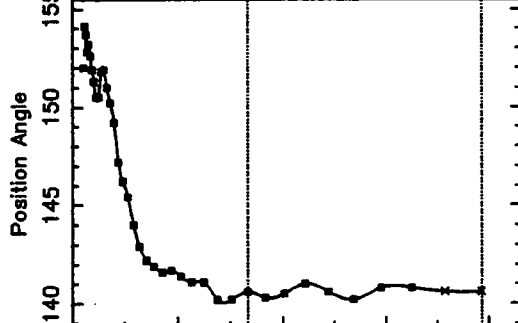
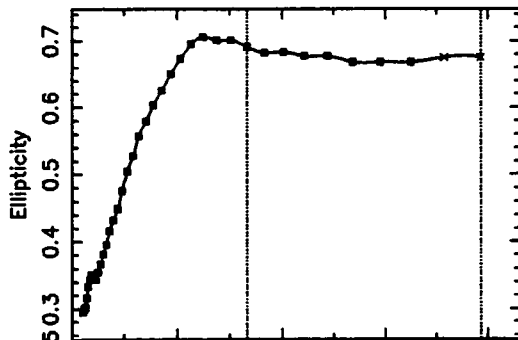
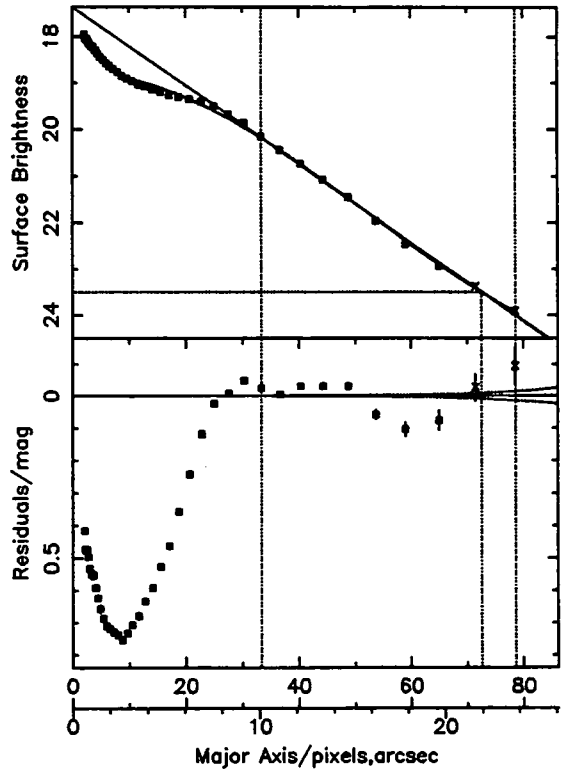
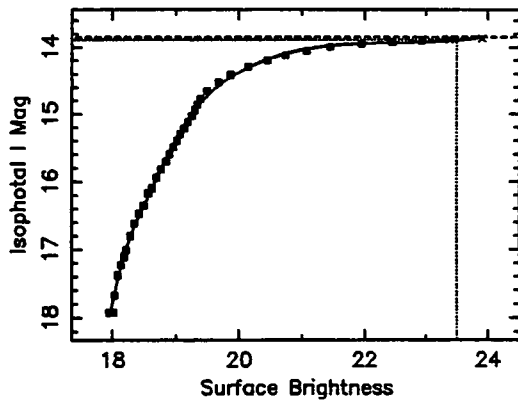


Ellipse Fitting Results For: 0123-0203

File: 0123_0203_i2334_clean.efot

$R_{22.5}=18.3''$ $\mu_0=17.35$ $R_{Scale}=3.9''$

$I_{22.5}=13.92$ $I_{23.5}=13.88$ $I_{Total}=13.85$

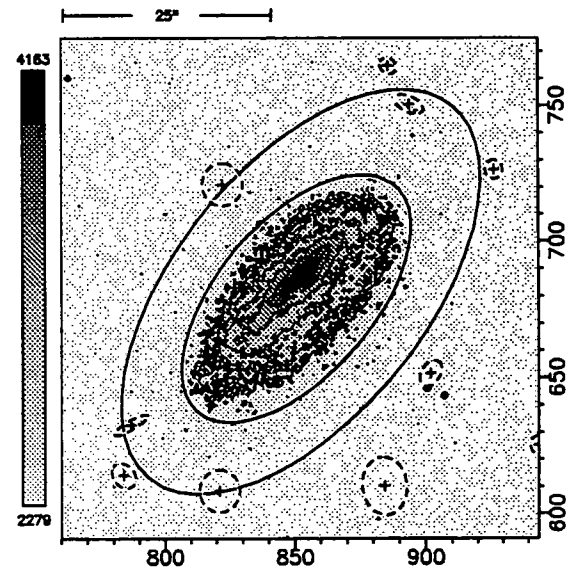
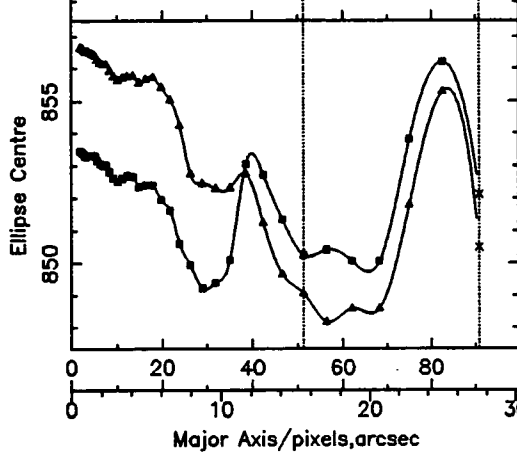
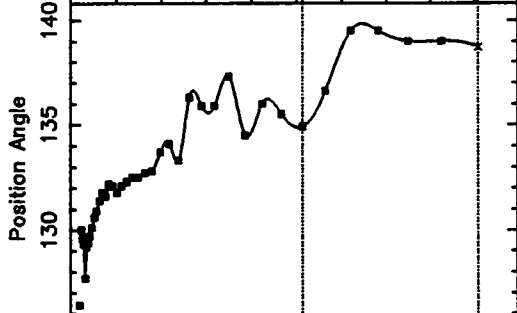
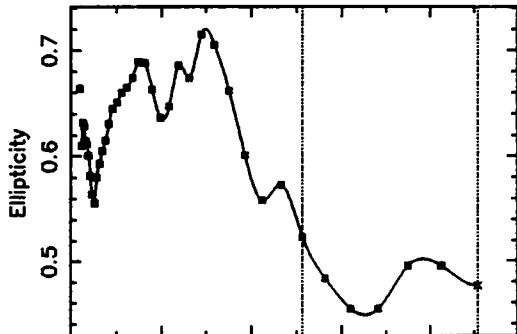
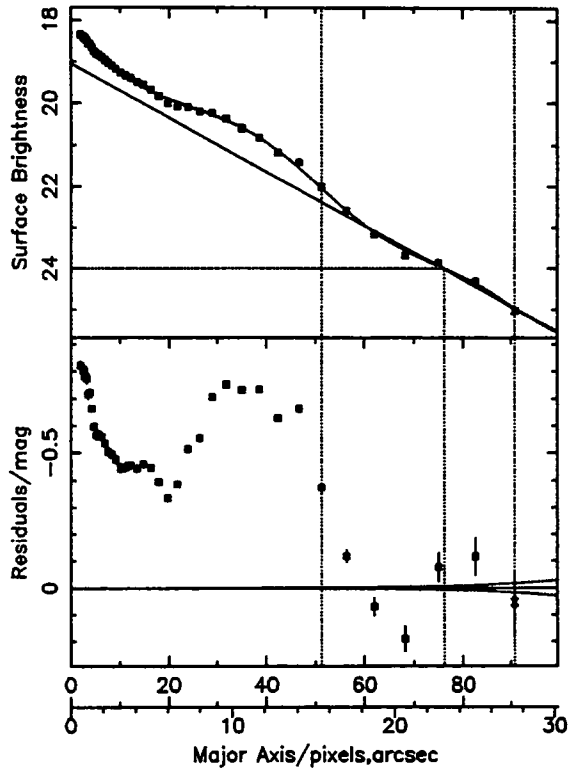
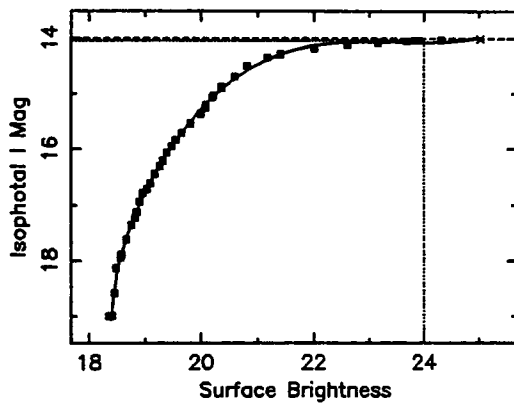


Ellipse Fitting Results For: 0124-0133

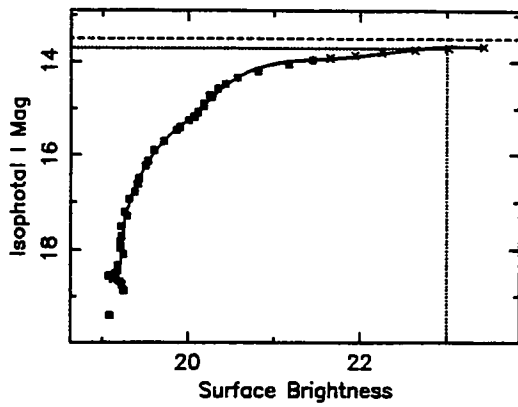
File: 0124_0133_i2627_clean.efot

$R_{22.5} = 16.8''$ $\mu_0 = 19.04$ $R_{Scale} = 5''$

$I_{22.5} = 14.13$ $I_{23.5} = 14.06$ $I_{Total} = 13.99$



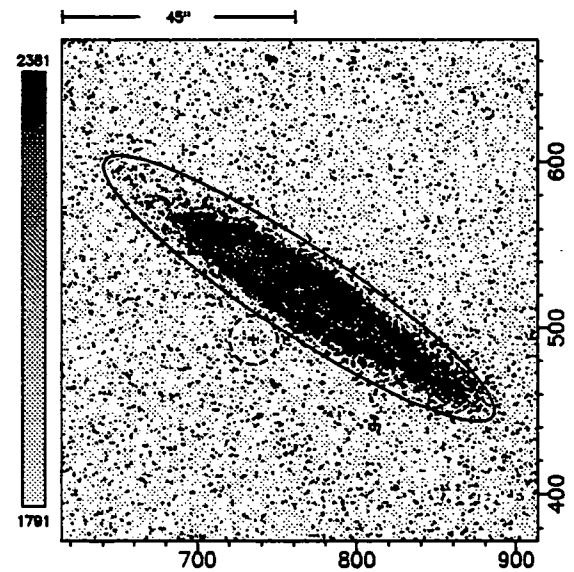
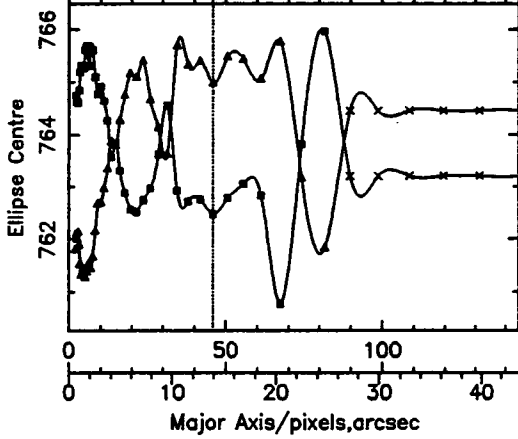
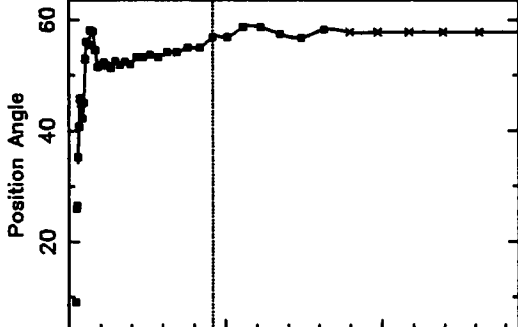
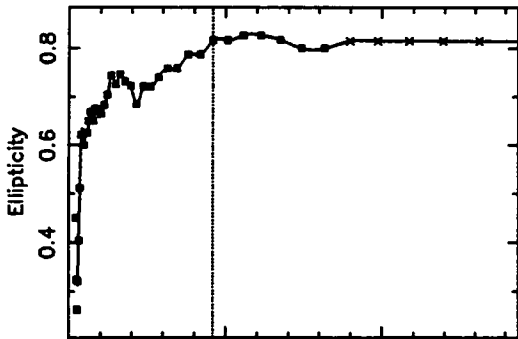
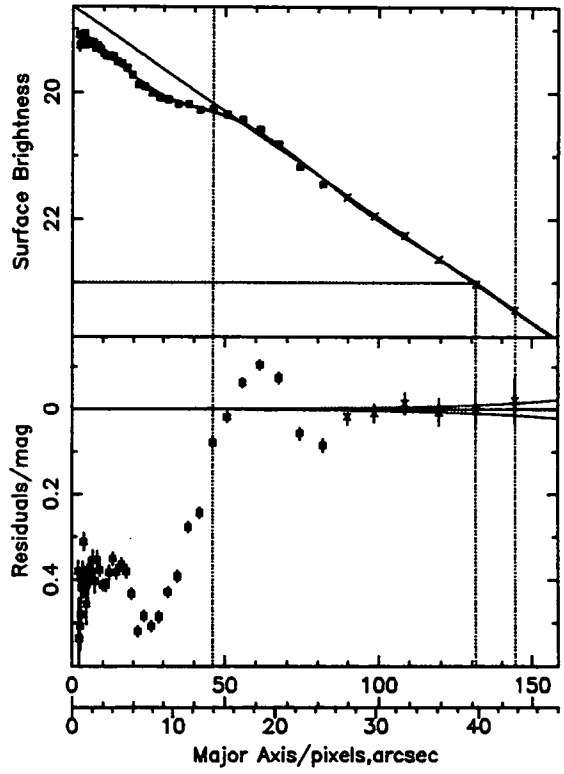
Ellipse Fitting Results For: 0125-0250



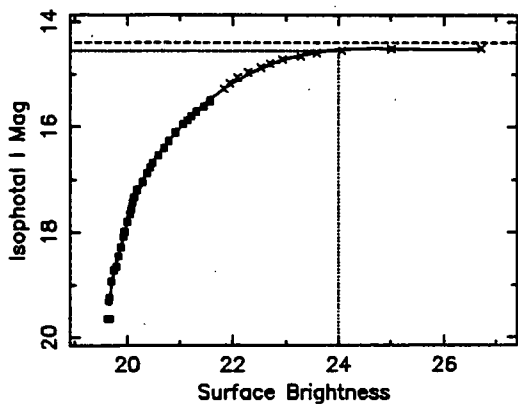
File: 0125_0250_i2535_clean.efot

$R_{22.5}=35''$ $\mu_0=18.63$ $R_{Scale}=9.8''$

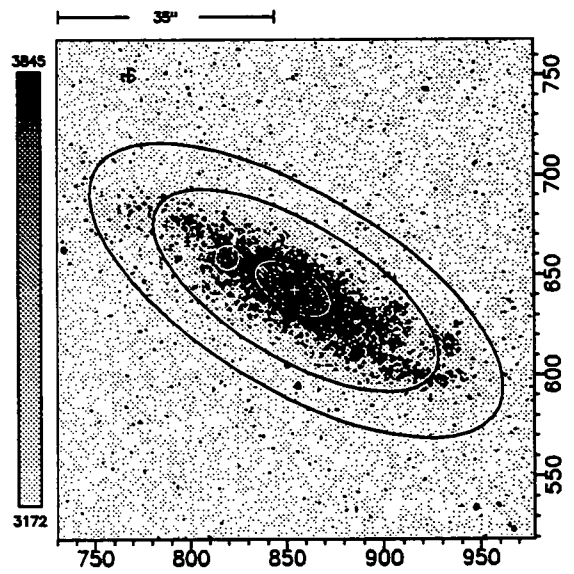
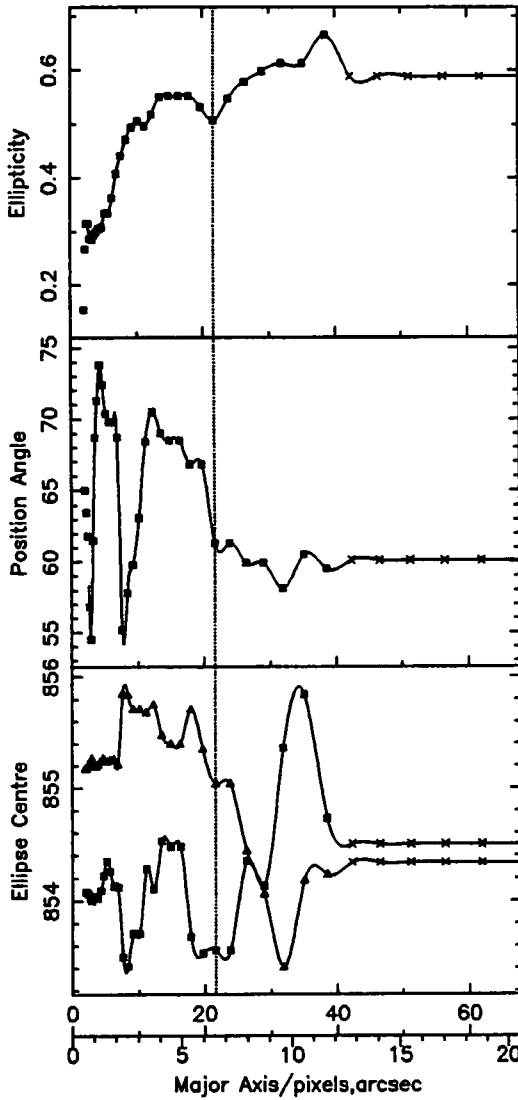
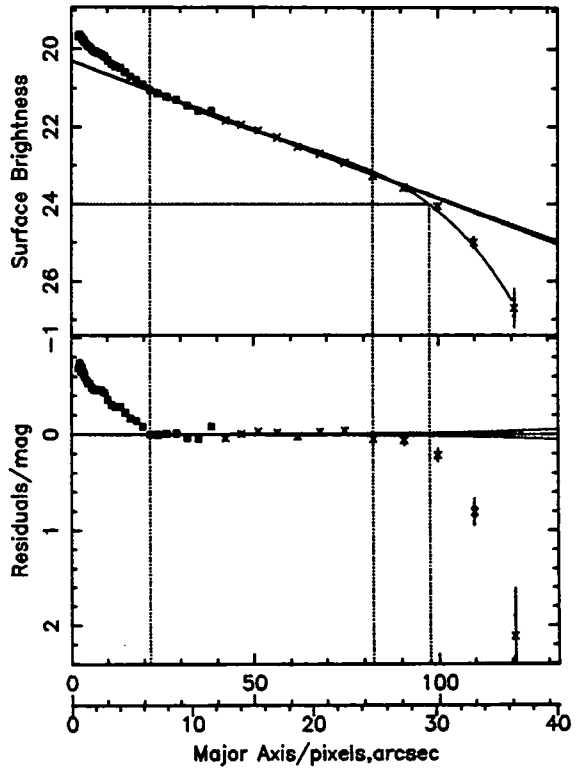
$I_{22.5}=13.76$ $I_{23.5}=99.99$ $I_{Total}=13.5$



Ellipse Fitting Results For: 0126-0241



File: 0126_0241_i2134_clean.efot
 $R_{22.5} = 19.2''$ $\mu_0 = 20.29$ $R_{Scale} = 9.2''$
 $I_{22.5} = 14.88$ $I_{23.5} = 14.61$ $I_{Total} = 14.39$

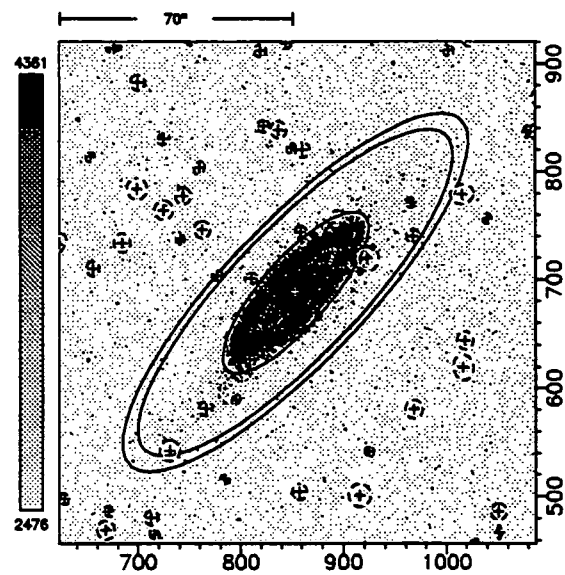
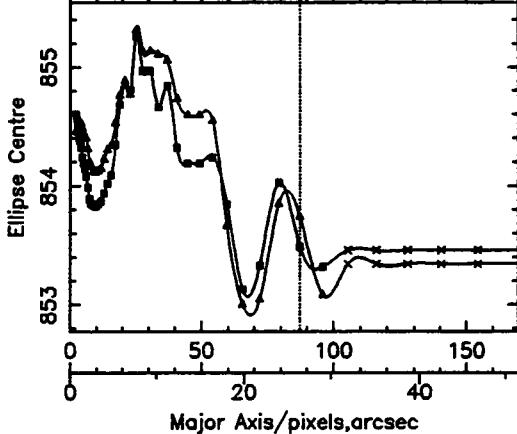
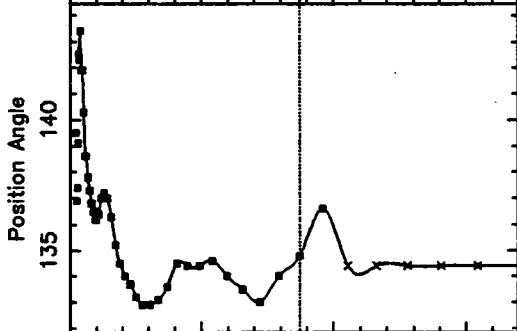
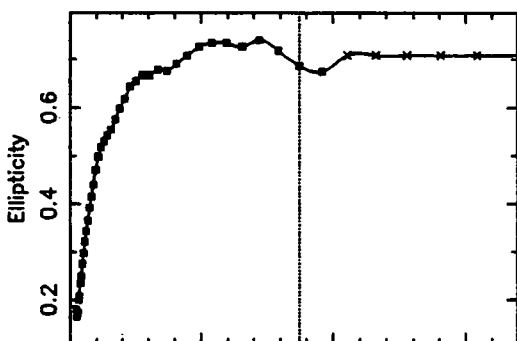
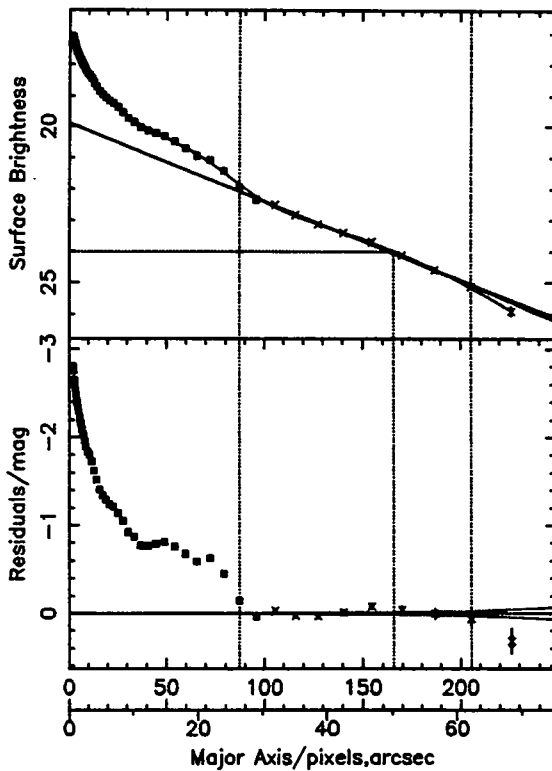
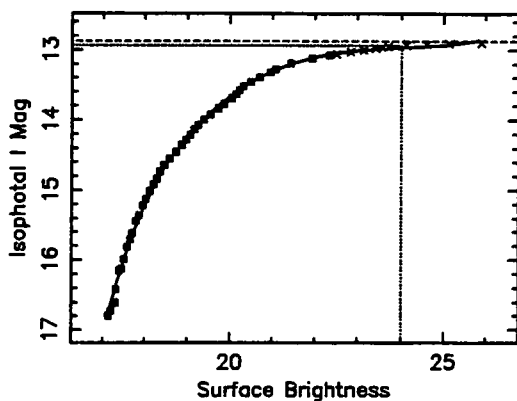


Ellipse Fitting Results For: 0131-0119

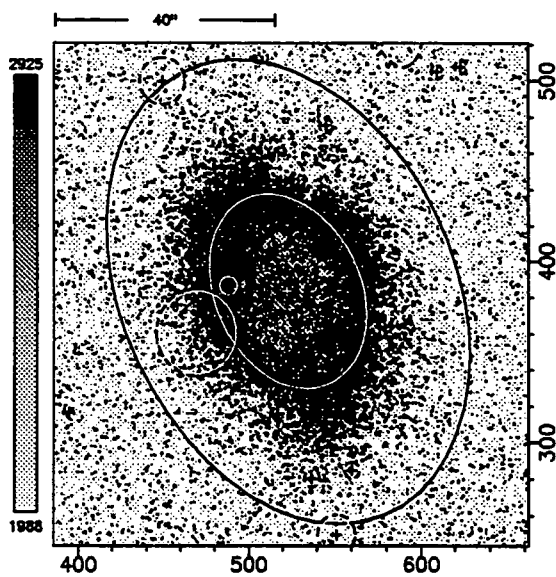
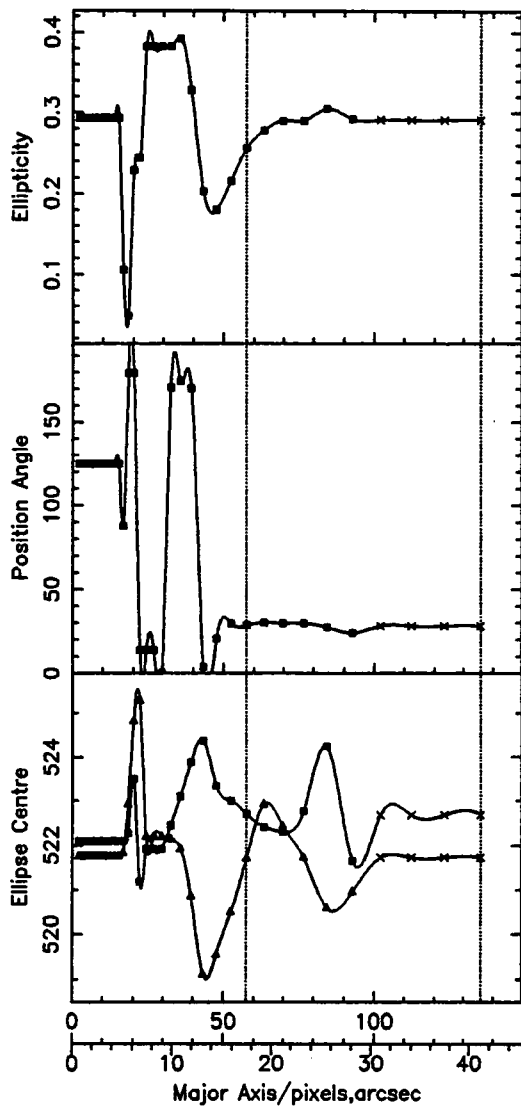
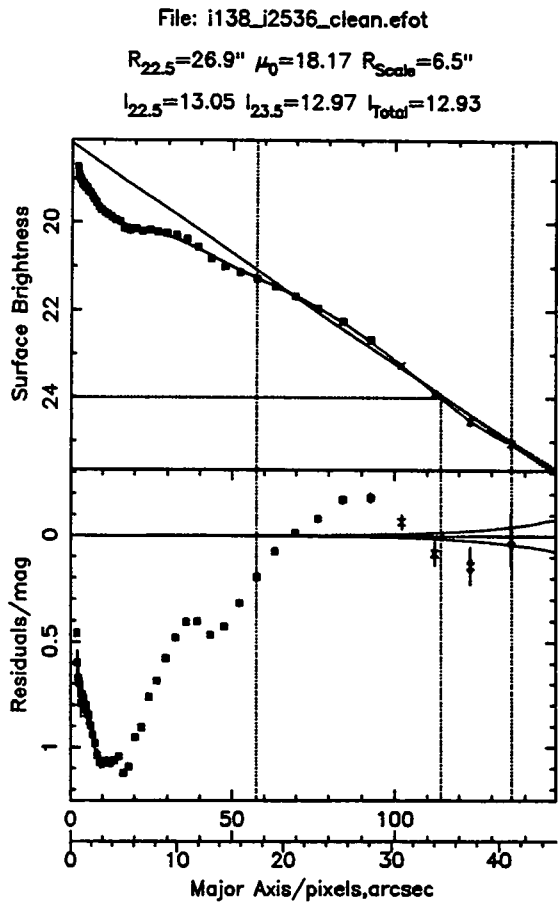
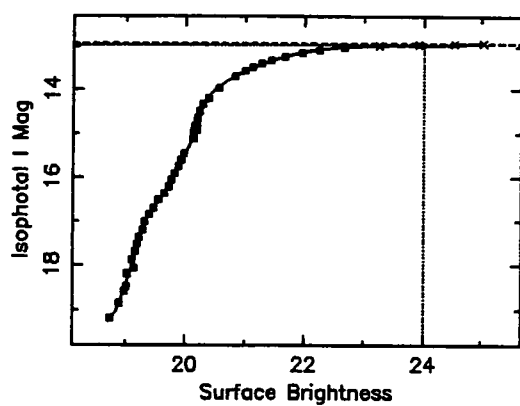
File: 0131_0119_j2628_clean.efot

$R_{22.5}=31.2''$ $\mu_0=19.88$ $R_{Scale}=13''$

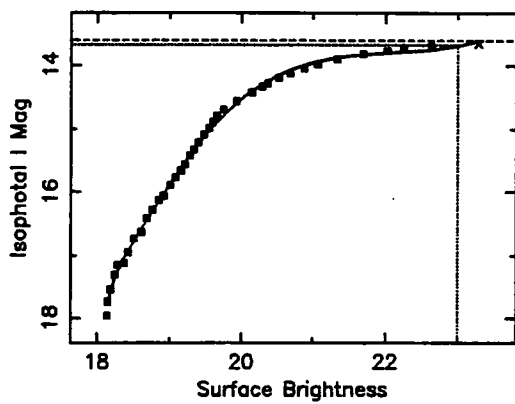
$I_{22.5}=13.06$ $I_{23.5}=12.97$ $I_{Total}=12.87$



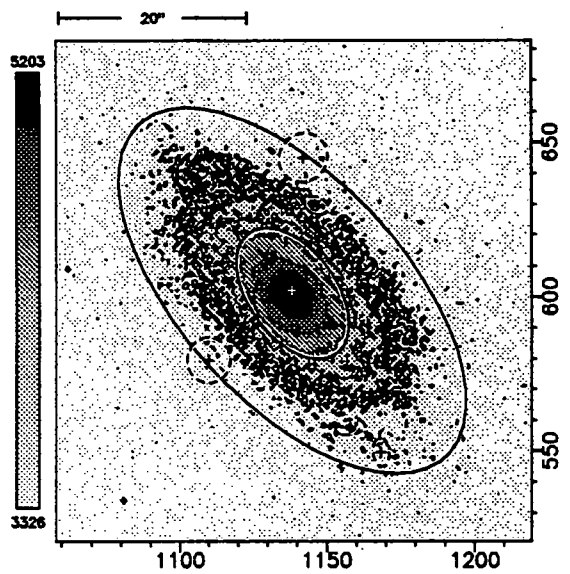
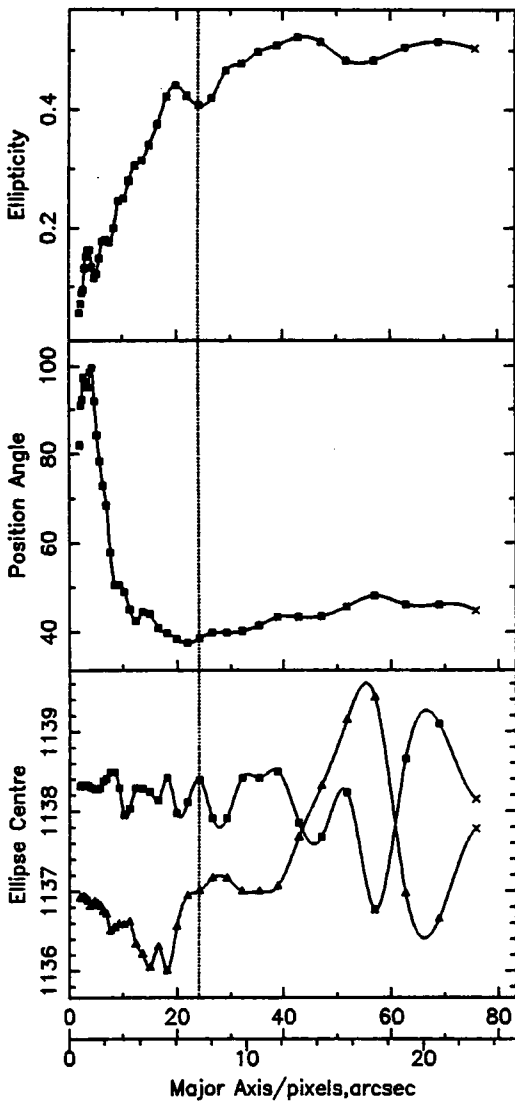
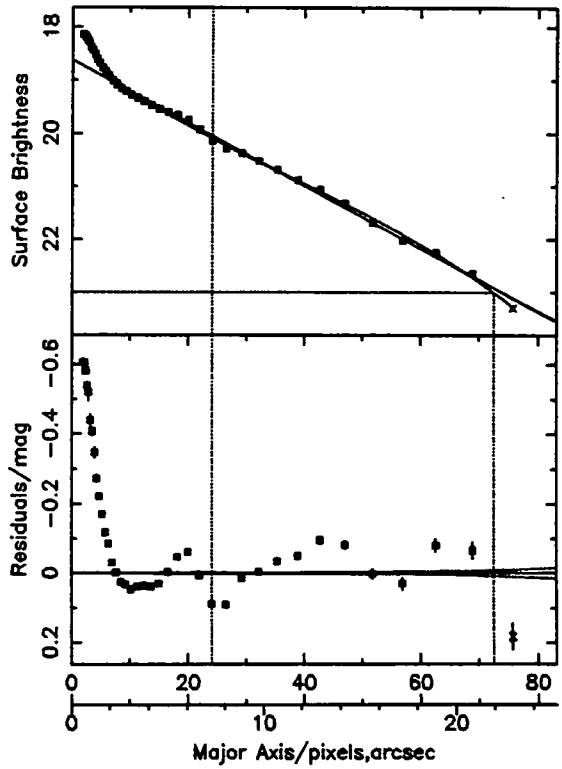
Ellipse Fitting Results For: I138



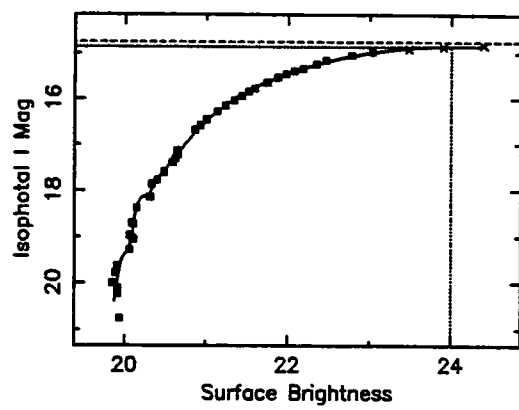
Ellipse Fitting Results For: U784



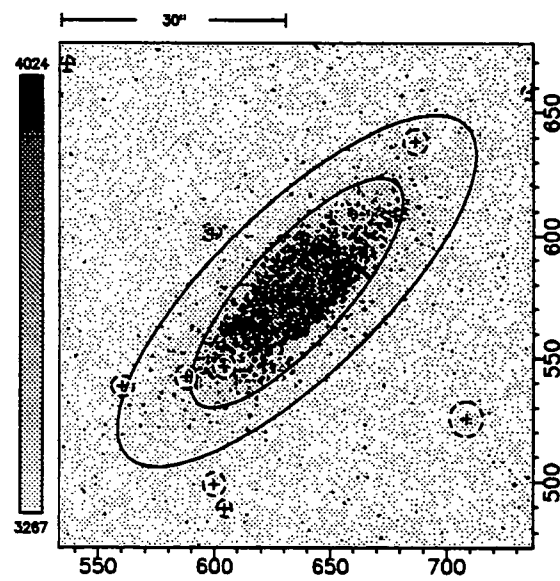
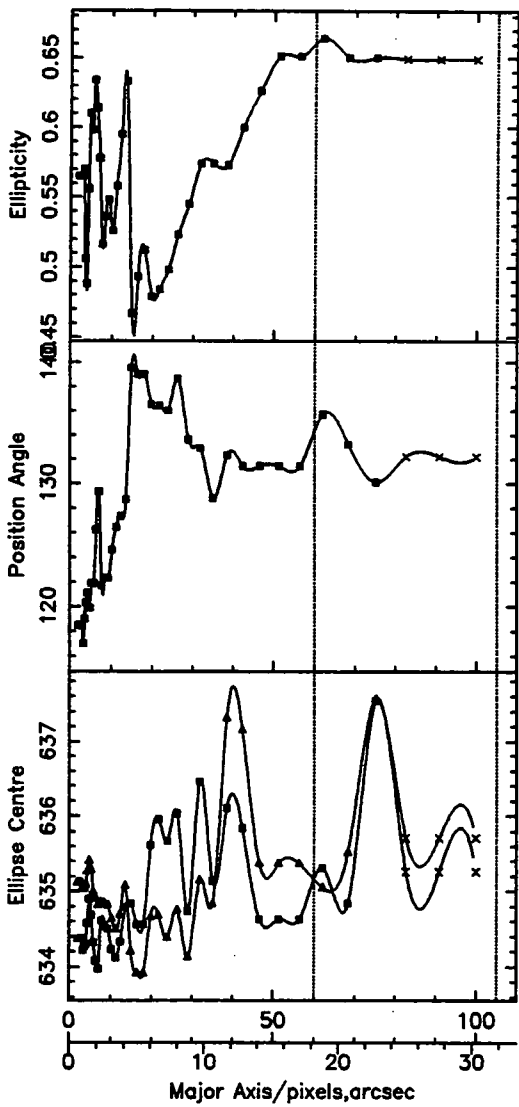
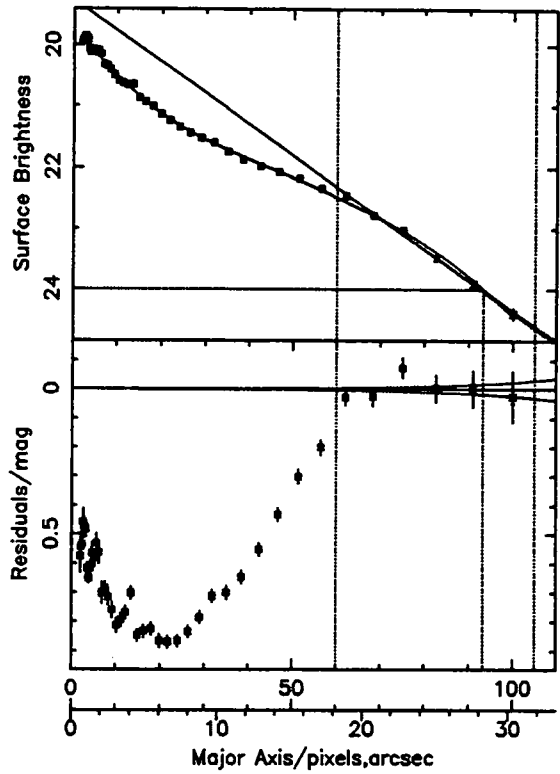
File: u784_i2631_clean.efot
 $R_{22.5} = 19.9''$ $\mu_0 = 18.63$ $R_{Scale} = 5.6''$
 $l_{22.5} = 13.7$ $l_{23.5} = 99.99$ $l_{Total} = 13.6$



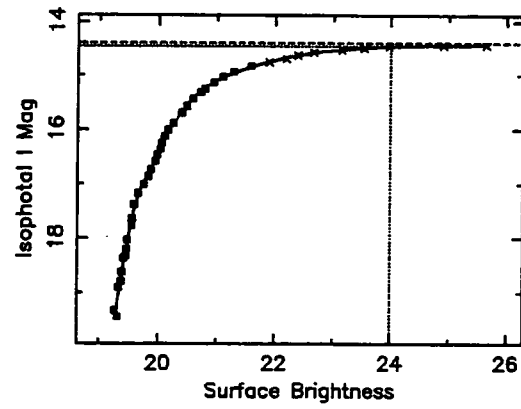
Ellipse Fitting Results For: U885



File: u885_j2734_clean.efot
 $R_{22.5} = 18.3''$ $\mu_0 = 19.26$ $R_{Scale} = 6.4''$
 $I_{22.5} = 15.15$ $I_{23.5} = 14.91$ $I_{Total} = 14.75$



Ellipse Fitting Results For: U1159



File: u1159_i2740_clean.efot
 $R_{22.5} = 17.5''$ $\mu_0 = 19.03$ $R_{Scale} = 5.5''$
 $I_{22.5} = 14.6$ $I_{23.5} = 14.49$ $I_{Total} = 14.39$

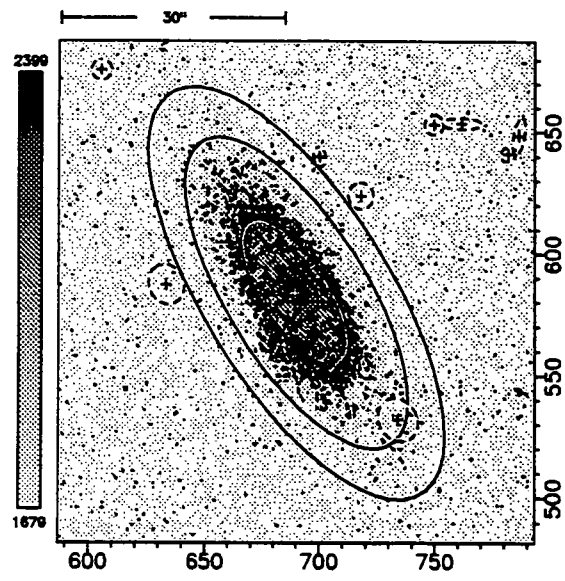
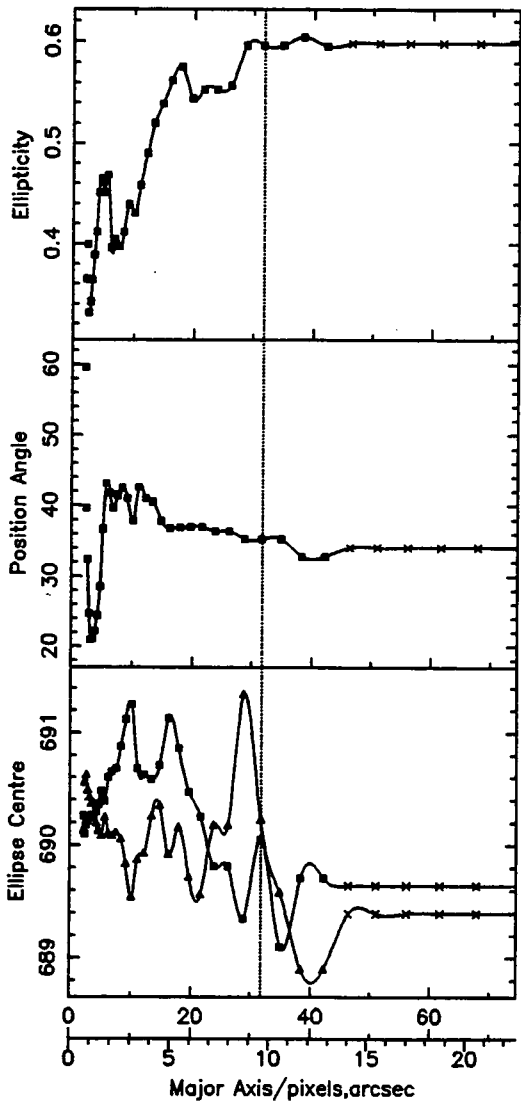
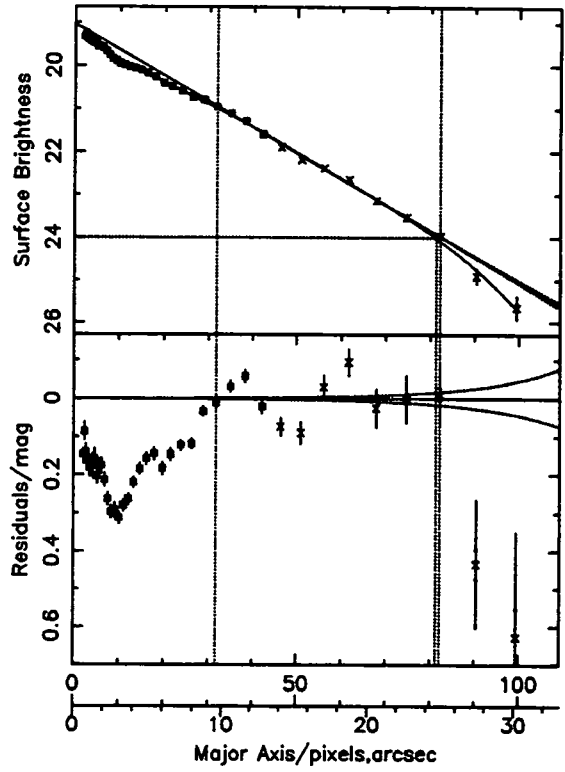


Table 9.1. Coma: Full Details of All Photometric Measurements. See §9.2 for Column Headings.

Object name	Phot	Run	Obj. No.	R.A. & Dec (B1950)	Exp. Time	I-23.5 Image	I-23.5 Image	I-Total	I-50%	e-50%	A1.5% of I-10	e-50%	Mean Diam. Parameters	pa	rms	R _{Scale}	I ₀	
	Qual			hh:mm:ss.ss dd:mm:ss.ss		mag	mag	mag	mag	mag	mag	mag	mag	mag	mag	mag	mag	
1251+2827	1	F1317		12:51:28.44 +28:27:27.3	2000	14.87	14.67	14.67	14.67	0.573	18.74	0.573	0.775	34.9	0.81	7.13	19.54	
1254+2924	3	F1321		12:54:03.96 +29:24:27.0	2000	16.10	10.72	10.72	15.61	0.604	13.20	0.604	0.992	171.3	1.01	6.86	20.40	
"	3	F1707		12:54:03.96 +29:24:26.3	500	16.10	10.72	10.72	16.44	0.534	17.0	0.534	0.539	177.0	0.00	3.92	20.00	
"	3	F1708		12:54:03.96 +29:24:26.3	1000	16.24	10.47	10.47	15.78	0.633	17.2	0.633	0.653	155.7	58.84	6.38	20.40	
1304+2854A	3	F1705		13:02:11.76 +28:52:13.1	500	15.22	9.50	9.50	15.03	0.394	13.03	0.394	0.666	86.6	1.49	2.82	18.93	
"	3	F1706		13:02:11.76 +28:53:42.7	500	15.16	9.65	9.65	15.01	0.400	13.01	0.400	0.400	85.0	2.20	3.01	19.01	
B0254	3	F1711		12:55:52.68 +28:07:03.0	2000	16.97	6.35	6.35	16.50	0.912	14.59	0.912	0.84	39.6	1.87	3.28	20.37	
B0254	2	F1119		12:55:53.04 +28:07:04.8	1000	17.33	5.44	5.44	16.98	0.467	17.19	0.467	0.490	39.2	1.87	3.28	20.37	
"	3	F1710		12:55:53.04 +28:07:03.4	1500	18.02	3.67	3.67	17.66	0.296	17.42	0.296	0.475	1.80	1.93	19.74	19.74	
D202	1	F1313		12:59:47.40 +28:28:28.0	2000	15.44	12.64	12.64	14.85	0.371	13.84	0.371	0.296	24.0	0.00	1.93	20.43	
D215	3	F1613		12:58:08.76 +27:46:21.7	1000	15.92	7.23	7.23	15.67	0.264	15.04	0.264	0.345	0.18	7.4	0.80	8.53	20.72
"	3	F1703		12:58:08.76 +27:46:22.1	1000	15.97	7.34	7.34	15.68	0.241	15.17	0.241	0.259	0.13	5.2	2.22	19.04	
"	3	F1704		12:58:08.76 +27:46:24.3	1000	16.11	7.00	7.00	15.87	0.271	15.39	0.271	0.254	0.07	5.7	3.92	19.35	
D3	1	F1323		12:57:49.32 +27:32:28.6	1500	15.12	11.87	11.87	14.55	0.543	19.0	0.543	0.270	53.7	4.08	2.38	19.33	
D38	1	F1319		12:58:10.92 +27:32:35.3	1500	14.31	19.88	19.88	14.19	0.790	14.19	0.790	0.543	0.021	19.0	0.41	3.97	18.78
I4040	1	F1325		12:58:11.44 +28:19:34.3	1000	14.09	18.28	18.28	13.94	0.568	14.70	0.568	0.730	0.009	49.9	0.82	4.76	18.08
"	1	F1512		12:58:13.08 +28:19:34.7	1000	14.14	18.89	18.89	14.21	0.522	14.62	0.522	0.567	0.012	146.9	2.13	3.83	18.05
N4585	1	F1514		12:55:45.60 +28:12:40.3	1000	13.96	23.31	23.31	13.20	0.442	12.1	0.442	0.518	0.012	148.2	0.79	3.92	18.10
N4735	2	F1111		12:48:36.00 +29:11:58.6	1000	13.49	20.55	20.55	13.34	0.386	17.43	0.386	0.442	0.018	121.1	3.25	7.72	18.68
N4788	2	F1109		12:51:50.04 +28:34:28.6	1000	13.23	23.85	23.85	13.13	0.617	15.68	0.617	0.386	0.00	174.3	0.00	3.11	18.19
N4858	1	F1126		12:56:38.76 +28:23:30.1	1000	12.54	22.64	22.64	12.39	0.151	11.82	0.151	0.619	0.007	136.8	0.08	5.93	18.18
TT13	1	F1326		12:58:15.96 +28:47:14.3	600	15.49	13.01	13.01	14.47	0.688	17.94	0.688	0.697	0.028	6.1	1.08	9.56	19.87
TT33	3	F1709		12:55:53.04 +27:34:49.4	1000	15.55	8.30	8.30	13.20	0.305	13.20	0.305	0.386	0.00	76.5	86.97	7.80	19.95
TT42	3	F1613		12:58:04.40 +27:47:03.2	1000	15.17	9.63	9.63	13.79	0.402	13.62	0.402	0.304	0.028	131.6	2.20	2.54	18.94
"	3	F1702		12:58:04.40 +27:47:03.2	1000	15.17	9.63	9.63	13.79	0.402	13.62	0.402	0.304	0.028	131.6	2.20	2.54	18.94
"	3	F1703		12:58:04.40 +27:47:03.2	1000	15.29	8.88	8.88	13.76	0.338	12.2	0.338	0.374	0.050	134.4	1.10	2.46	19.00
"	3	F1704		12:58:04.40 +27:47:03.2	1000	15.99	6.54	6.54	13.76	0.338	12.2	0.338	0.341	0.015	161.9	0.25	2.41	18.61
TT5	3	F1712		12:58:04.40 +27:47:03.2	1500	16.96	8.26	8.26	16.05	0.611	16.05	0.611	0.361	0.001	163.5	0.75	2.64	18.94
U8013	1	F1315		12:55:32.88 +28:19:30.9	2000	14.73	12.41	12.41	14.45	0.286	16.23	0.286	0.596	0.034	50.4	1.85	6.12	20.96
U8013	2	F1121		12:50:09.96 +27:01:16.7	1000	15.13	13.64	13.64	14.77	0.505	9.0	0.505	0.770	0.015	59.8	2.45	4.92	19.76
U8017	2	F1123		12:50:27.96 +28:39:30.9	1000	12.68	28.75	28.75	12.62	0.655	36.2	0.655	0.655	0.042	90.0	0.00	6.18	20.10
U8023	1	F1223		12:50:27.96 +28:39:31.9	1000	12.78	28.97	28.97	12.72	0.669	29.2	0.669	0.669	0.024	30.2	0.99	5.42	16.71
U8100	1	F1510		12:51:32.40 +28:52:29.6	500	12.63	43.52	43.52	12.51	0.713	68.6	0.713	0.662	0.004	29.3	0.45	4.98	16.55
U8140	1	F1205		12:59:15.52 +28:16:47.9	1000	12.97	36.53	36.53	12.57	0.713	10.4	0.713	0.778	0.008	68.6	0.14	11.57	18.28
U8161	1	F1227		13:01:04.44 +28:49:05.9	1000	13.96	16.08	16.08	12.76	0.698	85.6	0.698	0.701	0.014	83.6	1.19	8.30	18.62
U8194A	1	F1225		12:53:54.00 +28:19:48.3	1000	13.39	22.25	22.25	13.26	0.446	130.3	0.446	0.444	0.000	134.4	1.10	3.46	17.40
U8220	1	F1520		12:50:06.84 +24:50:00.5	1000	12.93	33.48	33.48	12.15	0.486	135.9	0.486	0.486	0.000	130.0	1.60	6.25	18.95
U8259	1	F1227		12:50:30.96 +28:27:01.8	1000	12.86	40.12	40.12	12.77	0.752	138.8	0.752	0.486	0.000	135.9	2.01	12.98	18.98
U8259	1	F1213		13:08:39.48 +28:52:37.7	1000	13.08	36.69	36.69	12.65	0.438	54.8	0.438	0.727	0.011	138.8	0.38	10.25	18.34
Z1304-4	1	F1211		12:53:50.04 +28:43:40.1	1000	13.96	16.08	16.08	12.86	0.671	168.0	0.671	0.671	0.013	54.8	1.19	8.30	18.62
Z159-75	2	F1113		12:45:01.80 +27:43:49.8	1000	13.17	17.63	17.63	13.07	0.418	114.3	0.418	0.292	0.000	143.2	0.00	4.36	17.40
"	2	F1219		12:45:01.84 +27:43:49.4	1000	13.20	17.29	17.29	13.14	0.425	114.3	0.425	0.444	0.035	131.4	0.31	3.46	18.04
Z159-105	2	F1125		12:51:23.92 +28:15:01.4	1000	14.24	17.01	17.01	14.31	0.536	174.2	0.536	0.455	0.026	23.2	1.92	3.56	17.25
"	2	F1221		12:51:26.28 +28:15:01.8	1500	14.26	17.44	17.44	14.12	0.568	175.1	0.568	0.568	0.014	175.1	1.13	4.86	18.32
Z159-117	2	F1127		12:52:23.16 +28:46:53.1	1000	14.59	16.67	16.67	14.12	0.390	141.2	0.390	0.568	0.014	175.1	1.13	4.86	18.32
Z159-144	2	F1127		12:52:07.68 +28:39:51.0	1000	13.43	21.54	21.54	13.26	0.373	133.8	0.373	0.568	0.012	153.6	0.22	3.27	18.88
Z159-80	2	F1115		12:46:13.24 +26:41:22.6	1000	13.69	23.66	23.66	13.59	0.743	4.7	0.743	0.390	0.009	63.8	1.30	8.83	19.75
"	2	F1111		12:46:13.24 +26:41:22.9	1000	13.71	23.90	23.90	13.53	0.718	5.0	0.718	0.390	0.009	63.8	1.30	8.83	19.75
Z159-98	2	F1117		12:48:37.08 +27:36:30.5	1000	14.18	18.84	18.84	14.15	0.417	196.1	0.417	0.370	0.002	99.1	0.94	6.24	16.64
Z160-67	1	F1215		12:55:44.76 +27:36:41.9	1000	13.81	29.30	29.30	13.75	0.719	83.3	0.719	0.370	0.002	99.1	0.94	6.24	16.64
Z160-137	1	F1217		12:56:12.12 +27:36:46.7	1000	14.55	11.20	11.20	14.42	0.330	19.1	0.330	0.370	0.000	83.3	0.52	10.03	19.19
"	1	F1209		13:02:02.04 +27:34:30.7	1000	14.99	11.94	11.94	14.66	0.297	83.0	0.297	0.313	0.010	81.4	3.15	4.97	19.84

Table 9.3. Abell 2634: Full Details of All Photometric Measurements. See §9.2 for Column Headings.

Object Name	Phot. Qual.	Run No.	R.A. & Dec (J2000)	Exp. Time	I _{22.5} bandpass		I _{23.5} bandpass		I _{Total}		AI 85% of I _{tot}		Mean Disk Parameters		R _{Scale}	I ₀ mag		
					I _{22.5} mag	σ _{I22.5} deg	I _{23.5} mag	σ _{I23.5} deg	I _{tot} mag	σ _{Itot} deg	I _{85%} mag	σ _{I85%} deg	σ ₀ deg	r _{ms} deg			pa deg	r _{ms} deg
U12626	1	12523	23:26:45.98	500	13.51	21.76	13.63	-0.3	13.52	13.30	13.53	20.88	0.573	189.4	0.863	0.000	12.74	21.08
"	2	12218	23:26:46.70	1000	13.61	21.40	13.78	-1.78	13.42	13.40	13.63	19.91	0.544	97.8	0.558	0.013	179.6	19.26
U12631	1	12732	23:27:32.01	500	13.24	29.63	14.83	14.83	13.15	13.15	13.35	23.82	0.701	143.4	0.702	0.007	143.4	17.36
"	1	12294	23:27:32.01	500	13.25	30.29	14.33	14.33	13.14	13.14	13.34	23.63	0.706	143.6	0.702	0.007	144.1	17.71
"	1	12621	23:27:32.01	1000	13.25	30.12	14.29	14.29	13.14	13.14	13.34	23.57	0.701	143.7	0.702	0.007	143.9	17.60
U12678	2	12129	23:32:14.25	1000	13.47	32.81	16.35	82.4	13.37	13.38	13.57	26.54	0.794	82.0	0.795	0.001	82.1	17.14
"	1	12626	23:32:18.59	1000	13.49	32.96	16.35	82.0	13.37	13.39	13.57	27.11	0.799	81.7	0.797	0.002	81.9	17.57
BU1000	2	12116	23:33:24.46	1000	17.22	6.86	14.19	7.72	16.79	16.80	16.99	7.72	0.660	141.9	0.668	0.000	142.6	19.81
"	1	12228	23:33:27.57	1000	17.38	5.74	13.83	13.83	16.96	16.96	17.16	8.30	0.975	133.8	0.900	0.022	133.8	19.99
D113	2	12222	23:33:33.29	1000	16.00	7.07	0.326	100.5	15.88	15.88	16.08	5.52	0.296	103.0	0.539	0.011	101.1	18.32
U12701	1	12624	23:33:53.82	1000	14.48	21.18	0.747	17.55	14.28	14.29	14.48	22.15	0.741	17.52	0.750	0.009	174.9	18.07
D124	2	12117	23:34:09.50	1000	15.69	8.25	0.216	59.3	15.48	15.47	15.68	8.09	0.215	59.4	0.215	0.004	59.4	18.32
D123	1	12531	23:34:26.03	1000	15.07	14.07	0.649	172.7	14.98	14.99	15.18	15.36	0.653	172.6	0.658	0.004	172.9	19.16
"	3	12417	23:34:26.42	1000	15.08	14.18	0.619	172.4	14.98	14.98	15.17	15.36	0.653	172.6	0.658	0.004	172.9	19.16
D85	2	12127	23:35:10.69	2000	16.18	6.30	0.524	131.2	16.03	16.03	16.22	5.00	0.542	134.2	0.534	0.007	134.2	18.81
D41	2	12125	23:35:22.94	2000	16.39	7.26	0.501	43.9	16.24	16.24	16.33	7.59	0.487	44.8	0.475	0.031	43.6	19.54
D131	2	12216	23:35:27.94	1000	16.56	6.49	0.196	100.7	15.69	15.67	15.89	12.98	0.196	100.7	0.199	0.017	101.8	21.43
U12721	1	12720	23:35:34.42	500	13.09	22.16	0.203	138.8	12.95	12.95	13.08	21.44	0.205	138.2	0.201	0.008	141.7	19.87
"	2	12220	23:35:34.81	1000	13.08	24.64	0.389	155.1	12.96	12.96	13.09	24.30	0.389	155.1	0.393	0.005	154.1	19.87
D21	1	12725	23:35:44.42	1000	14.70	16.79	0.719	69.6	14.63	14.63	14.77	13.85	0.723	69.2	0.722	0.012	69.6	19.79
"	3	12422	23:35:44.42	500	14.73	16.50	0.700	68.4	14.66	14.66	14.80	13.25	0.723	69.3	0.713	0.013	69.3	17.68
D39	2	12121	23:35:47.72	1000	15.93	11.63	0.777	141.5	15.83	15.83	15.93	10.87	0.777	141.5	0.781	0.005	141.0	18.59
D59	1	12618	23:35:45.96	1000	15.97	11.18	0.759	142.7	15.87	15.87	15.96	10.78	0.759	142.7	0.759	0.006	142.8	18.89
D129	1	12730	23:36:01.07	1000	15.61	14.66	0.736	128.7	15.50	15.50	15.57	12.95	0.641	128.7	0.641	0.023	128.7	19.87
"	1	12532	23:36:01.07	1000	15.72	12.82	0.680	130.1	15.42	15.42	15.57	12.95	0.641	128.7	0.641	0.023	128.7	19.87
D19	1	12925	23:36:12.60	1000	16.05	6.82	0.319	38.6	15.86	15.86	16.05	15.61	0.319	38.6	0.319	0.026	38.6	19.50
D109	1	12325	23:36:12.60	1000	16.05	6.82	0.319	38.6	15.86	15.86	16.05	15.61	0.319	38.6	0.319	0.026	38.6	19.50
D101	1	12324	23:36:19.41	500	13.61	19.17	0.378	116.6	13.51	13.51	13.63	13.45	0.378	116.6	0.383	0.005	116.6	19.14
D11	2	12217	23:36:31.33	500	14.26	13.90	0.355	12.6	13.07	13.07	13.18	12.14	0.302	12.1	0.301	0.021	12.1	18.11
"	1	12217	23:36:35.62	1000	18.15	4.44	0.407	13.3	17.42	17.42	18.15	12.14	0.302	12.1	0.301	0.021	12.1	18.11
D9	1	12322	23:36:36.39	2000	17.50	6.22	0.530	14.3	16.99	16.99	17.30	9.91	0.407	13.3	0.412	0.026	13.6	19.40
"	1	12322	23:36:39.24	1000	16.05	7.69	0.387	113.7	15.95	15.95	16.05	6.92	0.386	113.6	0.383	0.008	113.6	19.59
D67	1	12322	23:36:41.39	500	13.22	23.15	0.379	59.5	13.07	13.07	13.18	12.14	0.302	12.1	0.301	0.021	12.1	18.11
"	1	12721	23:36:41.39	500	13.23	24.68	0.483	82.1	13.05	13.05	13.18	12.14	0.302	12.1	0.301	0.021	12.1	18.11
D97	1	12328	23:37:03.97	1000	14.94	11.51	0.314	108.9	14.81	14.81	14.81	10.87	0.314	108.9	0.314	0.044	108.9	19.59
D47	1	12727	23:37:03.97	1000	16.39	6.82	0.389	38.6	16.22	16.22	16.34	7.46	0.389	38.6	0.403	0.032	38.6	19.52
"	1	12329	23:37:23.90	1000	16.41	7.82	0.533	43.1	16.23	16.23	16.34	7.46	0.389	38.6	0.403	0.032	38.6	19.52
D30	1	12623	23:37:37.91	1000	15.28	9.09	0.532	86.4	16.26	16.26	16.34	8.27	0.513	86.4	0.513	0.018	86.4	19.68
"	1	12722	23:37:38.29	1000	15.25	8.97	0.524	94.4	15.01	15.01	15.14	13.36	0.532	94.4	0.538	0.022	94.4	19.68
"	1	12931	23:37:38.29	500	15.20	6.95	0.169	78.1	14.92	14.92	15.06	14.30	0.304	93.4	0.289	0.105	93.8	20.79
BU108	1	12925	23:37:42.25	1000	15.63	14.75	0.735	108.2	15.28	15.28	15.48	16.82	0.735	108.2	0.734	0.013	108.1	21.99
"	1	12932	23:37:42.25	1000	15.63	14.56	0.733	106.2	15.34	15.34	15.54	16.94	0.733	106.2	0.732	0.019	106.2	19.46
"	3	12415	23:37:43.58	500	15.63	14.80	0.737	104.1	15.49	15.49	15.54	16.94	0.733	106.2	0.732	0.019	106.2	19.46
BU91	1	12415	23:38:02.41	500	15.17	11.57	0.494	176.3	15.00	15.00	15.32	19.05	0.494	176.3	0.494	0.010	176.3	19.09
"	1	12622	23:38:02.41	1000	15.11	11.95	0.593	179.2	15.03	15.03	15.32	19.05	0.494	176.3	0.494	0.010	176.3	19.09
BU171	1	12729	23:38:19.66	1000	16.19	16.11	0.833	73.7	13.81	13.81	14.97	9.65	0.832	179.1	0.833	0.008	178.8	18.73
ZW76-112	1	12731	23:38:44.87	1000	13.03	22.93	0.491	58.1	12.99	12.99	13.16	19.12	0.492	58.2	0.492	0.003	58.2	20.64
U12746	1	12725	23:40:15.95	500	13.25	41.97	0.823	46.9	13.29	13.29	13.31	44.51	0.823	46.9	0.824	0.001	47.1	18.80
ZW76-012	2	12123	23:44:49.56	1000	13.35	24.62	0.534	172.7	13.29	13.29	13.46	17.11	0.534	171.1	0.538	0.022	171.1	19.13
ZW477-024	1	12726	23:49:26.73	500	13.87	13.69	0.521	59.3	13.75	13.75	13.87	18.31	0.521	59.5	0.517	0.013	59.7	17.31

Table 9.4. Abell 194: Full Details of All Photometric Measurements. See §9.2 for Column Headings.

Object name	Phot Qual	Run No.	Run	R.A. & Dec (J1950)	diameter	Exp. Time	I=22.5 mag/arcsec		I=23.5 mag/arcsec		I=Total		At 85% of I=1.0		Mean Disk Parameters		R _{Scale}	H ₀	
							I22.5 mag	e22.5 deg	I23.5 mag	e23.5 deg	I=1.0 mag	eI=1.0 deg	I=1.0 mag	eI=1.0 deg	I=1.0 mag	eI=1.0 deg			pa deg
U734	1	12735	01:08:04.63	-02:32:37.0	1000	13.66	29.72	0.732	174.4	13.58	33.54	0.694	174.6	13.70	26.06	0.745	173.3	7.00	17.88
MCG-01-04-013	1	12741	01:09:58.65	-02:02:31.2	1000	13.40	26.97	0.377	151.1	13.28	34.38	0.427	153.2	13.24	23.23	0.326	147.2	5.22	16.42
U771	1	12737	01:11:08.20	-02:22:02.2	200	12.94	26.89	0.514	100.1	12.87	33.11	0.514	100.0	12.83	21.29	0.319	99.9	100.1	18.52
"	1	12737	01:11:08.20	-02:22:02.2	200	12.94	27.42	0.517	100.6	12.87	34.77	0.517	100.6	12.84	21.68	0.313	100.8	100.3	18.63
U764	1	12538	01:11:29.90	-02:00:39.1	300	99.90	13.87	0.215	48.4	99.99	13.77	0.215	48.4	12.84	20.75	0.212	48.6	7.97	18.46
"	1	12538	01:11:29.90	-02:00:39.1	300	99.90	13.87	0.215	48.4	99.99	13.77	0.215	48.4	12.84	20.75	0.212	48.6	7.97	18.46
U885	1	12531	01:11:33.99	-02:00:04.5	1000	13.70	19.93	0.513	45.8	99.99	22.81	0.566	45.1	13.60	17.63	0.488	47.9	4.00	18.70
U885	1	12794	01:18:27.98	-02:41:34.2	1000	13.15	18.33	0.661	134.7	14.91	25.62	0.649	132.5	14.75	23.56	0.650	130.5	1.763	16.63
U885	1	12639	01:18:41.90	-02:47:59.0	1000	12.26	40.19	0.408	59.0	99.99	53.36	0.409	51.7	12.04	38.99	0.408	52.0	51.7	20.13
"	1	12639	01:18:41.90	-02:47:59.0	1000	12.19	39.17	0.333	52.1	12.02	57.08	0.333	52.2	11.92	41.83	0.333	52.2	2.900	18.49
01:20-01:39	1	12337	01:20:13.96	-01:39:09.9	1000	12.23	46.89	0.711	104.2	12.17	58.40	0.694	104.3	12.10	34.11	0.715	104.5	104.2	18.70
"	1	12337	01:20:13.96	-01:39:09.9	1000	12.23	46.89	0.711	104.2	12.17	58.40	0.694	104.3	12.10	34.11	0.715	104.5	104.2	18.70
01:20-02:14	2	12333	01:20:13.99	-01:39:08.9	500	12.23	45.94	0.710	103.8	12.18	58.18	0.707	104.1	12.13	34.27	0.709	104.2	103.9	11.00
"	2	12133	01:20:44.27	-02:14:16.5	1000	13.15	27.46	0.626	199.4	13.10	33.54	0.627	160.5	13.07	21.05	0.620	160.3	160.4	16.86
1106	2	12133	01:22:07.28	-01:49:13.2	1000	16.00	10.56	0.578	167.0	15.78	14.98	0.578	167.0	15.59	15.55	0.578	167.0	167.0	19.80
01:23-01:34	3	12423	01:23:18.46	-01:34:38.3	500	13.36	17.70	0.245	94.5	13.30	22.23	0.240	99.0	13.26	13.06	0.243	104.5	3.10	18.79
01:23-02:03	1	12534	01:23:44.92	-02:03:09.4	500	13.92	17.99	0.633	141.0	13.88	21.99	0.639	139.6	13.84	13.36	0.650	141.2	140.4	17.71
"	1	12334	01:23:44.95	-02:03:09.4	1000	13.92	18.28	0.668	140.9	13.88	21.99	0.676	140.6	13.85	13.00	0.679	140.9	3.88	17.35
11703	2	12256	01:23:46.44	-01:58:14.6	500	12.37	30.32	0.426	132.3	12.44	49.56	0.544	124.5	12.19	62.51	0.497	126.7	29.79	21.40
01:24-01:22	3	12424	01:24:02.69	-01:22:20.0	500	13.85	16.69	0.268	42.6	13.75	21.20	0.270	39.9	13.68	16.06	0.290	43.1	4.08	19.52
01:24-01:33	2	12229	01:24:07.63	-01:34:26.1	500	14.15	20.96	0.664	136.2	14.07	26.28	0.664	136.2	14.00	17.83	0.664	136.2	136.1	18.59
"	1	12627	01:24:10.51	-01:35:57.2	1000	14.13	16.83	0.488	136.2	14.06	20.39	0.451	139.6	13.99	14.20	0.453	133.1	5.04	19.94
01:25-01:23	2	12230	01:25:06.99	-01:24:18.0	500	13.23	20.62	0.365	25.3	13.14	26.61	0.295	23.3	13.08	17.48	0.271	19.3	2.33	7.67
1119	2	12235	01:25:18.55	-02:18:42.0	500	12.39	46.64	0.628	74.7	12.17	87.39	0.628	74.7	11.91	98.15	0.628	74.7	7.67	19.65
01:25-02:50	3	12425	01:25:33.22	-02:50:46.6	500	13.75	34.41	0.803	39.6	13.66	42.84	0.807	39.3	13.54	33.42	0.801	36.7	33.70	20.89
"	1	12335	01:25:33.22	-02:50:47.0	500	13.76	33.02	0.815	37.8	13.59	43.47	0.815	37.8	13.50	37.75	0.815	37.8	58.3	18.47
N570	2	12331	01:26:23.32	-01:13:07.2	500	12.06	38.36	0.433	94.5	11.91	58.59	0.433	94.5	11.86	12.09	0.433	94.5	94.5	18.63
01:26-02:41	2	12134	01:26:25.69	-02:40:56.9	1000	14.88	19.18	0.389	60.1	14.61	27.16	0.389	60.1	14.39	27.23	0.389	60.1	60.1	19.19
N577	2	12232	01:26:04.15	-02:15:45.4	500	12.01	46.32	0.544	131.1	99.99	60.85	0.544	131.1	11.86	41.04	0.544	131.1	9.24	20.29
"	1	12742	01:26:07.75	-02:15:05.8	500	12.00	38.39	0.341	149.6	11.89	52.16	0.341	148.1	11.83	36.36	0.342	149.8	141.5	19.32
1138	2	12233	01:30:24.01	-02:57:00.1	500	13.11	26.92	0.304	24.5	13.03	31.08	0.306	23.2	12.96	42.93	0.286	24.2	24.8	11.89
"	1	12336	01:30:24.05	-02:55:59.2	500	13.05	26.91	0.300	24.8	12.97	32.13	0.292	28.6	12.93	23.78	0.293	29.3	27.5	2.333
01:31-01:20	3	12426	01:31:01.67	-01:22:12.8	500	14.13	23.02	0.751	112.7	14.00	33.85	0.752	113.9	13.70	13.73	0.746	112.9	0.741	18.85
01:31-01:19	1	12628	01:31:29.32	-01:19:54.4	1000	13.06	31.21	0.700	135.0	12.97	43.85	0.708	134.4	12.87	20.06	0.674	136.6	0.024	13.69
01:31-01:17	1	12333	01:31:54.07	-01:17:23.0	1000	12.48	38.37	0.755	68.1	12.45	44.25	0.762	68.2	12.42	26.64	0.763	68.1	68.2	13.05
U1159	1	12740	01:33:03.48	-02:12:31.0	600	14.60	17.49	0.598	34.1	14.49	22.39	0.598	34.1	14.39	17.99	0.598	34.1	34.1	7.80
"	1	12632	01:33:03.51	-02:12:48.1	200	14.66	14.27	0.500	39.8	14.52	19.59	0.500	39.8	14.45	13.00	0.500	39.8	5.00	19.03
"	1	12633	01:33:03.51	-02:12:48.1	200	14.64	14.71	0.465	32.0	99.99	15.96	0.465	32.0	14.50	13.13	0.465	32.0	32.4	4.51

Appendix C

H α Rotation Curves

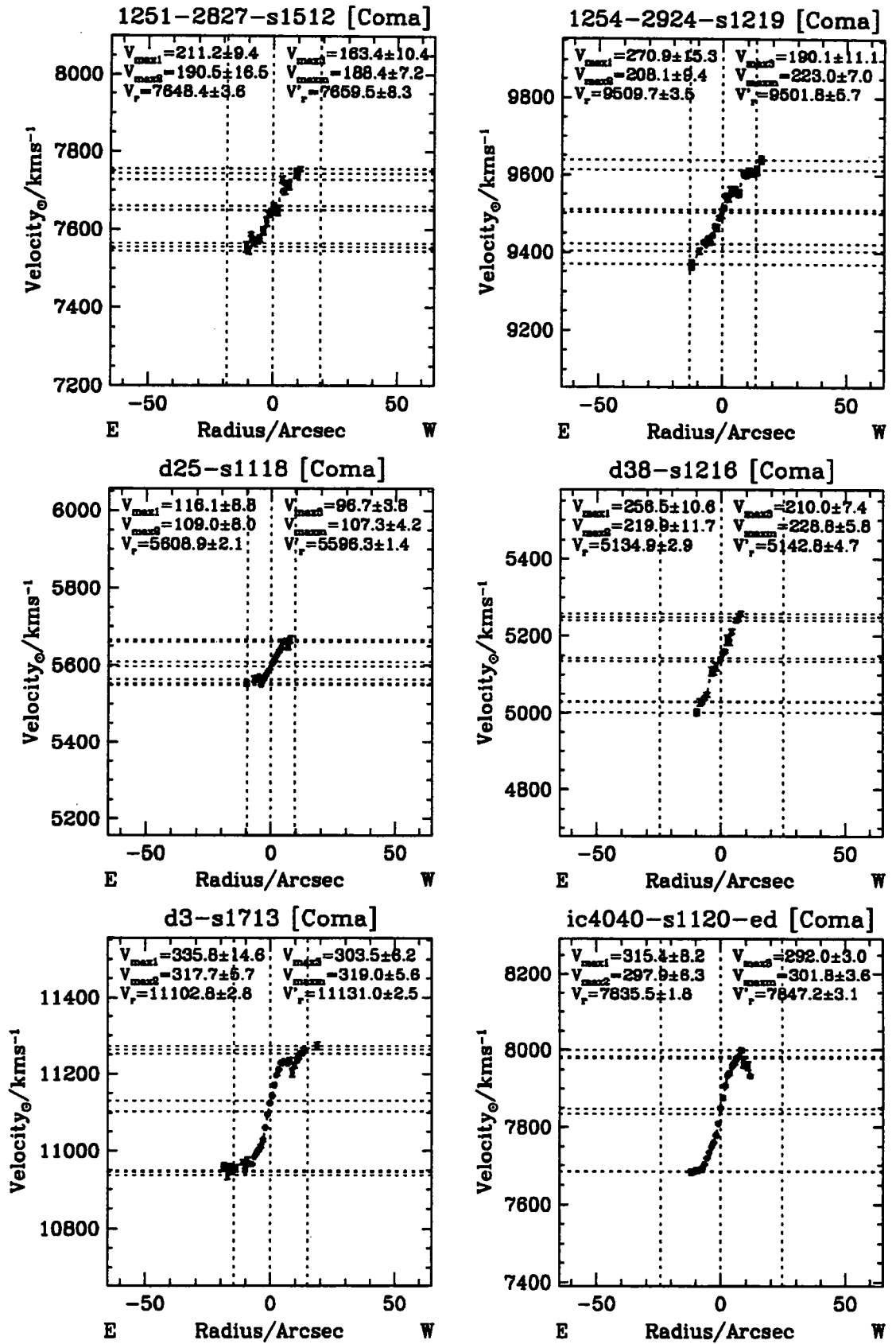
10.1 Rotation Curves

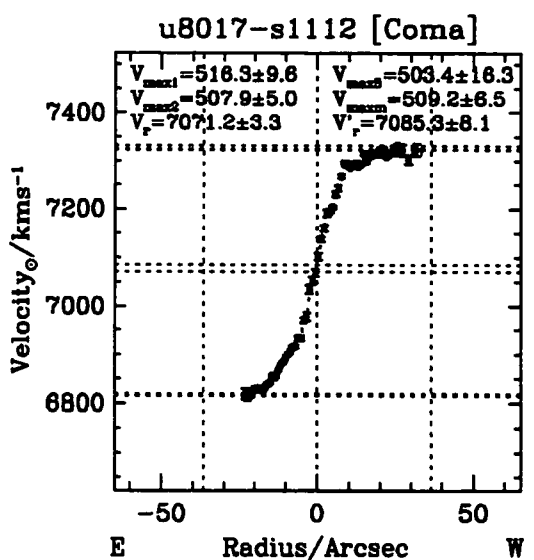
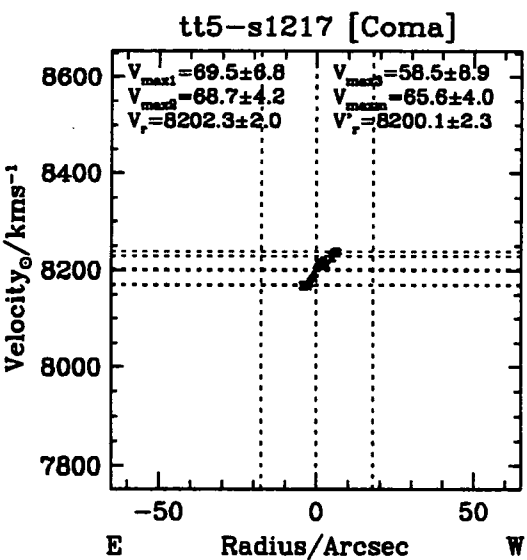
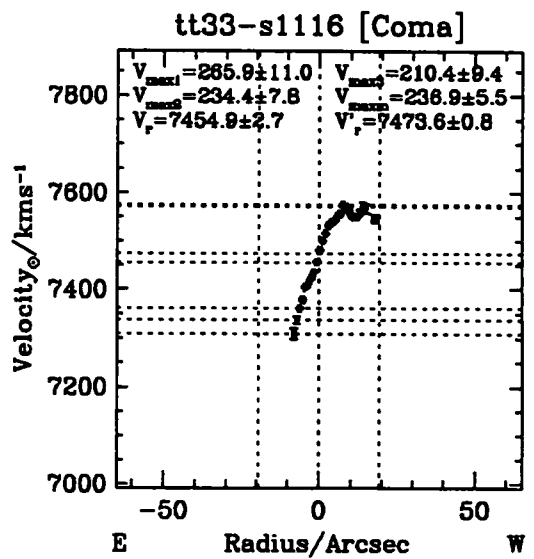
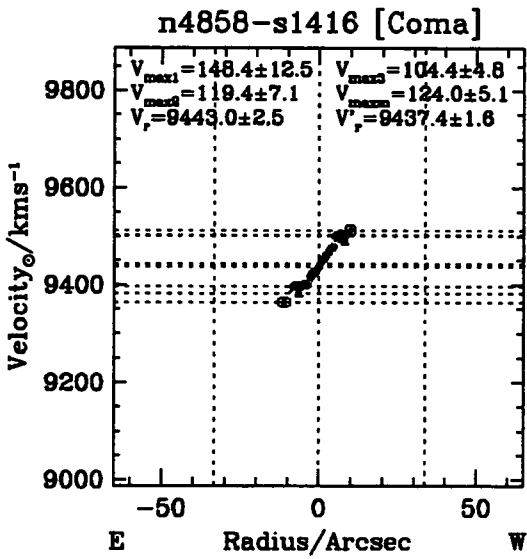
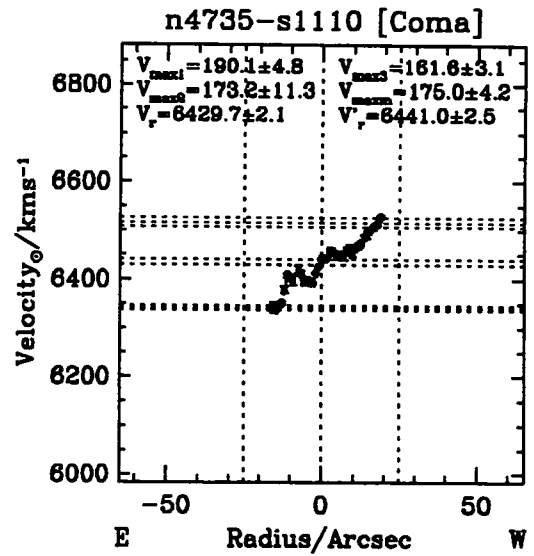
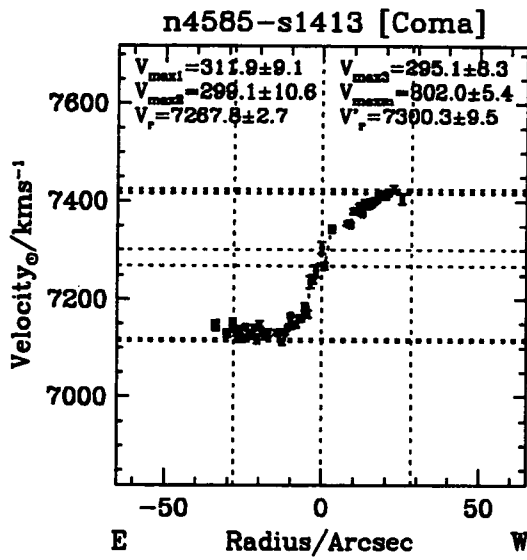
The following appendix contains the full and folded rotation curves for all galaxies within the final Tully-Fisher sample. Galaxies from the four clusters appear in the order; Coma, Abell 2199, Abell 2634 and Abell 194. Within each cluster the normal rotation curves appear first followed by the same curves folded about their centre of symmetry.

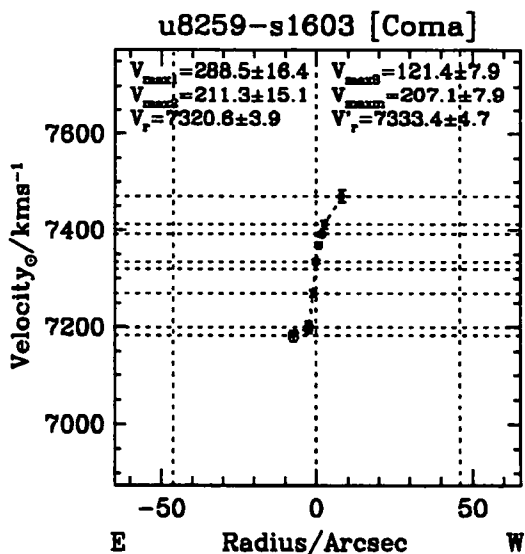
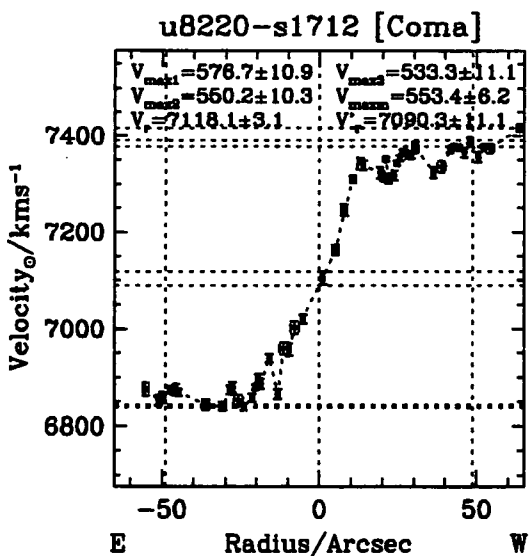
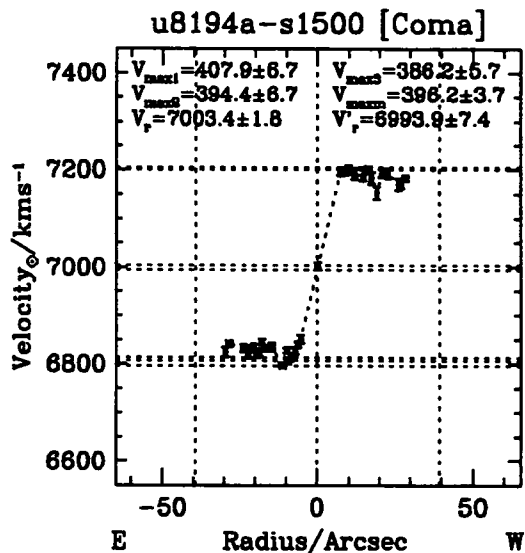
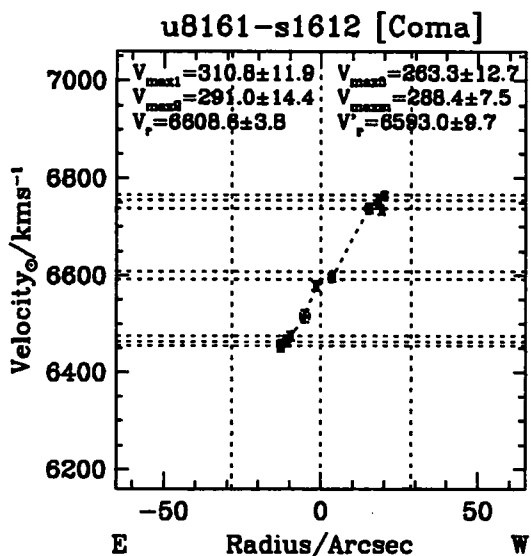
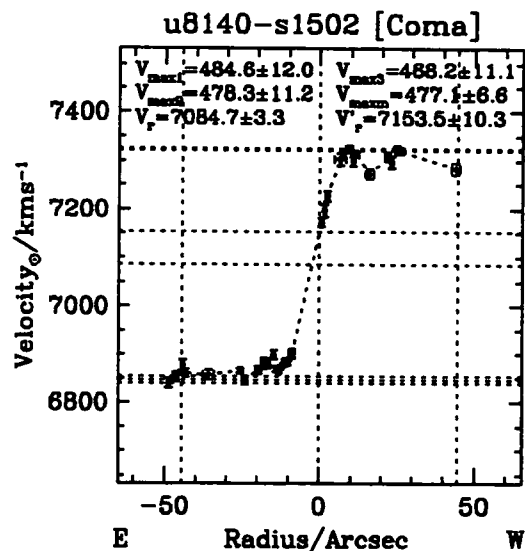
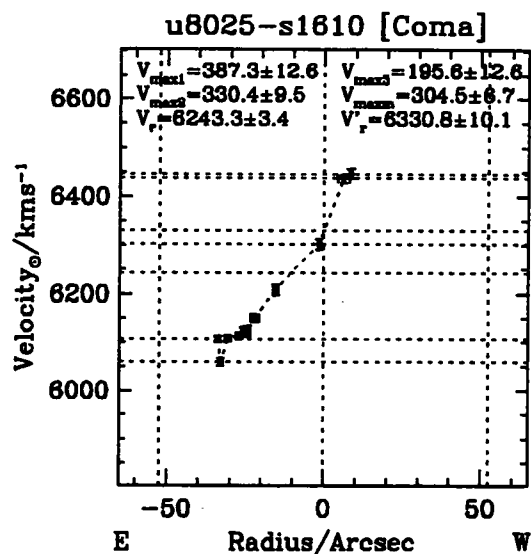
All initial curves are plotted on the same spatial and velocity scales. The middle vertical line marked on each plot indicates the Gaussian fitted centre of each galaxy's continuum. Other vertical lines mark the 23.5 isophotal radius. The two horizontal lines passing through the middle of each curve represent two possible ways of measuring the recession velocity. One is denoted as the velocity at the brightest point in the continuum the other is half way between the minimum and maximum rotation velocities. Note these can differ by as much as 100km^{-1} .

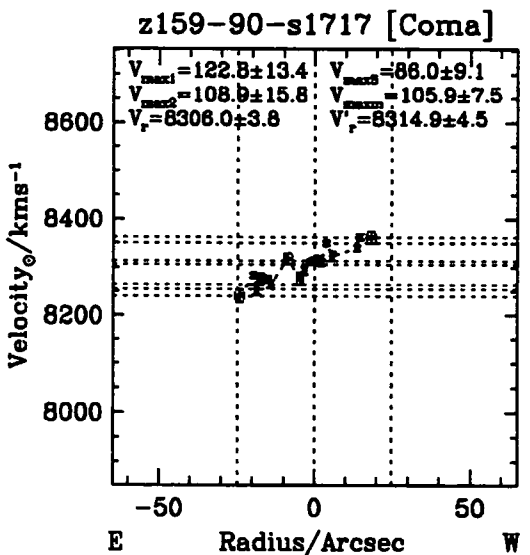
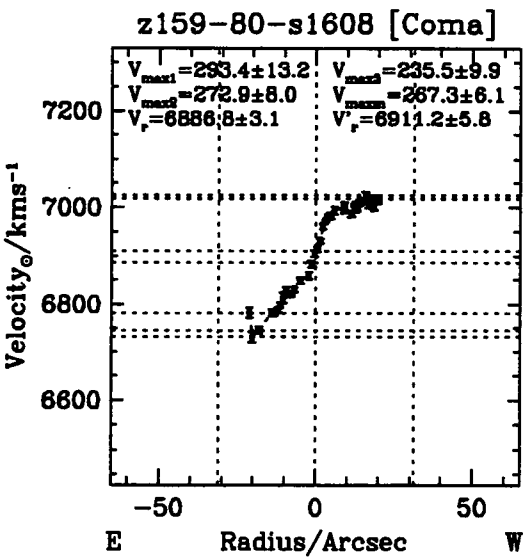
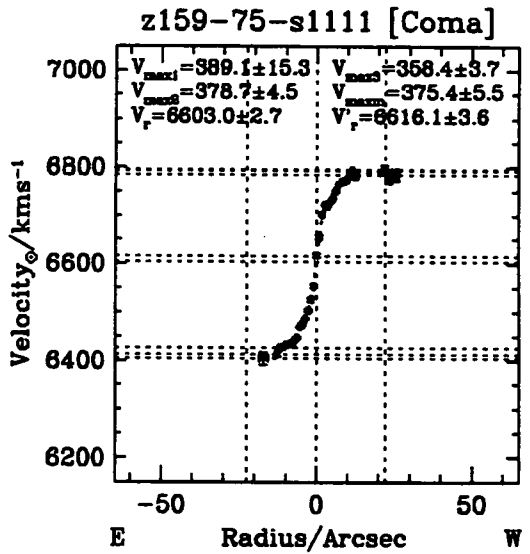
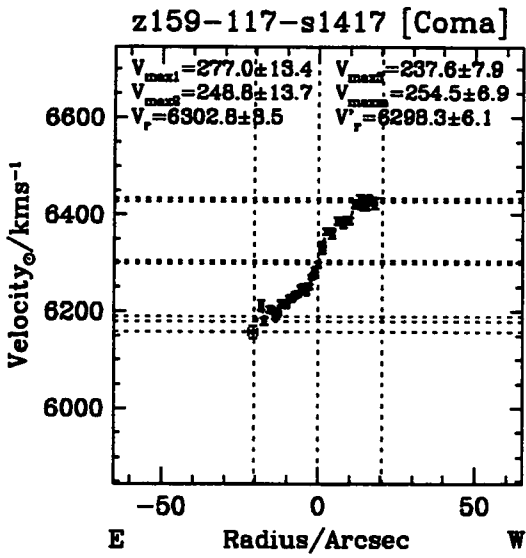
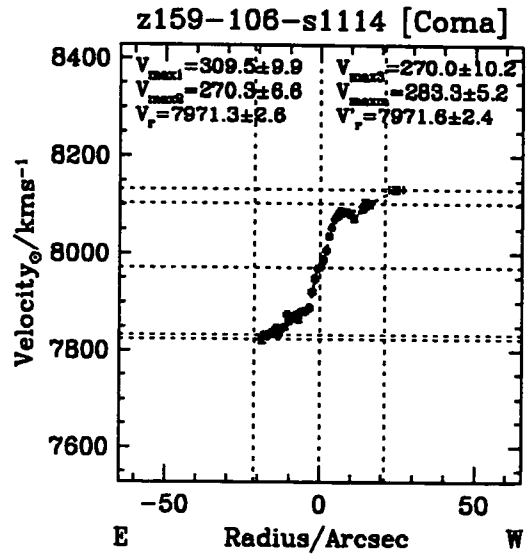
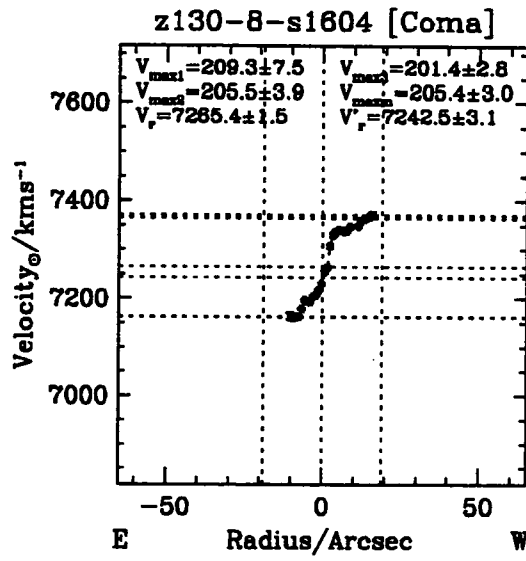
Three possible ways of measuring the rotation velocities are marked on each plot. Horizontal lines are drawn passing through the first, second and third most extreme point on each side of the curve. Rotation velocities are calculated as the difference of these and the mean are indicated at the top of each plot.

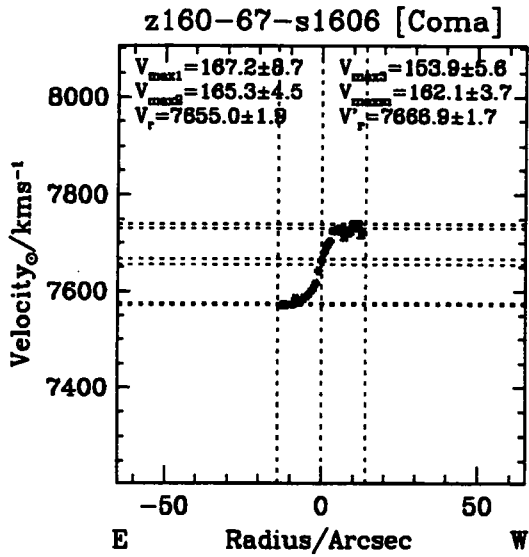
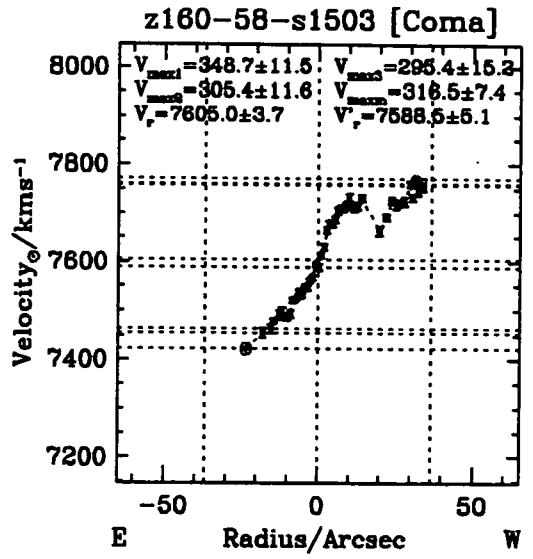
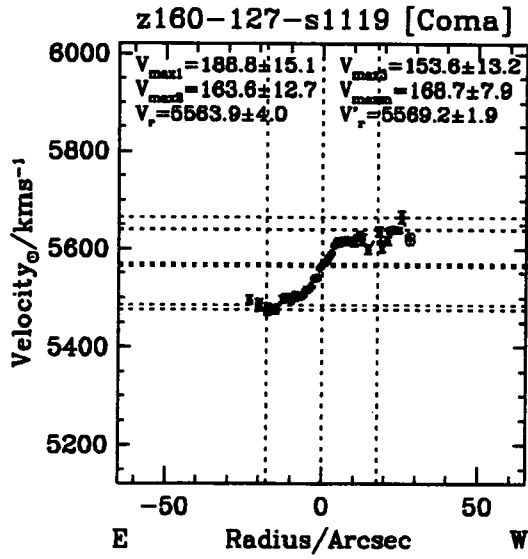
The folded plots that follow indicate the two sides of each curve with open circles and filled triangles respectively. The solid line represents the three parameter rotation curve fit as described in §4.2.2. The dotted curve is a smoothed spline fit to the data points. A dashed line marks the interpolated rotation velocity at $0.6R_{\text{Opt}}$ which is displayed at the top of each panel.

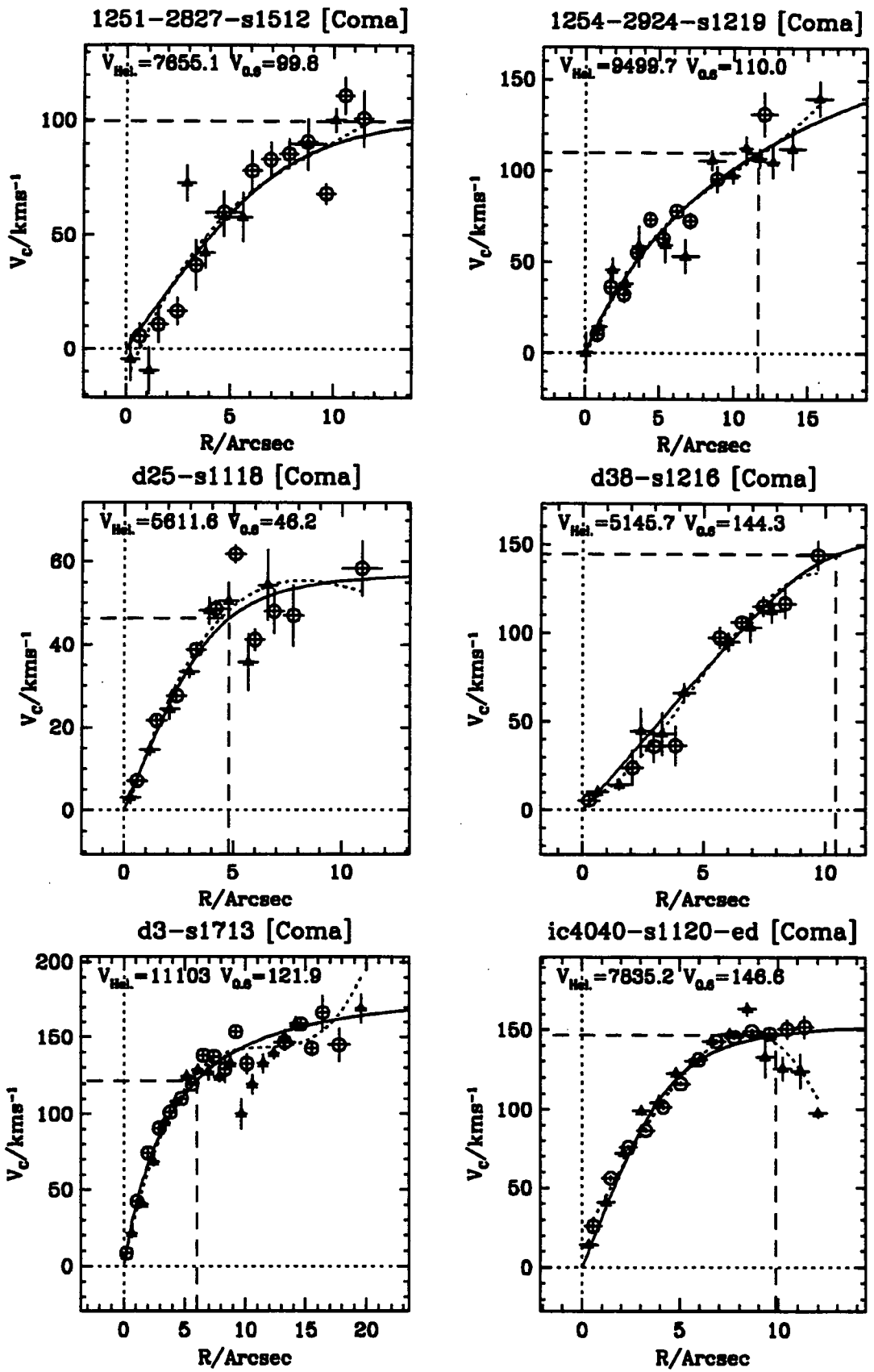


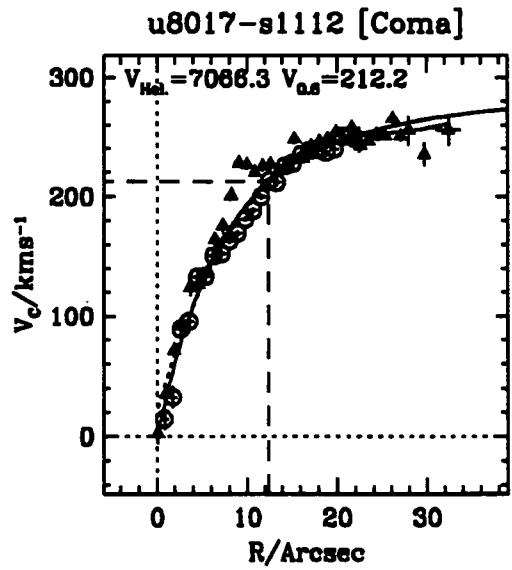
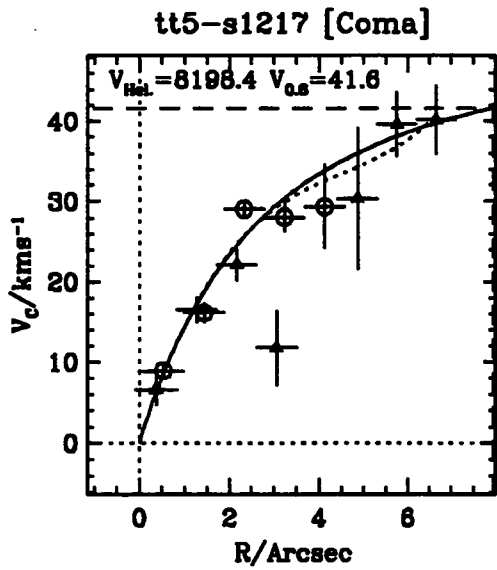
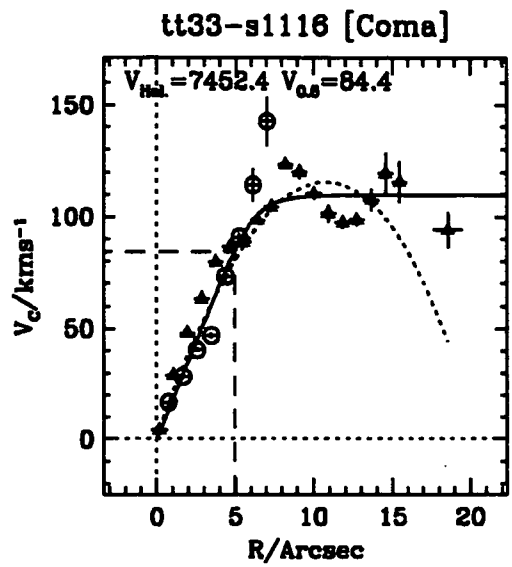
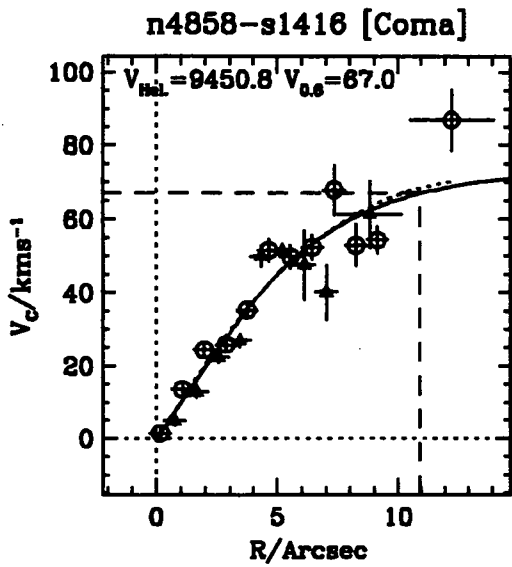
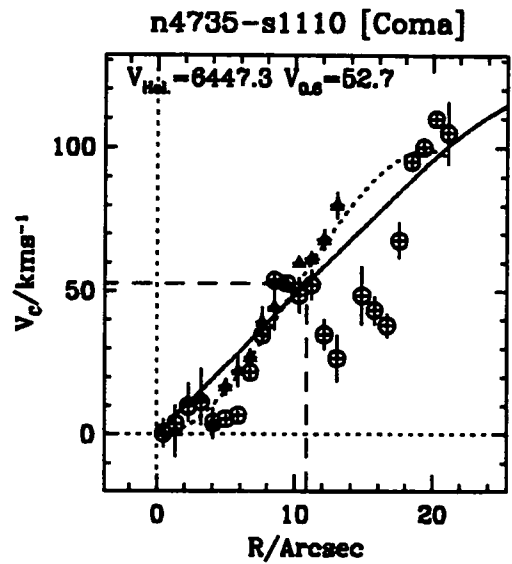
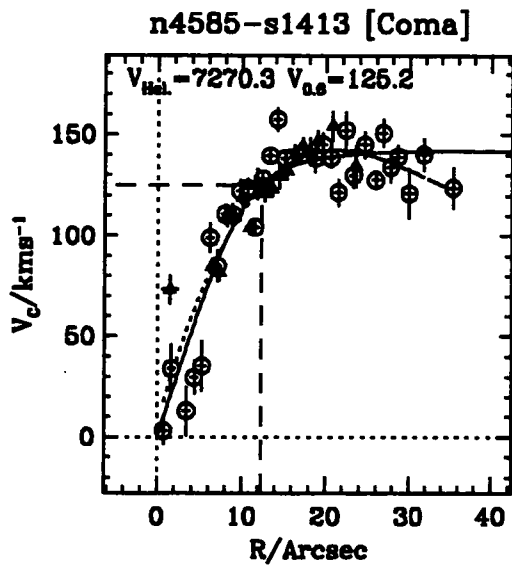


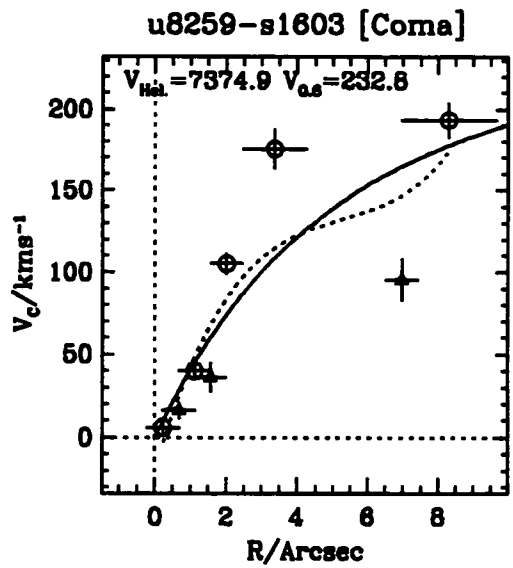
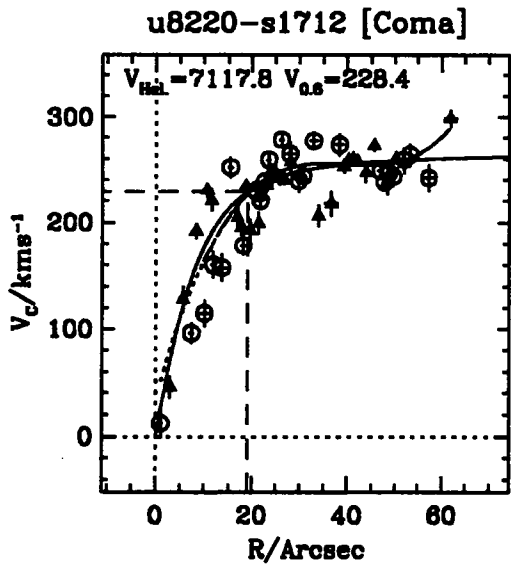
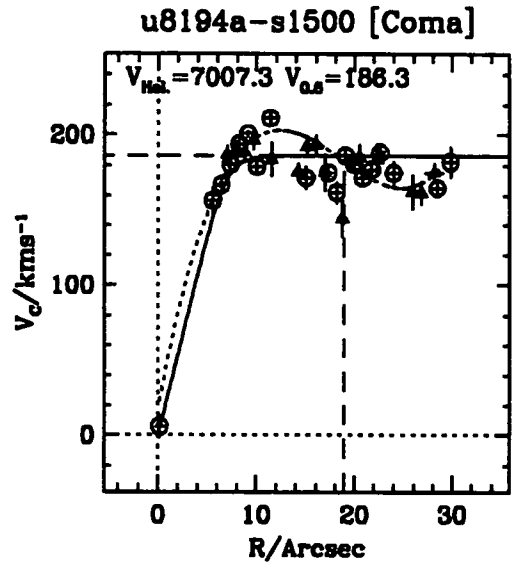
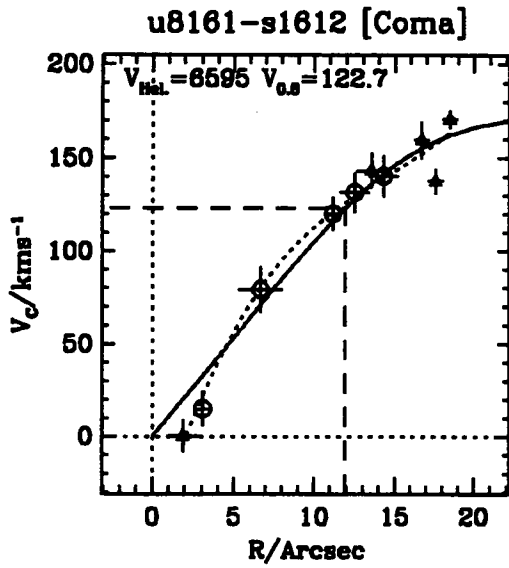
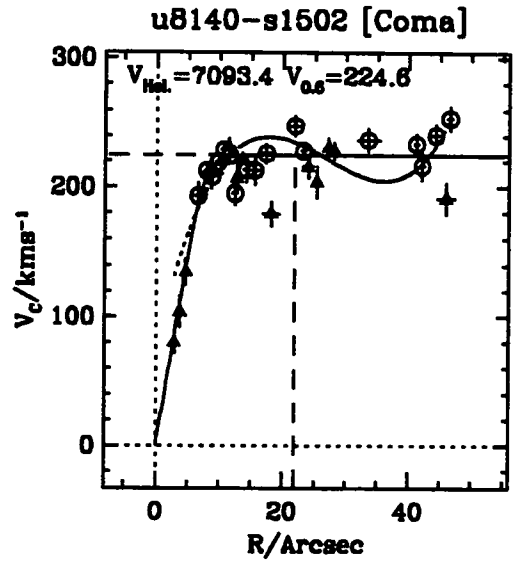
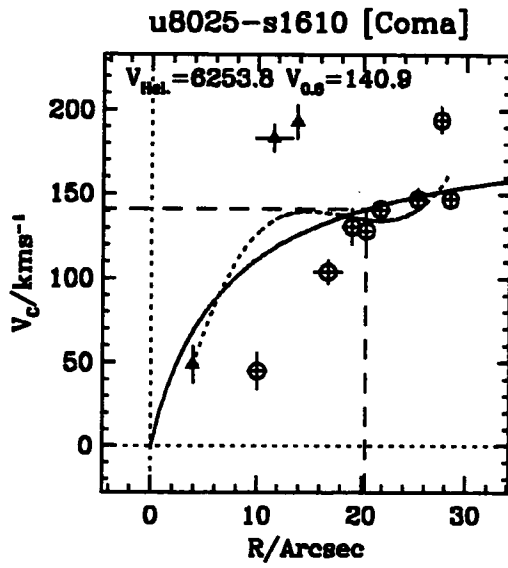


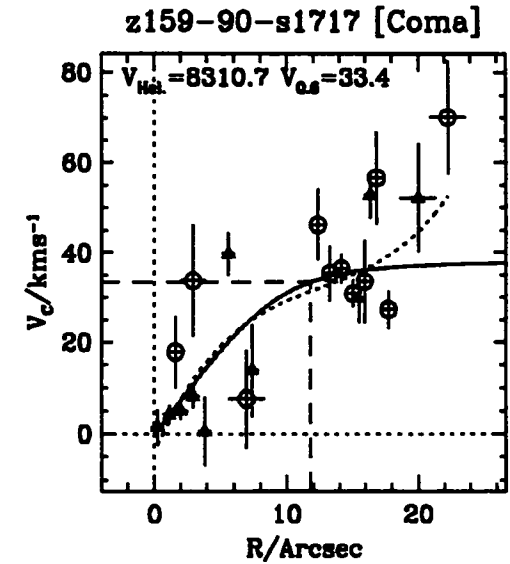
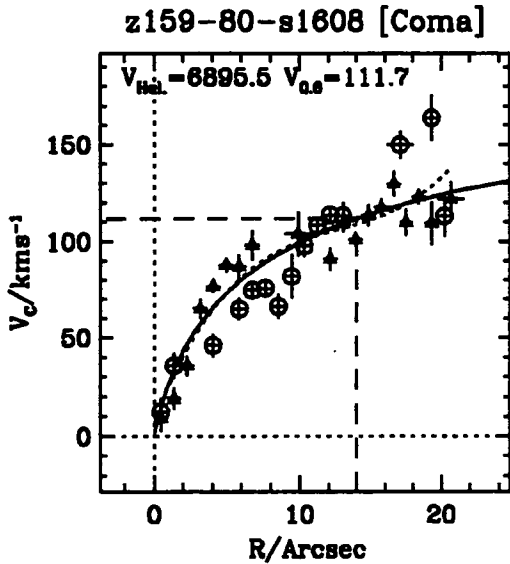
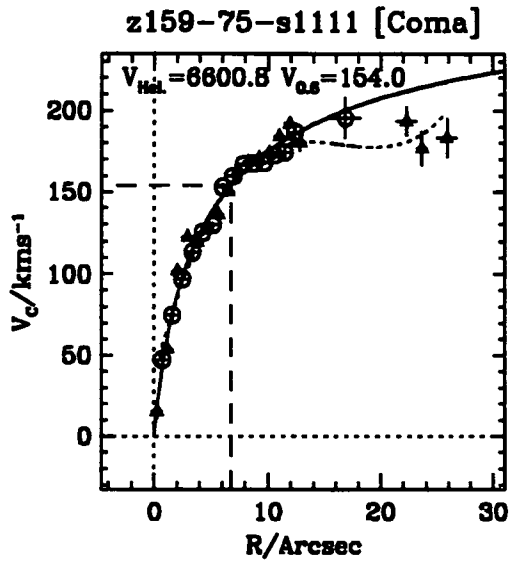
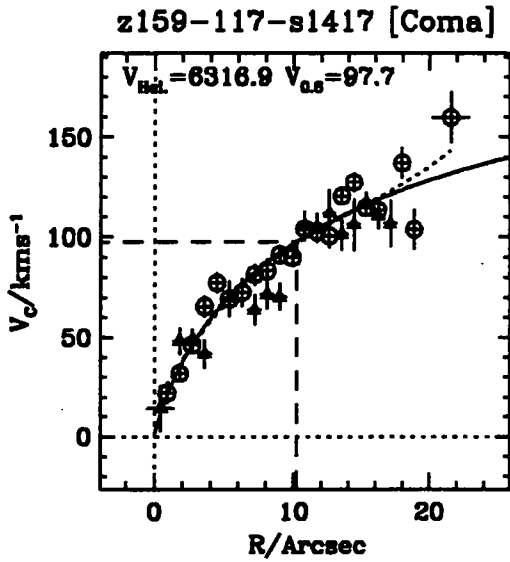
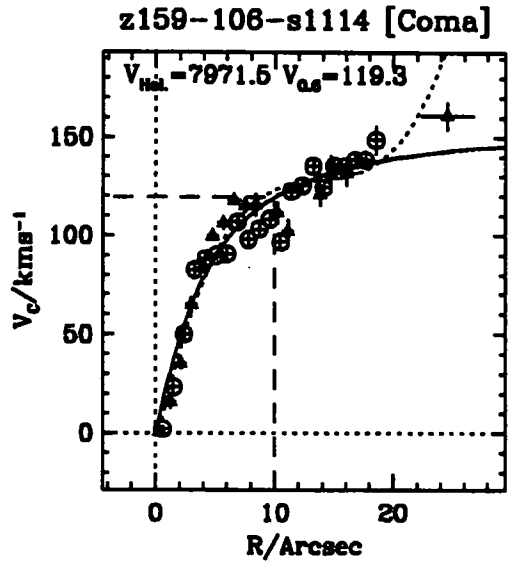
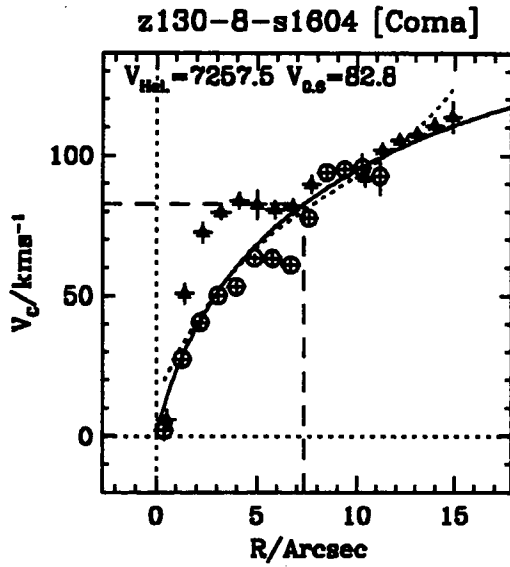


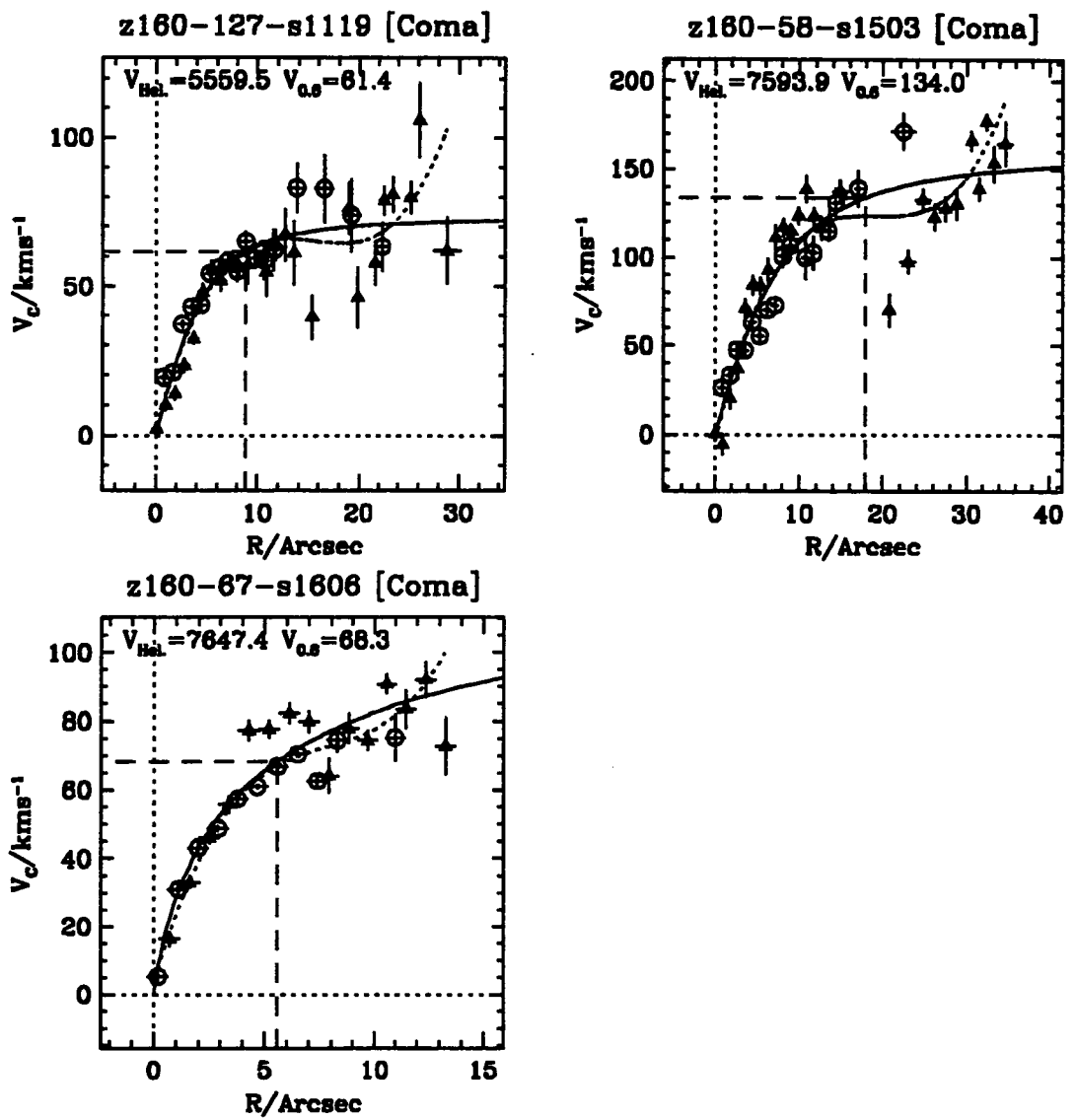


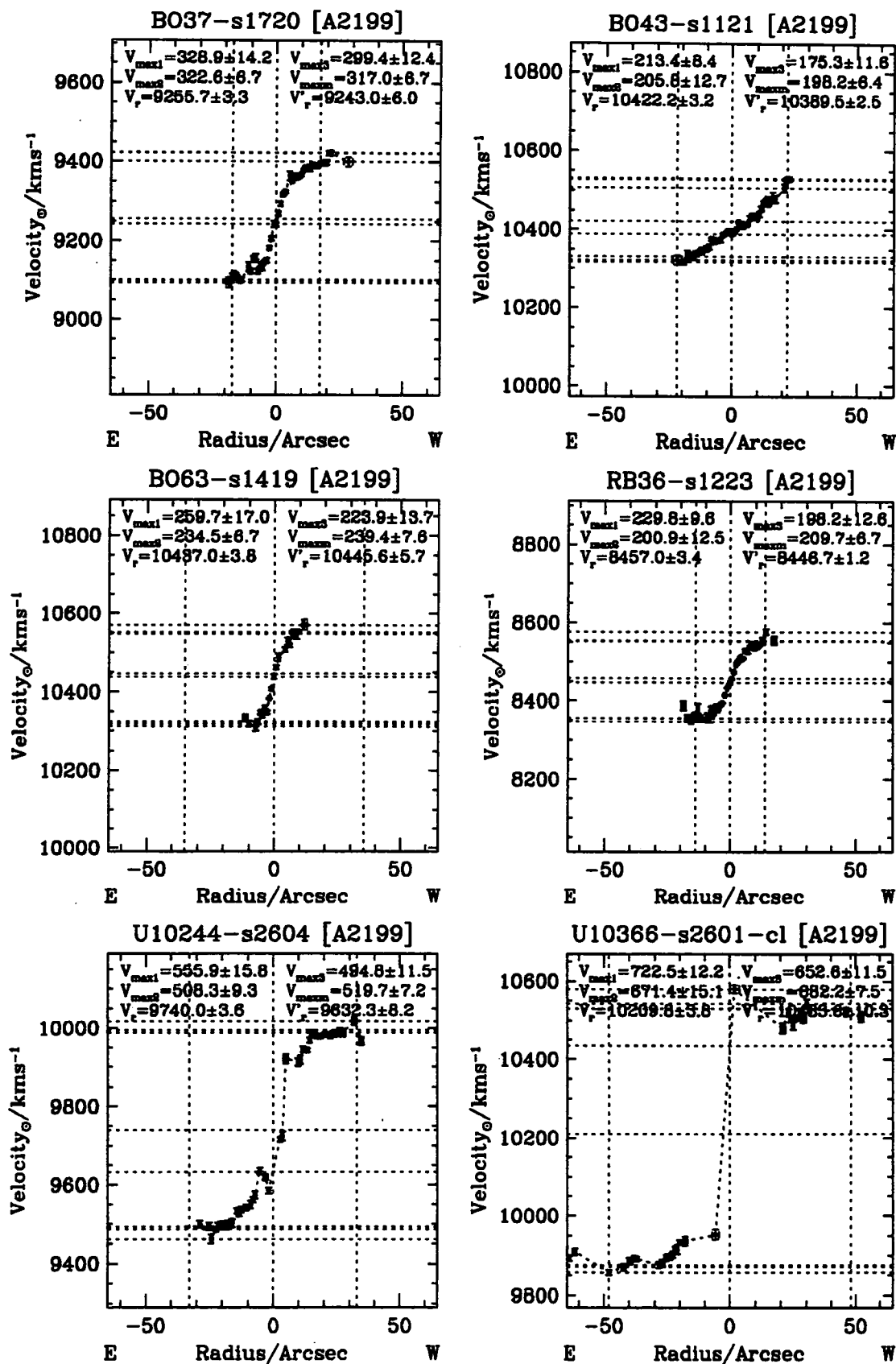


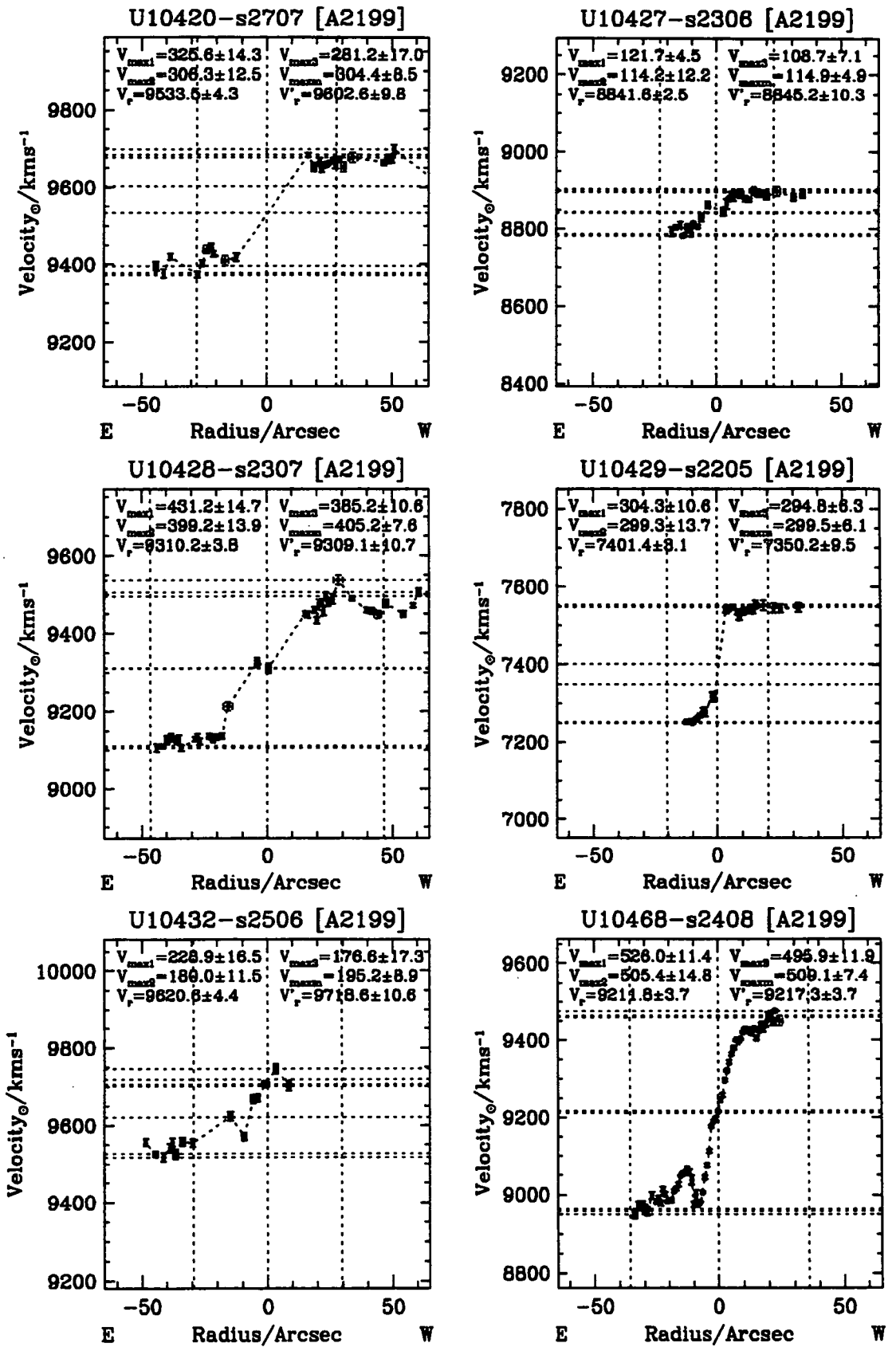


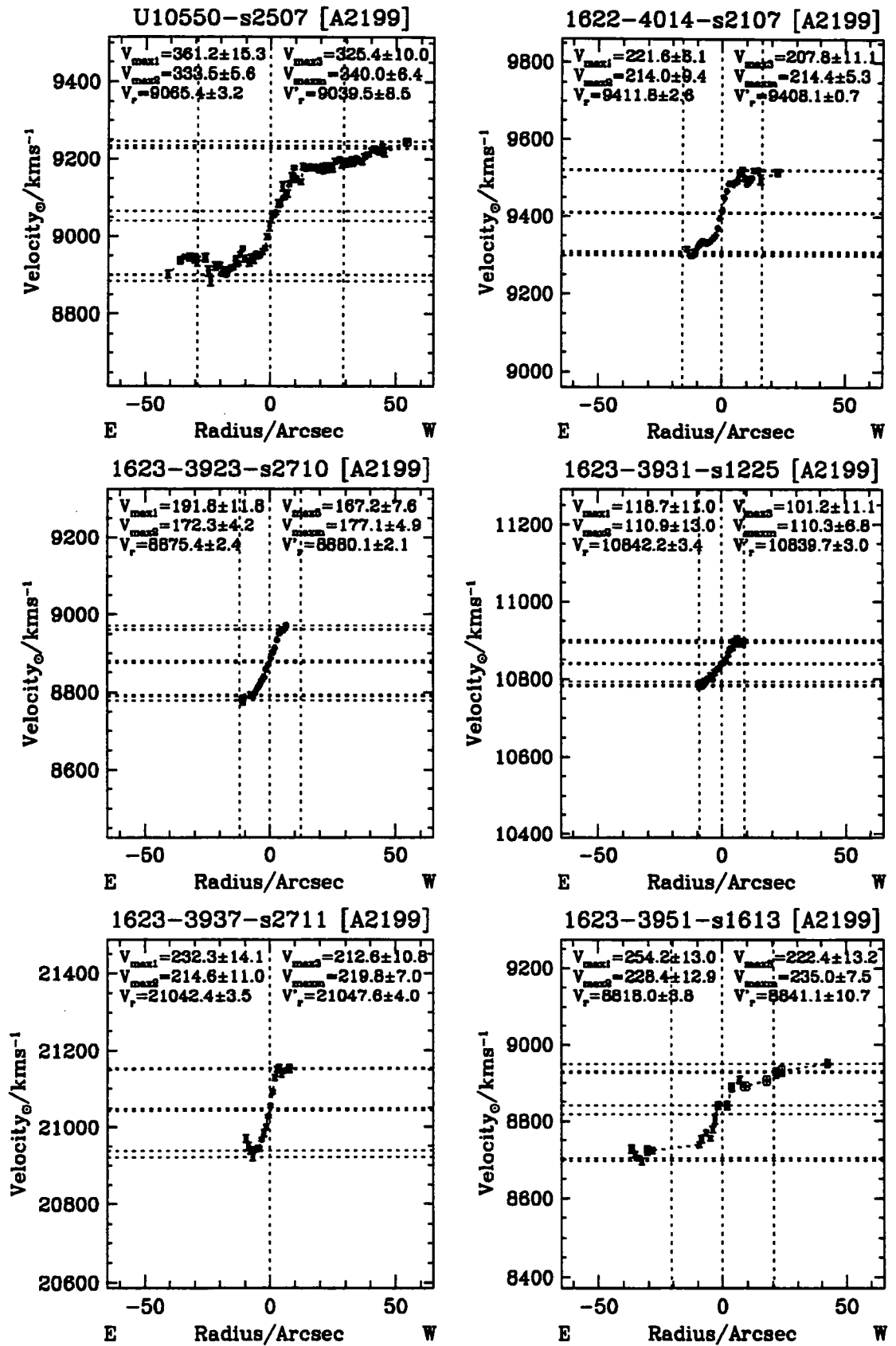


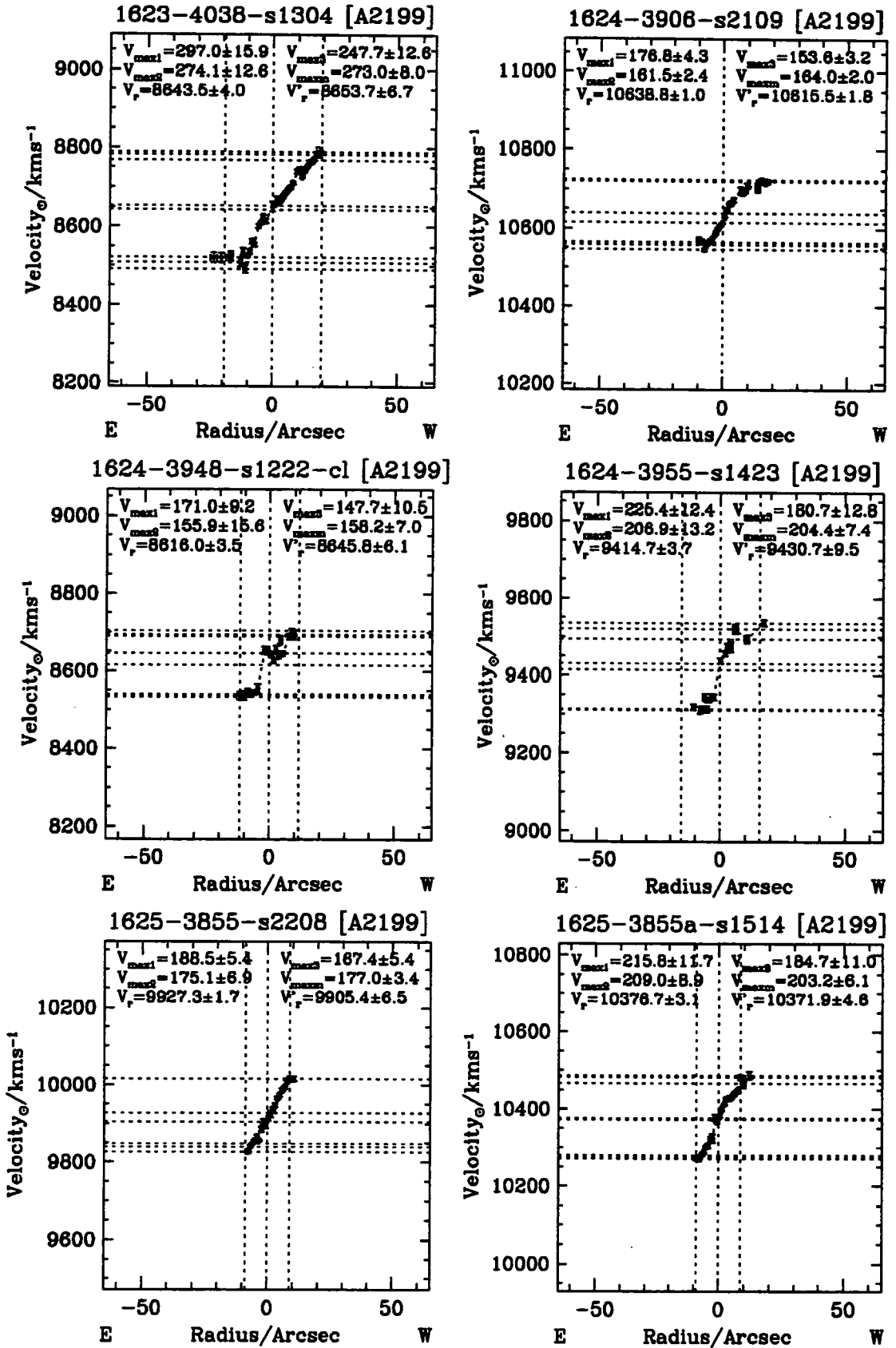


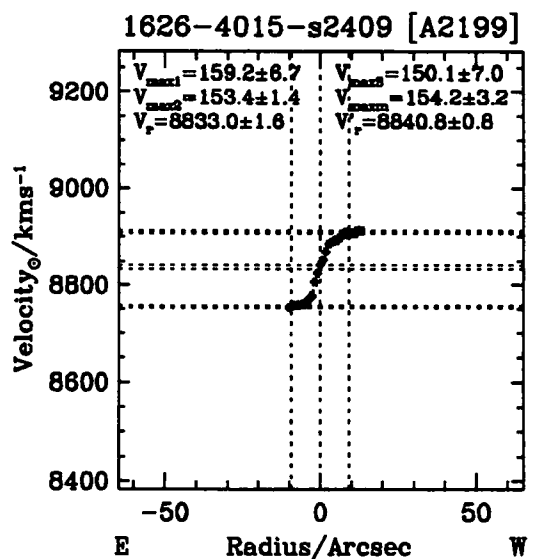
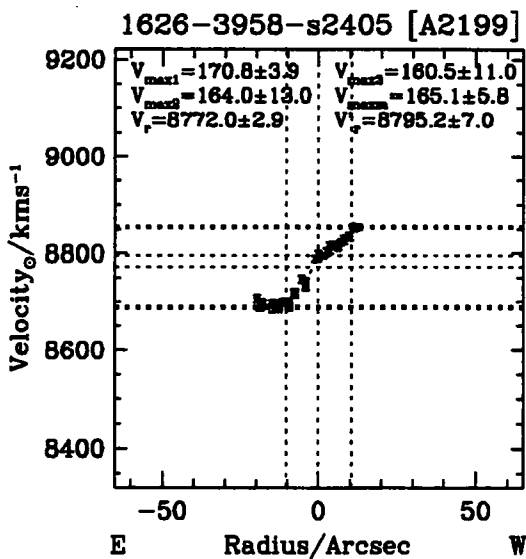
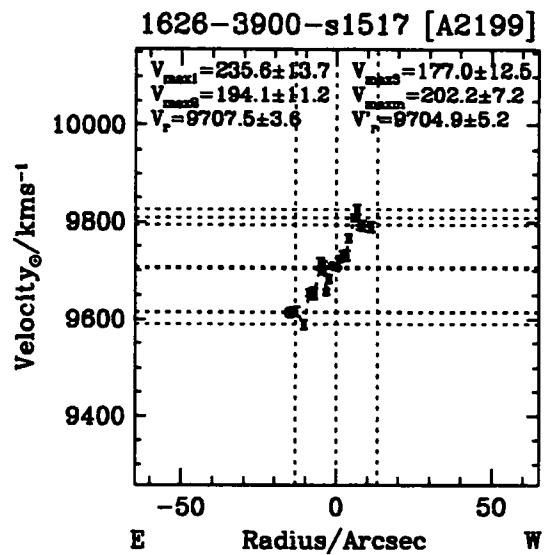
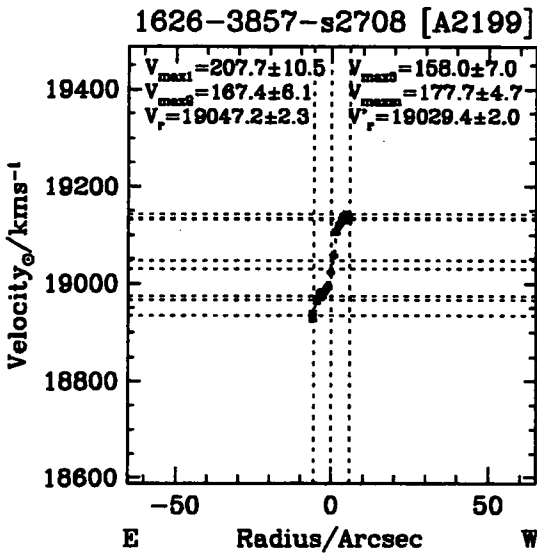
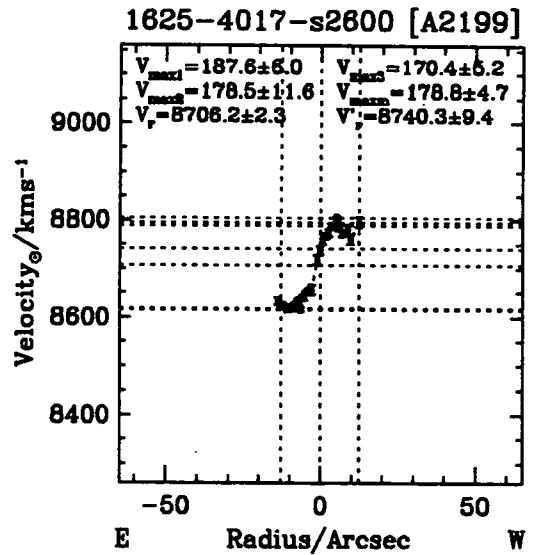
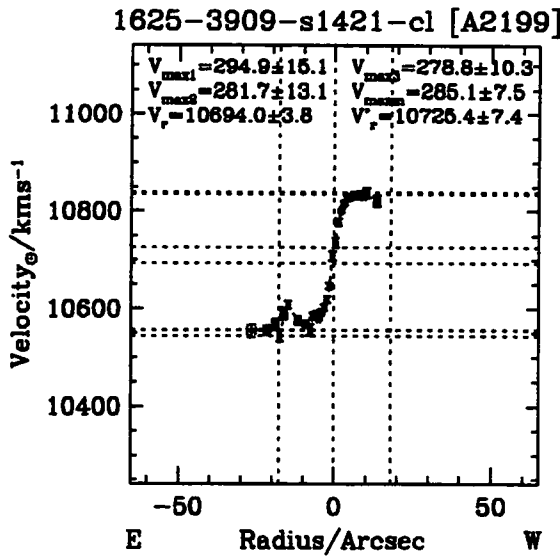


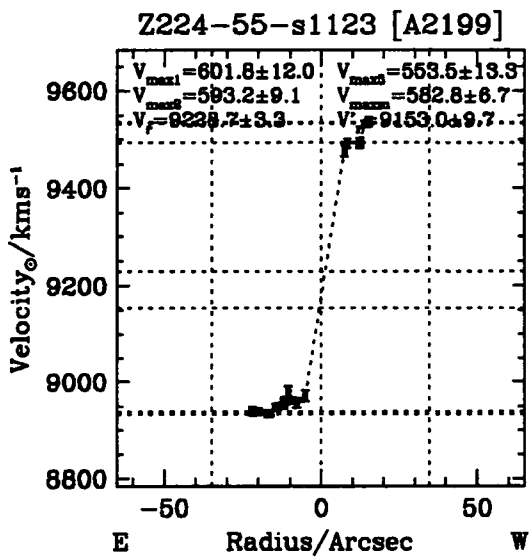
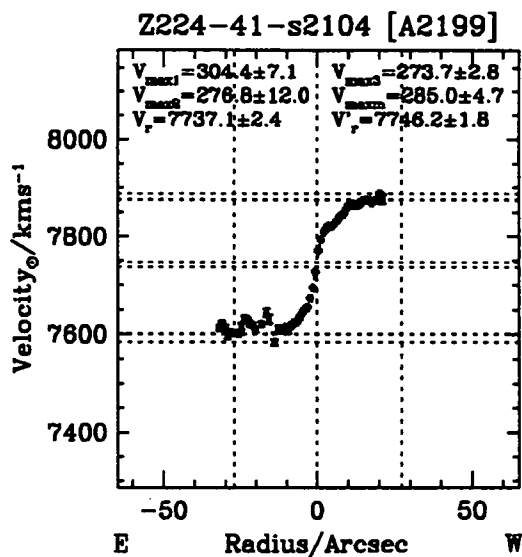
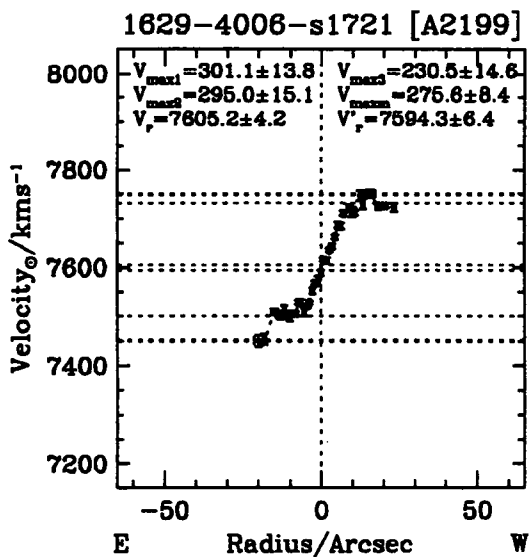


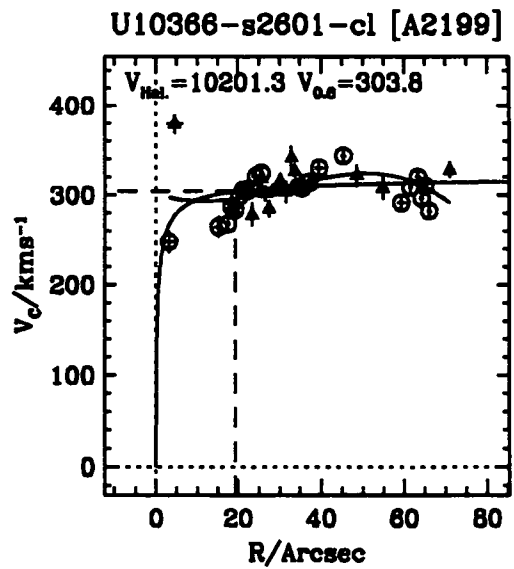
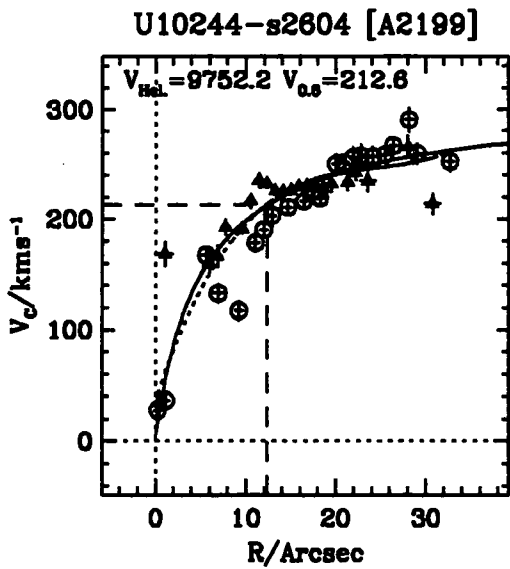
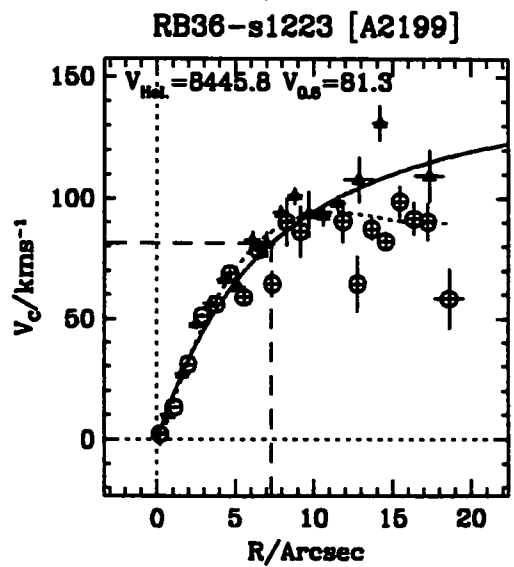
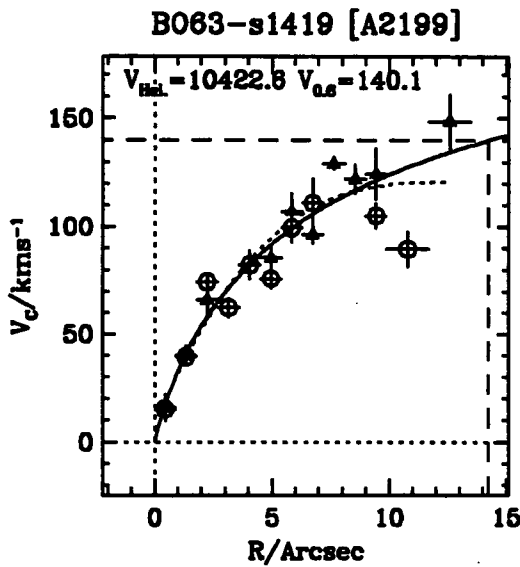
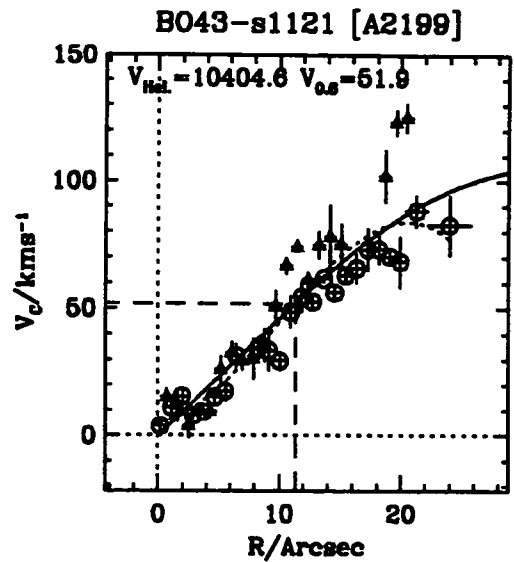
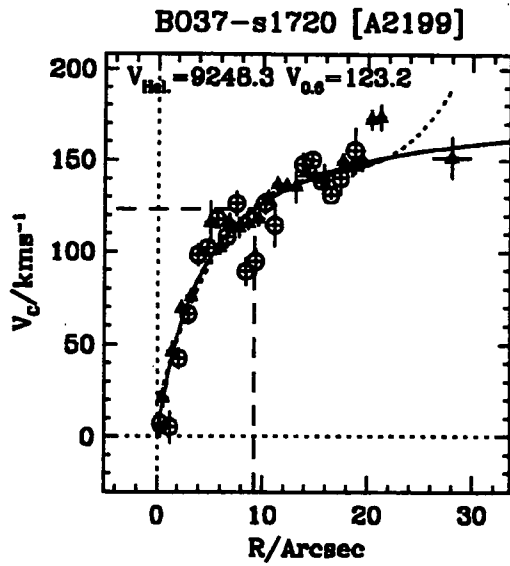


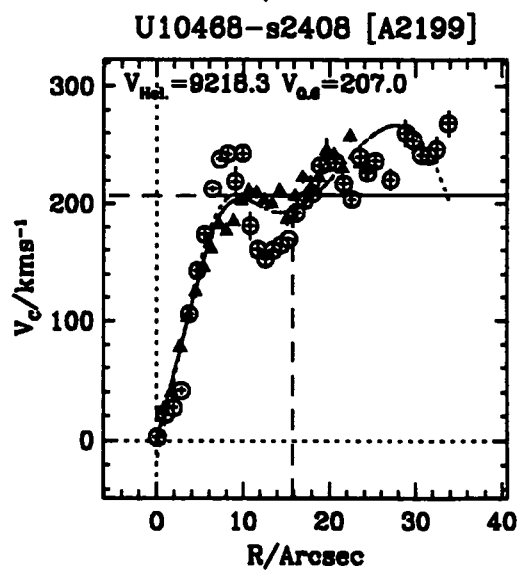
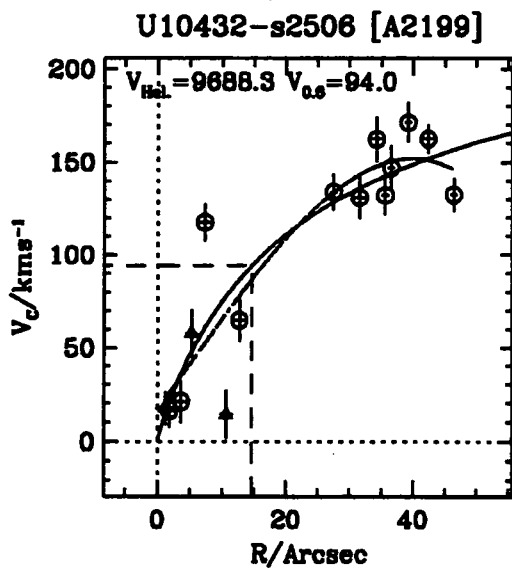
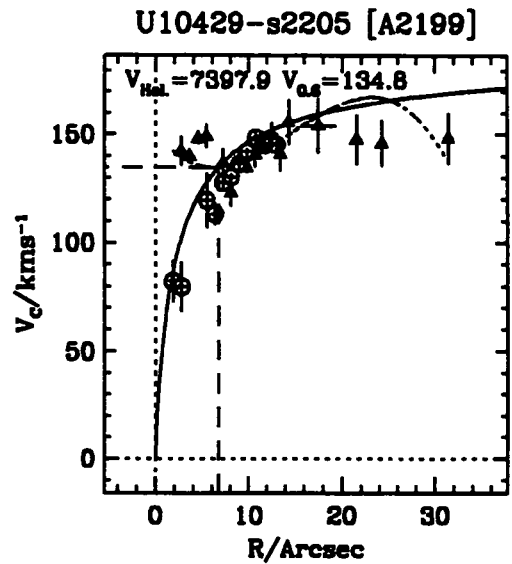
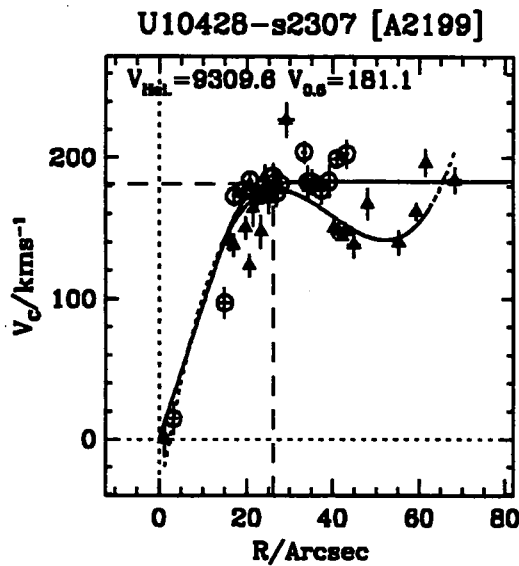
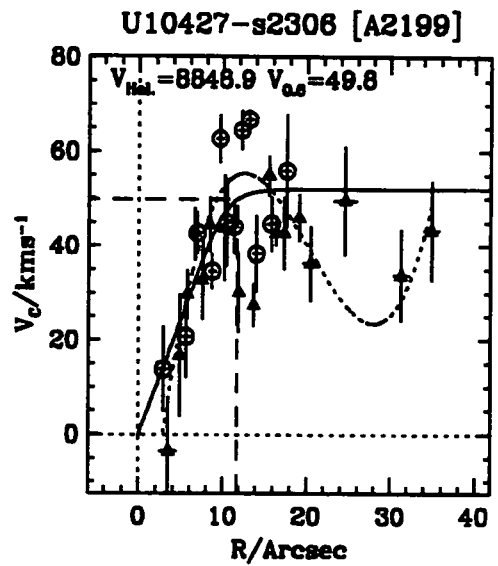
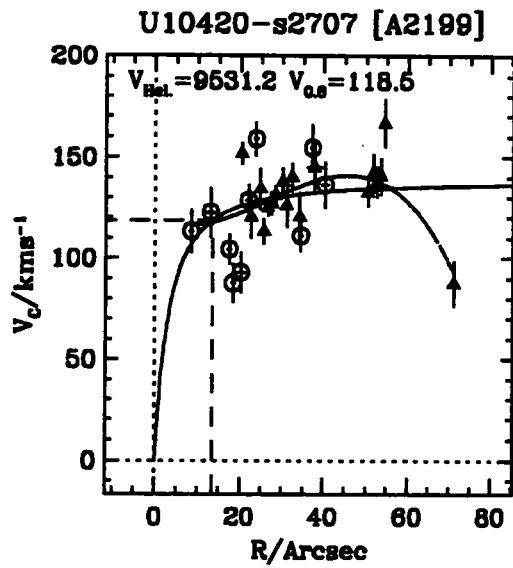


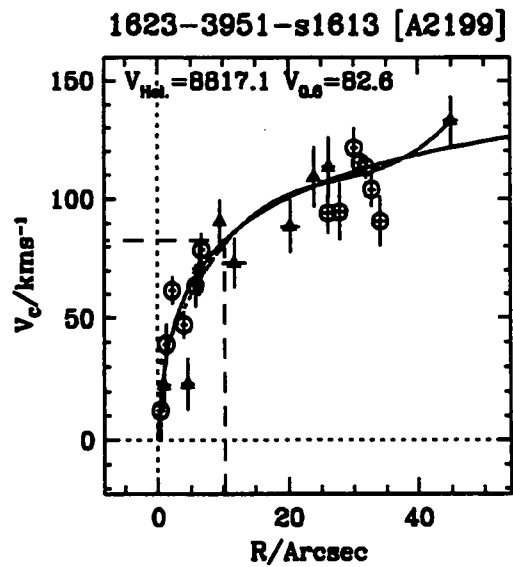
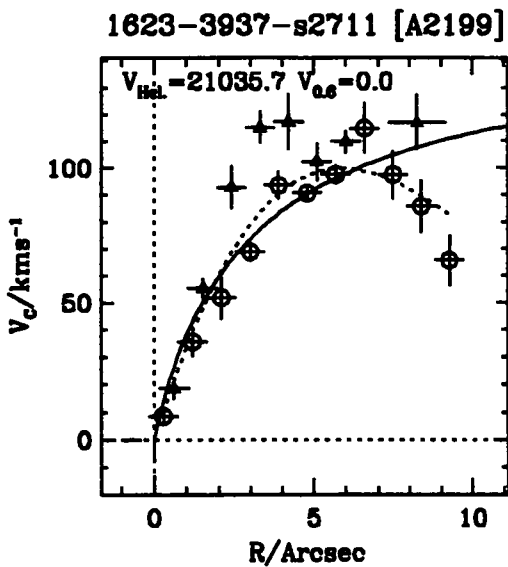
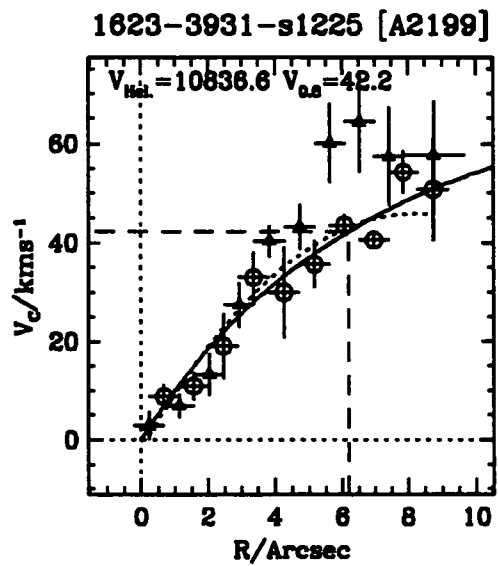
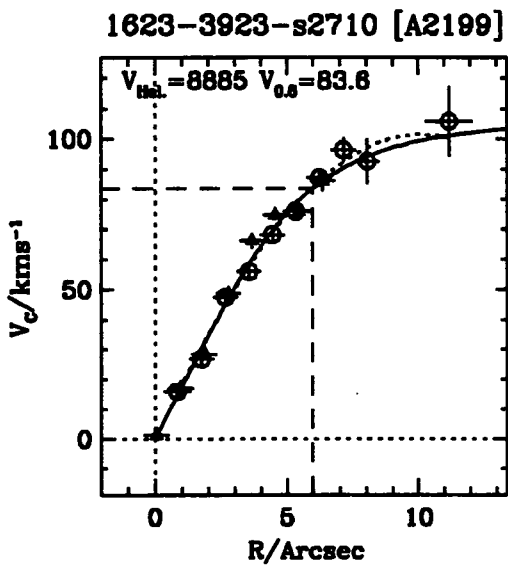
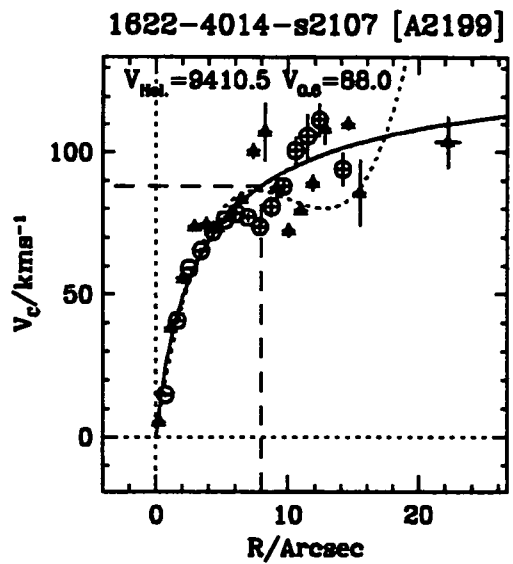
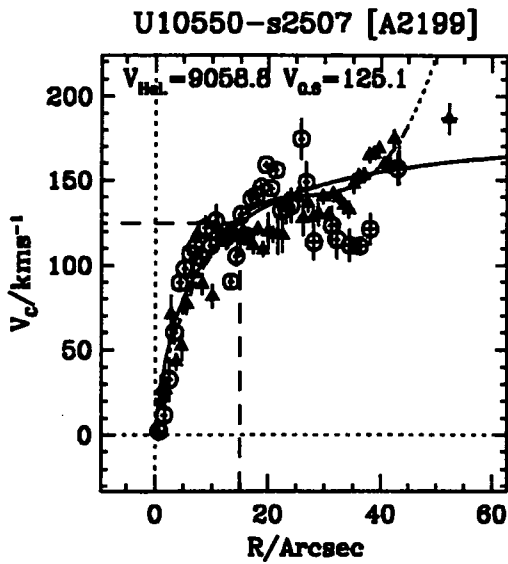


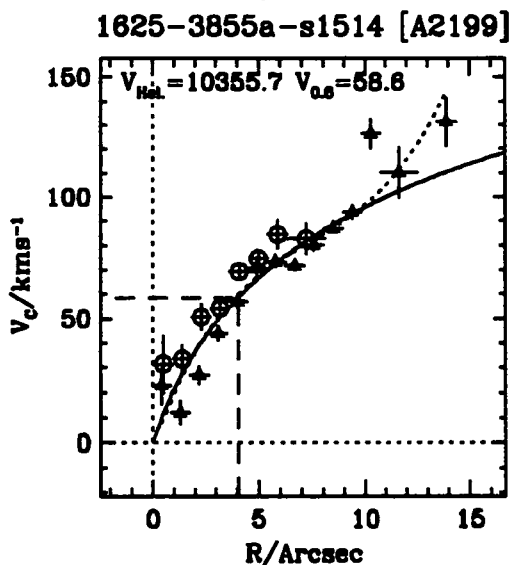
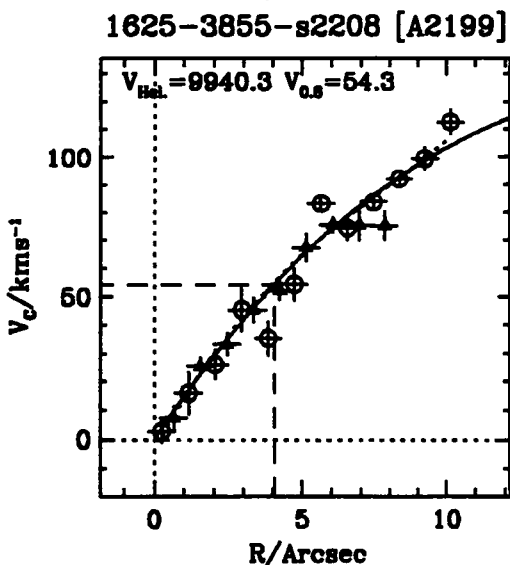
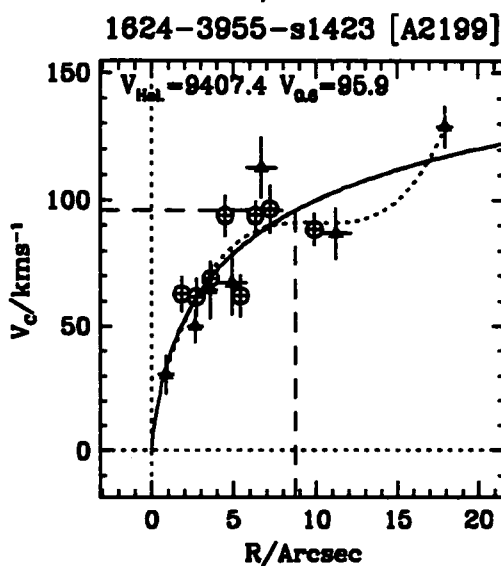
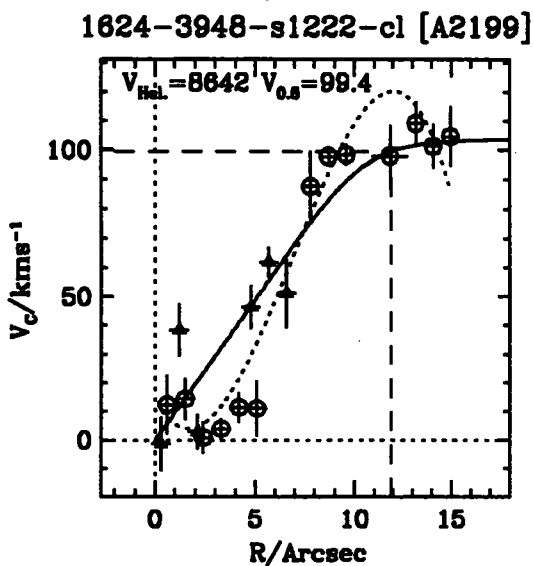
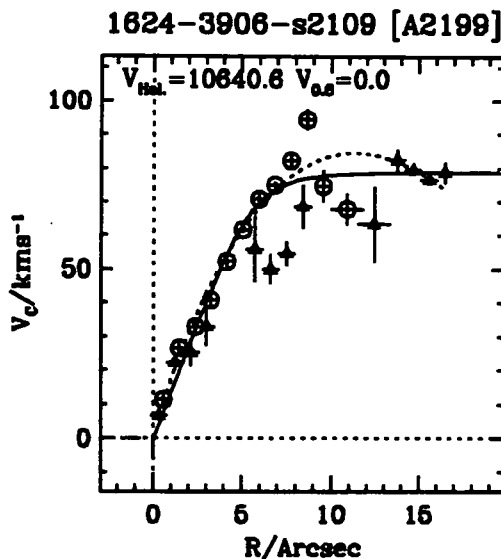
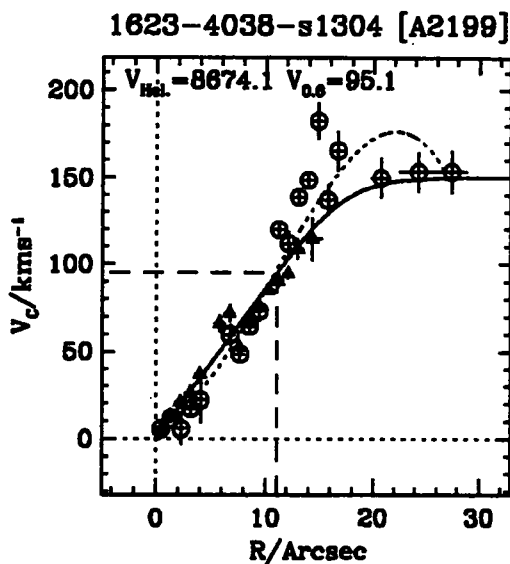




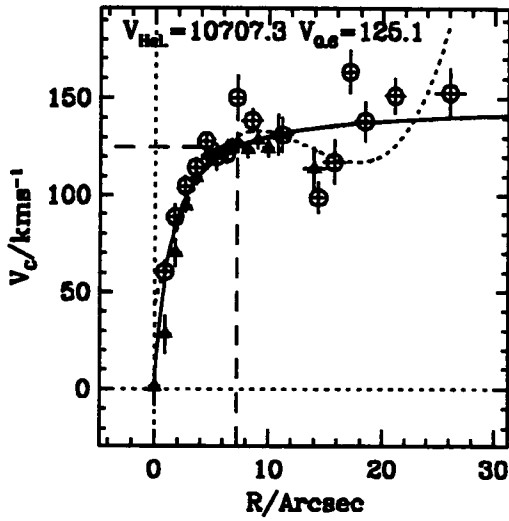




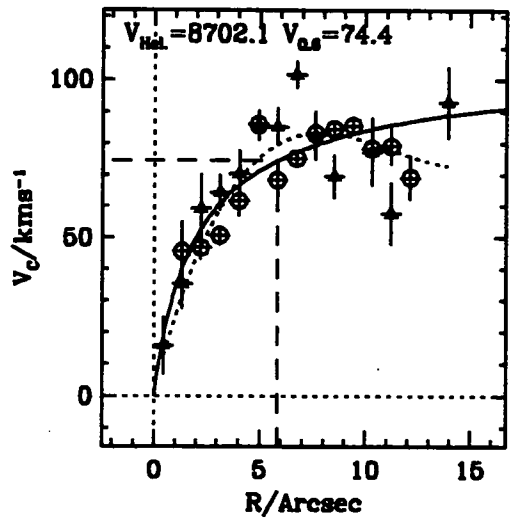




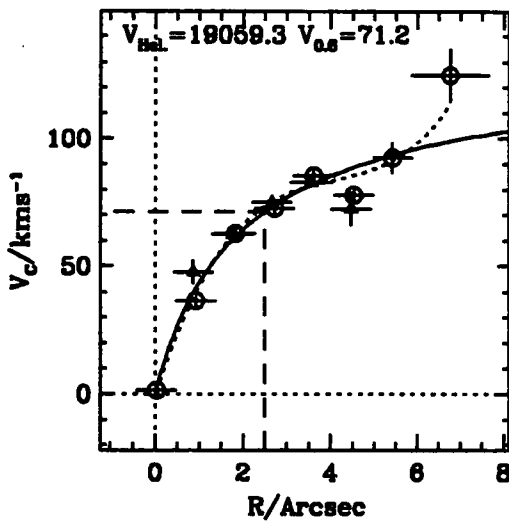
1625-3909-s1421-cl [A2199]



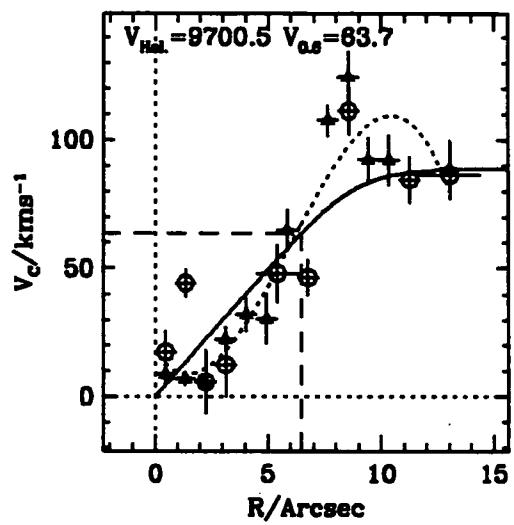
1625-4017-s2600 [A2199]



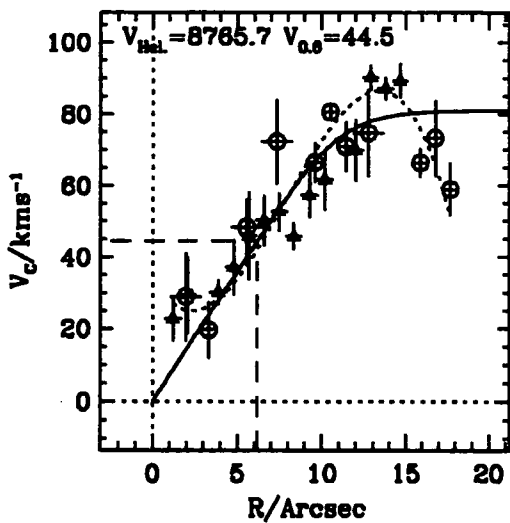
1626-3857-s2708 [A2199]



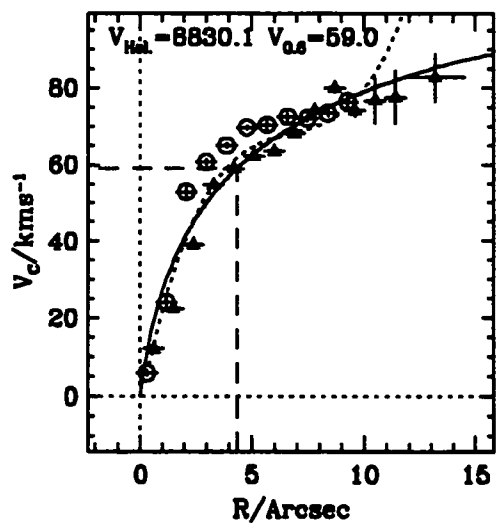
1626-3900-s1517 [A2199]



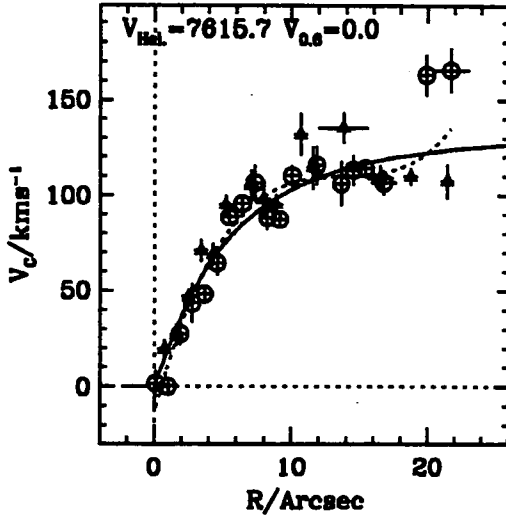
1626-3958-s2405 [A2199]



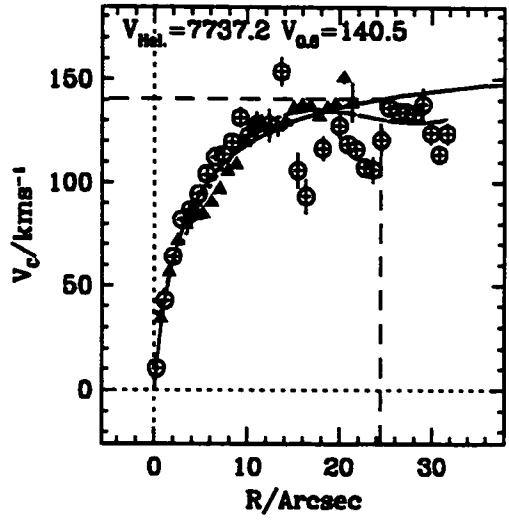
1626-4015-s2409 [A2199]



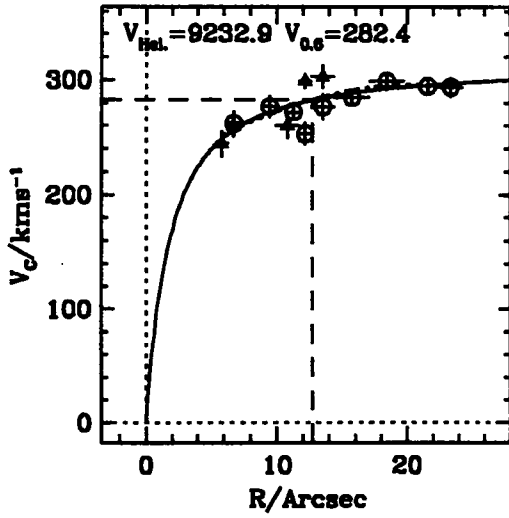
1629-4006-s1721 [A2199]

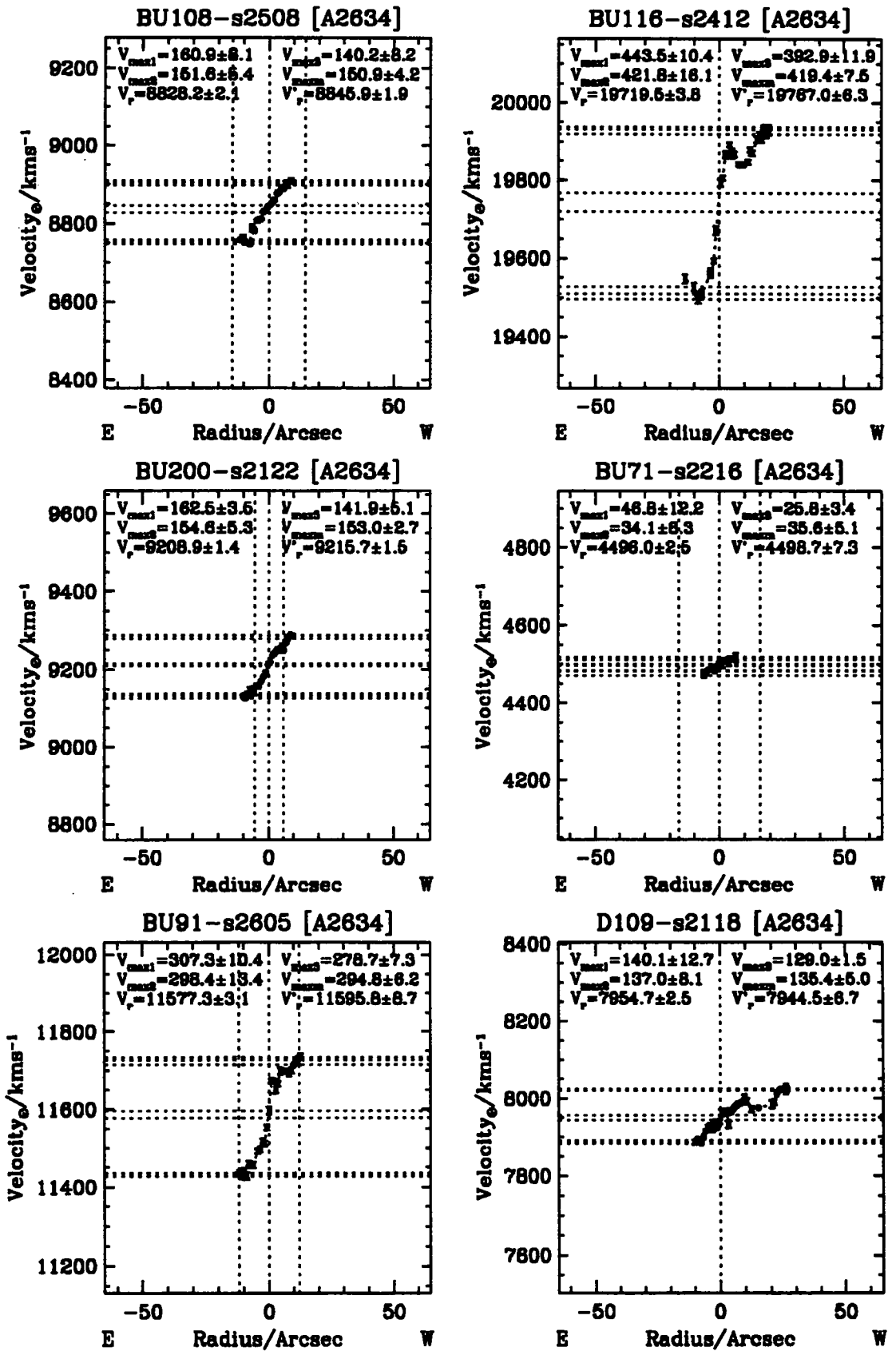


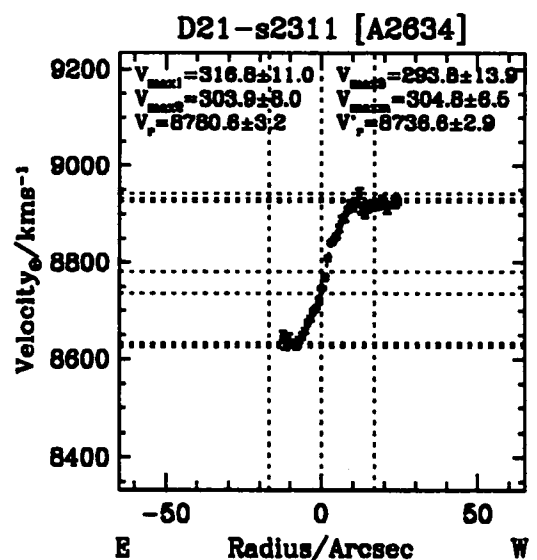
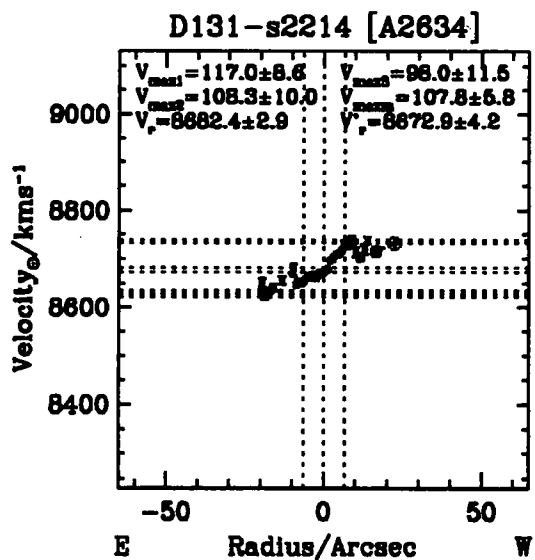
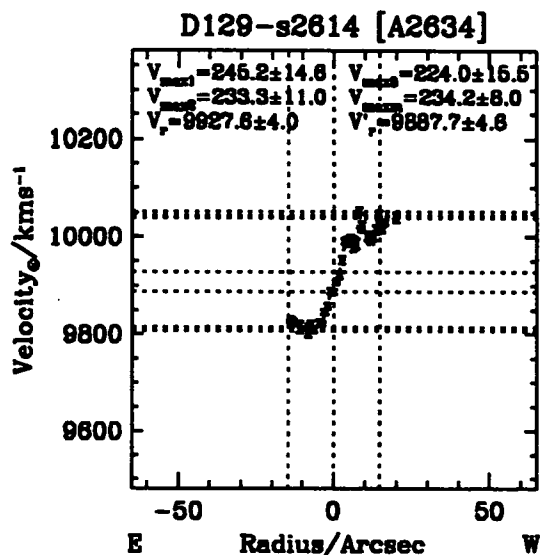
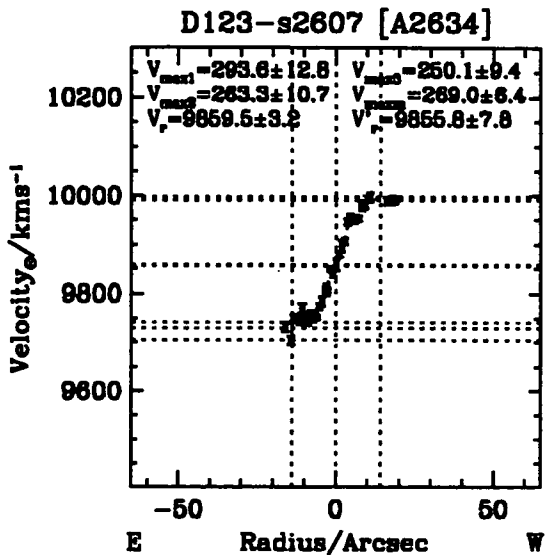
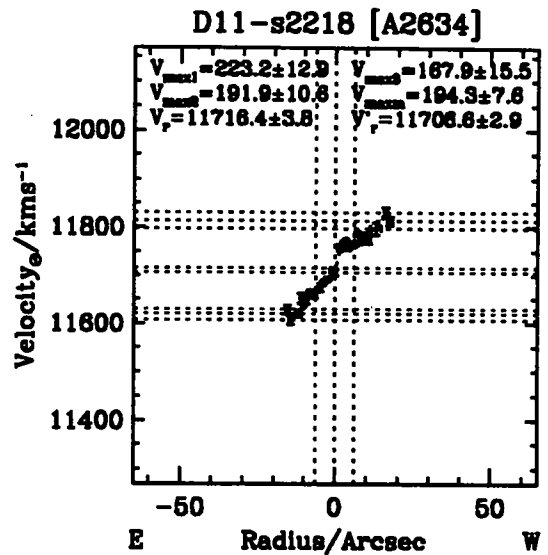
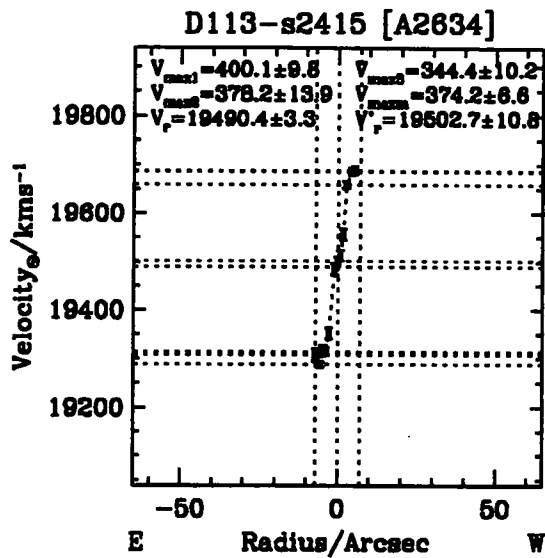
Z224-41-s2104 [A2199]

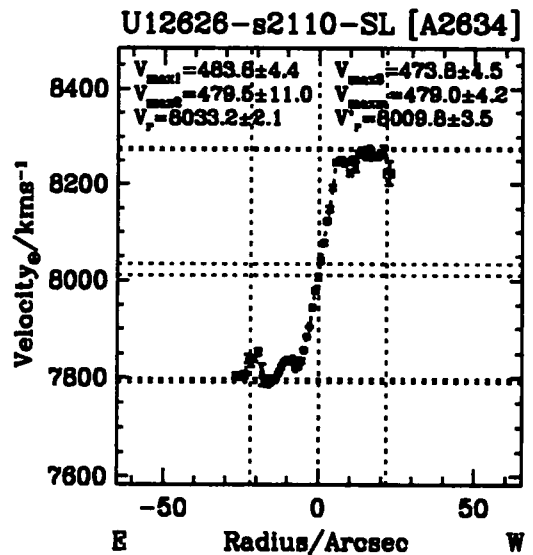
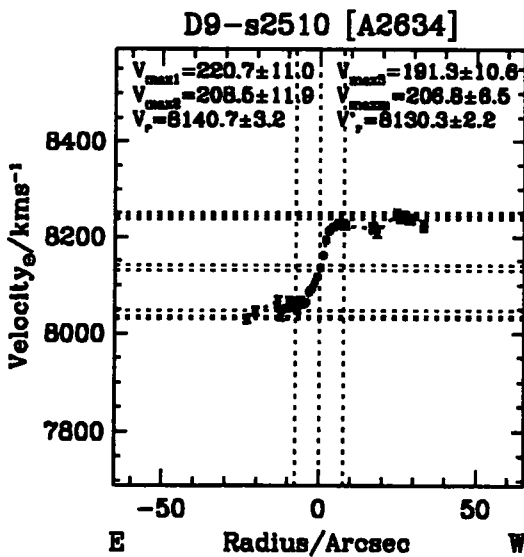
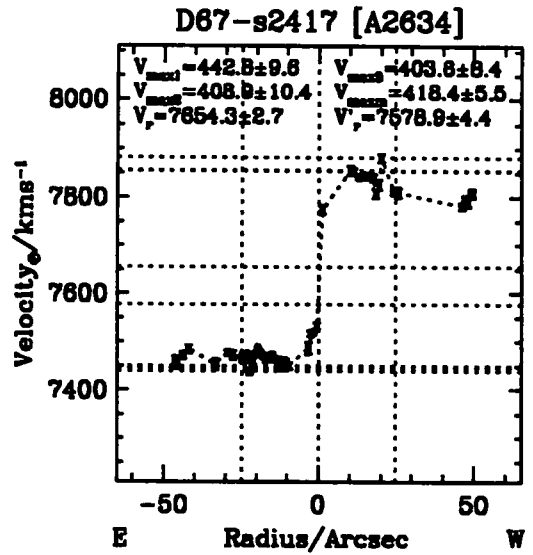
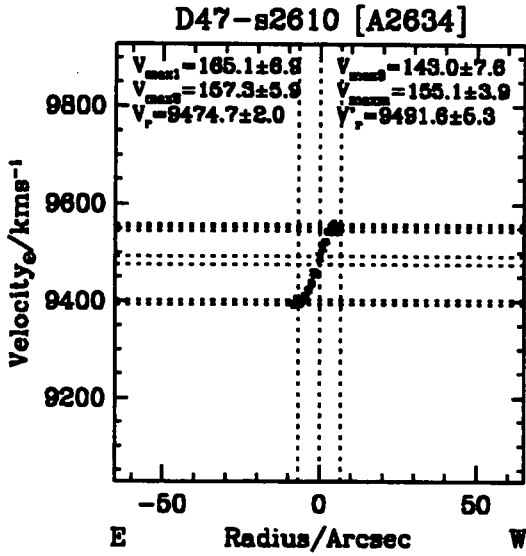
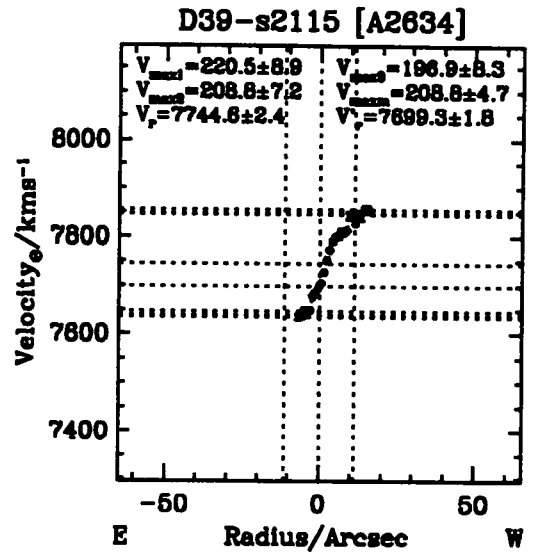
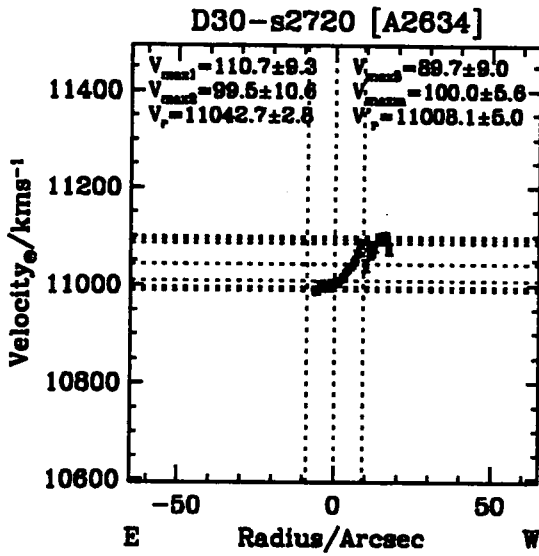


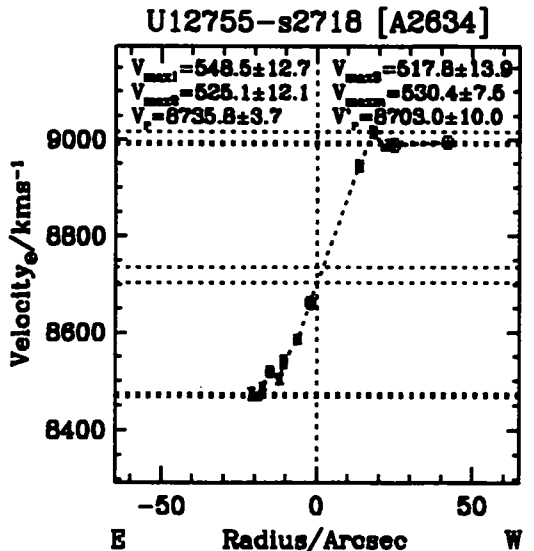
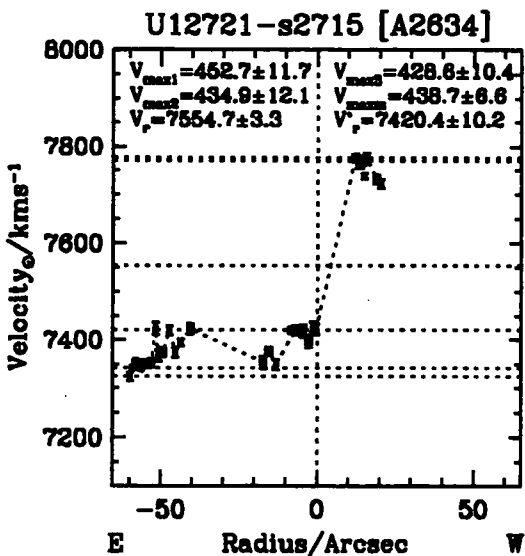
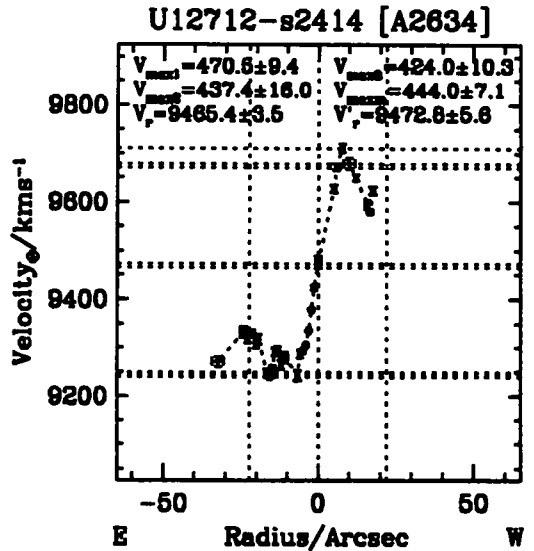
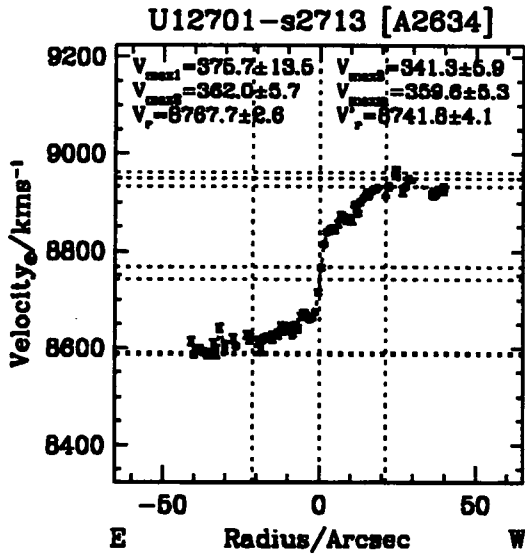
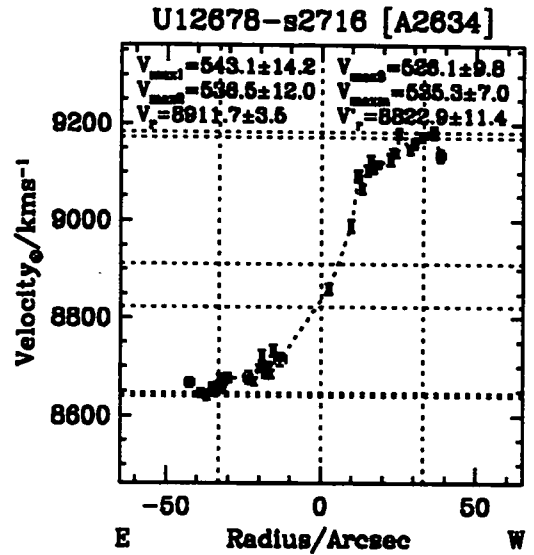
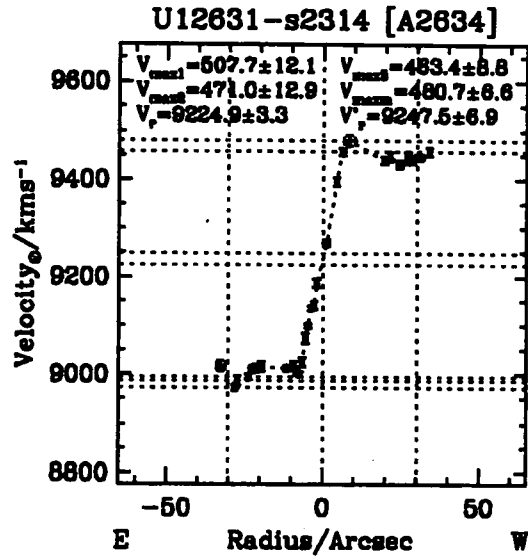
Z224-55-s1123 [A2199]

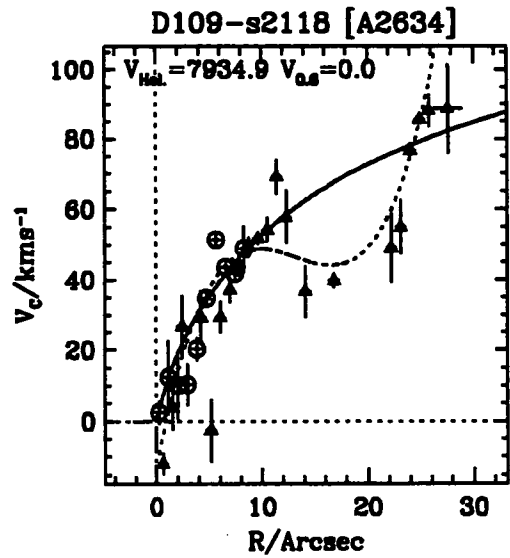
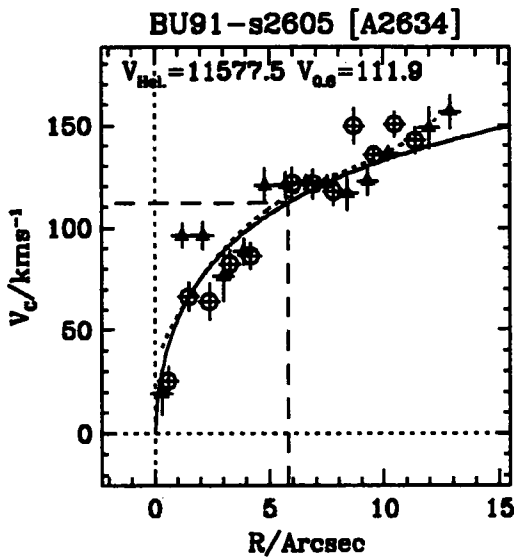
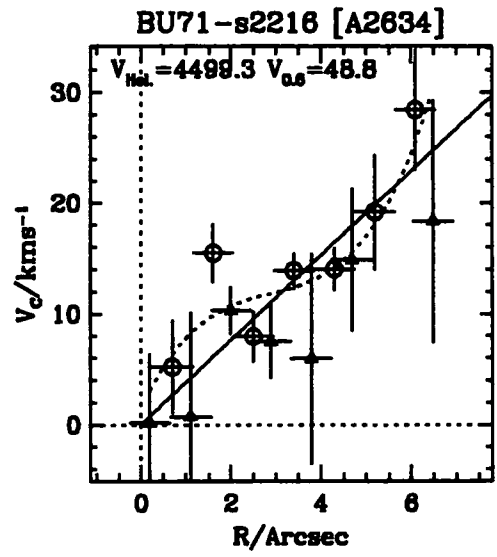
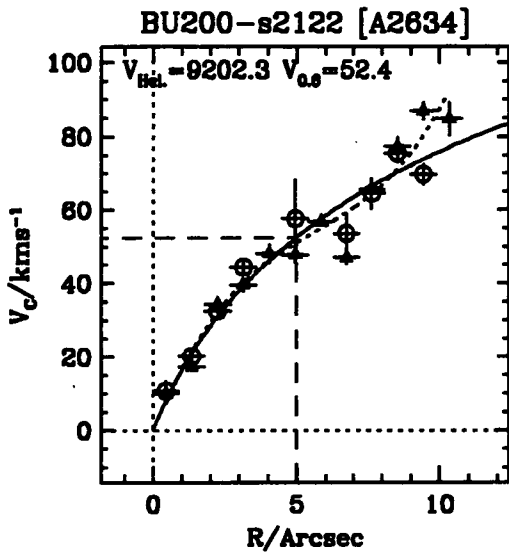
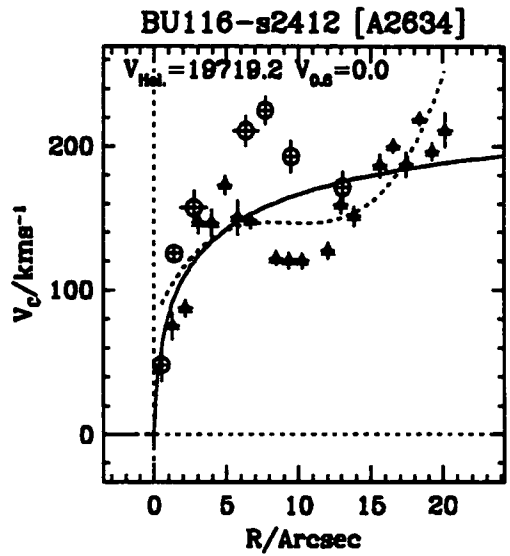
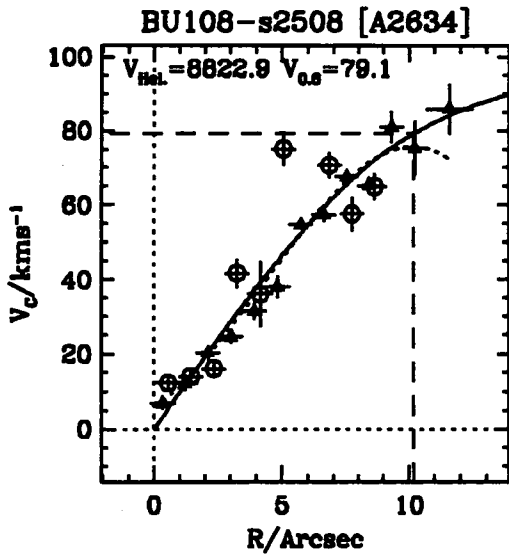


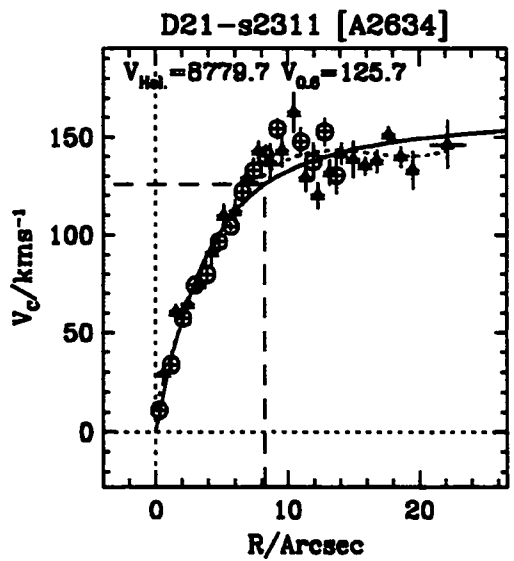
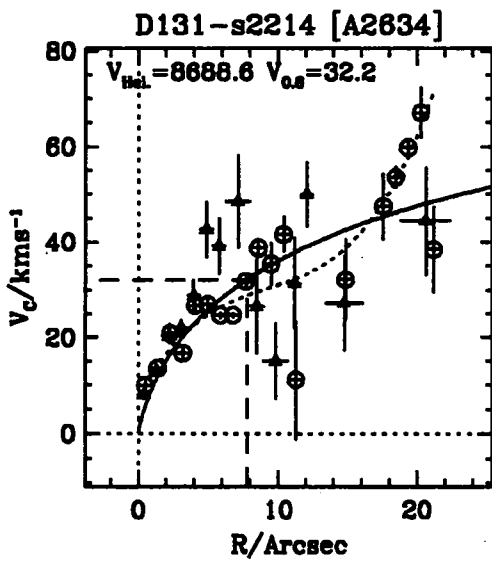
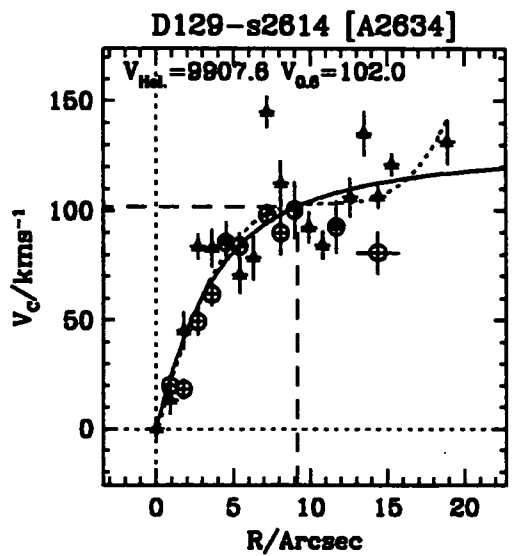
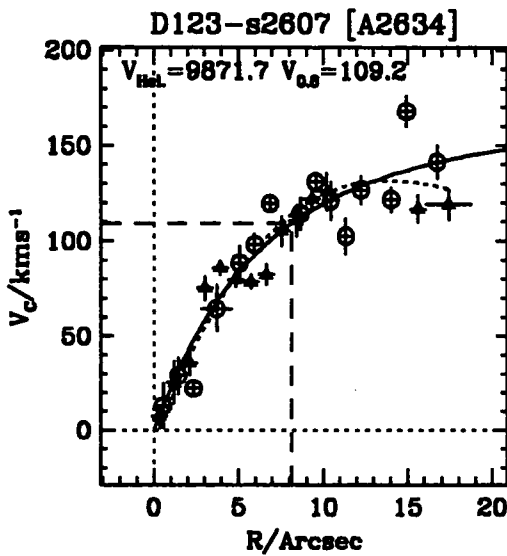
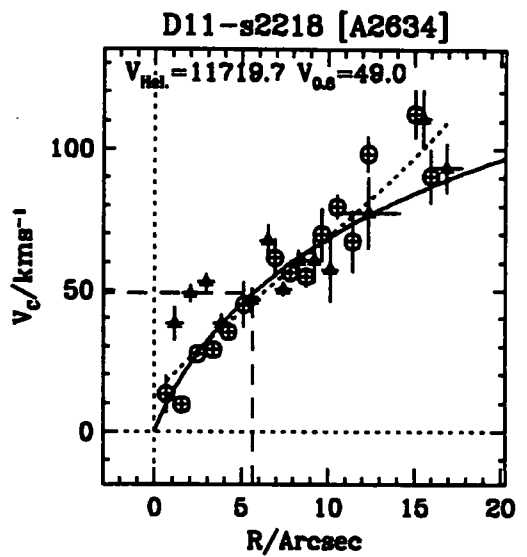
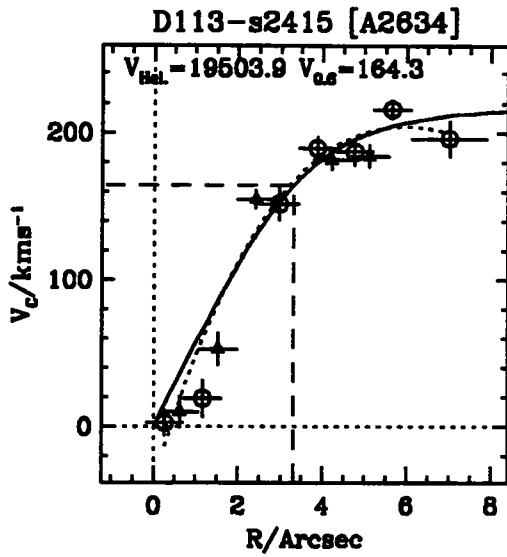


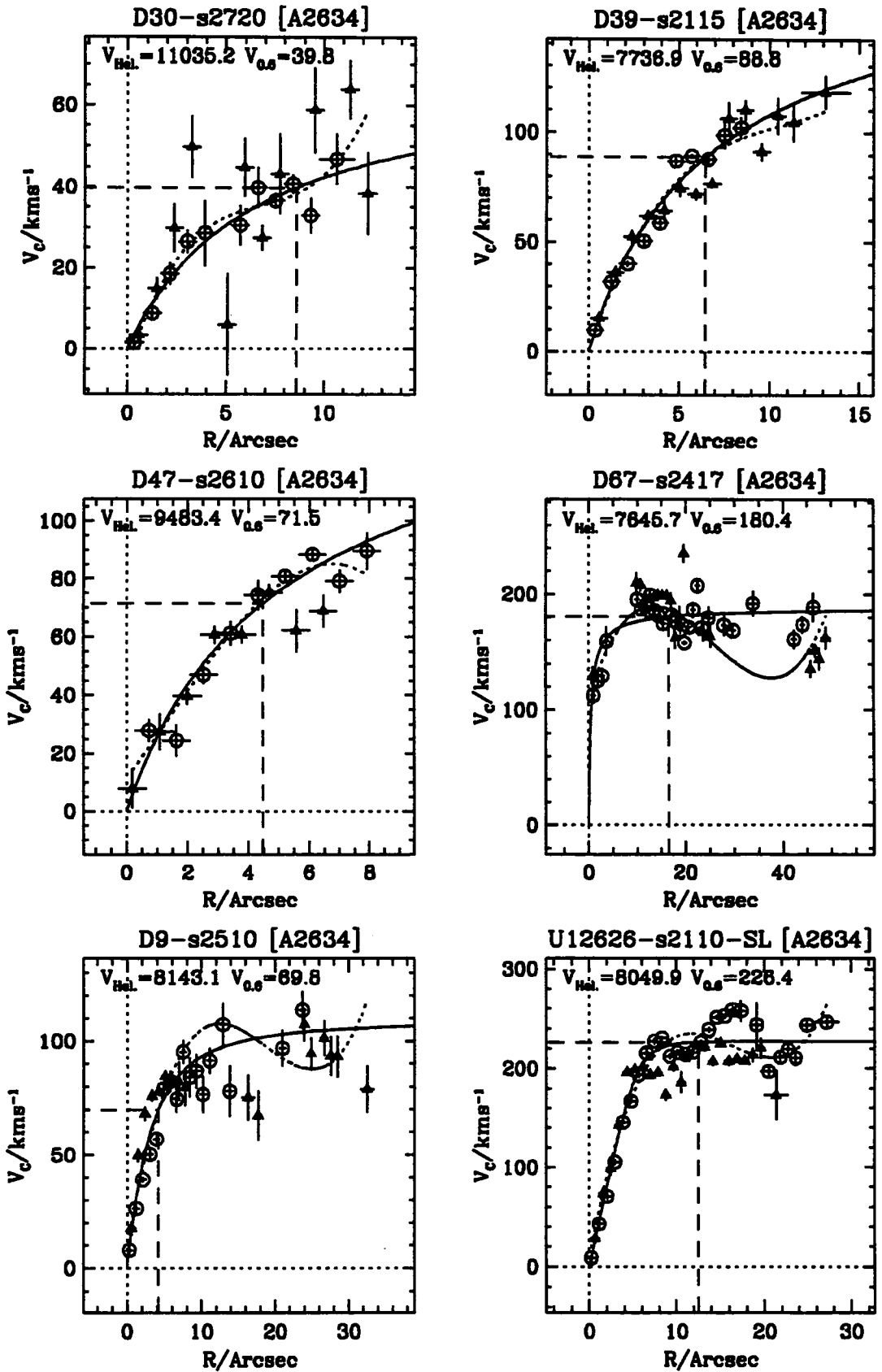


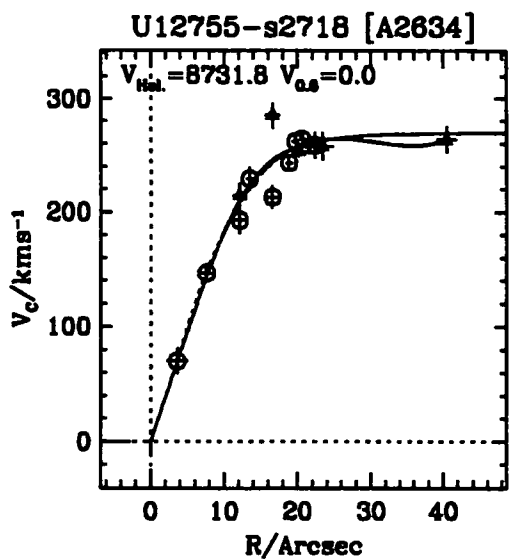
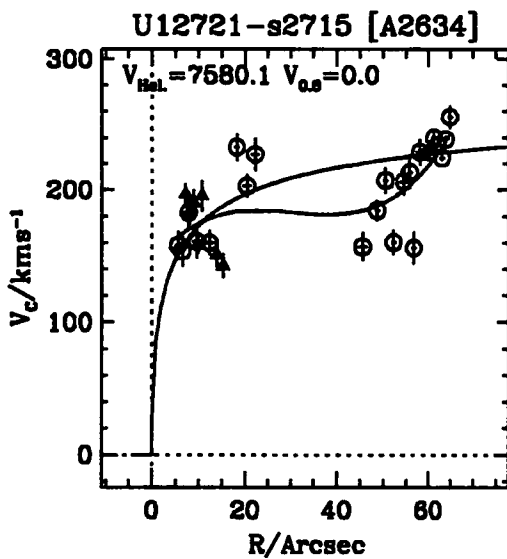
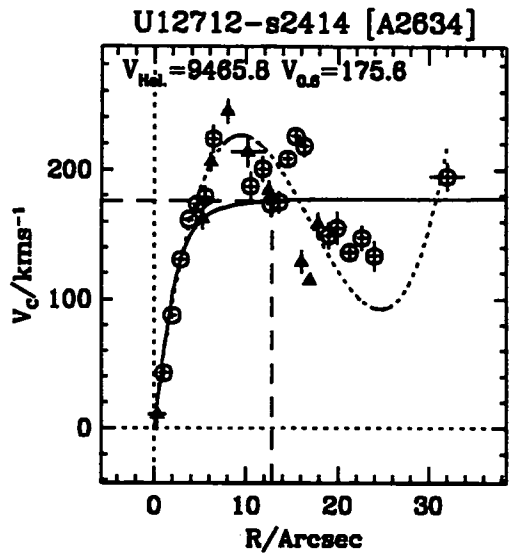
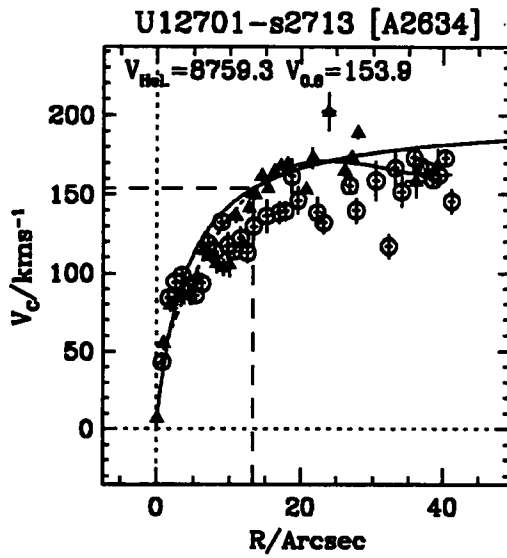
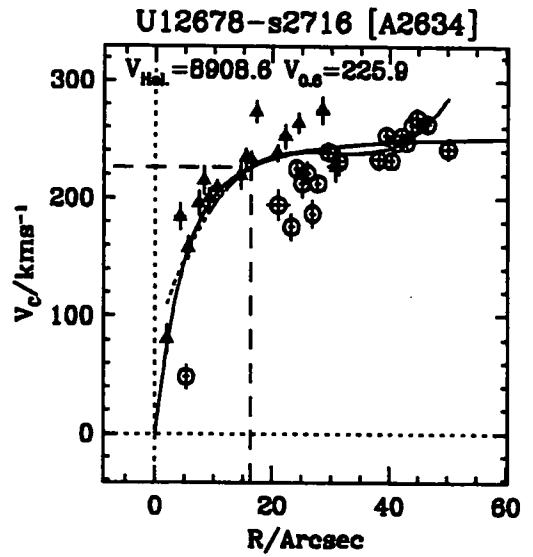
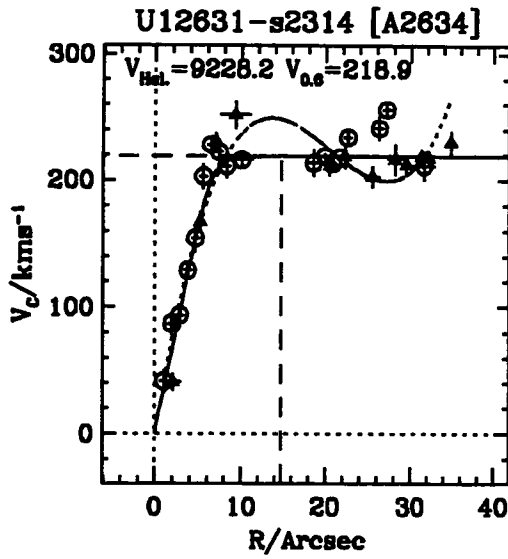


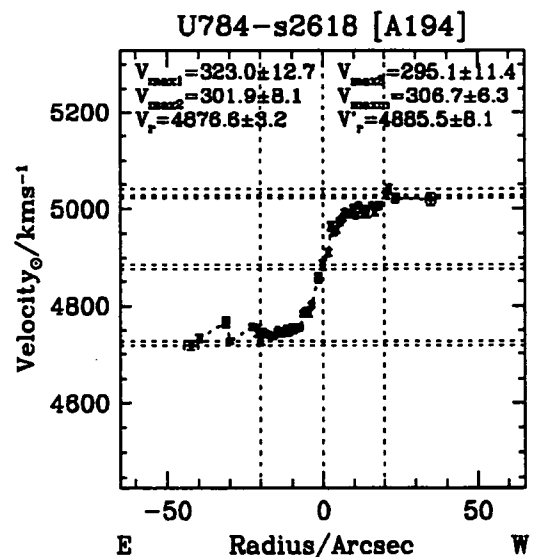
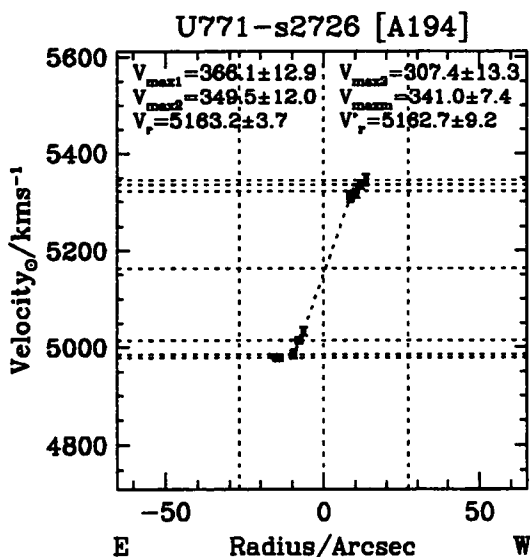
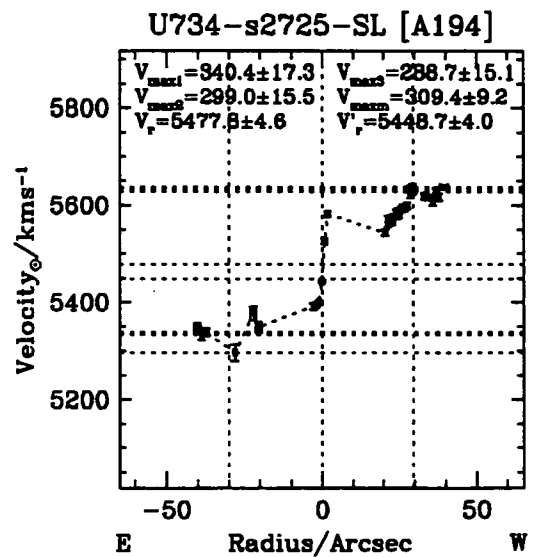
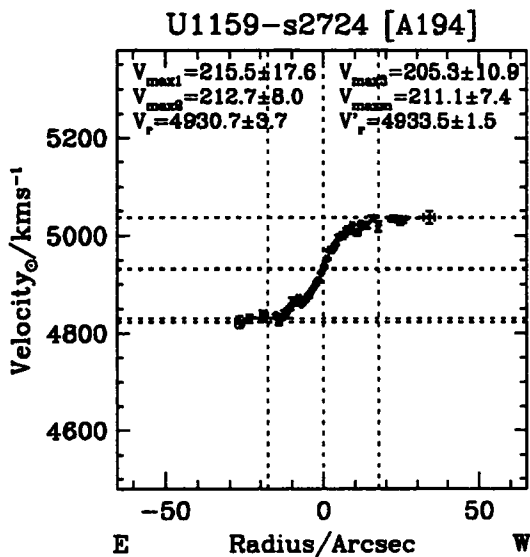
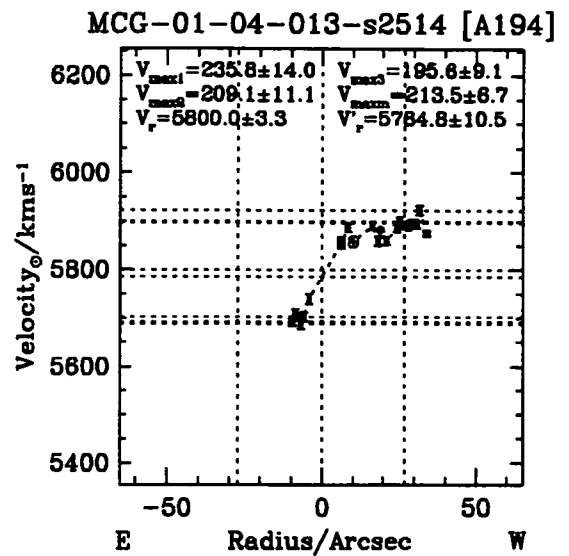
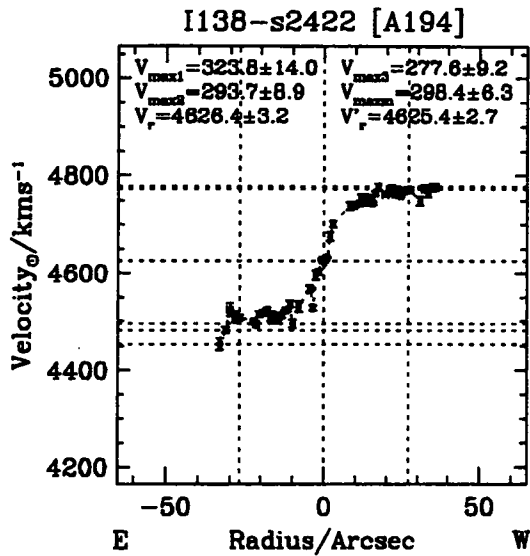


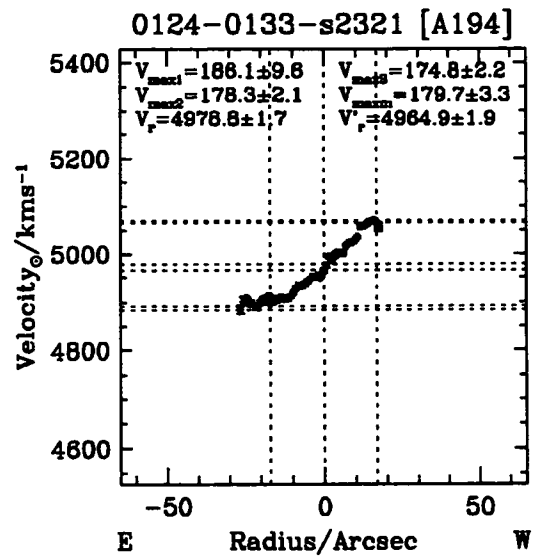
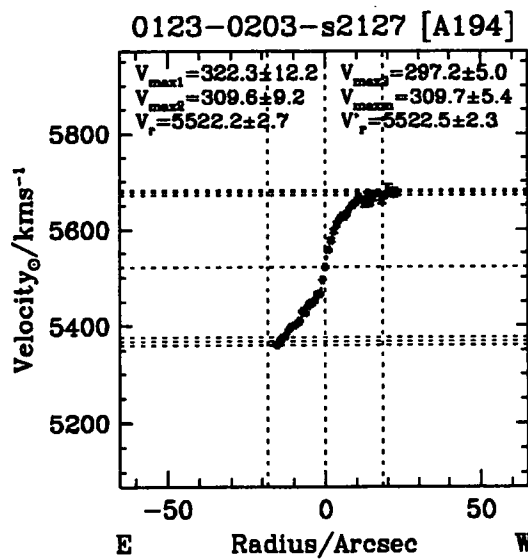
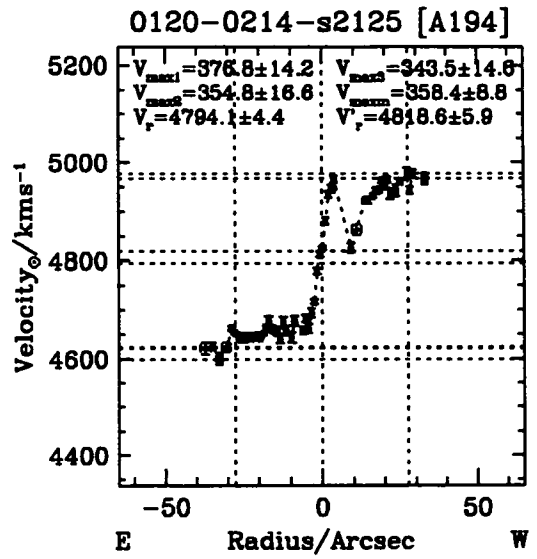
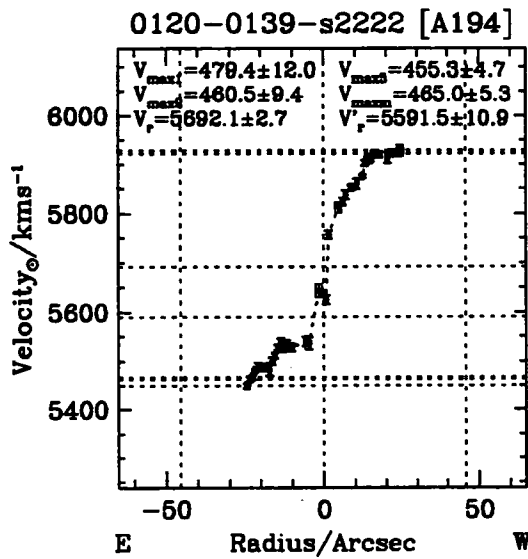
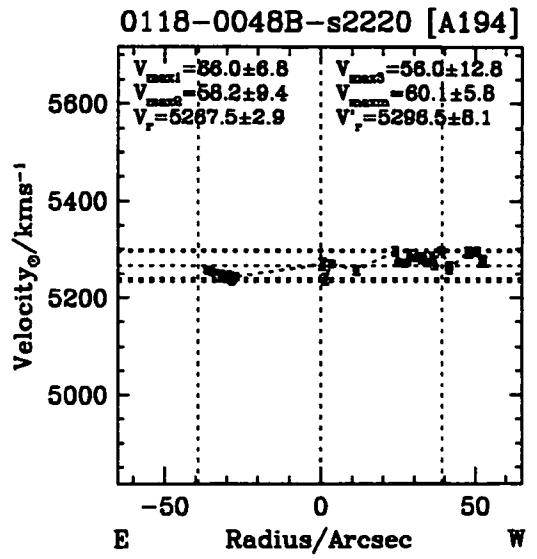
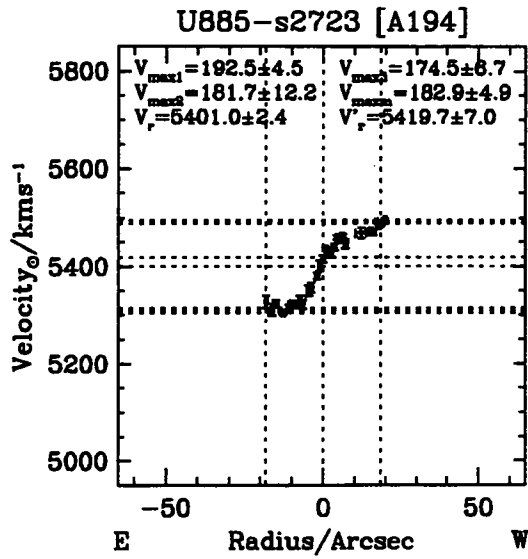


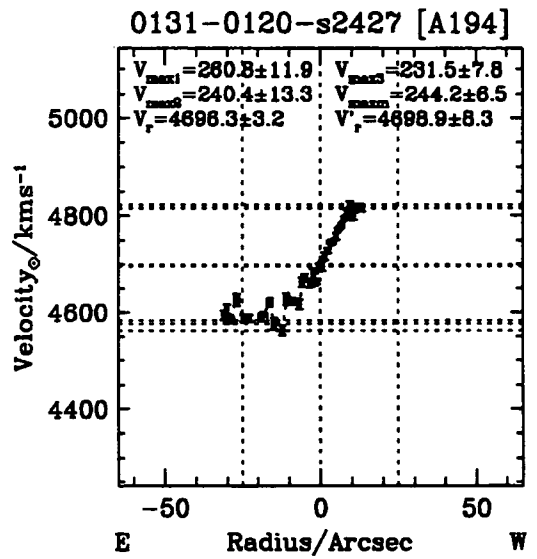
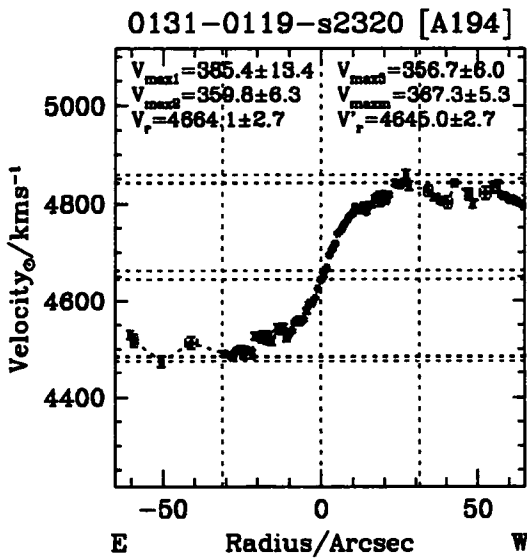
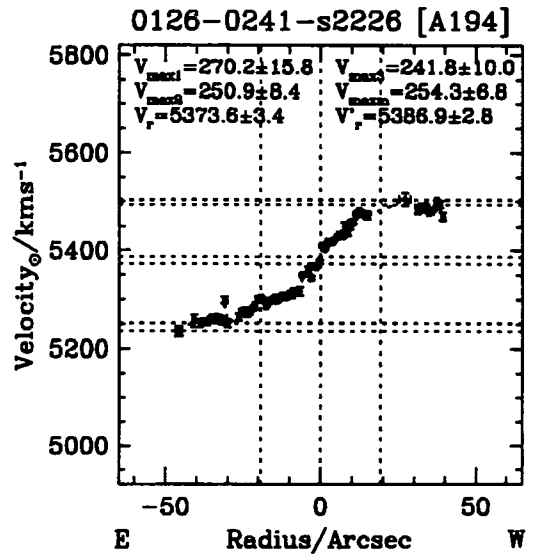
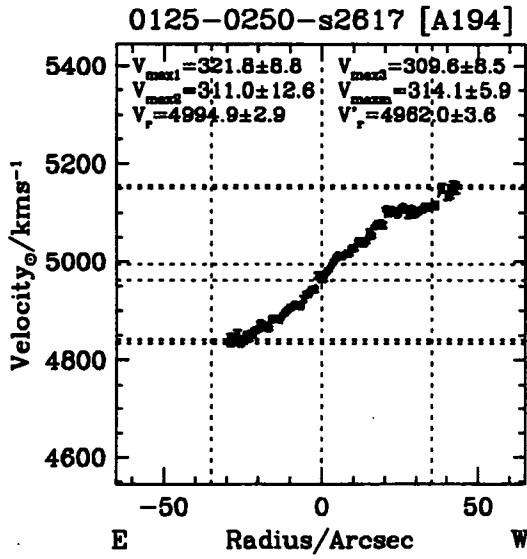




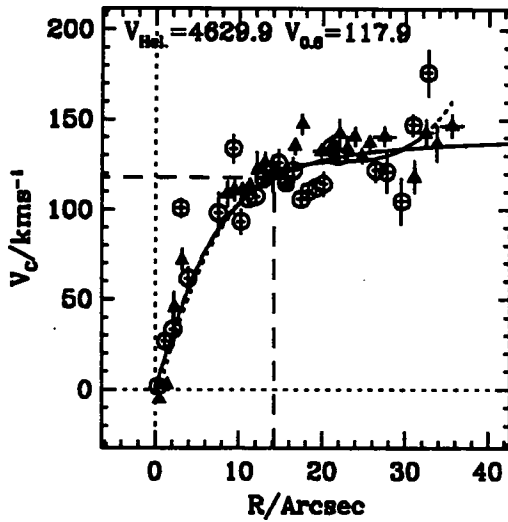




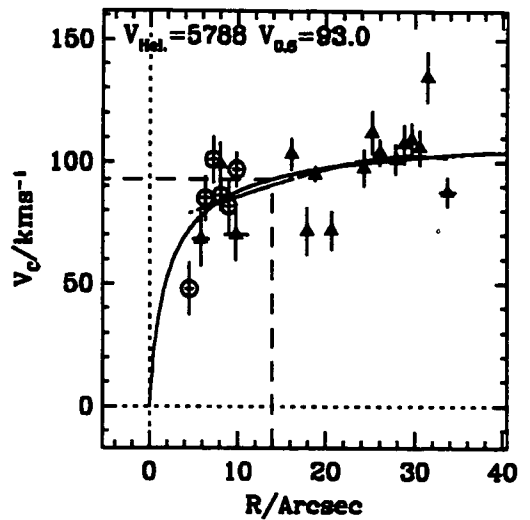




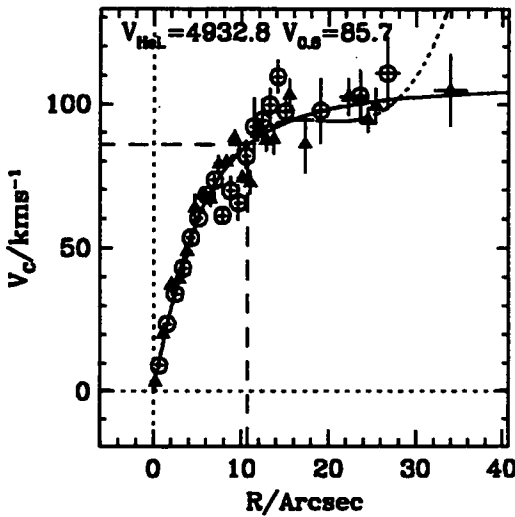
I138-s2422 [A194]



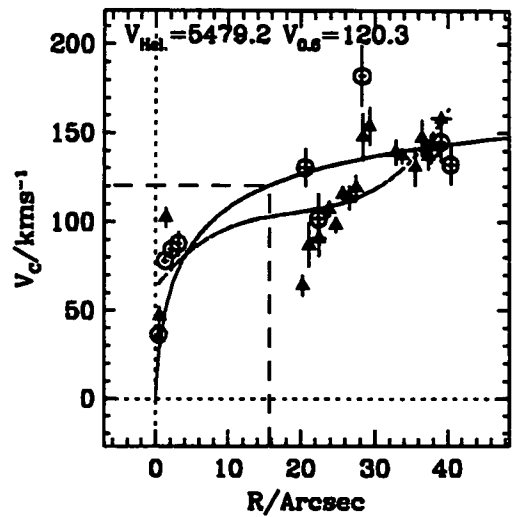
MCG-01-04-013-s2514 [A194]



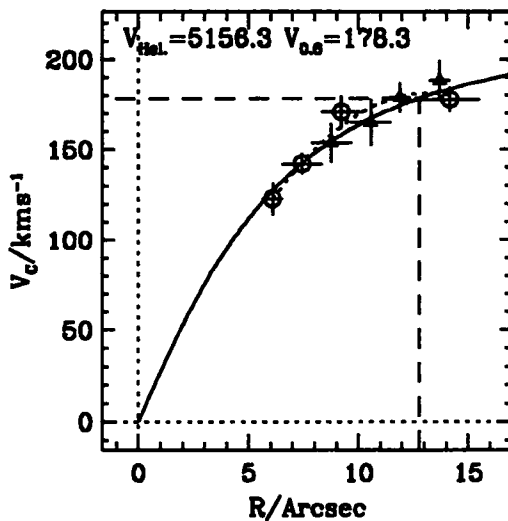
U1159-s2724 [A194]



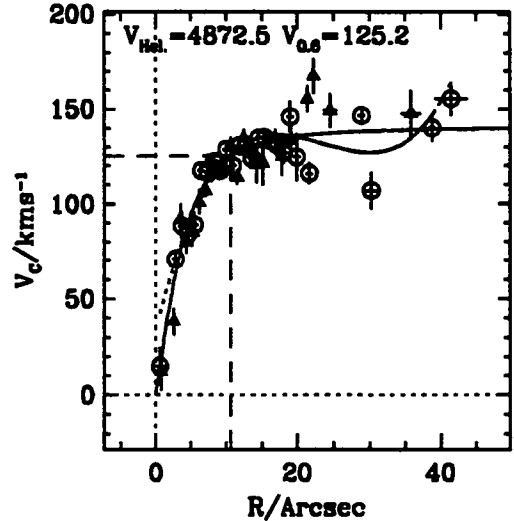
U734-s2725-SL [A194]

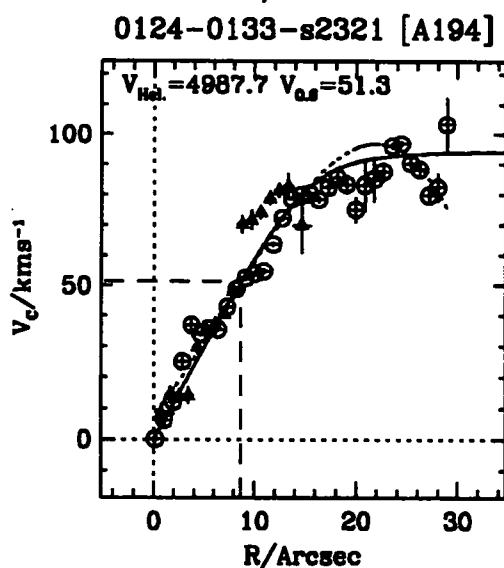
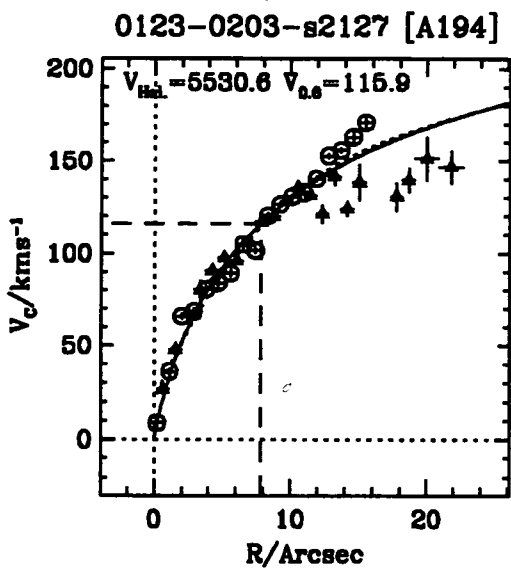
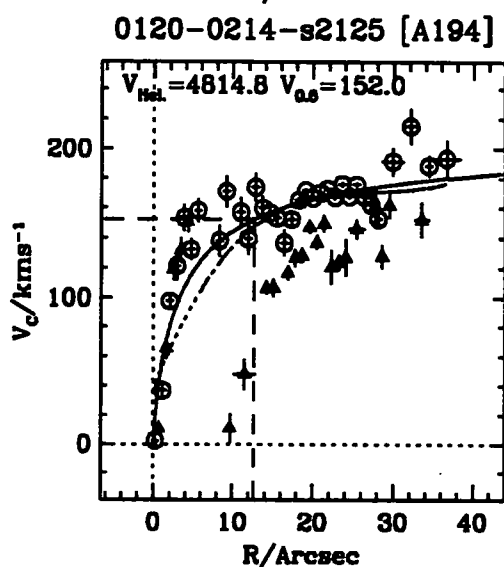
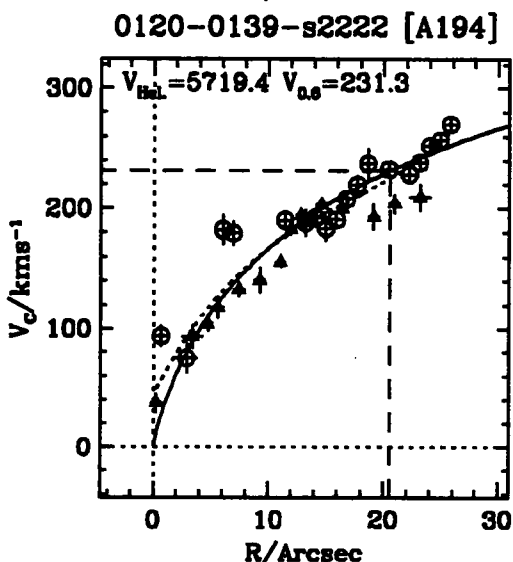
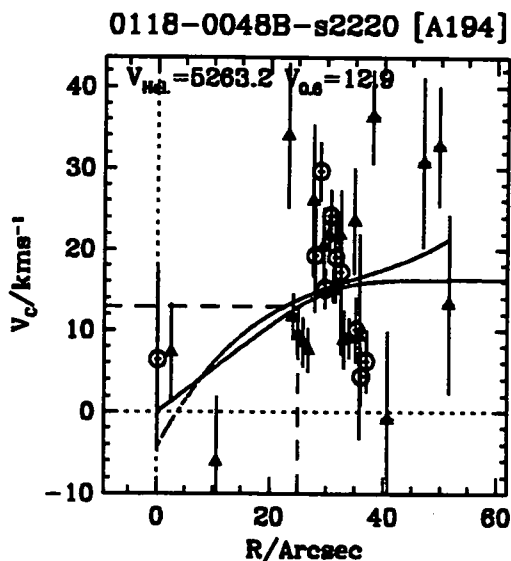
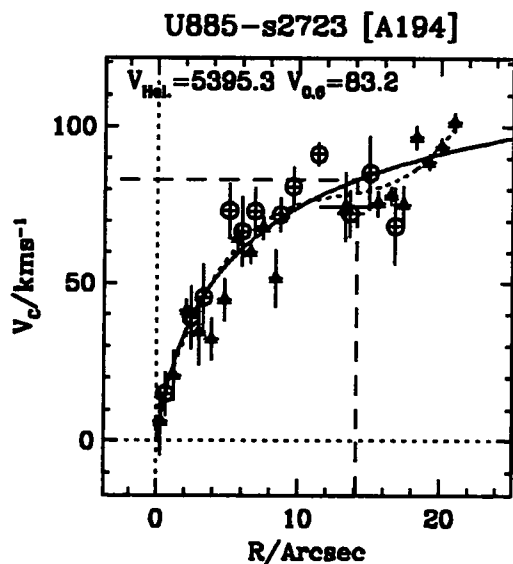


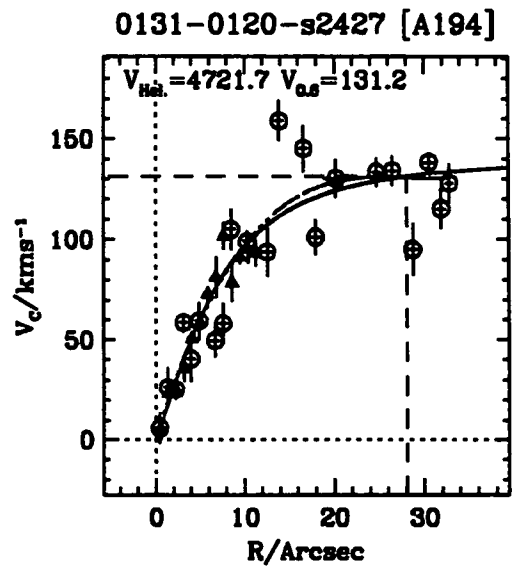
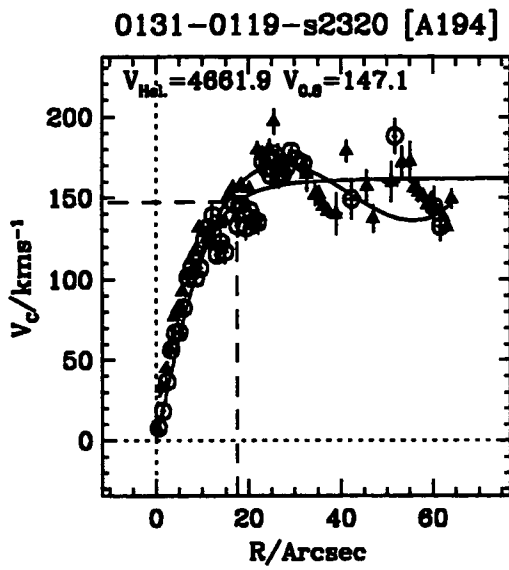
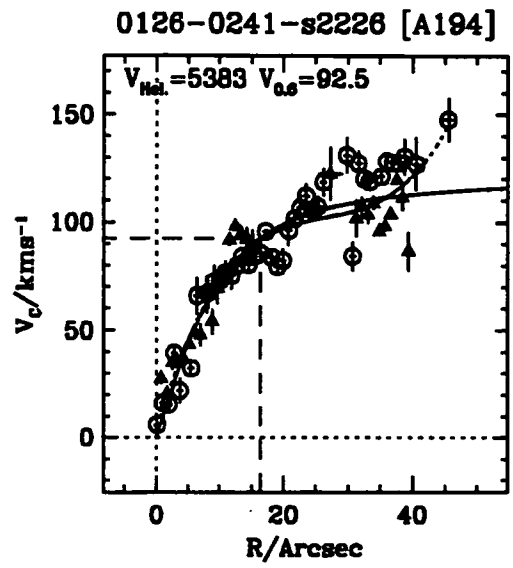
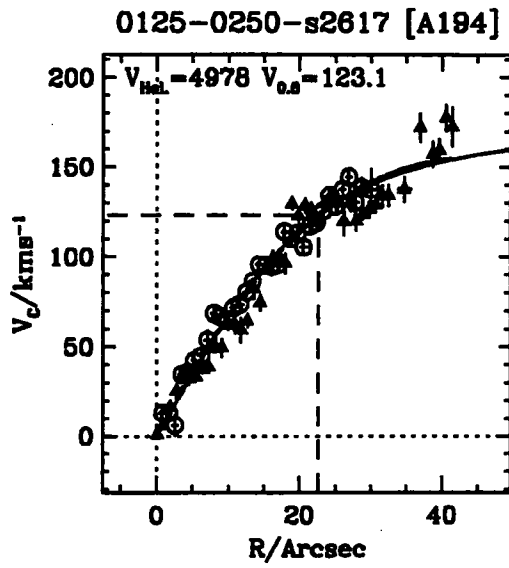
U771-s2726 [A194]



U784-s2618 [A194]







Appendix D

Final TF Sample

11.1 TF Sample Data Table

The tables that appear on the following pages list all the relevant data on the final TF sample for each cluster. Column headings are, in order; galaxy name, photometric quality code, Q_P , 22.5 mag arcsec⁻² isophotal magnitude, $I_{22.5}$, extrapolated total magnitude, $I_{T\alpha}$, ellipticity, e , major-axis position angle, PA, 23.5 mag arcsec⁻² isophotal radius in arcsec, $R_{23.5}$, optical radius in arcsec, R_{Opt} , Galactic extinction, A_{Gal} , heliocentric recessional velocity in kms⁻¹, V_{hel} , recessional velocity in local group frame, V_{lg} , velocity in CMB frame, V_{CMB} , interpolated rotation velocity at $0.6R_{Opt}$, $V_{0.6R_0}$, maximum rotation velocity, V_{max3} , maximum rotation velocity error, δV_{max3} , spectroscopic quality code, Q_S . The three parameters of the rotation curve fitting function, velocity at infinity, radius of turn-over in arcseconds and sharpness of turn-over, V_{inf} , R_0 and α respectively. The maximal extent in arcsecs of the rotation curve, $R_{H\alpha}$, the disk scale length in arcsecs, R_S and the disk central surface brightness, μ_0 . Notes are given in the last column.

The final table that appears in this appendix lists all the objects that were observed but rejected from the final TF sample. Column headings are the same, the final column indicates the main reason for rejection.

Table 11.1. Final Coma TF sample. See text §11.1 for full details.

Galaxy	Q _P	I _{22.5}	I _{Tot}	e	PA	R _{23.5}	R _{Opt}	Ab _{Gal}	V _{hel}	V _{lg}	V _{CMB}	V _{0.650}	V _{max3}	ΔV _{max3}	Q _S	V _{inf}	R ₀	α	R _{Hα}	R _S	μ ₀	Notes
1251+2827	1	14.87	14.44	0.575	35.1	18.74	27.62	0.018	7655.1	7909.6	7926.4	99.8	163.45	10.36	2	103.44	8.229	3.06	10.71	7.13	19.54	large fit extrap.
D38	1	14.31	14.19	0.730	49.9	24.65	17.40	0.012	5145.7	5399.4	5414.9	144.3	210.00	7.38	2	155.23	9.945	7.30	8.63	4.76	18.08	
I4040	1	14.09	13.97	0.567	146.9	24.32	16.41	0.022	7835.2	8089.5	8102.7	146.6	292.00	3.02	1	153.69	4.930	2.82	11.49	3.83	18.05	
N4585	1	13.36	13.20	0.442	112.1	28.09	20.60	0.032	7270.3	7525.5	7547.6	125.2	295.07	8.29	1	142.20	10.945	3.82	32.37	7.72	18.88	
U8017	1	12.78	12.72	0.662	29.3	36.52	20.70	0.018	7066.3	7321.0	7337.5	212.2	503.45	16.27	1	294.20	8.934	1.47	30.04	4.98	16.35	
U8140	1	12.97	12.76	0.701	85.6	44.56	36.50	0.004	7093.4	7348.8	7356.9	224.6	468.24	11.06	1	224.62	7.573	6.78	45.63	13.03	19.26	
U8220	1	12.89	12.76	0.757	138.8	48.76	31.75	0.014	7117.8	7367.6	7390.8	228.4	533.29	11.10	1	264.91	10.933	1.96	57.42	10.25	18.34	
Z130-8	1	13.56	13.49	0.292	145.2	18.87	12.27	0.006	7257.5	7508.3	7529.8	82.8	201.45	2.76	1	202.30	6.199	0.71	13.99	3.46	17.40	
Z159-75	1	13.20	13.14	0.455	23.2	22.29	11.28	0.020	6600.8	6854.3	6878.3	154.0	358.37	3.67	1	282.87	3.050	0.73	23.90	3.56	17.23	
Z159-106	1	14.26	14.12	0.568	175.1	21.02	16.58	0.014	7971.5	8226.8	8240.0	119.3	270.01	10.21	1	155.69	5.636	1.40	20.27	4.86	18.52	
Z159-117	2	14.59	14.38	0.587	153.6	20.34	16.99	0.026	6316.9	6573.2	6579.3	97.7	237.64	7.93	2	253.59	7.778	0.64	19.47	5.27	18.88	
Z160-58	1	13.81	13.55	0.728	83.5	36.79	29.85	0.022	7593.9	7849.0	7860.8	134.0	295.41	15.17	1	158.21	9.484	1.73	33.45	10.03	19.19	
Z160-67	1	14.55	14.42	0.335	19.4	13.88	9.27	0.008	7647.4	7900.5	7919.2	68.3	153.90	5.58	1	132.53	2.528	0.69	12.39	3.48	18.54	
Z160-127	1	14.99	14.66	0.313	82.4	17.63	14.73	0.008	5559.5	5812.8	5827.1	61.4	153.62	13.23	1	73.04	5.625	1.98	26.76	4.97	19.84	

Table 11.2. Final Abell 2199 TF sample. See text §11.1 for full details.

Galaxy	Q _p	I _{22.5}	I _{Tot}	e	PA	R _{23.5}	R _{Opt}	Ab _{Gal}	V _{hel}	V _{Ig}	V _{CMB}	V _{0.6R₀}	V _{max3}	δV _{max3}	Q _S	V _{inf}	R ₀	α	R _{Hα}	R _S	μ ₀	Notes
1622+4014	1	15.04	14.83	0.426	83.4	16.01	13.27	0.000	9410.5	9673.6	9441.2	88.0	207.79	11.14	1	134.38	2.725	0.82	17.42	4.82	19.68	
1623+3931	1	17.06	16.46	0.395	135.6	9.08	10.33	0.000	10836.6	11099.3	10867.0	42.2	101.20	11.06	2	88.86	8.341	1.19	8.46	3.67	20.63	
1623+3923	1	16.13	15.90	0.656	21.4	12.36	9.96	0.000	8885.0	9147.6	8915.5	83.6	167.24	7.58	2	189.03	9.714	1.31	8.78	3.12	19.19	
1624+3955	2	15.62	15.29	0.614	10.1	15.66	14.58	0.000	9407.4	9670.3	9436.6	95.9	180.74	12.80	2	199.28	1.986	0.52	13.02	5.06	20.07	
1625+3855	1	15.41	15.19	0.519	100.0	8.76	6.74	0.002	9940.3	10202.6	9969.8	54.3	184.70	10.97	2	173.69	11.577	1.57	9.24	3.57	19.15	
1625+3909	1	14.46	14.28	0.289	56.6	17.87	12.08	0.000	10707.3	10969.7	10736.0	125.1	278.80	10.33	1	146.13	1.467	1.07	21.84	3.63	18.79	
1625+4017	1	15.41	15.21	0.364	161.5	12.53	9.71	0.000	8702.1	8965.3	8729.5	74.4	170.41	5.21	1	105.92	1.904	0.89	12.43	2.97	18.96	
1626+3900	2	16.17	15.85	0.581	161.9	13.16	10.78	0.000	9700.5	9962.9	9728.7	63.7	176.99	12.49	2	88.90	8.945	8.00	12.43	3.48	19.48	
1626+3958	1	17.25	16.42	0.301	4.7	10.38	10.32	0.000	8765.7	9028.7	8792.7	44.5	160.46	11.00	2	80.95	11.250	8.00	16.79	3.55	20.87	
1626+4016	1	16.06	15.91	0.668	30.9	9.26	7.23	0.000	8830.1	9093.2	8856.3	59.0	150.11	6.97	1	132.73	2.572	0.66	11.69	2.39	18.51	
BO37	1	14.62	14.43	0.604	158.1	17.23	15.31	0.000	9248.3	9511.3	9276.0	123.2	291.06	3.91	1	179.23	4.752	1.07	23.19	5.02	18.88	
BO43	1	15.46	15.13	0.687	149.9	22.05	18.92	0.000	10404.6	10667.2	10432.2	51.9	175.30	11.64	2	112.97	24.547	4.65	21.93	5.24	19.64	
BO63	1	12.75	12.57	0.232	81.7	35.16	23.74	0.000	10422.6	10685.3	10449.9	140.1	223.90	13.73	2	224.04	5.009	0.78	10.93	9.14	19.57	
RB36	1	15.57	15.30	0.492	144.6	13.83	12.19	0.002	8445.8	8708.2	8474.2	81.3	198.24	12.60	1	151.91	8.029	1.20	17.73	4.11	19.65	
U10244	1	13.43	13.35	0.763	124.9	32.86	20.60	0.006	9752.2	10017.0	9792.7	212.6	494.79	11.52	1	308.75	5.142	0.96	30.80	5.82	17.36	
U10366	1	12.78	12.66	0.639	163.1	48.08	32.14	0.000	10201.3	10462.6	10234.9	303.8	652.62	11.46	1	321.63	0.152	0.67	67.39	8.05	17.32	
U10420	1	13.45	13.30	0.770	124.5	27.72	22.37	0.002	9531.2	9796.1	9573.3	118.5	281.24	17.01	2	138.88	3.785	1.22	59.70	6.57	17.76	
U10428	1	12.72	12.41	0.418	18.0	46.51	43.64	0.004	9309.6	9569.5	9339.1	181.1	385.22	10.56	2	182.79	18.965	8.00	62.99	6.51	15.74	
U10429	1	13.69	13.57	0.210	119.2	20.22	11.19	0.000	7397.9	7660.8	7421.1	134.8	294.80	6.29	2	188.80	1.491	0.79	25.75	3.01	17.79	
U10468	1	13.64	13.49	0.813	172.9	35.72	26.35	0.000	9218.3	9484.2	9228.7	207.0	495.93	11.93	1	207.04	7.216	8.00	32.59	7.00	17.74	
U10550	1	14.21	13.90	0.604	31.7	28.97	24.90	0.018	9058.8	9321.9	9059.8	125.1	325.41	10.03	1	186.24	5.571	0.88	46.19	8.96	19.95	
Z224-41	1	13.68	13.29	0.414	142.1	27.12	40.72	0.000	7737.2	8000.3	7762.3	140.5	258.02	10.16	1	167.89	2.675	0.83	30.76	11.55	19.75	v. nearby star
Z224-55	2	12.99	12.89	0.618	155.1	34.66	21.18	0.000	9232.9	9495.7	9256.5	282.4	553.54	13.33	2	312.63	2.069	1.15	21.13	7.25	18.27	

Table 11.3. Final Abell 2634 TF sample. See text §11.1 for full details.

Galaxy	QP	I _{22.5}	I _{Tot}	e	PA	R _{23.5}	R _{Opt}	Ab _{Gal}	V _{hel}	V _{lg}	V _{CMB}	V _{0.6R_o}	V _{max3}	ΔV _{max3}	Q _S	V _{inf}	R ₀	α	R _{Hα}	R _S	μ ₀	Notes
BU200	1	17.38	16.96	0.580	133.8	5.74	8.30	0.085	9202.3	9455.9	8856.4	52.4	141.88	5.06	2	177.87	8.379	0.74	9.74	2.49	19.99	
BU91	1	15.11	14.97	0.585	178.8	11.95	9.65	0.065	11577.5	11831.1	11232.3	111.9	278.70	7.29	2	343.41	0.832	0.36	12.09	3.14	18.41	
D9	1	16.05	15.86	0.588	115.9	7.69	6.92	0.069	8143.1	8396.4	7797.3	69.8	191.31	10.59	1	109.23	3.844	1.43	29.49	2.92	19.76	
D11	1	17.50	16.80	0.531	14.3	6.22	9.45	0.069	11719.7	11973.0	11373.8	49.0	167.90	15.48	2	240.96	13.522	0.63	16.11	2.67	19.59	
D21	1	14.70	14.57	0.722	69.6	16.79	13.85	0.069	8779.7	9033.2	8433.9	125.7	293.80	13.93	1	161.05	4.833	1.49	20.10	4.07	17.99	
D39	1	15.97	15.76	0.759	142.8	11.18	10.78	0.069	7736.9	7990.5	7391.4	88.8	196.93	8.28	2	192.26	6.387	0.89	11.65	3.35	18.89	
D67	1	13.23	12.96	0.483	82.1	24.68	27.52	0.077	7645.7	7899.6	7300.8	180.4	403.58	8.39	1	188.62	0.360	0.85	47.71	11.51	19.99	
D123	1	15.07	14.90	0.638	172.9	14.07	13.56	0.087	9871.7	10125.9	9527.0	109.2	250.08	9.42	2	172.64	7.535	1.40	16.59	4.42	19.16	
D129	1	15.61	15.37	0.727	128.8	14.66	15.30	0.077	9907.6	10161.9	9563.2	102.0	224.02	15.51	1	128.41	4.702	1.42	16.18	4.26	19.00	
U12626	1	13.51	13.32	0.565	2.5	21.76	20.88	0.093	8049.9	8302.8	7702.1	226.4	473.80	4.48	1	227.24	5.629	4.96	25.25	12.74	21.08	
U12631	1	13.25	13.14	0.702	143.9	30.12	24.57	0.071	9228.2	9482.1	8882.1	218.9	463.38	8.84	1	218.96	6.560	8.00	32.90	6.69	17.60	
U12678	1	13.49	13.37	0.797	81.9	32.96	27.11	0.059	8908.6	9161.4	8561.4	225.9	526.13	9.80	1	254.65	6.223	1.61	47.17	7.18	17.57	
U12701	1	14.48	14.28	0.750	174.9	21.18	22.15	0.061	8759.3	9014.4	8415.9	153.9	341.27	5.94	1	198.71	3.965	1.01	40.32	6.00	18.67	

Table 11.4. Final Abell 194 TF sample. See text §11.1 for full details.

Galaxy	Q _p	I _{22.5}	I _{Tot}	e	PA	R _{23.5}	R _{Opt}	AbGal	V _{hel}	V _{ig}	V _{CMB}	V _{0.68σ}	V _{max3}	δV _{max3}	Q _S	V _{inf}	R ₀	α	R _{Hα}	R _S	μ ₀	Notes
0120-0139	1	12.23	12.10	0.707	104.2	45.54	34.27	0.032	5719.4	5456.3	5411.0	231.3	455.28	4.73	2	572.03	10.329	0.57	24.91	13.31	18.70	
0120-0214	2	13.15	13.07	0.623	160.4	27.46	21.05	0.039	4814.8	4556.1	4507.3	152.0	343.52	14.57	1	211.94	2.055	0.72	34.82	5.32	16.86	
0123-0203	1	13.92	13.85	0.675	140.6	18.28	13.00	0.039	5530.6	5270.7	5225.6	115.9	297.21	4.96	2	280.54	7.006	0.74	20.14	3.88	17.35	
0124-0133	1	14.13	13.99	0.468	139.3	16.83	14.54	0.014	4987.7	4723.5	4682.6	51.4	174.81	2.15	2	94.14	15.927	6.06	28.01	5.04	19.04	
0125-0250	1	13.76	13.50	0.814	58.0	35.02	37.75	0.024	4978.0	4722.3	4675.6	123.1	309.61	8.53	2	171.60	24.393	2.36	40.53	9.84	18.63	
0126-0241	2	14.88	14.39	0.589	60.1	19.18	27.23	0.034	5383.0	5126.3	5081.0	92.4	241.81	10.04	2	119.83	12.571	1.85	41.84	9.24	20.29	
0131-0119	1	13.06	12.87	0.708	134.4	31.21	29.06	0.028	4661.9	4395.2	4363.2	147.1	356.66	6.01	1	162.16	12.514	3.12	63.24	13.05	19.88	
I138	1	13.05	12.93	0.294	27.5	26.91	23.78	0.008	4629.9	4360.3	4329.8	117.9	277.56	9.23	1	139.88	9.190	2.02	34.03	6.53	18.17	
U784	1	13.70	13.60	0.505	45.2	19.93	17.63	0.053	4872.5	4613.2	4557.2	125.2	295.13	11.42	1	140.36	5.621	2.08	38.69	5.56	18.63	
U885	1	15.15	14.75	0.654	132.9	18.33	23.56	0.034	5395.3	5577.9	5082.3	83.2	174.47	6.66	1	139.26	3.944	0.68	20.06	6.43	19.26	
U1159	1	14.60	14.39	0.600	34.1	17.49	17.90	0.020	4932.8	4980.7	4636.5	85.7	205.29	10.86	1	107.07	6.852	1.71	28.69	5.47	19.03	

Table 11.5. Table of objects rejected from Final TF sample. See text §11.1 for full details.

Galaxy	Q _p	I _{2.5}	I _{tot}	e	PA	R _{23.5}	R _{opt}	Ab _{Gal}	V _{hel}	V _{lg}	V _{CMB}	V _{0.68σ}	V _{max3}	δV _{max3}	Q _s	V _{inf}	R ₀	α	R _{Hα}	R _s	μ ₀	Notes
Coma																						
1248+2912	1	13.54	13.41	0.320	111.0		0.016		6400.0	6655.2	6670.4	227.00	227.00		3	227.00						v. poor rc
1254+2722	1	13.75	13.63	0.610	146.9		0.000		7000.0	7253.0	7273.1	356.00	356.00		3	356.00						v. poor rc
1254+2924	1	16.10	15.41	0.592	177.5	13.20	19.46	0.018	9499.7	9755.1	9766.1	110.0	190.13	11.12	3	264.33	13.162	0.85	14.15	6.86	20.40	v. unsymmetric rc
1258+2750	1	14.26	14.15	0.750	54.1			0.012	5100.0	5353.7	5369.2	220.00	220.00		3	220.00						v. poor rc
D25	3	16.11	15.87	0.270	53.7	9.57	8.01	0.012	5611.6	5865.2	5881.0	46.2	96.69	3.84	2	57.39	4.479	2.78	8.54	2.38	19.33	No phot. z.p.
N4735	2	13.49	13.38	0.386	174.3	25.02	18.10	0.016	6447.3	6702.5	6717.7	52.7	161.58	3.11	3	127.37	26.247	8.00	20.23	3.11	18.19	v. poor rc
N4858	1	12.54	12.39	0.149	118.2	33.41	18.25	0.024	9450.8	9705.2	9719.1	67.0	104.37	4.81	3	75.30	7.549	2.69	10.09	6.31	18.72	v. poor rc/S07
TT33	1	15.55	15.34	0.304	132.6	19.30	8.19	0.008	7452.4	7705.7	7723.9	84.4	210.36	9.36	2	160.53	7.491	1.47	16.17	2.54	18.94	v. unsymmetric rc
TT5	1	14.73	14.45	0.270	59.8	17.78	13.25	0.034	8198.4	8452.7	8467.6	41.6	58.51	8.87	3	74.37	11.845	8.00	5.76	4.92	19.76	v. poor rc
U8025	1	12.63	12.51	0.778	68.6	52.36	33.94	0.014	6253.8	6509.5	6520.1	140.9	195.61	12.56	3	195.64	6.722	0.93	27.10	11.37	18.28	v. poor rc
U8160	1	13.21	13.14	0.770	103.0			0.024	6100.0	6354.3	6365.9	318.00	318.00		3	318.00						v. poor rc
U8161	1	13.39	13.26	0.444	130.0	28.58	19.86	0.000	6595.0	6847.3	6865.7	122.7	263.28	12.71	3	176.18	16.603	5.32	17.59	6.25	18.95	v. poor rc
U8194A	3	12.33	12.14	0.486	135.9	39.43	31.47	0.014	7007.3	7262.7	7267.7	186.3	386.19	5.71	3	186.28	7.024	8.00	28.81	12.38	18.98	Nearby Star
U8259	1	13.08	12.86	0.671	168.1	46.07	37.34	0.012	7374.9	7630.7	7630.4	232.8	121.37	7.89	3	268.37	6.144	1.26	6.22	12.42	19.26	v. poor rc
Z159-80	1	13.71	13.51	0.718	5.0	31.18	23.33	0.008	6895.5	7147.6	7175.8	111.7	235.50	9.89	2	196.31	4.773	0.69	20.07	8.24	18.64	face on
Z159-90	2	14.18	13.95	0.370	99.1	24.66	19.61	0.018	8310.7	8564.1	8586.4	33.4	85.96	9.10	3	37.90	10.348	3.78	20.00	5.93	19.20	v. poor rc
A2199																						
1623+3951	3	14.99	14.63	0.313	43.8	20.46	17.05	0.000	8817.1	9080.0	8847.4	82.6	222.36	13.20	2	202.43	1.963	0.44	37.28	4.13	19.73	No phot. z.p.
1623+4038	1	15.15	14.84	0.640	92.4	19.21	18.51	0.004	8674.1	8937.5	8703.0	95.0	247.74	12.65	3	150.37	17.513	8.00	24.14	6.14	19.59	v. poor rc
1624+3948	1	17.05	16.13	0.581	19.2	11.69	19.79	0.000	8642.0	8904.8	8670.8	99.4	147.71	10.52	3	103.75	10.618	8.00	14.08	6.29	21.12	v. poor rc
U10427	1	14.03	13.73	0.199	18.5	22.88	19.61	0.000	8848.9	9112.6	8870.7	49.8	108.74	7.06	3	51.97	10.494	8.00	30.25	8.88	20.58	face on
U10432	1	14.06	13.76	0.525	175.6	29.49	24.43	0.000	9688.3	9952.1	9709.5	94.0	176.65	17.33	3	253.70	19.715	0.83	42.65	7.75	19.59	v. poor rc

Table 11.6. Table of objects rejected from Final TF sample. See text §11.1 for full details.

Galaxy	Q _P	I _{22.5}	I _{tot}	e	PA	R _{23.5}	R _{Opt}	AbGal	V _{hel}	V _{lg}	V _{CMB}	V _{0.6R₀}	V _{max3}	δV _{max3}	Q _S	V _{inf}	R ₀	α	R _{Hα}	R _S	μ ₀	Notes	
A2634																							
BU108	1	15.63	15.31	0.757	104.0	14.56	16.94	0.083	8822.9	9077.1	8478.6	79.1	140.23	8.16	3	100.06	10.460	3.15	10.37	5.06	19.36	v. poor rc	
BU71	1	16.19	15.37	0.832	75.7	16.12	33.20	0.089	4499.3	4753.7	4155.5	48.8	25.79	3.39	3	49.02	12.834	8.00	5.93	9.41	20.64	Foreground	
D113	2	16.00	15.88	0.539	101.1	7.07	5.52	0.069	19503.9	19758.0	19158.8	164.3	344.40	10.18	3	439.22	9.439	1.80	5.93	1.82	18.32	Background	
D131	2	16.56	15.69	0.199	101.8	6.49	12.98	0.077	8688.6	8942.9	8344.1	32.2	97.95	11.51	3	112.58	6.259	0.51	20.69	6.42	21.43	v. poor rc	
D30	1	15.25	14.88	0.289	93.8	8.97	14.30	0.065	11035.2	11288.8	10690.0	39.8	89.70	9.03	3	69.72	6.363	0.99	11.42	5.92	20.79	v. poor rc	
D47	1	16.39	16.14	0.405	38.6	6.82	7.46	0.065	9483.4	9737.1	9138.3	71.5	142.98	7.60	3	165.16	5.016	0.89	7.13	2.47	19.52	v. poor rc	
U12712	1	13.09	12.88	0.201	141.7	22.16	21.44	0.036	9465.8	9717.8	9117.8	175.6	423.99	10.35	3	177.73	2.978	2.42	26.19	9.14	19.87	v. poor rc	
A194																							
0118-0048B	1	12.19	11.92	0.327	51.7	39.17	41.83	0.016	5263.2	4994.6	4952.7	12.9	56.05	12.78	3	16.31	31.022	8.00	49.42	17.87	20.07	v. poor rc	
0131-0120	3	14.13	13.70	0.741	113.1	25.02	46.83	0.032	4721.7	4455.3	4422.6	131.2	231.50	7.82	2	140.70	10.369	1.94	31.71	20.88	21.99	No phot. z.p.	
MCG-01-04-013	1	13.40	13.24	0.428	153.2	26.97	23.23	0.067	5788.0	5534.7	5472.5	93.0	195.60	9.09	3	114.10	1.680	0.81	31.88	5.22	16.42	v. poor rc	
U734	1	13.66	13.50	0.714	174.4	29.72	26.06	0.014	5479.2	5212.4	5159.8	120.3	288.70	15.07	3	198.67	1.395	0.51	39.53	7.00	17.88	v. poor rc	
U771	1	12.93	12.83	0.514	100.1	26.89	21.29	0.018	5156.3	4890.9	4839.2	178.3	307.36	13.33	3	218.75	7.891	1.75	13.25	7.27	18.52	v. poor rc	

References

References

- Aaronson M., Bothun G., Mould J., Huchra J., Schommer R. A., Cornell M. E., 1986, *ApJ*, 302, 536
- Aaronson M., Huchra J., Mould J., Schechter P. L., Tully R. B., 1982, *ApJ*, 258, 64
- Aaronson M., Mould J., Huchra J., 1979, *ApJ*, 229, 1
- Abell G. O., 1958, *ApJS*, 3, 211
- Abell G. O., Corwin H. G., Olowin R., 1989, *ApJS*, 70, 1
- Argyle R. W., 1988, ING User Manual No. XVIII, RGO, Cambridge UK
- Ashman K. M., Salucci P., Persic M., 1993, *MNRAS*, 260, 610
- Bernstein G., Guhathakurta P., Raychaudhury S., Giovanelli R., Haynes M. P., Herter T., Vogt N. P., 1994, *AJ*, 107, 1962
- Bothun G., 1986, in *Galaxy Distances and Deviations from Universal Expansion*, ed. B. F. Madore and R. B. Tully (Dordrecht: Reidel), Vol. symp. p. 87
- Bothun G. D., Aaronson M., Schommer R. A., Mould J. R., Huchra J., Sullivan W. T., 1985a, *ApJS*, 57, 423
- Bothun G. D., Mould J. R., 1987, *ApJ*, 313, 629
- Bothun G. D., Mould J. R., Schommer R. A., Aaronson M., 1985b, *ApJ*, 291, 586
- Bottinelli L., Chamaroux P., Gerard E., Gougenheim L., Heidman J., Kazes I., Lauque R., 1971, *A&A*, 12, 264
- Bottinelli L., Gougenheim L., Fouque P., Paturel G., Teerikorpi P., 1987, *A&A*, 181, 1
- Bottinelli L., Gougenheim L., Paturel G., G. De Vaucouleurs, 1983, *A&A*, 118, 4
- Burstein D., Davies R. L., Dressler A., Faber S. M., Lynden-Bell D., 1986, in *Galaxy Distances and Deviations from Universal Expansion*, ed. B. F. Madore and R. B. Tully (Dordrecht: Reidel), Vol. symp. p. 123
- Burstein D., Heiles C., 1978, *ApJ*, 225, 40
- Butcher H., Oemler A., 1984, *ApJ*, 285, 426
- Butchins S. A., 1983, Ph.D. thesis, The University of Oxford, Oxford, U.K.
- Byun Y. I., Freeman K. C., 1995, *ApJ*, 448, 563
- Chapman G. N. F., Geller M. J., Huchra J. P., 1988, *AJ*, 95, 999
- Chiba M., Yoshi Y., 1995, *ApJ*, 442, 82
- Cole S., Aragon-Salamanca A., Frenk C. S., Navarro J. F., Zepf S. E., 1994, *MNRAS*, 271, 781
- Courteau S., 1992, Ph.D. thesis, University of California, Santa Cruz
- Courteau S., Faber S. M., Dressler A., Willick J. A., 1993, *ApJL*, 412, L51
- Cousins A. W. J., 1976, *MNRAS*, 81, 25
- David L. P., Slyz A., Jones C., Forman W., Vrtilik S. D., 1993, *ApJ*, 412, 479
- de Jong R. S., 1995, Ph.D. thesis, Kapteyn Laboratory, Groningen, The Netherlands.
- de Vaucouleurs G., 1948, *Ann. d'Astrophys.*, 11, 247
- de Vaucouleurs G., 1959, *ApJ*, 130, 728
- de Vaucouleurs G., de Vaucouleurs A., Corwin H., 1976, *Second reference catalogue of bright galaxies*
- Dekel A., Rees M. J., 1994, *ApJL*, 422, L1
- Dekel A., Silk J., 1986, *ApJ*, 303, 39
- Disney M., Davies J., Philipps S., 1989, *MNRAS*, 239, 939
- Dixon K. L., Godwin J. G., Peach J. V., 1989, *MNRAS*, 239, 459
- Djorgovski S., De Carvalho R., Han M. S., 1988, in *The extragalactic distance scale; Proceedings of the ASP 100th Anniversary Symposium, Victoria, Canada, June 29-July 1, 1988 (A90-14129 03-90)*. San Francisco, CA, Astronomical Society of the Pacific, 1988, p. 329-341, Vol. symp. p. 329
- Draper P. W., 1993, CCDPACK data reduction package, Starlink User Note 139.0, CCLRC / RAL
- Dressler A., 1980, *ApJS*, 42, 565
- Dressler A., Faber S., 1990, *ApJ Lett.*, 354, L45
- Eisenstein D. J., Loeb A., 1996, *ApJ*, 459, 432
- Freudling W., Da Costa L. N., Wegner G., Giovanelli R., Haynes M. P., Salzer J. J., 1995, *AJ*, 110, 920
- Freudling W., Martel H., Haynes M. P., 1991, *ApJ*, 377, 349
- Fukugita M., 1991, *ApJ*, 376, 8
- Giovanelli R., Haynes M. P., Salzer J. J., Wegner G., da Costa L. N., Freudling W., 1994, *AJ*, 107, 2036
- Godwin J. G., Metcalfe N., Peach J. V., 1983, *MNRAS*, 202, 113 (GMP83)

- Gregory S. A., Thompson L. A., 1984, *ApJ*, 286, 422
- Han M. S., 1991, Ph.D. thesis, California Institute of Technology, Pasadena, California.
- Han M. S., Mould J. R., 1992, *ApJ*, 396, 453
- Helou G., Madore B., Schmitz M., Bica M., Wu X., Bennett J., 1991, *The NASA/IPAC Extragalactic Database, Databases and On-Line Data in Astronomy*, ed. D. Egret & M. Albrecht (Dordrecht: Kluwer)
- Hendry M. A., Simmons J. F. L., 1994, *ApJ*, 435, 515
- Holmberg E. B., 1958, *Lund Medd. Astron. Obs. Ser. II*, 136, 1
- Holmberg E. B., Lauberts A., Schuster H. E., West R. M., 1975, *A&AS*, 22, 327
- Hudson M. J., 1994, *MNRAS*, 266, 468
- Jacoby G. H. et al., 1992, *PASP*, 104, 599
- Jedrzejewski R. I., 1987, *MNRAS*, 226, 747
- Jones C., Forman W., 1984, *ApJ*, 276, 38
- Jorgensen I., Franx M., Kjaergaard P., 1996, *MNRAS*, 280, 167
- Kent S. M., Gunn J. E., 1982, *AJ*, 87, 945
- Knapen J. H., van der Kruit P. C., 1991, *A&A*, 248, 57
- Landolt A. U., 1983, *AJ*, 88, 439
- Lucey J. R., Gray P. M., Carter D., Terlevich R., 1991a, *MNRAS*, 248, 804
- Lucey J. R., Guzman R., Carter D., Terlevich R., 1991b, *MNRAS*, 253, 584
- Lucey J. R., Steel R. G. J., Carter D., 1996, *MNRAS*, -, Preprint
- Lupton R. H., Monger P., 1994, SM 2.3.8, Starlink MUD, CCLRC / RAL
- Lynden-Bell D., D. S. M. F., Burstein, Davies R. L., Dressler A., Terlevich R. J., Wegner G., 1988, *ApJ*, 302, 536
- Maddox S. J., Loveday J., Sutherland W. J., Efstathiou G., 1988, in *Large-scale structures in the universe - Observational and analytical methods*. Springer-Verlag, p. 90
- Mathewson D. S., Ford V. L., Buchhorn M., 1992a, *ApJ Lett.*, 389, L5
- Mathewson D. S., Ford V. L., Buchhorn M., 1992b, *ApJS*, 81, 413
- Mazure A., Proust D., Mathez G., Mellier Y., 1988, *A&AS*, 76, 339
- McGaugh S. S., 1996, *MNRAS*, 280, 337
- McLeod B. A., 1993, *AJ*, 88, 439
- Meyerdiercks H., 1995, FIGARO, A general data reduction system, Starlink User Note 86.10, CCLRC / RAL
- Mould J. R., Akeson R. L., Bothun G. D., Han M., Huchra J. P., Roth J., Schommer R. A., 1993, *ApJ*, 409, 14
- Navarro J. F., Frenk C. S., White S. D. M., 1996, *ApJ*, 462, 563
- Nilson P., 1973, *Uppsala general catalogue of galaxies*
- Oepik E., 1922, *ApJ*, 55, 406
- Peletier R. F., Willner S. P., 1993, *ApJ*, 418, 626
- Persic M., Salucci P., Stel F., 1996, *MNRAS*, 281, 27
- Pierce M. J., Tully R. B., 1988, *ApJ*, 330, 579
- Pierce M. J., Tully R. B., 1992, *ApJ*, 387, 47
- Pinkney J., Ree G., Burns J., 1993, *ApJ*, 416, 36
- Rhee M.-H., 1996, Ph.D. thesis, Kapteyn Laboratorium, Groningen, The Netherlands.
- Roberts M. S., 1962, *AJ*, 67, 431
- Salucci P., Frenk C. S., Persic M., 1992, *MNRAS*, 262, 392
- Sandage A., Tammann G. A., 1976, *ApJ*, 210, 7
- Sandage A., Tammann G. A., 1981, *A revised shapley-ames catalogue of bright galaxies*
- Sandage A., Tammann G. A., Federspiel M., 1995, *ApJ*, 452, 1
- Schlegel D. J., 1995, Ph.D. thesis, University of California, Berkeley
- Schommer R. A., Bothun G. D., 1987, *AJ*, 92, 60
- Schommer R. A., Bothun G. D., Williams T. B., Mould J. R., 1993, *AJ*, 105, 97
- Scodreggio M., Solanes J. M., Giovanelli R., Haynes M. P., 1995, *ApJ*, 444, 91
- Silk J., 1995, *ApJ*, 438, L41
- Sofue Y., 1994, *PASJ*, 46, 173
- Strauss M. A., Willick J. A., 1995, *Physrep*, 261, 271
- Struble M. F., Rood H. J., 1987, *ApJS*, 63, 555
- Struble M. F., Rood H. J., 1991, *ApJS*, 77, 363
- Szomoru A., Guhathakurta P., Van Gorkom J. H., Knapen J. H., Weinberg D. H., Fruchter A. S., 1994, *AJ*, 108, 491
- Tully R. B., Fisher J. R., 1977, *A&A*, 54, 661
- Tully R. B., Fouque P., 1985, *ApJS*, 58, 67
- Valentijn E. A., 1990, *Nat*, 346, 153
- Van Den Bergh S., 1981, *ApJL*, 248, L9
- van Haarlem M. P., 1992, Ph.D. thesis, Leiden, Sterrewacht, Postbus 9513, Leiden, 2300RA, Netherlands.
- van Haarlem M. P., Cayon L., Gutierrez De La Cruz C., Martinez-Gonzalez E., 1993, *MNRAS*, 264, 71
- Vogt N. P., C. D. A. F. A., Phillips, Gronwall C., Faber S. M., Illingworth G. D., Koo D. C., 1996, *ApJL*, 465, L15
- White R. A., 1978, *ApJ*, 226, 591
- Wilkins T. N., 1994, TWODSPEC, Some Additions to Figaro, Starlink User Note 16.4, CCLRC / RAL
- Willick J. A., 1991, Ph.D. thesis, University of California, Berkeley
- Willick J. A., 1994, *ApJS*, 92, 1

- Willick J. A., Courteau S., Faber S. M., Burstein D.,
Dekel A., 1995, *ApJ*, 446, 12
- Willick J. A., Courteau S., Faber S. M., Burstein D.,
Dekel A., Kolatt T., 1996, *ApJ*, 457, 460
- Zwaan M. A., Van Der Hulst J. M., De Blok W. J. G.,
McGaugh S. S., 1995, *MNRAS*, 273, L35
- Zwicky F., Herzog E., Wild P., 1960, *Catalogue of galaxies
and of clusters of galaxies*

